Food Engineering Series
Series Editor: Gustavo V. Barbosa-Cánovas

Nesli Sozer *Editor*

Imaging Technologies and Data Processing for Food Engineers

Springer

Food Engineering Series

Springer's *Food Engineering Series* is essential to the Food Engineering profession, providing exceptional texts in areas that are necessary for the understanding and development of this constantly evolving discipline. The titles are primarily reference- oriented, targeted to a wide audience including food, mechanical, chemical, and electrical engineers, as well as food scientists and technologists working in the food industry, academia, regulatory industry, or in the design of food manufacturing plants or specialized equipment.

More information about this series at http://www.springer.com/series/5996

Nesli Sozer
Editor

Imaging Technologies and Data Processing for Food Engineers

Springer

Editor
Nesli Sozer
VTT Technical Research Centre of Finland
Espoo
Finland

ISSN 1571-0297
Food Engineering Series
ISBN 978-3-319-24733-5 ISBN 978-3-319-24735-9 (eBook)
DOI 10.1007/978-3-319-24735-9

Library of Congress Control Number: 2015958075

Springer Cham Heidelberg New York Dordrecht London

Printed on acid-free paper

Springer International Publishing AG Switzerland is part of Springer Science+Business Media (www.springer.com)

Preface

This book includes various perspectives on applicability of imaging technologies and data-processing tools for food structure analysis. Recent studies from worldwide peers are presented to provide an in-depth understanding on raw material characterization, process control, structure–function and structure–texture relationships by utilizing imaging and data analysis tool boxes. The book covers wide range of food matrices and also introduces applications from innovative and emerging areas of food science with an insight into future trends.

The information in this book is of interest to food scientists and engineers working in both academia and food industries. It can also be used as a textbook for food science and engineering students. There are eleven chapters in the book; Chaps. 1 and 2 introduce microstructural analysis of cereal grains and provide examples of chemometric analysis, Chaps. 3 and 4 focus on emulsions and gels, Chaps. 5–7 discuss the process–structure–texture relationship in various cereal-based food matrices and Chaps. 8–11 are dedicated to protein films, fruits and vegetables, and chocolates and nuts.

The editor acknowledges all the authors for their effort and expertise which enabled the publication of this book.

Espoo, Finland — Nesli Sozer

Contents

Contributors

Syed Ariful Alam University of Helsinki, Helsinki, Finland

VTT Technical Research Centre of Finland, Espoo, Finland

Richard Bernewitz Institute of Process Engineering in Life Sciences, Section I: Food Process Engineering, KIT, Karlsruhe, Germany

Carlo G. Bertinetto Department of Forest Products Technology, Aalto University, Espoo, Finland

Xin Chen Bioimaging and Machine Vision Labs, University of Maryland, College Park, MD, USA

Dilek Ercili-Cura VTT Technical Research Center of Finland, Espoo, Finland

Leonardo Galvis Rojas Department of Forest Products Technology, Aalto University, Espoo, Finland

Gisela Guthausen Pro2NMR, IBG2 and IMVM, KIT, Karlsruhe, Germany

Natalia Hernández-Sánchez Physical Properties Laboratory-Advanced Technologies in Agri-Food (LPF-TAGRALIA), Technical University of Madrid, Madrid, Spain

Ana Herre-ro-Langreo Irstea, UMR ITAP, Montpellier Cedex 5, France

Ulla Holopainen-Mantila VTT Technical Research Centre of Finland, Espoo, Finland

Anna-Stiina Jääskeläinen VTT Technical Research Centre of Finland, Espoo, Finland

Lu Jiang Department of Radiology and Oncology, Johns Hopkins University, Baltimore, MD, USA

Jozef L. Kokini Department of Food Science, Purdue University, West Lafayette, IN, USA

Filiz Koksel University of Manitoba, Winnipeg, MB, Canada

Jarupat Luecha Division of Food Technology, Mahidol University Kanchanaburi Campus, Kanchanaburi, Thailand

Ángela Melado-Herreros Physical Properties Laboratory-Advanced Technologies in Agri-Food (LPF-TAGRALIA), Technical University of Madrid, Madrid, Spain

Ilkem Demirkesen Mert Department of Food Engineering, Middle East Technical University, Ankara, Turkey

Guillermo P. Moreda Physical Properties Laboratory-Advanced Technologies in Agri-Food (LPF-TAGRALIA), Technical University of Madrid, Madrid, Spain

Mari Raulio Vantaa, Finland

Dérick Rousseau Department of Chemistry and Biology, Ryerson University, Toronto, ON, Canada

Serpil Sahin Department of Food Engineering, Middle East Technical University, Ankara, Turkey

Martin G. Scanlon University of Manitoba, Winnipeg, MB, Canada

Heike P. Schuchmann Institute of Process Engineering in Life Sciences, Section I: Food Process Engineering, KIT, Karlsruhe, Germany

Nesli Sozer VTT Technical Research Centre of Finland, Espoo, Finland

Gulum Sumnu Department of Food Engineering, Middle East Technical University, Ankara, Turkey

Yang Tao Bioimaging and Machine Vision Labs, University of Maryland, College Park, MD, USA

Chapter 1
Cereal Grain Structure by Microscopic Analysis

Ulla Holopainen-Mantila and Mari Raulio

1.1 General Structure of Cereal Grains

Cereal species covers monocotyledonous plant species from the family Poaceae, which are domesticated and cultivated for their grains rich in starch. This chapter focusses on the microscopical analysis of kernels of wheat (*Triticum aestivum* L.), rye (*Secale cereale* L.) and barley (*Hordeum vulgare* L.) belonging to the tribe Triticeae and oats (*Avena sativa* L.) belonging to the tribe Aveneae. However, most of the microscopy techniques referred are applicable to other cereal grains such as rice and corn.

Botanically, cereal kernels represent an indehiscent fruit type called caryopsis. Most of them have elongated shape. Caryopses of members of the tribes Triticeae and Aveneae can be distinguished by the presence of a crease or a longitudinal furrow. The crease extends along the grain's entire length, and it is deepest in the middle part of the grain. It is most apparent in the grain of wheat, but clearly detectable also in the grains of rye, barley and oat (Evers and Millar 2002). The crease is located in the ventral side of the grain, and the opposite part of the grain is called dorsal side.

Until maturity, cereal grains are covered by a hull. The adherence mechanism of the hull on the pericarp layer below varies among cereal species. Thus, hulls of wheat and rye kernels are usually removed by threshing, but in regular oat and barley varieties, the hull is attached by specific structural devices or through a cementing layer, respectively (Evers and Millar 2002; Olkku et al. 2005). Underneath the hull, there is the pericarp (fruit coat), which in turn surrounds the testa or seed coat. Both the pericarp and the testa consist of distinguishable layers of different cell types. Most of the cells in the outer layers of mature cereal kernels are dry and empty, and some

U. Holopainen-Mantila (✉)
VTT Technical Research Centre of Finland, Tietotie 2, Espoo FI-02044 VTT, Finland
e-mail: ulla.holopainen@vtt.fi

M. Raulio
Kuninkaalantie 1, P.O. Box 53, 01301 Vantaa, Finland
e-mail: mari.raulio@tikkurila.com

N. Sozer (ed.), *Imaging Technologies and Data Processing for Food Engineers,*
Food Engineering Series, DOI 10.1007/978-3-319-24735-9_1

of them are shrunken, leaving large intercellular spaces (Freeman and Palmer 1984; Evers and Millar 2002). The pericarp is rich in insoluble dietary fibres consisting mostly of branched heteroxylans and cellulose (Fincher and Stone 1986).

Between the testa and the endosperm lies a nucellar epidermis which is a hyaline layer containing no pigments. It is a remnant of a maternal tissue that served nutrients to the embryo and endosperm during grain development (Duffus and Cochrane 1992). Layers of cutin are present in the outer surfaces of the nucellar epidermis and the testa (Evers and Millar 2002). In barley, there is a cutin layer also on the outer surface of the pericarp (Olkku et al. 2005).

The endosperm consists of aleurone and sub-aleurone layers as well as starchy endosperm. In addition to the embryo, the aleurone layer is the only part of the grain containing living cells. Aleurone cell walls of cereals consist mainly of arabinoxylan (AX) with (1→3;1→4)-β-D-glucan being the second most abundant component in the aleurone cell walls of most of the cereals (Fincher and Stone 1986; Collins et al. 2010). The aleurone cells contain plenty of protein, lipids, vitamins and minerals (Pomeranz 1973; Fincher 1976; Evers and Millar 2002).

The starchy endosperm serves as nutrient storage for the growing embryo during germination. It is comprised of dead cells lacking nuclei. These cells contain starch granules embedded in a matrix consisting of storage proteins. The cell walls in the starchy endosperm of cereal grains are mainly formed of (1→3;1→4)-β-D-glucan and AX, and their relative proportions differ among the cereal species (Fincher and Stone 1986; Collins et al. 2010). The sub-aleurone layer below the aleurone differs from the starchy endosperm by the smaller cell size and higher amount of protein in cells (Duffus and Cochrane 1992; Evers and Millar 2002).

In the mature kernel, the embryo is located in the proximal end of the grain or near the place of attachment to rachis. The embryo consists of embryonic axis and scutellum. The scutellum is a specific cell layer, which separates embryonic axis from the endosperm and originates from a modified cotyledon (Evers and Millar 2002).

The starchy endosperm is by far the largest morphological part of the grain (Table 1.1). In hulled cereal species such as barley and oats, the hull forms a substantial part of the grain. The proportion of the embryo is less than 4 % in all cereals even when the hull is not taken into account. The proportion of aleurone, testa and pericarp varies from 8.8 to 15.2 % among cereal species.

Table 1.1 Typical proportions of different cereal kernel structures of total grain weight (from Kent and Evers 1994 and Evers and Millar 2002). Values in parentheses are proportions excluding the hull

Grain part	Proportion of grain dry weight (%)			
	Barley	Oat	Rye	Wheat
Hull	13.0	25.0	–	–
Testa and pericarp	2.9 (3.3)	9.0 (12.0)	10.0	8.5
Aleurone layer	4.8 (5.5)			6.7
Starchy endosperm	76.2 (87.6)	63.0 (84.0)	86.5	82.0
Embryo	1.7 (1.9)	1.2 (1.6)	1.8	1.3
Scutellum	1.3 (1.5)	1.6 (2.1)	1.7	1.5

1.2 Using Microscopy Techniques in Imaging of Cereal Grains

1.2.1 Stereomicroscopy

Stereomicroscope is an optical microscope intended for low-magnification observation of a specimen using light reflected from the surface of an object rather than transmitted through it (i.e. light microscopy). Stereomicroscopy can be utilized in collecting data on the appearance and colour features of the cereal grains, their processing products or end products containing cereals. A great advantage of stereomicroscopy in comparison to imaging with digital camera is the scale bar available when an imaging system with an imaging software is utilized. Most often, cereal samples are imaged with a stereomicroscope as such whether they are wet or dry without any pretreatments. The material and colour of the surface where the sample is imaged should be selected in order to improve the distinctiveness of the sample from the background. For proper illumination conditions needed in stereoimaging, usually both ring light (e.g. LED device) and goose-neck illuminators with continuous adjustment of luminosity are required.

1.2.2 Light Microscopy

In light microscopy (or optical microscope), visible light and a system of lenses are used to magnify images of small specimens. Light microscopy provides an option for analysis of cereal grain structures with higher magnification compared to stereomicroscopy. Furthermore, the embedding and cutting of cross sections of samples enable the examination of the microstructure of cereal grains and their tissues present in samples. Characterization and localization of grain components is possible by using different staining methods. For more detailed information on fixation, choice of resin, embedding and theory of staining, the reader is referred to, for example, Harris et al. (1994), Leitch (1994), Ruzin (1999) and Kiernan (2008).

Only rather seldom, cereal samples are imaged with a light microscope without fixation, embedded in resin, cut into sections and stained. The imaging of cereal samples without laborious sample preparation, that is, embedding and cutting, is applicable, for example, for flour and bran particles in water or ethanol, but the thickness of particles might complicate the imaging of this type of cereal samples.

In the sections cut from resin-embedded samples and attached to microscopy slides, many grain components such as starch and protein present inside the cells or β-glucan present in the cell walls can be visualized with different stains. For example, Light Green and Lugol's iodine can be used in the staining of protein and starch, respectively (Holopainen et al. 2005; Andersson et al. 2011; Jääskeläinen et al. 2013) and Oil Red O for visualization of lipids containing tissues like cutin layers of barley grain (Olkku et al. 2005). In addition to traditional stains, antibodies raised

against different components can be utilized in localization of compounds present in cereal grain. When planning the use of antibodies, the compatibility of fixation solution and resin with immunolabelling reagents should be carefully checked.

When using fluorescing stains, it is important to verify the autofluorescence of the sample prior to staining in order to avoid misinterpretations. In the cereal samples, the autofluorescence is mainly caused by the substances containing aromatic phenol rings such as lignin and ferulic acid (Fulcher et al. 1972; Rudall 1994). Due to the presence of these autofluorescing components, testa, pericarp and hulls of cereal grains are usually visible without staining, at least when the excitation is carried out between 330 and 410 nm and the emission from 420 to 455 nm is detected. The autofluorescence of the aleurone cell walls is not due to lignin but minor amounts of other aromatic substances such as *para*-coumaric and diferulic acids (Hernanz et al. 2001; Antoine et al. 2003; Jääskeläinen et al. 2013). Only weak autofluorescence is observed in the cell walls of starchy endosperm which can be explained by the low amount of phenolic substances (Saadi et al. 1998; Philippe et al. 2007).

1.2.3 Confocal Laser Scanning Microscopy

In the confocal laser scanning microscopy (CLSM), the sample is illuminated with a scanning laser light, and the reflected or fluorescing light is detected with photomultiplier tubes. Images are acquired point-by-point and reconstructed with a computer, allowing also three dimensional reconstructions. CLSM can provide in-focus information of the structure in selected depths by optical sectioning. This is enabled by using a confocal aperture, or pinhole, which allows only the signal from the focal plane pass to the photomultiplier, whereas the out-of-focus signal is omitted.

Confocal microscopy is typically applied for imaging of fluorescing samples. Confocal microscopy can be combined with transmitted light imaging of transparent samples by contrast methods like differential interference contrast (DIC) microscopy. Cereal grain samples, which often contain components having autofluorescence properties, can be imaged with CLSM without staining depending on the structures of interest. The advantage in using CLSM in the imaging of cereal grains or their processing products is that only minimal sample preparation is required. In comparison to resin embedding, no fixation, dehydration or infiltration procedures are necessarily needed, and thus the components such as lipids, which are destructed by the solvent treatments, can be visualized by CLSM. In addition, sections cut from resin-embedded samples stained with fluorescent dyes or labelled using antibodies coupled with fluorochromes can be imaged with CLSM.

1.2.4 Scanning Electron microscopy

An electron microscope is a microscope that uses the beam of accelerated electrons as a source of illumination to create an image of the specimen. Electron microscopes

apply the same principles as optical microscopes but use electrons rather than photons for generating the image. Since the wavelength of an electron is much shorter than that of visible light, the electron microscope has a higher resolving power than a light microscope.

Electron microscopy of biological samples requires pretreatments, fixation and dehydration. The specimen needs to be mounted on a sample holder and be coated with metallic vapours. Extensive sample preparation can cause severe artefacts, distort the structures and change interactions between the components, for instance, by removing the lipids soluble in solvents used for the dehydration. Yet, electron microscopy has a major advantage compared to light microscopy: its ultrahigh resolution. Highest possible magnification in light microscopy is 1000×, in electron microscopy, 200,000× can be reached. Nevertheless, the results acquired using electron microscopy should be confirmed by other techniques to rule out artefacts.

Cereal samples, being most often dry, do not necessarily need fixation or dehydration. Whole kernels can be cut by a sharp blade to reveal the content or outer layers of the hull which can be removed mechanically to reveal the seed coat. Kernels can also be fractured either mechanically of by freezing.

The ultrastructure of tissues and components of the kernel can be visualized using scanning electron microscopy (SEM). Size and distribution of starch granules and protein bodies of flour samples, efficiency of enzyme treatment, malting of fermenting and location of indigenous microorganisms can be revealed using higher magnification.

1.3 Examination of Cereal Grain Structure by Microscopy

1.3.1 Stereomicroscopy of Cereal Grains

The appearance of the ventral side of an oat grain with a hull imaged by a stereomicroscope is shown in Fig. 1.1a. When the grain is cut either longitudinally or diagonally, the inner structure of grain can be examined. The longitudinal cut reveals the starchy endosperm and the embryo (Fig. 1.1b). The division of the grain into two lobes by the crease can be seen in the cross-cut surface of the grain (Fig. 1.1c). The cross-cut also shows the thickness of the hull layers present in the oat kernel which explains the high proportion of the hull of the total grain weight.

1.3.2 Visualization of Starch, Protein and Cell Walls in Cereal Grains

Staining of the main storage compounds in the cereal grains, namely starch and protein, gives important information on the structure of the grain for many purposes.

Fig. 1.1 Stereomicroscopy image of **a** whole, **b** longitudinally cut surface and **c** cross-cut surface of oat grain

For example, for studying the localization of protein and starch granules in the cells of aleurone or starchy endosperm, they can be stained in the sections cut from the resin-embedded sample blocks. Protein can be stained with 0.1 % (w/v) Light Green in water and starch with Lugol's iodine solution (I_2 0.33 % (w/v) and KI 0.67 % (w/v), diluted 1:10; Holopainen et al. 2005; Andersson et al. 2011; Jääskeläinen et al. 2013). In stained specimens, protein appears green or yellow, while iodine stains the amylose component of starch blue and amylopectin brown. As the amylopectin masks the amylose, native starch granules appear dark blue. In Fig. 1.2, the microstructure of the aleurone layer and the starchy endosperm of wheat and barley grain are demonstrated by using these stains. The staining of starch reveals the

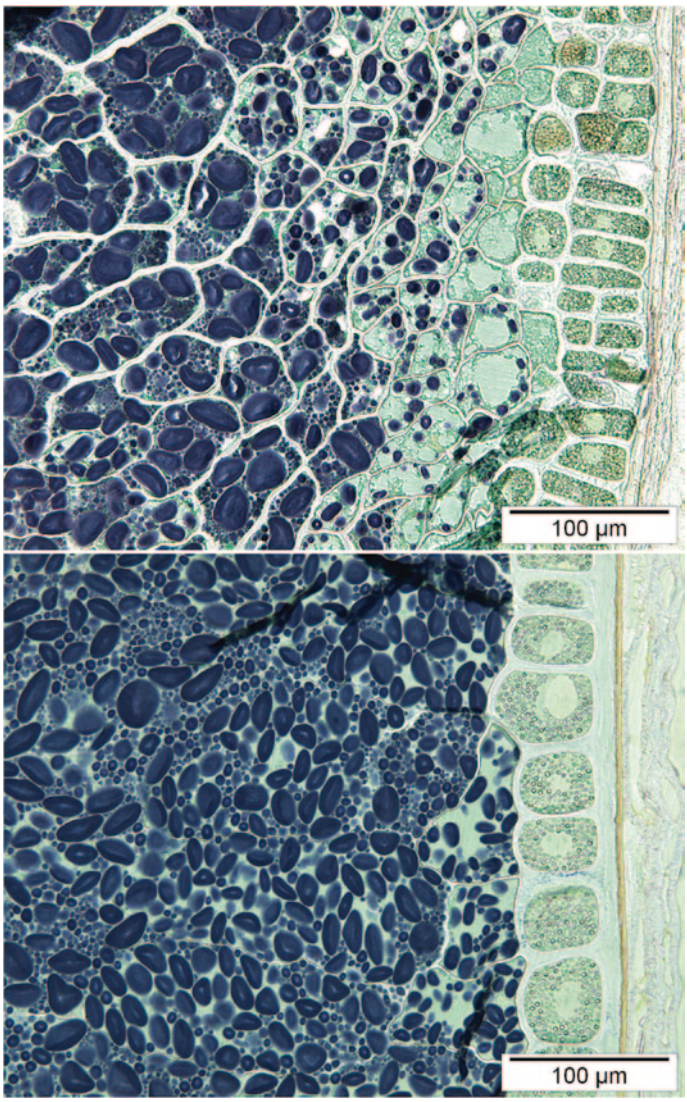

Fig. 1.2 Protein and starch stained with Light Green and Lugol's iodine in the cross sections of **a** barley and **b** wheat grain. Light Green stains protein *green* and starch appears *dark blue* due to iodine staining. Aleurone layer is located on the *right* in the images. (Reproduced from Jääskeläinen et al. 2013 with the permission from the publisher)

bimodal distribution of starch granules in the starchy endosperm. The protein staining shows that in the barley grain the sub-aleurone layer located adjacent to aleurone contains higher concentration of protein in comparison to wheat grain. Iodine staining can be utilized also in the examination of the state of starch in the processed cereal samples. It reveals the changes in the appearance of the starch granules and also the separation of amylose and amylopectin components after gelatinization.

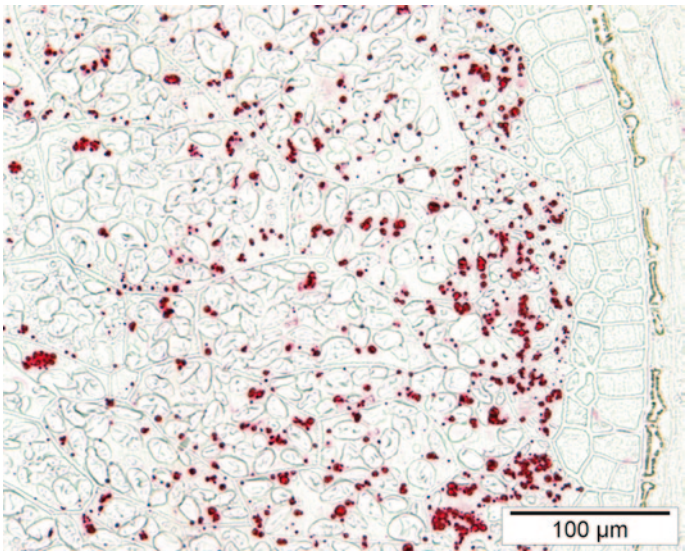

Fig. 1.3 B hordein storage proteins localized by immunolabelling in the cross section of developing barley grain collected 21 days after pollination. (Reproduced from Holopainen et al. 2012 with the permission from the publisher)

If only certain proteins present in cereal grains are of interest, specific antibodies can be utilized in their localization (Fig. 1.3). The primary antibody can be detected using a secondary antibody labelled either fluorescently or with a substrate producing a coloured compound after enzyme reaction (e.g. Dornez et al. 2011b; Holopainen et al. 2012).

Cell walls and polysaccharides as their constituents play an important role in the processing properties of cereal grains. As a part of the dietary fibre, they are also of interest from the nutritional point of view. As the cell walls in cereal endosperm are mainly constituted of mixed-linkage β-glucan and AX, visualization of these polysaccharides is essential when investigating the structure of the cereal samples.

Mixed-linkage β-glucan can be stained with Calcofluor (commercial names among others: Calcofluor White and Fluorescent Brightener 28). Calcofluor is not specific to β-glucan but bounds also to cellulose, which is a non-branching glucose polymer (Maeda and Ishida 1967). However, the low cellulose content of cereal endosperm enables the use of this stain as a specific label for mixed-linkage β-glucan (Wood et al. 1983; Wood and Fulcher 1983). To obtain a better contrast between cell walls and cell content, Calcofluor is often used in combination with protein stain Acid Fuchsin (Fulcher and Wong 1980; Wood et al. 1983; Parkkonen et al. 1994). For example, the resin-embedded cereal samples can be stained sequentially first with aqueous 0.1% (w/v) Acid Fuchsin in 1.0% acetic acid and then with aqueous 0.01% (w/v) Calcofluor White (Wood et al. 1983; Parkkonen et al. 1994). These stains are fluorescent, and they can be imaged under exciting light ($\lambda_{ex.}$ = 400–410 nm; $\lambda_{em.}$ > 455 nm). Using these imaging conditions, intact cell walls stained with Calcofluor appear blue, and

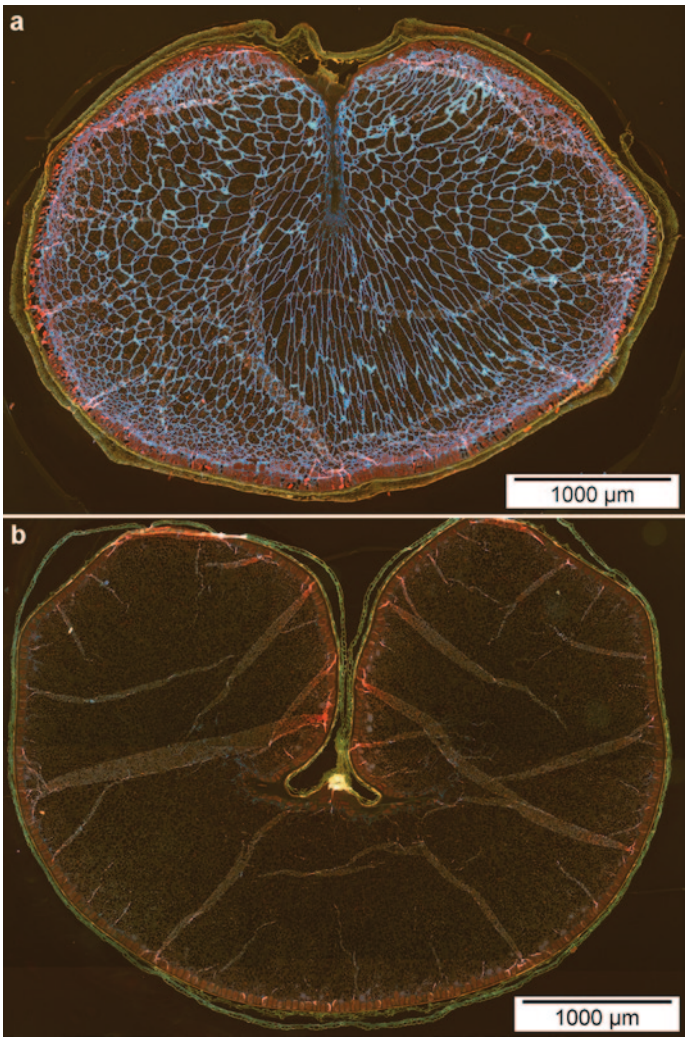

Fig. 1.4 Cross sections of **a** barley and **b** wheat grain stained with Calcofluor and Acid Fuchsin. Cell walls rich in β-glucan appear *blue* and protein appears *red*

proteins stained with Acid Fuchsin appear red when the fluorescing signal is recorded using long pass filters. Starch remains unstained and appears black. Pericarp and other grain outer structures are visualized by their autofluorescence.

By means of the bright fluorescence of the cell walls containing mixed-linkage β-glucan stained with Calcofluor, the structure of cereal grains can be examined, for example, on the level of the whole grain and of the tissue types present in the different parts of the endosperm. In Fig. 1.4a, the shape and distribution of the cells in the starchy endosperm of barley grain is shown by Calcofluor staining. For comparison, the similarly stained starchy endosperm of wheat shows no cell structure

due to thinner cell walls with lower content of mixed-linkage β-glucan (Fig. 1.4b). These images also illustrate the differences in the shape of the crease typical to these cereal species.

Calcofluor staining of cross sections of barley, oat, rye and wheat grains shows certain morphological differences in the endosperm structure (Dornez et al. 2011b; Fig. 1.5). The aleurone layer of wheat, oat and rye consists of one row of thick-walled cells, while the aleurone in barley grain is constructed of 2–4 rows of cells. Short regions with multiple cell layers exist also in oat aleurone. The shape of the aleurone cells also differs between cereal species. Wheat aleurone cells appear to be more squared in comparison to those of oat and rye. Barley aleurone cells are smaller and more irregularly shaped. With this higher magnification in comparison to Fig. 1.4, the distribution of β-glucan in the endosperm cell walls is also seen in more detailed way. In the grains of barley, oat, rye and wheat, the aleurone cell walls contain more AX than β-glucan (Collins et al. 2010), which is seen as a lower stainability of this cell layer by Calcofluor (Fig. 1.5). In rye grain, the periclinal cell walls adjacent to the nucellar epidermis seem to contain more β-glucan than the other cell walls.

Cell walls in the sub-aleurone layer of oat are clearly the thickest of the cereal species examined (Fig. 1.5). On the basis of the Calcofluor staining, the β-glucan is clearly concentrated in the sub-aleurone region of oat. Barley has the second thickest sub-aleurone cell walls, while in rye and wheat the Calcofluor staining of these cell walls was notably less intensive.

Central starchy endosperm cell walls of barley and rye are clearly visualized with Calcofluor. Also in oat, the cell walls of this region are detected with Calcofluor, but in wheat only the cell walls in the proximity of the crease are stainable with Calcofluor (Fig. 1.5; Dornez et al. 2011b). Calcofluor staining thus indicates that barley and rye grains contain more β-glucan in the central starchy endosperm than those of oat and wheat. In the central starchy endosperm of barley and rye, the inner walls next to the cell cavity tend to be more intensively stained with Calcofluor than the middle lamella. This suggests that β-glucan is not evenly distributed in these cell walls.

For comparison, the respective grain sections were labelled with a monoclonal β-glucan antibody (Dornez et al. 2011b; Fig. 1.6). Likely due to differing specificity compared to Calcofluor, the β-glucan antibody shows differences in the localization of this component in the aleurone and starchy endosperm cell wall. The inner parts of the aleurone cell walls adjacent to cell contents in rye and wheat grains were labelled with the antibody, and there was no clear difference between anticlinal and periclinal walls. However, the middle lamella was not stained. In the aleurone of barley and oat, the staining with β-glucan antibody was more limited.

In contrast to Calcofluor staining, the β-glucan antibody was more sensitive in visualization of the cell walls in the central starchy endosperm of all cereal grains studied. The antibody labelling of β-glucan was more distinctive in barley and rye compared to wheat. It is worth to note that central starchy endosperm cell walls in wheat grain were not stainable with Calcofluor, but were with the β-glucan antibody.

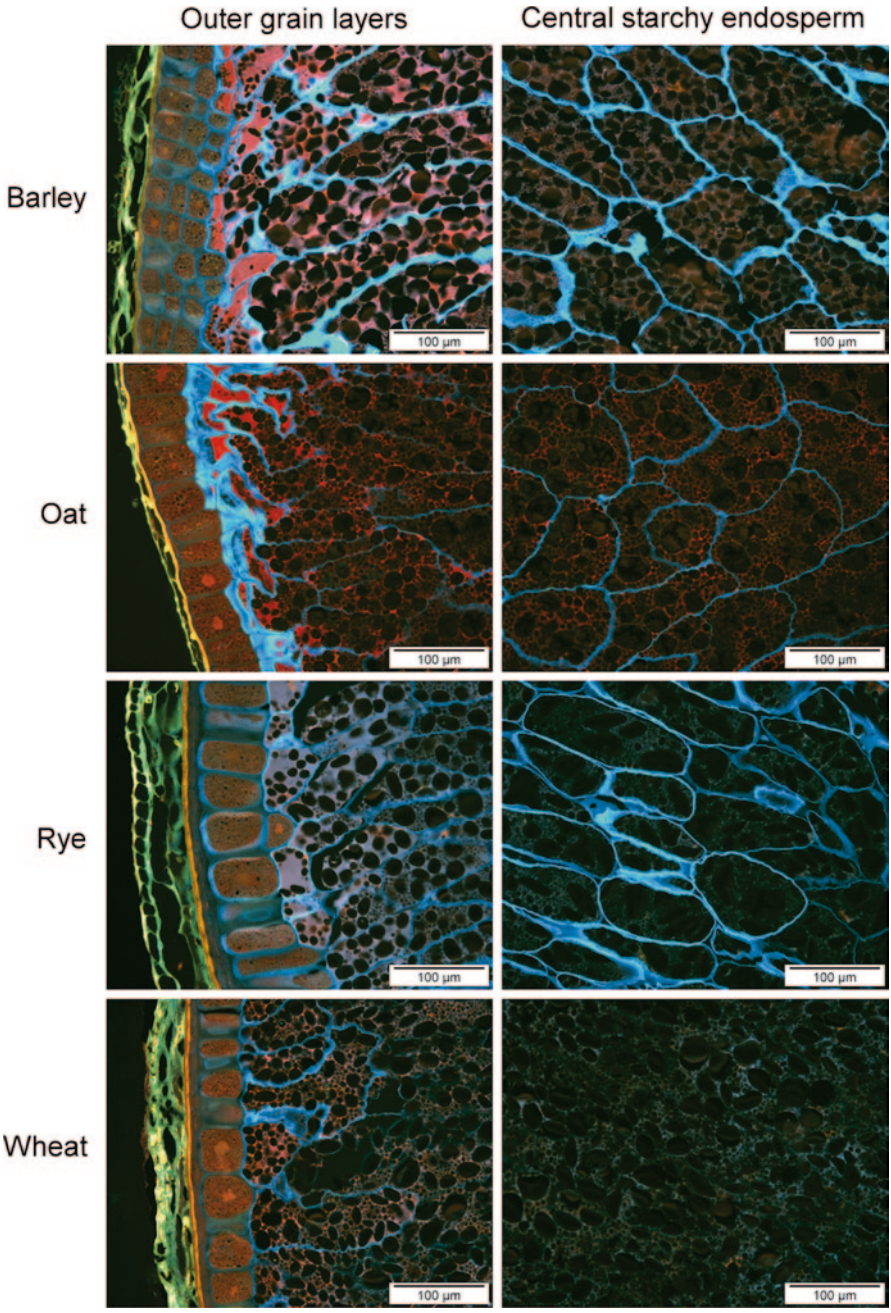

Fig. 1.5 Outer kernel layer and central starchy endosperm of kernel cross sections of barley, oat, rye and wheat stained with Calcofluor and Acid Fuchsin. Cell walls rich in β-glucan appear *blue* and protein appears *red*. (Reproduced from Dornez et al. 2011b with the permission from the publisher)

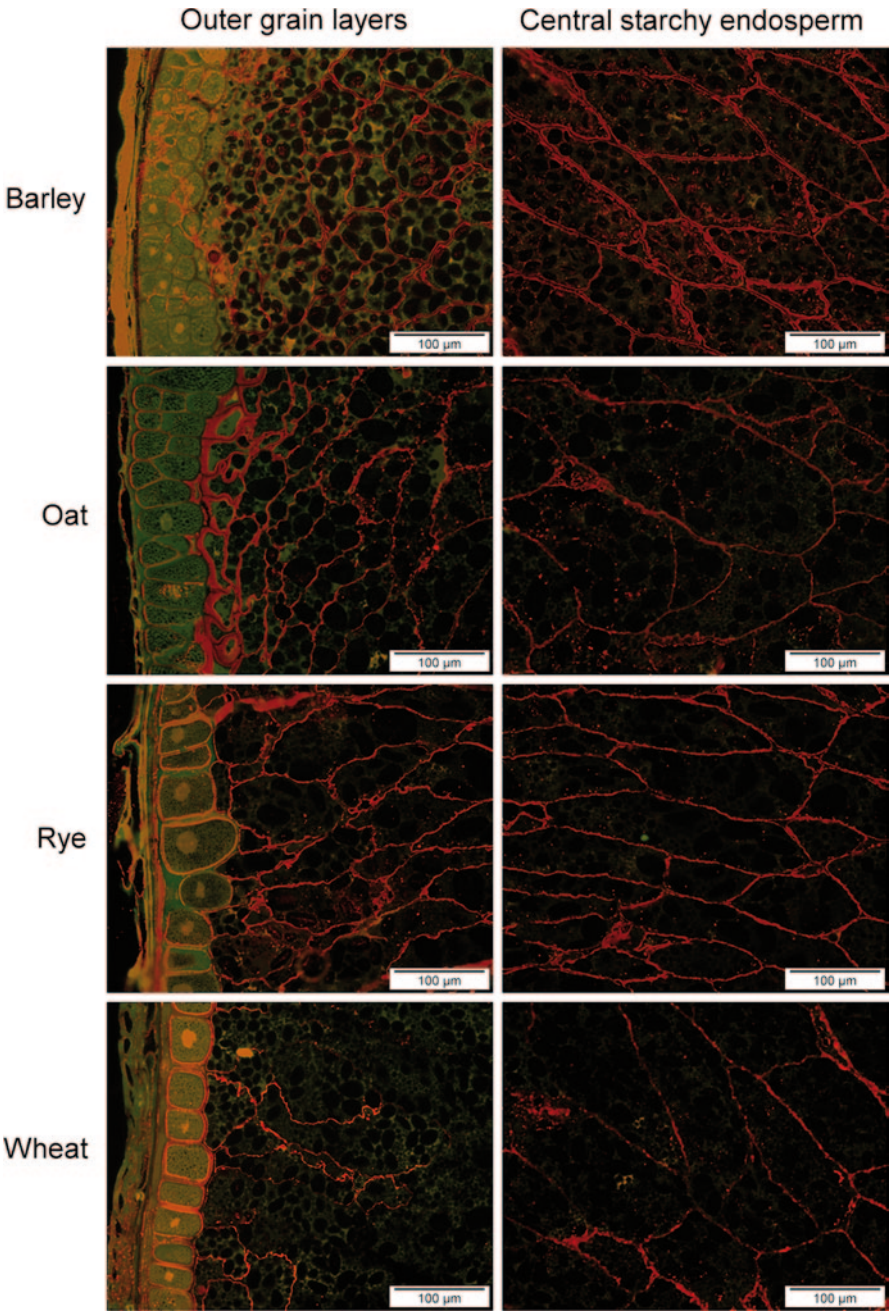

Fig. 1.6 Outer kernel layer and central starchy endosperm of kernel cross sections of barley, oat, rye and wheat stained with the mixed-linkage β-glucan antibody. The structures stained by the β-glucan antibody are detected as *red,* while the background signal is seen as *green*. The images are overlays of two pictures acquired with distinct parameters. (Reproduced from Dornez et al. 2011b with the permission from the publisher)

Due to the differing specificity or sensitivity, these two staining methods provided complementary information on localization of the cell wall component β-glucan. In comparison to the Calcofluor staining procedure, the immunolabelling technique is laborious and time-consuming. The advantage of the Acid Fuchsin and Calcofluor staining over the other techniques is the simultaneous staining of two grain components. In addition, the grain outer layers are visualized at the same time due to their autofluorescence.

AX, another important cell wall component of cereal grains can be visualized using specific antibodies (e.g. McCartney et al. 2005). Also an inactivated xylanase labelled with fluorochrome has been used in the detection of this cell wall polysaccharide (Dornez et al. 2011a, b).

1.4 Microstructure of Processed Cereal Products

In the following sections, several studies on the influence of different processing methods on the microstructure of cereal components are introduced.

1.4.1 Milling

1.4.1.1 The Effect of Temperature on Milling Behaviour of Wheat Bran

The reduction of particle size has been shown to improve the physicochemical, nutritional and physiological properties of various food materials (Jenkins et al. 1999; Chau et al. 2007; Wu et al. 2009; Stewart and Slavin 2009). One effective way to influence the dissociation of the material into smaller particles is to mill it in low temperatures. For example, the extensibility and brittleness of wheat bran can be decreased and increased, respectively, in temperatures below −46 °C (Hemery et al. 2010b). Therefore, cryogenic grinding serves as a potential technology for micronization of wheat bran.

In the study of Hemery et al. (2011a), the effect of ultra-fine grinding on coarse wheat bran either in ambient temperature or under cryogenic conditions was investigated. The microstructure was examined of the bran samples that were ground once, twice or three times in ambient temperature or once under cryogenic conditions. The number of successive grinding steps clearly influenced the microstructure of bran particles (Fig. 1.7a–c). The size of particles containing intact aleurone cells correlated negatively with the number of grinding steps. After one grinding, bran particles consisted mostly of more than ten intact aleurone cells. The second and third grinding step decreased the number of intact aleurone cells in bran particles to c. 2–7 and c. 1–4, respectively. Similarly, the fibre-rich pericarp particles were the smallest in the sample ground three times. Grinding also affected the adherence of tissue layers present in bran particles. Aleurone, testa and pericarp tissues were

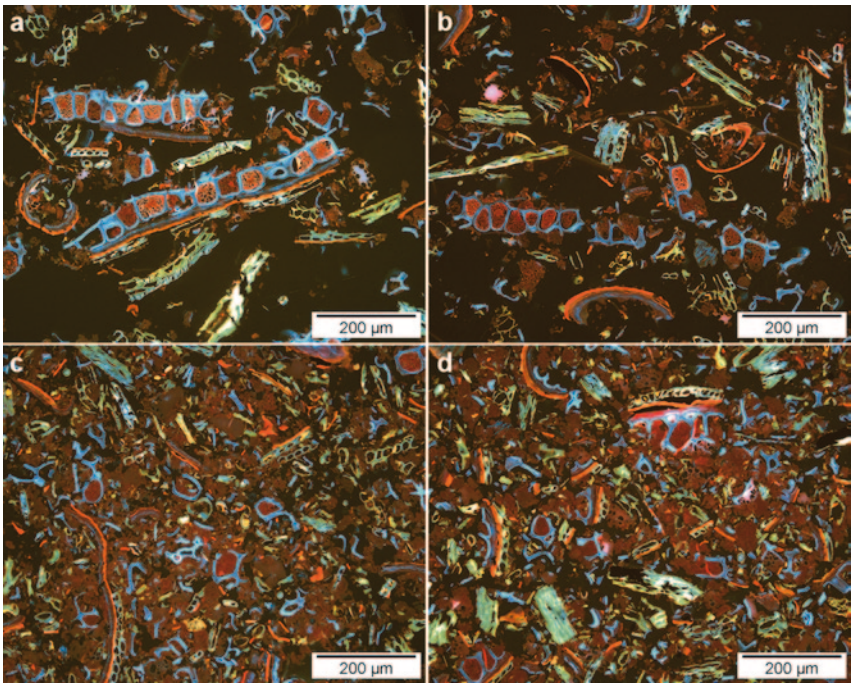

Fig. 1.7 Microstructure of coarse wheat bran samples ground **a** once, **b** twice or **c** three times in ambient temperature and **d** once under cryogenic conditions. Cell walls and protein are stained with Calcofluor and Acid Fuchsin, respectively. Aleurone cell walls appear *blue* and protein *brownish-red*. Fibre-rich material from the pericarp appears as *light greenish-yellow* and the testa appears *orange*. Starch is not stained. (Reproduced from Hemery et al. 2011a with the permission from the publisher)

more dissociated from each other after each grinding step. In ambient temperature, the degree of grinding was detected also in the increased amount of both aleurone cell walls and protein released from the aleurone cells.

The median particle diameter of the cryogenically ground sample was 55 µm being nearly the same as after three grinding steps at ambient temperature (51 µm). Nevertheless, there were substantial differences in the microstructure of the bran particles milled in different temperatures (Fig. 1.7c, d). Cryogenic grinding had not dissociated the pericarp from the testa and the testa from the aleurone in the bran particles. These interfaces were present as intact in most of the particles in the cryogenically ground sample, while after three grinding steps in ambient temperature only few composite particles were observed. In addition, testa particles observed as red were smaller (<200 µm) after cryogenic grinding at −100 °C in comparison with the ambient grinding (c. 200–500 µm). This indicates that the brittleness of the testa was increased at low temperature.

The milling temperature thus clearly affects the production mechanism of finer particles. At low temperature, the increased brittleness of tissues, in particular the testa, contributes to the breakage or fragmentation of bran particles and results in

more rapid production of finer particles in comparison to ambient grinding. However, in cryogenic conditions bran layers stayed adherent, while in milling at ambient temperature, they were separated from each other due to their different extensibility properties.

1.4.1.2 Extensive Dry Ball Milling Leads to Fragmentation of Arabinoxylan of Wheat Bran

Arabinoxylan oligosaccharides (AXOS) derived from wheat bran have potential prebiotic properties (Glitsø et al. 1999; Cloetens et al. 2008). They can be produced by solubilizing and degrading water-unextractable AX with endo-β-(1,4)-xylanases (Courtin and Delcour 2001). This enzymatic treatment affects the AX in aleurone layer but cannot release AXOS from the AX with higher A/X ratio located in the pericarp (Benamrouche et al. 2002). Water solubility can be, however, also affected by mechanical means. Water solubility of AX in psyllium seed husk has been increased with simultaneous decrease in molecular size by ball milling (Van Craeyveld et al. 2008).

The increase in the water solubility of AX due to ball milling of wheat bran has been related to the changes in the microstructure (Van Craeyveld et al. 2009). Both the reduction of particle size down to the nanoscale level and the aggregation of milled bran components were observed upon ball milling. In the unmilled sample, large bran particles with pericarp, testa and aleurone attached to each other were distinguished (Fig. 1.8a). These large particles contained also fragments of sub-aleurone cell walls located below the aleurone. Ball-milled samples consisted of fine material in which only few recognizable structures, including small fragments of aleurone cell walls and some protein aggregates, were observed (Fig. 1.8b–d). In comparison to ball milling for 24 h with 50% filling degree, the longer ball-milling treatment (48 h, 50% filling degree) resulted in less and smaller aleurone cell wall fragments observable by staining with Calcofluor (Fig. 1.8b, c). Wheat bran that was ball milled for 24 h at a lower filling degree (16%) contained even fewer and smaller pieces of the cell wall (Fig. 1.8d).

Thus, the fragmentation of the cell walls upon ball milling was observed as the low number of discernible cell wall structures. Individual, recognizable cell wall structures produced upon ball milling were in the low-micrometre to high-nanometre range. Also the low stainability of cell wall fragments with Calcofluor in the ball-milled samples reflected the fragmentation occurred during ball milling, as only β-glucan molecules with molecular mass > 10,000 can be detected by Calcofluor. On the basis of the molecular weight of the AXOS produced, the ball milling abled the breakdown of covalent bonds inside AX molecules and the reduction of the particle size to the nanoscale level. The fragmentation of cell wall polymers occurred as an effect of both the high-energy impact in the ball-milling process and the considerable development of heat in the milling jar. This combined influence of mechanical forces and heat could explain why extended milling times are necessary to significantly increase the water solubility of AX. In addition, the effect of ball milling on the fragmentation of bran was intensified by decreasing the filling degree.

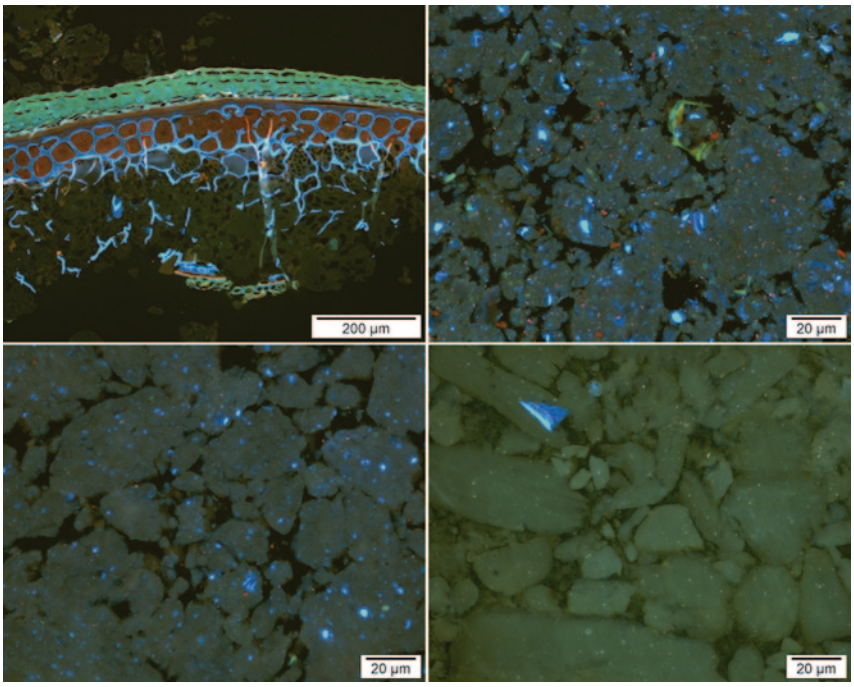

Fig. 1.8 Microstructure of **a** untreated wheat bran, **b** wheat bran ball milled for 24 h (50% filling degree), **c** wheat bran ball milled for 48 h (50% filling degree) and **d** wheat bran ball milled for 24 h (16% filling degree). Cell wall β-glucan stained with Calcofluor appears *blue,* and proteins stained with Acid Fuchsin appear *red*. Starch is unstained and appears *black*. (Adapted with permission from Van Craeyveld et al. 2009. Copyright 2014 American Chemical Society)

The aggregation of the milled bran material visualized by light microscopy was in line with the particle size analysis by laser diffraction (e.g. in the sample ball milled for 24 h with 50% filling degree d_{50} was 32 µm). Thus, the particle sizes observed by laser diffraction reflect the aggregation of very finely ground bran material and not the actual particle size of the bran material after milling treatment.

An extensive single-stage, dry ball-milling process can reduce the size of wheat bran to the nanoscale level. AXOS produced by ball-mill treatment had a higher A/X ratio in comparison to AXOS produced enzymatically from wheat bran. This implies that ball milling renders AX from both the aleurone layer as well as the pericarp layer water-extractable. Ball milling resulted in also higher AXOS yields compared to enzymatic treatment. Ball milling thus facilitates the more efficient use of the cereal bran, in particular the pericarp.

1.4.1.3 Effect of a Milling Pretreatment on the Microstructure of Brewer's Spent Grain

Brewer's spent grain is a by-product of the brewing industry containing mainly the insoluble residues of malt separated from wort before fermentation (Fig. 1.9a). The components such as AX, cellulose, lignin and protein present in this side stream could be utilized in food, chemical or energy production (Mussatto et al. 2006). As millions of tonnes of brewer's spent grain is produced worldwide annually, a cost-efficient fractionation method would enable its better valorization. Carbohydrates present in brewer's spent grain are rather resistant to enzymatic hydrolysis (Forssell et al. 2008; Treimo et al. 2009) and set thus certain requirements for the fractionation of this material. However, the decrease of the particle size is known to open up the cell wall structures and to reduce cellulose crystallinity thus making the biomass more accessible to enzymes (Hendriks and Zeeman 2009). The particle size reduction should be severe enough in order to influence the cell wall structures or the crystallinity of cellulose (Beldman et al. 1987).

The effect of different milling pretreatments on the microstructure of brewer's spent grain and further on its enzymatic hydrolysis has been demonstrated by Niemi et al. (2012a). Light microscopy shows that the unmilled brewer's spent grain contains large fragments of grain outer layers and aleurone and protein (Fig. 1.9b). After pin-disc milling, brewer's spent grain contained still the same recognizable structures, which were present in the unmilled sample, although the size of the particles was clearly reduced (Fig. 1.9c). The grinding with TurboRotor was more effective to break down the aleurone cell walls in comparison to pin-disc milling (Fig. 1.9c, d). Wet milling either with Masuko mill or microfluidisizer resulted in the thin particles with hardly any recognizable cellular structures (Fig. 1.9e, f). The similarity of these wet-milled samples was confirmed by the particle size distribution. The higher stainability of protein in the Masuko-milled sample could reflect, for example, the change in the physicochemical properties of the brewer's spent grain components due to heating up during milling. Ball milling of brewer's spent grain for 1 h did not totally break down the cellular structures, but extending the milling time to 24 h resulted in a very fine powder with no distinguishable or clearly stainable structures (Fig. 1.9g, h). Similarly with the results of Van Craeyveld et al. (2009), large aggregates of fine particles were observed after long ball-milling treatment and also contributed to the presence of larger particles in the particle size distribution. Aggregation could be due to the charges caused by the frictional electricity of the milling or mixing of lipids with protein and carbohydrates.

The solubilization of brewer's spent grain carbohydrates was clearly increased by the milling pretreatment, and the highest rates were observed in the samples ball milled for 24 h. Cellulose in particular was more hydrolysable after milling, while the solubilization of AX was not notably affected by milling pretreatments. Considering the need of a cost-efficient process, wet milling is a good option, as no drying is required for the material and the size reduction is sufficient to improve hydrolysis of cell wall carbohydrates.

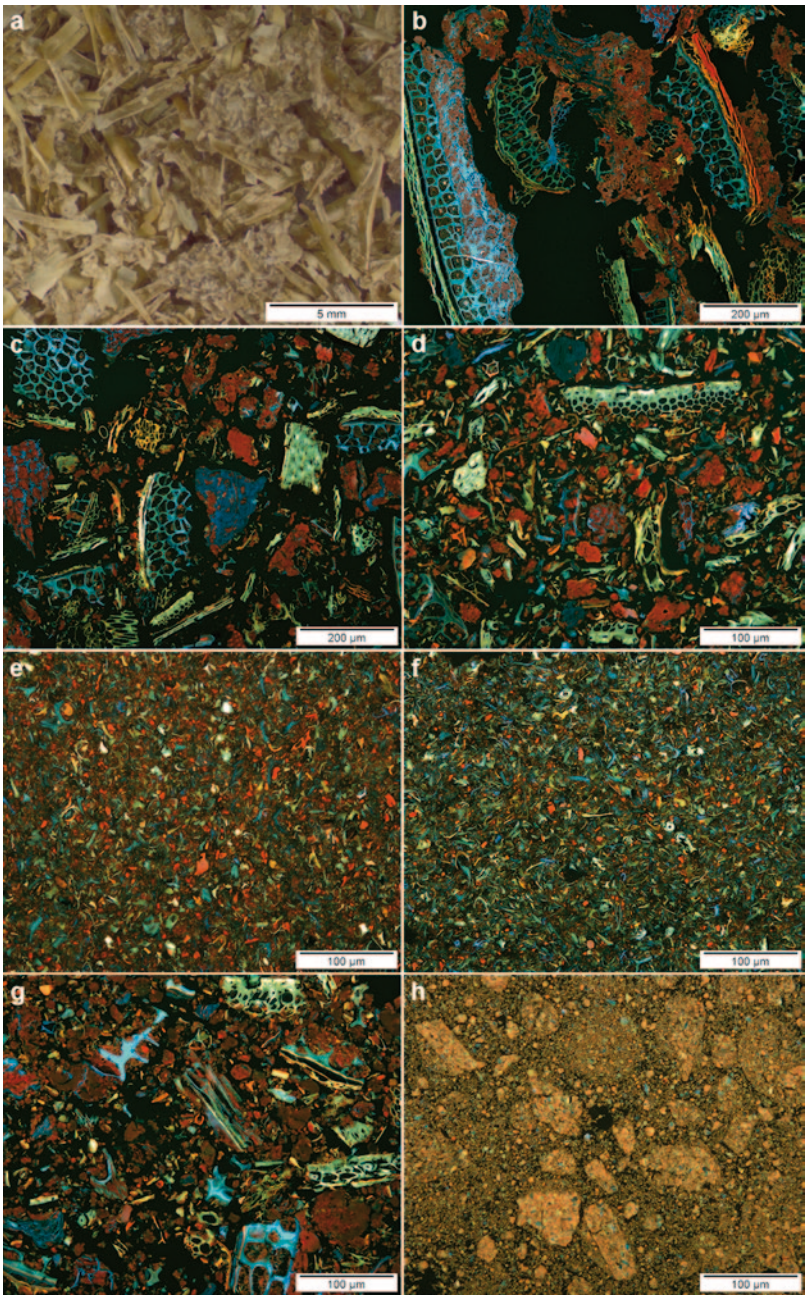

Fig. 1.9 Microstructure of **a, b** initial unmilled brewer's spent grain and brewer's spent grain milled with **c** pin-disc mill, **d** TurboRotor, **e** Masuko, **f** microfluidizer, **g** ball mill for 1 h and **h** ball mill for 24 h. Image **a** is a stereomicrograph and images **b**–**h** are light microscopy images of samples stained with Acid Fuchsin and Calcofluor showing protein *red* and cell wall β-glucan *blue,* respectively. Due to autofluorescence, lignified cell walls appear *yellowish-green*. (Reproduced from Niemi et al. 2012a with the permission from the publisher)

1.4.2 Enzymatic Processing

1.4.2.1 The Release of Ferulic Acid Metabolites from Wheat Aleurone Is Increased by Enzymatic Disintegration

In wheat grain, the nutritionally interesting component, namely dietary fibre, is concentrated in the cell walls of the aleurone layer. These cell walls are present in bran and consist mainly of AX with β-glucan, cellulose and phenolic acids as minor components (Bacic and Stone 1981). AX of wheat aleurone is highly esterified with phenolic acids, ferulic acid as the most abundant substituent. These phenolic compounds are carried by AX as co-passengers into the digestive tract. In fact, the health benefits of wheat aleurone may not be due only to the fermentation of its dietary fibre but also to the action of its co-passengers. The physiological activity of the different parts of the gut can be affected by the phenolic co-passengers released from cereal matrix (Jones 2010). Mechanically or enzymatically processed wheat bran has been shown to increase the bioaccessibility of phenolic compounds in an in vitro model of the upper gastrointestinal tract (Fardet 2010; Hemery et al. 2010a).

The microstructural integrity of wheat aleurone has been linked also to its colonic fermentability (Rosa et al. 2013a). The disintegration of aleurone layer fractions was carried out by dry processing (grinding) and wet processing (treatment with xylanase or xylanase and feruloyl esterase). The microstructure of the treated fractions was visualized by microscopy (Fig. 1.10). The native aleurone fraction comprises clusters of c. 5–8 intact aleurone cells (Fig. 1.10a, b). Ground aleurone fraction contained fragments of aleurone cell walls and protein released from the broken cells, but also recognisable cell clusters from the aleurone layer (Fig. 1.10c, d). The autofluorescence observed in the native and ground aleurone fractions was due to ferulic acid bound to AX in the aleurone cell walls (Fig. 1.10b, d).

The size of the aleurone layer fragments was not pronouncedly influenced by the treatments with xylanase or xylanase and feruloyl esterase (Fig. 1.10e–h). However, the composition and the appearance of the aleurone cell walls were clearly affected by the enzyme treatments. As indicated by the lower stainability with Calcofluor, β-glucan in the aleurone cell walls was degraded in both enzymatic treatments (Fig. 1.10e, g). The enzyme-treated aleurone cell walls were also thinner in comparison to the cell walls present in the starting material. Especially the combined influence of xylanase and feruloyl esterase plasticized the cell walls and made them appear in wrinkles (Fig. 1.10g). The degradation of both AX and β-glucan was confirmed by chemical analyses. Enzymatic treatment was also noticed to release protein from aleurone cells. In addition, the loss of autofluorescence due to enzyme treatment indicated the release of ferulic acid from the aleurone cell walls. In the xylanase-treated sample, the autofluorescence was lost from the periclinal cell walls leaving anticlinal cell walls between aleurone cells intact (Fig. 1.10f). The treatment with xylanase and feruloyl esterase was found to decrease also the autofluorescence of these anticlinal cell walls (Fig. 1.10h). The higher solubilization of ferulic acid in these two fractions was confirmed by higher quantities of conjugated and free forms of ferulic acid present in the enzymatically treated samples.

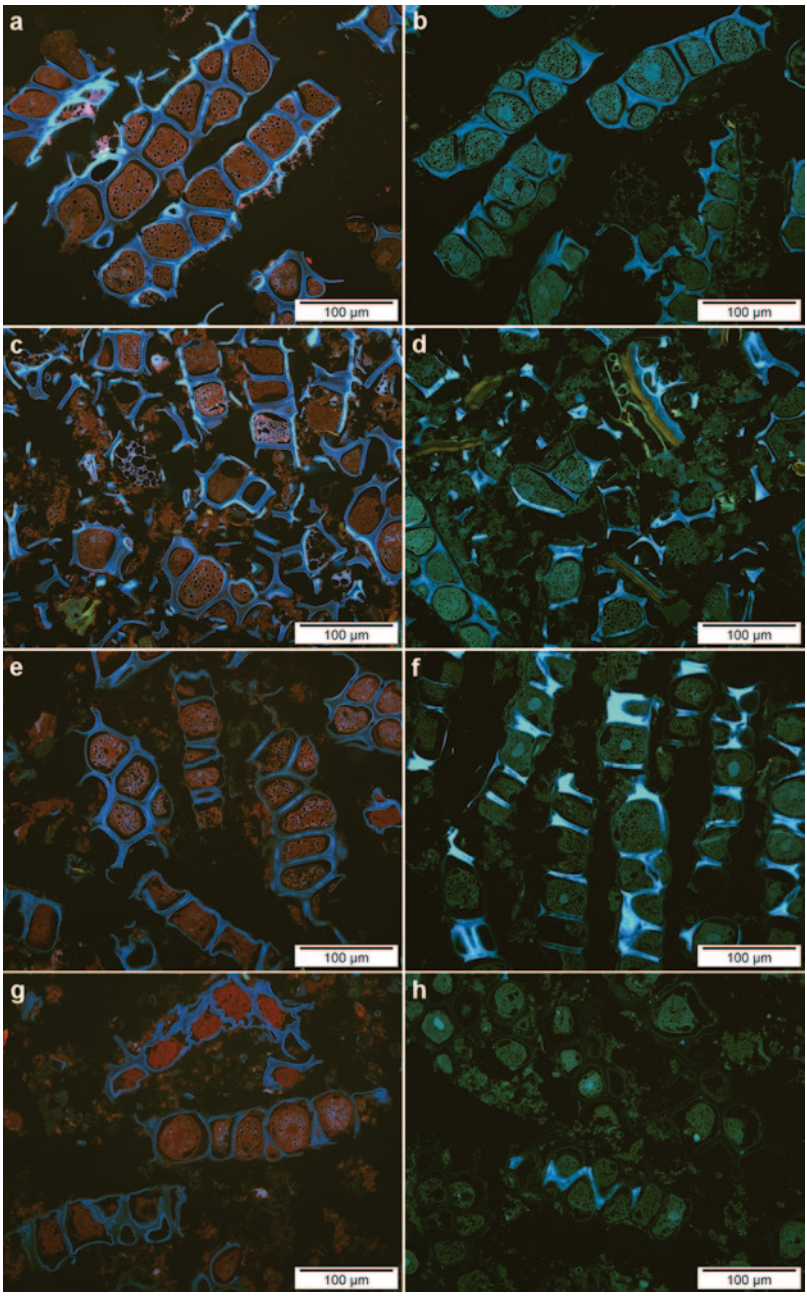

Fig. 1.10 Microstructure of wheat aleurone fractions **a, b** as native, **c, d** as ground, **e, f** as treated with xylanase and **g, h** as treated with xylanase and feruloyl esterase. Images **a, c, e** and **g** show cell wall β-glucan *blue* stained with Calcofluor and protein *red* stained with Acid Fuchsin. Images **b, d, f** and **h** show autofluorescence (λ_{ex} = 400–400 nm, λ_{em} > 455 nm) mainly due to the aromatic structures of ferulic and *para*-coumaric acids present in the aleurone cell walls. (Adapted with permission from Rosa et al. 2013a. Copyright 2014 American Chemical Society)

Fermentability of the aleurone samples was tested in the in vitro colon model. The fermentation of ground aleurone fraction showed increased production of total gas and short-chain fatty acids in comparison to the native aleurone fraction. This can be taken as an indication of enhanced microbial accessibility due to decreased particle size. The enzymatic disintegration of the aleurone fraction increased the formation of the colonic metabolites of ferulic acid (especially phenylpropionic acids) as a consequence of ferulic acid released by the enzymatic hydrolysis but did not change significantly the formation of short-chain fatty acids. Combined with the earlier results on the influence of the inhibition of lipid peroxidization by the bioavailable ferulic acid (Rosa et al. 2013b), these results indicate that bioactive compounds released from processed aleurone can benefit both in the upper and lower part of the digestive tract.

1.4.2.2 Microstructural Changes in Brewer's Spent Grain Due to Milling Pretreatment and Enzymatic Hydrolysis of Carbohydrates

Cost-efficient separation of components is needed for the valorization of brewer's spent grain, a remarkable side stream of brewing industry consisting mainly of water insoluble structures of malt. In the study of Niemi et al. (2012b), a two-step enzymatic hydrolysis of brewer's spent grain was carried out, and along with the compositional analyses, the microstructure of the material was monitored throughout the procedure by light microscopy. Prior to the sequential treatments with carbohydrate- and protein-degrading enzymes, brewer's spent grain was wet milled with a Masuko grinder. The intact cellular structures of husk, grain outer layers and aleurone present in the unmilled brewer's spent grain were broken in Masuko grinding, and the particle size was significantly decreased (Fig. 1.11a, b).

As the result of carbohydrase treatment carried out with two enzyme preparations, 26% of the brewer's spent grain was solubilized. No Calcofluor-stainable, β-glucan-containing cell walls were detected after this treatment (Fig. 1.11c). The non-lignified endosperm cell walls were more accessible for enzymes in comparison with the grain outer layers. The higher resistance to enzymatic hydrolysis of the grain outer layers may be due to their higher degree of arabinose substitution (Beaugrand et al. 2005). Despite the proteinase side activity of one of the carbohydrases, the protein stained by Acid Fuchsin was concentrated due to hydrolysis of carbohydrates.

The degree of solubilization of the protease treatment step was 40%, and at this point, 93% of original protein present in brewer's spent grain was solubilized. The removal of protein was detected by microscopy as a clear decrease of particles stained with Acid Fuchsin in the insoluble residue (Fig. 1.11e). Thus, the protein of brewer's spent grain consisting mainly of water-insoluble barley storage proteins and precipitated protein from wort boiling was efficiently hydrolysed in this treatment. The orange particles visible in the insoluble residue after the protease treatment should not be mistaken as protein. On the basis of their thin and longish shape, they most probably are fragments of cutin. Cutin is a polyester present in the hy-

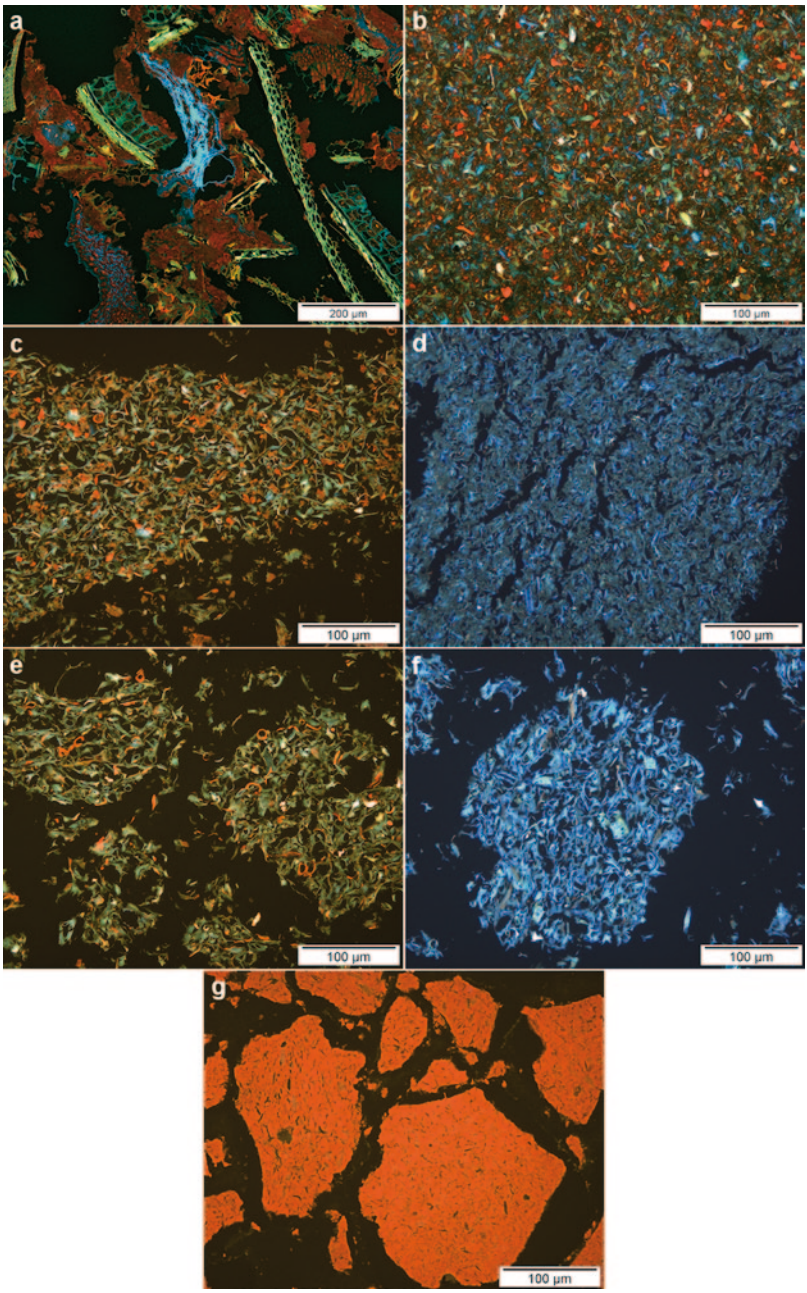

Fig. 1.11 Microstructure of brewer's spent grain and the enzyme-treated fractions: **a** unmilled brewer's spent grain, **b** Masuko-milled brewer's spent grain, **c** and **d** insoluble residue after the carbohydrase treatment, **e**–**f** insoluble residue after the protease treatment and **g** protease-alkaline extracted fraction. In the images **a**–**c**, **e** and **g**, protein and cell wall β-glucan stained with Acid Fuchsin and Calcofluor appear *red* and *blue,* respectively. Due to autofluorescence, lignified cell walls appear *yellowish-green*. Images **d** and **f** show autofluorescence (λ_{ex} = 330–385 nm, λ_{em} > 420 nm) mainly due to the aromatic structures. (Adapted with permission from Niemi et al. 2012a. Copyright 2014 American Chemical Society)

drophobic cuticle layers of the grain outer parts. Cutin fragments, which are visible due to their autofluorescence, became easier to distinguish after removal of protein.

The autofluorescence of the insoluble hydrolysis residue was increased by the protease treatment (Fig. 1.11d, f). This is according to the enrichment of lignin along with the enzymatic hydrolyses. In fact, the major autofluorescent compound in brewer's spent grain is lignin, although several other aromatic compounds are present as well (Jay et al. 2008). The autofluorescence of lignin may become more visible as the protein and carbohydrates covering it were removed. The supernatant containing the solubilized material from the protease treatment was further acidified in order to precipitate lignin. The yield of this precipitate was 11 % of the solubilized material. In this material, precipitated proteinaceous material presumably covered lignin and thus its autofluorescence (Fig. 1.11g).

The two-step enzymatic treatment solubilized 66 % of brewer's spent grain.

Carbohydrates were partially resistant to the action of the carbohydrate-degrading enzymes, whereas the proteins were almost completely solubilized by the protease treatment. Further analysis of the supernatant from protease treatment proved the presence of lipids and lignans in this fraction.

1.4.3 Fractionation Processing

1.4.3.1 Enrichment of Grain Outer Layers and Aleurone Cell Walls Present in Wheat Bran by Electrostatic Separation

The utilization of wheat bran could be increased by fractionating this currently undervalued side-stream product into purified fractions. One of the promising dry-fractionation technologies is electrostatic separation, in which finely ground material is separated depending on charge acquired in tribo-electrification, and the positively and negatively charged fractions can be collected separately (Stone and Minifie 1988; Bohm et al. 2003). In the study of Hemery et al. (2011b), two types of ultrafine wheat bran was fractionated using electrostatic separation, and the microstructure composition and the particle size distribution of the resulting fractions were analysed.

In addition to protein and the fragments of individual bran layers, the cryogenically ground wheat bran contains composite particles, in which the pericarp, testa and aleurone layers are attached to each other (Fig. 1.12a). The material attracted by the negative electrode in the electrostatic separation consisted mainly of rather large fibre-rich particles originating from the pericarp and to smaller extent the cell walls and cell contents originating from the aleurone layer (Fig. 1.12b). Accordingly, the composition of this fraction showed high contents of arabinose and dimers and trimer of ferulic acid, which are characteristic for the complex heteroxylans present in the pericarp (Fincher and Stone 1986). The cell walls and proteinaceous cell contents of the aleurone layer were enriched in the positive fraction, although some smaller pericarp fragments were also present (Fig. 1.12c). In line with the microstructure, the compositional analysis underlined aleurone as the origin of the particles present in this positive fraction. The β-glucan and ferulic acid monomers typical to aleurone cell walls and folates and phytates localized in aleurone cells (Pomeranz 1988) were

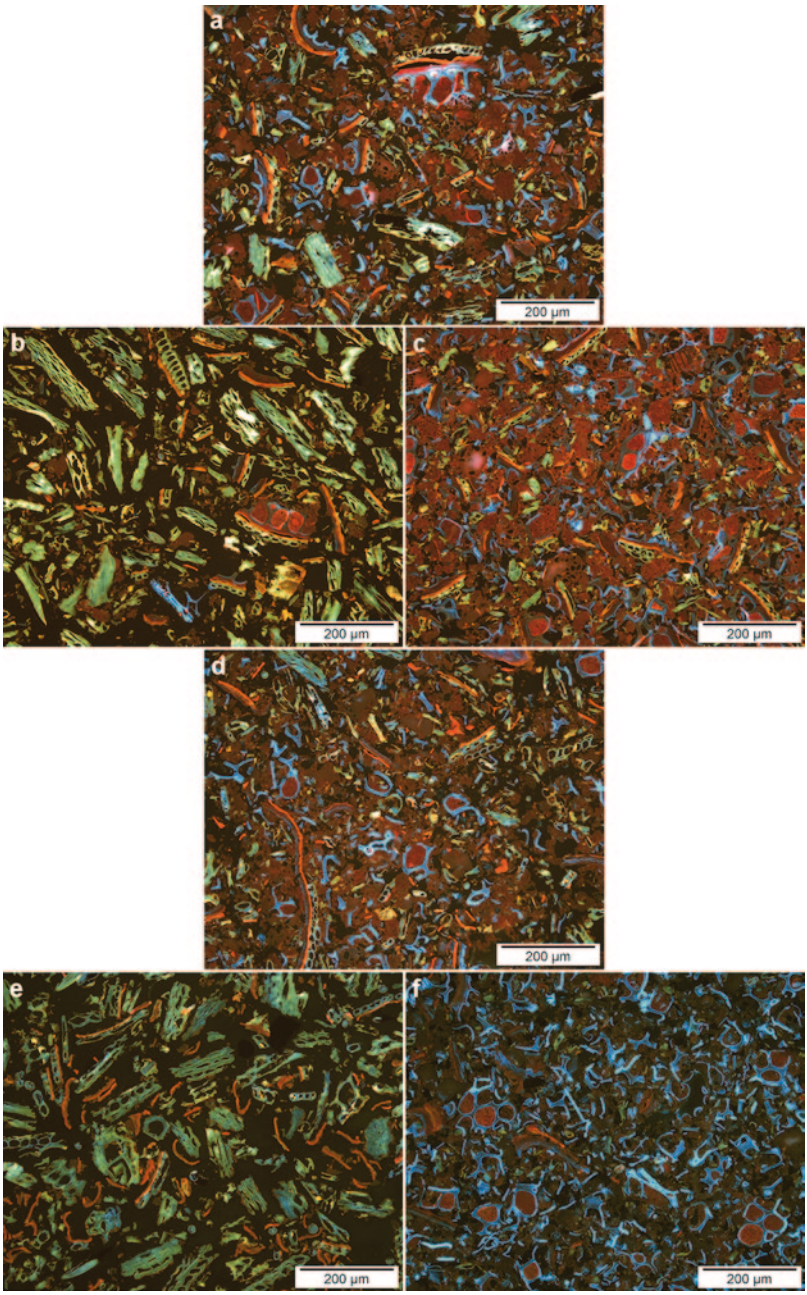

Fig. 1.12 Micrographs of ground wheat bran samples and their fractions obtained after two or three successive steps of electrostatic separation: **a** the cryogenically ground bran sample and its **b** negative and **c** positive fractions and **d** bran sample ground three times in ambient temperature and its **e** negative and **f** positive fractions. The cross sections of the resin-embedded powders were stained with Calcofluor and Acid Fuchsin. Aleurone cell walls appear *blue* and protein *brownish-red*. Fibre-rich material from the pericarp appears as *light greenish-yellow,* testa appears *reddish-orange,* whereas starch and aleurone granules stay unstained *(black)*. (Reproduced from Hemery et al. 2011b with the permission from the publisher)

enriched in this fraction. The negative fraction exhibited higher median particle size (88.3 μm) in comparison to the positive fraction (26.5 μm). However, the composite particles made of adhering bran layers were present in both purified fractions. This indicates that these composite particles limited the enrichment of bran components. As bran tissues are more efficiently dissociated in grinding at ambient temperature in comparison to cryogenic grinding (Hemery et al. 2011a), electrostatic separation was carried out with an ultrafine bran sample produced by ambient grinding.

The wheat bran ground in ambient temperature contained structures originating from the pericarp, testa, aleurone and starchy endosperm (Fig. 1.12d). Almost all the pericarp and aleurone particles were apart from those of the testa, and no composite particles were observed. The negative fraction obtained after three successive electrostatic separations was composed of fibre-rich pericarp particles and fragments of the testa (Fig. 1.12e). Only few cell wall structures from the aleurone or starchy endosperm were present in this fraction. The compositional analysis supported the enrichment of pericarp structures and the decrease of particles from the aleurone as the contents of arabinose, ferulic acid dimers and ferulic acid trimer were higher and the contents of aleurone cell contents such as folates, phytic acid, and ash were lower than in the fractions of positively charged particles. The positively charged fraction obtained after three successive electrostatic separations consisted mainly of aleurone cell wall fragments, loose protein matrix and intact aleurone cells as single or in entities of 2–4 cells (Fig. 1.12f). Few composite particles with a fragment of the testa attached to aleurone cell walls and some small pericarp particles were present in this fraction. The enrichment of structures originating from the aleurone and starchy endosperm in the positively charged fraction was reflected as the enrichment of β-glucan, protein, *para*-coumaric acid, ferulic acid monomers and starch.

In addition to the compositional enrichment, the median particle size was also affected by the electrostatic separation. The positively charged fraction was composed of finer particles than the corresponding negatively charged fraction. This indicates the resistance of pericarp fragments to milling as these were enriched to negative fraction.

Electrostatic separation allows the fractionation of wheat bran to fractions with very different biochemical compositions and grain tissue proportions depending on the degree of the dissociation of the starting material. It enables the production of fractions containing the pericarp which are thus rich in insoluble dietary fibre or fractions containing mainly structures from aleurone cell walls which are rich in β-glucan and ferulic acid monomer. These fractions could serve as food ingredients, or they could be purified further with other processing methods.

1.4.4 Malting

1.4.4.1 Using Starter Culture as a Tool to Reduce Extracellular Polymeric Substances Accumulation in Barley Kernel Tissues During Malting

Microbial communities are an integral part of all cereals (Fig. 1.13a–c). The natural microbiota of grains has great impact on the technical performance and the quality of cereal products (Noots et al. 1999; Laitila et al. 2007a). The steeping in water

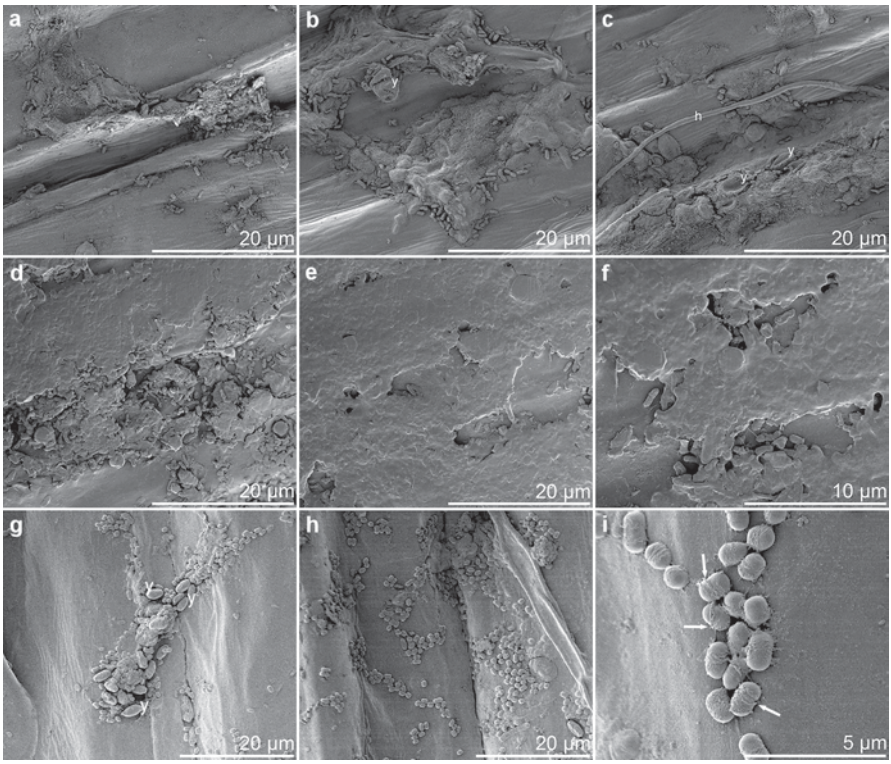

Fig. 1.13 Scanning electron micrographs of surfaces of the epidermis layers of barley kernels. **a**–**c** Clusters of bacteria on a dry kernel of barley, collapsed fungal hyphae *(h)* and yeast cells *(y)*. **d**–**f** 2 days old biofilms on a steeped barley kernel. Most of the kernel surface and the attached bacteria are embedded in amorphous slime. **g**–**i** 2 days old biofilms on a barley kernel steeped in the presence of the starter *Lactobacillus plantarum* E76 with *Wickerhamomyces anomalus* C565 (synonym *Pichia anomala*). Cells looking like *L. plantarum (short rods)* have colonized the kernel surface. In **g**, yeast cells *(y),* putative *W. anomalus,* are in close proximity to putative *L. plantarum* cells. In **i**, the belt-like structures of *L. plantarum* cells are visible *(white arrows)*. (Images by Mari Raulio, unpublished)

stimulates the microbiota in the barley kernel to grow and to produce extracellular substance (Fig. 1.3d–f). Biofilms and extracellular polymeric substances (EPS) can deteriorate grain germination (Kelly and Briggs 1992; Doran and Briggs 1993; Laitila et al. 2007a) and be harmful in brewing by reducing the separation of wort and filterability of the mash (Laitila et al. 1999).

We previously reported changes in ultrastructural details of the natural microbiota of barley kernels before and after the steeping step of malting by field emission scanning electron microscopy (FESEM; Raulio et al. 2009). Amending the steeping water with a culture of *Lactobacillus plantarum* E76 reduced the accumulation of EPS during the subsequent steeping. The strain of *L. plantarum* as a starter culture was capable of colonizing the tissues of barley kernel (Raulio et al. 2009; Fig. 1.13g–i). This colonization resulted into reduced growth of slime-producing

bacteria. A positive effect on mash filterability was also observed. Lactic acid starter bacteria have been shown effective in controlling undesirable microbial contaminants, particularly pseudomonads and the *Fusarium* fungi in malting elsewhere (reviewed by Lowe and Arendt 2004; Laitila et al. 2006).

Laitila et al. (2007b) have shown that adding the yeast *Wickerhamomyces anomalus* C565 (synonym *Pichia anomala*) neither noticeably affected bacterial growth in grain nor disturbed the germination. The final malts were good quality, but the separation of wort slowed down. On the other hand, use of *W. anomalus* as starter culture suppressed the growth of contaminating yeasts and filamentous fungi. Based on this knowledge, we decided to use two starters simultaneously, *Lactobacillus plantarum* E76 and *W. anomalus* C565 in the steeping water. When we examined biofilms on the barley kernel surfaces with FESEM, we found that both the *L. plantarum* and the *W. anomalus* strains had entered the husk layer of the barley grain and adhered on the surfaces of the kernel suppressing the growth of the EPS-producing bacteria (Laitila et al. 2011; Fig. 1.13g–i).

1.4.5 Baking

1.4.5.1 Fermentation

In the sourdough process, flour and water are fermented with microbes originating from preceding sourdough, commercial starter culture, bakery equipment or from flour. Using sourdough as a part of the dough is an ancient way to improve flavour, texture and microbiological shelf life of bread, and this technique is widely utilized in whole grain rye baking (Valjakka et al. 2003). What comes to wheat baking, the use of sourdough is less common. Products made from endosperm wheat flour have usually mild flavour, and thus the addition of acidic sourdough has a great influence on it. Although the sourdough process is rather widely studied, the localization of the bacterial cells in the cereal material is not well detected and documented.

The location of microbes and exopolysaccharides as well as the ultrastructure of microorganisms adhering onto the wheat bran surface after fermentation can be demonstrated using electron microscopy. In our study, first the structure of native wheat bran was examined (Fig. 1.14). This revealed the structures present in wheat bran, namely the outer layers including pericarp, aleurone and sub-aleurone layers. The pericarp was a distinguishable layer, and some starch granules originating from the inside of the grain were attached on it. The still alive cells of the aleurone had distinguishable, thick cell walls enclosing the protein and lipids. Starchy endosperm cells were also observed in these native, non-fermented wheat bran samples. The cells of the starchy endosperm were packed with starch granules and storage protein and have quite thin walls.

In the fermented wheat bran, lactic acid bacteria and yeast cells were observed attached to wheat aleurone cell walls and other surfaces of wheat bran (Fig. 1.15). Some bacterial cells were noticed to be attached on a surface of starch granules.

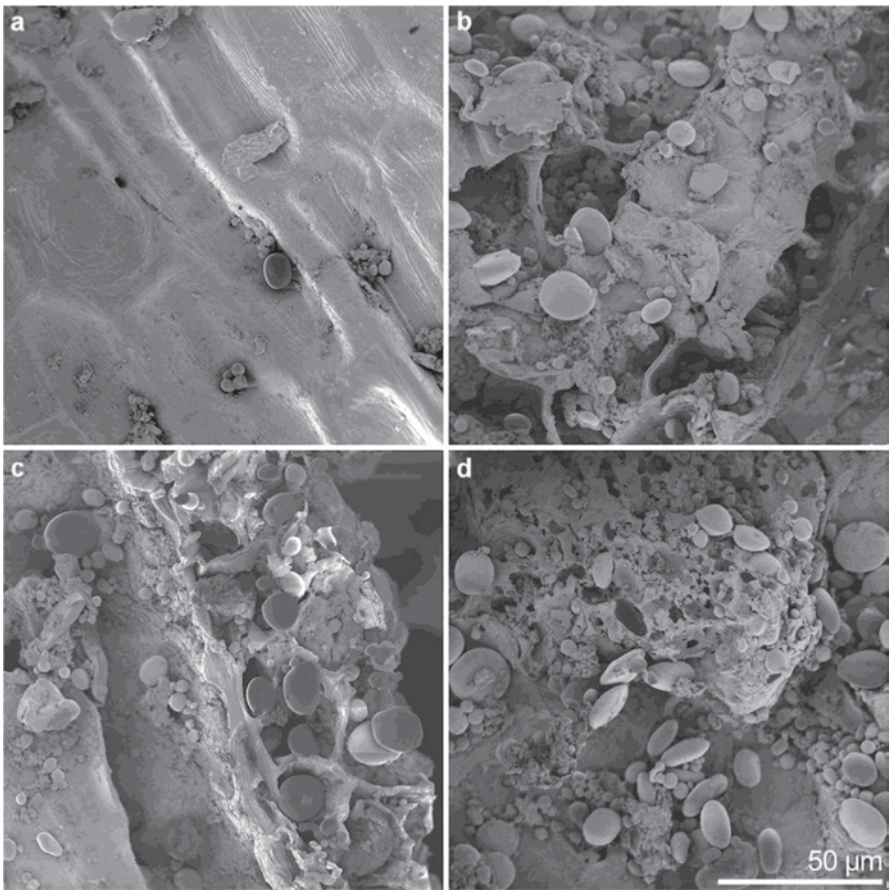

Fig. 1.14 Scanning electron micrographs of native wheat bran. **a** The inner pericarp. **b** and **c** The structure of aleurone and sub-aleurone layers. **d** Cells of the starchy endosperm. (Images by Mari Raulio, unpublished)

1.4.5.2 Microstructure of Pasta Made with Wheat Flour Rendered Gluten-Free

There is a growing demand for novel gluten-free products with acceptable flavour and structure, and thus new technologies need to be developed. One option is to render gluten-containing wheat flour to gluten-free one by lactic acid bacteria fermentation and fungal proteases (Rizzello et al. 2007). The major technological challenge is achieving adequate structural properties in a product lacking the viscoelastic properties of gluten proteins. Curiel et al. (2014) have studied the structure of pasta made with wheat flour, which is rendered gluten-free, in comparison to commercial durum wheat and gluten-free pastas. In addition, pre-gelatinized rice flour was used as a part of the experimental gluten-free pasta to enable the use of same production procedure as routinely applied for durum wheat pasta (Arendt et al. 2008).

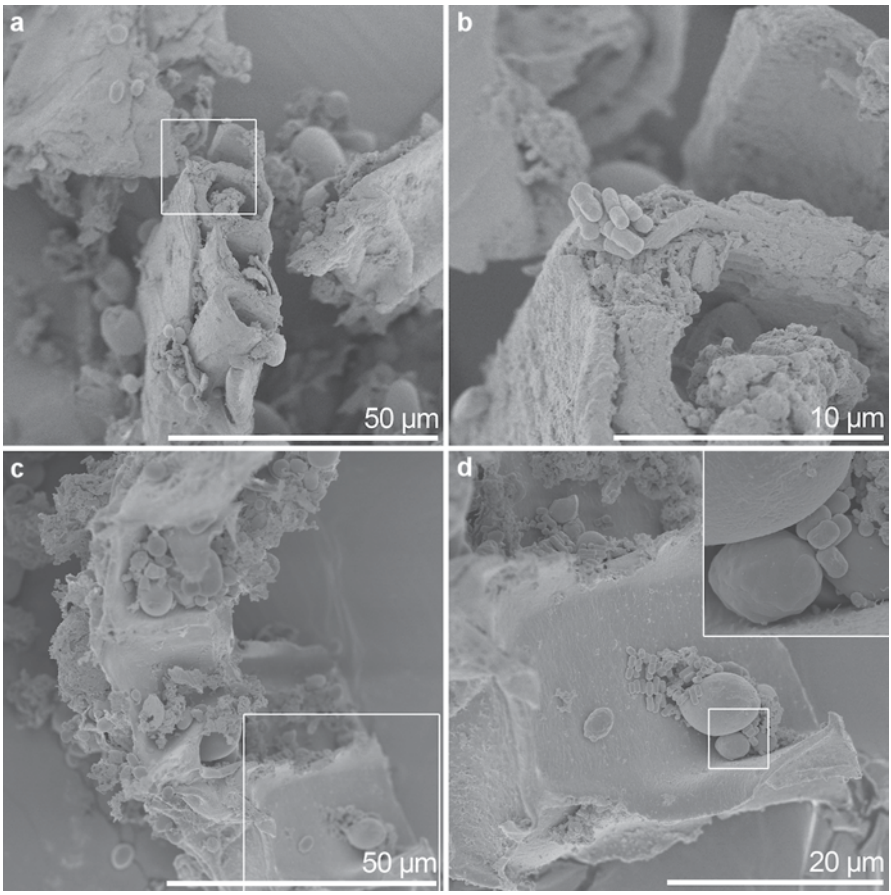

Fig. 1.15 Scanning electron micrographs of wheat bran inoculated with lactic acid bacteria and fermented for 20 h. **a** A low magnification micrograph of a piece of aleurone layer. **b** An enlargement of an area from **a** showing a group of lactic acid bacteria attached on the aleurone cell wall. **c** A low-magnification micrograph of a piece of bran. **d** An enlargement of an area from **c** showing the surface of the bran colonized by lactic acid bacteria and yeasts. (Images by Mari Raulio, unpublished)

The microstructure of cooked pasta samples was examined using light microscopy (Fig. 1.16). In the experimental gluten-free pasta, only few and scattered protein spots were observed (Fig. 1.16a). These protein aggregates were likely derived exclusively from rice flour on the basis of the very low gluten content present after fermentation and enzymatic hydrolysis. In the commercial durum wheat pasta, an intact protein network was detected (Fig. 1.16c). Starch granules were entrapped in this protein network (Fig. 1.16d). Similarly to the experimental gluten-free pasta, the commercial gluten-free pasta contained only few protein aggregates (Fig. 1.16e). Due to the lack of protein network, starch granules were not surrounded by protein matrix in either of the gluten-free pasta samples (Fig. 1.16b, f). Although starch

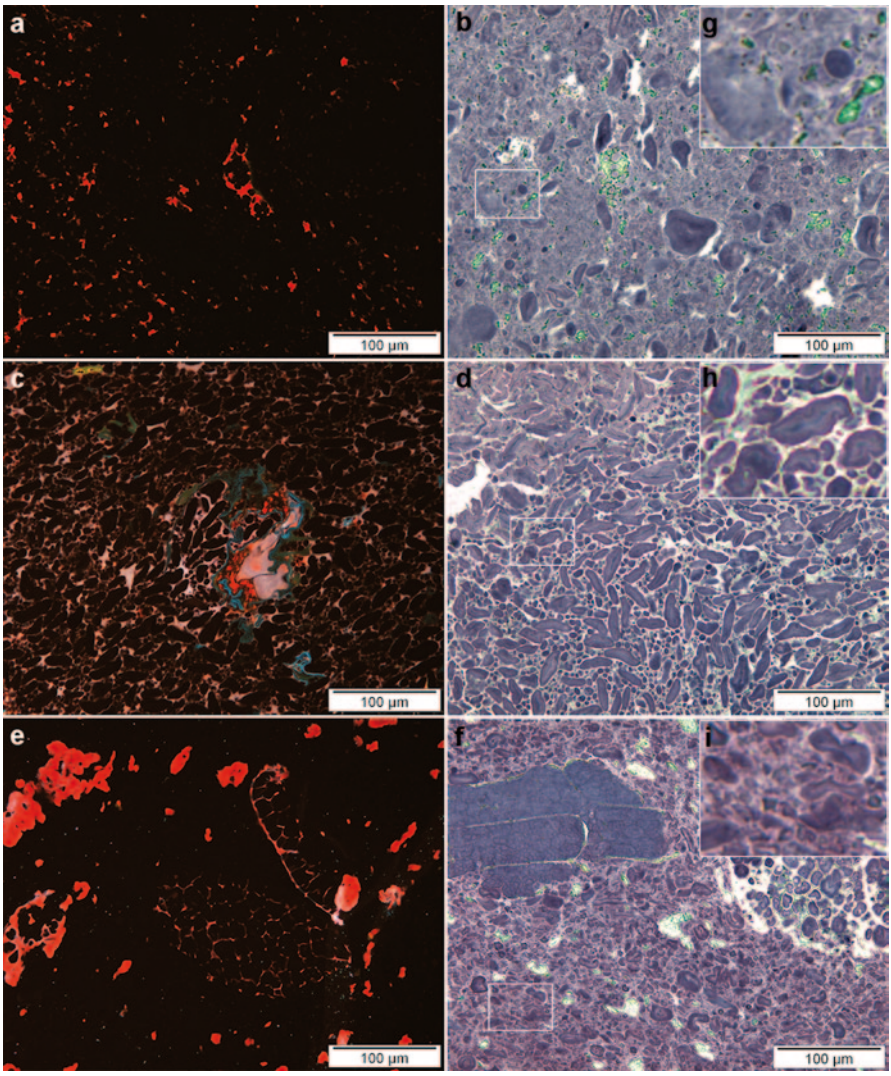

Fig. 1.16 Micrographs of cross sections of pasta samples. **a** and **b** Experimental gluten-free pasta. **c** and **d** Commercial durum wheat pasta. **e** and **f** Commercial gluten-free pasta. In the fluorescence images (**a**, **c** and **e**), cell walls β-glucan stained with Calcofluor appear *blue,* proteins stained with Acid Fuchsin appear *red* or *pink* and starch is unstained and appears *black*. In the bright field images (**b**, **d** and **f**), protein shows *light green* and the amylose component of starch *blue* and amylopectin *brown*. The starch granules are represented in the enlarged framed area (**g**, **h**, and **i**). (The image from Curiel et al. 2014 is reproduced with the permission from the publisher)

granules in all three samples were gelatinized, they were more swollen and deformed in the experimental or commercial gluten-free pastas in comparison to durum wheat pasta (Fig. 1.16g–i). In the gluten-free pasta samples, the leakage of amylose from the starch granules confirmed the further gelatinization. Thus, the

gluten network present in durum wheat pasta probably prevented the swelling and further deformation of starch granules.

All in all, the microstructure of the experimental gluten-free pasta was very similar to that of commercial gluten-free pasta, even though the former contained wheat flour. The experimental gluten-free pasta was intermediate between the two commercial samples in the structural characteristics such as hardness, gumminess and chewiness. It also had faster water absorption and shorter optimal cooking time. Most probably the structure of experimental gluten-free pasta despite the lack of gluten network was maintained by pre-gelatinized rice flour, which has been reported to improve the texture of gluten-free pasta (Mastromatteo et al. 2011). As the sensory properties of the experimental gluten-free pasta were also acceptable, fermented, gluten-free wheat flour appears as a promising ingredient for gluten-free pasta and also other types of food products.

1.4.5.3 The Effect of Alkylresorcinols on Microstructure of Bread

Addition of whole grain flour or bran to dough increases not only the fibre content but also the amount of alkylresorcinols in final breads. Alkylresorcinols are phenolic compounds naturally found in high amounts in the outer layers of wheat and rye kernels. It is known that whole grain flour or bran influences the technological properties of bread by decreasing volume and making the structure more compact (Katina 2003). However, the impact of alkylresorcinols on bread properties is not well understood. In the study of Andersson et al. 2011, the influence of alkylresorcinols purified from rye, wheat and durum wheat on yeast-leavened bread microstructure as well as on bread volume, height and porosity was demonstrated.

In order to investigate the effect of alkylresorcinols on the microstructure, pieces from breads with added alkylresorcinol were fixed, embedded into resin and examined by light microscopy. It was noticed that addition of purified alkylresorcinol extracts from rye, wheat or durum wheat had a clear influence on the degree of starch granule aggregation. In the breads with 1.0% added alkylresorcinol, starch granules were the most aggregated, while in the breads with 0.1% added alkylresorcinol, only minor effects on starch granule aggregation were observed and the breads resembled the control samples with no alkylresorcinol added (Fig. 1.17). Starch granule aggregation in breads with 0.5% added alkylresorcinol was intermediate in comparison with breads containing 0.1 and 1.0% added alkylresorcinol. Starch granules also were more swollen in breads with higher contents of added alkylresorcinol.

In addition to higher degree of starch aggregation, breads with 1.0% added alkylresorcinol showed separation of the protein phase. Breads with 0.1% added alkylresorcinol had a protein phase showing a similar dispersion to that observed in reference samples with no added alkylresorcinol (Fig. 1.17a, b, d, f). However, in the breads with 0.5 and 1.0% added alkylresorcinol, the separation of the protein phase increased along with the higher content of added alkylresorcinols (Fig. 1.17c, e, g). Separation of the protein and starch phases may be a consequence of starch

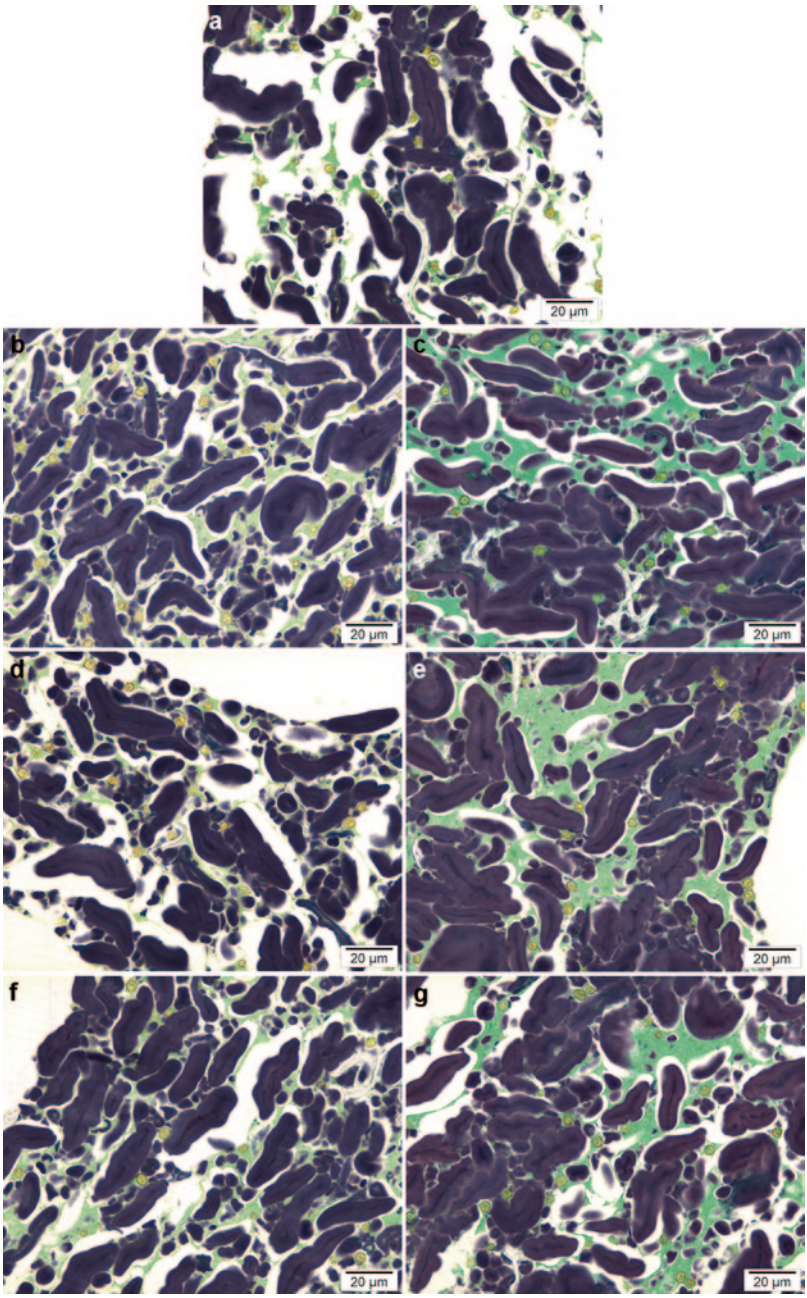

Fig. 1.17 Microstructure of wheat breads with added and purified alkylresorcinol extracts. **a** Reference bread without alkylresorcinol addition. **b** 0.1% rye alkylresorcinol added. **c** 1.0% rye alkylresorcinol added. **d** 0.1% wheat alkylresorcinol added. **e** 1.0% wheat alkylresorcinol added. **f** 0.1% durum wheat alkylresorcinol added. **g** 1.0% durum wheat alkylresorcinol added. Protein and starch were stained with Light Green and Lugol's iodine solution, respectively. Light Green stains protein *green,* and starch appears *dark blue* due to iodine staining. (Adapted with permission from Andersson et al. 2011. Copyright 2014 American Chemical Society)

swelling and may lead to uneven distribution of protein network. A similar effect on protein was observed with another protein stain, Acid Fuchsin. Based on the staining with Calcofluor, cell wall components were not clearly influenced by addition of alkylresorcinols.

Thus, addition of alkylresorcinols to dough seemed to change the protein–protein interaction and aggregation of starch granules in bread. Based on the data, it was not possible to deduce which one of the effects are direct consequences of alkylresorcinols or what are the mechanisms behind these effects. Alkylresorcinols are known to have different homologue composition for each cereal (Chen et al. 2004). However, the alkylresorcinols purified from wheat, rye and durum wheat had the same effects on bread microstructure.

The results of the microstructure of breads with added alkylresorcinols were well in line with the bread quality parameters. Irrespective of homologue composition of alkylresorcinols added, the breads with high amounts of added alkylresorcinols had a lower volume and a more compact structure compared with breads with no or low levels of added alkylresorcinols. Despite their amphiphilic nature, alkylresorcinols did not seem to have positive influence on the bread properties, although amphiphilic emulsifiers are frequently used in order to increase dough strength, give higher water absorption and improve crumb structure and gas retention during fermentation in the baking industry (Stampfli and Nersten 1995).

1.4.5.4 The Impact of Tyrosinase on the Microstructure of Gluten-Free Oat Dough

The network of gluten proteins accounts for the viscoelastic properties of wheat-based dough and the structure of final bread. Thus, the formation of adequate textural quality is the main challenge in baking gluten-free bread. The rheological properties of dough and bread could, however, significantly be altered by oxidative enzymes, which generate covalent bonds within or between cereal biopolymers (Gujral and Rosell 2004; Flander et al. 2008; Renzetti et al. 2010). Tyrosinase (EC 1.14.18.1) is an oxidative enzyme, which is capable of catalysing cross-linking biopolymers, such as tyrosine side chains in proteins and monophenols via their phenolic moieties (Xu 1997; Takasaki and Kawakishi 1997; Buchert et al. 2007; Selinheimo et al. 2007).

Flander et al. 2011 have studied the effect of tyrosinase on the dough microstructure and further on the quality of final bread. Light microscopy enabled the examination of individual flour component, namely protein and β-glucan. Proteins were stained with 0.2% (w/v) Xylidine Ponceau (Fig. 1.18a–c). Protein in the doughs treated with the highest tyrosine dosage (30 nkat tyrosine/g flour; Fig. 1.18c) seemed to be more aggregated than in the control sample and in the dough treated with lower dose of tyrosinase (Fig. 1.18a, b). To confirm this visual observation, the particle size distributions of proteins stained with Xylidine Ponceau were analysed from 20 images/sample by classifying the particles according to their area and calculating their number. The proteinaceous particles were divided into four different classes shown by false colours in Fig. 1.18d–f. The significantly ($p < 0.05$) higher

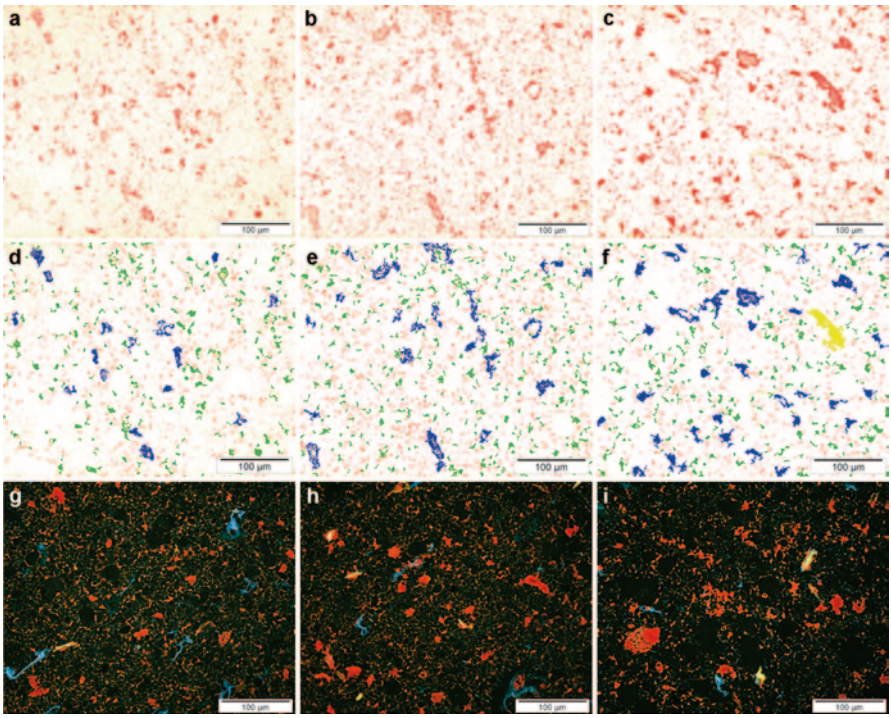

Fig. 1.18 Microstructure of oat doughs with reference treatment (**a**, **d**, **g**), with 10 nkat of added tyrosinase/g of flour (**b**, **e**, **h**) and with 30 nkat of added tyrosinase/g of flour (**c**, **f**, **i**). Images **a**–**c** represent doughs stained with Xylidine Ponceau showing protein *red***.** Images **d**–**f** show the particle size distribution of the proteins stained with Xylidine Ponceau. The size classes of protein particles were detected by image analysis and coded by colours as follows: 4–10 µm^2 *(red),* 10–100 µm^2 *(green),* 100–1000 µm^2 *(blue),* >1000 µm^2 *(yellow)*. Images **g**–**i** represent doughs stained with Acid Fuchsin and Calcofluor showing cell wall β-glucan *blue* and protein *red*. Scale bars = 100 µm. (Adapted with permission from Flander et al. 2011. Copyright 2014 American Chemical Society)

mean area and the mean count of protein particles between 100 and 1000 µm^2 (false coloured as blue in Fig. 1.8d–f) in the dough with 30 nkat tyrosinase/g flour proved the higher protein aggregation in comparison to the control dough. Together with the results of sodium dodecyl sulfate polyacrylamide gel electrophoresis (SDS-PAGE) separations of these dough proteins, this microscopical analysis suggests that the blue areas represent probably aggregated oat globulins formed by tyrosine-induced cross-linking.

The same protein aggregation was observed also in the staining with Calcofluor and Acid Fuchsin (Fig. 1.18g–i). Similar particle analysis as that of protein stained with Xylidine Ponceau was performed of cell wall structures stained with Calcofluor. The area and count of particles with diameter from 10 to 1000 µm^2 stained with Calcofluor decreased significantly ($p < 0.05$) as the dosage of tyrosine increased (Fig. 1.18g–i). This is in line with the fact that oat endosperm cell walls consist

mainly of β-glucan in oat (Henry 1987; Shewry et al. 2008). The effect of tyrosinase treatment on β-glucan may have been caused by the side activities of xylanase and β-glucanase present in the tyrosine preparation.

Possibly as a result of the more intensive protein aggregation, tyrosinase increased the firmness of the dough. In addition, tyrosinase improved the textural quality of final bread by increasing significantly the specific volume of the bread. The results thus indicate that cross-linking of oat globulins by tyrosinase is beneficial for improving the texture of gluten-free oat bread.

1.5 Summary

Microscopy techniques enable the examination of cereal grain structure on different levels. The structural features as well as the localization of grain components in whole grains as well as in their processing and end products can be carried out. Alongside with the chemical data and information on the processing and end use quality properties, the visualization of grain structures and composition assists in understanding the processability of cereal grains and products derived from them.

References

Andersson AA, Landberg R, Söderman T et al (2011) Effects of alkylresorcinols on volume and structure of yeast-leavened bread. J Sci Food Agric 91:226–232. doi:10.1002/jsfa.4174

Antoine C, Peyron S, Mabille F et al (2003) Individual contribution of grain outer layers and their cell wall structure to the mechanical properties of wheat bran. J Agric Food Chem 51:2026–2033. doi:10.1021/jf0261598

Arendt EK, Morrissey A, Moore MM, Dal Bello F (2008) Gluten-free breads. Gluten-free cereal products and beverages. Academic, Ireland, pp 289–319

Bacic A, Stone B (1981) Chemistry and organization of aleurone cell wall components from wheat and barley. Aust J Plant Physiol 8:475. doi:10.1071/PP9810475

Beaugrand J, Paës G, Reis D et al (2005) Probing the cell wall heterogeneity of micro-dissected wheat caryopsis using both active and inactive forms of a GH11 xylanase. Planta 222:246–257. doi:10.1007/s00425-005-1538-0

Beldman G, Hennekam J, Voragen AG (1987) Enzymatic hydrolysis of beer brewers' spent grain and the influence of pretreatments. Biotechnol Bioeng 30:668–671. doi:10.1002/bit.260300511

Benamrouche S, Crônier D, Debeire P, Chabbert B (2002) A chemical and histological study on the effect of (1→4)-β-endo-xylanase treatment on wheat bran. J Cereal Sci 36:253–260. doi:10.1006/jcrs.2001.0427

Bohm A, Bogoni C, Behrens R, Otto T (2003) Method for the extraction of aleurone from bran (US Patent US20030175384 A1)

Buchert J, Selinheimo E, Kruus K et al (2007) Using crosslinking enzymes to improve textural and other properties of food. In: Rastall R (ed) Novel enzyme technology for food applications. Woodhead Publishing, Cambridge, pp 101–139

Chau C, Wu S, Lee M (2007) Physicochemical changes upon micronization process positively improve the intestinal health-enhancement ability of carrot insoluble fibre. Food Chem 104:1569–1574. doi:10.1016/j.foodchem.2007.02.035

Chen Y, Ross AB, Aman P, Kamal-Eldin A (2004) Alkylresorcinols as markers of whole grain wheat and rye in cereal products. J Agric Food Chem 52:8242–8246. doi:10.1021/jf049726v

Cloetens L, Delaedt Y, Ollevier F et al (2008) The bifidogenic potential of arabinoxylo-oligosaccharides in healthy volunteers depends on the degree of polymerisation. Gastroenterology 134:A-692. doi:10.1016/S0016-5085(08)63232-1

Collins HM, Burton RA, Topping DL et al (2010) Variability in fine structures of noncellulosic cell wall polysaccharides from cereal grains: potential importance in human health and nutrition. Cereal Chem 87:272–282. doi:http://dx.doi.org/10.1094/CCHEM-87-4-0272

Courtin CM, Delcour JA (2001) Relative activity of endoxylanases towards water-extractable and water-unextractable arabinoxylan. J Cereal Sci 33:301–312. doi:10.1006/jcrs.2000.0354

Curiel JA, Coda R, Limitone A et al (2014) Manufacture and characterization of pasta made with wheat flour rendered gluten-free using fungal proteases and selected sourdough lactic acid bacteria. J Cereal Sci 59:79–87. doi:10.1016/j.jcs.2013.09.011

Doran P, Briggs D (1993) Microbes and grain germination. J Inst Brew 99:165–170

Dornez E, Cuyvers S, Holopainen U et al (2011a) Inactive fluorescently labeled xylanase as a novel probe for microscopic analysis of arabinoxylan containing cereal cell walls. J Agric Food Chem 59:6369–6375. doi:10.1021/jf200746g

Dornez E, Holopainen U, Cuyvers S et al (2011b) Study of grain cell wall structures by microscopic analysis with four different staining techniques. J Cereal Sci 54:363–373. doi:10.1016/j.jcs.2011.07.003

Duffus CM, Cochrane MP (1992) Grain structure and composition. In: Shewry PR (ed) Biochemistry, molecular biology and biotechnology. C.A.B. International, Wallingford, pp 291–317

Evers T, Millar S (2002) Cereal grain structure and development: some implications for quality. J Cereal Sci 36:261–284. doi:10.1006/jcrs.2002.0435

Fardet A (2010) New hypotheses for the health-protective mechanisms of whole-grain cereals: what is beyond fibre? Nutr Res Rev 23:65–134. doi:10.1017/S0954422410000041

Fincher GB (1976) Ferulic acid in barley cell walls: a fluorescence study. J Inst Brew 82:347–349. doi:10.1002/j.2050-0416.1975.tb06961.x

Fincher GB, Stone BA (1986) Cell walls and their components in cereal grain technology. Adv Cereal Sci Technol 8:207–295

Flander L, Rouau X, Morel M-H et al (2008) Effects of laccase and xylanase on the chemical and rheological properties of oat and wheat doughs. J Agric Food Chem 56:5732–5742. doi:10.1021/jf800264a

Flander L, Holopainen U, Kruus K, Buchert J (2011) Effects of tyrosinase and laccase on oat proteins and quality parameters of gluten-free oat breads. J Agric Food Chem 59:8385–8390. doi:10.1021/jf200872r

Forssell P, Kontkanen H, Schols HA et al (2008) Hydrolysis of brewers' spent grain by carbohydrate degrading enzymes. J Inst Brew 114:306–314. doi:10.1002/j.2050-0416.2008.tb00774.x

Freeman PL, Palmer GH (1984) The structure of the pericarp and testa of barley. J Inst Brew 90:88–94. doi:10.1002/j.2050-0416.1984.tb04244.x

Fulcher RG, Wong SJ (1980) Inside cereals—a fluorescence microchemical view. In: Inglett GE, Munck L (eds) Cereal. Food beverages. Academic, New York, pp 1–26

Fulcher R, O'Brien T, Lee J (1972) Studies on the aleurone layer I. Conventional and fluorescence microscopy of the cell wall with emphasis on phenol-carbohydrate complexes in wheat. Aust J Biol Sci 25:23–34. doi:10.1071/BI9720023

Glitsø LV, Gruppen H, Schols HA et al (1999) Degradation of rye arabinoxylans in the large intestine of pigs. J Sci Food Agric 79:961–969. doi:10.1002/(SICI)1097-0010(19990515)79:7<961::AID-JSFA311>3.0.CO;2-1

Gujral HS, Rosell CM (2004) Improvement of the breadmaking quality of rice flour by glucose oxidase. Food Res Int 37:75–81. doi:10.1016/j.foodres.2003.08.001

Harris N, Spence J, Oparka K (1994) General and enzyme histochemistry. In: Harris N, Oparka KJ (eds) Plant cell biology: a practical approach. Oxford University Press, Oxford, pp 51–68

Hemery YM, Anson NM, Havenaar R et al (2010a) Dry-fractionation of wheat bran increases the bioaccessibility of phenolic acids in breads made from processed bran fractions. Food Res Int 43:1429–1438. doi:10.1016/j.foodres.2010.04.013

Hemery YM, Mabille F, Martelli MR, Rouau X (2010b) Influence of water content and negative temperatures on the mechanical properties of wheat bran and its constitutive layers. J Food Eng 98:360–369. doi:10.1016/j.jfoodeng.2010.01.012

Hemery Y, Holopainen U, Lampi A-M et al (2011a) Potential of dry fractionation of wheat bran for the development of food ingredients, part I: influence of ultra-fine grinding. J Cereal Sci 53:1–8. doi:10.1016/j.jcs.2010.09.005

Hemery Y, Holopainen U, Lampi A-M et al (2011b) Potential of dry fractionation of wheat bran for the development of food ingredients, part II: electrostatic separation of particles. J Cereal Sci 53:9–18. doi:10.1016/j.jcs.2010.06.014

Hendriks ATWM, Zeeman G (2009) Pretreatments to enhance the digestibility of lignocellulosic biomass. Bioresour Technol 100:10–18. doi:10.1016/j.biortech.2008.05.027

Henry RJ (1987) Pentosan and (1→3),(1→4)-β-Glucan concentrations in endosperm and wholegrain of wheat, barley, oats and rye. J Cereal Sci 6:253–258. doi:10.1016/S0733-5210(87)80062-0

Hernanz D, Nuñez V, Sancho AI et al (2001) Hydroxycinnamic acids and ferulic acid dehydrodimers in barley and processed barley. J Agric Food Chem 49:4884–4888

Holopainen URM, Wilhelmson A, Home S et al (2012) Day-length effects on protein localisation affect water absorption in barley *(Hordeum vulgare)* grains. J Sci Food Agric 92:2944–2951. doi:10.1002/jsfa.5706

Holopainen URM, Wilhelmson A, Salmenkallio-Marttila M et al (2005) Endosperm structure affects the malting quality of barley (*Hordeum vulgare* L.). J Agric Food Chem 53:7279–7287. doi:10.1021/jf050349b

Jay AJ, Parker ML, Faulks R et al (2008) A systematic micro-dissection of brewers' spent grain. J Cereal Sci 47:357–364. doi:10.1016/j.jcs.2007.05.006

Jenkins DJ, Kendall CW, Vuksan V et al (1999) The effect of wheat bran particle size on laxation and colonic fermentation. J Am Coll Nutr 18:339–345

Jones JM (2010) Dietary fibre's co-passengers: is it the fibre or the copassengers? In: Van Der Kamp JW, Jones JM, McCleary BV, Topping DJ (eds) Dietary fibre: new frontiers for food and health. Wageningen Academic Publishers, Wageningen, pp 365–378

Jääskeläinen A-S, Holopainen-Mantila U, Tamminen T, Vuorinen T (2013) Endosperm and aleurone cell structure in barley and wheat as studied by optical and Raman microscopy. J Cereal Sci 57:543–550. doi:10.1016/j.jcs.2013.02.007

Katina K (2003) High-fibre baking. In: Cauvain S (ed) Bread making, Improving quality. Woodhead Publishing, Campbridge, pp 487–499

Kelly L, Briggs D (1992) The influence of the grain microflora on the germinative physiology of barley. J Inst Brew 98:395–400

Kent NL, Evers AD (1994) Technology of cereals, 4th ed. Pergamon Press Ltd., Oxford

Kiernan JA (2008) Histological and histochemical methods: theory and practice, 4th ed. Scion Publishing, Oxford

Laitila A, Schmedding D, van Gestel M, Vlegels P (1999) Lactic acid starter cultures in malting—An application for prevention of wort filtration problems caused by bacteria present in barley containing split kernels. Proc. 26th Eur. Brew. Conv. Congr. Cannes 1999. IRL Press, Oxford, pp 559–566

Laitila A, Sweins H, Vilpola A et al (2006) Lactobacillus plantarum and Pediococcus pentosaceus starter cultures as a tool for microflora management in malting and for enhancement of malt processability. J Agric Food Chem 54:3840–3851. doi:10.1021/jf052979j

Laitila A, Kotaviita E, Peltola P, Home S (2007a) Indigenous microbial community of barley greatly influences grain germination and malt quality. J Inst Brew 113:9–20

Laitila A, Sarlin T, Kotaviita E et al (2007b) Yeasts isolated from industrial maltings can suppress Fusarium growth and formation of gushing factors. J Ind Microbiol Biotechnol 34:701–713. doi:10.1007/s10295-007-0241-5

Laitila A, Sarlin T, Raulio M et al (2011) Yeasts in malting, with special emphasis on Wickerhamomyces anomalus (synonym *Pichia anomala*). Antonie Van Leeuwenhoek 99:75–84. doi:10.1007/s10482-010-9511-8

Leitch AR (1994) In situ hybridization: a practical guide. BIOS Scientific Publishers in association with the Royal Microscopical Society, Oxford

Lowe D, Arendt E (2004) The use and effects of lactic acid bacteria in malting and brewing with their relationships to antifungal activity, mycotoxins and gushing: a review. J Inst Brew 110:163–180

Maeda H, Ishida N (1967) Specificity of binding of hexopyranosyl polysaccharides with fluorescent brightener. J Biochem 62:276–278

Mastromatteo M, Chillo S, Iannetti M et al (2011) Formulation optimisation of gluten-free functional spaghetti based on quinoa, maize and soy flours. Int J Food Sci Technol 46:1201–1208. doi:10.1111/j.1365-2621.2011.02613.x

McCartney L, Marcus SE, Knox JP (2005) Monoclonal antibodies to plant cell wall xylans and arabinoxylans. J Histochem Cytochem 53:543–546. doi:10.1369/jhc.4B6578.2005

Mussatto SI, Dragone G, Roberto IC (2006) Brewers' spent grain: generation, characteristics and potential applications. J Cereal Sci 43:1–14. doi:10.1016/j.jcs.2005.06.001

Niemi P, Faulds CB, Sibakov J et al (2012a) Effect of a milling pre-treatment on the enzymatic hydrolysis of carbohydrates in brewer's spent grain. Bioresour Technol 116:155–160. doi:10.1016/j.biortech.2012.04.043

Niemi P, Tamminen T, Smeds A et al (2012b) Characterization of lipids and lignans in brewer's spent grain and its enzymatically extracted fraction. J Agric Food Chem 60:9910–9917. doi:10.1021/jf302684x

Noots I, Delcour J, Michiels C (1999) From field barley to malt: detection and specification of microbial activity for quality aspects. Crit Rev Microbiol 25:121–153

Olkku J, Salmenkallio-Marttila M, Swiens H, Home S (2005) Connection between structure and quality of barley husk. J Am Soc Brew Chem 63:17–22

Parkkonen T, Härkönen H, Autio K (1994) Effect of baking on the microstructure of rye cell walls and protein. Cereal Chem 71:58–63

Philippe S, Tranquet O, Utille J-P et al (2007) Investigation of ferulate deposition in endosperm cell walls of mature and developing wheat grains by using a polyclonal antibody. Planta 225:1287–1299. doi:10.1007/s00425-006-0422-x

Pomeranz Y (1973) Structure and mineral composition of cereal aleurone cells as shown by scanning electron microscopy. Cereal Chem 50:504–511

Pomeranz Y (1988) Chemical composition of kernel structures. In: Pomeranz Y (eds) Wheat: chemistry and technology. AACC, St Paul, pp 97–158

Raulio M, Wilhelmson A, Salkinoja-Salonen M, Laitila A (2009) Ultrastructure of biofilms formed on barley kernels during malting with and without starter culture. Food Microbiol 26:437–443. doi:10.1016/j.fm.2009.02.004

Renzetti S, Courtin CM, Delcour JA, Arendt EK (2010) Oxidative and proteolytic enzyme preparations as promising improvers for oat bread formulations: rheological, biochemical and microstructural background. Food Chem 119:1465–1473. doi:10.1016/j.foodchem.2009.09.028

Rizzello CG, De Angelis M, Di Cagno R et al (2007) Highly efficient gluten degradation by lactobacilli and fungal proteases during food processing: new perspectives for celiac disease. Appl Environ Microbiol 73:4499–4507. doi:10.1128/AEM.00260-07

Rosa N, Aura A, Saulnier L et al (2013a) Effects of disintegration on in vitro fermentation and conversion patterns of wheat aleurone in a metabolical colon model. J Agric Food Chem 61:5805–5816. doi:10.1021/jf4001814

Rosa NN, Dufour C, Lullien-Pellerin V, Micard V (2013b) Exposure or release of ferulic acid from wheat aleurone: impact on its antioxidant capacity. Food Chem 141:2355–2362. doi:10.1016/j.foodchem.2013.04.132

Rudall P (1994) Investigation of the presence of phenolic compounds in monocotyledonous cell walls, using UV fluorescence microscopy. Ann Bot 74:483–491. doi:10.1006/anbo.1994.1145

Ruzin SE (1999) Plant microtechnique and microscopy. Oxford University Press, New York

Saadi A, Lempereur I, Sharonov S et al (1998) Spatial distribution of phenolic materials in durum wheat grain as probed by confocal fluorescence spectral imaging. J Cereal Sci 28:107–114. doi:10.1006/jcrs.1998.0195

Selinheimo E, NiEidhin D, Steffensen C et al (2007) Comparison of the characteristics of fungal and plant tyrosinases. J Biotechnol 130:471–480. doi:10.1016/j.jbiotec.2007.05.018

Shewry PR, Piironen V, Lampi A-M et al (2008) Phytochemical and fiber components in oat varieties in the HEALTHGRAIN Diversity Screen. J Agric Food Chem 56:9777–9784. doi:10.1021/jf801880d

Stampfli L, Nersten B (1995) Emulsifiers in bread making. Food Chem 52:353–360. doi:10.1016/0308-8146(95)93281-U

Stewart ML, Slavin JL (2009) Particle size and fraction of wheat bran influence short-chain fatty acid production in vitro. Br J Nutr 102:1404–1407. doi:10.1017/S0007114509990663

Stone BA, Minifie J (1988) Recovery of aleurone cells from wheat bran (US Patent US4746073 A)

Takasaki S, Kawakishi S (1997) Formation of protein-bound 3,4-dihydroxyphenylalanine and 5-S-cysteinyl-3,4-dihydroxyphenylalanine as new cross-linkers in gluten. J Agric Food Chem 45:3472–3475. doi:10.1021/jf9701594

Treimo J, Westereng B, Horn SJ et al (2009) Enzymatic solubilization of brewers' spent grain by combined action of carbohydrases and peptidases. J Agric Food Chem 57:3316–3324. doi:10.1021/jf803310f

Valjakka TT, Katina K, Kerojoki H (2003) Sourdough bread in Finland and Eastern Europe. In: Kulp K, Lorenz K (eds) Handbook. Dough Ferment. Marcel Dekker Inc., New York, pp 269–297

Van Craeyveld V, Delcour JA, Courtin CM (2008) Ball milling improves extractability and affects molecular properties of psyllium (Plantago ovata Forsk) seed husk arabinoxylan. J Agric Food Chem 56:11306–11311. doi:10.1021/jf802668x

Van Craeyveld V, Holopainen U, Selinheimo E et al (2009) Extensive dry ball milling of wheat and rye bran leads to in situ production of arabinoxylan oligosaccharides through nanoscale fragmentation. J Agric Food Chem 57:8467–8473. doi:10.1021/jf901870r

Wood PJ, Fulcher RG (1983) Dye interactions. A basis for specific detection and histochemistry of polysaccharides. J Histochem Cytochem 31:823–826. doi:10.1177/31.6.6841974

Wood PJ, Fulcher RG, Stone BA (1983) Studies on the specificity of interaction of cereal cell wall components with Congo Red and Calcofluor. Specific detection and histochemistry of (1→3),(1→4),-β-D-glucan. J Cereal Sci 1:95–110. doi:10.1016/S0733-5210(83)80027-7

Wu S-C, Wu S-H, Chau C-F (2009) Improvement of the hypocholesterolemic activities of two common fruit fibers by micronization processing. J Agric Food Chem 57:5610–5614. doi:10.1021/jf9010388

Xu R (1997) Catecholamine and histidyl protein cross-linked structures in sclerotized insect cuticle. Insect Biochem Mol Biol 27:101–108. doi:10.1016/S0965-1748(96)00083-5

Chapter 2
Localization of Cereal Grain Components by Vibrational Microscopy and Chemometric Analysis

Anna-Stiina Jääskeläinen, Leonardo Galvis Rojas and Carlo G. Bertinetto

2.1 Introduction

The structure and composition of cereal grains are important factors when considering their usage in industrial food processes such as milling, bread-making, malting, and brewing. Grain composition also affects its digestion in human and animal gut, contributing to the nutritional value and possible health benefits. From these aspects follows an increasing importance in finding ways to characterize cereal structure quickly and accurately. This chapter shows how two spectroscopic imaging techniques, Fourier transform infrared (FTIR) microspectroscopy and confocal Raman microspectroscopy (CRM), can provide powerful tools for this purpose. The basic functioning and some practical issues of these experimental techniques will be illustrated in Sect. 2 and 3, respectively. An extensive overview of methods for chemometric analysis focusing on data preprocessing and spectral unmixing and resolution is provided in Sect. 4. Finally, Sect. 5 will present a case study demonstrating the application of CRM combined with chemometric processing to investigate samples of barley (*Hordeum vulgare* L.), one of the most commonly cultivated agricultural cereal crops. For information about the general structure of cereal kernels, the reader is invited to refer to Chap. 1 of this book.

A.-S. Jääskeläinen (✉)
VTT Technical Research Centre of Finland, Tietotie 2, Espoo FI-02044 VTT, Finland
e-mail: anna-stiina.jaaskelainen@vtt.fi

L. G. Rojas
Aalto University, Kirstinmäki 7, 02760 Espoo, Finland
e-mail: leonardo.galvisrojas@aalto.fi

C. G. Bertinetto
Aalto University, Joupinmäenrinne 4 B 33, 02760 Espoo, Finland
e-mail: carlo.bertinetto@aalto.fi

N. Sozer (ed.), *Imaging Technologies and Data Processing for Food Engineers,*
Food Engineering Series, DOI 10.1007/978-3-319-24735-9_2

2.2 FTIR Microspectroscopy

Infrared spectroscopy is a widely applied, noninvasive technique to characterize the chemical structure of plant materials. In the vast majority of experiments, infrared spectroscopy has been utilized to characterize the bulk structure of the samples (Gholizadeh et al. 2014). However, a few research groups have applied the potential of location specificity of infrared microspectroscopy to determine the structural features of selected regions in cereal grains (Mills et al. 2005). Hence, the changes in, for example, aleurone and endosperm cell walls (Barron et al. 2005; Jamme et al. 2008; Saulnier et al. 2009) or secondary structure of protein (Bonwell et al. 2008) during grain maturation (Toole et al. 2007) or rumen degradation (Walker et al. 2009) have been investigated.

Infrared microspectroscopy is most commonly applied for thin-sectioned grain samples, which are deposited on infrared inactive discs, such as barium fluoride or zinc selenium. These samples are measured in transmission mode using either conventional globar or synchrotron infrared light source. The main advantage of the latter is a much higher (1000x) light density but the utilization is limited due to few instruments available.

Alternatively, attenuated total reflectance (ATR) infrared spectroscopy can be applied in grain cell wall microspectroscopic analysis (Barron and Rouau 2008). In this technique, the sample is pressed against a high- refractive index crystal and the infrared spectrum is measured through the crystal in the total reflection angle. In this technique, the infrared irradiation does not actually penetrate the sample but the evanescent wave at the crystal–sample interface generates the infrared spectrum at the sample surface. Hence, the analysis depth of the sample is small, only ca. 0.5–4 μm, depending on the wavelength range and the refractive indices of the ATR crystal and sample materials. Barron and Rouau (2008) estimated that, in their setup, the sampling volume was ca. <2 mm $\times$ 2 mm $\times$ 6 μm.

The spatial resolution of infrared spectroscopy is limited by diffraction. In theory, the highest achievable resolution depends on the microscope magnification (numerical aperture) and infrared wavelength. Theoretically, the calculated diffraction limit is ca. 5 μm, indicating that two points that are separated with a distance shorter than this are detected as a single object. In practice, it is commonly stated that the spatial resolution of FTIR microspectroscopy is approximately 5.5–6 μm (Barron et al. 2005; Bonwell et al. 2008). When this resolution is compared to the dimensions of cereal grain structures, it can be revealed that the cell walls of endosperm or aleurone cells are typically 2–3 μm thick (Bacic and Stone 1981) and hence much thinner than the lateral resolution of FTIR microspectroscopy. Therefore, even with the most careful focusing on the cell walls, some signals from the surrounding areas influence the spectra. Consequently, FTIR microspectroscopy is mainly employed to visualize grain features at a cellular scale, as shown in the example in Fig. 2.1.

Interpretation of FTIR spectra The spectral assignment is critical when interpreting the data. The FTIR spectra of several cereal grain components are illustrated in Fig. 2.2. The most important information on the chemical structure of components is in the fingerprint region of the spectra (800–1800 cm^{-1}). The high

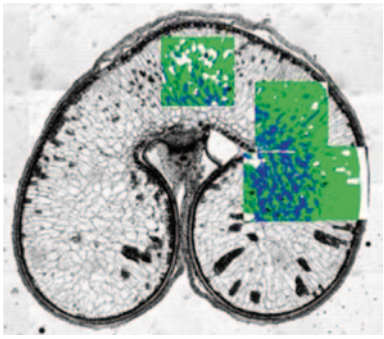

Fig. 2.1 Overlaid FTIR images of cross-section of wheat *(Triticum aestivum)* kernel: *blue* = arabinoxylan (highly branched); *green* = arabinoxylan (low branched); *white* = starch; *black* = holes. (Toole et al. 2007). Reproduced with permission from Springer

wavenumber range at 3800–2800 cm^{-1} contains mostly information on the OH, CH, and NH stretching vibrations. This spectral range is sensitive to sample moisture and, due to the broad and overlapping bands, this region is only occasionally used in quantitative analysis of the samples.

The characteristic infrared bands from protein and carbohydrates are clearly seen in the fingerprint region, as illustrated in Fig. 2.2. The wavenumber range of 1710–1500 cm^{-1} shows the most intense vibrational modes of cereal grain proteins.

Amide I and II have bands at 1710–1580 cm^{-1} and 1560–1500 cm^{-1}, respectively (Walker et al. 2009). Typically, the highest intensities are observed at 1650 and 1543 cm^{-1}, as reported by Thygesen et al. (2003) and as illustrated in the FTIR spectrum of gluten in Fig. 2.2. When investigating the protein spectra in more detail, the absorption band at 1658 cm^{-1} has been assigned to originate from the alpha helix and beta-sheet of amide (Bonwell et al. 2008).

The strong absorption at spectral range 1300–800 cm^{-1} is characteristic for cereal carbohydrates (Kačuráková and Wilson 2001). These bands arise from different stretching and bending modes of CO, CC, COH, and COC structures in carbohy-

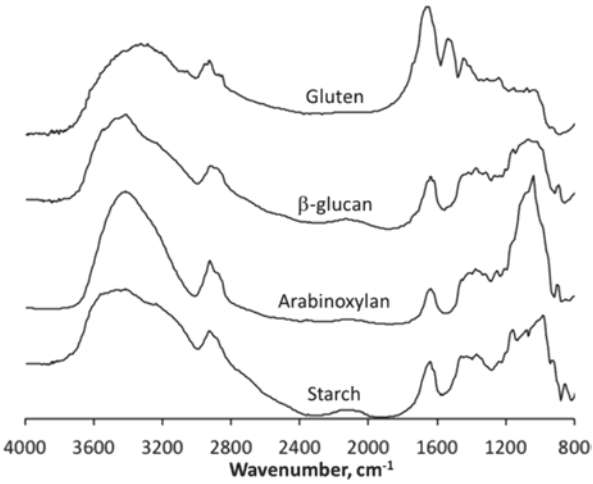

Fig. 2.2 FTIR spectra of main cereal grain components: protein (gluten) and three different carbohydrates (arabinoxylan, β-glucan, and starch)

drate polymers (Cael et al. 1973). It has not been possible to assign these bands unambiguously because most of these bands result from highly coupled vibrational modes. In addition, some of the bands are poorly resolved and severely overlapping, thus making the assignment challenging even when using advanced computational techniques, such as multivariate analysis or deconvolution (see below and Sect. 4.2). Nevertheless, all carbohydrate polymers have their own characteristic infrared absorption bands, which enable us to investigate the carbohydrate composition of the sample as well as identify selected features in the polymer structure at a molecular level (e.g., substitution, chain conformation, helicity, crystallinity, and retrogradation process) (van Soest et al. 1995).

The proportion of different carbohydrates in the sample can be performed using the FTIR spectra. Jamme et al. (2008) stated that arabinoxylan exhibits strong bands at 1045 and 970 cm^{-1}, whereas in β-glucan the band at 1155 and 1078 cm^{-1} is stronger. On the other hand, Barron et al. (2005) proposed that the band at 1075 cm^{-1} is influenced by the degree of branching and hydration of arabinoxylan, illustrating the difficulty of precise assignment of certain spectral bands.

Cereal grain arabinoxylan may have variable amount of ferulic acid substituents which can be observed by the presence of a band at 1595 cm^{-1}. This band is characteristic for the C=C stretching bond in the aromatic ring of ferulic acid. However, this spectral region overlaps with the bands from proteins and possible other aromatics (e.g., lignin) and therefore ferulic acids are not easy to detect or quantify.

The impact of, for example, starch can be removed by spectral subtraction, but this typically causes a distortion of the spectra. To overcome this problem, Barron et al. (2005) developed a method to prepare transverse thin sections of pure grain cell walls by removing the cell contents in the samples with 70 % ethanol solution. This treatment leaves the cell walls intact, and then it has been possible to investigate the structure of endosperm cell walls at different positions of the grain without the interference of neighboring starch granules.

As illustrated above, the infrared bands are overlapping and hence univariate analysis, that is, considering a single peak at a time, is usually not possible. Hence, the utilization of multivariate methods is necessary to highlight the small changes in composition or architecture of different sampling positions, for example, in different positions of grain cell walls. The most common approach is to apply principle component analysis (PCA) (Barron et al. 2005; Saulnier et al. 2009). Alternatively, the second derivative of the spectrum can be utilized to identify the minor changes in the spectra, as has been performed by Bonwell et al. (2008), to determine the secondary structure of the endosperm proteins. The spectral analysis is discussed in more detail in Sect. 4.

2.3 Confocal Raman Microscopy

Raman spectroscopy is based on the inelastic scattering of light interacting with molecules in which the frequency shift between the incident and the scattered light is associated with a particular vibration mode of a chemical bond (Tsuboi

and Thomas JR 1997; Tanaka and Young 2006; Masic et al. 2011). When incident radiation encounters molecules, the electric field of the light induces the polarization of the electron cloud and the formation of a short-lived "virtual state" (Tanaka and Young 2006). Different energy transitions take place during this interaction. In elastic energy transition, molecules from the ground state are promoted to the "virtual state" level and return to the ground state with emission of scattered light in a process called Rayleigh scattering. However, the scattering process may also involve inelastic energy transitions to different energy levels from their initial one. These energy transitions are called *Raman scattering*. Raman scattering is inherently a very weak process, since only one in every 10^6–10^8 photos experiences a frequency shift (Gierlinger et al. 2013).

One tool that is suited to study cereal kernels is CRM , which can obtain maps of the chemical composition and orientation of materials present in a sample with high resolution (0.6–1 μm) in a nondestructive manner. The main advantage of confocal mapping is an improvement in lateral discrimination with simultaneous reduction of the fluorescence background and an important improvement in axial resolution (depth discrimination) that allows "optical sectioning" in transparent samples (Chalmers and Griffiths 2001). CRM has been used to image the distribution of different components with at least micron resolution in different plant-based samples, including cereal grains (Gierlinger and Schwanninger 2006). For instance, it allowed the study of the relationship between interstitial protein structure in wheat grain and its hardness, through the characterization of the arabinoxylans present in the cell wall during the development of wheat endosperm and the revelation of the structure of starch granules in the endosperm of wild and mutant maize kernels, thus obtaining the compound distribution on the aleurone layer in wheat and barley kernels (Piot et al. 2002; Wellner et al. 2011; Jääskeläinen et al. 2013).

Experimental setups Different approaches can be used to produce Raman images such as scanning mapping (point-by-point scanning), line scanning, and wide-field illumination. Figure 2.3 depicts a point-by-point scanning where the laser is focused onto the sample surface using an objective, and a spectrum is taken by the detector at each spatial position over the region of interest (ROI) in the x and y directions. The integration values of a particular band (band intensity) are visualized as image where the bright pixels correspond to higher values of the integration. The Raman intensity value is linearly related not only to the number of chemical bonds but also to the orientation of molecules present in a confocal volume (Kneipp et al. 1999; Tanaka and Young 2006). Depth scan (x-z) direction is also possible as well as their reconstruction into 3D stack images (x, y, z). The time for the acquisition of every single spectrum at each pixel (integration time) depends usually on the Raman signal of the sample and also on the instrument setup. Integration time values between 0.1 and 1 s are commonly used in this mapping strategy; the duration of an experiment will be proportional to the integration time and also to the number of image pixels.

For the line imaging approach, cylindrical optics is used to distribute the laser beam in one direction over the sample. The laser line is oriented in a parallel fashion to the direction of the entrance slit of the dispersive spectrometer and a 2D charge-coupled device (CCD) detector located at the exit port of the spectrograph collects simultaneously spatial and spectral data of the illuminated sample (Chalmers and

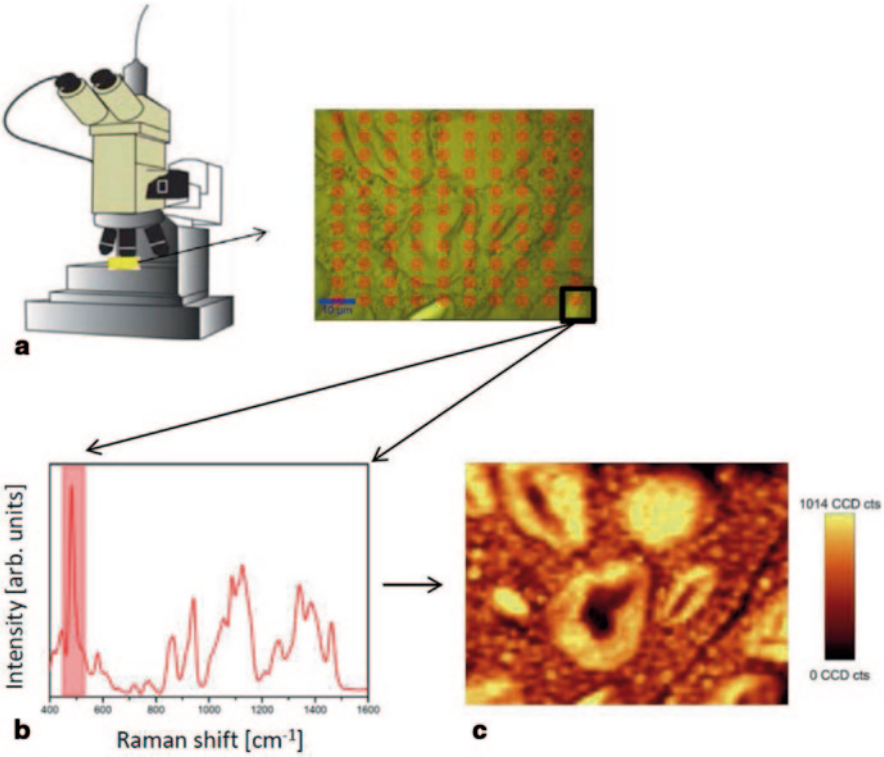

Fig. 2.3 Raman imaging procedure: **a** The selected region of interest (ROI) is scanned and Raman spectra of the ROI are taken at certain spatial steps. **b** Subsequently, the intensity of a single Raman band is obtained by integration (univariate analysis) for each spatial location on the ROI. **c** The result of this integration procedure is shown as chemical distribution image where the brightness of each pixel is associated with the intensity of the selected Raman band

Griffiths 2001; Schlücker et al. 2003). As a result of this setup, only the dimension perpendicular to the laser line is required to be scanned, thus reducing the experimental time. Finally, in wide-field Raman imaging, the entire ROI of the sample is illuminated and analyzed simultaneously by recording an image at discrete wavenumber increments through the spectrometer (Chalmers and Griffiths 2001).

Typical point-by-point Raman microspectroscopy maps are performed in a confocal Raman microscope equipped with linearly polarized lasers with a wavelength comprised in the visible range (e.g., Ar^+, He-Ne, Kr^+, and doubled Nd:YAG lasers) coupled to a dispersive spectrometer and a CCD detector. Figure 2.4 shows a standard configuration of the confocal microscope in Raman mode where the excitation laser is focused onto the sample with an objective, and the reflected Raman radiation resulting from the interaction of the laser and the sample is collected with the same objective and focused into a pinhole in front of the detector. The spectra are acquired using an air-cooled CCD camera behind a grating spectrograph. The Raman images are obtained by moving the sample with a piezoelectric scan table in x and y directions. The lateral resolution of the technique is calculated according

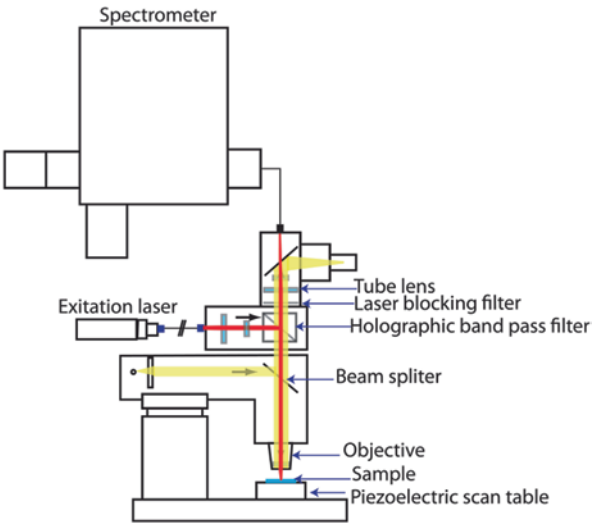

Fig. 2.4 Confocal Raman setup and optical pathway in Raman mode. The laser is delivered by an optical fiber and focused onto the sample with an objective lens. The reflected Raman radiation is collected with the same objective and focused into a multimode fiber, which sends the radiation to the spectrometer

to the Rayleigh criterion: $\Delta x = 0.61\lambda/NA$, where Δx is the smallest distance between two point objects that will appear separated in the image plane, λ is the wavelength of the laser, and *NA* is the numerical aperture of objective that is described by the equation: $NA = n \sin\theta$, where *n* is the refractive index in which the objective is immersed (e.g., 1.0 for air and up to 1.56 for oils) and θ is the half-angle of the maximum cone of light that can enter or exit the objective. In order to obtain reliable spectral data from Raman mapping experiments, different aspects should be taken into consideration such as sample preparation, damage threshold of the sample under excitation radiation (laser), and presence of fluorescent compounds. The first requirement is to have a very flat sample surface because correct spectral analysis is only possible by mapping even surfaces; otherwise, it is recommended to normalize all spectra with a reference band (see Sect. 4.1). Histological sections of kernels are usually selected for point-by-point Raman mapping. There are several protocols for preparation of kernel sections, but in general they involve several steps like dehydration of kernels in a series of ethanol solutions followed by embedding (in resin, paraffin, polyethylene glycol) and cutting of the kernels into semi-thin sections using a rotary microtome (Holopainen et al. 2005; Gierlinger et al. 2012). The use of polyethylene glycol as embedding media has proven to be useful in plant materials because the dehydration step is unnecessary and the embedding polymer can be easily removed from sections by rinsing with water. It is also important that the section thickness is never lower than the confocal depth of laser beam (depending on the particular setup). For the most common CRM setups, kernel sections with a thickness of 4–8 µm are suitable for Raman mapping. Another important aspect to be considered is the selection of the appropriate excitation laser. The Raman scattering intensity is proportional to ν^4, where ν is the wavelength of the excitation laser (Gierlinger et al. 2013). Therefore, excitation lasers at 400 nm produce a Raman scattering intensity about 16 times higher than others at 800 nm. However, in confocal microscopes equipped with lasers at 532 nm, the improvement in lateral

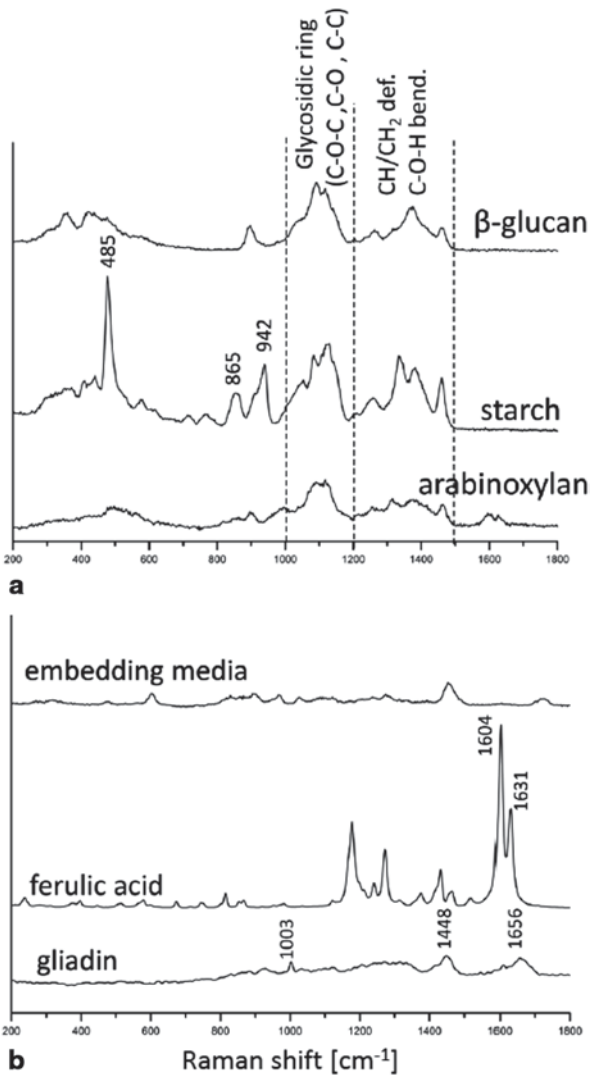

Fig. 2.5 **a** Raman spectra of model compounds of main carbohydrates present in sectioned wheat kernels; **b** spectra of other components as embedding media, ferulic acid and protein (gliadin)

resolution and Raman intensity is accompanied by an increase in fluorescence that can hamper the Raman signal. In this case, it is advisable to use setups with higher wavelength lasers, such as 633 or 785 nm. Finally, kernels sections also need to be tested for laser power density to determine the level at which samples do not suffer from degradation or burning. A laser power between 5 and 20 mW in green laser setups is commonly used in plant materials (Gierlinger et al. 2012).

Raman signature of main components in cereal starchy endosperm kernels As the first step in Raman spectral analysis of cereal kernels, a previous knowledge of the Raman fingerprint of pure components present in the cereal kernel material is necessary. For example, Fig. 2.5 shows the Raman spectra of the main components

in embedded sections of cereal starchy endosperm. This information will serve to elaborate chemical images based on the Raman intensity of a particular band (univariate analysis) in case there is no band overlapping from other components in the sample. Polysaccharides spectra in Fig. 2.5a are represented by β-glucan, starch, and arabinoxylan that show bands in the three major regions: 1000–1200 cm^{-1} that are the typical fingerprint of carbohydrates assigned to C-O-C, C-O, and C-C stretching; 1200–1500 cm^{-1} associated to CH/CH_2 deformation and C-O-H bending modes, and below 800 cm^{-1} that is attributed to the skeletal and torsional vibration modes (Barron et al. 2006; Philippe et al. 2006). It is in the last region that starch displays a strong band at 485 cm^{-1} that is assigned to the skeletal vibration of the glucopyranose unit (Kizil et al. 2002; Liu et al. 2004).

The starch spectrum also exhibits a band located at 865 cm^{-1}assigned to stretching C-O-C/ ring-breathing that could indicate sensitivity to the molecular orientation of ordered structures in starch grains (Wellner et al. 2011). The protein component is represented by a spectrum of gliadin (wheat protein) that shows the characteristic signature given by the amide I band that is assigned to the vibration of the trans-peptide group (CONH) in the range 1600–1700 cm^{-1}, the amide III band (1230–1340 cm^{-1}) that arises from the combination of N-H bending and C-N stretching of the peptide group, and the sharp band at 1003 cm^{-1} assigned to the phenylalanine ring vibration (Tsuboi and Thomas JR 1997; Movasaghi et al. 2007). Phenolic compounds are represented by ferulic acid, which exhibits sharp bands at 1604 and 1631 cm^{-1} that are assigned to the aromatic ring vibration and to C=C side-chain stretching, respectively (Sebastian et al. 2009). The same doublets on the region 1590–1630 cm^{-1} are observed in the arabinoxylan spectrum due to the presence of covalently bonded ferulic acid to its structure (Kačuráková et al. 1999; Calheiros et al. 2008). The spectrum of the embedding media needs to be taken into account for further Raman spectral analysis of histological sections.

2.4 Data Analysis of Spectral Images

Further chemical and structural knowledge can be extracted from spectral images by means of computational processing. Several methods are available, depending on the analyzed sample and desired information, which can be classified into two main categories. The first is commonly referred to as preprocessing and comprises algorithms for correcting noises, distortions, or any other unwanted effect in the signal. The second category consists of those methods that perform qualitative and quantitative evaluation of chemical composition and structure. In this chapter, we focus on multivariate methods for unmixing and resolution of spectral components. There are several other uses of spectral data by chemometric techniques, such as classification of substances or prediction of their properties, for which the reader is invited to consult other texts (Tauler et al. 2009). These operations are normally executed either using programming languages (most codes are in MATLAB, R, and C++) or by means of dedicated software often incorporated with the instrument.

2.4.1 Preprocessing

The various operations collectively called preprocessing range from simple format conversions to sophisticated algorithms to filter the signal from certain types of noise, instrumental artifacts, nonrelevant sources of variation and/or nonlinear behavior (Rinnan et al. 2009). These issues may not hamper peak detection or basic univariate analysis but are usually detrimental to precise quantification by multivariate analysis. Choosing the most suitable combination of preprocessing methods is not always easy: it depends on the particular case under study, it often involves additional human knowledge on the data, and there are normally no objective criteria to help the decision (Engel et al. 2013). Some studies have been carried out to address this issue (Bocklitz et al. 2011; Laxalde et al. 2011; Polshin et al. 2011; Bertinetto and Vuorinen 2014a), but they only apply to certain problems and contexts. As a general rule, it is better not to perform a computational transformation on the data when it is not strictly necessary.

For the spectral techniques treated in this chapter, the most common preprocessing operations include restriction of the wavenumber range, removal of cosmic ray peaks, correction of random noise, of baseline distortion, and of intensity variations not related to the phenomenon under study. These operations can be performed in different order and their *effect is illustrated in Fig.* 2.6.

Restriction of the wavenumber range The purpose of this operation is to remove the region that does not contain meaningful information (e.g., singling out the fingerprint region as discussed in Sect. 2 and 3) to simplify the calculations and reduce the influence of noise on the result. The selection is usually based on experience and chemical knowledge of the problem, although there are ways to automate this step using partial least squares, genetic algorithms, or other machine learning tools (Devos and Duponchel 2011; Polshin et al. 2011).

Removal of Cosmic Ray (CR) peaks CR peaks are large, positive, unidirectional, and narrow features that emerge when a CCD detector, such as those typically present in Raman spectrometers, is accidentally stricken by a cosmic ray. They vary randomly in magnitude, bandwidth, and wavenumber, often appearing on top of other spectral features. They are computationally detected by observing a sudden jump in signal intensity that is anomalous with respect to the overall standard deviation and signal-to-noise ratio. The detection can be done by comparing adjacent wavenumbers (Zhang and Henson 2007), adjacent pixels for the same wave number (Cappel et al. 2010; Schulze and Turner 2013), or using wavelets (Ehrentreich and Sümmchen 2001). The CR peaks thus found are then removed by substituting the affected spectral points with an interpolation curve or with an average of neighboring spectra at the same wavenumbers.

Very small CR peaks are likely to be missed by most methods but they can be handled in a subsequent smoothing step (see next paragraph).

Smoothing of random noise Signals are also contaminated by random high-frequency oscillations, which can be reduced by smoothing, that is, some sort of weighted averaging that decreases the curvature of the sharpest signal features. The

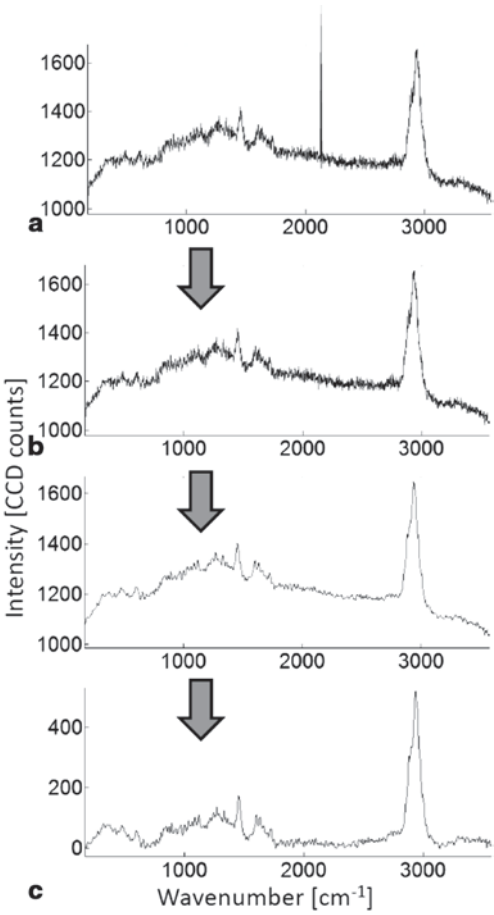

Fig. 2.6 Visualization of the effect of the most common preprocessing operations: **a** raw data; **b** after cosmic ray peak removal; **c** after smoothing; **d** after baseline correction

most widely used smoothing method is perhaps the Savitzky-Golay filtering (Savitzky and Golay 1964), based on a convolution operation with a low-order polynomial through a shifting data interval. Another popular and more recent method is the Whittaker smoother (Eilers 2003), based on the concept of penalized least squares. It is usually faster than Savitzky-Golay and better at dealing with signal boundaries and with missing spectral points. A third popular approach is Fourier and wavelet filtering (Strang and Nguyen 1996), which exploits the concepts of "frequency" or "scale" to separate signal components and remove those with very high curvature (the term "low-pass filter" is often used to refer to this approach). They are particularly effective when the shape of components to be separated resembles that of the basis function (i.e., sinusoidal or wavelet) but may otherwise cause distortions (Eilers 2003).

It is difficult to objectively know how much smoothing can be applied without removing useful information from the signal. Some authors have tried to determine it systematically (Bocklitz et al. 2011; Devos and Duponchel 2011; Laurens and

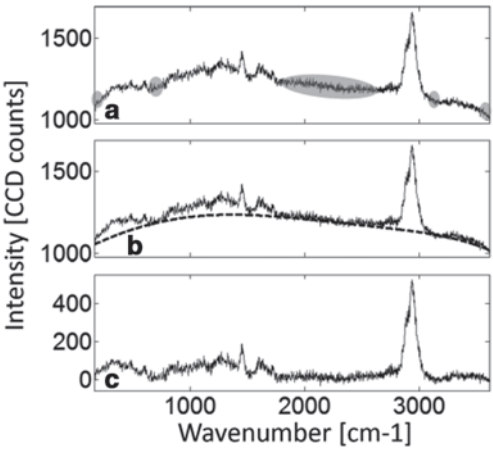

Fig. 2.7 Example demonstrating the principle of detrending: **a** regions without peaks (highlighted by *shadings*) are identified; **b** peak-free points are fitted with a suitable curve; **c** the fitted curve is subtracted from the spectrum

Wolfrum 2011; Weakley et al. 2012) but their results can seldom be generalized beyond the specific case they are treating. As a rule of thumb, a slight smoothing that still leaves a little random noise is usually beneficial (Bertinetto and Vuorinen 2014a).

Correction of baseline distortions Nearly all quantification criteria in spectral analysis assume that peaks arise from a flat baseline but this case seldom occurs in practice. Although the deviations from ideal behavior can sometimes be separated and accounted for by multivariate analysis, they are typically removed or at least reduced in the preprocessing stage. The most common way to do this is probably by detrending, that is, evaluating the baseline by fitting the regions without peaks with a curve function and then subtracting the fit from the spectrum, see Fig. 2.7. For Raman spectra affected by fluorescence of the sample, a fifth degree polynomial is widely agreed to be a suitable curve (Zhao et al. 2007), but for simple cases even a straight line can be enough. For large amounts of spectra with peaks at varying positions, the recognition of peak-free regions can also be carried out automatically (Bertinetto and Vuorinen 2014b).

Another simple and common approach is to use the derivative of the spectrum, usually first or second, which suppresses features with wide curvature and highlights the narrower ones. Derivatives can also be employed to locate small spectral features more precisely. However, this approach severely amplifies random noise (it is often combined with smoothing to limit this effect) and transforms the spectra in a way that is not suitable for any subsequent chemometric treatment.

Baseline correction is normally the most delicate preprocessing step because of the considerable influence it has on the result and because of the difficulty in determining the baseline objectively. A great number of methods based on different mathematical criteria exist in the literature and new ones are continuously devised to treat specific spectroscopies or data sets more effectively.
Relatively recent reviews can be found in the works of Schulze et al. (2005) and Rowlands and Elliott (2010).

Normalization *In confocal microscopy, the overall intensity may be affected by factors that are not related to the* analytes' *concentration, such as a not perfectly smooth* sample surface that causes some parts of the image to be off the laser focus. In such cases, spectra are usually normalized to make quantifications less arbitrary and pixels more comparable. The most accurate and objective way to do this is by exploiting an internal standard, that is, a peak corresponding to a substance with a known concentration or constant throughout all spectra. If such standard is not available, commonly used alternative normalization criteria are: total spectral intensity, intensity of the highest peak, and Euclidean length of the spectral vector. Among these, there is no general consensus on which one is most appropriate; in most cases, this choice does not have a great influence on the final results. Some studies (Bertinetto and Vuorinen 2014a) suggest that normalizing by the total spectral intensity may be more suitable for data with a high signal-to-noise ratio, but for noisy data it is better to use Euclidean or max-peak normalization, which are less influenced by small noise features. It is worth noting that normalization without internal standard does not allow for determining absolute concentration, but only comparing relative abundances among pixels of the same image.

Other preprocessing operations In certain contexts, multivariate techniques that are normally employed to perform the final qualitative or quantitative analysis can be used as a preprocessing step. PCA and cluster analysis are worth mentioning here. The former (Abdi and Williams 2010), which will be better described in the next section, can be used to remove noise by identifying the spectral components with the greatest contribution to the overall variance and exclude the rest. However, it must be remembered that there can sometimes be useful information that does not entail large variance in the data. Cluster analysis is a wide family of algorithms for the unsupervised classification of data (Jain and Dubes 1988). It can be used to suppress noise and other distortions by grouping similar spectra together and then computing their mean, although at the expense of spatial and spectral detail.

2.4.2 Spectral Analysis

As mentioned in Sect. 2 and 3, univariate analysis can be used only when the integration peak does not overlap with others. In case of partial overlap, it is possible to do a deconvolution using suitable curves, usually Gaussians, Lorentzians, or mixtures of both, for example, a Voigt profile. It may not always be easy to decide how many curves should be employed, especially when information on the active vibration modes is insufficient. As a rule of thumb, it is best to use the lowest number of curves that allows for a reasonably accurate fit.

Multivariate methods For more complex systems with significant peak overlap, multivariate approaches that exploit the information contained in all the spectral range are necessary. All methods described in this section rely on the assumption that the signal intensity is linearly proportional to the concentration of the analyte. Following this, the spectral data can be modeled as:

$$\mathbf{M} = \mathbf{CS} + \mathbf{E}, \tag{2.1}$$

where M is the n × w matrix of the spectral image (n = number of pixels, w = number of wavechannels), C is the n × p matrix of concentrations or relative abundances (p = number of components), S is the p × w matrix of spectra of pure components, and E accounts for noise. If the components present in the sample and their relevant spectra are known, their abundances, that is, C, can simply be obtained by a linear least-squares (LLS) fit of S into M, with the same limitations as explained above for determining the absolute concentrations. This method is sometimes referred to as linear spectral unmixing (Zimmermann et al. 2014) or basis analysis (Dieing and Ibach 2011). It must be stressed that for it to be effective, all the component spectra must be known because the lack of even one influences the fit of those that are accounted for. Moreover, the accuracy of these spectra must be carefully checked as this method can yield results that make mathematical (and sometimes physical) sense even with spectra that bear no relation to the actual chemical composition.

If the spectra of the individual components are unknown, the problem must be tackled with techniques that analyze relationships among variables. Their basic idea is that if intensities at certain wavenumbers are observed to vary in the same proportion throughout the data, they are likely to originate from the same chemical component. From this follows that this approach is not able to distinguish chemical components whose abundances vary together proportionally. On the other hand, factors that affect the signal without being an actual substance are sometimes observed as an independent component (see below in Sect. 5.2).

The most widely known multivariate analysis technique is PCA (Abdi and Williams 2010), which transforms the data by projecting it into a new set of variables, called principal components or loading factors, obtained by linear combination of the original ones. The loading factors are defined to be mutually orthogonal and to account for the maximum possible variance in the given data. They contain spectral features of chemical compounds present in the sample and they can be used to fit Eq. (2.1), obtaining a rough distribution of these compounds (Miljković et al. 2010; Bonifacio et al. 2010); an example is shown in Sect. 5.2. A similar type of result can be obtained by independent component analysis (ICA; Hyvärinen and Oja 2000; Hao et al. 2009), which finds new components that have the maximum statistical independence, usually by imposing that their probability distribution be as dissimilar as possible to a Gaussian. However, the loading factors from both PCA and ICA are different than the actual spectral signals of the chemical compounds: they often contain features from more than one component and they do not even comply with physical requirements; most notably, they have negative intensities. Consequently, such results are approximate and of no direct physical interpretation.

Other methodologies aim at finding the spectra of the real components in the sample. The simplest approach consists in identifying the pixels with the composition closest to the pure compounds. These pixels can be searched with methods such as N-FINDR (Winter 1999) and vertex component analysis (VCA; Nascimento and Bioucas Dias 2005). These methods are fast and reliable, but they can provide the

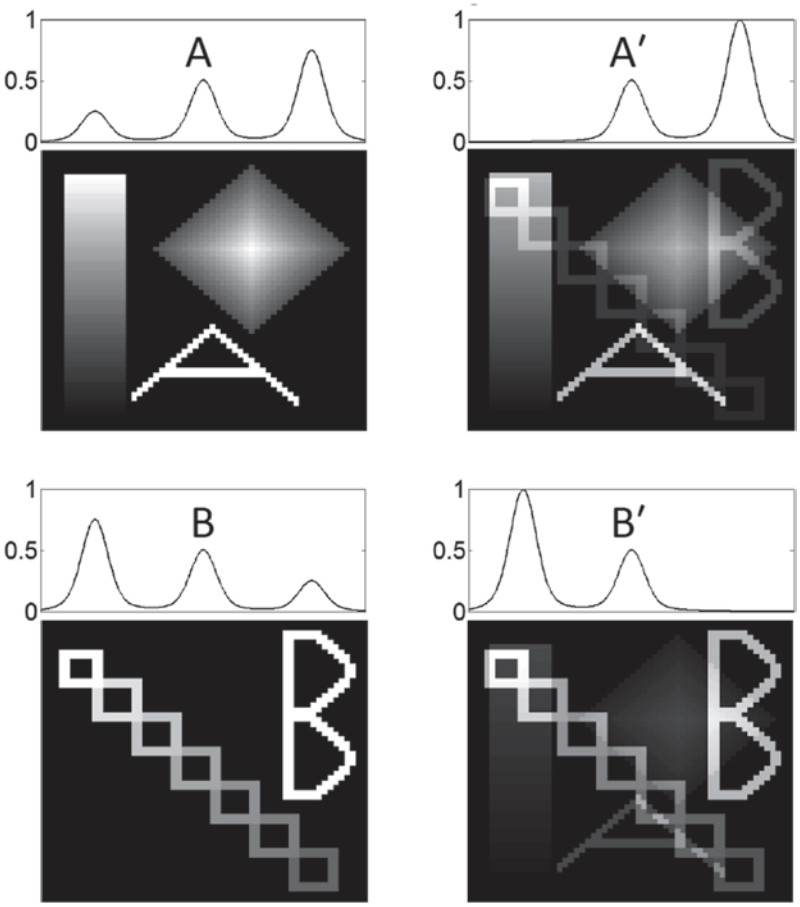

Fig. 2.8 Simulated example demonstrating the concept of rotational ambiguity. A spectral image has been made with an **S** matrix composed of spectra A and B and a **C** matrix plotted by the two maps on the left side (*lighter* color indicates higher abundance of the respective component). The same image can be represented using A' and B', which have less overlap than A and B, but the resulting **C**' matrix would be less resolved, as observable by the color plots on the right side

actual spectra of pure components only if they are present somewhere in the sample, a requirement that is seldom met in experimental situations.

Pure-component methods The problem of finding the spectra of the pure components when they cannot be directly observed in the sample is complicated by the so-called *rotational ambiguity* of Eq. (2.1), meaning that an infinite number of solutions can be found for C and S if no additional constraints are specified (Windig and Keenan 2011). These solutions are related so that a greater resolution in the spectra (i.e., fewer and sharper peaks) yields a lower resolution in the concentrations and vice versa; this concept is better illustrated in Fig. 2.8. Three different methodologies for tackling this issue are briefly presented here.

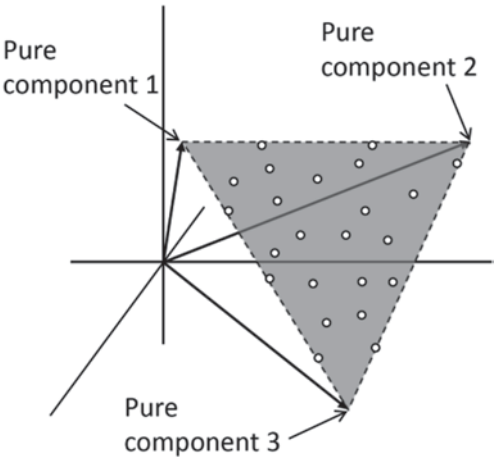

Fig. 2.9 Example demonstrating the principle of minimum simplex volume for three components in three spectral dimensions. The pure components are the vertices of the grey triangle, which is the simplex with minimum area/volume that comprises all data points *(small white circles)*

The first one, multivariate curve resolution-alternate least squares (MCR-ALS) (Jaumot et al. 2005) solves Eq. (2.1) iteratively: it starts from initial estimates of **C** and **S** (e.g., the purest pixels) and alternates their LLS resolution to optimization steps in which either matrix is modified by imposing constraints that reflect chemical or physical information on the studied system. Several types of constraints are possible, e.g., non-negativity, stoichiometric balances, or absence of certain compounds in some pixels. Moreover, MCR-ALS can handle systems in which more than one spectrum is taken, at different conditions, for each data point. This situation, attainable by various experimental means (Van Benthem et al. 2011; Buckley et al. 2014), allows for a unique resolution of Eq. (2.1; in such cases another viable technique is the parallel factor analysis method, or PARAFAC (Bro 1997)). The possibility of tailoring the constraints according to the specific case gives MCR-ALS a flexibility that allows it to be effective in very different situations, such as spectral images, chromatograms, reaction profiles, and gene expression profiles. However, the information required for the necessary constraints may not always be available.

The second methodology consists in finding the simplex with the minimum volume that encloses the data points of abundance fractions, that is, the **C** matrix. A simplex is the simplest shape (i.e., with lowest number of vertices) that can be obtained for a given number of dimensions. For example, the 2D simplex is a triangle and the 3D one is a tetrahedron. For a 3-component system, the principle of this methodology can be easily visualized in Fig. 2.9. Various algorithms are available to solve this problem, such as minimum volume enclosing simplex (MVES) (Chan et al. 2009), minimum volume simplex analysis (MVSA) (Li and Bioucas-Dias 2008), nonnegative matrix factorization minimum volume transform (NMF-MVT) (Tao et al. 2007) and simplex identification via split augmented Lagrangian (SISAL) (Bioucas-Dias 2009).

The latter is probably more recommended for large spectral images because of its speed and robustness to noise and outliers. The requirement for the minimum-simplex-volume approach is that the data contains, per each component, at least a

few pixels in which this component is absent (in the 3-component case they correspond to points lying on the side of the triangle).

The third methodology aims at reconstructing the spectra of pure components without directly solving Eq. (2.1). This is done by initially performing a PCA (or the substantially equivalent singular value decomposition, SVD) on the spectral matrix and then finding linear combinations of the loading factors that satisfy the conditions of non-negativity and minimum entropy.

Entropy, which can be mathematically defined in slightly different ways, is a way to quantify the concept of simplicity. The principle behind entropy minimization methods is that a pure component (and so its spectrum) is always more simple, that is, has a lower entropy, than a mixture containing it. Band-target entropy minimization (BTEM) (Widjaja et al. 2003) adds the condition that the reconstructed spectra must contain a certain peak, named *band-target* in this context; each band-target yields a different reconstruction. BTEM thus searches for pure spectra by exploring the solutions produced by all the prominent peaks observed in the loading factors. Since the set of these solutions is usually redundant (and some of them may just reproduce noise), a post-screening is necessary to identify the best ones. The chosen set of reconstructed pure spectra can then be fitted in Eq. (2.1) to obtain the **C** matrix. One advantage of BTEM is that it needs virtually no chemical knowledge of the sample, not even about the number of components, although some knowledge is useful for the post-screening. The other advantage is that BTEM is particularly good at identifying minor components whose signal easily gets overwhelmed by other components or by noise deviations. On the other hand, BTEM is not very effective in reconstructing spectra with wide and low features, such as background components. Its solutions may also have too narrow peaks, which yield a suboptimal resolution in the concentrations, as illustrated in Fig. 2.8. BTEM is the technique employed in the case study shown in Sect. 5.

Obtaining the spectra of pure components with one of the above-described methods is also a powerful tool for qualitative analysis. Not only does it allow for determining which substances are present in a certain sample (at least those responding to the employed spectroscopy), but also for observing details relative to the condition of the analyte in its current environment, for example, an interaction that produces a shift or a different peak as compared to the spectrum of corresponding model compounds (see Sect. 5.2).

2.5 Study of Barley Grains Using CRM and Multivariate Analysis

This case study (Galvis et al. 2015) aimed at evaluating chemical and structural changes in the endosperm of barley (*Hordeum vulgare* L.) upon malting by using CRM. The spectra of the main components were reconstructed with multivariate computational analysis and their distribution was mapped for native and malted kernels, respectively.

2.5.1 Materials and Methods

Barley samples *The analyzed barley* kernels were of cultivar *Fairytale,* crop 2010. Some of them were malted by steeping the kernels twice in conical vessels at 15 °C during 13 and 3 h, respectively, with a 16 h air-rest between the steeps. After steeping, the barley kernels were transferred to germination boxes for 6 days at 16 °C. The germination process was terminated during kilning using air at 50 °C for 17 h and finally at 84 °C for 4 h.

Malted and native barley kernels were then fixed with a solution of 3 % paraformaldehyde and 1 % glutaraldehyde in 0.10 M sodium potassium phosphate buffer pH 7. Subsequently, kernels were dehydrated in a series of ethanol solutions, embedded in Historesin© (Leica microsystem; Mensheim, Germany) and cut into semi-thin sections (4 μm thick) with a rotary microtome (Microm Labogeräte GmbH, Walldorf, Germany) using a tungsten carbon knife. Cross-sections of native and malted barley kernels were then mounted onto glass slides and dried on a heating plate at 40 °C.

Raman spectroscopy For Raman experiments, a continuous excitation laser beam was focused down to a micrometre-sized spot on the barley sections through a confocal Raman microscope equipped with a piezo-scanner. A frequency-doubled Nd:YAG, 532 nm linear polarized excitation laser (~20 mW) was used in combination with a ×100 (Nikon, NA = 0.90) microscope objective. The polarization angle of the laser was rotated using a half-wave plate in the optical pathway. The spectra were acquired using a CCD camera (Andor Newton DU970-BV, Andor Technology plc, Belfast, UK) behind a grating (600 g mm^{-1}) spectrograph with a spectral resolution of ~6 cm^{-1}. For mapping, the surface of the barley sections was scanned with steps of 1 μm, integrating the signal for 0.3 s and using 0 ° polarization of the exciting laser.

Analysis of Raman images All spectra were preprocessed by performing the following operations in order: (i) CR removal using an algorithm written in-house; (ii) baseline correction with an automatic detrending method (Bertinetto and Vuorinen 2014b); restriction of the wavenumber range to 320–1800 cm^{-1}; (iii) smoothing using Whittaker smoother (Eilers 2003); (iv) normalization by Euclidean norm. Spectra of pure components were reconstructed with BTEM (Widjaja et al. 2003), employing an automatic identification of band-targets (Tan et al. 2009) and a particle swarm optimizer (Singh 2004). The number of loading factors used for the spectral reconstructions was chosen by visual inspection; in a few cases, different numbers were tried.

BTEM was applied to all preprocessed spectra, as well as two sets of cluster-averaged spectra. Cluster analysis (Jain and Dubes 1988) was performed on the preprocessed data compressed by PCA, retaining the principal components explaining 85–90 % of the total variance. The first set was obtained using hierarchical clustering, city-block distance, complete linkage, and selecting a partition with a number of clusters approximately equal to 1/100 of the total number of pixels in the image. The second set was obtained using *k*-means clustering, city-block distance,

and setting a number of clusters ~1/10 of the total number of pixels. Prior to the clustering step, the noisiest spectra were filtered out to avoid the risk of averaging them with good ones and thus severely distorting the signal.

The results from all these BTEM runs (i.e., on whole image, on two sets of cluster-averaged spectra and on occasional alternate sets of loading factors) underwent a post-screening, in which the best solutions were selected by removing near-identical ones, by comparing with the spectra of model compounds and using some available chemical knowledge. Images of the relative concentration of each identified compound were generated by an LLS fit of the set of selected BTEM solutions (basis set) on the Raman spectra. In a few cases, different basis sets were tried and the one with the best fit and no negative concentrations (with some tolerance for noisy points) were retained.

2.5.2 Results and Discussion

The mapping by CRM focused on two selected regions of the barley endosperm: the centre of starchy endosperm and the boundary between starchy endosperm and aleurone layer. An example of the spectra of pure components reconstructed by BTEM (from the endosperm-aleurone boundary) is shown in Fig. 2.10. They match very well with the spectra measured from model compounds corresponding to protein, starch, non-starch carbohydrates, and the embedding media (see Fig. 2.5). The

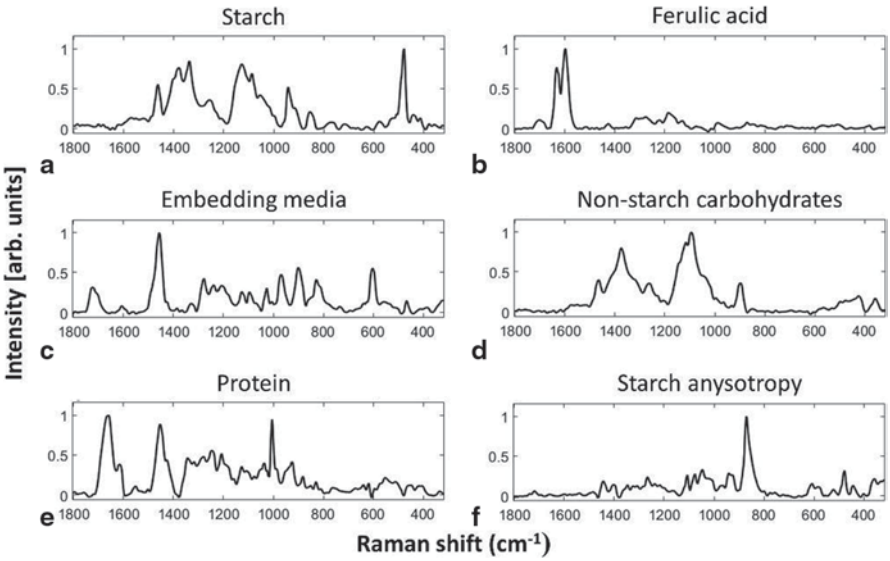

Fig. 2.10 Reconstructed spectra (A-F) from BTEM analysis performed on native barley kernel at the boundary of the starchy endosperm and the aleurone layer. The reconstructed spectrum F appears as a result of anisotropic Raman bands in starch spectrum

spectrum B in Fig. 2.10 shows the typical doublet band of ferulic acid but with a slight frequency shift of the band located at 1604 cm^{-1} in pure ferulic acid to 1599 cm^{-1} in the reconstructed spectra. This shifting has been attributed to the influence of the environment on the esterified form of ferulic acid present in the aleurone cell wall (Piot et al. 2000). Another interesting aspect of this reconstructed spectrum is the presence of a small band at ~1660–1725 cm^{-1} that is associated with the carbonyl group present in esters (Movasaghi et al. 2007; Calheiros et al. 2008). Moreover, peaks in the range ~1100–1500 cm^{-1} are much less sharp than in the model compound, probably due to the pure crystalline state of the latter as opposed to the complex mixture of substances present in the barley kernel. The reconstructed spectrum E, related to proteins, clearly shows the characteristic amide I (1600–1700 $cm^{-}1$), amide III (1230–1340 cm^{-1}), and phenylalanine ring (~1003 cm^{-1}) vibrations.

The spectrum F did not match with any of the model compounds, but appears as a result of the contribution of anisotropic starch bands, especially the glycosidic one at 865 cm^{-1}that is sensitive to the orientation of molecules within starch granules.

On the other hand, it was not possible to obtain clearly distinct reconstructions for the spectra of arabinoxylan and β-glucan, probably because of their highly similar spectral features or insufficient signal-to-noise ratio in the relevant areas of the image. In this sense, it is better to account for this spectrum as "non-starch cell wall carbohydrate" that, according to its location in barley seed, might represent arabinoxylan (71 %) in the endosperm aleurone layer or β-glucan (75 %) in the starchy endosperm (Bacic and Stone 1981).

The relative concentration of each component was mapped by fitting the corresponding BTEM-reconstructed spectrum. Figure 2.11 shows the resulting images from areas located at the boundary between starchy endosperm and aleurone layer in native and malted barley, respectively. Color bars indicate the coefficient of the LLS fit (with the sum of coefficients normalized to 1 for each pixel), which is proportional to the relative abundance of the component. Starch images reveal small rounded and large ellipsoidal starch granules ranging from 2 to 20 μm inside the starchy endosperm cells. In native barley, proteins appear distributed in the cells of the aleurone layer and the starchy endosperm. Malted barley endosperm exhibits a reduction in protein matrix concentration inside the starchy endosperm cells quite likely caused by the enzymatic action during malting.

Esterified ferulic acid in both native and malted barley is disseminated throughout cell walls of the aleurone layer. Non-starch carbohydrates (arabinoxylan and β-glucan) are distributed throughout the cell wall of the aleurone layer and the endosperm in the native barley but appear completely degraded in the starchy endosperm of malted barley. In several images, a pale "halo" is observable outside the areas of high concentration, probably due to an excessive peak resolution in some BTEM reconstructions, as commented at the end of Sect. 4.2.

For the sake of comparing different spectral analysis methods, Fig. 2.12 shows the images obtained from the same native sample in Fig. 2.11 by mapping the PCA coefficients (or *scores*) of the first four loadings, which are plotted alongside each image. These images present clear similarities with those observed with the BTEM processing, but they are considerably more blurred and of more difficult interpretation because the relevant loadings mix features from different components.

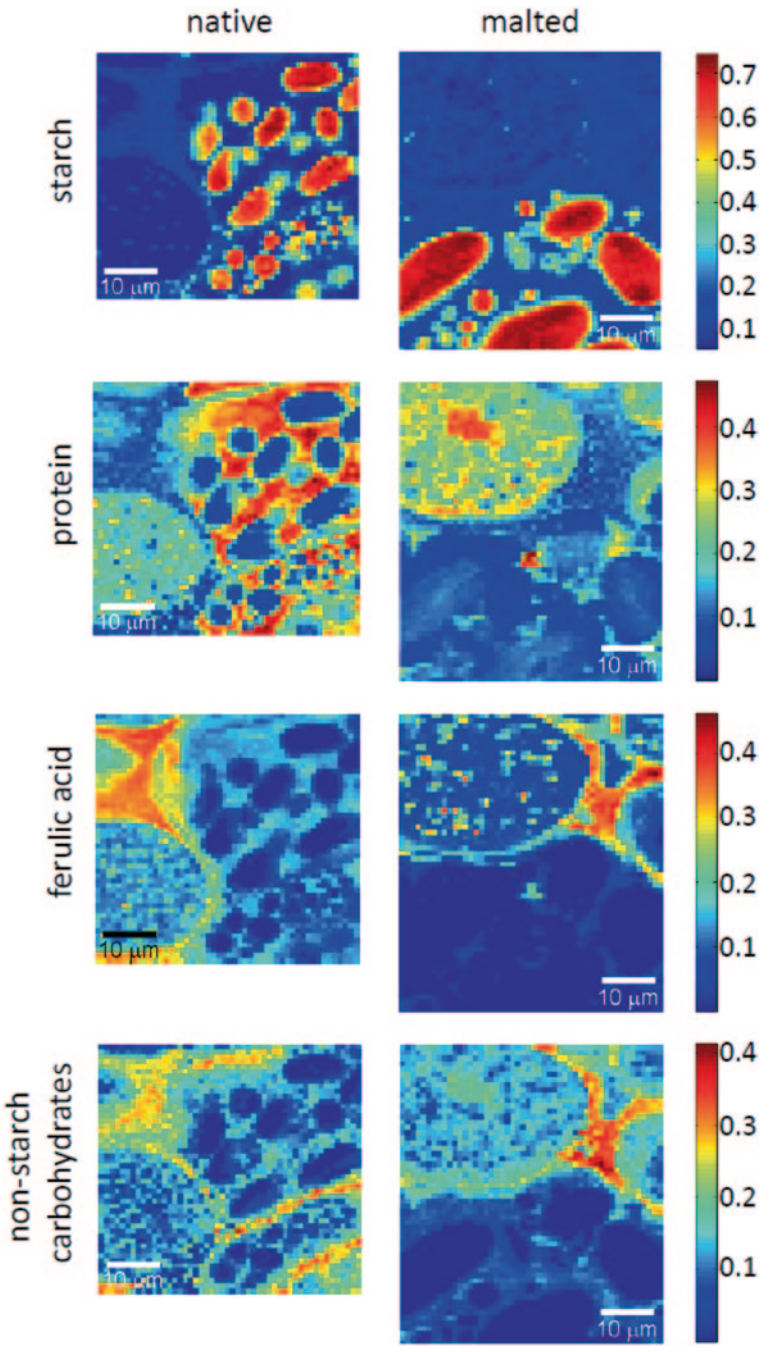

Fig. 2.11 Raman images based on the BTEM-reconstructed spectra of compounds present in the boundary aleurone layer-endosperm in native and malted barley. They correspond to: starch, protein, ferulic acid, non-starch carbohydrates. *Color bars* indicate the fraction of the LLS fit coefficient, which is proportional to the relative concentration of the component (Galvis et al. 2015). Reproduced with permission from Elsevier

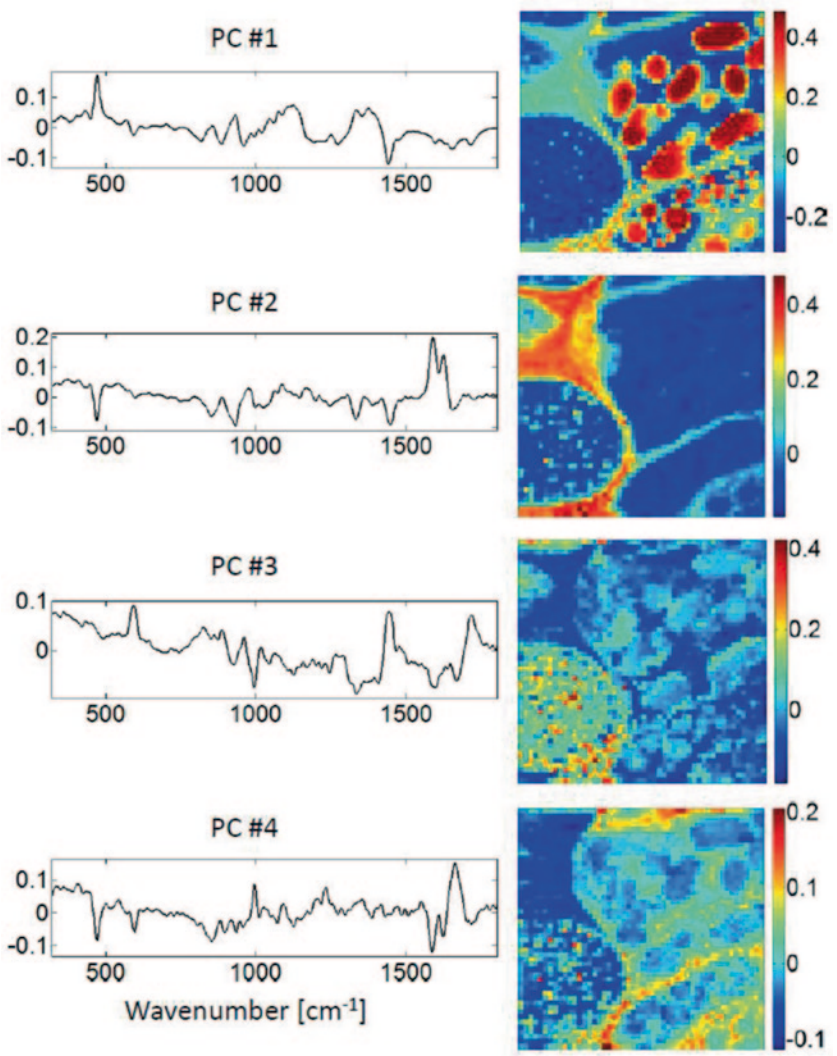

Fig. 2.12 Plots of the first four principal components (PC) for the Raman image from the boundary aleurone layer-endosperm in native barley and corresponding maps. The *color bar* indicates the coefficient (score) of the relevant loading

Consequently, and also because PCA scores can have negative values, it is always problematic to relate them to precise chemical concentrations or other physical quantities.

Raman images taken from the center of the starchy endosperm in both native and malted barley are shown in Fig. 2.13. Large starch granules (10–20 μm) and small rounded granules (2–5 μm) embedded in the cells can be observed. The small starch granules in malted barley appear partially degraded because of the hydrolytic action of amylases (Pomeranz 1972; Tarr et al. 2012). Changes in the shape of large starch

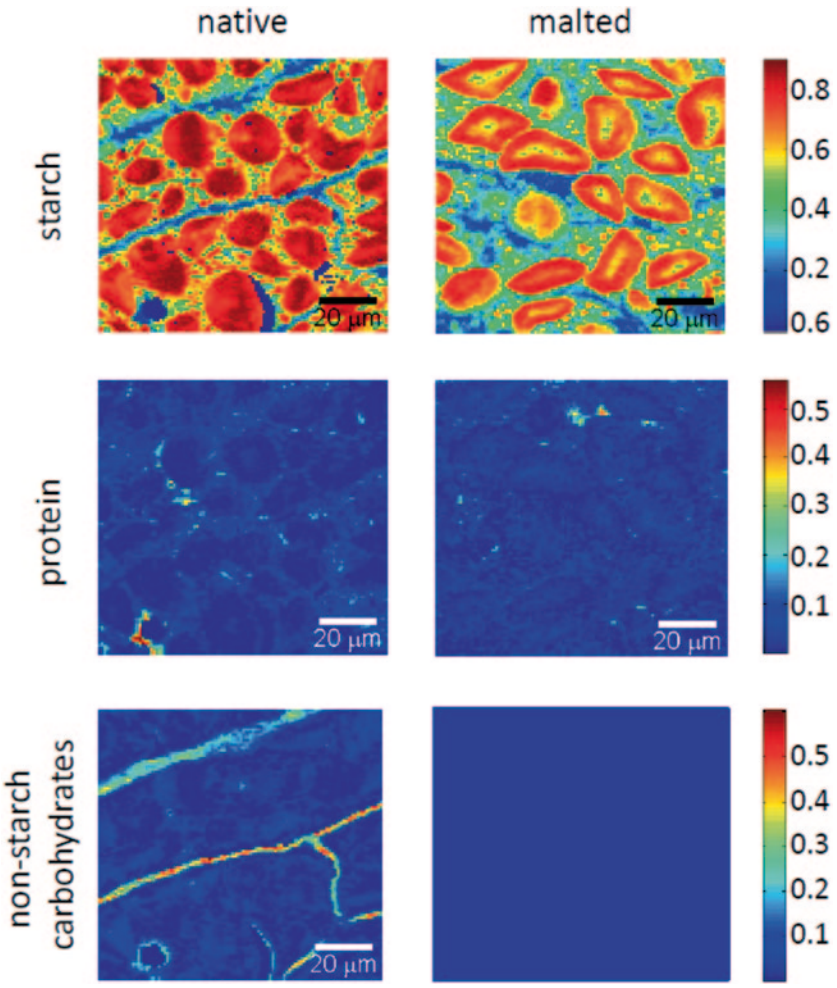

Fig. 2.13 Raman images based on the BTEM-reconstructed spectra of starch, protein, and non-starch carbohydrates present in the middle of endosperm of native and malted barley. Reconstructed spectra of non-starch carbohydrates were not resolved for malted barley. Color bars indicate the fraction of the LLS fit coefficient as in Fig. 2.3 (Galvis et al. 2015). Reproduced with permission from Elsevier

granules were observed in the malted grains. In this case, the equatorial groove appears bigger when compared to starch granules in the native kernel, an effect that might be caused by the thermal treatment during kilning. The cells and the cell walls in the central endosperm in native barley show smaller protein concentration compared to the native endosperm areas close to the aleurone layer (Fig. 2.11), but after malting almost no protein matrix was detected (Wijngaard et al. 2007). Similarly, the spectrum of ferulic acid is not found in the cell walls in the central endosperm in native barley, in accordance with observations reported in the literature (Fincher and Stone 1986; Jääskeläinen et al. 2013).

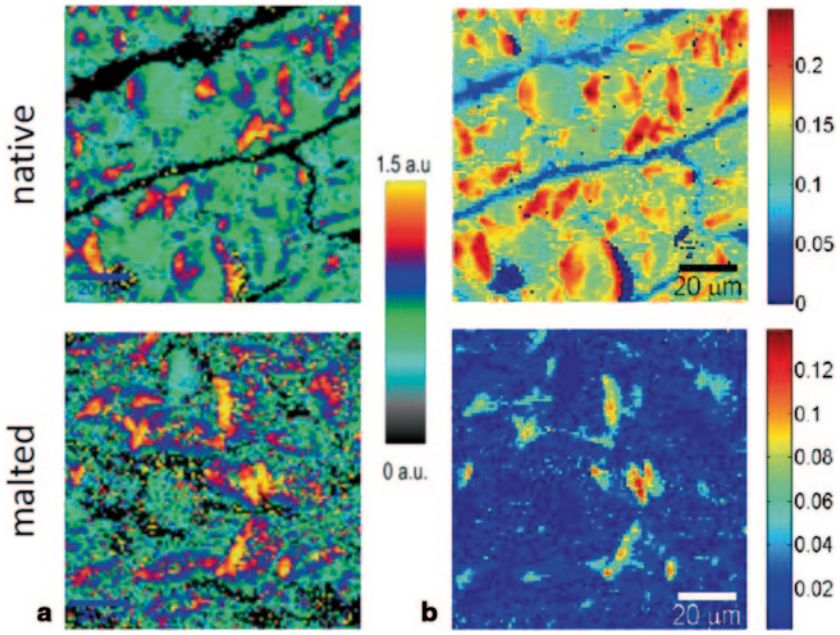

Fig. 2.14 **a** Raman images of the integrated 865 cm^{-1} band from a region located on the center of the endosperm for native *(top)* and malted *(bottom)* barley kernel. **b** Raman images for the same samples based on the BTEM-reconstructed spectrum F (Fig. 2.10) (Galvis et al. 2015). Reproduced with permission from Elsevier

Non-starch carbohydrates (mainly β-glucan) are distributed within the cell wall of native barley but not in the malted barley, thus indicating cell wall hydrolysis during malting.

As can be seen in Fig. 2.14, maps obtained from spectrum F of Fig. 2.10 are very similar to those produced by simple integration of the highly anisotropic starch peak at 865 cm^{-1}. This outcome supports the interpretation that spectrum F does not correspond to a chemical substance, but rather expresses the orientation of ordered structures in the sample, mainly inside large starch granules.

2.6 Conclusions

In this chapter, the FTIR microspectroscopy and CRM techniques were illustrated, explaining their functioning principles and main experimental setups. Their applicability in the analysis of cereal grains was discussed, presenting their strengths, limits, and other issues to be taken into consideration. Most grain components can be effectively identified and imaged based on their infrared or Raman features. In case of overlapping peaks, many chemometric methods are available to process the signal and resolve the various components in the sample. The case study shown here

is a clear example of how the combination of these spectral and computational techniques allows for a fast and noninvasive mapping of several chemical and structural details in cereal kernels.

The topics covered here provide an extensive and critical picture to all those who are interested in using vibrational microscopy for the imaging and analysis of cereals. We hope that this paper helps them choose the right technique for their purpose and gives stimuli to dig deeper into the subject.

References

Abdi H, Williams LJ (2010) Principal component analysis. Wiley Interdiscip Rev Comput Stat 2:433–459. doi:10.1002/wics.101

Bacic A, Stone BA (1981) Chemistry and organization of aleurone cell wall components from wheat and barley. Funct Plant Biol 8:475–495.

Barron C, Parker ML, Mills ENC et al (2005) FTIR imaging of wheat endosperm cell walls in situ reveals compositional and architectural heterogeneity related to grain hardness. Planta 220:667–677

Barron C, Robert P, Guillon F et al (2006) Structural heterogeneity of wheat arabinoxylans revealed by Raman spectroscopy. Carbohydr Res 341:1186–1191

Barron C, Rouau X (2008) FTIR and Raman signatures of wheat grain peripheral tissues. Cereal Chem 85:619–625

Bertinetto CG, Vuorinen T (2014a) Influence of pre-processing and distance on spectral classification: a simulation study. Vib Spectrosc 74:110–119

Bertinetto CG, Vuorinen T (2014b) Automatic baseline recognition for the correction of large sets of spectra using continuous wavelet transform and iterative fitting. Appl Spectrosc 68:155–164. doi:10.1366/13–07018

Bioucas-Dias JM (2009) A variable splitting augmented Lagrangian approach to linear spectral unmixing. First Work. Hyperspectral image signal process. Evol Remote Sensing, 2009. WHISPERS'09. IEEE, pp 1–4

Bocklitz T, Walter A, Hartmann K et al (2011) How to pre-process Raman spectra for reliable and stable models? Anal Chim Acta 704:47–56. doi:10.1016/j.aca.2011.06.043

Bonifacio A, Beleites C, Vittur F et al (2010) Chemical imaging of articular cartilage sections with Raman mapping, employing uni- and multi-variate methods for data analysis. Analyst 135:3193–3204. doi:10.1039/c0an00459f

Bonwell ES, Fisher TL, Fritz AK, Wetzel DL (2008) Determination of endosperm protein secondary structure in hard wheat breeding lines using synchrotron infrared microspectroscopy. Vib Spectrosc 48:76–81

Bro R (1997) PARAFAC. Tutorial and applications. Chemom Intell Lab Syst 38:149–171

Buckley K, Kerns JG, Parker AW et al (2014) Decomposition of in vivo spatially offset Raman spectroscopy data using multivariate analysis techniques. J Raman Spectrosc 45:188–192

Cael SJ, Koenig JL, Blackwell J (1973) Infrared and Raman spectroscopy of carbohydrates: part III: Raman spectra of the polymorphic forms of amylose. Carbohydr Res 29:123–134

Calheiros R, Machado NFL, Fiuza SM et al (2008) Antioxidant phenolic esters with potential anticancer activity: a Raman spectroscopy study. J Raman Spectrosc 39:95–107

Cappel UB, Bell IM, Pickard LK (2010) Removing cosmic ray features from Raman map data by a refined nearest neighbor comparison method as a precursor for chemometric analysis. Appl Spectrosc 64:195–200

Chalmers JM, Griffiths PR (2001) Vibrational spectroscopy: sampling techniques and fiber-optic probes. Handb Vib Spectrosc. doi:10.1002/0470027320.s8936

Chan TH, Chi CY, Huang YM, Ma WK (2009) A convex analysis-based minimum-volume enclosing simplex algorithm for hyperspectral unmixing. Signal Process IEEE Trans 57:4418–4432

Devos O, Duponchel L (2011) Parallel genetic algorithm co-optimization of spectral pre-processing and wavelength selection for PLS regression. Chemom Intell Lab Syst 107:50–58. doi:10.1016/j.chemolab.2011.01.008

Dieing T, Ibach W (2011) Software requirements and data analysis in confocal Raman microscopy. In: Dieing T, Hollricher O, Toporski J (eds) Confocal Raman microscopy. Springer, Berlin, pp 61–89

Ehrentreich F, Sümmchen L (2001) Spike removal and denoising of Raman spectra by wavelet transform methods. Anal Chem 73:4364–4373

Eilers PHC (2003) A perfect smoother. Anal Chem 75:3631–3636. doi:10.1021/ac034173t

Engel J, Gerretzen J, Szymańska E et al (2013) Breaking with trends in pre-processing? TrAC Trends Anal Chem 50:96–106. doi:10.1016/j.trac.2013.04.015

Fincher GB, Stone BA (1986) Cell walls and their components in cereal grain technology. In: Pomeranz Y (ed) Advances in cereal science and technology vol 8. American Association of Cereal Chemists, Minnesota, pp 207–296

Galvis L, Bertinetto C, Holopainen U et al (2015) Structural and chemical analysis of native and malted barley kernels by polarized Raman spectroscopy (PRS). J Cereal Sci 62:73–80. doi:10.1016/j.jcs.2014.12.008

Gholizadeh H, Naserian AA, Xin H et al (2014) Detecting carbohydrate molecular structural makeup in different types of cereal grains and different cultivars within each type of grain grown in semi-arid area using FTIR spectroscopy with uni- and multi-variate molecular spectral analyses. Anim Feed Sci Technol 194:136–144. doi:http://dx.doi.org/10.1016/j.anifeedsci.2014.05.007

Gierlinger N, Keplinger T, Harrington M (2012) Imaging of plant cell walls by confocal Raman microscopy. Nat Protoc 7:1694–1708

Gierlinger N, Keplinger T, Harrington M, Schwanninger M (2013) Raman imaging of lignocellulosic feedstock. Ed by Theo van Ven John Kadla 159

Gierlinger N, Schwanninger M (2006) Chemical imaging of poplar wood cell walls by confocal Raman microscopy. Plant Physiol 140:1246–1254. doi:pp.105.066993

Hao J, Zou X, Wilson MP et al (2009) A comparative study of feature extraction and blind source separation of independent component analysis (ICA) on childhood brain tumour 1H magnetic resonance spectra. NMR Biomed 22:809–818

Holopainen URM, Wilhelmson A, Salmenkallio-Marttila M et al (2005) Endosperm structure affects the malting quality of barley (*Hordeum vulgare* L.). J Agric Food Chem 53:7279–7287

Hyvärinen A, Oja E (2000) Independent component analysis: algorithms and applications. Neural Netw 13:411–430

Jääskeläinen A-S, Holopainen-Mantila U, Tamminen T, Vuorinen T (2013) Endosperm and aleurone cell structure in barley and wheat as studied by optical and Raman microscopy. J Cereal Sci 57:543–550

Jain AK, Dubes RC (1988) Algorithms for clustering data. Prentice-Hall Inc., Upper Saddle River

Jamme F, Robert P, Bouchet B et al (2008) Aleurone cell walls of wheat grain: high spatial resolution investigation using synchrotron infrared microspectroscopy. Appl Spectrosc 62:895–900

Jaumot J, Gargallo R, de Juan A, Tauler R (2005) A graphical user-friendly interface for MCR-ALS: a new tool for multivariate curve resolution in MATLAB. Chemom Intell Lab Syst 76:101–110

Kačuráková M, Wellner N, Ebringerová A et al (1999) Characterisation of xylan-type polysaccharides and associated cell wall components by FT-IR and FT-Raman spectroscopies. Food Hydrocoll 13:35–41. doi:http://dx.doi.org/10.1016/S0268-005X(98)00067-8

Kačuráková M, Wilson RH (2001) Developments in mid-infrared FT-IR spectroscopy of selected carbohydrates. Carbohydr Polym 44:291–303

Kizil R, Irudayaraj J, Seetharaman K (2002) Characterization of irradiated starches by using FT-Raman and FTIR spectroscopy. J Agric Food Chem 50:3912–3918

Kneipp K, Kneipp H, Itzkan I et al (1999) Ultrasensitive chemical analysis by Raman spectroscopy. Chem Rev 99:2957–2976

Laurens LML, Wolfrum EJ (2011) Feasibility of spectroscopic characterization of algal lipids: chemometric correlation of NIR and FTIR Spectra with exogenous lipids in algal biomass. Bioenergy Res 4:22–35. doi:10.1007/s12155-010-9098-y

Laxalde J, Ruckebusch C, Devos O et al (2011) Characterisation of heavy oils using near-infrared spectroscopy: optimisation of pre-processing methods and variable selection. Anal Chim Acta 705:227–234. doi:10.1016/j.aca.2011.05.048

Li J, Bioucas-Dias JM (2008) Minimum volume simplex analysis: a fast algorithm to unmix hyperspectral data. Geosci Remote Sens Symp 2008. IGARSS 2008. IEEE Int. IEEE, pp III–250–III–253

Liu Y, Himmelsbach DS, Barton FE (2004) Two-dimensional Fourier transform Raman correlation spectroscopy determination of the glycosidic linkages in amylose and amylopectin. Appl Spectrosc 58:745–749

Masic A, Bertinetti L, Schuetz R et al (2011) Observations of multiscale, stress-induced changes of collagen orientation in tendon by polarized Raman spectroscopy. Biomacromolecules 12:3989–3996. doi:10.1021/bm201008b

Miljković M, Chernenko T, Romeo MJ et al (2010) Label-free imaging of human cells: algorithms for image reconstruction of Raman hyperspectral datasets. Analyst 135:2002–2013. doi:10.1039/c0an00042f

Mills ENC, Parker ML, Wellner N et al (2005) Chemical imaging: the distribution of ions and molecules in developing and mature wheat grain. J Cereal Sci 41:193–201

Movasaghi Z, Rehman S, Rehman IU (2007) Raman spectroscopy of biological tissues. Appl Spectrosc Rev 42:493–541

Nascimento JMP, Bioucas Dias JM (2005) Vertex component analysis: a fast algorithm to unmix hyperspectral data. Geosci Remote Sens IEEE Trans 43:898–910

Philippe S, Barron C, Robert P et al (2006) Characterization using Raman microspectroscopy of arabinoxylans in the walls of different cell types during the development of wheat endosperm. J Agric Food Chem 54:5113–5119

Piot O, Autran JC, Manfait M (2000) Spatial distribution of protein and phenolic constituents in wheat grain as probed by confocal Raman microspectroscopy. J Cereal Sci 32:57–71

Piot O, Autran JC, Manfait M (2002) Assessment of cereal quality by micro-Raman analysis of the grain molecular composition. Appl Spectrosc 56:1132–1138

Polshin E, Aernouts B, Saeys W et al (2011) Beer quality screening by FT-IR spectrometry: impact of measurement strategies, data pre-processings and variable selection algorithms. J Food Eng 106:188–198. doi:10.1016/j.jfoodeng.2011.05.003

Pomeranz Y (1972) Scanning electron microscopy of the endosperm of malted barley. Cereal Chem pp 5–19

Rinnan Å, van den Berg F, Engelsen SB (2009) Review of the most common pre-processing techniques for near-infrared spectra. TrAC Trends Anal Chem 28:1201–1222. doi:10.1016/j.trac.2009.07.007

Rowlands C, Elliott S (2010) Automated algorithm for baseline subtraction in spectra. J Raman Spectrosc 42:363–369

Saulnier L, Robert P, Grintchenko M et al (2009) Wheat endosperm cell walls: spatial heterogeneity of polysaccharide structure and composition using micro-scale enzymatic fingerprinting and FT-IR microspectroscopy. J Cereal Sci 50:312–317

Savitzky A, Golay MJE (1964) Smoothing and differentiation of data by simplified least squares procedures. Anal Chem 36:1627–1639

Schlücker S, Schaeberle MD, Huffman SW, Levin IW (2003) Raman microspectroscopy: a comparison of point, line, and wide-field imaging methodologies. Anal Chem 75:4312–4318

Schulze G, Jirasek A, Yu MML et al (2005) Investigation of selected baseline removal techniques as candidates for automated implementation. Appl Spectrosc 59:545–574

Schulze HG, Turner RFB (2013) A fast, automated, polynomial-based cosmic ray spike-removal method for the high-throughput processing of Raman spectra. Appl Spectrosc 67:457–462

Sebastian S, Sundaraganesan N, Manoharan S (2009) Molecular structure, spectroscopic studies and first-order molecular hyperpolarizabilities of ferulic acid by density functional study. Spectrochim Acta Part A Mol Biomol Spectrosc 74:312–323

Singh J (2004) The PSO toolbox. http://psotoolbox.sourceforge.net/. Accessed 9 Feb 2015
Strang G, Ngyen T (1996) Wavelets and filter banks. Wellesley-Cambridge Press: Wellesley MA
Tan S-T, Zhu H, Chew W (2009) Self-modeling curve resolution of multi-component vibrational spectroscopic data using automatic band-target entropy minimization (AutoBTEM). Anal Chim Acta 639:29–41
Tanaka M, Young RJ (2006) Review Polarised Raman spectroscopy for the study of molecular orientation distributions in polymers. J Mater Sci 41:963–991
Tao X, Wang B, Zhang L, Zhang JQ (2007) A new scheme for decomposition of mixed pixels based on nonnegative matrix factorization. Geosci Remote Sens Symp 2007. IGARSS 2007. IEEE Int. IEEE, pp 1759–1762
Tarr A, Diepeveen D, Appels R (2012) Spectroscopic and chemical fingerprints in malted barley. J Cereal Sci 56:268–275
Tauler R, Walczak B, Brown SD (2009) Comprehensive chemometrics: chemical and biochemical data analysis. Elsevier
Thygesen LG, Løkke MM, Micklander E, Engelsen SB (2003) Vibrational microspectroscopy of food. Raman vs. FT-IR. Trends Food Sci Technol 14:50–57
Toole GA, Wilson RH, Parker ML et al (2007) The effect of environment on endosperm cell-wall development in *Triticum aestivum* during grain filling: an infrared spectroscopic imaging study. Planta 225:1393–1403
Tsuboi M, Thomas JR GJ (1997) Raman scattering tensors in biological molecules and their assemblies. Appl Spectrosc Rev 32:263–299
Walker AM, Yu P, Christensen CR et al (2009) Fourier transform infrared microspectroscopic analysis of the effects of cereal type and variety within a type of grain on structural makeup in relation to rumen degradation kinetics. J Agric Food Chem 57:6871–6878
Van Benthem MH, Lane TW, Davis RW et al (2011) PARAFAC modeling of three-way hyperspectral images: endogenous fluorophores as health biomarkers in aquatic species. Chemom Intell Lab Syst 106:115–124. doi:10.1016/j.chemolab.2010.09.003
Van Soest JJG, Tournois H, de Wit D, Vliegenthart JFG (1995) Short-range structure in (partially) crystalline potato starch determined with attenuated total reflectance Fourier-transform IR spectroscopy. Carbohydr Res 279:201–214
Weakley AT, Warwick PC, Bitterwolf TE, Aston DE (2012) Multivariate analysis of Micro-Raman spectra of thermoplastic polyurethane blends using principal component analysis and principal component regression. Appl Spectrosc 66:1269–1278. doi:10.1366/12-06588
Wellner N, Georget DMR, Parker ML, Morris VJ (2011) In situ Raman microscopy of starch granule structures in wild type and ae mutant maize kernels. Starch-Stärke 63:128–138
Widjaja E, Li C, Chew W, Garland M (2003) Band-target entropy minimization. A robust algorithm for pure component spectral recovery. Application to complex randomized mixtures of six components. Anal Chem 75:4499–4507
Wijngaard HH, Renzetti S, Arendt EK (2007) Microstructure of buckwheat and barley during malting observed by confocal scanning laser microscopy and scanning electron microscopy. J Inst Brew 113:34–41
Windig W, Keenan MR (2011) Angle-constrained alternating least squares. Appl Spectrosc 65:349–357
Winter ME (1999) N-FINDR: an algorithm for fast autonomous spectral end-member determination in hyperspectral data. SPIE's Int Symp Opt Sci Eng Instrum. International Society for Optics and Photonics, pp 266–275
Zhang L, Henson MJ (2007) A practical algorithm to remove cosmic spikes in Raman imaging data for pharmaceutical applications. Appl Spectrosc 61:1015–1020
Zhao J, Lui H, McLean DI, Zeng H (2007) Automated autofluorescence background subtraction algorithm for biomedical Raman spectroscopy. Appl Spectrosc 61:1225–1232
Zimmermann T, Marrison J, Hogg K, O'Toole P (2014) Clearing up the signal: spectral imaging and linear unmixing in fluorescence microscopy. Methods Mol Biol 1075:129–148

Chapter 3
Imaging of Double Emulsions

Richard Bernewitz, Gisela Guthausen and Heike P. Schuchmann

3.1 Introduction: Double Emulsions—Structure and Challenges for Imaging

Emulsions are disperse systems that can be found in many food systems. Their droplets can be loaded with various substances, among others with colours, flavouring or active agents. Process and recipe parameters influence the emulsions' structure and consequently their properties. The physical properties of emulsions depend on structure parameters such as droplet size distribution (DSD) and disperse phase ratio (DPR). Not only texture and colour tone can be adjusted (Schuchmann 2007; Ribeiro et al. 2009), also rheological (Weipert et al. 1993) and biochemical (Badolato-Bönisch 2009), as well as physical storage stability (Stokes 1851) are determined by DSD and DPR while keeping the recipe of the emulsion constant.

The structure of double emulsions is more complex (Schuchmann and Köhler 2012; Muschiolik 2007; Muschiolik 2006); they can be described as an emulsion within an emulsion: Inner droplets are dispersed in intermediate droplets, which are dispersed in the outer phase (Fig. 3.1). A variety of potential applications make research in this field attractive. An often discussed application is fat reduction without compromising textural properties (Ficheux et al. 1998; Lobato-Calleros et al. 2008), which is of interest especially for high-fat products such as mayonnaise. Functional food products should provide active substances. Release kinetics (also release rate) becomes important as an additional parameter in multiple emulsion systems. Adjustable release kinetics is nowadays often realised via coated (microporous)

H. P. Schuchmann (✉) · R. Bernewitz
Institute of Process Engineering in Life Sciences, Section I: Food Process Engineering, KIT, Karlsruhe, Germany
e-mail: heike.schuchmann@kit.edu

G. Guthausen
Pro2NMR, IBG2 and IMVM, KIT, Karlsruhe, Germany
e-mail: gisela.guthausen@kit.edu

N. Sozer (ed.), *Imaging Technologies and Data Processing for Food Engineers,*
Food Engineering Series, DOI 10.1007/978-3-319-24735-9_3

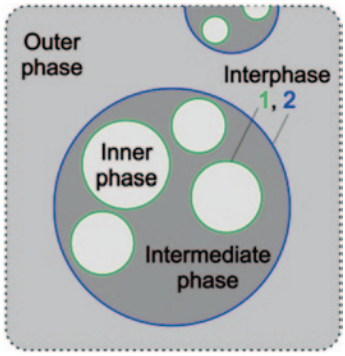

Fig. 3.1 Scheme of a double emulsion showing inner droplets dispersed in intermediate droplets which are dispersed in the outer phase. The inner and the outer phases are usually of similar chemical composition (oil or water, with some additives). Two interfaces are present, the inner *(1)* and the outer *(2)*. They are typically covered by at least two different emulsifiers that stabilise both emulsions

particles, which can also be synthesised via double emulsion polymerisation (Shum et al. 2009; Liang et al. 2011). In double emulsions, the inner droplets can be loaded with active substances (Ribeiro et al. 2009; Ax 2004; Frank 2012). The fact that double emulsions are in liquid aggregate state leads to a variety of diffusion phenomena. The release kinetics is influenced by diffusion between the inner and outer phase, where molecules pass the intermediate phase and both interfaces. These exchange phenomena have to be considered with respect to a controlled release of active substances (McClements et al. 2009b; Garti and Benichou 2011; Lakkis 2007; Bernewitz et al. 2013).

During (double) emulsions characterisation (Bernewitz 2013; Guthausen 2012) in product design and development as well as in quality control, parameters such as DSD, DPR, chemical composition, release kinetics and the disperse character itself have to be known. Besides other measuring techniques for these parameters (Schuchmann and Köhler 2012), diverse imaging techniques are extensively applied.

Generally, an appropriate image contrast between the three phases has to be created for successful imaging. Distorting effects such as droplet movement, diffusion or optical overlay effects have to be overcome. Droplets dispersed within droplets require the inner droplets to be small. Their diameters d are usually between $0.1\ \mu m < d < 20\ \mu m$. Temporal and spatial resolutions of the imaging technique have to match the system's characteristics, especially in the case of time-resolved observation of processes. Apart from the appropriate imaging modality, data processing is an issue particularly in the case of quantitative analysis. In the following session, an overview of imaging techniques and data processing will be given with a focus on double emulsion systems.

3.2 Imaging Techniques: Principles and Application to Double Emulsions

3.2.1 Optical Microscopy

Since the early days of multiple emulsion science, the emulsions' structure has been examined with optical microscopes (Seifriz 1925). Over time, light sources changed, and imaging principles have been developed further. Optical transmission microscopes (e.g. Török and Kao 2007) can often be found in double emulsion characterisation (Lee and Weitz 2009). Figure 3.2a shows such an image of a water in oil in water (WOW) double emulsion. The multiple emulsion structure is clearly visible. Apart from a polydispersity check, the technique also allows for the observation of reactions inside the droplets (Shum et al. 2009). However, the contrast between the phases and the projection technique limit the application towards a statistical analysis. Optical overlay of droplets leads to distorting effects especially in concentrated emulsions. Additionally, the optical resolution is strictly limited by flared light and the *Abbe* limit (Abbe 1873), which is determined by the light's wave number.

Overlay effects can be overcome by confocal microscopes (Price and Jerome 2011; Pawley 2006): The excitation light is focussed on an optical plane within the sample. As a result, an optical slice image is obtained (Figs. 3.2b and 3.3), and emission light from other distances outside the slice is excluded from the image acquisition. The confocality and therefore the optical slice thickness can be varied via

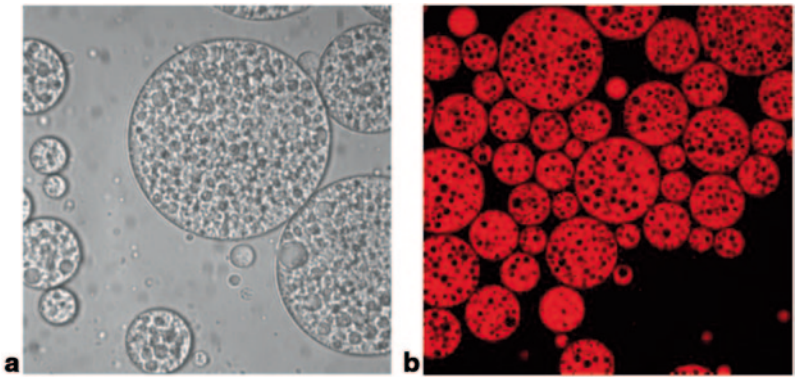

Fig. 3.2 **a** Transmitted light microscope image of a double emulsion. As the third spatial dimension is not resolved, projections of the sample are observed. The size of the droplets can be deduced from the image. Overlay effects of the inner and intermediate droplets hamper a detailed image analysis regarding the inner droplets. **b** Confocal laser scanning microscopy (CLSM) image of a double emulsion (image size: 142 × 142 µm). A good contrast between the phases is achieved by the addition of fluorescent dyes (*here:* Nile Red). The confocal principle allows a minimisation of overlay effects, leading to an appropriate image quality for statistical image analysis. (Schuster et al. 2012)

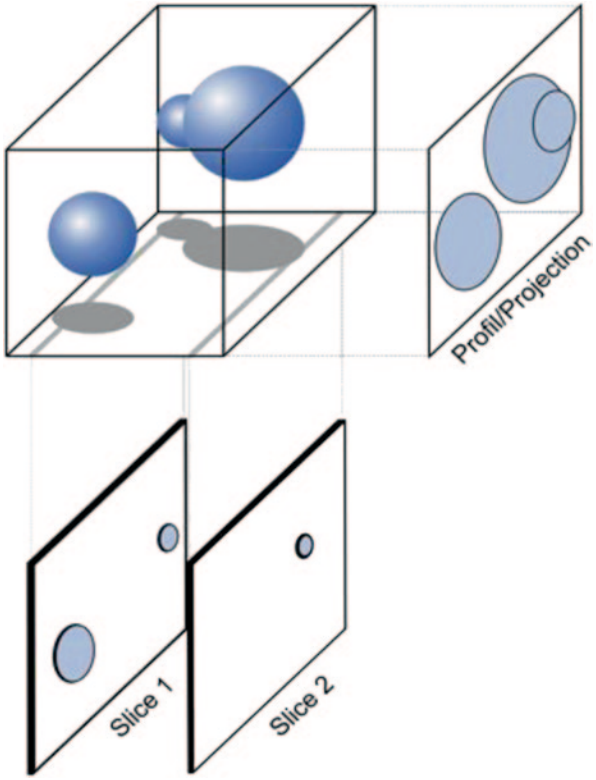

Fig. 3.3 Projection versus slice imaging: The profile of droplets, which is obtained by, for example, a transmission light microscope, suffers from overlay effects. Structural parameters can hardly be extracted. Nevertheless, representative diameters and the circumferences can be extracted from the projections. When a spatial resolution along the third spatial dimension, often called depth, is available, slices through the samples can be observed, which represent the sample at a certain depth. Droplets are optically cut, and overlay effects are reduced to nearly zero. This slicing can either be achieved technically, resulting in a non-destructive slicing (e.g. optical imaging, magnetic resonance imaging (MRI) and computer tomography) or mechanically (e.g. transmission electron microscopy, TEM)

the diameter of an aperture, often named pinhole. Depending on the microscope's parameters, overlay effects can be reduced to nearly zero.

Additionally, the third spatial dimension can be resolved in confocal microscopy: When performing a multi-slice experiment, 3D images can be reconstructed from 2D spatially resolved images taken at different depths, but continuously over a certain height (also called 2.5D). This results in a comprehensive quasi 3D view of the imaged sample. Therefore, one of the main differences compared to conventional transmission light microscopy is that the projection technique is replaced by a slicing technique via the focus of the laser beam in a certain depth of the sample. By scanning the lateral dimensions, an optical slice can be observed instead of the projection in transmission light microscopy.

A second difference concerns the image contrast: When observing liquid phases with similar refraction index with light microscopes, the contrast between the phases is relatively poor. For a better contrast between the phases, dyes can be used. When choosing dyes with largely different solubility in the different phases (i.e. oil or water), specific image contrast can be obtained (Adams et al. 2012). Fluorescent dyes (e.g. Haugland 2002) have special advantages regarding double emulsions. Solubility, excitation and emission wave length are specific for a dye molecule. In fluorescence microscopes (e.g. Pawley 2006) the spontaneous emission of photons after excitation, the fluorescence of dye molecules, is exploited. The excitation wave length can be adjusted when using lasers, the common light sources in fluorescence microscopy nowadays. Due to the *Franck–Condon* principle and the Stoke's shift, the wave number of the emitted light equals or is larger than the wave number of the excitation. This leads to a comfortable way to create contrast between excitation and detected light, as well as between different phases—an optimal condition for optical imaging of double emulsion.

Another point to be mentioned is the lateral dimension of a light beam. Focussing the light effectively into a small spot allows the application of the scanning technique, well known in electron and atomic force microscopy (AFM). It is usually combined with the confocal principle (Pawley 2006): The excitation light is focussed not only on a plane in the sample but also laterally. Thus the focused laser beam is scanned pixel by pixel over the complete optical mask, which defines the area of the sample to be imaged. The complete image is subsequently calculated. This leads to drastically reduced flare light, that is, to better contrast and better spatial resolution.

All these technical details improve the image quality in confocal laser scanning microscopy (CLSM; Pawley 2006), which has been applied on emulsions in various ways:

- Visualisation of particles (Balakrishnan et al. 2012) and proteins (Saglam et al. 2011) at the droplets' interface
- Visualisation of the morphological character of (food) emulsions (Blonk and Vanaalst 1993) with high DPR (Romero et al. 2008; Manoi and Rizvi 2009)
- Visualisation of the distribution of active substances (Nilkumhang et al. 2009)
- Observation of the multiple character (Blonk and Vanaalst 1993; Mao et al. 2007) of an emulsion and complex particles produced of multiple emulsions (Lamprecht et al. 2000)
- DSD of (food) single emulsions (van Dalen 2002b; Emin and Schuchmann 2013; Langton et al. 1999; Ríos et al. 2002)
- DSD of double emulsions (Schuster et al. 2012)
- Observation and quantification of release processes (Bernewitz et al. 2013)

A rather interesting application of CLSM concerns the above-mentioned release kinetics: In the case of an impermeable interfacial structure, the dye molecules are concentrated in a certain phase. An osmotic pressure exists, which drives the system towards concentration equilibrium. In the case of more or less permeable interfaces and boundary layers of emulsions, diffusion of dye molecules between the phases

leads to an equilibration of the dye molecule concentration in different compartments or even throughout the whole double emulsion. For a constant contrast in a CLSM image, diffusion of the dye molecules between the phases has to be precluded. On the other hand, with respect to observation of release kinetics, diffusion between the phases in double emulsions can be exploited (Sect. 4.3).

The minimal resolution of a common CLSM is in the order of 0.4 μm/pixel, depending on the hardware, the emission wave number and the aperture. The resolution is also limited by the *Abbe* limit. Progress in the field of microscopy led to new techniques, which overcome these limits. 4π-microscopy (Hell and Stelzer 1992; Hell et al. 1994; Cremer and Cremer 1971) improves the spatial resolution by using two lenses that are installed in opposite to each other with the sample in between. Its name is derived from the maximum possible angle at which the sample can be excited and signal can be detected. The excitation can be realised via both lenses (depending on the geometric arrangement of the lens) at the same time, leading to an improvement of the optical resolution. Another fluorescence method to improve the image quality is the stimulated emission depletion (STED; Hell and Wichmann 1994; Klar and Hell 1999). It uses a second emission beam of a certain wave number which deactivates fluorescence molecules by stimulated emission. The geometry of this light beam is such that only molecules in the centre of gravity of both beams contribute to the image which therefore shows a largely reduced spatial resolution. With the STED technique, lateral resolutions down to 2.6 nm have been realised (Wildanger et al. 2012), being no longer restricted by the *Abbe*-limit. The 4π and STED techniques can advantageously be combined (Dyba and Hell 2002; Schmidt et al. 2008).

Some challenges and limitations are presently known when examining double emulsions with optical microscopes. *Brownian* and forced motion of the droplets due to temperature and density gradients have an increasing impact on the image quality with higher magnification and beam power. Especially temperature gradients caused by the microscope's light beam are unavoidable and often lead to changes of the emulsion's composition or aggregate state. Motion blurred images are a result of moving droplets in combination with high light power and high exposure times during image acquisition. The effect is shown in Fig. 3.4 on the example of a water-in-oil-in-water (W/O/W) triple emulsion. It is observed more often in aqueous than in oily emulsions, due to the lower viscosity of water. The small aperture of scanning microscopes leads to longer exposure times of a smaller area, therefore to larger temperature gradients and finally to motion blurring. Not only is the lateral image quality influenced, but the effect is especially visible in the 3D reconstruction of multi-slice experiments (Fig. 3.4) due to the long experiment times. An optimisation of aperture size, exposure time and scan number is necessary for a good image quality with as little artefacts as possible and an optimal contrast. Digital image size is another important parameter. The optimal parameters need to adjusted based on individual sample and experiment conditions.

The variability of liquid multi-dispersed systems increases with the degree of dispersity. As shown in (Adams et al. 2012), transmitted light microscopy can be used to check the poly-disperse character of dyed droplets also. The inner droplets in these experiments were low concentrated and are arranged in a way that overlay

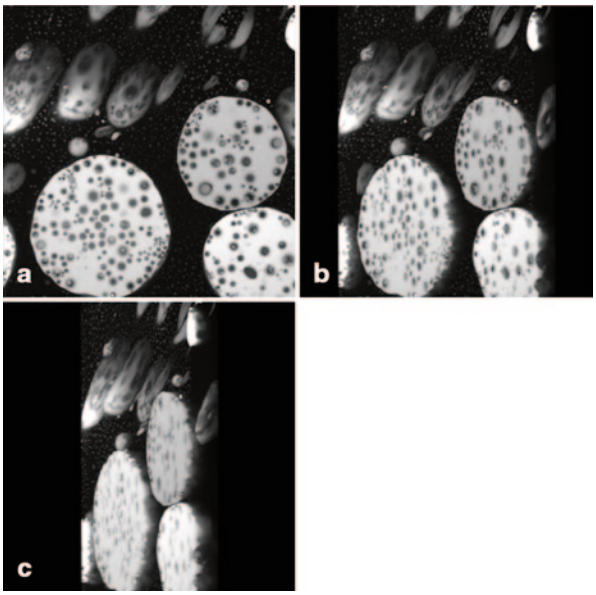

Fig. 3.4 Confocal laser scanning microscopy (CLSM) on a W/O/W triple emulsion. In a multi-slice experiment, the observed 2D images were reconstructed to a 2.5D image. Rotations of the resulting image are shown here. **a** No rotation. The upper slice nearest to the glass slide already shows the triple emulsion character. Optical effects due to the glass slide are visible in the form of small bright spots. Oil droplets sticking at the glass slide are deformed (*lower* and *right* area). Other droplets (*upper left* area) move during light exposure causing motion blurring. **a**–**c** show slices obtained by a left hand rotation of the 3D reconstruction with 100 slices and a resulting slice thickness of 0.149 µm. The multiple image acquisition time was about 1.5 h. The different observation angles, in **b** 40° and in **c** 70°, reveal the structure of the two inner emulsions (especially for the two droplets in the *lower right* corner), which are not visible in the 2D image in **a**

effects are excluded in this case. Figure 3.4 shows a CLSM multi-slice experiment on a W/O/W triple emulsion where the advantages of CLSM for imaging of multiple emulsion structures are summarised. It is an example showing different aspects of disperse systems' imaging.

- The image contrast depends on the dye and its concentration.
- Droplets stick to the glass slides commonly used in optical microscopy. They are partially deformed due to the glass contact.
- Due to temperature gradients, the long experiment duration of 1.5 h and the viscosity of the quasi-continuous outer oil phase, motion blurring occurs.
- The reconstruction of the 2D slice images to a 3D data set allows the optical rotation into all directions and a volumetric reconstruction, which results in a more comprehensive view of the structural details in this multiple emulsion.

The images can be statistically evaluated for DSD determination of the disperse phases (Sect. 3.2). The sample depths have to be chosen to image round droplets that are not deformed while being adhered at the glass slide for this purpose.

3.2.2 Electron Microscopy

Electron microscopy (Egerton 2005a, 2005b) relies on the interaction of emitted electrons with matter. Two main techniques are known, the surface-sensing scanning electron microscopy (SEM) working in reflection and the TEM, which exploits the attenuation of energy of the electron beam while passing through the sample. These techniques are of high interest in industry and research and are applied in various fields (Li 2002) with a spatial resolution down to a few nanometres. This spatial resolution is required, for example in nanoscience, where nanoparticles can also be prepared from double emulsions (Cohen-Sela et al. 2009).

In the case of double emulsions, TEM provides images of the complete double emulsion structure. Good contrast is achieved due to the specific electronic properties of oil and water phases. One consequence of the good spatial resolution is that motion processes within the sample and of the sample itself have to be avoided on the length and time scales of the experiment. Freezing of double emulsions satisfies this technical prerequisite.

Cryo-TEM is a destructive method. First, the emulsion is frozen. Depending on the freezing temperature and time scale, ice crystals can penetrate interfaces and change the structure dramatically. This aspect has to be considered when preparing emulsion samples. Once frozen, a very thin piece of sample is cut from the frozen emulsion, to achieve sufficient transmission of the electron beam. As a result, slice images are obtained. These images could lead to both DSD and DPR. Several error sources have to be considered in such analysis: Apart from the destructive nature of the method, the statistical significance has to be taken into account, which is discussed in more detail in Sect. 3. Due to the elaborate sample preparation of the Cryo-TEM technique, this aspect leads to high effort when aiming for statistical parameters of double emulsions. Therefore, this technique is appropriate to investigate the multiple disperse character as well as interface structure.

The Cryo-TEM technique was applied to WOW double emulsions (Hanson et al. 2008). Droplets could be observed on a 100-nm scale, revealing the multiple emulsion character. Additionally, a first vague insight into the stabilisation properties of co-polypeptides could be observed. Although this example shows how electron microscopy can be used, the laborious and destructive sample preparation procedure does not make electron microscopy techniques appropriate standard measuring techniques, but well-suited techniques for unraveling spatial details on a very small length scale.

3.2.3 Atomic Force Microscopy

In contrast to the imaging modalities mentioned before, AFM (Binnig et al. 1986; Butt et al. 2007) relies on interactions between a surface under examination and the tip of a micromechanical cantilever. Samples can be investigated under ambient conditions, which is a big advantage compared to electron microscopy. Forces as small

as a few pN can be measured. By scanning a given area of up to 100 μm in square by AFM, surface maps of specific forces can be obtained, which reflect surface specific properties such as molecular arrangement, composition, magnetic moments, etc. Lateral resolution is currently in the order of 2–10 nm, the depth dimension can be resolved on the atomic scale. Apart from the imaging capability of AFM, forces are studied most often as a function of distance from a surface, while keeping the lateral position constant. In the case of emulsions, colloidal probes allow direct measurements of adhesion phenomena and interactions between droplets. Care has to be taken with respect to pressure, stress and temperatures on the location of the measurement in order to retain the molecular structure during the measurement.

Against the background of the imaging methods mentioned before, it is clear that each technique has its unique length and time scales on which it delivers valuable information. In the case of AFM on emulsions, the relevant length scales are the dimension of the colloidal tip, which determines the spatial resolution together with the surface roughness. The geometry of the tip is another important quantity, which determines sensitivity as well as the resolvable time scales of AFM measurements (Butt et al. 2007). It is clear that the instrumental time and length scales should ideally match with those of the investigated samples and the processes taking place in the sample (i.e. diffusion). Although AFM investigations in emulsion science consider only single emulsions, interesting results are generated by this technique, while the focus is currently on three main aspects:

- *Force measurements:* In this measurement mode, the lateral resolution is of minor importance. Forces between the colloidal tip and a fixed droplet are investigated as a function of speed and direction (approach or retraction; Gillies and Prestidge 2004). Surface forces determine the stability of the dispersion and are accessible by AFM. Adhesion, caused by electrostatic and van der Waals forces, play a major role in flow properties and nano-rheology. These forces have also an impact regarding macroscopically observable phenomena such as coalescence. Recently, it was shown that AFM measurements could also be performed in the non-linear range and under oscillatory motion. Although AFM allows access to a rather limited surface area, it reveals elementary parameters for modelling emulsion systems (Tabor et al. 2011a, b, 2012, 2013; Lockie et al. 2012).
- *Imaging of emulsion surfaces* and distribution of surface active molecules and their molecular conformation: The molecular scale in emulsions is of special importance in investigations of permeability and controlled release of active agents. Surface coverage and molecular conformations determine these macroscopically relevant parameters. AFM allows a detailed view into the arrangements of surface molecules, also in the case of mixtures of these macromolecules and as a function of chemical parameters such as pH-value (Morris et al. 2011; Touhami et al. 2011).
- *Combination with other imaging techniques:* A fascinating question concerns the deformation of droplets under shear, under pressure and during approach of another droplet in an emulsion. Combining AFM with CLSM allows investigation of these processes. While measuring forces with AFM, CLSM can be used to observe the mechanical responses in real time. The surface layer of the droplets

is usually fluorescent, allowing the optical detection of the deformation directly (Manor et al. 2012; Wackerbarth et al. 2009).

As nanoparticle research currently widens towards possible applications, an interesting approach should be mentioned, where AFM and TEM are used to probe properties of nanoparticles relevant as MRI contrast agents (Ashjari et al. 2012): Meanwhile, relaxation agents play a major role in medical MRI, which have the prerequisite of being very effective and biocompatible. Relaxation active agents were implemented into double emulsions. Their structure was examined by AFM and TEM, the relevance for MRI by means of relaxation measurements. This study shows that the combination of several analytical techniques allows drawing a comprehensive picture and deepening the understanding of structured substances substantially.

3.2.4 Nuclear Magnetic Resonance

MRI is known to be a powerful imaging tool in medicine and increasingly also in material and food science. It relies on Nuclear Magnetic Resonance (NMR) and employs magnetic field gradients for generation of spatial resolution (Kimmich 1997; Callaghan 1991, 2011). Typical values for spatial resolution are in the range of several 10 μm in material science and up to the millimetre range for medical imaging. Often, it is limited by the achievable signal-to-noise ratio, which is given by the number of nuclear spins in a volume element, that is, voxel. The diffusion limit at spatial resolutions of a few micrometre in liquid samples is important: As the spatial resolution in MRI is created by a linearly varying magnetic field on a given spatial coordinate, every sort of motion of the detected nuclear spins is detected in the images. Brownian motion leads to displacements of molecules in the micrometre range on the typical time scales of image acquisition and therefore to artefacts in the micrometre-resolved images. By the way, the diffusion limit restricts the spatial resolution not only of MRI, but also of the other techniques, dependent on the time scales and other specific properties of the corresponding techniques.

There are mainly three schemes for spatial encoding via gradients in MRI summarised below. They can be combined for pure 2D, multi-slice 2.5D, or real 3D images. Also profiling along one spatial dimension is known:

- Read gradient: A magnetic field gradient is applied during data acquisition. A Fourier transform of the acquired data finally reveals a profile along the selected spatial coordinate.
- Phase gradient: Data are acquired which are encoded by a gradient before data acquisition. By incrementing the phase gradient and a subsequent Fourier transform along this direction of the two dimensional data set, the spatial information can be obtained.
- The third possibility is to use slice selection by a gradient combined with a shaped pulse. Almost rectangular slices can be imaged and reveal information just of the chosen slice. This technique can also be applied as a multi-slice experiment, where

slices can be acquired in parallel and with arbitrary orientation without spending measurement time for a detailed representation of the chosen spatial dimension.

The three encoding techniques can be combined in a very flexible and variable way such that an MRI experiment can be individually designed for the sample and question under investigation. This is a major advantage of MRI, which on the other hand requires users with some knowledge.

Despite the limitations concerning mainly spatial resolution, signal-to-noise ratio and temporal resolution, MRI is unique concerning the image contrast: Different from, for example, optical and x-ray techniques, which use absorption or emission contrast also by adding dyes as contrast agents, MRI utilises diversity of intrinsic contrast parameters. The most elementary is the spin density, which determines the NMR signal amplitude of each voxel directly. Additionally, the NMR relaxation times T_1 and T_2 are quite different and specific for substances and materials. For example, oil and water as fundamental ingredients in double emulsions have T_1 values in the order of 350 ms and 2–3 s, T_2 values around 50 ms and 1.6 s at a ^{1}H Larmor frequency of 200 MHz. Diffusion is not only a limited factor when using small voxel sizes, but it can also be exploited as a contrast parameter. Water shows a self-diffusion coefficient of about 2×10^{-9} m^2/s, whereas oil is characterised by a mean self-diffusion coefficient of about 8×10^{-12} m^2/s at room temperature. Further techniques exploit the chemical shift as contrast parameter. In this respect, NMR is known as a versatile tool for determination of chemical structures. The use of this contrast is extremely useful, for example, in functional imaging for revealing metabolic activities. As in optical imaging, contrast agents can be added. Most of them consist of paramagnetic molecules or ions (Aime et al. 2005; Bertini et al. 2001), which shorten both relaxation times T_1 and T_2. Other studies exploit the magnetic susceptibility contrast due to magnetic nanoparticles (Choo et al. 2013; Courant et al. 2013; Fardis et al. 2012; Chaughule et al. 2012). Especially in the context of hyperthermia, these particles can be applied not only for diagnostic but also for dedicated therapeutic purposes.

An important point to mention is that MRI is completely non-destructive in both senses that the samples do not have to be cut physically nor the energy intake is such that destruction can occur. The energy quanta are in the radio frequency range and therefore, they do not ionise tissue or other sample materials (compared to x-ray tomography, for example). Temperature gradients are usually of minor importance.

Regarding emulsions, NMR imaging techniques are applied in various ways (Mariette 2009). An MRI study was performed on a millimetre-scale emulsion (Henning et al. 2012), aiming for detection of release. Microcapsules of polysaccharides were investigated with respect to the permeability of the membranes and the influence of environmental parameters. Concretely, the permeability of a common MRI relaxation agent gadolinium-diethylenetriamine penta-acetic acid (Gd-DTPA) was investigated and quantitatively analysed via the change in relaxation contrast of 2D MRI images. The comparison of the experimental MRI results with results from the numerical solution of the diffusion equation reveals good agreement. By this means, a variation of environmental parameters such as pH-value could be investigated with respect to their influence following the experimental and numerical procedures (Henning et al. 2012).

As mentioned above, the length scale of most food emulsions is in the range of 0.1–50 µm. The spatial resolution of a common MRI, also called *k*-space imaging, is therefore hardly sufficient to directly image the droplets over the complete range of sizes. On the other hand, pulsed field gradient (PFG)-NMR, also called *q*-space imaging (Callaghan 2011, 1990; Lee et al. 1998), can be applied, which is not directly an imaging method in the sense of visualisation along spatial coordinates, but an indirect method to investigate length scales of diffusing molecules, that is, it is an imaging method for the observation of molecular displacements within a given time. Apart from PFG-NMR in porous media (Callaghan 2011; Kärger et al. 2013), this approach is applied to analyse DSD of single and double emulsions (Johns 2009; Hollingsworth et al. 2004; Hollingsworth and Johns 2003; Bernewitz et al. 2011a, b; Wolf et al. 2009; Hindmarsh et al. 2005; Mezzenga et al. 2004; Lönnqvist et al. 1997). It relies on the measurement of *Brownian* motion in the presence of geometrical hindrance or restriction. Dedicated mathematical models allow the calculation of, for example, DSD (Packer et al. 1972; Murday and Cotts 1968; Veeman 2003; Balinov et al. 1993, 2003). In the case of single emulsions, standard routines and procedures are used in food design and production (van Duynhoven et al. 2002, 2010; Voda and van Duynhoven 2009). Some insight into release kinetics was obtained in a diffusion exchange study. It revealed the exchange of molecules in polyelectrolyte multilayer structures (Wende and Schönhoff 2010; Qiao et al. 2005).

On double emulsions, PFG-NMR was successfully applied for a comprehensive characterisation. Topics of release kinetics and exchange of molecules between similar phases across an intermediate phase were addressed as well as the determination of DPRs and droplet size determination (Bernewitz et al. 2011b, 2013, 2014a; Hindmarsh et al. 2005; Mezzenga et al. 2004; Lönnqvist et al. 1997; Guan et al. 2010; Johns and Hollingsworth 2007). In contrast to the above-mentioned CLSM and MRI experiments, the difference in the effective diffusion coefficient between the quasi-continuous phase and the geometrically restricted inner phase of a double emulsion is explored. This allows the investigation of double emulsions in concentration equilibrium, that is, the osmotic forces can be neglected. Even in this case it was found, that molecules penetrate the intermediate phase and exchange between the two similar phases (Wolf et al. 2009; Bernewitz et al. 2011a; Guan et al. 2010). This phenomenon can be described in analogy to water exchange in biological tissues (Hindmarsh et al. 2005; Pfeuffer et al. 1998a, b) and will further be discussed in Sect. 4.3.

3.3 Image Processing

3.3.1 Contrast and Quantitative Image Analysis

Apart from the diverse underlying physical principles leading to different possibilities and limits of the mentioned imaging methods, data processing and analysis has to be considered as an important step towards reliable interpretation of spatially resolved data. Particularly with regard to quantitative data analysis, image contrast

is a rather important parameter. Depending on the imaging technique chosen, the physical origin of contrast is different; a general statement for optimisation is therefore not possible in the present context. However, on the examples of CLSM and MRI some essential points can be discussed, which can be transferred to other techniques:

- CLSM: Image contrast is created by fluorescence which depends strongly on structure and concentration of molecules being present in the imaged section. The contrast can therefore be designed by using the appropriate concentration of molecules, which fluoresce in a specific range of wavelength. Additionally, technical parameters such as focus and aperture size, slice thickness, size of the image section and digitisation rate are important to obtain images of good quality (Sect. 2.1).
- MRI: Contrast is often achieved due to the intrinsic spin density distribution, relaxation and diffusion in MRI in material science. Additionally, contrast agents might be applied, often in form of paramagnetic substances which influence the relaxation times or in form of magnetic particles with their influence on the main magnetic field. Interaction of the sample with the apparatus is rather small in the case of NMR and can be neglected in the presently know investigation of double emulsions (Sect. 2.4).

In both cases it is essential that the structures which should be quantified show a sufficient signal difference from other parts of the image as well as a sufficient signal-to-noise ratio. It is not only the signal-to-noise ratio of the image, which is important in the context of structural analysis. Most often, the first step is to create an intensity histogram, which is the basis for setting thresholds for structural differentiation. Binning of the image data is of course crucial for the quality of the deduced parameters, irrespective of the spatial dimensionality. Both, statistical significance and detail recognition are important and often interfere. Compromises have to be made in real imaging, well knowing that a final uncertainty remains. It is also due to the fact that the signal intensity is not constant over the complete field of view due to technical imperfections. Apart from thresholding, intensity gradients are explored to unravel structures. Separation of nearby and unresolved structures can be treated by water shed algorithms, leading to an improved recognition of structures. An example for image treatment can be found in the work of Al-Raoush 2007; Al-Raoush and Alshibli 2006. Also algorithms are known which use prior knowledge, for example, about the shape of the structure to be quantified. Modern numerical mathematics opens a variety of possibilities, which currently introduces image analysis in the field of material science.

3.3.2 Profiling Versus Slice Selective Imaging

Imaging methods can be divided into projection methods, for example, classic light microscopy and slicing methods such as x-ray imaging, CLSM and MRI (Fig. 3.3).

It is rather clear, that projections, also named profiles, have to be treated differently concerning information along the third spatial dimension. With respect to imaging of double emulsions, profiling methods often reveal diffuse images which do not allow a quantitative interpretation and description of the sample under investigation. Nevertheless, qualitative information about the dispersion degree of the inner emulsion can be obtained as well as a first impression about the DSD of the outer emulsion, separation and coalescence processes.

In contrast, slicing methods usually reveal 2D spatially resolved images. The third spatial dimension is averaged over the generally very small slice thickness. In CLSM, this is done by a dedicated focus of laser light, in MRI by slice gradients in combination with shaped rf-pulses, in x-ray tomography by mathematical treatment of the angle dependent projections via Radon transformation. All three methods are in principle capable to measure 3D images. In practice, requirements of data representation and restrictions of measurement time often lead to the reduction to slicing of the most interesting parts of the sample. The three mentioned imaging modalities work more or less non-destructively and are therefore able to describe the double emulsion as it is. Destructive slicing methods have to be distinguished. Most often, surface sensitive methods such as SEM and other electron spectroscopic methods have to be mentioned here. Emulsions are frozen and cut into slices, which are subsequently imaged. With the assumption that these processes do not influence the structure and composition of the sample, electron microscopy images reveal details on an atomic length scale, which is complementary to the scales of CLSM and MRI mentioned before.

An important characterising parameter is the DSD where the aspect of slicing methods versus projection (Fig. 3.3) has to be considered in the context of quantitative image analysis. In a projection, always the largest dimension of an object determines the shape. Smaller objects may be obscured by these large objects, especially in highly concentrated emulsions. On the other hand, slicing leads to a selection of a certain area which is not necessarily representative in several respects:

- Slicing error: In the case of a slice thickness smaller than the diameter of a droplet, it is obvious that the droplet is not necessarily *cut* in the equatorial plane. The measured diameter in the image is therefore equal or smaller than the true diameter of a droplet. Therefore, statistical data treatment was developed early in stereology, in the context of mineralogy and medicine (Gegner et al. 2004; Goldsmith 1967; Wicksell 1925; Reverter et al. 1993; Cruzorive 1976; Jeppsson et al. 2011; Saltykov 1974), which can be adapted to the special needs of the present noninvasive imaging techniques (Schuster et al. 2012; Van Dalen 2002a): The apparent diameter of droplets in a CLSM image are equal or smaller than the diameter, leading to an underestimation of the droplet sizes. The probability of being captured in an image is larger for large droplets, which leads to an overestimation of the larger fraction in the DSD. Both consequences can be statistically corrected by the corresponding algorithms according to *Wicksell, Gegner* and others (Gegner et al. 2004; Goldsmith 1967; Wicksell 1925; Reverter et al. 1993; Cruzorive 1976; Jeppsson et al. 2011; Saltykov 1974; Van Dalen 2002a).
- Error due to the image mask: Apart from the systematic error due to slicing the influence of the image mask, also named field of view, has to be considered: In

optical imaging and in AFM, TEM and SEM, only small sections of the sample are observed. Boundary effects are to be considered especially in cases when the dimensions of typical structures are comparable to the image mask. One possibility is to reject droplets from the quantitative analysis which are only partially visible in the image, which, however, decreases the statistical significance. A second possibility is to estimate the *true* diameter via statistical mask error correction (Schuster et al. 2012).

It should be mentioned, that both effects lead to systematic errors, which can be corrected only statistically. Special emphasis should be put on magnification, choice of slice thickness and image mask to minimise the impact of errors. A comparison with alternative techniques such as PFG-NMR and light scattering techniques could reveal systematic errors, too. These techniques are not capable to produce direct visual inspection but lead to DSD of a representative amount of sample.

3.3.3 Determination of Structural Parameters

The importance of structural parameters for product properties leads to intense investigations of deducing them from images. Quantitative image interpretation needs first of all suitable images which are acquired with appropriate contrast and signal-to-noise ratio as stated above. Imaging of structures is often sufficient for qualitative interpretation but not for qualitative and even more for automated analysis. An equally distributed intensity over the image section is preferable, however, in reality this is difficult to achieve during imaging and thus requires corrections already in the early stage of data interpretation. Additional to the mentioned steps of setting thresholds, binning of images and other numerical data treatment, typical characterising parameters have to be extracted from the corrected images. One of them is the DSD. The final step in data treatment is therefore to count droplets with a diameter in the experimentally accessible range. Two main approaches have to be mentioned: One method is counting pixels within a given area determined by the boundaries in a black–white image. This approach is independent on the shape of the object but depends on the quality of the watershed separation and the image contrast, that is, the thresholding procedure. In the second approach, prior knowledge on the droplets' spherical symmetry is utilised. In the case of double emulsions of reasonable concentration, this assumption is appropriate, whereas deviations might occur at high concentrations. In the most common imaging modality, that is, optical imaging, these emulsions are problematic anyway because of multiple scattering effects influencing the image quality significantly. Both methods are implemented in current imaging software. Nevertheless, quantitative image analysis is still a crucial step which should be critically observed in order to gain correct data for further steps of design and development of complex food structures.

A typical ratio of inner to outer droplets in double emulsion depends on the DPR, the dilution factor and the preservation degree due to the emulsification process. In the work by Schuster et al. 2012, the DSD of a WOW double emulsion was

determined by CLSM showing a ratio of inner to outer droplets of approximately 6. A DSD is, on the other hand, a statistical quantity. Therefore, a consideration of the statistical significance of an image analysis has to be performed. An empirical way of doing so can be found in the work by Schuster et al. 2012, where a varying amount of droplets was analysed in order to find a stable cumulative DSD. The number of droplets to be counted is rather large, leading to a considerable effort in data processing. The statistically relevant number of analysed droplets can also be found by application of statistical tools as hypothesis tests, which are implemented in common numerical data treatment software.

From these considerations, it is clear that a statistically significant amount of samples has to be analysed. Imaging modalities with spatial resolution in the nanometre range reveal detailed insight into forces and interfaces but hardly in a statistical description of structural parameters. Combining the complementary techniques mentioned above, however, completes and deepens our understanding of multiple emulsions to an enormous extend which would not be possible when just analysing the results from one technique.

3.4 Insights into Double Emulsions

3.4.1 Geometric Structure

The DSD determination of the inner and outer emulsion in multiple emulsions is a challenge for standard measuring techniques such as laser diffraction due to the need of dilution and multiple scattering (Bernewitz et al. 2014b). Other techniques such as PFG-NMR were adapted and currently reveal the inner DSD.

Imaging techniques have the potential to give a direct insight into structural details of double emulsions. Combined with statistical image processing, both DSD of double emulsions were determined applying CLSM (Schuster et al. 2012). Apart from the challenges to acquire appropriate images with sufficient contrast and a small amount of artefacts, the data analysis step has to be performed.

Critical points in deducing DSD of inner and outer dispersed phases from CLSM slice images are the following and need special emphasis:

- Adding dye molecules to the distinct phases is necessary for a good contrast. This could change, for example, the pH-value, which, then again, can have an impact on the structural parameters of a double emulsion. Care has to be taken that the double emulsion is not altered, neither with respect to structural nor with respect to physico-chemical parameters.
- To reduce motion blurring, the outer phase can be thickened, for example, by a gel-forming agent in water-based emulsions. However, many of these substances often used as food thickeners (e.g. xanthan, pectin, gelatine, etc.) are known to be surface active (Garti and Leser 2001; Dickinson 2011).
- Energy intake is not negligible. Temperature effects have to be critically considered.

- The optical slice thickness and the field of view should be adequate compared to the size of the structural elements to be analysed.
- Diffusion of dye molecules, concentration gradients and bleaching effects of the dye molecules should be considered when analysing the fluorescence intensity quantitatively. Setting thresholds in automated data processing should take these effects into account which can also exhibit a spatial dependence.
- The number of analysed objects have to be statistically relevant, especially when applying statistical corrections for slicing and mask errors.
- Depending on the underlying physical principle, different information about the distribution is gained: In PFG-NMR, volume-related distributions densities $q_3(d)$ or cumulative distributions $Q_3(d)$ are measured, other techniques such as CSLM reveal number or area-related distributions. The distributions can be converted mathematically.

The diversity of ingredients in double emulsions (at least two emulsifiers are required, and other stabilising agents as hydrocolloids often are added) means that the system is susceptible to chemical manipulation. A shift in pH-values can lead to a change in proteins' conformation, which can change the emulsions properties when using protein emulsifiers (Lam and Nickerson 2013; Benjamin et al. 2012). This was confirmed also by AFM measurements (Morris et al. 2011; Touhami et al. 2011). Salt-based dyes applied in fluorescence microscopy could also lead to a concentration gradient when added to the outer phase of double emulsions. Concentration gradients are usually equilibrated; in the case of WOW emulsion they often lead to driven diffusion from the inner water phase to the outer. The influence of added substances should always be known or investigated, in order to interpret the imaging data correctly. Due to their surface tension and thermodynamics, the assumption of droplets being spheres and showing circles in 2D-images is justified experimentally. Nevertheless, deformations occur, for example, in highly concentrated emulsions (Balinov et al. 1996) or due to adhesion at surfaces especially in optical microscopy and AFM. In such cases, the form factor has to be considered in data processing and interpretation.

The big advantage of applying CLSM to determine DSD of double emulsions is the direct access and visibility of a variety of droplets, which is the basis for a reliable determination of both DSDs. In Fig. 3.5, the outer and inner DSD of a WOW double emulsion is shown (Schuster et al. 2012). They have been extracted from one set of CLSM images with a ratio of inner to outer droplets of 6.

As mentioned, q-space imaging (PFG-NMR, Sect. 2.4) is capable to determine the inner DSD of a highly representative amount of double emulsions noninvasively and non-destructively. The sample can be measured as it is, without any additives or dilution, which shifts the thermodynamic equilibrium. The DSD is usually determined by fitting a mathematical model to the data. The most common ones are the model by Murday and Cotts (Murday and Cotts 1968) and the model of short gradient pulse approximation (Veeman 2003). Quantitative analysis of signal attenuation as a function of the q-value reveals the characteristic parameters of the droplets, median volume-related diameter $d_{50,3}$ and associated standard deviation σ, which corresponds to the distribution's width, of a log-normal distribution function.

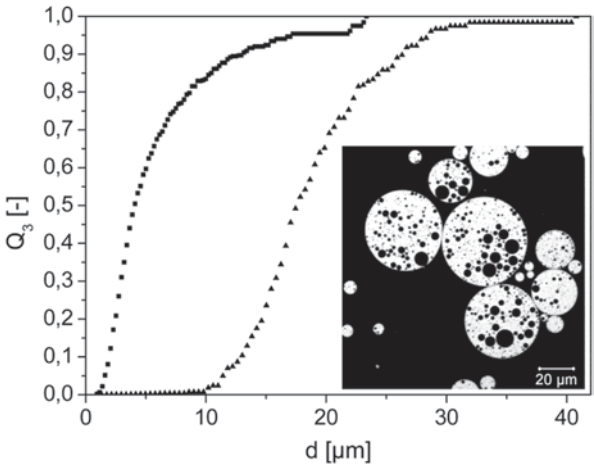

Fig. 3.5 Simultaneous determination of both, the inner (W1, ■) and outer (O, ▲) cumulative volume-related droplet size distributions (DSDs) of a water in oil in water (WOW) double emulsion. The oil phase was dyed with Nile Red. The *insert* shows the confocal laser scanning microscopy (CLSM) image of the W/O/W with the oil phase dyed (field of view 142.9 × 142.9 µm. (Reproduced from Schuster et al. 2012)

Currently, model-free approaches were investigated on single emulsions, which justify the assumption of a log-normal distribution (Johns and Hollingsworth 2007). In several investigations of *q*-space imaging on WOW double emulsions, it was found that dynamic exchange of water molecules has to be considered for a consistent DSD determination (Hindmarsh et al. 2005; Guan et al. 2010). This will be discussed in Sect. 4.3.

With CLSM and NMR *q*-space imaging, there are two possibilities to obtain valuable information about the DSD of double emulsions after their production. The CLSM technique shows good agreement for the outer DSD when compared to laser diffraction measurements (Schuster et al. 2012). Regarding CLSM and *q*-space imaging, good agreement was found for single emulsions (van Duynhoven et al. 2002; Johns and Gladden 2002; Van Lent et al. 2008) as well as for the inner DSD of double emulsions (Bernewitz et al. 2013).

3.4.2 Chemical Composition and Morphology

During production and storage, the ratios of the phases can change due to the emulsification process (Schuch et al. 2013), diffusion phenomena (Guan et al. 2010; Mezzenga et al. 2004) and physical processes during storage such as coalescence (Magdassi and Garti 1984) and Ostwald ripening (Marqusee and Ross 1984; Sect. 4.3). A loss of inner phase into the outer phase influences the emulsion's properties drastically. It can lead to the loss of active agents, a change in viscosity and therefore sensorial properties, an increase of the water activity (spoilage of food) or even the loss of the double emulsion character itself. These are usually unwanted effects. Two DPRs, the inner and outer, have to be measured for determination of the preservation degree (often *yield*).

In principle, both DPR can be determined from 3D images (Fig. 3.4). However, multiple slice experiments require measurement times in the order of several 10 min

to hours, depending on the required quality and accuracy of the images. The imaged objects have to keep their position during the complete acquisition time. This hardly is the case in phases of low viscosity. Therefore, the sample has to be solidified either by freezing or by thickening via additives that keep the sample translucent.

In fluorescence imaging, the light intensity can be analysed spectrally and spatially resolved (Lakowicz 2007; Gauglitz and Vo-Dinh 2006). With respect to DPR determination of double emulsions a prerequisite is that the fluorescence dyes, dissolved in the different phases of a double emulsion, emit fluorescence light of different wave number. Therefore, mixing of dyes in a given phase due to molecular diffusion has to be prevented which is achieved by polarity, that is, specific solubility.

A direct access to chemical information is given in NMR. As known from analytical chemistry, this technique is unsurpassed with respect to determination of chemical structure and quantification of mixtures' composition. Regarding double emulsions, the situation is complicated by the fact that phases of similar chemical structures have to be quantified, whereas oil and water can be differentiated and quantified easily in NMR spectroscopy (Guthausen and Kamlowski 2009), quantification of the similar phases of a double emulsions has to be discussed in more detail.

In fluorescence microscopy, this differentiation is achieved by adding specific dyes. In NMR, relaxation agents or diffusion contrast can be exploited, the latter being discussed in Sect. 4.3. Molecular displacements are strongly influenced by the geometry of the environment, which is clearly different in the outer and in the inner phases. The mechanisms of hindered and restricted diffusion influence the NMR signals characteristically and can therefore be used for the mentioned differentiation. If the molecular displacements are known from PFG-NMR experiments, the DPR can be determined with two methods (Bernewitz et al. 2014b):

- Diffusion weighted spectroscopy: In the case of double emulsions with strong signal attenuation of the outer phase (usually WOW emulsions), the DPR can be extracted from spectroscopic data by separation of the inner and outer phases' signals via application of magnetic field gradients and integration of the corresponding lines in the spectra, taking into account the influence of relaxation times and diffusion.
- Signal reconstruction: The differentiation of inner and outer phases is more complicated in case of highly concentrated double emulsions or OWO emulsions which have outer phases with small diffusion coefficients. The phase contributions to the oil signal are reconstructed via the molecular displacement signature. The single contributions of hindered and restricted diffusion have to be determined before by PFG-NMR experiments on the corresponding single emulsions, and deformation of droplets has to be excluded.

Prerequisite for these two NMR methods is that the time scale of molecular exchange, which will be discussed in Sect. 4.3, is long compared to the experimental time. If this assumption is fulfilled, the DPR can be determined with an accuracy of about 3 %.

As double emulsions are composed not only of water and oil, but also of emulsifiers in the percent range and as interfaces play a major role in stabilisation of emulsion structures, it is of special interest to image emulsifier distributions and even the

molecular configuration of these macromolecules. AFM is a suitable technique in this respect, requiring good spatial resolution. Images reveal surface and interface composition also as a function of local concentration (Morris et al. 2011).

^{13}C-NMR can be used to characterise emulsifiers. Valuable structure information from ^{13}C-NMR spectroscopy can be combined with information of other measuring techniques to gain a profound understanding of the emulsifier systems (e.g. Alberola et al. 2006; Parra et al. 1989).

3.4.3 Dynamic Processes: Exchange and Instabilities

Processes on the molecular scale determine encapsulation and controlled release of active agents. Also osmotic tailoring (Mezzenga et al. 2004) and physical instabilities such as Ostwald ripening (Yao et al. 1993; Marqusee and Ross 1984) are driven by diffusion phenomena. Diffusion phenomena are a special challenge for measuring techniques in emulsion science due to the involved time and length scales. Nowadays, imaging techniques are not fully capable of monitoring diffusion of molecules in real time, although new techniques can image on the nanometre scale (Sect. 2.1). Diffusion is a statistical process; the comprehensive description requires therefore the observation of an ensemble of molecules. Regarding double emulsions, dye diffusion in and between phases can be imaged leading to an estimation of the time scales of driven diffusion. Double emulsions of different recipes can be compared in order to get an insight into boundary properties of interfaces and intermediate phases. In the work by Bernewitz et al. 2013, an experiment is presented to monitor driven diffusion of fluorescein in WOW double emulsions by CLSM. Initially the double emulsion is dyed only in the intermediate phase. An appropriate CLSM set-up can be adjusted to perform the main experiment: A drop of dye solution is added, and a time series of images is acquired with a time resolution of about half a second. Two WOW emulsions of different recipes (see differences in legend) have been compared (Fig. 3.6): The concentration equilibrium is reached within few minutes in one double emulsion, but the concentration equilibrium was not reached after hours in another emulsion (Bernewitz et al. 2013). From these observations, diffusion kinetics could be extracted. This type of experiment can also be applied to OWO double emulsions (Bernewitz et al. 2014b).

A more detailed look into the molecular processes can be obtained by NMR. Whereas the above-described CLSM-related experiment allows the observation of concentration equilibration by driven diffusion, PFG-NMR can be used to measure diffusion properties of double emulsions in concentration equilibrium, which is of importance with respect to controlled release of active agents. Molecular exchange of water in WOW emulsions has been investigated and proven (Hindmarsh et al. 2005; Guan et al. 2010). It takes place on time scales of several up to a few hundred milliseconds. The exchange model (Pfeuffer et al. 1998a, b) was originally developed for the water exchange in tissue. Transferred to double emulsions, the residence times of molecules can be determined, which is another essential parameter for the characterisation of emulsions of different recipes.

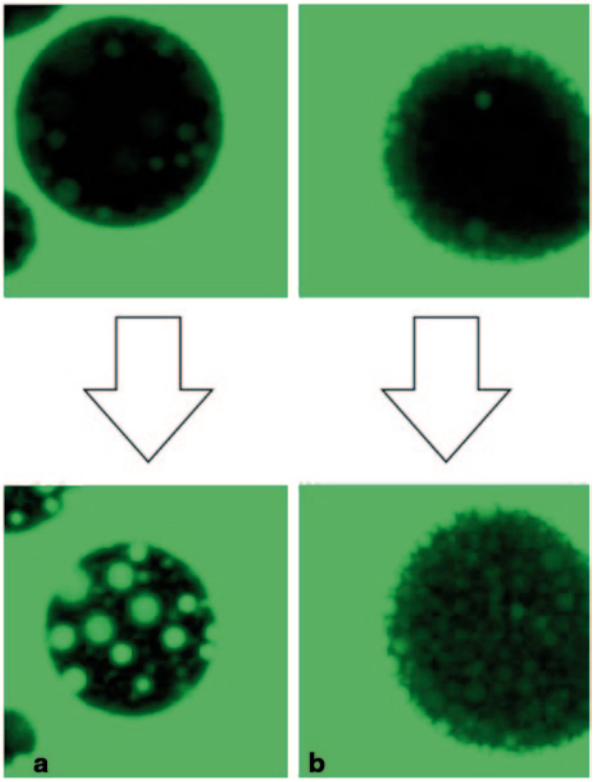

Fig. 3.6 Observation of fluorescein diffusion by confocal laser scanning microscopy (CLSM). According to the concentration gradient, a net transfer of dye to the inner phase occurs via driven diffusion from the outer to the inner water phase. Two emulsions of different recipes are shown. **a** The inner droplets were dyed within several minutes. In this case, polyglycerol polyricinoleate (PGPR) and Lutensol TO-10 were used as emulsifiers. **b** The emulsion was still not fully dyed after 4 h. The emulsifiers were PGPR and a whey protein isolate

The application of paramagnetic relaxation agents in NMR is in principle similar to the application of dyes in fluorescence microscopy. Due to the different nature of NMR, conclusions about the diffusion mechanisms can be drawn additionally to the diffusion kinetics. As the effect of paramagnetic relaxation is strongly dependent on distance, the direct environment of a paramagnetic molecule will be influenced, whereas molecules at larger distances will not be influenced. The experiments show that in a WOW emulsion the oil relaxation is enhanced—in addition to the water relaxation, which is expected in the case of exchange. This observation can only be interpreted when assuming that the diffusion mechanism takes place on the molecular scale, rather than in micelles.

3.4.4 Imaging of Emulsion: Characterisation of Physical Parameters from Processing to Digestion

The quantities in Sects. 4.1–4.3 describe mainly double emulsions in a thermodynamic equilibrium state and reveal a basic understanding of this type of food materials. Especially in the context of single emulsions, further studies are known, which

should be mentioned in this chapter, as an outlook for possibilities of future imaging based research on double emulsions.

During production, emulsions are exposed to considerable mechanical stress. Rheological quantities allow an integral characterisation of these processes. When combined with imaging methods, additional spatial information can be obtained. Several attempts are reported, combining a Couette shear cell with MRI for revealing the local shear stress and droplets deformation (d'Avila et al. 2005; Fridjonsson et al. 2011; Hollingsworth and Johns 2006).

Interactions between droplets are essential for ripening and coalescence, for example. These interactions can be characterised via force microscopy and combined methods (Sect. 2.3). Sensory properties are determined also by interactions of droplets with more or less solid surfaces, which are addressed via optical microscopy (Dresselhuis et al. 2008).

In the understanding and modelling of drying, for example, of milk, the behaviour of a single droplet as well as of an ensemble of droplets is essential to know. Publications report on the in situ observation of droplets drying (Lin and Chen 2004; Reis et al. 2006), which allow the determination of relevant model parameters.

Double emulsions often tend to separate. In the example of a WOW, several possibilities exist: Either only the outer water phase separates from the oil phase, the inner emulsion is stable such that the separated oil layer still contains the inner water droplets. This separation could also be incomplete. Or the emulsion separates completely, and the separated compartments are no longer in the dispersed state but rather completely coalesced and separated. Combined MRI and PFG-NMR reveal the microscopic character of a separated WOW emulsion (Caro 2014). In contrast to the WO single emulsion, from which the double emulsion was produced, the WOW separated into different phases: an oily phase in the supernatant and a watery phase being underneath. Additionally, part of the emulsifier is found on the bottom of the NMR tube. A sample from each phase was taken with a pipette for PFG-analysis. The MRI images show the phase separation clearly (Fig. 3.7a), whereas the PFG-NMR experiments show the structural composition: Comparing the signal decays of the oil rich phase of the separated WOW emulsion with the corresponding observation on the single emulsion (Fig. 3.7b), the conclusion is that the inner emulsion is more or less retained, but water molecules are still present in a spatial very restricted, perhaps layered form, leading to a rather slow signal decay at large gradients. A similar investigation of creaming by optical micrographs led to a model for depletion in the presence of protein sub-micelles (Jang et al. 2004).

Motivation for further development of double emulsions in the field of foods can be seen in the context of health benefits with fat reduction and encapsulation of active ingredients (Jiménez-Colmenero 2013). Digestion is therefore an important topic for possible applications of these structures. Imaging activities are also found in this context (McClements et al. 2009a), using—amongst others—fluorescence for the observation of processes in the mouth (Adams et al. 2007).

These few examples show the variety of beneficial application of analytical imaging techniques in the context of emulsion science and might be considered as a starting point for further investigations.

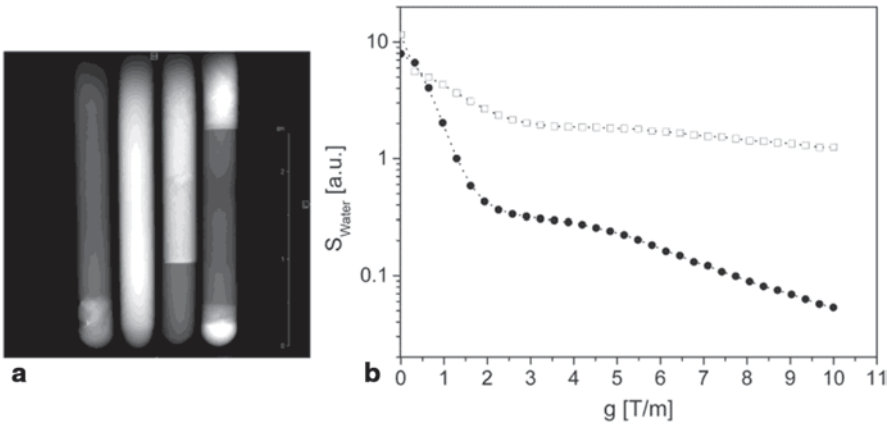

Fig. 3.7 Separation study on a WOW double emulsion. **a** Magnetic resonance imaging (MRI), from *left* to *right:* separated water phase, inner water in oil (WO) single emulsion, separated oily phase (supernatant) and separated water in oil in water (WOW) double emulsion. The time from sample preparation until the measurement was 2 h. *Dark* areas correspond to the water, *light* areas to the oil and emulsifier-rich phases. Additional diffusion measurements showed almost no difference between pure water (Sect. 2.4) and the separated watery phase. **b** *q*-space imaging of the water in oil (WO) single emulsion (●) and the water signal in the separated oil rich phase (□). The signal attenuation curves show that the oily supernatant consist of inner droplets and of boundary water

3.5 Summary

Imaging techniques on multiple emulsions were presented, and analytical techniques were shortly summarised with respect to their impact on emulsion science. The methods are rather complementary regarding spatial resolution and physical and chemical parameters, which can be obtained from the images. Slicing and profiling imaging techniques were compared. Structural parameters most often are distributed measures; therefore slice imaging techniques are more appropriate for characterisation of double emulsions, also with respect to overlay effects. The use of paramagnetic ions in MRI and *q*-space imaging and dyes, especially fluorescence dyes, in optical microscopy can lead to very good contrasts between the different phases of multiple emulsions. Dedicated experiments with these contrast agents allow the investigation of diffusion properties of double emulsions. On the example of molecular diffusion imaging, it is clear that time scales and dynamics of the system under investigation are reflected differently. These facts can be used to choose a well-suited technique for an actual question. More useful for a comprehensive description of complex food systems such as double emulsions, however, is the combination of the methods, all with their specific strength and weak points. On the examples of CLSM and NMR, this approach was shown to reveal many parameters relevant to describe double emulsions in product design and development as well as in quality control.

Acknowledgments The authors acknowledge financial support of the DFG in the project SCHU 1417/4-1 and for the NMR instrumental facility Pro²NMR. The members of the research groups of LVT and SRG10-2 are thanked for fruitful discussions and for assistance during experiments. Special thanks to Sandy Schuster, Esteban Caro and Frederic Schöffel who contributed to the work during their research thesis at KIT. The *Centre of Functional Nanostructures* (CFN) of KIT, especially Prof. Bastmeyer is thanked for the opportunity to work with a CLSM.

References

Abbe E (1873) Beiträge zur Theorie des Mikroskops und der mikroskopischen Wahrnehmung. Archiv für mikroskopische Anatomie 9

Adams lLA, Kodger TE, Kim SH, Shum HC, Franke T, Weitz DA (2012) Single step emulsification for the generation of multi-component double emulsions. Soft Matter 8:10719–10724

Adams S, Singleton S, Juskaitis R, Wilson T (2007) In-vivo visualisation of mouth-material interactions by video rate endoscopy. Food Hydrocolloid 21:986–995

Aime S, Botta M, Terreno E (2005) Gd(III)-based contrast agents for MRI. Advances in Inorganic Chemistry. Academic Press.

Alberola C, Blümich B, Emeis D, Wittern K-P (2006) Phase transitions of monoglyceride emulsifier systems and pearlescent effects in cosmetic creams studied by 13C NMR spectroscopy and DSC. Colloids Surf Physicochem Eng Asp 290:247–255

Al-Raoush R (2007) Microstructure characterization of granular materials. Physica A 377:545–558

Al-Raoush R, Alshibli KA (2006) Distribution of local void ratio in porous media systems from 3D X-ray microtomography images. Physica A 361:441–456

Ashjari M, Khoee S, Mahdavian AR (2012) Controlling the morphology and surface property of magnetic/cisplatin-loaded nanocapsules via W/O/W double emulsion method. Colloids Surf Physicochem Eng Asp 408:87–96

Ax K (2004) Emulsionen und Liposomen als Trägersystem für Carotinoide. Dr. Dissertation, Universität Karlsruhe (TH)

Badolato-Bönisch G (2009) Untersuchung zur mikrobiologischen Stabilisierung von Emulsionen. Dissertation, KIT

Balakrishnan G, Nicolai T, Benyahia L, Durand D (2012) Particles trapped at the droplet interface in water-in-water emulsions. Langmuir 28:5921–5926

Balinov B, Jonsson B, Linse P, Soederman O (1993) The NMR self-diffusion method applied to restricted diffusion—simulation of echo attenuation from molecules in spheres and between planes. J Magn Reson A 104:17–25

Balinov B, Linse P, Soederman O (1996) Diffusion of the dispersed phase in a highly concentrated emulsion: emulsion structure and film permeation. J Colloid Interf Sci 182:539–548

Balinov B, Marini D, Soederman O (2003) NMR studies of emulsions with particular emphasis on food emulsions. In: Friberg SE, Larsson K, Sjoblom J (eds) Food emulsions, 4th ed, Marcel Dekker

Benjamin O, Lasse M, Silcock P, Everett DW (2012) Effect of pectin adsorption on the hydrophobic binding sites of beta-lactoglobulin in solution and in emulsion systems. Int Dairy J 26:36–40

Bernewitz R (2013) Charakterisierung von Doppelemulsionen mittels NMR und CLSM—Struktur und Diffusion. PhD Dissertation, Karlsruher Institut für Technologie (KIT)

Bernewitz R, Guan X, Guthausen G, Wolf F, Schuchmann HP (2011a) PFG-NMR on double emulsions: a detailed look into molecular processes. In: Renou J-P, Belton PS, Webb GA (eds) Magnetic resonance in food science: an exciting future, RSC Publishing Cambridge, Clermont-Ferrant, pp 39–46

Bernewitz R, Guthausen G, Schuchmann HP (2011b) NMR on emulsions: characterisation of liquid dispersed systems. Magn Reson Chem 49:93–104

Bernewitz R, Dalitz F, Köhler K, Schuchmann HP, Guthausen G (2013) Characterisation of multiple emulsions by NMR spectroscopy and diffusometry. Microporous Mesoporous Mater 178:69–73

Bernewitz R, Schmidt US, Schuchmann HP, Guthausen G (2014a) Structure of and diffusion in O/W/O double emulsions by CLSM and NMR—comparison with W/O/W. Colloids Surf A Physicochem Eng Asp 458:10–18

Bernewitz R, Schmidt US, Schuchmann HP, Guthausen G (2014b) Structure of and diffusion in O/W/O double emulsions by CLSM and NMR—comparison with W/O/W. J Colloids Surf A Physicochemical and Engineering Aspects, in press

Bertini I, Luchinat C, Parigi G (2001) Solution NMR of paramagnetic molecules: applications to metallobiomolecules and models. Elsevier Science B.V., Amsterdam

Binnig G, Quate CF, Gerber C (1986) Atomic force microscope. Phys Rev Lett 56:930–933

Blonk JCG, Vanaalst H (1993) Confocal scanning light-microscopy in food research. Food Res Int 26:297–311

Butt HJ, Berger R, Bonaccurso E, Chen Y, Wang J (2007) Impact of atomic force microscopy on interface and colloid science. Adv Colloid Interface Sci 133:91–104

Callaghan PT (1990) Pgse Massey, a sequence for overcoming phase instability in very-high-gradient Spin-Echo NMR. J Magn Reson 88:493–500

Callaghan PT (1991) Principles of nuclear magnetic resonance microscopy. Oxford University Press, New York

Callaghan PT (2011) Translational dynamics and magnetic resonance: principles of pulsed gradient spin echo NMR. Oxford University Press Inc., New York

Caro E (2014) Investigations of diffusion phenomena in double emulsions with PFG-NMR. MA Master Thesis, KIT

Chaughule RS, Purushotham S, Ramanujan RV (2012) Magnetic nanoparticles as contrast agents for magnetic resonance imaging. Proc Natl Acad Sci India Sect a-Phys Sci 82:257–268.

Choo ESG, Peng E, Rajendran R, Chandrasekharan P, Yang CT, Ding J, Chuang KH, Xue J (2013) Superparamagnetic nanostructures for off-resonance magnetic resonance spectroscopic imaging. Adv Funct Mater 23:496–505

Cohen-Sela E, Chorny M, Koroukhov N, Danenberg HD, Golomb G (2009) A new double emulsion solvent diffusion technique for encapsulating hydrophilic molecules in PLGA nanoparticles. J Control Release 133:90–95

Courant T, Roullin GV, Cadiou C, Callewaert M, Andry MC, Portefaix C, Hoeffel C, De Goltstein MC, Port M, Laurent S, Vander EL, Muller RN, Molinari M, Chuburu F (2013) Biocompatible nanoparticles and gadolinium complexes for MRI applications. Comptes Rendus Chimie 16:531–539

Cremer C, Cremer T (1971) 4p Punkthologramme: Physikalische Grundlagen und mögliche Anwendungen, aus: Verfahren zur Darstellung bzw. Modifikation von Objekt-Details, deren Abmessungen außerhalb der sichtbaren Wellenlängen liegen. Deutschland patent application de 2116521

Cruzorive LM (1976) Particle-size—shape distributions—general spheroid problem.1. mathematical-model. J Microsc Oxford 107:235–253

D'avila MA, Powell RL, Phillips RJ, Shapley NC, Walton JH, Dungan SR (2005) Magnetic resonance imaging (MRI): a technique to study flow an microstructure of concentrated emulsions. Braz J Chem Eng 22:49–60

Dickinson E (2011) Double emulsions stabilized by food biopolymers. Food Biophys 6:1–11

Dresselhuis DM, Van Aken GA, De Hoog EHA, Stuart MAC (2008) Direct observation of adhesion and spreading of emulsion droplets at solid surfaces. Soft Matter 4:1079–1085

Dyba M, Hell SW (2002) Focal spots of size λ/23 open up far-field florescence microscopy at 33 nm axial resolution. Phys Rev Lett 88:163901-1–163901-4

Egerton R (2005a) Physical principles of electron microscopy: an Introduction to TEM, SEM, and AEM. Springer

Egerton RF (2005b) Analytical electron microscopy. Physical principles of electron microscopy. Springer US

Emin MA, Schuchmann HP (2013) Droplet breakup and coalescence in a twin-screw extrusion processing of starch based matrix. J Food Eng 116:118–129
Fardis M, Douvalis AP, Tsitrouli D, Rabias I, Stamopoulos D, Kehagias T, Karakosta E, Diamantopoulos G, Bakas T, Papavassiliou G (2012) Structural, static and dynamic magnetic properties of dextran coated gamma-Fe2O3 nanoparticles studied by Fe-57 NMR, Mossbauer, TEM and magnetization measurements. J Phys-Condens Mat 24
Ficheux MF, Bonakdar L, Leal-Calderon F, Bibette J (1998) Some stability criteria for double emulsions. Langmuir 14:2702–2706
Frank K (2012) Formulieren von Anthocyanen in Doppelemulsionen. PhD Dissertation, KIT
Fridjonsson EO, Chandrasekera TC, Sederman AJ, Johns ML, Zhao CX, Middelberg APJ (2011) Imaging the effects of peptide bio-surfactants on droplet deformation in a Taylor-Couette shear cell. Soft Matter 7:2961–2967
Garti N, Benichou A (2011) Double emulsions for controlled release applications—progress and trends. In: Sjoblom J (ed) Encyclopedic handbook of emulsions technology. Marcel Dekker, Inc., New York
Garti N, Leser ME (2001) Emulsification properties of hydrocolloids. Polym Advan Technol 12:123–135
Gauglitz G, Vo-Dinh T (2006) Handbook of spectroscopy, Wiley
Gegner J, Henninger C, Öchsner A (2004) Stereologic analysis and modelling of object distributions from sectional micrographs. Materialwiss Werkst 35:36–44
Gillies G, Prestidge CA (2004) Interaction forces, deformation and nano-rheology of emulsion droplets as determined by colloid probe AFM. Adv Colloid Interfac 108:197–205
Goldsmith PL (1967) The calculation of true particle size distributions from the sizes observed in a thin slice. Br J Appl Phys 18:813–830
Guan XZ, Hailu K, Guthausen G, Wolf F, Bernewitz R, Schuchmann HP (2010) PFG-NMR on W1/O/W2-emulsions: evidence for molecular exchange between water phases. Eur J Lipid Sci Technol 112:828–837
Guthausen G (2012) Produkt- und Prozesscharakterisierung mittels NMR-Methoden. PD Habilitationsschrift, KIT Karlsruhe
Guthausen G, Kamlowski A (2009) Developments in time domain and single sided NMR. In: Guojonsdottir M, Belton P, Webb GA (eds) Magnetic resonance in food science: challenges in a changing world. RSC Publisher, Nordic House, Reykjavik (Sep 15–17, 2008 2009), pp 46–56
Hanson JA, Chang CB, Graves SM, Li Z, Mason TG, Deming TJ (2008) Nanoscale double emulsions stabilized by single-component block copolypeptides. Nature 455:85–88
Haugland RP (2002) Handbook of fluorescent probes and research products, Eugene, OR, Molecular Probes
Hell S, Stelzer EHK (1992) Properties of a 4Pi confocal fluorescence microscope. J Opt Soc Am 9:2159–2166
Hell SW, Wichmann J (1994) Breaking the diffraction resolution limit by stimulated emission: stimulated-emission-depletion fluorescence microscopy. Opt Lett 19:780–782
Hell SW, Stelzer EHK, Lindek S, Cremer C (1994) Confocal microscopy with an increased detection aperture: type-B 4Pi confocal microscopy. Opt Lett 19:222–224
Henning S, Edelhoff D, Ernst B, Leick S, Rehage H, Suter D (2012) Characterizing permeability and stability of microcapsules drug delivery by dynamic NMR microscopy. J Magn Reson 221:11–18
Hindmarsh JP, Su J, Flanagan J, Singh H (2005) PFG-NMR analysis of intercompartment exchange and inner droplet size distribution of WOW emulsions. Langmuir 21:9076–9084
Hollingsworth KG, Johns ML (2003) Measurement of emulsion droplet sizes using PFG NMR and regularization methods. J Colloid Interf Sci 258:383–389
Hollingsworth KG, Johns ML (2006) Droplet migration in emulsion systems measured using MR methods. J Colloid Interf Sci 296:700–709
Hollingsworth KG, Sederman AJ, Buckley C, Gladden LF, Johns ML (2004) Fast emulsion droplet sizing using NMR self-diffusion measurements. J Colloid Interf Sci 274:244–250

Jang W, Nikolov A, Wasan DT (2004) Effect of depletion force on the stability of food emulsions. J Disper Sci Technol 25:817–821
Jeppsson J, Mannesson K, Borgenstam A, Agren J (2011) Inverse Saltykov analysis for particle-size distributions and their time evolution. Acta Mater 59:874–882
Jiménez-Colmenero F (2013) Potential applications of multiple emulsions in the development of healthy and functional foods. Food Res Int 52:64–74
Johns ML (2009) NMR studies of emulsions. Curr Opin Colloid In 14:178–183
Johns ML, Gladden LF (2002) Sizing of emulsion droplets under flow using flow-compensating NMR-PFG techniques. J Magn Reson 154:142–145
Johns ML, Hollingsworth KG (2007) Characterisation of emulsion systems using NMR and MRI. Prog Nucl Magn Reson Spectrosc 50:51–70
Kärger J, Chmelik C, Valiullin R (2013) Die innere Größe macht's Moleküldiffusion in nanoporösen Materialien. Phys Today 12:39–45
Kimmich R (1997) NMR—tomography diffusometry relaxometry. Springer, Berlin
Klar TA, Hell SW (1999) Subdiffraction resolution in far-field fluorescence microscopy. Opt Lett 24:954–956
Lakkis JM (ed) (2007) Encapsulation and controlled release technologies in food systems. Blackwell, Ames
Lakowicz JR (2007) Principles of fluorescence spectroscopy. Springer
Lam RSH, Nickerson MT (2013) Food proteins: a review on their emulsifying properties using a structure-function approach. Food Chem 141:975–984
Lamprecht A, Schäfer U, Lehr CM (2000) Structural analysis of microparticles by Confocal Laser scanning microscopy. AAPS PharmSciTech 1
Langton M, Jordansson E, Altskär A, Sørensen C, Hermansson A-M (1999) Microstructure and image analysis of mayonnaises. Food Hydrocolloid 13:113–125
Lee D, Weitz DA (2009) Nonspherical colloidosomes with multiple compartments from double emulsions. Small 5:1932–1935
Lee H-Y, Mccarthy MJ, Dungan SR (1998) Experimental characterization of emulsion formation and coalescence by nuclear magnetic resonance restricted diffusion techniques. Am Oil Chem Soc 75:463–475
Li Z (2002) Industrial applications of electron microscopy. Taylor & Francis
Liang SS, Chen SL, Chen SH (2011) Diverse macroporous spheres synthesized by multiple emulsion polymerization for protein analyses. Chem Commun 47:8385–8387
Lin SXQ, Chen XD (2004) Changes in milk droplet diameter during drying under constant drying conditions investigated using the glass-filament method. Food Bioprod Process 82:213–218
Lobato-calleros C, Sosa-Perez A, Rodriguez-Tafoya J, Sandoval-Castilla O, Perez-Alonso C, Vemon-Carter EJ (2008) Structural and textural characteristics of reduced-fat cheese-like products made from W-1/O/W-2 emulsions and skim milk. Lwt-Food Sci Technol 41:1847–1856
Lockie H, Manica R, Tabor RF, Stevens GW, Grieser F, Chan DYC, Dagastine RR (2012) Anomalous pull-off forces between surfactant-free emulsion drops in different aqueous electrolytes. Langmuir 28:4259–4266
Lönnqvist I, Haakansson B, Balinov B, Soederman O (1997) NMR Self-diffusion studies of the water and the oil components in a WOW emulsion. J Colloid Interf Sci 192:66–73
Magdassi S, Garti N (1984) Release of electrolytes in multiple emulsions—coalescence and breakdown or diffusion through oil phase? Colloids Surf 12:367–373
Manoi K, Rizvi SSH (2009) Emulsification mechanisms and characterizations of cold, gel-like emulsions produced from texturized whey protein concentrate. Food Hydrocolloid 23:1837–1847
Manor O, Chau TT, Stevens GW, Chan DYC, Grieser F, Dagastine RR (2012) Polymeric stabilized emulsions: steric effects and deformation in soft systems. Langmuir 28:4599–4604
Mao SR, Xu J, Cai CF, Germershaus O, Schaper A, Kissel T (2007) Effect of WOW process parameters on morphology and burst release of FITC-dextran loaded PLGA microspheres. Int J Pharm 334:137–148

Mariette F (2009) Investigations of food colloids by NMR and MRI. Curr Opin Colloid In 14:203–211
Marqusee JA, Ross J (1984) Theory of ostwald ripening—competitive growth and its dependence on volume fraction. J Chem Phys 80:536–543
Mcclements DJ, Decker EA, Park Y (2009a) Controlling lipid bioavailability through physicochemical and structural approaches. Crit Rev Food Sci Nutr 49:48–67
Mcclements DJ, Decker EA, Park Y, Weiss J (2009b) Structural design principles for delivery of bioactive components in nutraceuticals and functional foods. Crit Rev Food Sci Nutr 49
Mezzenga R, Folmer BM, Hughes E (2004) Design of double emulsions by osmotic pressure tailoring. Langmuir 20:3574–3582
Morris VJ, Woodward NC, Gunning AP (2011) Atomic force microscopy as a nanoscience tool in rational food design. J Sci Food Agr 91:2117–2125
Murday JS, Cotts RM (1968) Self-diffusion coefficient of liquid lithium. J Chem Phys 48:4938–4945
Muschiolik G (2006) Multiple Emulsionen: Herstellung und Eigenschaften. Behr's Verlag, Hamburg
Muschiolik G (2007) Multiple emulsions for food use. Curr Opin Colloid In 12:213–220
Nilkumhang S, Alhnan MA, Mcconnell EL, Basit AW (2009) Drug distribution in enteric microparticles. Int J Pharm 379:1–8
Packer KJ, Tomlinso DJ, Rees C (1972) Studies of diffusion and flow by pulsed NMR techniques. Adv Mol Relax Int Pr 3:119- &
Parra JL, Guinea J, Manresa MA, Robert M, Mercadé ME, Comelles F, Bosch MP (1989) Chemical characterization and physicochemical behavior of biosurfactants. J Am Oil Chem Soc 66:141–145
Pawley JB (2006) Handbook of biological confocal microscopy. Springer, New York
Pfeuffer J, Flögel U, Dreher W, Leibfritz D (1998a) Restricted diffusion and exchange of intracellular water: theoretical modelling and diffusion time dependence of 1H NMR measurements on perfused glial cells. NMR Biomed 11:19–31
Pfeuffer J, Flögel U, Leibfritz D (1998b) Monitoring of cell volume and water exchange time in perfused cells by diffusion-weighted 1H NMR spectroscopy. NMR Biomed 11:11–18
Price RL, Jerome WG (2011) Basic Confocal Microscopy. Springer, Heidelberg
Qiao Y, Galvosas P, Adalsteinsson T, Schönhoff M, Callaghan PT (2005) Diffusion exchange NMR spectroscopic study of dextran exchange through polyelectrolyte multilayer capsules. J Chem Phys 122:214912
Reis NC, Griffiths RF, Mantle MD, Gladden LF, Santos JM (2006) MRI investigation of the evaporation of embedded liquid droplets from porous surfaces under different drying regimes. Int J Heat Mass Transfer 49:951–961
Reverter JC, Feliu E, Climent C, Rozman M, Berga L, Rozman C (1993) Stereological study of human bone-marrow adipocytes—a comparison of 4 methods for estimating size distributions. Pathol Res Pract 189:1215–1220
Ribeiro HS, Schuchmann HP, Engel R, Briviba K, Walz E (2009) Encapsulation of carotenoids and vitamins. In: Zuidam NJ, Nedovic VA (eds) Encapsulation technologies for food active ingredients and food processing. Springer, Heidelberg
Ríos G, Benito JM, Pazos C, Coca J (2002) Drop size distribution of o/w emulsions by drop immobilization with agarose. J Disper Sci Technol 23:721–728
Romero A, Cordobés F, Puppo MC, Guerrero A, Bengoechea C (2008) Rheology and droplet size distribution of emulsions stabilized by crayfish flour. Food Hydrocolloid 22:1033–1043
Saglam D, Venema P, De Vries R, Sagis LMC, Van Der Linden E (2011) Preparation of high protein micro-particles using two-step emulsification. Food Hydrocolloids 25:1139–1148
Saltykov SA (1974) Stereometrische Metallographie. Deutscher Verlag für Grundstoffindustrie
Schmidt R, Wurm CA, Jakobs S, Engelhardt J, Egner A, Hell SW (2008) Spherical nanosized focal spot unravels the interior of cells. Nat Methods 5:539–544
Schuch A, Deiters P, Henne J, Kohler K, Schuchmann HP (2013) Production of W/O/W (water-in-oil-in-water) multiple emulsions: droplet breakup and release of water. J Colloid Interf Sci 402:157–164

Schuchmann HP (2007) Emulsification techniques for the formulation of emulsions and suspensions. In: Bröckel U, Meier W, Wagner G (eds) Product design and engineering: best practices. Wiley-VCH, Weinheim

Schuchmann HP, Köhler K (eds) (2012) Emulgiertechnik. Behr's Verlag, Hamburg

Schuster S, Bernewitz R, Guthausen G, Zapp J, Greiner AM, Köhler K, Schuchmann HP (2012) Analysis of W1/O/W2 double emulsions with CLSM: statistical image processing for droplet size distribution. Chem Eng Sci 81:84–90

Seifriz W (1925) Studies in emulsions. III-V. J Phys Chem 29:738–749

Shum HC, Bandyopadhyay A, Bose S, Weitz DA (2009) Double emulsion droplets as microreactors for synthesis of mesoporous hydroxyapatite. Chem Mater 21:5548–5555

Stokes GG (1851) On the effect of the internal friction of fluids on the motion of pendulums. Camb Philos Soc Trans 9:8–106

Tabor RF, Chan DYC, Grieser F, Dagastine RR (2011a) Structural forces in soft matter systems. J Phys Chem Lett 2:434–437

Tabor RF, Lockie H, Chan DYC, Grieser F, Grillo I, Mutch KJ, Dagastine RR (2011b) Structural forces in soft matter systems: unique flocculation pathways between deformable droplets. Soft Matter 7:11334–11344

Tabor RF, Grieser F, Dagastine RR, Chan DYC (2012) Measurement and analysis of forces in bubble and droplet systems using AFM. J Colloid Interf Sci 371:1–14

Tabor RF, Wu C, Grieser F, Chan DYC, Dagastine RR (2013) Non-linear and cyclical collisions between drops and bubbles: using AFM to understand droplet interactions in micro-scale flows. Soft Matter 9:2426–2433

Török P, Kao FJ (2007) Optical imaging and microscopy: techniques and advanced systems. Springer, Heidelberg

Touhami A, Alexander M, Kurylowicz M, Gram C, Corredig M, Dutcher JR (2011) Probing protein conformations at the oil droplet-water interface using single-molecule force spectroscopy. Soft Matter 7:10274–10284

Van Dalen G (2002a) Determination of the water droplet size distribution of fat spreads using confocal scanning laser microscopy. J Microsc Oxford 208:116–133

Van Dalen G (2002b) Determination of the water droplet size distribution of fat spreads using Confocal Scanning Laser Microscopy. J Microsc 208:116–133

Van Duynhoven JPM, Goudappel GJW, Van Dalen G, Van Bruggen PC, Blonk JCG, Eukelenboom APAM (2002) Scope of droplet size measurements in food emulsions by pulsed field gradient NMR at low field. Magn Reson Chem 40:51–59

Van Lent K, Vanlerberghe B, Van Oostveldt P, Thas O, Van Der Meeren P (2008) Determination of water droplet size distribution in butter: pulsed field gradient NMR in comparison with confocal scanning laser microscopy. Int Dairy J 18:12–22

Van Duynhoven J, Voda A, Witek M, Van As H (2010) Time-domain NMR applied to food products. Ann R NMR S 69:145–197

Veeman WS (2003) Diffusion in a closed sphere. Ann R NMR S 50:201–216

Voda MA, Van Duynhoven JPM (2009) Characterization of food emulsions by PFG-NMR. Trends Food Sci Tech 20:533–543

Wackerbarth H, Schon P, Bindrich U (2009) Preparation and characterization of multilayer coated microdroplets: droplet deformation simultaneously probed by atomic force spectroscopy and optical detection. Langmuir 25:2636–2640

Weipert D, Tscheuschner HD, Escher F, Windhab E (1993) Rheologie der Lebensmittel. Behr's Verlag, Hamburg

Wende C, Schönhoff M (2010) Dynamics of water in polyelectrolyte multilayers: restricted diffusion and cross-relaxation. Langmuir 26:8352–8357

Wicksell SD (1925) The corpuscle problem: a mathematical study of a biometric problem. Biometrika 17:84–99

Wildanger D, Patton BR, Schill H, Marseglia L, Hadden JP, Knauer S, Schönle A, Rarity JG, O'BRIEN JL, Hell SW, Smith JM (2012) Solid immersion facilitates fluorescence microscopy with nanometer resolution and Sub-Ångström Emitter Localization. Adv Mater 24:309–313

Wolf F, Hecht L, Schuchmann HP, Hardy EH, Guthausen G (2009) Preparation of W1/O/W2 emulsions and droplet size distribution measurements by pulsed-field gradient nuclear magnetic resonance (PFG-NMR) technique. Eur J Lipid Sci Tech 111:723–729

Yao JH, Elder KR, Guo H, Grant M (1993) Theory and simulation of Ostwald ripening. Phys Rev B 47:14110–14125

Chapter 4
Imaging of Fermented Dairy Products

Dilek Ercili-Cura

4.1 Introduction

4.1.1 Colloidal Components of Milk

Milk is an oil-in-water emulsion and a dispersion of colloidal protein particles in a liquid phase which contains sugar and salts. The interaction between and within the colloidal and the soluble fractions determine the processing behaviour and the final structure of the milk products.

Protein composition of bovine milk is distributed among caseins (~80%) and whey (or serum) proteins (~20%). Caseins consist of four major proteins, α_{s1}-, α_{s2}-, β- and κ-caseins, which show differences in their electrophoretic mobility, degree of phosphorylation, glycosylation and genetic polymorphism (Fox 2003; Fox and Brodkorb 2008). Owing to their structural properties and the calcium phosphate content of milk, caseins are found as association colloids, namely casein micelles. Casein micelles are assembled mainly by hydrophobic interactions and calcium phosphate bridges. While calcium sensitive caseins form the interior structure, κ-caseins, which are glycoproteins, are located at the micelle surface protruding their hydrophilic domain out to the serum phase forming a hairy layer on the micelle surface and rendering micelles with steric (and electrostatic) stabilization (De Kruif 1999; Horne 1986; Dalgleish 2011; Dalgleish et al. 2004). Casein micelles are highly hydrated, polydisperse colloidal particles with a large size distribution (50–500 nm). Studies on the micelle structure (how they are formed and stabilized) are vast and various models have been proposed until today (see reviews by Horne 2006; Farrell Jr et al. 2006; Fox and Brodkorb 2008; Dalgleish 2011; Dalgleish and Corredig 2012; McMahon and Oommen 2013). Even though there is a consensus about the surface location of the κ-caseins, the interior structure of the micelles, that is how the calcium sensitive caseins are assembled and glued with colloidal

D. Ercili-Cura (✉)
VTT Technical Research Center of Finland, Tietotie 2, Espoo FI-02044 VTT, Finland
e-mail: Dilek.ercili-cura@vtt.fi

N. Sozer (ed.), *Imaging Technologies and Data Processing for Food Engineers,*
Food Engineering Series, DOI 10.1007/978-3-319-24735-9_4

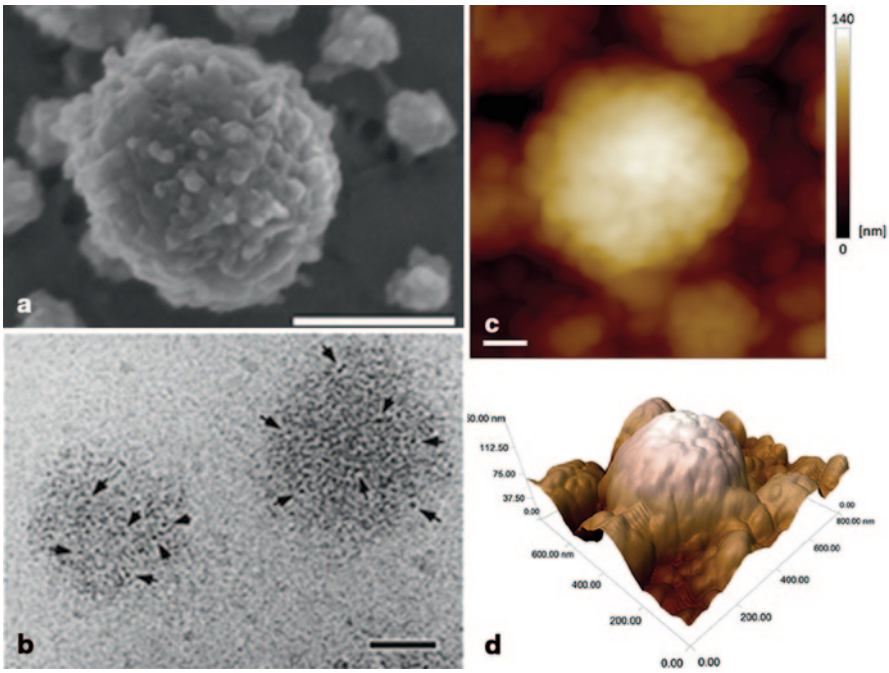

Fig. 4.1 **a** Scanning electron microscopy (SEM) image of a casein micelle. The bar represents 200 nm. Reprinted from Dalgleish et al. (2004), **b** Cryo-transmission electron microscopy (TEM) image of casein micelles. The bar represents 50 nm. Reprinted from Marchin et al. (2007), **c** and **d** Atomic force microscopy (AFM) images of casein micelles in close to native state. (Reproduced from Ouanezar et al. 2012)

calcium phosphate (CCP), still needs further elucidation. Advances in microscopy techniques enabled detailed imaging of the surface as well as the interior of the casein micelles facilitating better evaluation of the existing models (Fig. 4.1).

The proteins that remain after the isoelectric precipitation of caseins (pI, ~pH 4.6) are called whey proteins and are comprised primarily of β-lactoglobulin (50% of whey proteins) and α-lactalbumin (20% of whey proteins) but also immunoglobulins, bovine serum albumin, lactoferrin and enzymes (lipases, proteinases, etc.). Whey proteins are compact globular proteins with well-defined secondary and tertiary structures which make them more heat sensitive and less calcium sensitive as compared to caseins (Fox 2003). Under physiological conditions, bovine β-lactoglobulin exist as a homodimer. The monomeric diameter of the β-lactoglobulin molecule was reported to be ~3.5 nm (Sawyer and Kontopidis 2000). α-Lactalbumin contains four intramolecular disulphide bridges and adopt an ellipsoid-like shape with dimensions between 2 and 4 nm in diameter (Fox 2003).

The other colloidal component of milk is the milk fat globule (MFG). Milk fat comprises around 4% of whole bovine milk and exists as globules with sizes ranging between 0.2 and 15 μm (4 μm on average), depending on the breed (Walstra 1995; Smith and Campbell 2007). Native MFG are essentially droplets of

triglycerides (~98% of milk fat) surrounded and stabilized in the milk's aqueous phase by a biological membrane (milk fat globule membrane, MFGM), which is composed of proteins, glycoproteins, phospholipids, enzymes, cholesterol and other small molecules. MFGM shows a complex multilayer structure with a thickness of around 10 nm. It acts both as an emulsifying agent and a protective layer against lipolysis of milk fat (Walstra 1995). Homogenization of milk causes an increase in the milk fat surface area by reduction in the size of the MFG to 1 μm, depending on the homogenization conditions (pressure, temperature, etc.). The composition of the MFGM after homogenization is highly altered and includes adsorbed casein micelles and whey proteins (Smith and Campbell 2007).

4.1.2 Fermented Dairy Products: Formation and Structural Components

Production of fermented milk products, such as yoghurt, relies on acid-induced gelation of milk proteins. Acidification is achieved by slow fermentation of lactose, sugar component in milk, into lactic acid by using various bacterial cultures, which depends on the type of product. The most common fermented dairy product yoghurt is produced by fermentation of milk by *Streptococcus thermophilus* and *Lactobacillus delbrueckii* subsp. *bulgaricus* thermophilic cultures. Set-type, stirred-type and drinking yoghurts are available in the market today. Various other products are locally available including Nordic-cultured buttermilk *(piimä, filmjölk, hapupiim, fil, syrnet melk)* produced from mesophilic lactic acid bacteria (*Lactococcus lactis* subsp. *cremoris, Lactococcus lactis* subsp. *lactis, Lactococcus lactis* subsp. *lactis biovar. diacetylactis, Leuconostoc mesenteroides* subsp. *cremoris* and some other probiotic cultures); kefir produced from a complex mixture of microorganisms and yeast known as kefir grains; and slimy, viscous products such as viili in Finland, which contains similar mesophilic cultures as in cultured buttermilk and their ropy exopolysaccharides (EPS) forming strains together with a mould *Geotrichum candidum* (Tamime et al. 2007; Tamime et al. 2005).

The main structural component in fermented dairy products is the colloidal protein aggregates but also fat globules, added or in situ produced (EPS) polysaccharides and water. During fermentation, the gradual decrease in milk pH from around 6.7 to around 4.5 causes aggregation of proteins due to gradual loss of electrostatic repulsion and other physical interactions such as hydrophobic and van der Waals attractions and steric and entropic effects (Roefs and Van Vliet 1990; Lucey 2007). The casein micelles undergo changes in their physicochemical characteristics during pH drop, which finally lead to micelle–micelle interactions and gradual formation of the three-dimensional protein network. Between pH 6.7 and 6.0, the casein micelles retain their size, shape and integrity. CCP solubilisation is very slow until pH 6.0–5.8 (Gastaldi et al. 1996). Below pH 6.0, till pH 5.0 the net negative charge continues to decrease resulting in the loss of electrostatic repulsion, which also leads to the collapse of κ-casein hairy layer on the surface of the micelles. Thus,

both electrostatic and steric stabilization mechanisms of the micelles are being lost gradually. CCP solubilisation speeds up after pH 5.8 and maximises at ~pH 5.1 (Gastaldi et al. 1996; Lucey 2007; Phadungath 2005). As CCP is largely responsible for the integrity of the casein micelles, its depletion causes dissociation of individual caseins, mainly β-caseins, from the micelles to some extent depending on both pH and temperature. Scanning electron microscopy (SEM) has revealed that the newly formed Ca-depleted micelle particles became deformed around pH 5.3 and coalescence of the particles started (Gastaldi et al. 1996). As acidification approaches the isoelectric point of caseins, pH 4.5, casein–casein aggregation via electrostatic, hydrophobic and other weak interactions (van der Waals, H-bonding) intensifies. Increased ionic strength of the serum phase due to the CCP solubilisation also strengthens electrostatic interactions. In raw milk, gel formation starts at a pH of around 4.9 unless a high acidification temperature is used (Lucey 2007; Phadungath 2005). For yoghurt production, milk is subjected to high temperature heat treatments (usually around 90°C, 5–10 min) prior to fermentation which causes whey protein denaturation and subsequent formation of soluble and micelle bound κ-casein/whey protein complexes. As a consequence, the surface hydrophobicity and the apparent pI of the micelles increase (towards the pI of whey proteins) and thus, the gel formation starts at higher pH values (~pH 5.4 depending on the preheating conditions and the acidification temperature) in heated milk compared to raw milk (Donato and Guyomarc'h 2009; Lucey et al. 1997, 1998). After that point, fusion of the casein particles, organisation of strands and clusters, and further rearrangement of the three-dimensional network continues.

Fermented milk gels are particle gels, meaning that they are formed of aggregated spherical particles forming a continuous network of clusters and strands (Fig. 4.2; Horne 1999; Kalab et al. 1983). However, they differ from gels formed of

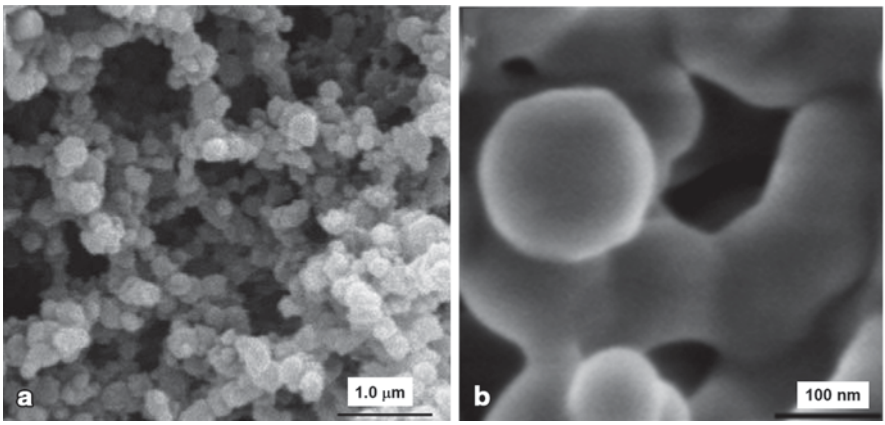

Fig. 4.2 **a** Scanning electron microscopy (SEM) micrograph of skim milk fermented with *Streptococcus thermophilus*. Casein particles form clusters and strands entrapping the water. (Reproduced from Aichinger et al. 2003), **b** Fusion of gel particles (primary particles) in an acid-induced milk gel imaged by SEM

hard spheres as the internal structure of the building blocks affects the gel properties greatly and due to fusion of the casein particles, the strand deformation is not limited to the interparticle regions (Fig. 4.2b; Horne 2003; Van Vliet et al. 2004). Accordingly, van Vliet et al. (2004) proposed that acid-induced milk gels can be considered as particle gels during gel formation but soon afterwards they would exhibit properties coherent with both particle and polymer gels. Rheological properties are associated with the number and type (strength) of the bonds between and inside the casein particles and their spatial distribution, meaning the curvature and thickness of the strands making up the gel network (Lakemond and van Vliet 2008; Mellema et al. 2002b; Mellema et al. 2002a; Van Vliet et al. 2004). In dynamic small deformation rheological measurements, the evolution of the moduli (G´, G″, or G*) is followed during gel formation. First, a lag period is observed until the gelation pH is reached and after that point, a sudden increase followed by a plateau is common. In large deformation measurements, usually the fracture stress (force) or strain is measured. Accordingly, the strands making up the gel network are straightened, stretched and finally broken.

Fermented dairy products, such as yoghurt contain ~90% water, basically are *structured water*. Retention of water inside the gel is an important functional property and is directly related to the network structure (Hermansson 2008; van Vliet and Walstra 1994). Syneresis, which refers to separation of water (or whey) from the gel without any applied external force, is a common defect in acid-induced milk gels, like yoghurt. Water is physically entrapped within the casein strands forming the gel network, meaning that the tendency for whey separation is primarily linked to dynamics of the network (van Vliet and Walstra 1994). Accordingly, proneness of the casein network to large-scale rearrangements during and after gel formation leading to contraction of the network is the cause of spontaneous syneresis in set-type milk gels (Walstra et al. 1985). In stirred-type products, such as fruit yoghurts or drinkable fermented milk products, the network of protein particles is destroyed due to mechanical stresses (shearing) during processing. Broken network particles rearrange into large clusters, referred to as microgel particles (Nöbel et al. 2014; Hahn et al. 2012) or super aggregates (van Marle et al. 1999) which are suspended in the milk serum. The microgel particles are fractal within, and show the same topology as the initial acid-induced gel network itself (Hahn et al. 2012).

Whey separation and poor texture are major problems especially in nonfat or low-fat fermented milk products. Addition of stabilizers such as pectin, starch, carrageenan, gum arabic, locust bean gum, etc.; increasing the solids nonfat content by adding milk or whey powders; or using protein cross-linking enzyme transglutaminase (when approved by the national legislations) are the methods adopted by the dairy producers today.

A natural way of improving the texture of fermented dairy products is in situ production of hydrocolloids known as EPS produced by many lactic acid bacteria. EPS are high molecular weight polysaccharides composed of repeated units of monosaccharides, D-glucose, D-galactose and L-rhamnose at varying ratios. The content of EPS in fermented products depends on the bacterial strain used and the fermentation conditions. EPS, even at low concentrations, may greatly affect

the texture, viscosity, creaminess and water-binding properties of fermented dairy products (Folkenberg et al. 2005). Moreover, depending on the bacterial strain used (capsular or non-capsular EPS forming bacteria), they may induce ropiness in the product leading to production of different types of products such as viili or piima of Finland. The structure of the EPS and their interactions with each other and with other milk components, especially the proteins and the protein network, determines their effects on the product's textural and sensorial properties.

4.2 Imaging Fermented Dairy Gels by CLSM

Imaging the microstructure of gels like yoghurt which consist of around 90 % water and where the structure is extremely shear sensitive necessitates that the gel pieces are analysed with the least possible external physical and chemical disturbance. This simply makes CLSM the best choice for visualising the 3D spatial distribution of the structural elements in an acidified milk gel. In CLSM, optical sectioning attained by moving the focal plane in steps of defined thickness through the depth of the specimen allows analysis of thick specimens, for example a piece of yoghurt or cheese, with the least possible external disturbance during sample preparation. The penetration depth achieved by the laser into the specimen usually exceeds the size of the structural components, allowing imaging the bulk properties and eliminating the possible defects at the outer surface (Tromp et al. 2003). Superiority of CLSM over widefield microscopy techniques originates from the elimination of out-of-focus light in CLSM which reduces the background fluorescence, improves signal-to-noise ratio leading to superior resolution and image quality. In contrast to most other light microscopy techniques, 3D image with sectional focus can be built by using CLSM. Advantages of CLSM over other light microscopy techniques in food and bio structure characterisation is discussed in a number of reviews (Dürrenberger et al. 2001; Ferrando and Spiess 2000; Rincón Cardona et al. 2013; Auty 2013; Claxton et al. 2006; Tromp et al. 2003).

Owing to above-mentioned factors, CLSM has been the choice of microscopy technique to visualise the 3D spatial arrangement of the protein aggregates and the distribution of fat and polysaccharides in fermented (or chemically acidified) milk gels. Alternatively, a few reports exist where a conventional fluorescence microscope with a motorized sample stage was used to analyse set-type milk gels in a similar manner to CLSM (Choi et al. 2007; Ozcan et al. 2011; Peng et al. 2010, 2009). The authors used acridine orange to label the milk proteins, and the labelled samples were let to gel between concave microscopy slides. By using the Z-stack module, a series of images from different positions in the gel matrix were acquired and the out-of-focus light was suggested to be eliminated by a 3D deconvolution procedure (Choi et al. 2007). Phase contrast microscopy has also been utilized for visualising the protein aggregation during acidification of milk (Singh and Kim 2009) or visualisation of the gel structure in thin sections obtained after extensive sample preparation for transmission electron microscopy (TEM) analysis (Sanchez et al. 2000).

Casein network can be visualised by CLSM basically in two modes; reflectance mode and after staining with protein-specific fluorescent dyes. The ability of casein micelles (and gel particles) to reflect laser beams have found use mainly when bacterial EPS were aimed to be visualised together with the protein network in fermented dairy products. In most other occasions, suitable fluorescent probes were used to visualise the structural components. Most fluorescent dyes that have traditionally been used in widefield fluorescence microscopy are used also in CLSM. A list of widely used fluorescent probes in imaging of structural components in milk protein gels is shown in Table 4.1. Most of the fluorescent labels used for labelling proteins and fats interact with the target molecules via hydrophobic, ionic interactions and hydrogen bonding, that is, non-covalently. Staining of added or in-situ-produced polysaccha-

Table 4.1 Widely used fluorescent probes for imaging of structural components in dairy products

Structural component	Fluorescent probe	Excitation wavelength (nm)	References (as examples)
Protein			
	Acridine orange	450	Ozcan et al. (2011), Peng et al. (2009, 2010), Choi et al. (2007)
	FITC	488	Lin et al. (2012), Guyomarc'h et al. (2009), Jensen et al. (2010), Torres et al. (2012)
	RITC	543	Guyomarc'h et al. (2009)
	Rhodamine B	543	Ercili Cura et al. (2009, 2010)
	Fast green	633	Ciron et al. (2010; 2012), Abhyankar et al. (2011, 2014)
	Acid fuchsin	488	Partanen et al. (2008), Herbert et al. (1999)
	Nile blue	633	Auty et al. (1999)
Fat			
	Nile red	488	Ciron et al. (2010, 2012), Abhyankar et al. (2014)
	V03-01136	647	Krzeminski et al. (2011), Heilig et al. (2009)
Added hydrocolloids			
Starch	FITC, Safranin O, Rhodamine B		van de Velde et al. (2003)
Pectin	FITC	568	Tromp et al. (2004)
Xanthan, konjac	FITC	488	Nayebzadeh et al. (2006), Abhyankar et al. (2011, 2014)
κ-carrageenan	FITC	488	Heilig et al. (2009)
Exopolysaccharides			
	WGA-AlexaFluor 488, conA-AlexaFluor 488	488	Hassan et al. (2002; 2003b); Folkenberg et al. (2005)

FITC fluorescein isothiocyanate, *RITC* rhodamine B isothiocyanate, *WGA*: wheat germ agglutinin, *conA* concanavalin A

rides, however, may require covalent labelling, which needs tedious sample preparation or use of special labels such as lectin-fluorescent probe conjugates. Methods of sample preparation for imaging of various components in commercial or model dairy protein gels will be briefly described in the following sections.

Fluorescence microscopy allows identification of multiple components in mixed biopolymer systems simultaneously when different fluorescent probes associated with different phases are used. Most confocal microscopes today are equipped with multiple laser excitation sources (UV, blue, green and red) and include integrated three electronic detectors (photomultiplier tubes), which enable simultaneous imaging of three different fluorophores in multiply labelled specimens. A fourth detector for transmitted or reflected light imaging also exists (Claxton et al. 2006). Signals from each detector can be collected simultaneously and the images merged into a single overlay file in which different colours represent associated components. The main constraint in simultaneous imaging of multiple components is to find fluorescent probes specific enough to the target components and have distinct excitation and emission spectra from each other. In modern instruments, the emission spectral overlaps can partly be resolved due to acousto-optical tuneable filters and beam splitters which replace conventional epi-fluorescence filters. For more information on CLSM and its use in visualising food structures, readers are directed to excellent book chapters by Auty (2013) and Tromp et al. (2003).

4.2.1 Imaging of Protein and Fat

Non-covalent labelling can usually be attained by free diffusion of the dye into the specimen. The relevant solutions of fluorescent probes such as Rhodamine B or Nile blue used to stain proteins and fats, respectively, for example are directly added to the specimen and analysed after an incubation period for homogeneous distribution, which may be from minutes to hours depending on the structure of the sample. Sample preparation for set-type gels usually starts during the initial stages of fermentation (or acidification when a chemical acidifier, e.g. glucono delta-lactone (GDL) is used) so as not to disturb the gel after formation. Fluorescent probes are added to the milk before or right after the inoculation with the starter bacteria or the addition of an acidulant. While the system is still liquid, the stained sample is placed onto a concave slide or in a well created by a silicone isolator sealed onto a microscopy slide. The cover slip is then carefully placed on top and the sides sealed for preventing drying of the sample during incubation at the desired acidification temperature. When the pH reaches predetermined levels, around pH 4.5 for yoghurt, the sample which gelled in place is imaged by fluorescence microscopy or CLSM without any external disturbance. This method has been adopted by many authors, especially when the spatial distribution of the structural elements and the dynamics of aggregation and gel formation were to be explored (examples may be found in Ercili Cura et al. (2009, 2010, 2014), Morand et al. (2012a, b), Partanen et al. (2008), Myllärinen et al. (2007), Guyomarc'h et al. (2009), and Kristo et al. (2011)).

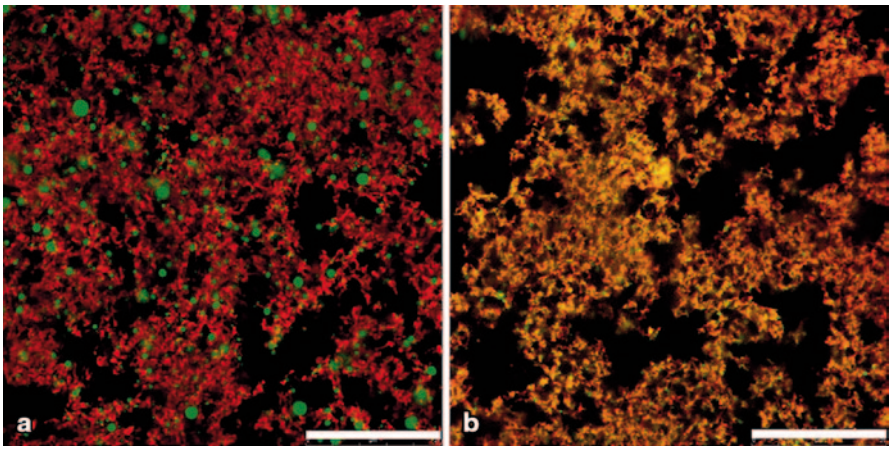

Fig. 4.3 CLSM images of low-fat stirred yoghurt produced from milk homogenised by: **a** Conventional homogenisation, **b** Microfluidisation. The protein matrix is red (stained with Fast green) and the fat globules are green (stained with Nile red). Yoghurt from microfluidised milk showed a different structure as a consequence of smaller fat globule size and more fat globules connected and bound to the protein. Accordingly, yellow colour in image **b** indicates intermixing of red and green channels due to co-localisation of pixels. Scale bar = 25 mm. (Reproduced from Ciron et al. 2010)

Samples of sheared gels, for example stirred-type yoghurt, may be prepared directly from the final product as the structure has already gone through extensive shear stresses. A generally adopted method is that a drop of the fluorescent probe solution is added onto a drop of sample which is placed on a microscopy slide. Imaging starts after homogeneous distribution of the dye is attained (Ciron et al. 2010; Kristo et al. 2011). Alternatively, a drop of the fluorescent probe solution can be placed on a cover glass and left exposed to air for evaporation of the solvent. Then the cover glass is placed on top of a sample drop and left for homogeneous diffusion of the dye molecules into the sample (Girard and Schaffer-Lequart 2007a, 2007b; Jensen et al. 2010; Torres et al. 2012). The microstructure of a low-fat stirred yoghurt product visualised after dual-labelling with Nile red (for fat) and Fast green (for protein) mixture is shown in Fig. 4.3. A drop of yoghurt sample was stained with 10 μL aqueous solution of the dye mixture and imaged with CLSM (Ciron et al. 2010).

4.2.2 Imaging of Added Stabilizers and Bacterial Exopolysaccharides

In the dairy industry, various hydrocolloids, starch and starch derivatives are added to certain fermented dairy products in order to improve the structural stability by, for example, increasing viscosity, limit or prevent whey separation or to improve mouthfeel. These may include pectin, xanthan gum, locust bean gum, guar gum,

carrageenan, cellulose derivatives, starch and gelatin. The structural properties of the added stabilizers as well as their interactions with the milk proteins and fat in the dairy system are crucial for the final product quality. The functionality of an added polysaccharide as well as in situ produced EPS are greatly affected by their molecular charge density and molecular structure (Pang et al. 2015a; Girard and Schaffer-Lequart 2007b, 2008). Neutral polysaccharides such as starch, guar gum and locust bean gum do not particularly interact with the milk proteins but increase the viscosity of the continuous phase by filling the pores in the gel network (Everett and McLeod 2005). Anionic polysaccharides such as pectin, carrageenan and xanthan gum interact with protein aggregates that are positively charged at the pH of, for example, yoghurt and aid in structural stabilisation by a different mechanism (Girard and Schaffer-Lequart 2007b; Pang et al. 2015a). For example, the stabilisation of acidified milk drinks against sedimentation is based on electrostatic adsorption of anionic polysaccharides, for example high methoxy pectins, on to gel particles during shearing (Tromp et al. 2004; Tuinier et al. 2002). Due to the block-wise distribution of the charges along the pectin chain (depending on the type and structure of the pectin), while charged blocks adsorb onto the gel particles, other parts of the molecule protrude from the surface as loops and tails introducing steric stabilisation to the system (Tromp et al. 2004). Besides molecular charge and structure, another crucial parameter that affects the functionality of polysaccharides in acid milk gel structure is their concentration. The concentration dependence of the interplay between proteins and polysaccharides is sourced from the destabilisation mechanisms such as bridging and depletion flocculation and phase separation (Rohart and Michon 2014; Rohart and Michon 2013; Everett and McLeod 2005; Aichinger et al. 2006). Protein–polysaccharide interactions and their significance in control of structures in dairy matrices have been reviewed by Corredig et al. (2011).

CLSM has been a valuable tool for localisation of the added polysaccharides in 3D protein spatial organisation of the proteins in fermented milk gels. Staining of polysaccharides, however, is not as trivial as for proteins and lipids as there are only few fluorescent probes that will non-covalently attach to those hydrophilic molecules and make it easy to use directly on the final product (Auty 2013; Tromp et al. 2004). In order to visualize those additives in milk gel structure, polysaccharides are pre-labelled (covalently) before being added to the milk during or after gelation. Covalent labelling involves high-temperature heating of the polysaccharide-fluorescent probe mixtures in nonaqueous environment followed by alcohol precipitation (Auty 2013). The tedious steps of covalent labelling of some commercial polysaccharides by fluorescein isothiocyanate (FITC) can be followed in Laneuville and Turgeon (2014) and Tromp et al. (2001). The necessity of harsh treatments for covalent labelling brings about unwanted structural and possibly functional changes to polysaccharides. Structural changes were observed in κ-carrageenan (Tromp et al. 2001; Laneuville and Turgeon 2014), konjac glucomannan (Abhyankar et al. 2011) and pectin (depending on the extent of modification; Tromp et al. 2004) due to covalent labelling procedures.

Laneuville et al. (2014) recently elucidated addition of various commercial polysaccharides (low-methoxy pectin, κ-carrageenan, xanthan gum, agar agar and modi-

fied corn starch) and a purified anionic EPS to skim milk prior to acidification and determined the effects on rheological and microstructural properties of the acid gels. Polysaccharides and EPS were covalently labelled by FITC and Rhodamine B isothiocyanate (RITC), respectively. They were able to visualise added polysaccharides and EPS together with the protein matrix which was stained non-covalently using 8-anilino-1-naphthalenesulfonic acid (ANS) and excited at 405 nm, far enough from the other two fluorophores. The approach was highly useful to assess the effects of single or multiple polysaccharides with different molecular weight and charge distributions on whey separation in acid milk gels linked to the microstructural organisation of the components. The results revealed existence of low-methoxy pectin co-localised with proteins but also forming an independent secondary network extending into the pores of the protein matrix which played a significant role in reduction of the whey separation (Laneuville and Turgeon 2014). Formation of a ramified pectin network and its effects in stabilisation of acidified milk drinks was previously elucidated by using a technique called fluorescence recovery after photobleaching (FRAP; Tromp et al. 2004). FRAP is based on applying a high-intensity beam on a certain area in the sample causing bleaching and loss of fluorescence. Recovery of the fluorescence in bleached area in time would indicate the ability of labelled molecules to diffuse from other parts of the sample to that area, that is indicate the mobility or immobility of the labelled molecules. Accordingly, covalently labelled pectin was added to yoghurt before homogenization into an acidified milk drink. Pectin was visualised by CLSM using FRAP (Fig. 4.4). No recovery of fluorescence was observed in the bleached area in 2 h indicating lack of diffusive mobility of pectin and existence of a weak secondary pectin network (Tromp et al. 2004). The same

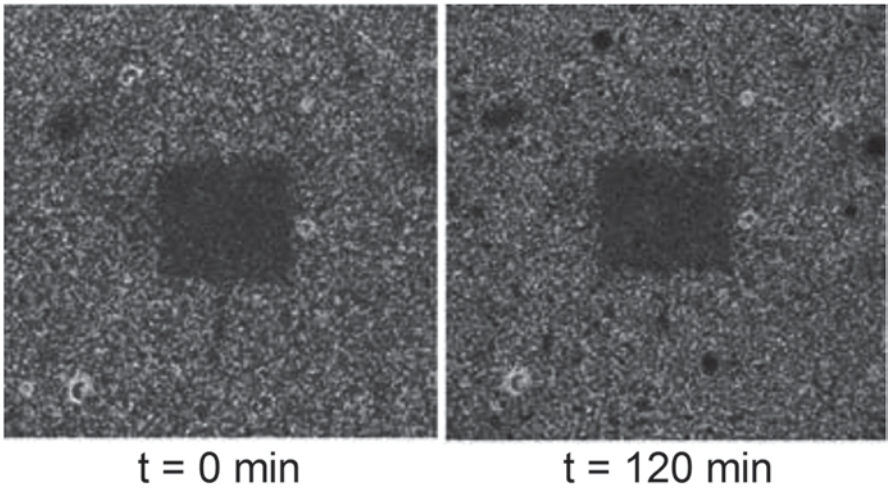

Fig. 4.4 Fluorescence recovery after photobleaching (FRAP) applied on an acidified milk drink sample. The fluorescence belongs only to pectin. Pectin was covalently labelled with fluorescein isothiocyanate (FITC). The persistency of the bleached area for 2 h indicates the immobility of pectin. (Reproduced from Tromp et al. 2004)

method was also used by Jensen et al. (2010) to assess the mobility of proteins in the presence of high-methoxy pectin in a model acidified milk drink.

Covalent labelling of polysaccharides is an effective but unpractical method and limits microscopy only to model systems as it is not possible to apply the technique to in situ labelling of the final products. Immunolabelling (or immunostaining) and use of fluorophore-conjugated lectins are the methods that are adopted for in situ labelling of added polysaccharides and EPS in fermented dairy products. Immunolabelling includes addition of a primary antibody onto the specimen which attaches to the specific compound that will be labelled. Then, a secondary antibody which is coupled to a fluorophore recognises and attaches to the primary antibody. Immunolabelling is a widely used technique for localisation of cell wall polysaccharides, especially pectins in plants (Willats et al. 2001; Liu et al. 2013; Guillemin et al. 2005; Van Buggenhout et al. 2013). The immunolabelling technique was adopted by a research group in Denmark for localising added pectin and carrageenan in the microstructure of fermented dairy products or dairy desserts (Arltoft et al. 2006a, b, 2007, 2008). The group developed a direct immunolabelling procedure which uses a commercially available primary antibody (e.g. JIM5 or JIM7 for pectin) and conjugated it to a fluorophore (Arltoft et al. 2006a; Arltoft et al. 2007) eliminating the need for a secondary antibody and washing steps which would be unpractical for in situ labelling of dairy gels.

Lectins are carbohydrate-binding proteins. Fluorescent conjugates of some lectins are commercially available and widely used in imaging of specific structures in cell biology. Concanavalin A, a lectin from leguminous plants and wheat germ agglutinin (WGA) from wheat are the two most commonly used lectins. Their fluorescent conjugates, for example with AlexaFluor 488, has been used to visualise added hydrocolloids (Arltoft et al. 2007) and EPS (Arltoft et al. 2007; Hassan et al. 2003a; Folkenberg et al. 2005; Hassan et al. 2002) in fermented dairy gels. Hassan et al. (2002) developed the technique for direct visualisation of bacterial EPS in fermented dairy products in their fully hydrated state by using lectin conjugates. Accordingly, a stock solution of the lectin–fluorophore conjugate is first prepared using a buffer at neutral (for WGA) or alkaline (for concanavalin A) pH (Hassan et al. 2002). Before staining of the sample, the stock solutions are diluted in the serum (whey) obtained from the fermented product in order to avoid changes in pH or osmolarity of the specimen. Some drops of the solution is added onto the undisturbed fermented milk sample and imaged using a CLSM after allowing the dye to diffuse homogeneously (Hassan et al. 2002, 2003a). Authors were able to simultaneously visualise the bacterial EPS produced by different ropy strains and the protein network (by using the reflectance mode of the confocal microscope) in set- and slightly stirred-fermented milk samples (Fig. 4.5). Interplay between the EPS and the protein aggregates as well as EPS–EPS upon stirring was successfully visualised and it was further used to explain the rheological properties, whey separation (Hassan et al. 2003a) and sensorial properties (Folkenberg et al. 2005) in fermented milk gels produced by various EPS-forming strains. Extensive information on the role of EPS produced by lactic acid bacteria in structure formation and stabilisation of fermented dairy products and examples of microstructure images obtained by various techniques can be found in Hassan (2008).

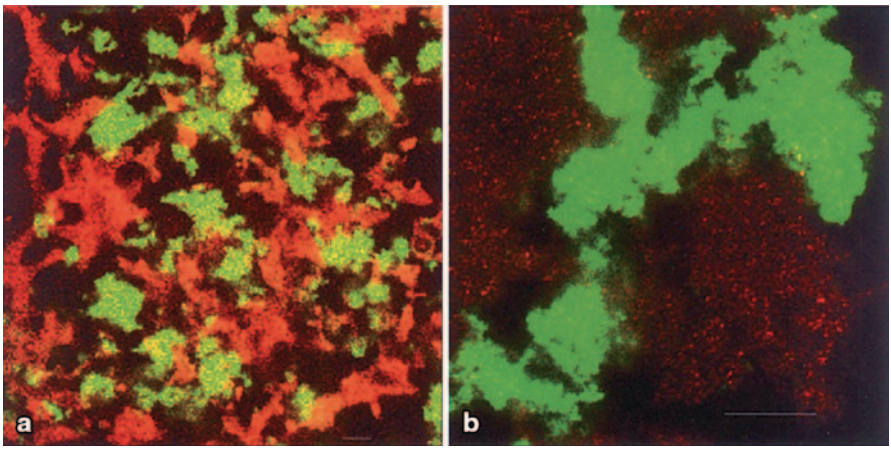

Fig. 4.5 Distribution of exopolysaccharide *(green)* and protein aggregates *(red)* in milk fermented by ropy Lactococcus lactis CHCC3367. **a** Set-type gel, **b** Stirred after addition of the lectin solution. Wheat germ agglutinin was used to stain EPS. Proteins were visualised by the reflectance mode of the confocal microscope. Bar = 10 μm. (Reproduced from Hassan et al. 2002)

4.2.3 Dynamic Confocal Microscopy

One highly valuable advantage of CLSM over other microscopy techniques is that as the samples are visualised in their natural, hydrated states without external disturbance, structural changes in dynamic systems can easily be recorded in situ. In fermented milk gels, such dynamic events may be an aggregation of the proteins during gradual pH drop, structure break down under shear, phase separation in time or dynamic changes due to, for example, temperature change. Hassan et al. (1995) may be the first ones to use CLSM to observe coagulum formation during acidification of milk on a temperature-controlled stage. In later years, many authors combined the technique of in situ visualisation of gelation with oscillatory rheology data (Guyomarc'h et al. 2009; Auty et al. 2005; Auty et al. 1999; Matia-Merino and Singh 2007; Ercili-Cura et al. 2014; Olsson et al. 2002) or diffusive wave spectroscopy (Nicolas et al. 2003a; Nicolas et al. 2003b) to investigate the onset of gel formation, particle–particle interactions and structural changes during gelation inherently. Development of tensile stages that can be mounted to CLSM made it possible to visualise structural changes directly during large deformation of soft matter.

Understanding the structural breakdown under stress is crucial for understanding the behaviour of materials during flow and fracture, mouth feel and sensory perception, water release and mobility, fat and active compound release, etc. The crack propagation in a complex food structure is directly related to the properties of the continuous matrix, structural interfaces, defects and heterogeneity (Hermansson 2008).

The principle of the measurement is based on creation of a small notch on the sample which will initiate further deformation at a specific location. The tensile stage (Deben MICROTEST, Deben UK Ltd.) consists of an extension/compression unit comprised of one stationary and one movable stage with sample clamps,

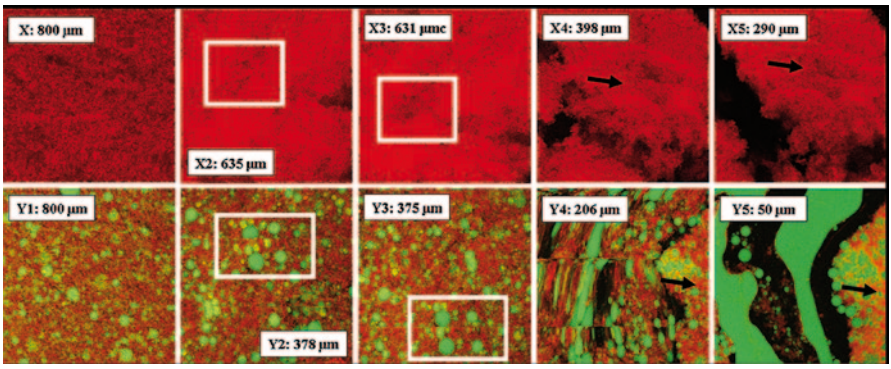

Fig. 4.6 CLSM images of stirred acid milk gels containing 0 (imagesX1–X5) and 10% (imagesY1–Y5)(w/w), emulsified sunflower oil, acquired at different compression heights (in µm as shown on the image), on compressing from 800 to 50 mm at a rate of 5 mm/s. The protein aggregates appear *red* while the oil phase appears *green*. The *white squares* indicate lateral flow in the stirred gels; *black arrows* indicate the large protein aggregates that are trapped between the parallel plates of the compression stage. Scale bar 100 µm. (Reprinted from Abhyankar et al. 2014)

motorised gear box unit to facilitate movement, a load cell and a computer control unit (Abhyankar et al. 2011). The propagation of the crack during tensile measurement is followed by the confocal microscope focused on the area close to the notch tip. This technique has been utilised to visualise structure breakdown in microscopic scale in whey protein/gelatin gels (Brink et al. 2007), heat-induced β-lactoglobulin gels (Olsson et al. 2002), emulsion filled whey protein gels (Abhyankar et al. 2014; Abhyankar et al. 2011) and acid milk gels (Abhyankar et al. 2014). For the acid milk gels, instead of a tensile measurement, a compression test was applied using a compression stage that is explained in Abhyankar et al. (2014). Deformation during compression of both fat-free and emulsion-filled acid milk gels (stirred) were observed with CLSM and images at different heights in the sample were recorded (Fig. 4.6). The study demonstrates the importance of microstructure on the fracture behaviour of gels and particularly the effect of protein aggregates (fine stranded or particulate) on fat mobility and release. Simultaneous analysis of microstructure and large deformation behaviour of multicomponent model systems (proteins, oil, polysaccharides, etc.) and relating those to sensory data will allow the food industry to design food products with novel textures and tailored mouthfeel and flavour perception (Abhyankar et al. 2014).

4.3 Electron Microscopy Techniques

4.3.1 Scanning Electron Microscopy

Electron microscopy, especially SEM, has widely been used for imaging the structure of fermented dairy products. Resolution in the fluorescence microscopy tech-

niques is limited by the wavelength of the light. Electron microscopy allows high resolution imaging by using electron beams which characteristically have short wavelength. By using SEM, main structural components such as individual protein aggregates, stabilisers and bacterial cells can be identified, and their morphological features and interactions can be visualised with high resolution (see Fig. 4.2).

A disadvantage of conventional SEM in food science is that it operates under vacuum which necessitates that the sample is effectively dried during sample preparation. For highly hydrated samples like fermented dairy products, dehydration procedures involve fixation of the sample in glutaraldehyde and osmium tetroxide solutions followed by dehydration in a series of ethanol or acetone concentrations. Those procedures necessitate that the sample is cut into thin slabs, which may not be possible for stirred or drinking type of fermented milk products. A common procedure for imaging biological dispersions with SEM is encapsulating them in small agar gel casings (tubes) which allow to treat samples as solid specimens afterwards. Kalab and Larocque (1996) used this technique successfully for stirred-type yoghurt. The yoghurt sample was filled into gelled agar tubes with defined dimensions and wall thickness. The sample-filled tubes were exposed to above-mentioned fixation and dehydration steps (Kalab and Larocque 1996). The dehydrated specimen is then dried by freeze-drying (van den Berg et al. 2009; Ercili Cura et al. 2010), critical point drying (Pang et al. 2015a, 2015b; Aichinger et al. 2003; Sandoval-Castilla et al. 2004) or even by air drying (Sanchez et al. 2000). Dried samples are cut or broken into pieces and mounted onto aluminium or carbon stubs. For conventional SEM, the surface of the sample has to be electrically conductive, thus, when biological samples are to be imaged, an ultrathin coating of an electrically conductive material, for example gold or platinum, is sputter coated onto the sample surface. For organic samples, the electron beam energy needs to be low enough to avoid damaging the specimen.

An alternative sample preparation method used for SEM imaging of acidified milk samples was immobilisation of proteins onto solid substrates creating self-assembled monolayers (SAM; Ayala-Hernandez et al. 2008, 2009). Immobilisation is achieved by covalent bonds between a linker molecule on a solid substrate and the proteins. Accordingly, SAM is formed by adsorption of 11-mercaptoundecanoic acid onto carbon planchets. SAM is then activated by modifying the terminal functional group via carbodiimide chemistry. Activated carbon planchets are then immersed in the samples and the nonadsorbed molecules are washed away. The samples then go through similar fixation and dehydration steps as explained above before imaging with SEM (Ayala-Hernandez et al. 2008; Martin et al. 2006). The method was developed by Martin et al. (2006) for studying the casein micelle-polysaccharide interactions directly in milk and it was then used by Ayala-Hernandez et al. (2008, 2009) for imaging protein–EPS interactions in fermented buttermilk or milk permeate.

Sample preparation steps are necessary for visualisation of sample morphology in biological samples with the least possible structural damage; however, some changes in sample structure are unavoidable and artefacts may occur. For example, EPS is visualised as thin filaments attached to protein aggregates and bacterial cells in conventional SEM images of fermented milk products (Fig. 4.7; Ayala-Hernandez

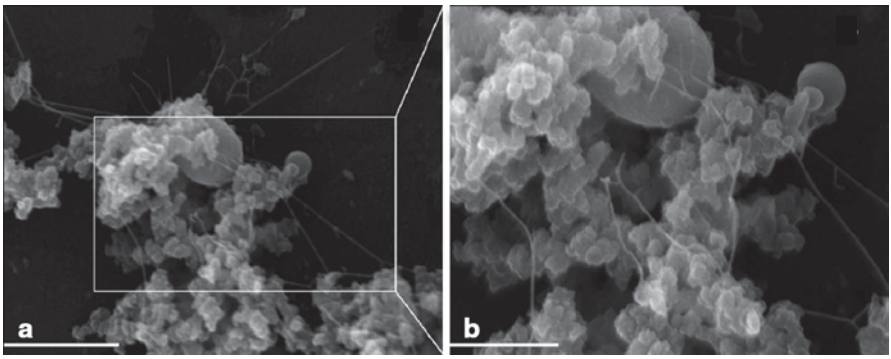

Fig. 4.7 Field emission SEM images of concentrated milk permeate fermented by *Lactococcus lactis ssp. cremoris*. *Panel b* (scale bar = 600 nm) is a magnification of *panel a* (scale bar = 1,200 nm). (Reprinted from Ayala-Hernandez et al. 2008)

et al. 2008, 2009; Hassan 2008; Hassan et al. 2003a). Those filamentous structures were, however, suggested to be an artefact sourced by dehydration steps during drying as EPS molecules would occupy much more volume than observed in their hydrated state (Hassan 2008; Ayala-Hernandez et al. 2008). Recently, Pang et al. (2015) also observed the formation of thin filament-like strands due to gelatin addition to acidified skim milk gels. In this case, however, CLSM images were complementary to SEM images indicating that thin strands were not necessarily due to formation of artefacts during sample preparation for SEM (Pang et al. 2015b). Comparison of conventional SEM images with other techniques that do not require harsh sample preparation is necessary for better judgement of evaluated structural features. Environmental SEM (ESEM) and cryo-SEM may be regarded as more advantageous techniques compared to conventional SEM as they do not require laborious and harsh sample preparation procedures before imaging of hydrated samples.

ESEM allows samples to be imaged in hydrated state and without the need of sputter coating of a metallic surface layer. Unlike the vacuum in conventional SEM, the sample chamber in ESEM is operated at low pressure. The most common gas used in ESEM is water vapour, which is especially advantageous for controlling the thermodynamic stability of the hydrated samples. Moreover, it allows performance of dynamic hydration and dehydration experiments. Other gases such as nitrogen and nitrous oxide are also used (Stokes 2013). Bromley et al. (2006) studied the microstructure of acid- and heat-induced β-lactobulin gels by using ESEM. ESEM allowed analysis of submicron sized protein aggregates in the particulate gel structure accurately, in their hydrated and natural state (Bromley et al. 2006). Similar to CLSM, a strain stage can be placed in the specimen chamber of ESEM configuration and the dynamic mechanical properties of the samples can be recorded simultaneously with a high-resolution microstructure imaging (Rizzieri et al. 2003; Donald 2003; 2012). The main limitation of ESEM is slightly lowered image quality compared to conventional SEM and obstructions caused by the presence of water (Ong et al. 2011). The working principle and the key applications of ESEM in food science can be followed from a recent compilation by Stokes (2013).

Cryo-SEM is another method which eliminates laborious fixation and dehydration steps in conventional SEM allowing visualisation of hydrated biopolymer systems in a state closer to their natural state. The specimen is kept frozen by a cryo-stage attached to SEM and imaged in similar conditions to conventional SEM, under high vacuum and at similar acceleration voltages (Dudkiewicz et al. 2011; El-Bakry and Sheehan 2014). In a typical experiment, bulk samples are first rapidly frozen by immersion into liquid nitrogen slush at around −210 °C (Ong et al. 2011; El-Bakry and Sheehan 2014) or by high-pressure freezing (Mellema et al. 2002a). Rate of freezing is a critical parameter in sample preparation for cryo-SEM. Rapid freezing lowers the tendency of water to form crystals and limits the time for crystal growth. Ice crystal growth causes distortions in the specimen microstructure, and thus needs to be eliminated before SEM imaging. Frozen specimens are transferred to a cryo-preparation chamber using a vacuum transfer device which prevents ice recrystallisation during transfer (Ong et al. 2011; Nguyen et al. 2014b). The sample is freeze-fractured and etched in the cryo-preparation chamber. Etching process is the removal of ice crystals from the surface of the fractured sample by vacuum sublimation and it is a crucial step in sample preparation for cryo-SEM. Etched sample surface is then sputter coated with a conductive metal and transferred to the cryo-stage attached to SEM for microscopical analysis. In cryo-SEM, samples are better protected from beam damage due to the low temperature of the specimen. Cryo-SEM sample preparation steps and the microstructure of the specimen at each stage for a milk gel sample are schematically explained in Ong et al. (2011). In recent years, the cryo-SEM technique has widely been used for microstructural characterisation of yoghurt-type fermented dairy products (Amatayakul et al. 2006; Hassan et al. 2003a; González-Martínez et al. 2002; Vargas et al. 2008; Riener et al. 2009; Prasanna et al. 2013; Martín-Diana et al. 2004; Nguyen et al. 2014b; Morell et al. 2015; Nguyen et al. 2014a; Siefarth et al. 2014), rennet-induced milk protein gels and cheese (Ong et al. 2011; Mellema et al. 2002a; Soodam et al. 2014; Ong et al. 2013a, b, 2015; El-Bakry et al. 2011), or cheese with EPS-forming bacteria (Hassan and Awad 2005; Hassan et al. 2004). Nguyen et al. (2015) revealed the microstructural differences in yoghurt gels produced from bovine and buffalo milk by using cryo-SEM and CLSM complementarily (Fig. 4.8). CLSM images reveal the protein network (green) and the fat droplets (red) distributed among the protein aggregates similarly in both buffalo and bovine yoghurt samples. Larger fat droplets are clearly observed in the buffalo yoghurt compared to that of bovine milk yoghurt as buffalo milk was not homogenised (Nguyen et al. 2014b). Cryo-SEM imaging made it possible to observe the morphology of the protein aggregates and the location of the fat globules inside the protein matrix (Fig. 4.8). The homogenised fat globules in bovine milk yoghurt were observed to be attached to the protein network, whereas fat globules in buffalo yoghurt were located within the pores, disrupting the protein network due to their large size (Nguyen et al. 2014b). High-resolution imaging of the mesostructures and their spatial distribution within yoghurt gels by using cryo-SEM gave insight into the differences between the rheological and water-holding properties of the sample yoghurts.

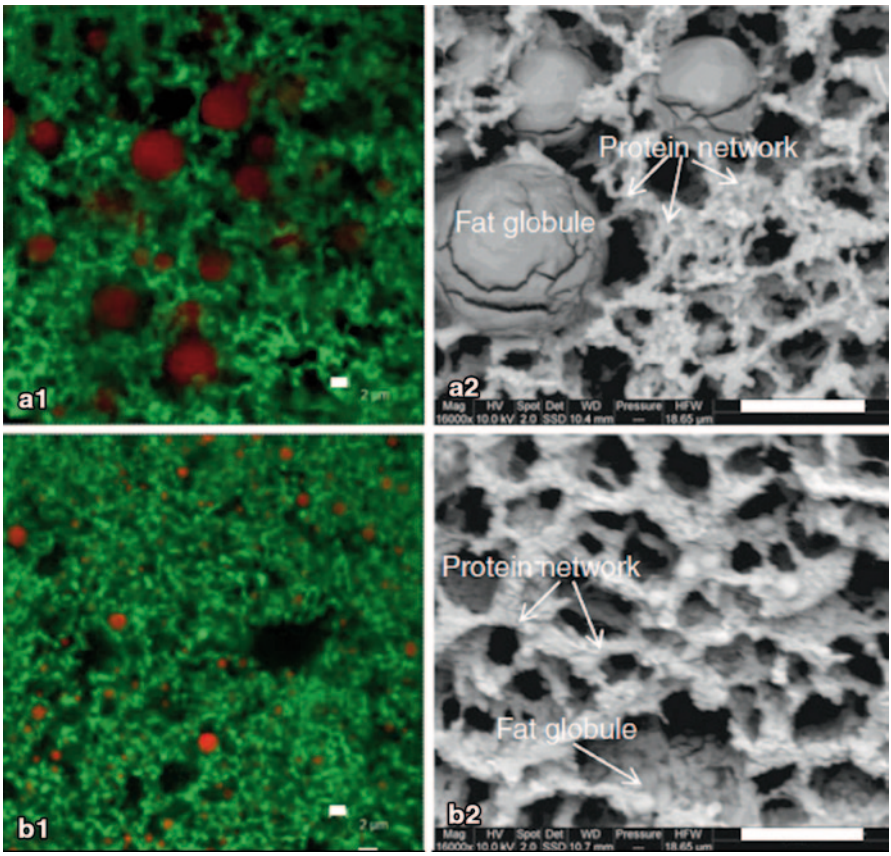

Fig. 4.8 **a** Microstructure of buffalo and **b** Bovine milk yoghurts imaged by CLSM (**a1**, **b1**) or cryo-SEM (**a2**, **b2**). In CLSM, fat was stained by Nile red (appears *red*) and proteins were stained by FCF (appears *green*). *Black areas* are serum pores in both CLSM and cryo-SEM images. The scale bars represent 2 μm and 5 μm in the CLSM and cryo-SEM images, respectively. (Reproduced from Nguyen et al. 2014b)

4.3.2 Transmission Electron Microscopy

TEM, especially cryo-TEM, has been extensively used in structural characterisation of casein micelles in milk as it allows imaging of nano-structural features of micelle interior as well as the outer surface (McMahon and Oommen 2013; Trejo et al. 2011; McMahon and Oommen 2008; Karlsson et al. 2007; Knudsen and Skibsted 2010; Marchin et al. 2007; Yahimi Yazdi et al. 2014). Examples of using TEM for imaging the structure of fermented dairy products, however, have been scarce as for such products, the 3D spatial organization of the structural components is most relevant for gaining understanding in product characteristics. TEM has higher resolution compared to other electron microscopy techniques, thus, it provides highly valuable insight into the morphology and interactions of nanostructures in soft

matter; however, conventional TEM only provides 2D images. The major drawback of TEM is the necessity of ultrathin sectioning of the specimen to allow electrons to pass through. Resolution strongly depends on the thickness of the specimen and the accelerating voltage for the electron beam (Dudkiewicz et al. 2011).

Preparation of fermented milk gel samples for TEM imaging follows similar sample preparation steps to SEM imaging initially. Effectively dehydrated samples are usually embedded in epoxy raisins and sectioned into ultrathin slices (60–90 nm) using ultramicrotomy. Finally, the slices are either imaged as such or stained by using uranyl acetate and lead citrate before imaging with TEM. Readers are directed to view publications by Aichinger et al. (2003), Sanchez et al. (2000), McMahon et al. (2009), Trejo et al. (2014) and Auty et al. (2005) for preparation of fermented milk gels for TEM imaging.

TEM provides insight into the lateral interactions of the casein micelles forming up the gel network. Aichinger et al. (2003) compared the microstructural features of fermented milk gels produced in existence or absence of chymosin by using both SEM and TEM. TEM images revealed that without chymosin, casein micelles were arranged like hard spheres touching each other with distinguished small contact area between two aggregated micelles (Fig. 4.9a). When a high concentration of chymosin was present during fermentation, extensive fusion of casein micelles into each other forming large junction zones was observed (Fig. 4.9b). Existence of larger and compact casein clusters, thicker strands, larger pores observed in SEM micrographs of the combined acid- and chymosin-induced gel were explained by those micellar interactions revealed by using TEM (Aichinger et al. 2003). A higher gel strength indicated by high-storage modulus in combined acid- and chymosin-induced gel compared to acid-induced gel was a consequence of higher number of junction zones, thus, higher number of bonds between strand-forming casein micelles while increased wheying off was explained by coarser network and larger pores as observed by SEM (Aichinger et al. 2003). The study reveals the high importance of understanding micro- and nano-structural organisation in order to elucidate the rheological and water-holding properties in acid milk gels. Sanchez et al.

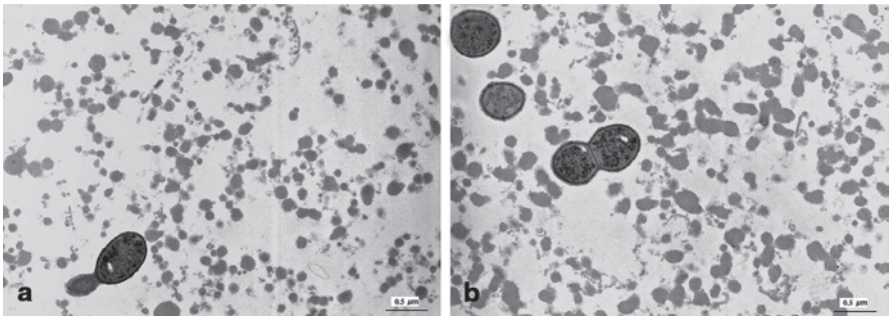

Fig. 4.9 TEM micrographs of milk gels fermented with *Streptococcus thermophilus* at 40 °C **a** without chymosin, and **b** at a high chymosin concentration. Scale bar represents 0.5 µm. (Reproduced from Aichinger et al. 2003)

(2000) also used SEM and TEM complementarily to study the effects of various hydrocolloids on the microstructure of acid-induced milk gels. TEM provided through characterisation of the size of the casein aggregates (modified micelles) forming the gel network and made it possible to visualise the filamentous structures or nano-aggregates forming a shell around the micellar aggregates (Sanchez et al. 2000).

The aggregation of proteins in milk during acidification and gradual formation of the gel network as the pH decreases has been visualised by CLSM or SEM as mentioned earlier. Changes in the supramolecular structure of casein micelles during acidification of skim milk at varying acidification temperatures (10–40 °C) have recently been followed by using TEM (McMahon et al. 2009). Based on TEM images, McMahon et al. (2009) proposed a three-phase model for formation of acid-induced gels from unheated milk. Phase 1 (pH 6.7–5.3) involves temperature-dependent dissociation of proteins from the casein micelles. Dissociated proteins were visualised as loosely entangled colloidal aggregates (50 nm in diameter; Fig. 4.10). Phase 2 (pH 5.3–4.9) involves the loosely entangled proteins forming more compact colloidal particles the size of which is affected by the acidification temperature. Phase 3 (pH 4.9–4.8) involves rapid aggregation of the colloidal casein supramolecules into

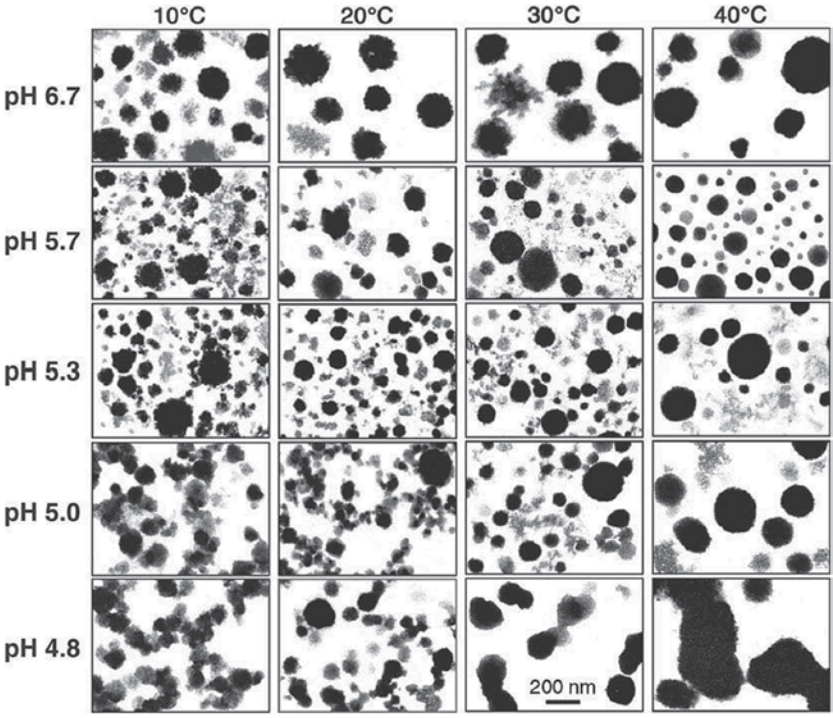

Fig. 4.10 TEM images revealing microstructural changes during acidification of unheated skim milk as a function of temperature and pH. Colloidal casein supramolecules depicted in *black,* loosely entangled protein aggregates depicted in *grey* and background digitally converted to white. (Reprinted from McMahon et al. 2009)

a gel network as the pH decreases. The nature of the gel, that is being coarse or fine stranded, is dependent on acidification temperature.

TEM images showing the structural details of more specific fermented dairy products such as kefir, viili and skyr can be viewed in Tamime et al. (2007).

4.4 Image Analysis

Image analysis on fermented milk gel micrographs has been performed mainly aiming at quantitation of relative phase area, fractal dimensions, size and shape of the protein aggregates, network pores and fat globules, etc. Most typical analysis are morphometry of individual particles and grey level granulometry (Ercili-Cura et al. 2014; Morand et al. 2012a, b; Rovira et al. 2011; Impoco et al. 2012; Silva et al. 2015). Grey-level granulometry involves image transformations based on a *structuring element* with a given shape and size. A detailed description of image analysis by using this technique can be found in Ercili-Cura et al. (2014) and Devaux et al. (2008). Grey-level granulometry was used to measure mean pore size from CLSM images of skim milk gels obtained during different stages of acidification (Ercili-Cura et al. 2014). Skim milk was treated with a protein cross-linking enzyme, namely transglutaminase, before acidification and the mean pore size of the gel networks of the control and the enzyme-treated gels were analysed during and at the end of acidification (Fig. 4.11). Quantitation of the pore size provided insight into the gel formation dynamics such as fixation of the network or further coarsening at intermediate pH values during the course of acidification (Ercili-Cura et al. 2014).

Thresholding is a crucial step in image analysis of greyscale images. Important parameters and optimisation of thresholding technique for analysis of pore size in acid-induced milk protein gels is extensively described in Pugnaloni et al. (2005). Fractal analysis techniques have been useful in characterising the structural

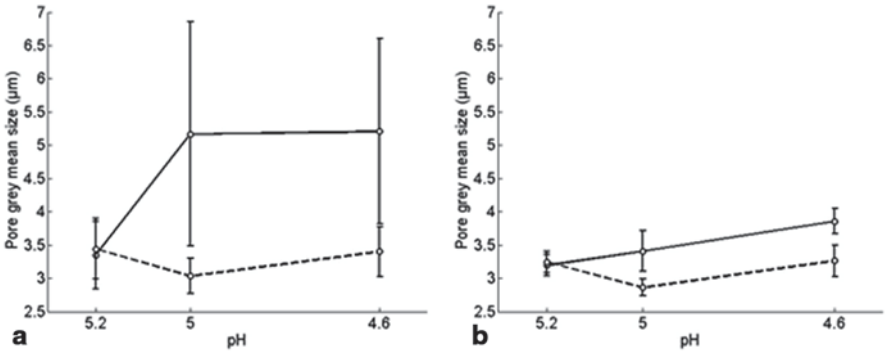

Fig. 4.11 Grey level mean sizes of pores obtained by image analysis on CLSM images of the control *(solid lines)* and the transglutaminase-treated *(dashed lines)* acid skim milk gels produced at **a** 40 °C, and **b** 20 °C. Vertical bars represent standard deviation. (Reproduced from Ercili-Cura et al. 2014)

component morphology in food systems with highly irregular structures (Torres et al. 2012). Determination of fractal dimensions from CLSM (Torres et al. 2012; Pugnaloni et al. 2005) or SEM (Kuhn et al. 2010) micrographs of milk protein gels have been used in order to compare microstructural details quantitatively and link the microstructural features to the gel mechanical properties. Torres et al. (2012) used fractal image analysis in combination with principal components analysis (PCA) to quantitate the structural changes in stirred yoghurt with addition of different microparticulated whey ingredients. CLSM images were analysed using an image analysis technique that combines an initial 2D-wavelet compression followed by fractal analysis and inspection of the fractal curves by PCA. The calculated degree of self-similarity or fractality was used to identify the most potential microparticulated whey ingredient as a fat replacer in yoghurt gels (Torres et al. 2012).

Silva et al. (2015) recently introduced an automated image analysis procedure to characterise the microstructure of various dairy systems. TEM images of two concentrated milk protein suspensions and two rennet-induced gels were used for the image analysis. Images were first normalised using a blank background image, converted to images based on 256 shades of grey, smoothed to remove the acquisition noise, contrasted and segmented using the *Otsu automated threshold* resulting in a binary image (Fig. 4.12). Microstructural parameters investigated involved global morphological parameters such as area fraction, porosity and boundary length per

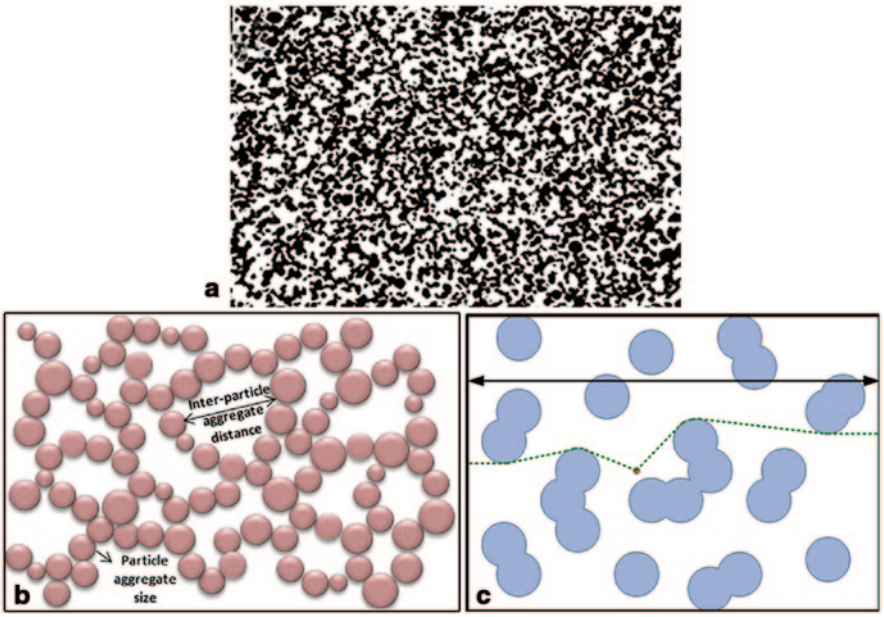

Fig. 4.12 **a** Binarised image from TEM micrograph of rennet-induced milk gel produced from milk concentrated by ultrafiltration, **b** Schematic representation of the microstructural parameters determined for dairy gels by the image morphological granulometry method, **c** Tortuosity computed as the ratio of the shortest lengths to borders *(dashed line)* over the image width *(black line)* in a synthetic binary structure. (Reproduced from Silva et al. 2015)

unit area; binary image granulometry which measures the typical sizes of particles/aggregates or of interparticle/aggregate distances; and tortuosity which describes the microstructure at a larger scale (Fig. 4.12). The analysis procedure was first validated on TEM images of concentrated milk protein suspensions and then applied to TEM images of rennet-induced gels of the corresponding suspensions. Developed image analysis method was found to be successful in differentiating the microstructural features of the studied milk gels. It enabled easy measurement of microstructural parameters which may even be used in routine measurements (Silva et al. 2015).

References

Abhyankar AR, Mulvihill DM, Chaurin V, Auty MAE (2011) Techniques for localisation of konjac glucomannan in model milk protein–polysaccharide mixed systems: Physicochemical and microscopic investigations. Food Chem 129(4):1362–1368. doi:http://dx.doi.org/10.1016/j.foodchem.2011.05.052

Abhyankar AR, Mulvihill DM, Auty MAE (2014) Combined confocal microscopy and large deformation analysis of emulsion filled gels and stirred acid milk gels. Food Struct 1(2):127–136. doi:http://dx.doi.org/10.1016/j.foostr.2013.12.001

Aichinger P-A, Michel M, Servais C, Dillmann M-L, Rouvet M, D'Amico N, Zink R, Klostermeyer H, Horne DS (2003) Fermentation of a skim milk concentrate with *Streptococcus thermophilus* and chymosin: structure, viscoelasticity and syneresis of gels. Coll Surf B Biointerfaces 31(1–4):243–255. doi:http://dx.doi.org/10.1016/S0927-7765(03)00144-9

Aichinger P-A, Dillmann M-L, Rami-Shojaei S, Michel M, Horne DS (2006) Xanthan gum in skim milk: designing structure into acid milk gels. In: Dickinson E, Leser ME (eds) Food colloids: self-assembly and material science. Royal Society of Chemistry, Cambridge, pp 283–296

Amatayakul T, Sherkat F, Shah NP (2006) Physical characteristics of set yoghurt made with altered casein to whey protein ratios and EPS-producing starter cultures at 9 and 14 % total solids. Food Hydrocoll 20(2–3):314–324. doi:http://dx.doi.org/10.1016/j.foodhyd.2005.02.015

Arltoft D, Ipsen R, Christensen N, Madsen F (2006a) Localising pectin in dairy products using direct immunostaining. In: Williams PA, Phillips GO (eds) Gums and Stabilisers for the Food Industry, vol 13. The Royal Society of Chemistry, Cambridge, pp 41–50

Arltoft D, Madsen F, Ipsen R (2006b) Characterizing low ester pectin microstructure in model milk gels by direct immunostaining and CLSM. In: 4th International Symposium on Food Rheology and Structure, Zurich, Switzerland. pp 91–95

Arltoft D, Madsen F, Ipsen R (2007) Screening of probes for specific localisation of polysaccharides. Food Hydrocoll 21(7):1062–1071. doi:http://dx.doi.org/10.1016/j.foodhyd.2006.07.020

Arltoft D, Madsen F, Ipsen R (2008) Relating the microstructure of pectin and carrageenan in dairy desserts to rheological and sensory characteristics. Food Hydrocoll 22(4):660–673. doi:http://dx.doi.org/10.1016/j.foodhyd.2007.01.025

Auty MAE (2013) Confocal microscopy: principles and applications to food microstructures. In: Morris VJ, Groves K (eds) Food microstructures: microscopy, meausrement and modelling. Woodhead Publishing, Cambridge, pp 96–131

Auty MAE, Fenelon MA, Guinee TP, Mullins C, Mulvihill DM (1999) Dynamic confocal scanning laser microscopy methods for studying milk protein gelation and cheese melting. Scanning 21(5):299–304. doi:10.1002/sca.4950210503

Auty MAE, O'Kennedy BT, Allan-Wojtas P, Mulvihill DM (2005) The application of microscopy and rheology to study the effect of milk salt concentration on the structure of acidified micellar casein systems. Food Hydrocoll 19(1):101–109. doi:http://dx.doi.org/10.1016/j.foodhyd.2004.04.019

Ayala-Hernandez I, Goff HD, Corredig M (2008) Interactions between milk proteins and exopolysaccharides produced by *Lactococcus lactis* observed by scanning electron microscopy. J Dairy Sci 91(7):2583–2590. doi:10.3168/jds.2007–0876

Ayala-Hernández I, Hassan AN, Goff HD, Corredig M (2009) Effect of protein supplementation on the rheological characteristics of milk permeates fermented with exopolysaccharide-producing *Lactococcus lactis* subsp. *cremoris*. Food Hydrocoll 23(5):1299–1304. doi:http://dx.doi.org/10.1016/j.foodhyd.2008.11.004

Brink J, Langton M, Stading M, Hermansson A-M (2007) Simultaneous analysis of the structural and mechanical changes during large deformation of whey protein isolate/gelatin gels at the macro and micro levels. Food Hydrocoll 21(3):409–419. doi:http://dx.doi.org/10.1016/j.foodhyd.2006.04.012

Bromley EHC, Krebs MRH, Donald AM (2006) Mechanisms of structure formation in particulate gels of β-lactoglobulin formed near the isoelectric point. Eur Phys J E 21(2):145–152. doi:10.1140/epje/i2006-10055-7

Choi J, Horne DS, Lucey JA (2007) Effect of insoluble calcium concentration on rennet coagulation properties of milk. J Dairy Sci 90(6):2612–2623. doi:http://dx.doi.org/10.3168/jds.2006-814

Ciron CIE, Gee VL, Kelly AL, Auty MAE (2010) Comparison of the effects of high-pressure microfluidization and conventional homogenization of milk on particle size, water retention and texture of non-fat and low-fat yoghurts. Int Dairy J 20(5):314–320

Ciron CIE, Gee VL, Kelly AL, Auty MAE (2012) Modifying the microstructure of low-fat yoghurt by microfluidisation of milk at different pressures to enhance rheological and sensory properties. Food Chem 130(3):510–519. doi:http://dx.doi.org/10.1016/j.foodchem.2011.07.056

Claxton NS, Fellers TJ, Davidson MW (2006) Laser scanning confocal microscopy. Department of Optical Microscopy and Digital Imaging, Florida State University, Tallahassee, http://ww-wolympusconfocalcom/theory/LSCMIntropdf

Corredig M, Sharafbafi N, Kristo E (2011) Polysaccharide–protein interactions in dairy matrices, control and design of structures. Food Hydrocolloids 25(8):1833–1841. doi:http://dx.doi.org/10.1016/j.foodhyd.2011.05.014

Dalgleish DG (2011) On the structural models of bovine casein micelles-review and possible improvements. Soft Matter 7(6):2265–2272. doi:10.1039/C0SM00806K

Dalgleish DG, Corredig M (2012) The structure of the casein micelle of milk and its changes during processing. Annu Rev Food Sci Technol 3(1):449–467. doi:10.1146/annurev-food-022811-101214

Dalgleish DG, Spagnuolo PA, Douglas GH (2004) A possible structure of the casein micelle based on high-resolution field-emission scanning electron microscopy. Int Dairy J 14(12):1025–1031. doi:10.1016/j.idairyj.2004.04.008

De Kruif CG (1999) Casein micelle interactions. Int Dairy J 9:183–188

Devaux M-F, Bouchet B, Legland D, Guillon F, Lahaye M (2008) Macro-vision and grey level granulometry for quantification of tomato pericarp structure. Postharvest Biol Technol 47(2):199–209. doi:http://dx.doi.org/10.1016/j.postharvbio.2007.06.017

Donald AM (2003) In situ deformation of hydrated food samples. In: Dickinson E, Van Vliet T (eds) Food colloids, biopolymers and materials. Royal Society of Chemistry, Cambridge, pp 245–255

Donato L, Guyomarc'h F (2009) Formation and properties of the whey protein/κ-casein complexes in heated skim milk—A review. Dairy Sci Technol 89(1):3–29

Dudkiewicz A, Tiede K, Loeschner K, Jensen LHS, Jensen E, Wierzbicki R, Boxall ABA, Molhave K (2011) Characterization of nanomaterials in food by electron microscopy. Trends Anal Chem 30(1):28–43. doi:http://dx.doi.org/10.1016/j.trac.2010.10.007

Dürrenberger MB, Handschin S, Conde-Petit B, Escher F (2001) Visualization of food structure by confocal laser scanning microscopy (CLSM). LWT Food Sci Technol 34(1):11–17. doi:http://dx.doi.org/10.1006/fstl.2000.0739

El-Bakry M, Duggan E, O'Riordan ED, O'Sullivan M (2011) Casein hydration and fat emulsification during manufacture of imitation cheese, and effects of emulsifying salts reduction. J Food Eng 103(2):179–187. doi:http://dx.doi.org/10.1016/j.jfoodeng.2010.10.014

El-Bakry M, Sheehan J (2014) Analysing cheese microstructure: a review of recent developments. J Food Eng 125:84–96. doi:http://dx.doi.org/10.1016/j.jfoodeng.2013.10.030

Ercili Cura D, Lantto R, Lille M, Andberg M, Kruus K, Buchert J (2009) Laccase-aided protein modification: effects on the structural properties of acidified sodium caseinate gels. Int Dairy J 19(12):737–745. doi:10.1016/j.idairyj.2009.06.007

Ercili Cura D, Lille M, Partanen R, Kruus K, Buchert J, Lantto R (2010) Effect of *Trichoderma reesei* tyrosinase on rheology and microstructure of acidified milk gels. Int Dairy J 20(12):830–837. doi:10.1016/j.idairyj.2010.06.008

Ercili-Cura D, Lille M, Legland D, Gaucel S, Poutanen K, Partanen R, Lantto R (2014) Structural mechanisms leading to improved water retention in acid milk gels by use of transglutaminase. Food Hydrocoll 30(1):419–427. doi:http://dx.doi.org/10.1016/j.foodhyd.2012.07.008

Everett DW, McLeod RE (2005) Interactions of polysaccharide stabilisers with casein aggregates in stirred skim-milk yoghurt. Int Dairy J 15(11):1175–1183. doi:http://dx.doi.org/10.1016/j.idairyj.2004.12.004

Farrell Jr HM, Malin EL, Brown EM, Qi PX (2006) Casein micelle structure: what can be learned from milk synthesis and structural biology? Curr Opin Coll Interf Sci 11(2–3):135–147. doi:10.1016/j.cocis.2005.11.005

Ferrando M, Spiess WEL (2000) Review: confocal scanning laser microscopy. A powerful tool in food science revision: Microscopía láser confocal de barrido. Una potente herramienta en la ciencia de los alimentos. Food Sci Technol Int 6(4):267–284. doi:10.1177/108201320000600402

Folkenberg DM, Dejmek P, Skriver A, Ipsen R (2005) Relation between sensory texture properties and exopolysaccharide distribution in set and stirred yoghurts produced with different starter cultures. J Texture Stud 36(2):174–189. doi:10.1111/j.1745-4603.2005.00010.x

Fox PF (2003) Milk proteines: general and historical aspects. In: Fox PF, McSweeney PLH (eds) Advanced dairy chemistry, vol 1 Part A. vol 3rd edition. Kluwer Academic/Plenum Publishers, New York, pp 1–48

Fox PF, Brodkorb A (2008) The casein micelle: historical aspects, current concepts and significance. Int Dairy J 18(7):677–684. doi:10.1016/j.idairyj.2008.03.002

Gastaldi E, Lagaude A, De La Fuente BT (1996) Micellar transition state in casein between pH 5.5 and 5.0. J Food Sci 61(1):59–64. doi:10.1111/j.1365-2621.1996.tb14725.x

Girard M, Schaffer-Lequart C (2007a) Gelation and resistance to shearing of fermented milk: role of exopolysaccharides. Int Dairy J 17(6):666–673. doi:http://dx.doi.org/10.1016/j.idairyj.2006.08.007

Girard M, Schaffer-Lequart C (2007b) Gelation of skim milk containing anionic exopolysaccharides and recovery of texture after shearing. Food Hydrocoll 21(7):1031–1040. doi:http://dx.doi.org/10.1016/j.foodhyd.2006.07.012

Girard M, Schaffer-Lequart C (2008) Attractive interactions between selected anionic exopolysaccharides and milk proteins. Food Hydrocolloids 22(8):1425–1434. doi:http://dx.doi.org/10.1016/j.foodhyd.2007.09.001

González-Martínez C, Becerra M, Cháfer M, Albors A, Carot JM, Chiralt A (2002) Influence of substituting milk powder for whey powder on yoghurt quality. Trends Food Sci Technol 13(9–10):334–340. doi:http://dx.doi.org/10.1016/S0924-2244(02)00160-7

Guillemin F, Guillon F, Bonnin E, Devaux M-F, Chevalier T, Knox JP, Liners F, Thibault JF (2005) Distribution of pectic epitopes in cell walls of the sugar beet root. Planta 222(2):355–371

Guyomarc'h F, Jemin M, Le Tilly V, Madec M-N, Famelart M-H (2009) Role of the heat-induced whey protein/κ-casein complexes in the formation of acid milk gels: a kinetic study using rheology and confocal microscopy. J Agric Food Chem 57(13):5910–5917. doi:10.1021/jf804042k

Hahn C, Sramek M, Nöbel S, Hinrichs J (2012) Post-processing of concentrated fermented milk: influence of temperature and holding time on the formation of particle clusters. Dairy Sci Technol 92(1):91–107. doi:10.1007/s13594-011-0046-1

Hassan AN (2008) ADSA Foundation scholar award: possibilities and challenges of exopolysaccharide-producing lactic cultures in dairy foods. J Dairy Sci 91(4):1282–1298

Hassan AN, Awad S (2005) Application of exopolysaccharide-producing cultures in reduced-fat cheddar cheese: cryo-Scanning electron microscopy observations. J Dairy Sci 88(12):4214–4220. doi:http://dx.doi.org/10.3168/jds.S0022-0302(05)73107-6

Hassan AN, Frank JF, Farmer MA, Schmidt KA, Shalabi SI (1995) Formation of yogurt microstructure and three-dimensional visualization as determined by confocal scanning laser microscopy. J Dairy Sci 78(12):2629–2636

Hassan AN, Frank JF, Qvist KB (2002) Direct observation of bacterial exopolysaccharides in dairy products using confocal scanning laser microscopy. J Dairy Sci 85(7):1705–1708

Hassan AN, Frank JF, Elsoda M (2003a) Observation of bacterial exopolysaccharide in dairy products using cryo-scanning electron microscopy. Int Dairy J 13(9):755–762. doi:http://dx.doi.org/10.1016/S0958-6946(03)00101-8

Hassan AN, Ipsen R, Janzen T, Qvist KB (2003b) Microstructure and rheology of yogurt made with cultures differing only in their ability to produce exopolysaccharides. J Dairy Sci 86(5):1632–1638

Hassan AN, Corredig M, Frank JF, Elsoda M (2004) Microstructure and rheology of an acid-coagulated cheese (Karish) made with an exopolysaccharide-producing *Streptococcus thermophilus* strain and its exopolysaccharide non-producing genetic variant. J Dairy Res 71(01):116–120. doi:10.1017/S0022029903006605

Heilig A, Göggerle A, Hinrichs J (2009) Multiphase visualisation of fat containing β-lactoglobulin–κ-carrageenan gels by confocal scanning laser microscopy, using a novel dye, V03-01136, for fat staining. LWT—Food Sci Technol 42(2):646–653. doi:http://dx.doi.org/10.1016/j.lwt.2008.08.006

Herbert S, Bouchet B, Riaublanc A, Dufour E, Gallant D, J. (1999) Multiple fluorescence labelling of proteins, lipids and whey in dairy products using confocal microscopy. Lait 79(6):567–575

Hermansson A-M (2008) Structuring water by gelation. In: Aguilera JM, Lillford PJ (eds) Food Materials Science. Food Engineering: principles and practice. Springer, New York. pp 255–280. doi:10.1007/978-0-387-71947-4_13

Horne DS (1986) Steric stabilization and casein micelle stability. J Coll Interface Sci 111(1):250–260

Horne DS (1999) Formation and structure of acidified milk gels. Int Dairy J 9(3–6):261–268

Horne DS (2003) Casein micelles as hard spheres: limitations of the model in acidified gel formation. Coll Surfaces A Physicochem Eng Asp 213(2–3):255–263. doi:10.1016/s0927-7757(02)00518-6

Horne DS (2006) Casein micelle structure: models and muddles. Curr Opin Coll Interface Sci 11(2–3):148–153. doi:10.1016/j.cocis.2005.11.004

Impoco G, FucÃ N, Pasta C, Caccamo M, Licitra G (2012) Quantitative analysis of nanostructures' shape and distribution in micrographs using image analysis. Comput Electron Agric 84:26–35. doi:http://dx.doi.org/10.1016/j.compag.2012.02.013

Jensen S, Rolin C, Ipsen R (2010) Stabilisation of acidified skimmed milk with HM pectin. Food Hydrocoll 24(4):291–299. doi:http://dx.doi.org/10.1016/j.foodhyd.2009.10.004

Kalab M, Allan-Wojtas P, Phipps-Todd BE (1983) Development of microstructure in set-style nonfat yoghurt-a review. Food Microstruct 2:51–66

Kalab M, Larocque G (1996) Suitability of agar gel encapsulation of milk and cream for electron microscopy. LWT Food Sci Technol 29:368–371

Karlsson AO, Ipsen R, Ardö Y (2007) Observations of casein micelles in skim milk concentrate by transmission electron microscopy. LWT Food Sci Technol 40(6):1102–1107. doi:http://dx.doi.org/10.1016/j.lwt.2006.05.012

Knudsen JC, Skibsted LH (2010) High pressure effects on the structure of casein micelles in milk as studied by cryo-transmission electron microscopy. Food Chem 119(1):202–208. doi:10.1016/j.foodchem.2009.06.017

Kristo E, Miao Z, Corredig M (2011) The role of exopolysaccharide produced by *Lactococcus lactis* subsp. cremoris in structure formation and recovery of acid milk gels. Int Dairy J 21(9):656–662. doi:http://dx.doi.org/10.1016/j.idairyj.2011.02.002

Krzeminski A, Großhable K, Hinrichs J (2011) Structural properties of stirred yoghurt as influenced by whey proteins. LWT Food Sci Technol 44(10):2134–2140. doi:http://dx.doi.org/10.1016/j.lwt.2011.05.018

Kuhn KR, Cavallieri ÂLF, Da Cunha RL (2010) Cold-set whey protein gels induced by calcium or sodium salt addition. Int J Food Sci Technol 45(2):348–357. doi:10.1111/j.1365-2621.2009.02145.x

Lakemond CMM, van Vliet T (2008) Rheological properties of acid skim milk gels as affected by the spatial distribution of the structural elements and the interaction forces between them. Int Dairy J 18(5):585–593

Laneuville SI, Turgeon SL (2014) Microstructure and stability of skim milk acid gels containing an anionic bacterial exopolysaccharide and commercial polysaccharides. Int Dairy J 37(1):5–15. doi:http://dx.doi.org/10.1016/j.idairyj.2014.01.014

Lin C, Chen J, Corredig M, Hill A (2012) Soy/milk cheese-type and yoghurt-type products and method of making.

Liu Q, Talbot M, Llewellyn DJ (2013) Pectin methylesterase and pectin remodelling differ in the fibre walls of two *Gossypium* species with very different fibre properties. PLoS ONE 8(6):e65131. doi:10.1371/journal.pone.0065131

Lucey JA (2007) Microstructural approaches to the study and improvement of cheese and yoghurt products. In: McClements DJ (ed) Understanding and controlling the microstructure of complex food. Woodhead Publishing, Cambridge, pp 600–621. doi:10.1533/9781845693671.4.600

Lucey JA, Teo CT, Munro PA, Singh H (1997) Rheological properties at small (dynamic) and large (yield) deformations of acid gels made from heated milk. J Dairy Res 64(4):591–600

Lucey JA, Tamehana M, Singh H, Munro PA (1998) Effects of interactions between denaturated whey proteins and casein micelles on the formation and rheological properties of acid skim milk gels. J Dairy Res 65:555–567

Marchin S, Putaux J-L, Pignon F, Leonil J (2007) Effects of the environmental factors on the casein micelle structure studied by cryo transmission electron microscopy and small-angle x-ray scattering/ultrasmall-angle x-ray scattering. J Chem Phy 126(4):1–10

Martín-Diana AB, Janer C, Peláez C, Requena T (2004) Effect of milk fat replacement by polyunsaturated fatty acids on the microbiological, rheological and sensorial properties of fermented milks. J Sci Food Agric 84(12):1599–1605. doi:10.1002/jsfa.1844

Martin AH, Douglas Goff H, Smith A, Dalgleish DG (2006) Immobilization of casein micelles for probing their structure and interactions with polysaccharides using scanning electron microscopy (SEM). Food Hydrocoll 20(6):817–824. doi:http://dx.doi.org/10.1016/j.foodhyd.2005.08.004

Matia-Merino L, Singh H (2007) Acid-induced gelation of milk protein concentrates with added pectin: effect of casein micelle dissociation. Food Hydrocoll 21(5–6):765–775. doi:http://dx.doi.org/10.1016/j.foodhyd.2006.12.007

McMahon DJ, Oommen BS (2008) Supramolecular structure of the casein micelle. J Dairy Sci 91(5):1709–1721

McMahon DJ, Oommen BS (2013) Casein micelle structure, functions, and interactions. In: McSweeney PLH, Fox PF (eds) Advanced Dairy Chemistry, vol 1A Proteins: basic Aspects. Springer, US, pp 185–209. doi:10.1007/978-1-4614-4714-6_6

McMahon DJ, Du H, McManus WR, Larsen KM (2009) Microstructural changes in casein supramolecules during acidification of skim milk. J Dairy Sci 92(12):5854–5867. doi:http://dx.doi.org/10.3168/jds.2009–2324

Mellema M, Walstra P, van Opheusden JHJ, van Vliet T (2002a) Effects of structural rearrangements on the rheology of rennet-induced casein particle gels. Adv Coll Interface Sci 98(1):25–50. doi:10.1016/s0001-8686(01)00089-6

Mellema M, van Opheusden JHJ, van Vliet T (2002b) Categorization of rheological scaling models for particle gels applied to casein gels. J Rheol 46(1):11–29

Morand M, Dekkari A, Guyomarc'h F, Famelart M-H (2012a) Increasing the hydrophobicity of the heat-induced whey protein complexes improves the acid gelation of skim milk. Int Dairy J 25(2):103–111. doi:http://dx.doi.org/10.1016/j.idairyj.2012.03.002

Morand M, Guyomarc'h F, Legland D, Famelart M-H (2012b) Changing the isoelectric point of the heat-induced whey protein complexes affects the acid gelation of skim milk. Int Dairy J 23(1):9–17. doi:http://dx.doi.org/10.1016/j.idairyj.2011.10.006

Morell P, Hernando I, Llorca E, Fiszman S (2015) Yogurts with an increased protein content and physically modified starch: rheological, structural, oral digestion and sensory properties related to enhanced satiating capacity. Food Res Int 70:64–73. doi:http://dx.doi.org/10.1016/j.foodres.2015.01.024

Myllärinen P, Buchert J, Autio K (2007) Effect of transglutaminase on rheological properties and microstructure of chemically acidified sodium caseinate gels. Int Dairy J 17(7):800–807

Nayebzadeh K, Chen J, Dickinson E, Moschakis T (2006) Surface structure smoothing effect of polysaccharide on a heat-set protein particle gel. Langmuir 22(21):8873–8880. doi:10.1021/la060419o

Nguyen HTH, Ong L, Kentish SE, Gras SL (2014a) The effect of fermentation temperature on the microstructure, physicochemical and rheological properties of probiotic buffalo yoghurt. Food Bioprocess Technol 7(9):2538–2548. doi:10.1007/s11947-014-1278-x

Nguyen HTH, Ong L, Lefèvre C, Kentish SE, Gras SL (2014b) The microstructure and physicochemical properties of probiotic buffalo yoghurt during fermentation and storage: a comparison with bovine yoghurt. Food Bioprocess Technol 7(4):937–953. doi:10.1007/s11947-013-1082-z

Nicolas Y, Paques M, Knaebel A, Steyer A, Munch J-P, Blijdenstein TBJ, van Aken GA (2003a) Microrheology: structural evolution under static and dynamic conditions by simultaneous analysis of confocal microscopy and diffusing wave spectroscopy. Rev Sci Instrum 74(8):3838–3844. doi:http://dx.doi.org/10.1063/1.1588747

Nicolas Y, Paques M, van den Ende D, Dhont JKG, van Polanen RC, Knaebel A, Steyer A, Munch J-P, Blijdenstein TBJ, van Aken GA (2003b) Microrheology: new methods to approach the functional properties of food. Food Hydrocoll 17(6):907–913. doi:http://dx.doi.org/10.1016/S0268-005X(03)00113-9

Nöbel S, Hahn C, Hitzmann B, Hinrichs J (2014) Rheological properties of microgel suspensions: viscoelastic modelling of microstructural elements from casein micelles to fermented dairy products. Int Dairy J 39(1):157–166. doi:http://dx.doi.org/10.1016/j.idairyj.2014.06.001

Olsson C, Langton M, Hermansson A-M (2002) Dynamic measurements of β-lactoglobulin structures during aggregation, gel formation and gel break-up in mixed biopolymer systems. Food Hydrocoll 16(5):477–488. doi:http://dx.doi.org/10.1016/S0268-005X(01)00125-4

Ong L, Dagastine RR, Kentish SE, Gras SL (2011) Microstructure of milk gel and cheese curd observed using cryo scanning electron microscopy and confocal microscopy. LWT Food Sci Technol 44(5):1291–1302. doi:http://dx.doi.org/10.1016/j.lwt.2010.12.026

Ong L, Dagastine R, Kentish S, Gras S (2013a) Microstructure and composition of full fat cheddar cheese made with ultrafiltered milk retentate. Foods 2(3):310–331

Ong L, Dagastine RR, Kentish SE, Gras SL (2013b) The effect of calcium chloride addition on the microstructure and composition of Cheddar cheese. Int Dairy J 33(2):135–141. doi:http://dx.doi.org/10.1016/j.idairyj.2013.03.002

Ong L, Soodam K, Kentish SE, Powell IB, Gras SL (2015) The addition of calcium chloride in combination with a lower draining pH to change the microstructure and improve fat retention in Cheddar cheese. Int Dairy J 46:53–62. doi:http://dx.doi.org/10.1016/j.idairyj.2014.07.003

Ouanezar M, Guyomarc'h F, Bouchoux A (2012) AFM imaging of milk casein micelles: evidence for structural rearrangement upon acidification. Langmuir 28(11):4915–4919. doi:10.1021/la3001448

Ozcan T, Horne D, Lucey JA (2011) Effect of increasing the colloidal calcium phosphate of milk on the texture and microstructure of yogurt. J Dairy Sci 94(11):5278–5288. doi:10.3168/jds.2010-3932

Pang Z, Deeth H, Bansal N (2015a) Effect of polysaccharides with different ionic charge on the rheological, microstructural and textural properties of acid milk gels. Food Res Int 72:62–73. doi:http://dx.doi.org/10.1016/j.foodres.2015.02.009

Pang Z, Deeth H, Sharma R, Bansal N (2015b) Effect of addition of gelatin on the rheological and microstructural properties of acid milk protein gels. Food Hydrocoll 43:340–351. doi:http://dx.doi.org/10.1016/j.foodhyd.2014.06.005

Partanen R, Autio K, Myllärinen P, Lille M, Buchert J, Forssell P (2008) Effect of transglutaminase on structure and syneresis of neutral and acidic sodium caseinate gels. Int Dairy J 18(4):414–421

Peng Y, Horne DS, Lucey JA (2009) Impact of preacidification of milk and fermentation time on the properties of yogurt. J Dairy Sci 92(7):2977–2990. doi:10.3168/jds.2008-1221

Peng Y, Horne DS, Lucey JA (2010) Physical properties of acid milk gels prepared at 37°C up to gelation but at different incubation temperatures for the remainder of fermentation. J Dairy Sci 93(5):1910–1917

Phadungath C (2005) The mechanism and properties of acid-coagulated milk gels. Songklanakarin J Sci Technol 27(2):433–448

Prasanna PHP, Grandison AS, Charalampopoulos D (2013) Microbiological, chemical and rheological properties of low fat set yoghurt produced with exopolysaccharide (EPS) producing *Bifidobacterium* strains. Food Res Int 51(1):15–22. doi:http://dx.doi.org/10.1016/j.foodres.2012.11.016

Pugnaloni LA, Matia-Merino L, Dickinson E (2005) Microstructure of acid-induced caseinate gels containing sucrose: quantification from confocal microscopy and image analysis. Coll Surfaces B Biointerfaces 42(3–4):211–217. doi:http://dx.doi.org/10.1016/j.colsurfb.2005.03.002

Riener J, Noci F, Cronin DA, Morgan DJ, Lyng JG (2009) The effect of thermosonication of milk on selected physicochemical and microstructural properties of yoghurt gels during fermentation. Food Chem 114(3):905–911. doi:http://dx.doi.org/10.1016/j.foodchem.2008.10.037

Rincón Cardona JA, Iriart HC, Herrera ML (2013) Applications of confocal laser scanning microscopy (CLSM) in foods. In: Lagali N (ed) Confocal laser microscopy—principles and applications in medicine, biology, and the food sciences. InTech. doi:10.5772/55653

Rizzieri R, Baker FS, Donald AM (2003) A tensometer to study strain deformation and failure behavior of hydrated systems via in situ environmental scanning electron microscopy. Rev Scient Instrum 74(10):4423–4428. doi:http://dx.doi.org/10.1063/1.1611618

Roefs SPFM, Van Vliet T (1990) Structure of acid casein gels 2. Dynamic measurements and type of interaction forces. Coll Surf A 50(c):161–175. (Physicochemical and Engineering Aspects)

Rohart A, Michon C (2013) Designing microstructure into acid skim milk/guar gum gels. Paper presented at the InsideFood Symposium, 9–12 April, Leuven, Belgium,

Rohart A, Michon C (2014) Designing microstructure into xanthan gum-enriched acid milk gels. Innov Sci Emerg Technol 25:53–57. doi:http://dx.doi.org/10.1016/j.ifset.2014.01.002

Rovira S, Lopez MB, Ferrandini E, Laencina J (2011) Hot topic: microstructure quantification by scanning electron microscopy and image analysis of goat cheese curd. J Dairy Sci 94(3):1091–1097

Sanchez C, Zuniga-Lopez R, Schmitt C, Despond S, Hardy J (2000) Microstructure of acid–induced skim milk–locust bean gum–xanthan gels. Int Dairy J 10(3):199–212. doi:http://dx.doi.org/10.1016/S0958-6946(00)00030-3

Sandoval-Castilla O, Lobato-Calleros C, Aguirre-Mandujano E, Vernon-Carter EJ (2004) Microstructure and texture of yogurt as influenced by fat replacers. Int Dairy J 14(2):151–159. doi:http://dx.doi.org/10.1016/S0958-6946(03)00166-3

Sawyer L, Kontopidis G (2000) The core lipocalin, bovine β-lactoglobulin. Biochimica et Biophysica Acta (BBA). Protein Struct Mol Enzymol 1482(1–2):136–148. doi:10.1016/s0167-4838(00)00160-6

Siefarth C, Tran T, Mittermaier P, Pfeiffer T, Buettner A (2014) Effect of radio frequency heating on yoghurt, II: microstructure and texture. Foods 3(2):369–393

Silva JVC, Legland D, Cauty C, Kolotuev I, Floury J (2015) Characterization of the microstructure of dairy systems using automated image analysis. Food Hydrocoll 44:360–371. doi:http://dx.doi.org/10.1016/j.foodhyd.2014.09.028

Singh M, Kim S (2009) Yogurt fermentation in the presence of starch–lipid composite. J Food Sci 74(2):85–89. doi:10.1111/j.1750-3841.2008.01028.x

Smith AK, Campbell BE (2007) Microstructure of milk components. In: Tamime AY (ed) Structure of dairy products. Blackwell Publishing, Oxford, pp 59–71

Soodam K, Ong L, Powell I, Kentish S, Gras S (2014) The effect of milk protein concentration on the microstructure and textural properties of full fat cheddar cheese during ripening. Food Bioprocess Technol 7(10):2912–2922. doi:10.1007/s11947-014-1342-6

Stokes DJ (2013) Environmental scanning electron microscopy (ESEM): principles and applications to food microstructures. In: Morris VJ, Groves K (eds) Food microstructures: microscopy, measurement and modelling. Woodhead Publishing, Cambridge, pp 3–26

Tamime AY, Hassan A, Farnworth E, Toba T (2007) Structure of fermented milks. In: Tamime AY (ed) Structure of dairy products. Blackwell Publishing, Oxford, pp 134–169

Tamime AY, Saarela M, Korslund Sondergaard K, Mistry VV, Shah NP (2005) Production and maintenance of viability of probiotic micro-organisms in dairy products. In: Tamime AY (ed) Probiotic dairy products. Blackwell Publishing, Oxford, pp 39–72

Torres IC, Amigo Rubio JM, Ipsen R (2012) Using fractal image analysis to characterize microstructure of low-fat stirred yoghurt manufactured with microparticulated whey protein. J Food Eng 109(4):721–729. doi:http://dx.doi.org/10.1016/j.jfoodeng.2011.11.016

Trejo R, Corzo-Martínez M, Wilkinson S, Higginbotham K, Harte FM (2014) Effect of a low temperature step during fermentation on the physico-chemical properties of fat-free yogurt. Int Dairy J 36(1):14–20. doi:http://dx.doi.org/10.1016/j.idairyj.2013.12.003

Trejo R, Dokland T, Jurat-Fuentes J, Harte F (2011) Cryo-transmission electron tomography of native casein micelles from bovine milk. J Dairy Sci 94(12):5770–5775. doi:http://dx.doi.org/10.3168/jds.2011–4368

Tromp RH, van de Velde F, van Riel J, Paques M (2001) Confocal scanning light microscopy (CSLM) on mixtures of gelatine and polysaccharides. Food Res Int 34(10):931–938. doi:http://dx.doi.org/10.1016/S0963-9969(01)00117-X

Tromp RH, Nicolas Y, Van de Velde F, Paques M (2003) Confocal scanning laser microscopy (CSLM) for monitoring food composition. In: Tothill IE (ed) Rapid and on-line instrumentation for food quality assurance. Woodhead Publishing Limited, Cambridge, pp 306–323

Tromp RH, de Kruif CG, van Eijk M, Rolin C (2004) On the mechanism of stabilisation of acidified milk drinks by pectin. Food Hydrocoll 18(4):565–572. doi:http://dx.doi.org/10.1016/j.foodhyd.2003.09.005

Tuinier R, Rolin C, de Kruif CG (2002) Electrosorption of pectin onto casein micelles. Biomacromolecules 3(3):632–638

Walstra P (1995) Physical chemistry of milkfat globules. In: Fox PF (ed) Developments in dairy chemistry. Chapman & Hall, London, pp 131–173

Walstra P, van Dijk HJM, Geurts TJ (1985) The syneresis of curd. 1. General considerations and literature review. Neth Milk Dairy J 39:209–246

Van Buggenhout S, Christiaens S, Moelants K, Ribas-Agusti A, Van Loey A, Hendrickx M (2013) The functionality of plant-based food systems as affected by process-induced changes in cell wall polysaccharides. In: InsideFood Symposium, 9–12 April 2013, Leuven, Belgium

van de Velde F, Weinbreck F, Edelman MW, van der Linden E, Tromp RH (2003) Visualisation of biopolymer mixtures using confocal scanning laser microscopy (CSLM) and covalent labelling techniques. Coll Surf B Biointerfaces 31(1–4):159–168. doi:http://dx.doi.org/10.1016/S0927-7765(03)00135-8

van den Berg L, Rosenberg Y, van Boekel MAJS, Rosenberg M, van de Velde F (2009) Microstructural features of composite whey protein/polysaccharide gels characterized at different length scales. Food Hydrocoll 23(5):1288–1298. doi:http://dx.doi.org/10.1016/j.foodhyd.2008.10.013

van Marle ME, van den Ende D, de Kruif CG, Mellema J (1999) Steady-shear viscosity of stirred yogurts with varying ropiness. J Rheol 43(6):1643–1662. doi:http://dx.doi.org/10.1122/1.551065

Van Vliet T, Lakemond CMM, Visschers RW (2004) Rheology and structure of milk protein gels. Curr Opin Coll Interface Sci 9(5):298–304. doi:10.1016/j.cocis.2004.09.002

van Vliet T, Walstra P (1994) Water in casein gels; how to get it out or keep it in. J Food Eng 22(1–4):75–88. doi:10.1016/0260-8774(94)90026-4

Vargas M, Cháfer M, Albors A, Chiralt A, González-Martínez C (2008) Physicochemical and sensory characteristics of yoghurt produced from mixtures of cows' and goats' milk. Int Dairy J 18(12):1146–1152. doi:http://dx.doi.org/10.1016/j.idairyj.2008.06.007

Willats WG, Orfila C, Limberg G, Buchholt HC, van Alebeek GJ, Voragen AG, Marcus SE, Christensen TM, Mikkelsen JD, Murray BS, Knox JP (2001) Modulation of the degree and pattern of methyl-esterification of pectic homogalacturonan in plant cell walls. Implications for pectin methyl esterase action, matrix properties, and cell adhesion. J Biol Chem 276(22):19404–19413

Yahimi Yazdi S, Corredig M, Dalgleish DG (2014) Studying the structure of β-casein-depleted bovine casein micelles using electron microscopy and fluorescent polyphenols. Food Hydrocoll 42:171–177. doi:http://dx.doi.org/10.1016/j.foodhyd.2014.03.022. (Part 1)

Chapter 5
Kinetics of Bubble Growth in Bread Dough and Crust Formation

Filiz Koksel and Martin G. Scanlon

5.1 The Importance of Gas Production and Gas Retention in Breadmaking

Bread dough is subject to a set of process operations during breadmaking where the rheology of the dough as well as the bubble size distribution are manipulated (Campbell et al. 1998). Therefore, the evaluation of the interactions between the process operations and bubbles is a key criterion in predicting dough performance. Of these process operations in breadmaking, mixing is critical since no new bubbles are entrained during later stages of breadmaking (Baker and Mize 1941). Moreover, dough aeration during mixing and dough rheology are linked (Chin and Campbell 2005a) as both the bubble concentration (Bloksma 1981; Chin et al. 2005; Chin and Campbell 2005a, b) and the bubble size (van Vliet 1999) affect the dough's rheological properties.

Volumetrically, the bubbles which arise either from air captured in the flour (Shimiya and Yano 1988) or from dough aeration during the mixing process (Campbell et al. 1991) represent a significant ingredient of dough and may contribute up to about 20% of the total dough volume at the end of mixing (Whitworth and Alava 1999). In the final baked product, air cells contribute to roughly 70% of the total bread volume. Consequently, dough aeration during mixing and the retention of these air bubbles until the dough matrix is set are crucial for the final character of the bread (Campbell et al. 1998, 2001; Cauvain et al. 1999).

Fermentation is another key operation in breadmaking, where available sugars are metabolized into CO_2 and ethanol by yeast (Chevallier et al. 2012). It has been

F. Koksel (✉) · M. G. Scanlon
University of Manitoba, 260 Ellis Building, 13 Freedman Crescent, Winnipeg, MB R3T 2N2, Canada
e-mail: filizkoksel@gmail.com

M. G. Scanlon
e-mail: Martin.Scanlon@ad.umanitoba.ca

N. Sozer (ed.), *Imaging Technologies and Data Processing for Food Engineers,* Food Engineering Series, DOI 10.1007/978-3-319-24735-9_5

reported that a typical gas production rate for a dough under standard fermentation conditions at 27 °C (2 % compressed yeast) is 25 μmol/s/l of dough (Bloksma 1990a), and it increases as yeast level and temperature are increased (Chiotellis and Campbell 2003a).

Bloksma (1990b) emphasized the uniqueness of the viscoelastic gluten–starch matrix as a cell membrane to stabilize the growing bubbles during fermentation and baking. Even though discontinuities in the gluten–starch matrix begin to appear during dough proving (as early as 15 min of proving), intact bubbles are still observed (Gan et al. 1990). The balance between the extensibility and the strength of the gluten–starch matrix, which depends largely on the gluten proteins, controls the timing and the extent of these discontinuities (Gan et al. 1995). It was proposed that growing bubbles are stabilized against coalescence by a secondary liquid lamella at the gas/liquid interface that is replete with surface-active materials (MacRitchie 1976). The stability of this liquid lamella depends on its composition (Gan et al. 1995; Keller et al. 1997; Mills et al. 2003; Sroan et al. 2009; Sroan and MacRitchie 2009) and how quickly the components at the gas/liquid interface move to the thinner sections of the liquid lamella as bubbles grow (Örnebro et al. 2000; Mills et al. 2003).

Some of the gas produced during fermentation, particularly at the later stages of breadmaking, cannot be retained. During the initial stages of breadmaking, gas diffuses to the exterior surface of the dough and is lost to the surrounding atmosphere as it evaporates at the dough surface. Both of these processes are relatively slow (Gan et al. 1995). Towards the later stages of proving, the rate of gas loss increases sharply owing to coalescence of adjacent bubbles. In order to obtain a high-quality bread with a light texture and an even bread crumb structure, as much gas as possible should be retained during proving and the early stages of baking and released at the later stages of baking (Mills et al. 2003). An illustration of the nature of the interactions of dough aeration and the physical properties of the dough during the breadmaking process is presented in Fig. 5.1.

5.2 Bubble Nucleation and Mixing

The sizes of bubbles and how they are distributed within the dough at the end of mixing are controlled by the interaction of the aeration processes taking place in the mixer (air entrainment, air disentrainment, bubble break-up, and bubble compression) as well as the physical properties of the dough (Martin et al. 2004; Fig. 5.1). Air entrainment and disentrainment mechanisms are relevant when overall gas content (gas volume fraction) of the dough is considered, while bubble break-up and compression mechanisms are relevant when bubble size distribution (BSD) is studied (Campbell and Shah 1999). Physical properties of the dough (e.g., viscosity, consistency), as affected by dough formulation and mixing conditions, influence both the gas volume fraction (Koksel and Scanlon 2012) and the BSD of the dough at the end of mixing (Bellido et al. 2006; Upadhyay et al. 2012; Koksel et al. 2014).

Considering the overall gas content of the dough, Campbell and Shah (1999) showed by means of manipulating the mixer headspace pressure that both

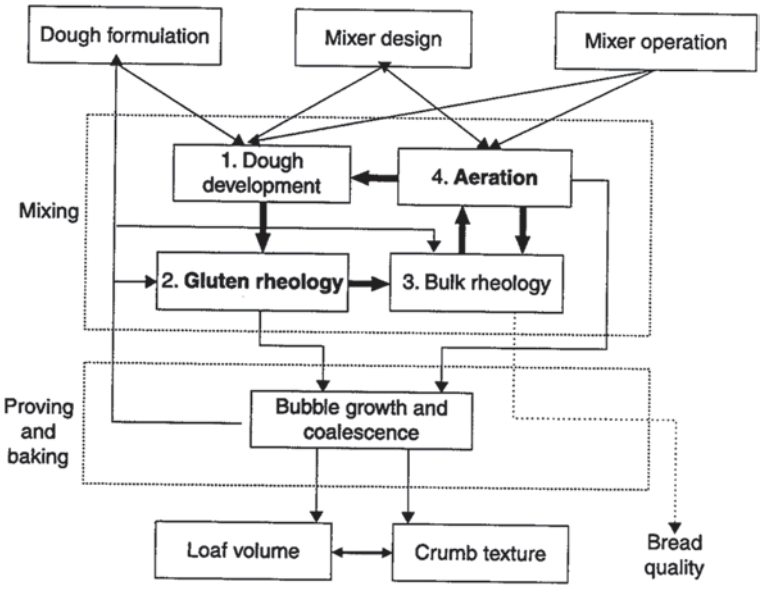

Fig. 5.1 Interactions of dough aeration and physical properties of dough during the breadmaking process. (From Campbell and Martin 2012)

entrainment and disentrainment occur during mixing. Dough aeration was modeled as a mass balance problem, and the overall gas content of the dough was calculated from the balance between air entrainment and disentrainment (Campbell and Shah 1999). Following this model, Chin et al. (2004) studied the effect of direction and size of the headspace pressure change on dough aeration and reported that the disentrainment rate was a function of pressure change direction and its size. Campbell and Shah's (1999) model was later modified by Martin et al. (2004) based on the probability of a particular bubble being entrained, disentrained, and broken-up. A population balance model was found to satisfactorily describe the overall gas volume fraction of the dough despite the simplifications employed, such as negligible bubble break-up and bubble compression (Martin et al. 2004).

The gas volume fraction and/or the BSD of the dough also depend on how mixing conditions interact with the physical properties of the dough (as manipulated by altering dough formulation). Therefore, several studies have investigated the effects of manipulation of single variables on the nature of dough aeration during mixing, such as mixer type (Whitworth and Alava 1999), mixing time (Mehta et al. 2009; Koksel and Scanlon 2012), mixing speed (Chin and Campbell 2005a, b), mixing headspace pressure (Baker and Mize 1937; Elmehdi et al. 2004; Chin and Campbell 2005b), and ingredients (Chin and Campbell 2005a; Bellido et al. 2006; Koksel and Scanlon 2012). For example, Whitworth and Alava (1999) reported that when the same dough formulation is used, the gas volume fraction at the end of mixing varied as much as ~30% with different mixers. When dough formulation was varied, changes up to 21 (Chin and Campbell 2005a) and 13% (Campbell et al. 2001) in total gas volume fraction were reported with different flour types.

The impact of dough rheology, as affected by the mixing conditions and dough formulation, on dough aeration during mixing, that indirectly affect gas retention during the later stages of the breadmaking process, has also been emphasized. For example, an increase in the dough gas volume fraction was reported to increase the failure strain and failure stress as measured using a dough inflation system (Chin et al. 2005), while variation in the gas retention ability of doughs developed with different mixers was observed during proving and baking (Peighambardoust et al. 2010b).

5.3 Kinetics of Bubble Growth in Bread Dough

5.3.1 Overview

In terms of bubble stabilization and gas retention in bread dough, contributions of water (MacRitchie 1976), proteins, and carbohydrates (Bloksma 1990b), lipids, and other surfactant materials (Gan et al. 1990) are relatively better understood compared to the dynamic physical behavior of bubbles and of the gas phase (Chiotellis and Campbell 2003a). For characterization of the dynamic behavior of bread dough, determining BSD and air content as well as understanding disproportionation, strain hardening, and coalescence mechanisms are fundamental (Campbell and Mougeot 1999; van Vliet 2008; Sroan et al. 2009).

At the end of dough mixing, disproportionation starts because a wide range of bubble sizes are entrained into the dough (Shimiya and Nakamura 1997), and gas diffuses from small bubbles to adjacent larger ones due to greater Laplace pressures in the smaller bubbles (Shimiya and Yano 1988; Kokelaar et al. 1996; Shimiya and Nakamura 1997; Murray and Ettelaie 2004). The wide range of bubble sizes in wheat flour doughs has the consequence that smaller bubbles tend to shrink and disappear while the larger ones tend to grow.

During dough expansion, the gluten–starch matrix around bubbles is stretched to large strains, and it gets thinner due to diffusion of CO_2 into the bubbles and by thermal expansion of gases during proving and baking respectively (Mills et al. 2003). If a bubble continues to expand further along these thin regions, it may rupture. However, if the resistance to expansion in a thin region of the gluten–starch matrix is disproportionate to the increase in strain, then the thin region will oppose further strain causing the bubble to grow along thicker regions (van Vliet et al. 1992). This increase in stress with increasing strain that prevents failure of the bubble walls is called strain hardening, and it is vital for obtaining good bread volume (Sroan et al. 2009).

Towards the end of breadmaking, during the later stages of proving and the early stages of baking, coalescence becomes important (Kokelaar et al. 1996). Due to interconnection of adjacent cells, coalescence of bubbles results in loss of gas, and this translates into a decrease in loaf volume and a broad cell size distribution characterized as a coarse bread crumb (van Vliet et al. 1992).

Also at later stages of the breadmaking process, simultaneous heat and mass transfer impact the conversion of bread dough to bread crumb and crust (Besbes et al. 2013). Two significant gradients present at the surface of the loaf are essentially absent in the interior, and these dictate the emergence of a distinct *crust* region: a CO_2 gradient engendered by the CO_2 sink associated with its 35-Pa partial pressure in the atmosphere (Van Dyck et al. 2014) and a moisture gradient associated with the non-saturated water vapor pressure in the proving cabinet (Vanin et al. 2009). The former gradient governs lack of bubble growth at the surface, even when surrounded by actively fermenting yeast cells, since CO_2 will diffuse out into the proving chamber rather than doing work to expand the bubbles. The latter gradient dictates a desiccation of the outer regions of the loaf so that a leathery texture develops, with the rate of growth of the *crust* determined largely by the relative humidity of the proving cabinet and air flow velocity. The enhanced viscosity of the desiccated layer is a further impediment to expansion of bubbles in this region.

5.3.2 Factors Affecting Changes in the Bubble Size Distribution

Understanding how to link dough aeration during mixing to bread quality requires a knowledge of how bubbles in the dough change during proving, since proving is the link between the dough leaving the mixer and the final baked loaf (Shah et al. 1998). The change in bubbles during the later stages of proving and during baking is also critically important to the quality of the bread (Zghal et al. 2001; Schirmer et al. 2011). Shifts in the distribution of the bubbles with time (Bisperink et al. 1992) are controlled by various physical processes, such as disproportionation, bubble growth, and coalescence (van Vliet 1999; Mills et al. 2003).

5.3.2.1 Disproportionation

The pressure difference *(ΔP)* across the surface of a spherical bubble can be defined in terms of the Laplace equation

$$\Delta P = \frac{2\gamma}{R} \tag{5.1}$$

where γ is the surface tension and R is the radius of the bubble (Stevenson 2010). This pressure difference is generated by the surface tension at the bubble surface, which acts to contract the bubble surface (Mills et al. 2003). According to Eq. 5.1, smaller bubbles have a higher gas pressure due to their smaller radii of curvature (Lemlich 1978; Murray et al. 2005). This higher pressure elevates the equilibrium gas concentration around the smaller bubbles (arising from Henry's law), which in turn causes diffusive transport of gas through the aqueous phase of dough from smaller to larger bubbles (van Vliet 1999). In Fig. 5.2, the disappearance of smaller

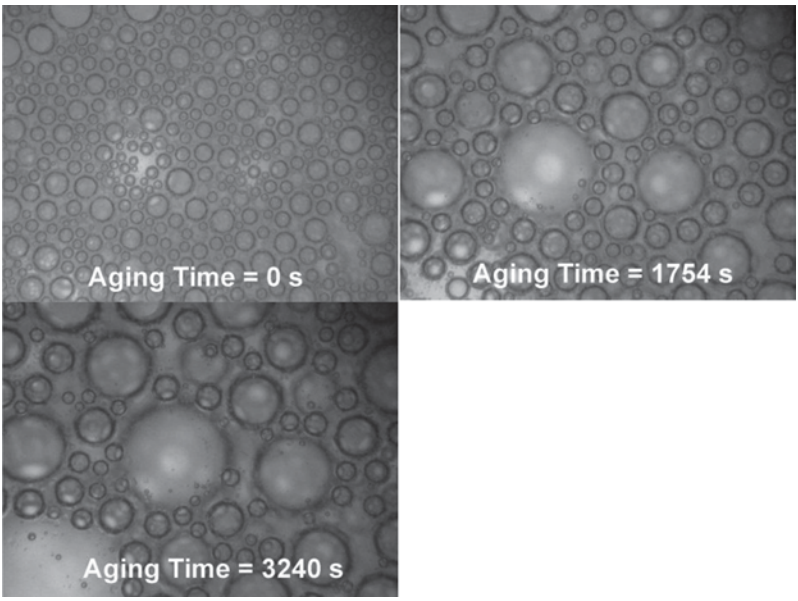

Fig. 5.2 Time evolution of bubbles in a well-mixed whole-egg foam with a gas volume fraction of 68 %. Images (0.7 × 0.52 mm) are obtained using a transmission light microscope. (Reproduced from Spencer et al. 2008)

bubbles at the expense of larger ones as a result of disproportionation is presented for a well-aerated whole-egg foam over the course of 3240s. The mechanism driving bubble growth also occurs in unyeasted doughs but at a much slower rate due to the greater separation between bubbles.

According to some researchers (Gan et al. 1995; Shah et al. 1999), disproportionation is unlikely to occur in yeasted doughs, not only because the CO_2 concentration in the liquid phase of the dough is higher than or equal to that in the bubbles at all times during dough proving, but also because the solubility of N_2 is very low and it is the only available gas at the early stages of proving. On the other hand, several researchers accept that disproportionation occurs in bread doughs (Shimiya and Yano 1988; Kokelaar and Prins 1995; Shimiya and Nakamura 1997; van Vliet 1999). Experimental evidence from Shimiya and Nakamura (1997) for both yeasted and unyeasted doughs showed that disproportionation was a major factor affecting the stability of bubbles and hence their size distributions. In Fig. 5.3, measurements of shrinkage and growth of bubbles in an unyeasted wheat flour dough sample at constant temperature (19 °C) is presented (Shimiya and Yano 1988).

For dough systems, the diameter of the bubbles visible by light microscopy at the onset of fermentation is between 10 and 100 μm, and the surface tension of approximately 40 mN/m is lower than that of pure water (~ 73 mN/m at 20 °C) because of adsorbed materials at the gas/liquid interface (Walstra 1989). As a result, the Laplace pressure difference in the bubbles within dough resides between 1600 and 16,000 Pa (van Vliet et al. 1992). The difference in gas pressures between small

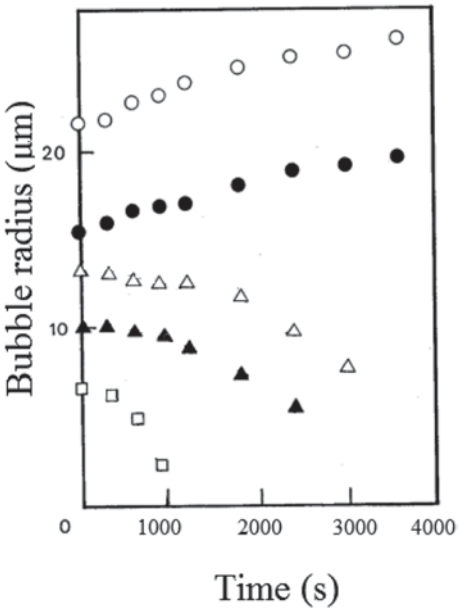

Fig. 5.3 Shrinkage and growth of bubbles in an unyeasted wheat flour dough sample (150–200 μm thick) at constant temperature (19 °C) measured with a microscope. Different symbols represent bubbles of different initial sizes. (Adapted from Shimiya and Yano 1988)

and large bubbles forces gas to diffuse initially into and through the aqueous phase of the dough and then into the larger bubbles, changing the BSD and even changing the number of bubbles if the smaller bubbles shrink to extinction (Lemlich 1978).

In a shrinking bubble, as the gas diffuses out of the bubble, the radius is reduced and the internal pressure increases (Campbell and Mougeot 1999). Thus, shrinkage is self-accelerating if the surface tension is constant, and the film surrounding the bubble has no significant surface viscoelasticity (Murray et al. 2005). However, for dough systems, where a number of surface-active materials compete at the gas/liquid interface, surface tension is not constant with respect to a change in bubble radius (Kokelaar and Prins 1995). As a result, disproportionation in bread doughs is not just an issue of simple gas diffusion between bubbles, since bubbles resist mechanical contraction/growth (Stevenson 2010). The gas diffusion rate and thus the rate of disproportionation depends on many factors, such as the range of bubble sizes, the degree of saturation of the aqueous phase of dough (Mills et al. 2003), and the adsorption and desorption speeds of surface-active materials at the gas/liquid interface during increases and decreases of the surface area, respectively (van Vliet et al. 1992).

According to van Vliet et al. (1992), disproportionation in dough slows down when its driving force reduces considerably, which happens once the small bubbles disappear or stabilize. Murray et al. (2005) investigated disproportionation kinetics of isolated air bubbles in food protein solutions so as to shed light on the key question of whether or not various food proteins adsorbed at the gas/liquid interface significantly reduce the rate of disproportionation or indeed prevent it. They concluded that air bubbles in their system shrank sufficiently slowly that the protein

films at the gas/liquid interface were able to rearrange themselves as the bubble surface area decreased. In doing so, protein films maintained a constant concentration on the surface as the protein desorbed into the bulk of the solution. With time, in a shrinking bubble they observed that all the protein at the interface gradually dissolved into the bulk solution, but the rates of desorption and dissolution depended on protein type. Mun and McClements (2006) confirmed for oil-in-water emulsions that disproportionation can be altered: Creating thicker and more elastic membranes provided mechanical resistance to shrinkage or growth and so slowed disproportionation. These studies showed that disproportionation can be retarded by manipulating the components or properties of the gas/liquid interface, although in none of these studies was disproportionation prevented completely.

As stated by van Vliet et al. (1992), the response of the surface tension during shrinkage can be expressed by the surface dilational modulus E_s:

$$E_s = \frac{d\gamma}{d \ln A} \tag{5.2}$$

where A is the surface area of the bubble. If E_s is greater than zero, shrinkage of the bubble is slowed down, and if $E_s \geq \gamma/2$, disproportionation stops (Walstra 1989). After considerable shrinkage, the remaining surface-active materials do not desorb from the surface, and E_s becomes greater than or equal to $\gamma/2$ for very small bubbles (van Vliet et al. 1992). However, except for the smallest bubbles, $E_s < \gamma/2$, and consequently this mechanism would not stop disproportionation in dough completely (van Vliet 1999).

5.3.2.2 Bubble Growth

When bubble growth during dough proving is described, the rate of CO_2 production by yeast, the degree of CO_2 retention within the dough piece, the rate of CO_2 diffusion from the liquid phase of the dough into the bubble nuclei, and the rate of bubble coalescence need to be considered (Shah et al. 1998). Two different approaches for investigating bubble growth can be seen in the literature. In one of these approaches, the rheological properties of the medium that surrounds the bubble are deemed important since the forces exerted by the expanding bubbles deform the dough matrix during fermentation. Hence, a better understanding of the extensional properties of the dough matrix would permit better control of dough fermentation and thus better-quality baked products (Lee et al. 2004). In this approach, the driving force for bubble growth is the pressure difference between the bubble and the surrounding medium (Huang and Kokini 1999). The second approach focuses on diffusion-controlled bubble growth where the rheological properties of the medium are neglected, and the rate of bubble growth is governed by the transfer of gas species across the bubble interface (Shah et al. 1998, 1999; Chiotellis and Campbell 2003a, b). In the middle of these two approaches, diffusion-induced bubble growth models, which are challenging to apply to real dough systems, take the viscoelastic

properties of the medium that surrounds the bubbles, bubble interactions, and the mass transfer across the bubble interface into account (Venerus et al. 1998; Chiotellis and Campbell 2003b).

Fermentation and CO_2 Transport in Fermenting Dough

According to Huang and Kokini (1999), bubble expansion in wheat flour dough can be modeled by considering biaxial extensional flow of dough around a bubble. By developing a bubble growth model to predict dough expansion, the biaxial extensional rheological properties of dough can be linked to the overall dough proving process. With this bubble growth model, Huang and Kokini (1999) used a circumferential stress equation where the viscous resistance of the dough was the only factor balancing the pressure increase in the bubble. The model predicted dough volume expansion reasonably well at early times of proving. However, as the proving time increased, the predictions of dough volume were larger than what was observed from dough height measurements. Huang and Kokini (1999) pointed out that strain hardening of the dough, which was not considered in their model, could be an important factor affecting bubble growth.

Grenier et al. (2010) investigated the contributions of surface tension and dough viscosity to gas pressure in bubbles and emphasized the importance of surface tension in determining bubble sizes when bubble expansion is slow, as in during dough proving. They studied two different water content conditions and showed that surface tension was critically important in modeling dough expansion at earlier stages of proving especially when the water content of the doughs was relatively high (0.45 kg kg^{-1}). When the water content was lower ($\leq$0.42 kg kg^{-1}), dough viscosity had a greater impact on the rate of dough expansion during proving compared to that of surface tension.

Shah et al. (1998) viewed the rate of CO_2 diffusion from the dough liquid phase into the bubble nuclei entrained into the dough during mixing as a classical mass transfer problem. They applied diffusion theory to predict the slow growth of a bubble at early stages of proving. Initially the CO_2 concentration in the bubble nuclei was taken to be zero so that a concentration gradient exists to act as driving force for CO_2 diffusion into the bubbles, resulting in bubble expansion. In this model, surface tension played a role in bubble expansion whereas dough rheology was not thought to influence bubble expansion significantly, in contrast to Huang and Kokini's (1999) model. According to Shah et al. (1998), when the dough is subsaturated, which according to them is the more realistic case for real dough systems at least for the first half of proving, all bubbles grow and eventually reach an upper limit where the final bubble size is approximately proportional to its initial size.

Shah et al. (1999), who studied the bubble growth throughout a dough piece that was allowed to expand only in one direction, improved Shah et al.'s (1998) model by extending the model to bring in the rates of CO_2 production and diffusion. They modeled the dough piece as a series of slices and solved a mass balance equation for CO_2 in the aqueous phase in a slice of dough. According to their model, the

mass of CO_2 accumulating in the aqueous dough phase is a total of the mass entering the slice by diffusion plus the mass generated by yeast minus the mass leaving the slice by diffusion minus the mass coming out of solution into the bubbles. The overall diffusion gradient is the reduction in CO_2 concentration in the top slice due to its exposure to the atmosphere. Shah et al. (1999) also reported that bubble sizes will keep increasing indefinitely during proving when the dough aqueous phase is saturated with CO_2, but pointed out that such a model overestimates bubble sizes compared to what is observed experimentally.

Chiotellis and Campbell (2003b) incorporated the initial BSD as well as proving temperature and yeast concentration into Shah et al.'s (1999) model and addressed several of the shortcomings of the previous models. According to their model, the mean bubble diameter increased during proving, and the bubbles grew at approximately similar rates. Chiotellis and Campbell (2003b) concluded that further improvements, including incorporation of dough rheology and bubble coalescence as well as evaluations of model predictions against experimental results, were needed for better predictions of bubble growth.

Chiotellis and Campbell (2003a) investigated the various factors affecting gas production and retention during proving and compared their results to the model developed by Chiotellis and Campbell (2003b). Decreasing the headspace pressure during mixing resulted in a small initial mass transfer rate due to a fewer number of bubbles entrained into the dough and thus a smaller interfacial area for mass transfer (Chiotellis and Campbell 2003a). The initial small mass transfer rate was followed by an increased mass transfer rate at later stages of proving due to a rapid increase in CO_2 in the aqueous phase of the dough, creating a large concentration gradient for mass transfer. Both of these observations were in agreement with the predictions of the model of Chiotellis and Campbell (2003b).

Strain Hardening and Gas Cell Expansion Rates

During proving, as the bubbles expand, the resistance to further deformation of the gluten–starch matrix at thinner regions increases due to strain hardening (Sroan et al. 2009; Campbell and Martin 2012). For a dough film, strain hardening occurs when the relative increase in stress ($d \ln \sigma$) is at least twice as large as the increase in the biaxial strain ($d\varepsilon_B$) (van Vliet et al. 1992; Kokelaar et al. 1996).

The stability of the dough film during gas expansion can be explained by the balance between resistance to extension and strength of the gluten proteins (Singh and MacRitchie 2001). Gluten's branched and entangled structure is expected to significantly contribute to bubble stability and resistance to extension during breadmaking (Dobraszczyk 2004). To ensure that bubbles do not undergo coalescence and lose gas too early in the breadmaking process, the dough needs to be sufficiently strong to resist rupture as well as extensible enough to stretch as a result of gas pressure increase (Sroan et al. 2009). For high molecular weight branched polymers, such as gluten, the strain hardening is believed to depend on the balance between entanglement of gluten branches with surrounding branches and stretching

of the flexible high molecular weight backbone between the entanglements. The expanding dough film resists rupture by increasing resistance to extension locally at the thinner regions, with the thinner regions stabilized against unstable necking and premature failure during large extensions (Dobraszczyk 2004).

5.3.2.3 Coalescence

During the later stages of proving and the early stages of baking, bubbles expand at a relatively faster rate as a result of both increased CO_2 by the yeast and release of water vapor from the matrix due to high temperature (Mills et al. 2003). At these stages, the dough is converted into a foam with polyhedral bubbles where flat films develop between bubbles and coalescence becomes important (Kokelaar et al. 1996). These flat films separating two bubbles are stabilized by repulsive forces (due to steric and electrostatic forces) counteracted by attractive van der Waals forces between them (Walstra 1989; Örnebro et al. 2000). As the liquid films get thinner and thinner with bubble growth, a critical distance is eventually reached when any small perturbation, such as a draught or a thermal disturbance, can cause the film to rupture because the balance between the attractive and repulsive forces is lost (Örnebro et al. 2000).

Babin et al. (2006) studied bubble growth during dough fermentation and baking processes using X-ray microtomography where bubble growth was visualized at various times during proving and baking. They reported that a few minutes after kneading, the dough has many small bubbles, and the bubbles grow freely leading to a smooth increase in the bubble size. Their 2D cross-sectional images obtained using synchrotron radiation demonstrating the evolution of the bubbles in bread dough during proving is presented in Fig. 5.4.

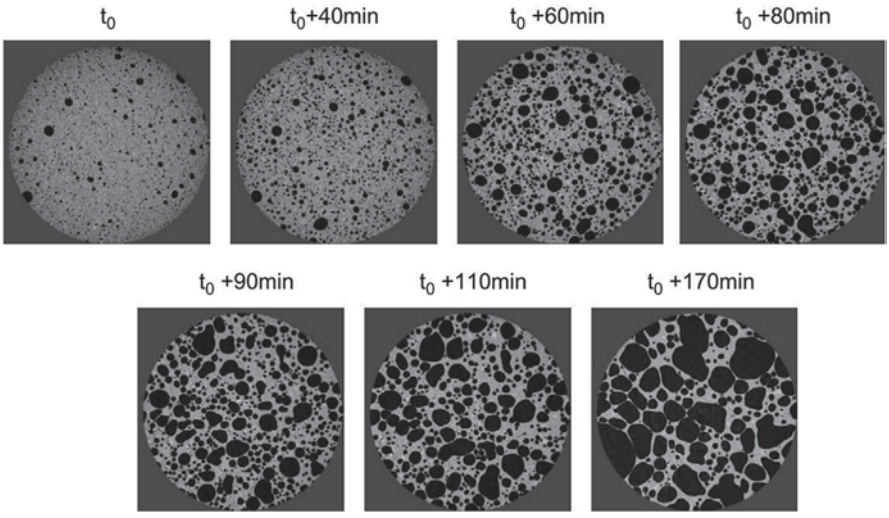

Fig. 5.4 Evolution of bubbles in bread dough during fermentation investigated by synchrotron-generated X-ray radiation; t_0 is a few minutes after kneading. (Adapted from Babin et al. 2006)

The free growth of bubbles at early stages of fermentation was also confirmed by Romano et al. (2013). In the second stage of fermentation, the dough structure becomes heterogeneous with many large bubbles due to bubble growth and coalescence (Babin et al. 2006). In the third stage, coalescence prevails over bubble growth, and the dough structure becomes more heterogeneous with large, nonspherical-shaped gas holes (second row of Fig. 5.4). Coalescence is affected by the properties of the adsorbed materials on the surface of the bubbles as well as the properties of the bulk liquid (Örnebro et al. 2000). It has been shown that the extent of coalescence can be lowered by using surface-active materials which aid in bubble stabilization during expansion (Kokelaar and Prins 1995).

5.3.2.4 Densification at the Crust

In the conclusion to their review on crust formation, Vanin et al. (2009) posed the question "can a definition of the crust region be proposed?" An equally relevant question is, when does the crust start forming? The review of Vanin et al. (2009) focused exclusively on baking, thereby neglecting the development of the crust that occurs prior to baking. This is likely an oversight, given the mechanisms at play (Sect. 5.3.1) and the research conducted to date. However, morphological investigations of the emergence of the distinct *crust* region during proving are few (see Sect. 5.6.4).

The primary focus for imaging evaluations of crust setting and its differentiation from the crumb region of the loaf has been those taking place during the baking process itself. Substantial changes in the mechanical properties and the color of the crust arise when the loaf is placed in the oven (Altamirano-Fortoul et al. 2012), and the difference in bubble structure between crust and crumb that is initiated during proving becomes even more pronounced (Tromp et al. 2008; Altamirano-Fortoul et al. 2012). In their review of crust formation, Vanin et al. (2009) covered the various processes that contributed to the formation of crust structure and how crust setting influenced structure formation in the crumb (and thus an effect on the overall quality of the loaf).

The rigidification of the crust that arises from the change in its mechanical properties during baking affects crumb structure because of the constraints that it imposes on additional bubble expansion in the dough that forms the crumb. Using an electrical resistance oven (where crust formation does not occur, but crumb setting does), Hayman et al. (1998a) showed that poor breadmaking flours were able to produce good crumb structure, which they were unable to do by conventional baking. From this study, the authors concluded that the crust contributed to an increased pressure within the gas bubbles so that bubble coalescence was enhanced in dough made from poor-quality flour. Such uniform pressure increases were not evident when Wagner et al. (2008) conducted detailed magnetic resonance imaging (MRI) investigations of the dough to crumb transition. Instead, they saw that after the crust had set, crust constraint caused local regions of crumb collapse as other regions of the dough continued to expand. Commending the insights gained from such studies, Vanin et al. (2009) advocated the use of quantitative nondestructive imaging techniques for studying structural changes in both crumb and crust.

5.4 Modeling Formation of Cellular Structure

Modeling breadmaking and quantification of the cellular structure of bread are challenging due to the complexity of the heat and mass transfer operations that take place during baking of this soft solid as well as the changes in the medium (i.e., temperature, moisture, and time dependence) in which these operations are taking place (Hussein and Becker 2010). The benefit of accurate quantification of structure using nondestructive techniques, such as MRI and X-ray tomography, and even destructive analyses of the finished product using image analysis, is that the structural data can be used to build high-quality structure-properties models (Falcone et al. 2005; Wang et al. 2013). Two approaches are primarily undertaken: analytical and numerical. The first approach is where one or more structural parameters are defined, for example, average crumb cell size, and these are used with material properties and an appropriate model to predict overall mechanical properties of the product (Zghal et al. 2002). The second approach is where more sophisticated numerical models, capable of exploiting the large amount of structural data put out by these techniques, more precisely predict the particular physical property of the bread of interest. For example, the properties of interest should be derived from larger strains if texture assessments are to be applicable to real mastication processes (Guessasma et al. 2011), while crumb permeability predictions (Chaunier et al. 2008) are important for gaining insights on the foam to sponge transition that occurs during baking.

5.4.1 Analytical Models

Early work relating image analysis quantification of crumb structure to density and mechanical properties was carried out by Zghal et al. (1999) and Scanlon and Zghal (2001), respectively. This work followed on from earlier studies on brittle cellular solids relating parameters such as elastic modulus and fracture strength (Hutchinson et al. 1987; Warburton et al. 1990) to structure using the relative density scaling arguments of Gibson and Ashby (1988). In these models, a mechanical parameter, M^* (that is related to one or more important quality parameters), scales according to the crumb's relative density (ρ^*/ρ_s):

$$M^* = M_s \left(\frac{\rho^*}{\rho_s} \right)^p \tag{5.3}$$

where p is the scaling parameter, and ρ_s and M_s are the density and the mechanical parameter of the material constituting the crumb cell walls, respectively. Using X-ray tomography from a synchrotron radiation source, but conducted dynamically during loaf proving, Babin et al. (2005) were able to calculate crumb density and show how bread crumb properties scaled according to Gibson and Ashby theory. Based on the scaling exponent from their structure-properties theoretical model, bread crumb would be characterized as an open cell foam. They were also able to

use data on dough structure during proving to predict relative density, thereby giving predictive capacity to texture evaluation based on structure quantification, and how it would be affected by changes in formulation.

Zghal et al. (2002) showed how expected changes in crumb morphology brought about by strain hardening during processing altered the density scaling relationship and that parameters derived from the model compared reasonably well with those obtained from biaxial extension measurements on dough. In this work, and that of others examining the suitability of these analytical models, the structure was defined by an average cell size or with the additional structural parameter, average cell wall thickness. Babin et al. (2005) tackled the more realistic situation for bread-making where homogeneous average values do not exist and instead a distribution of bubble sizes is evident. The group later analyzed how structural heterogeneity would affect predictions of the mechanical properties in brittle extrudates (Babin et al. 2007), a result of direct relevance to consumer appreciation of bread crust's sensory crispness (Van Vliet and Primo-Martín 2011).

As with other studies conducted by the French National Institute for Agricultural Research (INRA) group at Nantes (Babin et al. 2005, 2006; Turbin-Orger et al. 2012) and Falcone's group at Trieste (Falcone et al. 2004, 2005), synchrotron X-ray radiation was used to quantify cell distributions in three dimensions. Both sets of researchers showed that structural heterogeneity should not be neglected in predictions of crumb properties since it influenced mechanical properties at an equivalent relative density.

A different analytical model was used by Meinders and van Vliet (2008) to evaluate how sound intensity in bread rolls scaled with work to fracture using a model for earthquake *crackling events*. The model's applicability to brittle crusts was deemed appropriate for both applications, with the authors' interest being its utility for understanding crispness perception in the rolls. Their modeling showed that even though relative density was controlled, the crust's structural heterogeneity as well as its humidity were confounding effects in the model's capacity to predict how crispness depended on the work to fracture.

5.4.2 Numerical Models

The capacity to generate large amounts of structural data puts pressure on modelers to utilize more sophisticated models for better prediction of the physical properties of crust and crumb (Guessasma et al. 2008), particularly when the heterogeneity of the crust and crumb is a significant determinant of properties (Falcone et al. 2005; Babin et al. 2005). Finite element models are especially suited for potentially mapping an element of the crumb or crust cell wall to each voxel defined by techniques such as X-ray tomography and MRI (should processing power permit!).

An early application of finite element modeling (Liu and Scanlon 2003) was to understand how measurements from the American Association of Cereal Chemists (AACC) standard bread texture test (AACC International 1983), which are conducted

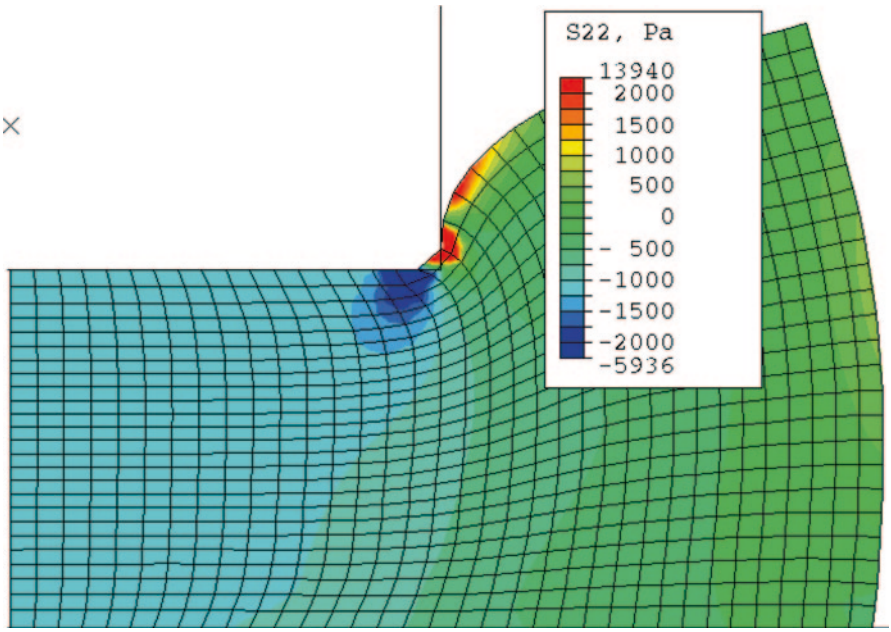

Fig. 5.5 Finite element predictions of principal stress contours for a cylindrical indenter indenting 10 mm into a *bread crumb* sample (diameter = 70 mm) whose Poisson's ratio was defined as 0.21. (Derived from Liu and Scanlon 2003)

at large strain, relate to standard assessments of crumb's mechanical properties under compression. In Fig. 5.5, finite element predictions of the principal stress contours for a 36-mm-diameter cylindrical indenter indenting 10 mm into a model bread crumb sample (diameter = 70 mm) is presented. Because indenter and sample sizes were large compared to crumb cell size, detailed structural information was not part of the modeling process of Liu and Scanlon (2003), and a standard mechanical model applicable at large strains was used to characterize the properties of the bread crumb as a whole. Despite the lack of specific microstructural information, load-displacement curves for the AACC test were well predicted from parameters derived from uniaxial compression tests used to calibrate the mechanical model.

In a fairly recent overview of the subject, Guessasma et al. (2011) justified the benefits of mechanical modeling of solid cereal products such as bread. Much emphasis was placed on how structural quantification provided the bedrock for good mechanical modeling of the crumb, a point endorsed by Wang et al. (2013) in their digital representation of bread crumb. With the proliferation of friendlier user interfaces and faster computational speeds (Gonzalez-Gutierrez and Scanlon 2012), finite element models will prove their worth for complementing microstructural information generated by a range of nondestructive structural characterization tools. Expected outcomes are that macroscopic mechanical relations can be predicted (Babin et al. 2005), that we can better understand how quality is affected by events during processing (Purlis 2012; Mack et al. 2013), and particularly so that we can

better understand the nucleation, growth, and transformation of bubbles (Babin et al. 2006; Wang et al. 2013) that are the basis for much of the quality of bread (Scanlon and Zghal 2001).

5.5 Methods Used to Investigate the Evolution of Cellular Structure of Crumb and Crust

In order to provide a reliable connection between the various process operations and final product characteristics, high-quality, and preferentially 3D, data need to be acquired (Clarke and Eberhardt 2002). High-quality data can be obtained by probing materials with waves (electromagnetic or mechanical), where the features of the material are determined by changes in the properties of the waves as a result of their transmission through or reflection from the material (Clarke and Eberhardt 2002).

5.5.1 Microscopy

Microscopy techniques make use of three fundamental components: an illumination source (beam of visible light in light microscopy, beam of electrons in electron microscopy, a laser beam for confocal laser scanning microscopy; CLSM), a system for focusing this source onto the sample being tested, and a means of generating images so that the information can be stored (Falcone et al. 2006). The images that the information is stored in are then used for extracting the spatial representations of the features of interest within the images (Gunasekaran 1996).

The resolution of a digital image can be expressed in terms of the number of individual picture elements (pixels) that are used to represent a unit area. Each pixel of a digital image has an intensity value that stores the number of brightness steps used in the image. This is termed as the color depth and is quoted in bits, for example, each pixel in a 4-bit image has 2^4 (=16) possible different brightness steps (gray levels), and the range of possible values are termed as the dynamic range of the image. The dynamic range of an image may be altered once the image is processed, for example, by histogram manipulation or filtering with the aim of decreasing image noise or increasing the prominence of a particular characteristic of interest (Clarke and Eberhardt 2002). Characteristics of interest can then be identified and their boundaries recognized. With binary images, this identification is performed through application of a threshold value and assigning values of either 1 or 0 to regions of interest and those not of interest to the user, respectively, for example, dough matrix and bubbles. The next step is characterization and classification of the features of interest (Clarke and Eberhardt 2002), for example, size, circularity, orientation, etc. Finally, a means of extracting statistically unbiased conclusions from the data is accomplished by techniques such as stereology (Bisperink et al. 1992; Sahagian and Proussevitch 1998).

Despite the usefulness of the stereological reconstruction techniques for characterizing BSDs in dough, the validity of the results obtained from these bubble data is still questionable since steps such as dough freezing, serial sectioning, or squashing are used during dough preparation. For example, Elmehdi et al. (2003a) reported an 8 % volume reduction of their bread crumb samples due to freeze drying. Therefore, in order to unambiguously evaluate the BSDs in the dough, techniques that require no additional treatment steps and are capable of nondestructively probing the bubble sizes in situ are desirable.

The earliest study where the bubbly structure of bread dough was reported utilized a transmission light microscope (Carlson and Bohlin 1978). In transmission light microscopy, the light from the illumination source is transmitted through the material being tested, and the part of the light that is not absorbed or scattered by the material is sent into the lens (Clarke and Eberhardt 2002). Carlson and Bohlin (1978) measured the cross-sections of bubbles in photographs of 30-μm slices of dough obtained by microtomy, converted these cross sections into bubble diameters, and fitted a one-parameter analytical function with only a scale parameter (mean bubble diameter) to describe the bubble distribution. Due to resolution limitations in the technique they used, measurement of bubble cross-sections corresponding to a diameter of less than 90 μm was not possible, and the mean bubble diameter reported was 112 μm.

A method with better resolution and accuracy for measurement of bubble diameter in doughs was developed by Campbell et al. (1991). They also used a transmission light microscope to examine circles on slices of frozen dough and utilized a stereological technique to reconstruct the BSDs that nucleated in two types of mixers. In their technique, the slice thickness and the maximum resolution were 30 and 39 μm, respectively. They analyzed at least 20 slices with 80× magnification, measured cross-sections of diameter between 25 and 500 μm, and characterized the BSD by two empirical parameters: the arithmetic mean bubble size and the standard deviation. For doughs mixed in a food processor and a Tweedy 10 mixer, they reported mean bubble diameters of 71 and 89 μm, respectively and standard deviations, which they defined as the spread of bubble sizes within the distribution, of 24 and 47 μm, respectively.

Shimiya and Nakamura (1997) utilized reflection light microscopy (an optical microscope of 100× magnification and a stereomicroscope of 50× and 4× magnifications), with a better resolution (3 μm) compared to previous studies, in order to measure the changes in BSD in unyeasted doughs. In optical reflection microscopy, the reflection coefficients (and hence refractive indices) of the components of the sample are critically important since the greater the difference between the reflection coefficients, the greater the image contrast (Clarke and Eberhardt 2002). Therefore, sample surface preparation, thus sectioning and surface polishing, significantly impact the resulting image quality (Clarke and Eberhardt 2002). In their technique, Shimiya and Nakamura (1997) excised a dough subsample immediately after mixing and squashed it between two pieces of glass and then observed it under a microscope. The soft nature of unfrozen dough therefore did not permit image enhancement by surface preparation. A median bubble diameter of 15 μm at the

end of mixing grew up to 35 μm as a result of disproportionation during 100 min of resting of the dough (Shimiya and Nakamura 1997). Their BSD was characterized as lognormal, and the width of 0.18 only changed slightly during resting. However, in their technique, the thickness of the dough subsample under the microscope was at least 150 μm, which resulted in a smaller number of bubbles being analyzed. For yeasted doughs, the total cross-sectional circle areas (m^2/m^2) on microphotographs were approximately three times larger than those of unyeasted doughs. They reported that the number and cross-sectional area of bubbles smaller than 50 μm decreased, and the number and cross-sectional area of bubbles larger than 100 μm increased. As fermentation progressed, a small number of bubbles that constituted the larger sized bubbles of the BSD grew substantially, while the median bubble diameter of 15 μm at the end of mixing did not change very much (grew up to 16 μm) following 100 min of fermentation. After baking, the air cell diameters were in the range of 0.1–5 mm. According to the authors, this range of bubble sizes indicated that bubble sizes smaller than a critical size did not grow, that is, smaller bubbles dissolved in the liquid phase of the dough, and the dissolved gas was preferentially delivered to the larger bubbles.

Another technique that has been used for investigation of dough and bread structure is scanning electron microscopy (SEM; Junge et al. 1981; Hayman et al. 1998b; Whitworth and Alava 1999; Esselink et al. 2003; Hirte et al. 2012a). SEM is a microscopy technique that requires lengthy sample preparation so that samples conduct electrons and the analysis can be carried out under vacuum (Esselink et al. 2003; Peighambardoust et al. 2010a). Just as light is focused in an optical microscope by an optical lens, an electron beam is focused in an electron microscope by appropriate use of electric and magnetic fields.

Hayman et al. (1998b), who studied bread crumb development throughout the breadmaking process by SEM, reported that no difference in dough microstructure was observed during mixing, punching, panning, or proving for doughs made from two different flours. Their images, representative of dough microstructure following mixing, are presented in Fig. 5.6a and b. Hayman et al. (1998b) concluded that changes in microstructures of doughs made from these two flours were only observed during the early stages of baking. In contrast, Létang et al. (1999), who used an environmental SEM (an SEM technique where desiccation of the sample is not necessary; Falcone et al. 2006), reported that the microscopic structure of the dough is affected by differences in ingredient concentrations as early as the mixing process. They manipulated the water content of doughs but mixed for the same time and concluded that dough morphology at the end of mixing differed depending on dough water content. SEM images of dough of low- and high water content (50% and 56% water on a flour weight basis) from their study are presented in Fig. 5.6c and d, respectively.

Whitworth and Alava (1999) measured bubble sizes using different imaging techniques: optical microscopy (for measuring bubble sizes in the range of 20–1500 μm), SEM (for bubble sizes in the range of 50–3500 μm), and X-ray tomography (for bubble sizes larger than 1 mm). With these different imaging techniques, Whitworth and Alava (1999) observed a wide range of bubble sizes during different

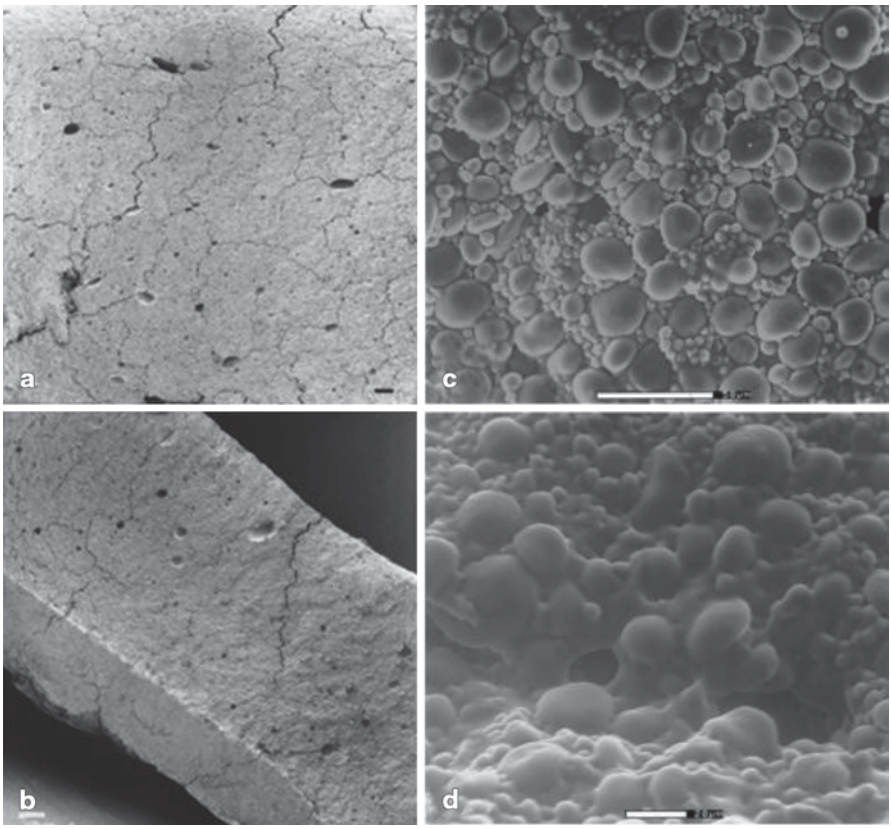

Fig. 5.6 **a**, **b** Dough microstructures of two different types of flour that produce "bread of similar loaf volume but different crumb grain when baked," from Hayman et al. (1998b), bar = 200 mm. Microstructure of doughs of **c** low water content, bar = 50 μm, and **d** high water content, bar = 20 μm, from Létang et al. (1999)

stages of the breadmaking process. In their technique, doughs were frozen and cut into thin sections before they were mounted on the appropriate imaging equipment. The image analysis and reconstruction of bubble sizes from circles on slices were performed based on the method of Campbell et al. (1991). They found that their mechanically developed doughs typically contained bubbles with a maximum diameter of 0.8–2.5 mm at the end of mixing, and the total gas volume fraction was about 5–8 %. After first molding, they reported an increase in the number of bubbles, while during intermediate proof they reported doubling of the maximum bubble diameter and total gas volume fraction.

Another technique that has been used for investigation of dough and bread structure is CLSM. The light source in CSLM is a highly narrow, coherent beam of electromagnetic radiation. CLSM's working principle is that the laser beam is focused on the sample resulting in illumination of one spot at a time, as opposed to uniform illumination in light microscopy techniques (Falcone et al. 2006). The laser beam

excites fluorescent dyes that selectively bind to different components of the sample (Hermansson et al. 2000). These components are detected using dyes with specific fluorescence wavelengths and by manipulating the wavelength of the incident laser (Upadhyay et al. 2012). The light reflected from the spot in focus passes through a pinhole to be detected by a light detector. Passing through the pinhole, light outside of the focal plane is eliminated, and background noise is reduced (Bosch et al. 2012). The sample is scanned spot by spot on one focal plane, and a 2D image is generated. By choosing different focal planes, information about different depths can be obtained, and 3D images, where the image resolution is a function of the pinhole gap, can be reconstructed (Ferrando and Spiess 2000).

CLSM has been successfully utilized in studies of the changes in dough microstructure during mixing (Peighambardoust et al. 2010a) and mechanical treatment (Boitte et al. 2013). It has also been used to study the effects of changes in sodium chloride concentration (Lynch et al. 2009), water and yeast concentration (Upadhyay et al. 2012) on dough microstructure, as well as the changes in the cellular structure of bread crumb (Deshlahra et al. 2009). Typical CLSM images of dough with different amounts of yeast (2 and 10 %) at a fixed water content from the study of Upadhyay et al. (2012) are presented in Fig. 5.7a and b. From these 2D CLSM images, Upadhyay et al. (2012) extracted the distributions of bubble diameters (Fig. 5.7c and d). However, a disadvantage of CLSM is that sample preparation, that is, stretching of the sample, or moisture loss during diffusion of the labeling dye may induce artifacts that distort image information parameters (Yusoff and Murray 2011; Boitte et al. 2013).

5.5.2 Magnetic Resonance Imaging

MRI is an imaging technique that is suitable for coping with soft fragile materials nondestructively (Takano et al. 2002; Esselink et al. 2003; Grenier et al. 2003; Rouille et al. 2005). Magnetic resonance images can be generated by using broadband radio frequency pulses that excite the nuclear spins of hydrogen nuclei when exposed to a strong magnetic field and then detecting the emitted radio frequency photons (Clarke and Eberhardt 2002; Falcone et al. 2006). MRI is widely used for medical diagnosis and makes use of differences in mobility of protons in the components that constitute a material in order to depict the internal structure of a material (Takano et al. 2002; Rouille et al. 2005).

Using MRI, Takano et al. (2002) followed the bubble growth, gluten development, and crumb grain network formation during the fermentation of bread dough as affected by freezing and thawing operations. They found that MRI was able to differentiate between the bread made from fresh and frozen dough, but they did not communicate BSDs for either the dough or for the bread. Rouille et al. (2005) studied bubble growth in bread dough during proving by MRI; however, their spatial resolution was not high enough to estimate the sizes of bubble nuclei even at 25 min after the end of mixing. To obviate bubble resolution limitations of their MRI techniques, Wagner et al. (2008) used layers of 0.5-mm-sized microcapsules in

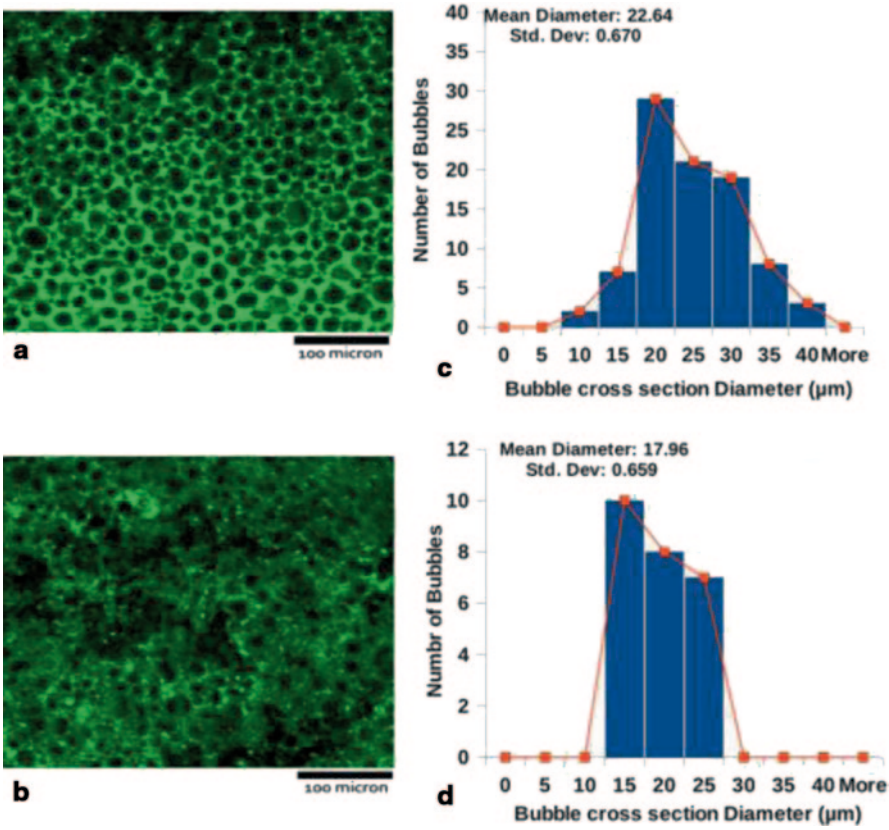

Fig. 5.7 Confocal laser scanning microscopy (CLSM) images of a dough sample containing **a** 2 and **b** 10% (on a flour weight basis) yeast at a constant water content (60%) and their respective bubble cross-section distributions (**c** and **d**). (Adapted from Upadhyay et al. 2012)

their analysis of bubble structure changes during baking. This permitted the authors to evaluate how crumb structure was affected by crust setting.

One of the first attempts to utilize quantitative MRI combined with image analysis was by van Duynhoven et al. (2003) who studied bubble development in bread dough during proving. In their 2D MRI technique, they reported circle distributions from dough cross-sections (real 3D bubble distributions were not reconstructed in this study). The authors evaluated bubble size changes with proving time as affected by kneading temperature and the magnitude of mechanical damage during molding. They reported that changes in both the kneading temperature and the magnitude of the deformation during molding affected the BSD, and these effects were detected by MRI.

De Guio et al. (2009) studied the bubble sizes in unyeasted and yeasted bread doughs during proving using MRI and reported that the estimated bubble sizes in unyeasted bread dough were represented by a normal distribution function. After

20 min of dough proving for yeasted doughs, BSDs were still described by normal distribution functions but with larger mean diameters as time progressed, consistent with the growth of bubbles due to the activity of yeast during fermentation. They concluded that their method overestimated the bubble sizes since small bubbles could not be discriminated. Bajd and Serša (2011) continuously monitored dough fermentation and bread baking by MRI and used image analysis to show that the increase in both the number of bubbles and the dough volume was slow at the beginning of fermentation, gradually increased but slowed down again at later stages of fermentation. No information on the BSD at the end of mixing was communicated in their study.

MRI has proven to be a powerful technique for studying bread dough and monitoring bubble expansion during proving; however, one of the disadvantages of MRI is its trade-off between spatial resolution (image quality) and temporal resolution, that is, it takes a long time to generate a high-quality image since data collection times are quite long (Clarke and Eberhardt 2002; Rouille et al. 2005). Moreover, magnetic susceptibility effects, such as distortions in images induced by magnetic field inhomogeneities, are undesirable and need to be corrected during post-processing of the data (De Guio et al. 2009).

5.5.3 *X-Ray Microtomography and Synchrotron Radiation Studies*

The key elements of an X-ray tomography measurement system are an X-ray source (which may vary widely from massive particle accelerators to small portable benchtop sources; Clarke and Eberhardt 2002), a rotation stage, and a detector (Fig. 5.8a). A complete X-ray microtomography analysis starts with acquiring a number of projections of the sample under gradually increasing viewing angles (Fig. 5.8b) and continues with a reconstruction step (Fig. 5.8c), where these projections are converted to a 3D representation of how the X-rays in the material are affected by structural features such as bubbles (Fig. 5.8d and e; Falcone et al. 2006).

X-ray attenuation depends on the local mass density in the sample (Proussevitch et al. 2007), allowing the 3D map of the attenuation in the material to be segmented so that components of a sample with high and low density can be differentiated. Attenuation of X-rays, due to absorption or scattering, can be expressed by Beer's law (Falcone et al. 2006):

$$I = I_0 \exp(-\alpha l), \tag{5.4}$$

where I and I_0 are the intensities of the transmitted and incident X-rays, respectively, α is the attenuation coefficient, and l is the path of the radiation in the sample. As the X-rays travel through the sample being tested, they pass along many different paths as the sample or the X-ray source is rotated (Lim and Barigou 2004). Therefore, the attenuation of X-rays is different at each rotation since the low-density components do not attenuate X-rays as much as the high-density components (Fig. 5.8b). As the number of projections increase, projections are superposed, and the reconstructed

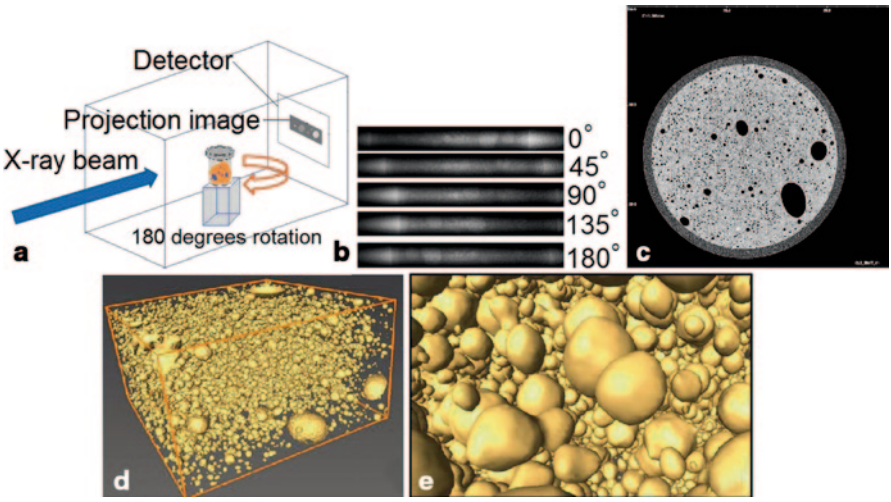

Fig. 5.8 **a** Key elements of an X-ray tomography measurement system, **b** X-ray projections of the sample under gradually increasing viewing angles, **c** a reconstructed 2D cross-sectional X-ray image of a dough piece (*black:* gas, *dark gray:* container walls, *light gray:* dough matrix), **d** the 3D representation of the volume of interest obtained using 2D images such as the one in **c**, and **e** an enlarged view of the 3D representation in **d**

cross-sectional image's quality increases (Clarke and Eberhardt 2002). In order to obtain higher quality images, contrast agents with higher atomic numbers can be employed (Clarke and Eberhardt 2002; Jakhmola et al. 2014). An alternative way of obtaining higher quality images compared to the ones obtained by benchtop X-ray tomography is using synchrotron radiation sources that can deliver several orders of magnitude greater photon flux (Falcone et al. 2006; Babin et al. 2006, 2008). With the greater photon flux, and thus greater X-ray intensity, higher quality images can be generated in shorter time scales.

Conventional benchtop X-ray tomography has proven to be very well suited for scrutinizing the 3D structure of cellular baked goods both qualitatively (Demirkesen et al. 2014) and quantitatively (Besbes et al. 2013; Van Dyck et al. 2014). However, the rapid dynamics of bubble populations in both unyeasted and yeasted doughs presents severe challenges to quantitative evaluation of structure in dough by benchtop X-ray microtomography. Bellido et al. (2006) studied the BSD in bread doughs made from strong breadmaking flour by benchtop X-ray microtomography and reported lognormal BSDs that had median diameters of 100 and 109 μm and geometric standard deviations of 1.79 and 1.62 μm, for two different unyeasted dough formulations tested 90 min after the end of mixing. Their resolution was 10 μm. Whitworth (2008) studied the structural changes in bread dough during proving and baking using benchtop X-ray tomography with a resolution of 0.7 mm but did not communicate a BSD. Trinh et al. (2013) studied the BSDs during a pressure-step dough mixing process using benchtop X-ray microtomography with a resolution of approximately 11 μm. However, they did not recognize any bubbles smaller than 43 μm, which meant that they excluded a part of their BSD (Trinh et al. 2013).

Synchrotron radiation interrogation of the evolution of the 3D microstructure of bread dough during fermentation has also been reported (Babin et al. 2006, 2008; Turbin-Orger et al. 2012), pointing to the ability of the more powerful X-rays of a synchrotron source to accurately capture the complexity of the morphology of bread dough three-dimensionally, and rapidly, in order that the changes taking place during fermentation can be followed. Babin et al. (2006) reported that bubbles in fermenting dough grow exponentially and freely until a critical time after which coalescence dominates and the dough structure becomes irregular (Fig. 5.4). Babin et al. (2008), who monitored fermenting bread doughs with a resolution of 15 μm, reported that the critical time for free bubble growth was affected by dough composition: The critical time increased either when yeast concentration was reduced or when water concentration decreased and oil concentration increased. In this study it was also stated that the cellular structure is entirely set at a temperature close to 75 °C. Turbin-Orger et al. (2012), who studied the bubbles in bread doughs during the later stages of proving (40–180 min), reported that both mean bubble size (410–675 μm on average) and mean cell wall thickness (200–230 μm on average) increased during proving for all dough compositions tested and that the size of the changes in the mean size and the mean cell wall thickness differed as dough composition varied.

In third generation X-ray sources (e.g., synchrotrons), in addition to greater photon flux, another important characteristic has been developed: The X-ray beam has small divergence. When the small divergence beams are combined with increased distance between the source and the sample, a new opportunity in the field of X-ray imaging emerges: phase contrast imaging. This imaging technique differs from conventional absorption X-ray tomography in the sense that it does not rely on the decrease in the X-ray beam's intensity (attenuation) but relies on the X-ray beam's phase. As X-rays travel through a material, their phase is altered due to regional variations in the refractive index of the material; these variations occur at borders or interfaces between the continuous phase of the material and the inclusions in it (Falcone et al. 2004). Therefore, even if a sample has poor intrinsic contrast due to low atomic number, high contrast may be generated by the interference of the X-ray wave front with components of the sample with different refractive indexes (Falcone et al. 2006). Phase of the X-rays has been shown to be sensitive to very small density variations (on the order of 10^{-9} g/cm^3) so that phase shifts of the X-rays can produce significantly greater contrast images (up to 1000 times) as compared to the ones achieved in X-ray absorption tomography (Falcone et al. 2004, 2005). However, extracting the variations in the phase of X-rays from the distorted wave front is challenging (Fitzgerald 2000).

5.5.4 Ultrasound

Sound waves which have a frequency above the upper limit audible to humans (> 16 kHz) are described as ultrasound waves (McClements and Gunasekaran,

1997). Due to its nondestructive nature, low-intensity ultrasound (<100 mW/cm^2) provides information about the physical properties of the material through which it propagates without altering its structure or physical properties (McClements 1991). Ultrasonic testing of materials requires three components: a signal generator that produces electrical pulses, a transducer that converts electrical pulses to mechanical vibrations, and a display system to detect and record the received signal (Falcone et al. 2006).

Investigation of BSD in bread doughs with ultrasound is a relatively recent phenomenon. It has been shown that the ultrasonic parameters measured in a material are affected by changes in matrix properties as well as the size and concentration of bubbles (Létang et al. 2001; Leroy et al. 2008). Ultrasonic velocity is defined as the distance an ultrasonic wave propagates per unit time (McClements and Gunasekaran 1997). As an ultrasonic wave travels through a medium, the amplitude of the ultrasonic wave decreases with the distance travelled, that is, it is attenuated (Cobus et al. 2007). The change in the amplitude of the ultrasonic wave, that is, how rapidly the ultrasonic energy is dissipated, is measured with the ultrasonic attenuation coefficient, α (Povey 1997; Coupland 2004). Ultrasonic parameters are measured as a function of frequency, and these can be linked to the BSD in the bubbly medium through models that describe wave propagation in bubbly media (Leroy et al. 2008).

Elmehdi et al. (2003b) studied dough fermentation by using an ultrasonic transmission technique and showed that the changes in the gas volume fraction as well as changes in the structure of the dough during fermentation could be monitored by low-frequency (50 kHz) ultrasound. They reported a substantial decrease in signal velocity (Fig. 5.9a) without a significant change in dough density (Fig. 5.9b) at early times of fermentation that was attributed to the modification of dough matrix elasticity by yeast activity. The modification of the dough matrix occurred as the CO_2 produced by the yeast diffused through the dough matrix, causing a reduction in the pH and thus weakening of gluten. Another study where the changes in the mechanical properties of doughs during fermentation were investigated using an ultrasonic transmission technique (2–10 MHz) is that of Lee et al. (2004). They determined the signal velocity and attenuation coefficient from which they calculated

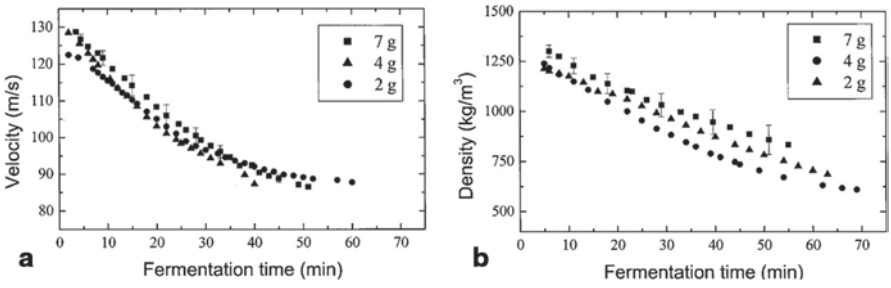

Fig. 5.9 **a** The ultrasonic signal velocity as a function of fermentation time measured using dough sample sizes of 2, 4, and 7 g, **b** the density of fermenting doughs as a function of fermentation time for the samples in (**a**). (Adapted from Elmehdi et al. 2003b)

the longitudinal moduli of the dough. They concluded that the longitudinal moduli of the dough were significantly affected by fermentation time resulting in a loss in elasticity of the dough, confirming the results they obtained from conventional extensional rheology.

Scanlon et al. (2011) studied the bubble evolution in unyeasted doughs at frequencies close to bubble resonance using an ultrasonic transmission technique. They showed that ultrasonic parameters were very sensitive to the changes in the BSD brought about by disproportionation. Strybulevych et al. (2012) used ultrasound to examine the evolution of bubble sizes in both unyeasted and yeasted doughs. For unyeasted doughs, they reported an increase in the normalized median diameter and the width of the lognormal BSD with time and attributed these changes to bubble disproportionation. For yeasted doughs, a decrease in normalized bubble size was observed at the beginning of the fermentation process due to consumption of oxygen by yeast. At later stages of fermentation, an increase in the normalized bubble size was observed which was attributed to the inflation of bubbles with CO_2 generated by yeast activity. Koksel et al. (2014) showed using an ultrasonic transmission technique that aeration processes of unyeasted dough during mixing are influenced by reducing sodium chloride content. They reported that the bubble diameter increased (40–50 %) for all sodium chloride contents over the course of 150 min for unyeasted doughs, consistent with changes in the BSD arising from disproportionation.

The only study that appears to report true BSDs in bread doughs measured by ultrasonic techniques is by Leroy et al. (2008). For unyeasted doughs tested 53 min after mixing, they reported a median bubble diameter of 28 μm with a width of 0.46 for a lognormal BSD. Approximately 45 min later, the median diameter had increased to 36 μm, and the width had decreased to 0.44.

One of the limitations of ultrasonic investigation of BSDs is that highly attenuating media are barriers to successful ultrasonic sizing (Povey 1997). When the sample under investigation is highly attenuating, reflection measurements, where the ultrasonic wave is reflected from the surface of the material, are useful (Kulmyrzaev et al. 2000). However, the drawback of the reflection technique is that only the boundary layer properties, rather than properties of the bulk of the material, are measured (Povey and McClements 1988).

5.6 Factors Affecting the Evolution of Cellular Structure of Crust and Crumb

Control and manipulation of dough properties are essential for high-quality and consistent baked products (Campbell and Martin 2012). Therefore, the effect of dough ingredients or dough processing conditions on the resulting loaf quality has been the subject of many studies. The evolution of the cellular structure of bread dough plays important roles in dough rheology (Carlson and Bohlin 1978; Bellido et al. 2006) as well as in the appearance, structure, texture, and thus the quality of

the final product (Zghal et al. 1999; Scanlon and Zghal 2001). Consequently, the occlusion of air as bubbles during mixing (Baker and Mize 1941), the subdivision of these air bubbles during later stages of breadmaking (Campbell and Martin 2012), their growth during fermentation, proof, and baking (Chiotellis and Campbell 2003b), and their retention until the final structure of bread is set (Gan et al. 1995) are all vital for the production of high-quality baked goods. Better knowledge of the factors affecting the evolution of cellular structure of crumb and crust requires a deeper appreciation of the phenomena governing changes in the aerated structure of this opaque medium (Shehzad et al. 2010).

5.6.1 The Role of Mixing Conditions

It has been shown that the gas volume fraction entrained during mixing may range as much as from 4 to over 20% (Cauvain et al. 1999). Since rates of physical processes such as disproportionation, bubble growth, and coalescence occurring during breadmaking depend on total gas volume fraction and the initial BSD, all of the factors that affect the BSD at the end of mixing (e.g., see Sect. 5.2) are likely to affect the evolution of the bubbles during later stages of breadmaking.

Shehzad et al. (2010) used different mixing conditions to prepare doughs with different rheological properties and investigated the stability of bubbles in dough during proving. Their results indicated that higher specific energy input during mixing promoted a stronger gluten network, which may cause better strain hardening properties and increase dough stability during proving. These results were later confirmed by Kansou et al. (2012) who studied the proving behavior of a wheat flour dough affected by mixing conditions such as mixing time and specific power input. Greater power input in a shorter time during mixing promoted gluten network formation and thus increased gas retention and dough stability during proving. An increase in dough stability would in turn prevent premature gas loss and collapse during proving and baking and therefore affect the final crumb texture and gas cell size distribution (Kansou et al. 2012).

5.6.2 The Role of Dough Rheology and Composition

Changes in flour components are very important since these changes affect the dough's rheological properties and so alter its mixing performance (Eliasson and Larsson 1993). When dough is mechanically stressed, it responds viscoelastically, and the viscoelastic behavior of dough under stress is affected by flour components such as proteins or dough ingredients such as salts and agents that affect disulfide bonding (Belton 2002). Among flour components, proteins undergo considerable changes from their structure in the flour particle to that at the end of the mixing process (Shewry et al. 2001). The changes in proteins during the dough mixing process

have been studied extensively, including techniques such as SEM (Bache and Donald 1998; Létang et al. 1999; Esselink et al. 2003) and CLSM (Peighambardoust et al. 2010a; Boitte et al. 2013).

When the effect of certain surfactants on crumb grain was investigated, it was found that surfactants did not change the amount of air incorporated into the dough during the mixing process (Junge et al. 1981; Mehta et al. 2009), but they improved bread crumb structure by allowing more and smaller bubbles to form during mixing, followed by more subdivision of these bubbles during punching (Junge et al. 1981).

When the influence of additives and mixing time on bread crumb properties was studied, inclusion of fat or emulsifiers and an increase in mixing time was found to significantly affect the total bubble area and number of bubbles per unit area in bread (Crowley et al. 2000). In another study where again effects of baking ingredients (surfactants and flour type) on dough aeration during mixing and gas retention during proving were studied, it was found that stronger flours occluded less air during mixing compared to weaker flours and that surfactants greatly improved the resulting baked loaf (Campbell et al. 2001).

Brooker (1996) studied the function of fat in bubble stabilization in bread dough by electron microscopy and CLSM and reported that fat crystals from shortening adsorb to the bubble gas/liquid interface during mixing and proving. These fat crystals melt during baking causing a transfer of interfacial material from the crystals to the bubble surfaces to maintain bubble expansion for longer without rupture (Brooker 1996).

Dough rheology literature usually disregards the contributions of the gas phase to the properties of dough and considers bubbles to be an independent variable. Although the fraction of gas in dough is significant (Whitworth and Alava 1999; Campbell and Martin 2012), one of the first studies to propose that the elastic character of the dough was affected by the surface tension at the gas/liquid interface was Carlson and Bohlin (1978). They accordingly linked dough rheology to dough gas content. However, an alternative model proposed by Bloksma (1981) predicted that the extent to which surface tension at the gas/liquid interface contributes to dough rheology was insignificant, except for doughs at a later stage of fermentation.

The relationship between dough rheology and dough gas content was later investigated by varying baking ingredients and processing factors (Chin et al. 2005; Chin and Campbell 2005a, b). Dough development and dough aeration, which are affected by mixing speed and mixing headspace pressure, influenced dough rheology assessed by mixing peak torque and work input during mixing (Chin and Campbell 2005b). Under large biaxial extensional deformation, the same researchers reported that both dough aeration and rheology were affected by flour type, total work input during mixing, and the rate at which this work input was delivered (Chin and Campbell 2005a). Using the same type of deformation, they stated that dough aeration affects dough rheology not only due to the contribution of air to oxidation and development of dough during mixing, but also due to the physical presence of bubbles in dough which promotes disruption of the integrity of dough structure through decreasing the strain hardening behavior of the dough and the resistance of the dough to failure (Chin et al. 2005).

Sahi (1994) investigated the effect of water on dough aeration and stated that a low level of water may limit the bubble nuclei that could be incorporated into the

dough during mixing and also limit the expansion of bubble nuclei during dough proving and baking. In contrast, a high level of water may destabilize bubbles and lead to loss of gas from the dough (Sahi 1994). For systems other than wheat flour doughs, Hanselmann and Windhab (1999) stated that rheological properties influence the shear field experienced by the bubbles during mixing, with higher viscosity systems being more likely to generate smaller bubbles for a given mixing speed in whey protein isolate–guar gum foams. The bidirectional relationship of dough rheology and aeration was further confirmed by investigation of dough rheological properties by ultrasound (Elmehdi et al. 2004; Scanlon et al. 2008). Rheological properties of doughs measured by changes in the longitudinal modulus (derived from ultrasonic pulse measurements) were significantly affected by concentration of bubbles in the dough (Elmehdi et al. 2004).

5.6.3 Dough Aeration and Mixing

Understanding dough aeration can enlighten the mechanisms by which the final loaf texture is affected by the BSD and how the aerated structure of the final loaf can be improved as early as right after the mixing stage. However, due to the paucity of tools for studying the fragile and rapidly changing bubbles in dough, resolving these questions for doughs tested right after mixing has been stymied so far. To our knowledge, determination of the BSD in dough shortly after mixing and its time evolution have not been reported unless a freezing step was involved. In Table 5.1, literature reports of bubble size analysis in dough are presented.

The wide variety of the results reported in Table 5.1 is likely due to the difference between the times that the dough samples were tested. For example, while a relatively longer time evolution was investigated in Leroy et al. (2008), Shimiya and Nakamura (1997) studied doughs right after mixing (3 min after the end of mixing). In spite of the pronounced influence of post-mixing time on bubble properties, literature usually disregards reporting the time at which the tests were performed.

It also needs to be pointed out that approximately half of the studies in Table 5.1 rely on the assumption that the BSD in bread dough at the end of mixing is lognormal, deemed appropriate because of the repetitive action of bubble subdivision during mixing. Among these studies, Shimiya and Nakamura (1997) and Bellido et al. (2006), who employed morphometric methods to investigate BSD, did not report the goodness of lognormal fits to their experimental BSDs, and Leroy et al. (2008), who used an ultrasonic transmission technique, did not confirm the lognormality of the BSD.

5.6.4 The Role of Proving and Baking Conditions

Altering the conditions operating during processing can have substantial effects on cellular structure, with temperature being a factor, either in yeast or chemical leavened bread systems. The impacts of proving time on crumb morphology

Table 5.1 Literature values reported for analyses of gas bubbles in dough

Reference	Method	Time after mixing	Resolution (μm)	ϕ (%)	Median (μm)	Width of the distribution
Carlson and Bohlin (1978)[a]	TLM	NC	90	10	56	23.8
Bloksma (1990b)	NC	NC	NC	10	17.5	NC
Campbell et al. (1991)[a]	TLM	NC	39	2.90	35.5	12.1
Campbell et al. (1991)[a]	TLM	NC	39	2.80	44.2	23.5
Shimiya and Nakamura (1997)[b]	RLM	3 min	10	3.5	7.5	0.18
Whitworth and Alava (1999)	B-XMT	NC (during proving)	20	5–8	1250[c]	NC
Bellido et al. (2006)[b]	B-XMT	90 min	10	7.6	50	0.58
Bellido et al. (2006)[b]	B-XMT	90 min	10	9.5	54.7	0.48
Babin et al. (2006; 2008)	S-XMT	NC (after kneading)	15	10	90[a]	NC
Leroy et al. (2008)[b]	T-US	53 min	–	12	14	0.46
Leroy et al. (2008)[b]	T-US	96 min	–	12	18	0.44
Trinh et al. (2013)	B-XMT	NC	10.8	NC	10–15[e]	NC

TLM transmission light microscopy, *NC* not communicated, *RLM* reflection light microscopy, *B-XMT* benchtop X-ray microtomography, *S-XMT* X-rays from a synchrotron source, *T-US* transmission ultrasound

[a] Arithmetic mean and standard deviation of the BSD

[b] Median and width of the lognormal BSD

[c] Maximum bubble radius

[d] Median and width derived from lognormal BSD function

[e] Minimum bubble radius

(Zghal et al. 2001; Primo-Martín et al. 2010) and oven air temperature and relative humidity on bread crust during baking (Vanin et al. 2009) have previously been reported. Whitworth (2008) showed from benchtop X-ray tomography imaging of whole loaves how structure developed differently in unlidded and lidded pans. High-resolution X-ray microtomography analyses by Turbin-Orger et al. (2012) confirmed the clear evolution in cellular structure with proving time. They concluded that the porosity varied from 0.3 to 0.4 (at 40 min of proving) to 0.6–0.74 (towards the end of proving, 160–180 min) with the range affected by different dough formulations.

Once placed in the oven, the massive temperature gradient rapidly sets the crust (Mack et al. 2013), but crust properties and structure are affected by the conditions employed during proving and baking. X-ray tomography was used by Primo-Martín et al. (2010) to show that longer proving times permitted more desiccation, thickening the "top solid layer" of the crust region that formed in the baked product. Our emphasis on the distinction within the crust region is important since their definition of crust was on the "basis of color difference," and their finding was that crust thickness decreased as proving time increased. This discrepancy in conclusion, based on how the crust is defined, is further exacerbated with the research results from autocorrelation measurements of image intensity as one moves inwards from the exterior

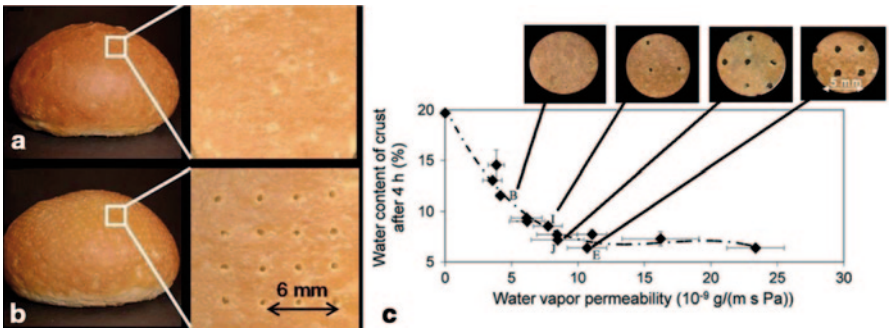

Fig. 5.10 Full roll and a detail of the crust for control roll (**a**) and punctured roll (**b**) after baking (adapted from Hirte et al. 2010), **c** relationship between the water content and the water vapor permeability of crust for different puncturing settings of the rolls; letters *B, I, J,* and *E* represent puncture diameters of 0.5, 0.8, 1.4, and 1.8 mm, respectively after baking. (Adapted from Hirte et al. 2012a)

of a loaf. In a study by Tromp et al. (2008), these measurements provided evidence that morphological differences associated with a crust region extended well beyond a color definition of the crust. Discrepancies were also evident between imaging definitions of crust thickness and those defined from a moisture content change criterion as a function of baking time when loaves were baked for increasing lengths of time in an oven with a vault temperature of 250 °C (Della Valle et al. 2012).

The importance of crust development to end product quality was shown in a definitive experiment on the relationship between moisture migration and the loss of crust crispness. Hirte et al. (2010) reported that crispness retention was enhanced in rolls where the parbaked roll was subject to an array of punctures applied to the partially developed crust. The punctures in the crust allowed a preferential moisture vapor migration route so that the crust retained a different moisture content to the crumb, and this translated into an eightfold increase in sensory crispness in the crust-punctured rolls (Hirte et al. 2010). Their images of a control roll with no punctures and a punctured roll are presented in Fig. 5.10a and b, respectively. The same group (Hirte et al. 2012a) used imaging techniques and SEM to show that the surface structure was not altered by the puncturing process and that with an increase in the surface area of the punctures, water vapor permeability, and thus crispness, increased. Their measurements for water vapor permeability of crust versus water content for crusts punctured differently are presented in Fig. 5.10c. The importance of the crust for control of moisture migration from the crumb was further emphasized by Hirte et al. (2012b) in a morphological analysis of the bread crumb made from doughs of different formulation using X-ray tomography and image analysis. Besbes et al. (2013) commented that quantification of the morphology of the crust by tortuosity parameters acquired by X-ray tomography techniques would be highly beneficial for investigations of the mechanisms of water migration during the shelf life of bread, since image analyses showed that tortuosity did change at the transition region between crumb and crust (Hussein and Becker 2010).

Crust formation can be enhanced by administering steam in the early stages of the oven (Schirmer et al. 2011) or by altering oven temperature and heating rate

(Besbes et al. 2013). A more significant factor, compared to temperature, which affects crust formation is the rate of moisture removal (dependent on air velocity and moisture vapor pressure deficit), a phenomenon predicted on the basis of modeling studies (Jefferson et al. 2006). Since the comment of Vanin et al. in their review of 2009, lamenting the lack of quantitative structural characterizations of crust, there have been a number of such assessments of crust formation. Besbes et al. (2013) examined how crust from different regions of the loaf was affected by processing regime and compared porosity values determined from X-ray tomography with helium pycnometry assessments. X-ray tomography was also used by van Dyck et al. (2014) to quantify crust's lower porosity (compared to the crumb) using a large number of bread samples. Altamirano-Fortoul et al. (2012) used both SEM and X-ray microtomography to demonstrate differences in porosity with crust depth and how this was affected by the quantity of steam injected during baking.

Using image analysis of loaf cross-sections, Tromp et al. (2008) defined autocorrelation functions of the change in pixel intensity with distance from the crust edge. From the longer range of correlations in the top crust compared to the sides and the bottom crusts, they deduced that the top crust was coarser. The technique was also used to show the dependence of structure changes in the crust when different bakery improvers were used. A color criterion of crust from color image analysis was used by Schirmer et al. (2011) to define crust thickness. From such analyses, crust thickness was observed to change with manipulation of process conditions during baking.

Addition of reagents to enhance the crust during proving affects both the porosity of the crumb (Jahromi et al. 2011) and the mechanical properties of the finished product. For example, we have found that glazing the crust during proving increased the fracture stress of the excised crusts (Scanlon unpublished data). Even though identical baking conditions were employed, crust fracture stresses at 129 kN/m^2 were substantially greater than those of unglazed loaves (55 kN/m^2).

5.7 Conclusions

Bread owes its appeal largely to the quality of its aerated structure that contributes to its acceptable appearance, delicate, spongy texture, and perceived freshness. All these attributes depend on the manipulation and control of bubbles, starting from mixing to the end of baking. Control of bubble structure is hampered somewhat by the experimental challenges of nondestructive monitoring of bubbles during their transformations in bread dough and during crust formation. Nevertheless, microscopy, MRI, X-ray microtomography, and ultrasound have all been utilized for the interrogation of the morphology of bread dough, crumb, and crust in order to obtain detailed information at different length scales and during various stages of the breadmaking process. Such information is providing new insights into the fundamentals of the aerated structure of dough and bread. This in turn can be translated into better quality assurance, insights into ingredient functionality, process operation optimization, and product improvement.

Acknowledgments The authors are grateful for research support from Natural Sciences and Engineering Research Council of Canada (NSERC) Discovery grants program.

References

AACC International (1983) Approved methods of the American Association of Cereal Chemists, 8th edn. AACC International, Inc., St. Paul

Altamirano-Fortoul R, Le-Bail A, Chevallier S, Rosell CM (2012) Effect of the amount of steam during baking on bread crust features and water diffusion. J Food Eng 108:128–134. doi:10.1016/j.jfoodeng.2011.07.015

Babin P, Della Valle G, Dendievel R et al (2005) Mechanical properties of bread crumbs from tomography based finite element simulations. J Mater Sci 40:5867–5873. doi:10.1007/s10853-005-5021-x

Babin P, Della Valle G, Chiron H et al (2006) Fast X-ray tomography analysis of bubble growth and foam setting during breadmaking. J Cereal Sci 43:393–397. doi:10.1016/j.jcs.2005.12.002

Babin P, Della Valle G, Dendievel R et al (2007) X-ray tomography study of the cellular structure of extruded starches and its relations with expansion phenomenon and foam mechanical properties. Carbohydr Polym 68:329–340. doi:10.1016/j.carbpol.2006.12.005

Babin P, Della Valle G, Chiron H et al (2008) In situ fast X-ray tomography study of the evolution of cellular structure in bread dough during proving and baking. In: Campbell GM, Scanlon MG, Pyle LD (eds) Bubbles in food 2: novelty, health and luxury. Eagan Press, St. Paul, pp 265–272

Bache IC, Donald AM (1998) The structure of the gluten network in dough: a study using environmental scanning electron microscopy. J Cereal Sci 28:127–133. doi:10.1006/jcrs.1997.0176

Bajd F, Serša I (2011) Continuous monitoring of dough fermentation and bread baking by magnetic resonance microscopy. Magn Reson Imaging 29:434–442. doi:10.1016/j.mri.2010.10.010

Baker JC, Mize MD (1937) Mixing doughs in vacuum and in the presence of various gases. Cereal Chem 14:721–734

Baker JC, Mize MD (1941) The origin of the gas cell in bread dough. Cereal Chem 18:19–34

Bellido GG, Scanlon MG, Page JH, Hallgrimsson B (2006) The bubble size distribution in wheat flour dough. Food Res Int 39:1058–1066. doi:10.1016/j.foodres.2006.07.020

Belton PS (2002) The molecular basis of dough rheology. In: Cauvain SP (ed) Bread making: improving quality, 2nd edn. CPC, UK, pp 273–287

Besbes E, Jury V, Monteau J-Y, Le Bail A (2013) Characterizing the cellular structure of bread crumb and crust as affected by heating rate using X-ray microtomography. J Food Eng 115:415–423. doi:10.1016/j.jfoodeng.2012.10.005

Bisperink CGJ, Ronteltap AD, Prins A (1992) Bubble-size distributions in foams. Adv Colloid Interface Sci 38:13–32

Bloksma AH (1981) Effect of surface tension in the gas-dough interface on the rheological behaviour of dough. Cereal Chem 58:481–486

Bloksma AH (1990a) Rheology of the breadmaking process. Cereal Foods World 35:228–236

Bloksma AH (1990b) Dough structure, dough rheology, and baking quality. Cereal Foods World 35:237–244

Boitte J-B, Hayert M, Michon C (2013) Observation of wheat flour doughs under mechanical treatment using confocal microscopy and classification of their microstructures. J Cereal Sci 58:365–371. doi:10.1016/j.jcs.2013.07.009

Bosch M, Torrejón-Escribano B, Bosch A, Calvo M (2012) Advanced light microscopy techniques. In: Seoane JR, Llovet Ximenes X (eds) Handbook of Instrumental techniques from CCiTUB. Scientific and Technological Centers of University of Barcelona, Spain, pp 1–11

Brooker BE (1996) The role of fat in the stabilisation of gas cells in bread dough. J Cereal Sci 24:187–198. doi:10.1006/jcrs.1996.0052

Campbell GM, Martin PJ (2012) Bread aeration and dough rheology: an introduction. In: Cauvain SP (ed) Bread making: improving quality, 2nd edn. CPC, UK, pp 299–336

Campbell GM, Mougeot E (1999) Creation and characterisation of aerated food products. Trends Food Sci Technol 10:283–296

Campbell GM, Shah P (1999) Entrainment and disentrainment of air during bread dough mixing, and their effect on scale-up of dough mixers. In: Campbell GM, Webb C, Pandiella SS, Niranjan K (eds) Bubbles in food. Eagan Press, St. Paul, pp 11–20

Campbell GM, Rielly CD, Fryer PJ, Sadd PA (1991) The measurement of bubble size distributions in an opaque food fluid. Trans IChemE 69:67–76

Campbell GM, Rielly CD, Fryer PJ, Sadd PA (1998) Aeration of bread dough during mixing: effect of mixing dough at reduced pressure. Cereal Foods World 43:163–167

Campbell GM, Herrero-sanchez R, Payo-rodriguez R, Merchan ML (2001) Measurement of dynamic dough density and effect of surfactants and flour type on aeration during mixing and gas retention during proofing. Cereal Chem 78:272–277

Carlson T, Bohlin L (1978) Free surface energy in the elasticity of wheat flour dough. Cereal Chem 55:539–544

Cauvain SP, Whitworth MB, Alava JM (1999) The evolution of bubble structure in bread doughs and its effect on bread structure. In: Campbell GM, Webb C, Pandiella SS, Niranjan K (eds) Bubbles in food. Eagan Press, St. Paul, pp 85–93

Chaunier L, Chrusciel L, Delisée C et al (2008) Permeability and expanded structure of baked products crumbs. Food Biophys 3:344–351. doi:10.1007/s11483-008-9073-8

Chevallier S, Zuniga R, Le-Bail A (2012) Assessment of bread dough expansion during fermentation. Food Bioprocess Technol 5:609–617

Chin NL, Campbell GM (2005a) Dough aeration and rheology: part 2. Effects of flour type, mixing speed and total work input on aeration and rheology of bread dough. J Sci Food Agric 85:2194–2202. doi:10.1002/jsfa.2237

Chin NL, Campbell GM (2005b) Dough aeration and rheology: part 1. Effects of mixing speed and headspace pressure on mechanical development of bread dough. J Sci Food Agric 85:2184–2193. doi:10.1002/jsfa.2236

Chin NL, Martin PJ, Campbell GM (2004) Aeration during bread dough mixing I. Effect of direction and size of a pressure step-change during mixing on turnover of gas. Trans IChemE 82:261–267

Chin NL, Martin PJ, Campbell GM (2005) Dough aeration and rheology: part 3. Effect of the presence of gas bubbles in bread dough on measured bulk rheology and work input rate. J Sci Food Agric 85:2203–2212. doi:10.1002/jsfa.2238

Chiotellis E, Campbell GM (2003a) Proving of bread dough II: measurement of gas production and retention. Trans IChemE 81:207–216

Chiotellis E, Campbell GM (2003b) Proving of bread dough I: modelling the evolution of the bubble size distribution. Trans IChemE 81:194–206

Clarke AR, Eberhardt CN (2002) Microscopy techniques for materials science. Woodhead Publishing Limited, UK, pp 1–85

Cobus LAEB, Ross KA, Scanlon MG, Page JH (2007) Comparison of ultrasonic velocities in dispersive and nondispersive food materials. J Agric Food Chem 55:8889–8895. doi:10.1021/jf071660r

Coupland JN (2004) Low intensity ultrasound. Food Res Int 37:537–543. doi:10.1016/j.foodres.2004.01.011

Crowley P, Grau H, Arendt EK (2000) Influence of additives and mixing time on crumb grain characteristics of wheat bread. Cereal Chem 77:370–375. doi:10.1094/CCHEM.2000.77.3.370

De Guio F, Musse M, Benoit-Cattin H et al (2009) Magnetic resonance imaging method based on magnetic susceptibility effects to estimate bubble size in alveolar products: application to bread dough during proving. Magn Reson Imaging 27:577–585. doi:10.1016/j.mri.2008.08.009

Della Valle G, Chiron H, Jury V et al (2012) Kinetics of crust formation during conventional French bread baking. J Cereal Sci 56:440–444. doi:10.1016/j.jcs.2012.05.004

Demirkesen I, Kelkar S, Campanella OH et al (2014) Characterization of structure of gluten-free breads by using X-ray microtomography. Food Hydrocoll 36:37–44. doi:10.1016/j.foodhyd.2013.09.002

Deshlahra P, Mehra A, Ghosal D (2009) Evolution of bubble size distribution in baked foods. J Food Eng 93:192–199. doi:10.1016/j.jfoodeng.2009.01.016

Dobraszczyk BJ (2004) The physics of baking: rheological and polymer molecular structure-function relationships in breadmaking. J Nonnewton Fluid Mech 124:61–69. doi:10.1016/j.jnnfm.2004.07.014

Eliasson A-C, Larsson K (1993) Cereals breadmaking: a molecular colloidal approach. Marcel Dekker, New York, pp 261–324

Elmehdi HM, Page JH, Scanlon MG (2003a) Using ultrasound to investigate the cellular structure of bread crumb. J Cereal Sci 38:33–42. doi:10.1016/S0733-5210(03)00002-X

Elmehdi HM, Page JH, Scanlon MG (2003b) Monitoring dough fermentation using acoustic waves. Trans IChemE 81:217–223

Elmehdi HM, Page JH, Scanlon MG (2004) Ultrasonic investigation of the effect of mixing under reduced pressure on the mechanical properties of bread dough. Cereal Chem 81:504–510. doi:10.1094/CCHEM.2004.81.4.504

Esselink E, van Aalst H, Maliepaard M et al (2003) Impact of industrial dough processing on structure: a rheology, nuclear magnetic resonance, and electron microscopy study. Cereal Chem 80:419–423. doi:10.1094/CCHEM.2003.80.4.419

Falcone PM, Baiano A, Zanini F et al (2004) A novel approach to the study of bread porous structure: phase-contrast X-Ray microtomography. J Food Sci 69:38–43

Falcone PM, Baiano A, Zanini F et al (2005) Three-dimensional quantitative analysis of bread crumb by X-ray microtomography. J Food Sci 70:265–272

Falcone PM, Baiano A, Conte A et al (2006) Imaging techniques for the study of food microstructure: a review. Adv Food Nutr Res 51:205–263. doi:10.1016/S1043-4526(06)51004-6

Ferrando M, Spiess WEL (2000) Review: confocal scanning laser microscopy. A powerful tool in food science. Food Sci Technol Int 6:267–284. doi:10.1177/108201320000600402

Fitzgerald R (2000) Phase-sensitive x-ray imaging. Phys Today 53:23. doi:10.1063/1.1292471

Gan Z, Angold RE, Williams MR et al (1990) The microstructure and gas retention of bread dough. J Cereal Sci 12:15–24. doi:10.1016/S0733-5210(09)80153-7

Gan Z, Ellis PR, Schofield JD (1995) Mini review gas cell stabilisation and gas retention in wheat bread dough. J Cereal Sci 21:215–230

Gibson LJ, Ashby MF (1988) Cellular solids. Pergamon Press, Oxford

Gonzalez-Gutierrez J, Scanlon MG (2012) Rheology and mechanical properties of fats. In: Marangoni AG (ed) Structure–function analysis of edible fats. AOCS Press, Urbana, pp 127–172

Grenier A, Lucas T, Collewet G, Le Bail A (2003) Assessment by MRI of local porosity in dough during proving. theoretical considerations and experimental validation using a spin-echo sequence. Magn Reson Imaging 21:1071–1086. doi:10.1016/S0730-725X(03)00194-2

Grenier D, Lucas T, Le Ray D (2010) Measurement of local pressure during proving of bread dough sticks: contribution of surface tension and dough viscosity to gas pressure in bubbles. J Cereal Sci 52:373–377. doi:10.1016/j.jcs.2010.06.016

Guessasma S, Babin P, Della Valle G, Dendievel R (2008) Relating cellular structure of open solid food foams to their Young's modulus: Finite element calculation. Int J Solids Struct 45:2881–2896

Guessasma S, Chaunier L, Della Valle G, Lourdin D (2011) Mechanical modelling of cereal solid foods. Trends Food Sci Technol 22:142–153. doi:10.1016/j.tifs.2011.01.005

Gunasekaran S (1996) Computer vision technology for food quality assurance. Trends Food Sci Technol 71:245–256

Hanselmann W, Windhab E (1999) Flow characteristics and modelling of foam generation in a continuous rotor/stator mixer. J Food Eng 38:393–405

Hayman D, Hoseney RC, Faubion JM (1998a) Effect of pressure (crust formation) on bread crumb grain development. Cereal Chem 75:581–584

Hayman D, Hoseney RC, Faubion JM (1998b) Bread crumb grain development during baking. Cereal Chem 75:557–580

Hermansson A-M, Langton M, Loren N (2000) New approaches to characterizing food microstructures. MRS Bull 30–36

Hirte A, Hamer RJ, Meinders MBJ, Primo-Martín C (2010) Permeability of crust is key to crispness retention. J Cereal Sci 52:129–135. doi:10.1016/j.jcs.2010.04.004

Hirte A, Hamer RJ, Meinders MBJ et al (2012a) Control of crust permeability and crispness retention in crispy breads. Food Res Int 46:92–98. doi:10.1016/j.foodres.2011.11.019

Hirte A, Primo-Martín C, Meinders MBJ, Hamer RJ (2012b) Does crumb morphology affect water migration and crispness retention in crispy breads? J Cereal Sci 56:289–295. doi:10.1016/j.jcs.2012.05.014

Huang H, Kokini JL (1999) Prediction of dough volume development which considers the biaxial extensional growth of cells. In: Campbell GM, Webb C, Pandiella SS, Niranjan K (eds) Bubbles in food. AACC International, Inc., St. Paul, pp 113–120

Hussein MA, Becker T (2010) An innovative micro-modelling of simultaneous heat and moisture transfer during bread baking using the lattice boltzmann method. Food Biophys 5:161–176. doi:10.1007/s11483-010-9156-1

Hutchinson RJ, Siodlak DE, Smith AC (1987) Influence of processing variables on the mechanical properties of extruded maize. J Mater Sci 22:3956–3962

Jahromi SHR, Yazdi FT, Karimi M et al (2011) Application of glazing for bread quality improvement. Food Bioprocess Technol 5:2381–2391. doi:10.1007/s11947-011-0594-7

Jakhmola A, Anton N, Anton H et al (2014) Poly-ε-caprolactone tungsten oxide nanoparticles as a contrast agent for X-ray computed tomography. Biomaterials 35:2981–2986. doi:10.1016/j.biomaterials.2013.12.032

Jefferson DR, Lacey AA, Sadd PA (2006) Understanding crust formation during baking. J Food Eng 75:515–521. doi:10.1016/j.jfoodeng.2005.04.051

Junge RC, Hoseney RC, Varriano-Marston E (1981) Effect of surfactants on air incorporation in dough and the crumb grain of bread. Cereal Chem 58:338–342

Kansou K, Chiron H, Della Valle G et al (2012) Modelling wheat flour dough proofing behaviour: effects of mixing conditions on porosity and stability. Food Bioprocess Technol 6:2150–2164. doi:10.1007/s11947-012-0854-1

Keller RCA, Orsel R, Hamer RJ (1997) Competitive adsorption behaviour of wheat flour components and emulsifiers at an air-water interface. J Cereal Sci 25:175–183. doi:10.1006/jcrs.1996.0089

Kokelaar JJ, Prins A (1995) Surface rheological properties of bread dough components in relation to gas bubble stability. J Cereal Sci 22:53–61. doi:10.1016/S0733-5210(05)80007-4

Kokelaar JJ, van Vliet T, Prins A (1996) Strain hardening properties and extensibility of flour and gluten doughs in relation to breadmaking performance. J Cereal Sci 24:199–214. doi:10.1006/jcrs.1996.0053

Koksel F, Scanlon MG (2012) Effects of composition on dough development and air entrainment in doughs made from gluten-starch blends. J Cereal Sci 56:445–450. doi:10.1016/j.jcs.2012.05.013

Koksel F, Strybulevych A, Page JH, Scanlon MG (2014) Ultrasonic characterization of unyeasted bread dough of different sodium chloride concentrations. Cereal Chem 91:327–332

Kulmyrzaev A, Cancelliere C, Mcclements DJ (2000) Characterization of aerated foods using ultrasonic reflectance spectroscopy. J Food Eng 46:235–241

Lee S, Pyrak-Nolte LJ, Campanella OH (2004) Determination of ultrasonic-based rheological properties of dough during fermentation. J Texture Stud 35:33–51

Lemlich R (1978) Prediction of changes in bubble size distribution due to interbubble gas diffusion. Ind Eng Chem Fundam 17:89–93

Leroy V, Fan Y, Strybulevych A et al (2008) Investigating the bubble size distribution in dough using ultrasound. In: Campbell GM, Scanlon MG, Pyle DL (eds) Bubbles in food 2: novelty, health and luxury. Eagan Press, St. Paul, pp 51–60

Létang C, Piau M, Verdier C (1999) Characterization of wheat flour–water doughs. Part I: rheometry and microstructure. J Food Eng 41:121–132. doi:10.1016/S0260-8774(99)00082–5

Létang C, Piau M, Verdier C, Lefebvre L (2001) Characterization of wheat-flour-water doughs: a new method using ultrasound. Ultrasonics 39:133–141

Lim KS, Barigou M (2004) X-ray micro-computed tomography of cellular food products. Food Res Int 37:1001–1012. doi:10.1016/j.foodres.2004.06.010

Liu Z, Scanlon MG (2003) Modelling indentation of bread crumb by finite element analysis. Biosyst Eng 85:477–484. doi:10.1016/S1537-5110(03)00093-X

Lynch EJ, Dal Bello F, Sheehan EM et al (2009) Fundamental studies on the reduction of salt on dough and bread characteristics. Food Res Int 42:885–891. doi:10.1016/j.foodres.2009.03.014

Mack S, Hussein MA, Becker T (2013) On the theoretical time-scale estimation of physical and chemical kinetics whilst wheat dough processing. Food Biophys 8:69–79. doi:10.1007/s11483-013-9285-4

MacRitchie F (1976) The liquid phase of dough and its role in baking. Cereal Chem 53:318–326

Martin PJ, Chin NL, Campbell GM (2004) Aeration during bread dough mixing II. A population balance model of aeration. Trans IChemE 82:268–281

McClements DJ (1991) Ultrasonic characterization of emulsions and suspensions. Adv Colloid Interface Sci 37:33–72

McClements DJ, Gunasekaran S (1997) Ultrasonic characterization of foods and drinks: principles, methods, and applications. Crit Rev Food Sci Nutr 37:1–46

Mehta KL, Scanlon MG, Sapirstein HD, Page JH (2009) Ultrasonic investigation of the effect of vegetable shortening and mixing time on the mechanical properties of bread dough. J Food Sci 74:E455–E461. doi:10.1111/j.1750–3841.2009.01346.x

Meinders MBJ, van Vliet T (2008) Scaling of sound emission energy and fracture behavior of cellular solid foods. Phys Rev E 77:036116. doi:10.1103/PhysRevE.77.036116

Mills ENC, Wilde PJ, Salt LJ, Skeggs P (2003) Bubble formation and stabilization in bread dough. Trans IChemE 81:189–193

Mun S, McClements DJ (2006) Influence of interfacial characteristics on Ostwald ripening in hydrocarbon oil-in-water emulsions. Langmuir 22:1799–1808. doi:10.1021/la0525751

Murray BS, Ettelaie R (2004) Foam stability: proteins and nanoparticles. Curr Opin Colloid Interface Sci 9:314–320. doi:10.1016/j.cocis.2004.09.004

Murray BS, Dickinson E, Du Z et al (2005) Foams and emulsions: disproportionation kinetics of air bubbles stabilized by food proteins and nanoparticles. In: Dickinson E (ed) Food colloids: interactions, microstructure and processing. Royal Society of Chemistry Special Publications, Cambridge, UK, pp 259–272

Örnebro J, Nylander T, Eliasson A-C (2000) Critical review—interfacial behaviour of wheat proteins. J Cereal Sci 31:195–221. doi:10.1006/jcrs.1999.0297

Peighambardoust SH, Dadpour MR, Dokouhaki M (2010a) Application of epifluorescence light microscopy (EFLM) to study the microstructure of wheat dough: a comparison with confocal scanning laser microscopy (CSLM) technique. J Cereal Sci 51:21–27. doi:10.1016/j.jcs.2009.09.002

Peighambardoust SH, Fallah E, Hamer RJ, van der Goot AJ (2010b) Aeration of bread dough influenced by different way of processing. J Cereal Sci 51:89–95. doi:10.1016/j.jcs.2009.10.002

Povey MJW (1997) Ultrasonic techniques for fluids characterization. Academic Press, CA, pp 1–46, 92–141

Povey MJW, McClements DJ (1988) Ultrasonics in food engineering. Part I: introduction and experimental methods. J Food Eng 8:217–245

Primo-Martín C, van Dalen G, Meinders MBJ et al (2010) Bread crispness and morphology can be controlled by proving conditions. Food Res Int 43:207–217. doi:10.1016/j.foodres.2009.09.030

Proussevitch AA, Sahagian DL, Carlson WD (2007) Statistical analysis of bubble and crystal size distributions: application to Colorado Plateau basalts. J Volcanol Geotherm Res 164:112–126. doi:10.1016/j.jvolgeores.2007.04.006

Purlis E (2012) Baking process design based on modelling and simulation: towards optimization of bread baking. Food Control 27:45–52. doi:10.1016/j.foodcont.2012.02.034

Romano A, Cavella S, Toraldo G, Masi P (2013) 2D structural imaging study of bubble evolution during leavening. Food Res Int 50:324–329. doi:10.1016/j.foodres.2012.10.040

Rouille J, Bonny JM, Della Valle G et al (2005) Effect of flour minor components on bubble growth in bread dough during proofing assessed by magnetic resonance imaging. J Agric Food Chem 53:3986–3994

Sahagian DL, Proussevitch AA (1998) 3D particle size distributions from 2D observations: stereology for natural applications. J Volcanol Geotherm Res 84:173–196. doi:10.1016/S0377-0273(98)00043-2

Sahi SS (1994) Interfacial properties of the aqueous phases of wheat flour doughs. J Cereal Sci 20:119–127

Scanlon MG, Zghal MC (2001) Bread properties and crumb structure. Food Res Int 34:841–864. doi:10.1016/S0963-9969(01)00109-0

Scanlon MG, Elmehdi HM, Leroy V, Page JH (2008) Using ultrasound to probe nucleation and growth of bubbles in bread dough and to examine the resulting cellular structure of bread crumb. In: Campbell GM, Scanlon MG, Pyle DL (eds) Bubbles in food 2: novelty, health and luxury. Eagan Press, St. Paul, pp 217–230

Scanlon MG, Page JH, Leroy V et al (2011) Examining the effect of dough matrix and bubbles on the properties of dough using low-intensity ultrasound. In: Chibbar RN, Dexter JE (eds) Proceedings of the 4th international wheat quality conference. AGROBIOS (International), Jodhpur, p 389

Schirmer M, Hussein WB, Jekle M et al (2011) Impact of air humidity in industrial heating processes on selected quality attributes of bread rolls. J Food Eng 105:647–655. doi:10.1016/j.jfoodeng.2011.03.020

Shah P, Campbell GM, Mckee SL, Rielly CD (1998) Proving of bread dough: modelling the growth of individual bubbles. Trans IChemE 76:73–79

Shah P, Campbell GM, Dale C, Rudder A (1999) Modelling bubble growth during proving of bread dough: predicting the output from the chopin rheofermentometer. In: Campbell GM, Webb C, Pandiella SS, Niranjan K (eds) Bubbles in food. AACC International, Inc., St. Paul, pp 95–106

Shehzad A, Chiron H, Della Valle G et al (2010) Porosity and stability of bread dough during proofing determined by video image analysis for different compositions and mixing conditions. Food Res Int 43:1999–2005. doi:10.1016/j.foodres.2010.05.019

Shewry PR, Popineau Y, Lafiandra D et al (2001) Wheat glutenin subunits and dough elasticity: findings of the EUROWHEAT project. Trends Food Sci Technol 11:433–441

Shimiya Y, Nakamura K (1997) Changes in size of gas cells in dough and bread during breadmaking and calculation of critical size of gas cells that expand. J Texture Stud 28:273–288. doi:10.1111/j.1745-4603.1997.tb00117.x

Shimiya Y, Yano T (1988) Rates of shrinkage and growth of air bubbles entrained in wheat flour dough. Agric Biol Chem 52:2879–2883

Singh H, MacRitchie F (2001) Application of polymer science to properties of gluten. J Cereal Sci 33:231–243. doi:10.1006/jcrs.2000.0360

Spencer JE, Scanlon MG, Page JH (2008) Drainage and coarsening effects on the time-dependent rheology of whole egg and egg white foams and batters. In: Campbell GM, Scanlon MG, Pyle DL (eds) Bubbles in food 2: novelty, health and luxury. Eagan Press, St. Paul, pp 117–129

Sroan BS, MacRitchie F (2009) Mechanism of gas cell stabilization in breadmaking. II. The secondary liquid lamellae. J Cereal Sci 49:41–46. doi:10.1016/j.jcs.2008.07.004

Sroan BS, Bean SR, MacRitchie F (2009) Mechanism of gas cell stabilization in bread making. I. The primary gluten–starch matrix. J Cereal Sci 49:32–40

Stevenson P (2010) Inter-bubble gas diffusion in liquid foam. Curr Opin Colloid Interface Sci 15:374–381. doi:10.1016/j.cocis.2010.05.010

Strybulevych A, Leroy V, Shum AL et al (2012) Use of an ultrasonic reflectance technique to examine bubble size changes in dough. IOP Conf Ser Mater Sci Eng 42:1–4. doi:10.1088/1757-899X/42/1/012037

Takano H, Ishida N, Koizumi M, Kano H (2002) Imaging of the fermentation process of bread dough and the grain structure of baked breads by magnetic resonance imaging. J Food Sci 67:244–250

Trinh L, Lowe T, Campbell GM et al (2013) Bread dough aeration dynamics during pressure step-change mixing: studies by X-ray tomography, dough density and population balance modelling. Chem Eng Sci 101:470–477. doi:10.1016/j.ces.2013.06.053

Tromp RH, Primo-Martín C, van de Zedde R, Koenderink N (2008) Quantifying the morphology of bread crusts. In: Campbell GM, Scanlon MG, Pyle DL (eds) Bubbles in food 2: novelty, health and luxury. AACC International, Inc., St. Paul, pp 61–72

Turbin-Orger A, Boller E, Chaunier L et al (2012) Kinetics of bubble growth in wheat flour dough during proofing studied by computed X-ray micro-tomography. J Cereal Sci 56:676–683. doi:10.1016/j.jcs.2012.08.008

Upadhyay R, Ghosal D, Mehra A (2012) Characterization of bread dough: rheological properties and microstructure. J Food Eng 109:104–113. doi:10.1016/j.jfoodeng.2011.09.028

Van Duynhoven JPM, van Kempen GMP, van Sluis R et al (2003) Quantitative assessment of gas cell development during the proofing of dough by magnetic resonance imaging and image analysis. Cereal Chem 80:390–395. doi:10.1094/CCHEM.2003.80.4.390

Van Dyck T, Verboven P, Herremans E et al (2014) Characterisation of structural patterns in bread as evaluated by X-ray computer tomography. J Food Eng 123:67–77. doi:10.1016/j.jfoodeng.2013.09.017

Van Vliet T (1999) Physical factors determining gas cell stability in a dough during bread making. In: Campbell GM, Webb C, Pandiella SS (eds) Bubbles Food. Eagan Press, St. Paul, pp 121–127

Van Vliet T (2008) Strain hardening as an indicator of bread-making performance: a review with discussion. J Cereal Sci 48:1–9. doi:10.1016/j.jcs.2007.08.010

Van Vliet T, Primo-Martín C (2011) Interplay between product characteristics, oral physiology and texture perception of cellular brittle foods. J Texture Stud 42:82–94. doi:10.1111/j.1745-4603.2010.00273.x

Van Vliet T, Janssen AM, Bloksma AH, Walstra P (1992) Strain hardening of dough as a requirement for gas retention. J Texture Stud 23:439–460. doi:10.1111/j.1745-4603.1992.tb00033.x

Vanin FM, Lucas T, Trystram G (2009) Crust formation and its role during bread baking. Trends Food Sci Technol 20:333–343. doi:10.1016/j.tifs.2009.04.001

Venerus DC, Yala N, Bernstein B (1998) Analysis of diffusion-induced bubble growth in viscoelastic liquids. J Nonnewton Fluid Mech 75:55–75. doi:10.1016/S0377-0257(97)00076-1

Wagner M, Quellec S, Trystram G, Lucas T (2008) MRI evaluation of local expansion in bread crumb during baking. J Cereal Sci 48:213–223. doi:10.1016/j.jcs.2007.09.006

Walstra P (1989) Principles of foam formation and stability. In: Wilson AJ (ed) Foams: physics, chemistry and structure. Springer, NY, pp 1–15

Wang S, Karrech A, Regenauer-Lieb K, Chakrabati-Bell S (2013) Digital bread crumb: creation and application. J Food Eng 116:852–861. doi:10.1016/j.jfoodeng.2013.01.037

Warburton SC, Donald AM, Smith AC (1990) The deformation of brittle starch foams. J Mater Sci 25:4001–4007

Whitworth MB (2008) X-ray tomography of structure formation in bread and cakes during baking. In: Campbell GM, Scanlon MG, Pyle DL (eds) Bubbles in food 2: novelty, health and luxury. Eagan Press, St. Paul, pp 273–286

Whitworth MB, Alava JM (1999) Imaging and measurement of bubbles in bread doughs. In: Campbell GM, Webb C, Pandiella SS, Niranjan K (eds) Bubbles in food. Eagan Press, St. Paul, pp 221–231

Yusoff A, Murray BS (2011) Modified starch granules as particle-stabilizers of oil-in-water emulsions. Food Hydrocoll 25:42–55. doi:10.1016/j.foodhyd.2010.05.004

Zghal MC, Scanlon MG, Sapirstein HD (1999) Prediction of bread crumb density by digital image analysis. Cereal Chem 76:734–742. doi:10.1094/CCHEM.1999.76.5.734

Zghal MC, Scanlon MG, Sapirstein HD (2001) Effects of flour strength, baking absorption, and processing conditions on the structure and mechanical properties of bread crumb. Cereal Chem 78:1–7. doi:10.1094/CCHEM.2001.78.1.1

Zghal MC, Scanlon MG, Sapirstein HD (2002) Cellular structure of bread crumb and its influence on mechanical properties. J Cereal Sci 36:167–176. doi:10.1006/jcrs.2001.0445

Chapter 6
Nondestructive Imaging of Cellular Solid Foods

Syed Ariful Alam and Nesli Sozer

6.1 Introduction

Food structure is an important quality-related parameter which has a direct impact on perceived texture; influenced by ingredients, their interaction, processing and storage history. Recent innovations in food imaging technologies or novel labelling strategies opens up new opportunities in the field of food technology to understand the food processing–structure–property–sensory relationship. To determine the food microstructure, several methods are used in food sector such as ultrasound, magnetic resonance imaging (MRI), stereomicroscopy, computer vision technique, digital imaging using charge coupled device (CCD) sensor, thermal imaging, flatbed scanning, radiography and most recently XMT. Most of the microscopy techniques is destructive and require sample preparation or treatments which would ultimately cause structural changes. Destructive imaging methods are usually time consuming and require costly instrumentation which runs with sophisticated software, therefore, not suitable to be used for "on-line" quality control tool. These techniques cannot provide accurate information on cell distribution, average cell wall thickness and interconnection between cells which are the most important microstructural features of open and solid cereal foams (Trater et al. 2005). It is also difficult to obtain adequate contrast between void and solid phase by scanning electron microscopy (SEM) and with optical imaging due to improper lightening and angle of illumination. Moreover, in these methods, algorithms such as Fourier transformation used for segmentation (combination of image subtraction and edge detection to distinguish void and solid phase), which require large computational time and also might give computational error and thus lead to inaccurate results (Trater et al. 2005).

N. Sozer (✉) · S. A. Alam
VTT Technical Research Centre of Finland, Tietotie 2, Espoo FI-02044 VTT, Finland
e-mail: nesli.sozer@vtt.fi

S. A. Alam
University of Helsinki, Helsinki, Finland
e-mail: ariful.alam@vtt.fi

N. Sozer (ed.), *Imaging Technologies and Data Processing for Food Engineers,*
Food Engineering Series, DOI 10.1007/978-3-319-24735-9_6

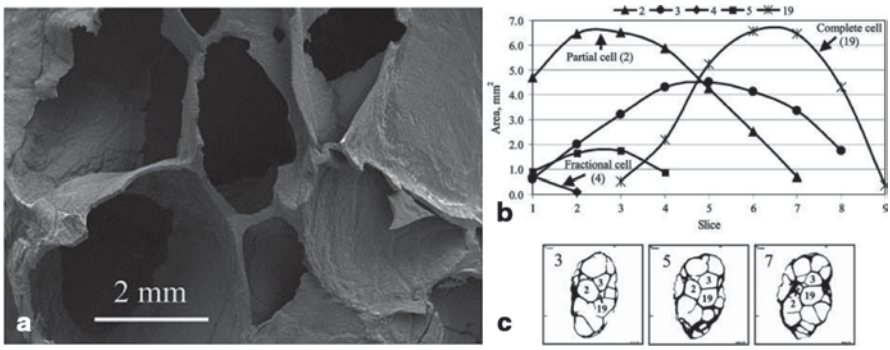

Fig. 6.1 **a** Scanning electron micrograph *(SEM)* image of extrudates of 5 % whey protein isolate *(WPC)* processed at 26 % feed moisture. **b** Development of cells 2, 3, 4, 5 and 19 over slices 1–9. **c** The appearance of cross section of the cells 2, 3 and 19 in the slices 3, 5 and 7 is shown in 2D *XMT* images of extrudate processed with same recipe and process condition. (Adapted with permission from Trater et al. (2005))

Cross-sectional area of air cells changes in a cellular solid matrix when depth of slice within the volume of interest (VOI) increases (6.1). The cells can be categorized into three groups: complete, partial or fractional cells according to their gradual development. Depth of slice had a significant effect on the cell area distribution pattern which was clearly shown in the XMT image where typical 2D imaging such as SEM is unable to characterize the distribution of actual 3D cell size distribution.

Due to the depth focus and high contrast between void and solid phase, XMT images were much better than SEM images. In SEM, sample preparation needs physical cutting which might cause partial damage and initiate crack through the pores. Multiple 2D images of the cross section facilitate imaging tremendously with incremental depth. Figure 6.1 demonstrates how cross-sectional area of air cells changes within the VOI of different consecutive slices in the form of complete, partial or fractional cells. It is clear that there is significant change in the cell-area distribution within the depth of cells. Traditional imaging tools such as SEM and light microscopy are unable to characterize accurate 3D cell area distribution of the extruded foams. However, the presence of partial and fractional cells within the VOI gives inaccurate results thus corrections are needed. After correction, although the trends are similar, estimates of cell size (average cell diameter and weighted average cell diameter) were 12 % larger. Similar trends observed for all parameters except open wall area ratio and weighted open wall area ratio, when processing corrections are made (Trater et al. 2005).

X-ray imaging or radiography should not be confused with XMT as radiography mostly used for determination of internal quality (i.e. internal damage or, volume of different internal features) of agricultural products such as nuts, fruits and grains (Kotwaliwale et al. 2010). In this method, high-energy X-ray beam penetrates into the test product. Depending on the food composition, properties and internal structure, photons of X-ray beam distributed in different ways: (1) transmitted, (2) scat-

tered and (3) absorbed. The transmitted X-ray beams later create visual contrast in the images showing the differences of test objects (Kotwaliwale et al. 2010).

XMT is one of the nondestructive techniques that would enable to visualize and characterize the internal structural architecture, porosity, cell wall thickness and cell diameter of processed cellular solid foods such as bread, extruded snacks, biscuits and cakes (Kotwaliwale et al. 2010). XMT enables to develop three-dimensional (3D) images of various food structures by combining 2D images with the help of dedicated software and programmes which would facilitate visualization and quantitative measurement without chemical fixation or tedious and time-consuming sample preparation protocols (Kiani and Sun 2011). MRI is another useful imaging technique which is capable to produce images through the proton mobility in foods using static magnetic fields and radio frequencies. The intensity of MRI signals originates from the water, fat or even from sugars present within the food matrix and allows accurate prediction of these components on structure at various time–temperature conditions. MRI has potential to determine several quality attributes such as presence of voids or foreign objects, internal damage caused by insects and larvae, dry/wet regions within test food, state of maturity and bruises, for example, in fruits and vegetables (Kotwaliwale et al. 2010). MRI requires complex and expensive system as it has certain material restrictions with high investment and operating costs (Kiani and Sun 2011). Special sample preparation is needed for both negative and positive imaging with MRI. A major advantage of XMT over MRI is the good spatial resolution which could be reached without using extensive sample preparation with statistically similar results (Horvat et al. 2014).

However, both MRI and XMT imaging methods are unable to represent optical properties; therefore, a correlation needs to be set between different features such as greyness and pixel bunches (2D) or voxels (3D). Although 2D image analysis is fast and relatively easy technique compared to 3D image analysis, image analysis of cereal solid foams need third orthogonal dimension to produce high-quality images representing proper structure of air cells and thus able to represent original size and shape of the cellular structure including cell size distribution, average cell wall thickness, average cell diameter and connectivity of cells through the quantitative analysis of projection data (Sozer et al. 2011b).

The interconnected pores can be segmented by watershed algorithm in order to accurately evaluate the pore sizes and shapes (Plews et al. 2009). The technique can be used to analyse samples with inhomogeneous porosity where pore size was based on volume fraction and aperture size was based on area fraction. The algorithm itself is an efficient tool for closing open cells to obtain pore size distributions as well as interconnecting pore aperture distributions (Plews et al. 2009). Average cell wall thickness and apparent pore size distribution can be obtained from 2D image analysis, although it is challenging to get accurate information about pore connectivity. Combined 2D and 3D analyses gives a thorough characterization of the porous food structure provided that they have sufficient density difference throughout the matrix.

Cell volume and cell connectedness of white bread and extrudates have been analysed by gas pycnometry (Bhatnagar and Hanna 1996; Hicsasmaz and Clayton

1992; Jones et al. 2000). The technique is an indirect method which utilizes the ideal gas law to determine the true volume of a solid. The method is weak as some closed adjoining cells could be considered as interconnected cells though they are not actually connected. Small cracks within the cell wall may allow gas to penetrate through the solid matrices surrounding the air cells but also applied pressure during the measurements can further cause cracks depending on sample type (Trater et al. 2005).

The cellular structure of solid cereal foams such as bread, cake, extruded snacks and biscuits has an effect on textural properties such as hardness, chewiness or crispiness based on product category. Sensory quality of baked and extruded cereal foods are strongly dependent on the structural architectures such as air cell size, shape and their distribution within the food matrix; therefore, it is important to evaluate these structural parameters to aid product design and optimize processing conditions (Sozer et al. 2011b).

6.2 X-Ray Microtomography for Foods

Basic principles of imaging by XMT rely on material density, atomic number and on X-ray absorption capacity (Babin et al. 2007). X-ray microtomography (XMT) is becoming an important tool for food microstructure analysis due to the high penetrating power, probing efficiency and noninvasive characteristics. However, as in the case of most imaging technologies benchtop XMT equipment might produce image artefacts which require special data handling procedures. When a polychromatic beam used in X-ray equipment a strong artefact appear known as “cupping effect” caused by beam hardening (Vidal et al. 2005). The fact is that when heterogeneous (combination of low- and high-energy photon) beam pass through an object the lower energy photon absorbed more readily and results in attenuated beam with higher average energy. Therefore, the longer the exposure time of the object to the X-ray radiation, the harder the X-ray become. The centre of the test sample usually exposed to the radiation longer period of time compared to the edges thus may appear less absorbent during reconstruction. However, pre-hardening of the X-ray beam by placing a filter between the X-ray source and test sample could help to reduce the cupping effect (Barigou et al. 2013). The “hot points” artefact usually appears after image reconstruction stage if the photons hit the CCD camera after passing through the scintillator. The hot points will be recognized by streaks or thin line throughout the sample volume (Barigou et al. 2013). On the other hand, dead pixels in the CCD camera may also cause a common artefact named “ring artefacts”, which appear when the detector response and the light intensity are not linearly proportional. This artefact is generally tackled by the XMT software. Besides the aforementioned artefacts, varying output of X-ray sources, sensitivity of the detector, nonuniform voltage supply, incomplete viewing and scattering of photons are reported to cause also artefacts (Vidal et al. 2005).

In desktop-based XMT, X-rays are generated by accelerating the electrons in a strong electric field through the collision of electrons from a cathode (source of

electron) to anode (metallic target such as tungsten block on a copper support). After collision, some electrons achieve higher energy than others and consequently knock out the electrons of lower energy from the inner shells of the target atoms. The higher energy electron fills up the vacant place and produce X-rays (Betz et al. 2007). Although desktop-based XMT can produce good-quality image from micron to submicron level, synchrotron-based XMT may perform well below 5 μm spatial resolution. Higher resolution and lower acquisition time makes synchrotron superior over desktop-based XMT. Samples can be imaged within a short period of time due to the wide energy range (4–200 keV) of synchrotron facility. Higher photon flux allows imaging with very narrow range ($\Delta E/E \rightarrow 10^{-2}$–$10^{-4}$) and advantageous for both quantitative absorption and phase contrast (Betz et al. 2007).

Detailed comparison between synchrotron and commonly used desktop-based XMT is summarized in Table 6.1 and their assembly and working principles are shown in Fig. 6.2.

6.3 Image Processing and Data Handling

The device for XMT imaging system consists of an X-ray source (mono or polychromatic), stage (fixed or rotational) containing sample holder and an X-ray detector. The X-ray detector transforms X-rays into visible light and transferred through optical lenses to CCD camera (Chaunier et al. 2007).

The energy decrease during exposure of a test sample to X-ray beam is called as attenuation. Attenuation coefficient is the term which describes how easily an X-ray beam will penetrate through a test sample, when exposed. The sample which is transparent to the X-ray beam showed small attenuation coefficient, on the other hand, large coefficient is the indicator of dense material. Equation 6.1 shows that the intensity of colliding photons exponentially reduces and directly related to the energy of the X-ray beam (Curry et al. 1990).

$$I = I_0 e^{-\mu_m Z \rho} \tag{6.1}$$

where I = intensity of photons through the matter, μ_m = mass attenuation coefficient, (in $mm^2\ g^{-1}$ ($M^{-1}\ L^2$)), Z the thickness of the matter (in mm (L)) and ρ is the material density (in g mm^{-3} (M L^{-3})).

The absorption of X-rays is different for different material depending on the material density, which is expressed as X-ray computed tomography (CT) number. In XMT analysis, the test material is exposed by X-rays from a specific direction emitted from X-ray source. The intensities of attenuated X-rays passing through a test object are first measured by detectors and used in the reconstrcution of digital image of the scanned object using CT numbers. The CT number depends on the linear attenuation coefficient which is further expressed by the brightness data of the obtained image. The CT number is defined as follows (Eq. 6.2):

Table 6.1 Comparison of synchrotron-based XMT and desktop XMT. (Betz et al. (2007); Mamlouk and Guessasma (2013); Kotwaliwale et al. (2014))

Synchrotron-based XMT	Desktop-based XMT
Monochromatic X-rays in a parallel beam geometry	Polychromatic X-rays operate with cone-geometry using raw spectrum from X-ray source
Higher resolution and lower acquisition time	Comparatively low resolution and high acquisition time
10–100 times faster	Comparatively lower
Lower construction error to build 3D image due to the use of filter-back projection algorithm for volume construction	Cone-beam construction method used which give high construction error, errors increase with distance from the central slice
Samples can be analysed at submicron level. Samples below 5 μm spatial resolution usually analysed using synchrotron	Not suitable for below 5 μm spatial resolution, gives blurry 3D images
Better resolution due to homogeneous signal	Lower resolution due to heterogeneous signal
Use of monochromatic source allows the selection of specific X-ray energy suitable for analysis	Selection of X-ray energy is not possible due to the use of polychromatic source
Smaller beam size restricts to use for small sample, if the dimension of the sample being equivalent to the beam size, this method is not suitable	Large beam size facilitate the use for large sample
Improved qualitative and quantitative analysis	Still good enough and comparable with the quality of synchrotron
High-resolution images with higher pixels but requires large storage capacity	Comparatively low-resolution images with low pixel density thus suitable for small storage capacity
Use of filter-back projection algorithms for 3D features offers low construction error	Cone beam construction method used to make, which usually give construction errors depending on the distance from the central slice
Fewer artefacts. Use of high energy and parallel beam geometry ensures final images free of geometrical and beam hardening artefacts	More artefacts: bright and dark streaks
Costly and needing large space	Comparatively cheap and requires small space

$$CT\ number = k \times \frac{\mu - \mu_{\mathrm{w}}}{\mu_{\mathrm{w}}}, \tag{6.2}$$

where

μ linear X-ray attenuation coefficient of object (m^{-1})
μ_{w} linear X-ray attenuation coefficient of water (m^{-1})
k constant (1000)

X-rays does not fully attenuate when passing through an object thus photons of X-rays transmitted through different layers of the object. X-ray converter called phosphor screen stops X-rays to reach to the imaging medium and finally produce visible output which is proportional to incident X-ray photons. The intensity of the transmitted photon creates different contrast in radiographs while casing protects

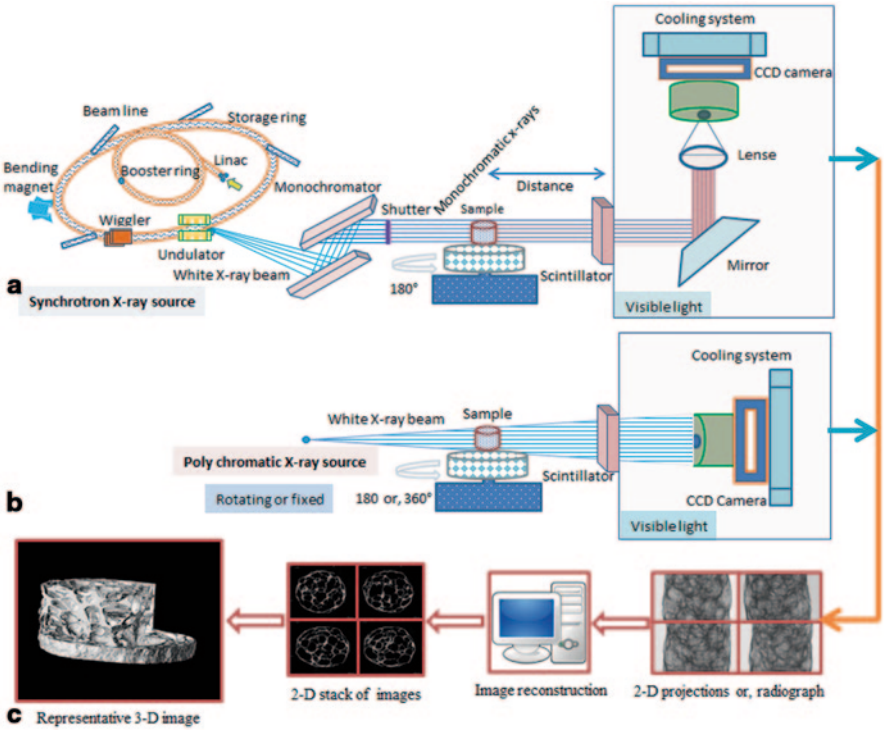

Fig. 6.2 Schematic drawing showing assembly and principle of **a** synchrotron and **b** desktop *XMT* **c** overview of image processing

the imaging medium from other visible radiation. Hence, the obtained image produced with X-ray imaging is a transmitted image rather than reflected image which is found in conventional visible light imaging method. The quality of the X-ray image depends on the consisting element mentioned above. However, recent developments in X-ray imaging elements such as X-ray source with small focal spot, high-resolution CCD device and image intensifier make this imaging system more convenient and induces better quality.

In X-ray imaging system, X-rays come either from radio-active substance (monochromatic X-ray source) or from commonly used X-ray tube (polychromatic X-ray beam) in which X-rays is produced by interaction between energetic electron and target atom in a vacuum place. During scanning, radiographs are produced by scanning of sample by rotating the sample over 180 or 360° with a small angular increment in an axis perpendicular to the X-ray beam. Different radiographs obtained for different angular rotation differ from each other as they have different attenuation value depending on the interior structure and density. The typical X-ray parameters such as source voltage (kV or keV or kVp) and source current (μA or mA) have strong influence on the emitted X-ray photon. The lower energy photons are attenuated more readily than the higher energy photons thus CT value increases

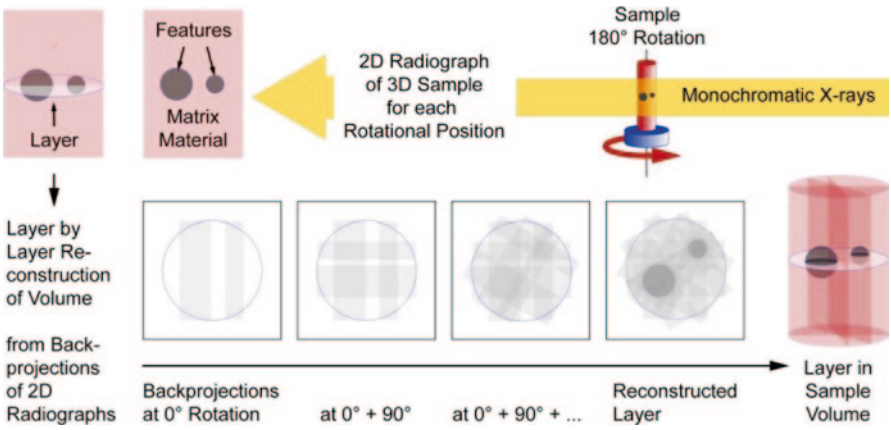

Fig. 6.3 Illustration of data acquisition and reconstruction of 3D image from 2D slices. (Adapted with permission from Betz et al. (2007))

with decreasing the source voltage. By controlling the max voltage, current and exposure time with manually adjustable hardware, XMT can produce images with varying intensity depending on the object properties. After X-ray exposure into the object, attenuated X-rays transmitted to the sensing film and form object image. Like conventional photography, high-resolution X-ray image is obtained after developing the film. The series of 2D radiographs are later combined using an appropriate mathematical algorithm (cone beam and back-projection software) and reconstruct a 3D data set consisting of a stack of 2D cross-sectional images. A series of 2D slices are obtained maintaining a constant distance in between two slices with a thickness of 1 voxel (Babin et al. 2007). Special software could be utilized for reconstruction of cross sections up to 1 μm resolution for a desired orientation of the plane of cut (Trater et al. 2005). The principle of data acquisition and reconstruction is shown in Fig. 6.3. Series of multiple 2D images obtained by XMT provides more structural information than the single 2D image obtained by SEM or optical microscopy (Trater et al. 2005).

6.4 Imaging of Cellular Solid Foods by XMT

For successful structural characterization and quality imaging, selection of right imaging parameters and accurate data processing is important. Thus, we have selected and summarized X-ray measurement parameters used to characterize the microstructure of various cellular solid foods such as cookies, crispy bread/roll (Table 6.2), extrudate snacks, breakfast cereals (Table 6.3) and some other cereal-based foods (Table 6.4). For cookies, X-rays generated mostly at 40–80 kV voltage and 100–180 μm, while for extrudates preferred voltage and current was 20–60 kV/100–250 μm so that maximum possible features of the sample could be

Table 6.2 X-ray parameters used in cookies, crispy bread and roll

Application: cookies, crispy bread and roll	Type of XMT	Voltage (kV or KeV) Current (μA or mA) Rotation and rotation step (°) Total scanning time (min or s) Image pixel size (μm) Exposure time (s or ms)	Structural analysis
Determination of cellular structure of commercial extruded corn ball and short dough wheat flour biscuit (Chevallier et al. 2014)	Skyscan 1174 and ESRF	50 kV and 17 keV, 180 μA, 75 and 2–15 min, 6.5, 16.2, 25.8 and 7.5 μm, 1600 and 100–200	Relative density, cell distribution, cell wall distribution, connectivity index, void volume and porosity
Correlation between microstructure, texture and sensory properties of commercial biscuits and breadsticks (Frisullo et al. 2010)	Skyscan 1172	59 kvP, 167 μA, 20 min, 180°(0.70), 15 μm, 147 ms	Object volume, surface/volume ratio, fragmentation index, structure model index, structure separation and degree of anisotropy
Microstructural properties of extruded crisp bread from whole grain rye flour (Gondek et al. 2013)	SkyScan 1172	49 kev, 200 μA, 180°(0.4), 21 min, 5.9 μm	Porosity, closed porosity, surface/volume ratio, cell diameter, structure thickness, Euler number and degree of anisotropy
Microstructure of crispy breads made of wheat, rye and rice flour (Herremans et al. 2011)	SkyScan 1172	40 and 59 kV, 200 and167 μA, 70 and 60 min, 26.43 and 5.91	Porosity, cell diameter, degree of anisotropy and matrix thickness
Effect of proving condition on crispiness of crispy roll (Primo-Martin et al. 2010)	Skyscan 1072	50 kV, 100 μA, 180°(0.45)	Porosity, cell size, object volume, cell diameter, cell wall thickness, cell density, sphericity of cells, aspect ratio of cell and cell equivalent diameter
Modelling for water migration in bread roll (Voogt et al. 2011)	Skyscan 1072	50 kv, 100 μA, 180°(0.45)	Porosity, cell wall thickness and water migration

Table 6.3 X-ray parameters used in extruded snacks and breakfast cereals

Applications: extruded snacks and breakfast cereals	Type of XMT	Voltage (kV or KeV) Current (μA or mA) Rotation and rotation step (°) Total scanning time (min or s) Image pixel size (μm) Exposure time (s or ms)	Structural analysis
Structure of rye flour extrudates at different temperature, moisture and screw speed (Chanvrier et al. 2009)	Skyscan 1172	40 kV, 100 μA, 180° (0.4), 45 min, 6 μm	Cell distribution, cell wall distribution, structure separation and structure thickness
Fibre and whole grain content on the quality attributes of extrudates (Chassagne-Berces et al. 2011)	Skyscan 1172	40 kV, 180°	Porosity, cell size, cell distribution and cell wall thickness
Microstructure of soy protein fortified corn starch extrudates (De Mesa et al. 2009)	Skyscan 1072	20 kV, 100 μA	Total void area and cell wall area
Microstructural properties of protein-rich sorghum snack (Devi et al. 2013)	Skyscan 1072	40 kV, 100 μA	Cell diameter, cell wall thickness and cell number density
Quality assessment of extruded breakfast cereals made of wheat (Herremans et al. 2011)	SkyScan 1172	30 kV, 200 μA, 108 min, 0.45 μm	Porosity, cell diameter, matrix thickness, connectivity density and degree of anisotropy
Relation between microstructural and textural properties of apple pomace-corn flour extrudates (Karkle et al. 2012a, b)	Skyscan 1072	40 kV, 244 and 248 μA, 180° (0.9 and 1.35), 1 and 1.34 s	Cell size, cell wall thickness and void fraction
Effect of extrusion process variables and whey protein isolate addition on barley extrudates (Kirjoranta et al. 2012)	Nanotom 180NF	80 kV, 150 μA, 360°(0.25), 6.25 μm	Porosity and cell wall thickness
Effect of salt and sugar on corn–wheat extrudates Pitts et al. 2014)	Skyscan 1172	60 kV, 167 μA, 360°(0.3), 20.7 μm, 79 ms	Cell size and cell wall thickness
Cellular structure WPI and polydextrose added wholegrain barley extudates (Penttilä et al. 2011)	Nanotom180NF	60 kV, 200–360 μA, 360°(0.25), 450 and 766 nm	Presence and position of starch in the matrix and void volume
Structure of starch extrudates using 3D watershed algorithm (Plews et al. 2009)	Phoenix X-ray systems (GmbH)	14.25 and 16.25 μm	Porosity, cell wall thickness, cell size, cell size distribution and void fraction
Textural and microstructural properties of soy protein–corn starch extrudates (Zhu et al. 2010)	Skyscan 1072	20 kV, 100 μA, (0.45)°, 60 min, 10.94 μm, 2240 ms	Void fraction, void cell wall and cell wall area

Table 6.4 X-ray parameters used in other cellular foods

Application: other cereal foods	Type of XMT	Voltage (kV or KeV) Current (μA or mA) Rotation and rotation step (°) Total scanning time (min or s) Image pixel size (μm) Exposure time (s or ms)	Structural analysis
Relation between texture and structure of corn flakes (Chaunier et al. 2007)	ESRF	15 μm	Cell number, cell size, cell size distribution, cell wall size and cell wall size distribution
Permeability of French bread crumb and expanded structure (Chaunier et al. 2008)	ESRF	1. 20 μm	Porosity, volumetric cell, relative density, cell size, cell size distribution and 3D particle size distribution
	Nanotom from Phoenix Xray	2. 7 μm	
Mechanical characterization and modelling to study the fragmentation of commercial airy and brittle product (Guessasma and Hedjazi, 2012)	ID19 beamline (ESRF)	7.46 μm	Porosity, cell size, cell size distribution, cell wall thickness and relative density
Mechanical modelling of food degradation to understand the starchy breakfast cereal structure (Hedjazi et al. 2014)	ID19 beamline ESRF	17.6 keV, 6.47 μm	Porosity, cell size, cell size distribution, cell wall thickness and relative density
Density determination of white and multigrain bread, cupcake, muffin, cereal bar, bread roll and cookies (Kelkar et al. 2011)	MicroCT 40	45 kVp, 177 μA	Porosity, apparent and true density
Cellular structure of chocolate muffins (Lim and Barigou, 2004)	Skyscan 1072	100 kV, 96 μA 180°(0.9), 30–45 min, 10–20 μm	Void volume, surface/volume ratio, cell wall thickness, connectivity index, cell number, cell area, cell diameter and degree of anisotropy of solid and air phase
Airy structure of breakfast cereals (chocapic, golden graham, miel pop, corn flakes) (Mamlouk and Guessasma, 2013)	Beamline ID19 ESRF	7.46 μm	Object volume, relative density, cell size, cell wall thickness, thickness dispersion, cell size dispersion and fragment dispersion
Microstructure and modelling of commercial wafer at different compression strain (Mohammad et al. 2014)	Phoenix v-tome-x "s" X-ray	80 kV, 125 μA, 5 μm	Porosity and internal structure change in deformation

Table 6.4 (continued)

Application: other cereal foods	Type of XMT	Voltage (kV or KeV) Current (µA or mA) Rotation and rotation step (°) Total scanning time (min or s) Image pixel size (µm) Exposure time (s or ms)	Structural analysis
Improving shelf life of cake and correlation between texture and cell structure of chocolate cake (Sozer et al. 2011a, b)	Skyscan 1172 and 1072	40 kV, 250 µA, 180°(1.33), 15 min, 23.3 µm, 1.3 s	Cell number, cell area, cell radius, density, cell size distribution, cell density, cell wall thickness, cell wall thickness/cell diameter ratio, fragmentation index and polydispersity index
Effect of baking on pound cake structure (Wilderjans et al. 2010)	HOMX 161	62 kV, 0.56 mA, 187° (0.5), 40 µm	Cell size, cell wall thickness and cell distribution
Microstructure of spaghetti during drying (Zhang et al. 2013)	Skyscan 1172	59 kV, 167 µA, 180° (0.5), 14–15 min, 1.9–3.3 µm	Axial and radial shrinkage, shrinkage rate and anisotropic shrinkage

ESRF synchrotron at European Synchrotron Radiation Facility

captured. Generally, higher voltage and/or higher current result in saturated image (i.e., photons of X-ray are not fully attenuated to show the optimum contrast between void and solid). On the other hand, use of lower voltage and current than the required limits could result in a darker image and loss of contrast which would disable accurate image analysis (Kotwaliwale et al. 2014).

6.4.1 Biscuits, Cookies and Crackers

Biscuits, cookies and crackers are low-moisture baked products where they contain high levels of fat, sugar and/or salt. In biscuits and cookies, gas cells of varying size and shape exist within the starch, fat and sugar matrix (Baltsavias et al. 1999). Structure, texture and sensory properties of cookies and biscuits mainly depend on the sugar content as it incorporates air into the fat and reduce the dough viscosity (Pareyt et al. 2009). Addition of fat in cookie and biscuit recipe affects volume due to air encapsulating capacity of fat but also provides tenderness and improve flavour intensity (Maache-Rezzoug et al. 1998; Rodríguez-García et al. 2013). The effect of fat and sugar on cookie structure with XMT was first studied by Pareyt et al. (2009). Microstructural analysis of cookies of 45.5 mm inner diameter was done with Philips HOMX 161 (Philips, Eindhoven, Netherlands) X-ray imaging system with a voltage of 68 kV and a current of 0.51 mA. The samples were scanned with an angular rotation of 180° and a 0.5° angular increment. Total image acquisition time was 15 min and the resolution of resulted images was 91 μm. Image reconstruction was done with NRecon reconstruction software (Skyscan NV, Kontich, Belgium). Feldkamp algorithm was utilized in reconstruction software. ImageJ software was used to analyse the 3D digital images and the quantitative data were obtained. Otsu thresholding was used for segmentation (greyscale images converted to black and white) for each voxel of the image by determining the void space or solid material. To eliminate any edge effects, artefacts and cutting damage, a rectangular region of each cookie sample was extracted from the middle part of the scanned region. 3D granulometric analysis was performed using CTAn analysis software (Skyscan NV) where volumetric mean cell size, mean cell wall thickness and their distributions were obtained. The degree of anisotropy of cells and cell walls was calculated based on mean intercept length and Eigen analysis and finally, the percentages of closed porosity were determined.

Increasing the amount of fat from 8.7 to 15.8% in the dough of sugar snap cookies increased porosity from 8.7 to 14.5%. However, no effect was seen on closed structure which clearly showed that cookies, in general, had an open structure. Increasing the fat content, increased the swelling of air cells during baking which further led to an increase in mean air cell size (643 → 719 μm). Number of air cells and average cell wall anisotropy were inversely related to the fat level. Cookies with reduced fat level had less spread and small diameter. Increasing the fat content did not influence the cell wall thickness but caused a reduction in the cookie break strength. On the other hand, increased sugar levels (17.6 → 31.2% in the dough)

increased porosity (37.3 → 46.4 %), mean cell size (399 → 719 μm) and cell wall thickness (419 → 535 μm) and reduced cookie height (10.6 → 7.1 mm) but no influence was observed on density and hardness (Pareyt et al. 2009). The mean cell size and cell wall thickness, and their distributions, were influenced by sugar level due to the influence of sugar on dough viscosity. Higher sugar levels in the recipe resulted in more and longer oven rise. A strong correlation between breaking strength and cell wall thickness observed particularly for sugar content varying between 18 and 26 %.

Soft wheat flour is generally preferred for cookie and biscuit making as it spreads faster and gives larger cookies compared to cookies from hard wheat flour possibly due to lower protein content and damaged starch levels (Pauly et al. 2013a). High levels of protein and damaged starch in the flour increased the water absorption level and thus increased dough viscosity (Gaines and Finney 1989). Wheat puroindolines (PINs) are proteins responsible for differences in wheat endosperm texture (Pauly et al. 2013b). When PINs are in their wild form, wheat kernel has a soft texture and when PINs are absent or mutated, wheat kernel has a hard texture (Pauly et al. 2013a). Semisweet biscuits were prepared from model flour consisting of starch and gluten fractions with varying PIN levels. PINs are located more at air–water interfaces (Biswas et al. 2001) and exhibit excellent foam-forming properties (Dubreil et al. 1997). Porosity and microstructure of biscuits were analysed by XMT (Bruker microCT, Kontich, Belgium) at 70 kV and 500 μA. The biscuits were scanned over an interval of 0–180° with 0.5 angular increments with a spatial resolution of 100 μm. The images were reconstructed by NRecon software (Bruker microCT, Kontich, Belgium) by using modified Feldkamp algorithm and converted into binary images by using Otsu thresholding to determine pore or solid material for each voxel in the image by utilizing ImageJ freeware. The biscuits made of higher level of PIN gave higher porosity, where porosity and matrix thickness were negatively correlated. Yang et al. (2012) studied on the impact of flavour solvent on biscuit structure, flavour stability and formation of 5-hydroxymethyl-furfural (HMF). Propylene glycol (PG) and triacetin (TA) are commonly used flavour solvents in food industry. Both PG and TA may also have an effect on the physical properties. For example, PG can act as a plasticizer and provide stickiness for hard candies (De Roos 2007) whereas TA gives a softer structure to chewing gum (Yang et al. 2012). The microstructure of biscuits made with TA and PG was analysed by Pheonix Nanotom NF180 X-ray CT System (GE Sensing & Inspection Technologies GmbH, Wunstorf, Germany) where 1440 projection images collected with a 360° rotation using electron acceleration energy of 80 kV, current of 180 μA and resolution of 22.5 μm. The obtained images were analysed by "Image J" processing software v1.44. The average pore diameter of PG biscuits was smaller than TA biscuits (0.105 vs. 0.11 mm) whereas average porosity of PG biscuits was greater (49.5 vs. 45.4 %). Both flavour compound and HMF was greater in TA biscuits due to restricted diffusivity associated with lower porosity.

Multicomponent cellular solid food products with a dry shell and wet filling inside are challenging due to water migration from wet filling towards the dry shell. A good understanding of relation between the microstructure and water mobility

will guide to develop moisture barrier systems which will prevent the undesirable water migration between the two different phases (Van Dalen et al. 2007a). Crackers are rather dry, thin and crisp which can be produced either leavened or unleavened. For leavened crackers the structure is mainly influenced from dough proofing time besides baking conditions and ingredients. Crackers with different porosity were made by changing the proofing time (10–130 min; Van Dalen et al. 2007b). Quantitative information related to inner structure of cracker cellular matrices was determined by 3D image analysis obtained from Skyscan 1072 XMT (Skyscan, Belgium) with a power setting of 50 kV and 100 μA. Image contrast was adjusted based on absorption of X-rays by fat, carbohydrate and air within the cracker matrices. Images were acquired with a rotation of 180° and 0.45° step size for 40 min. Image processing and analysis was done by MATLAB and 3D visualization was done by isosurface rendering (Amira 4.1 from Mercury Computer Systems). Moisture transport in crackers was modelled from the actual imaged samples. Air cells were segmented from the solid matrix with a manual thresholding by using a watershed transform of the Euclidean distance map of the solid material. During this process isolated air cells smaller than 40 voxels were removed. Watershed transform of the image-created boundaries which were further used to mark each air cell and the solid matrix surrounding it. The marked pore images enabled to evaluate volume, surface area and location of air cells. The relations between adjacent air cells were described by pore-to-pore properties. The network model was used to calculate the resistance between air cells. A simple model (Eq. 6.3) was developed to evaluate the point-to-point resistance in each cereal matrix. The conduction between two air cells (pores i and j) were defined by

$$C_{ij} = \left(Ad_{ij} + \frac{Ai_{ij}}{100} \right) \times \left(\frac{1}{SA\_pore} \right), \tag{6.3}$$

where *Ad* is the area between direct connected pores, *Ai* is the area of indirect connected pores and (*SA*_pore) is the pore surface. The point-to-point resistance was calculated by using eigenvalues and eigenfunctions of the Laplacian matrix associated with the network (Wu 2004).

Increasing the cracker proofing time increased porosity and average air cell diameter which varied between 0.4–0.6 mm for proofing times 10–60 min and 1.2–1.3 mm for proofing times 115–130 min. Air cells which are more far away from each other had larger resistance than the two adjacent ones. The average pore-to-pore resistance of samples with large air cells was lower than the samples containing small air cells. The authors concluded that the obtained quantitative microstructural information by XMT could be utilized as an input to predict moisture diffusion.

Structural features of cellular solid matrices have an impact on liquid migration. Advanced noninvasive image analysis techniques can be utilized to develop predictive models to link structure and material properties to have better control over liquid migration**.** Esveld et al. (2012) developed an effective diffusivity model by utilizing cellular decomposition-based network model to study the dynamics of moisture sorption in crackers produced with different structures by varying proof-

ing time (10–115 min). Images were obtained with a Skyscan 1072 desktop XMT system (Skyscan, Belgium) by using power setting of 50 kV and 100 μA under different rotations over 180° with a step size of 0.45° and a resolution of 7.8 μm. The water vapour transport between air cells and open pores and the sorption kinetics in the lamellae were simulated using 3D network model and then compared with experimental sorption results of cracker with distinct structures (fine vs. coarse) yet identical recipe. Predictive models had good correlation with experimental results. This study revealed that differences in relative vapour conductivity for distinct structures such as fine vs. coarse crackers (33 vs. 64%) depends on the open surface fraction of the cell and porosity (18 vs. 22 and 66 vs. 78%, fine vs. coarse, respectively). Therefore, shelf life of the cracker products could be increased based on liquid migration by decreasing the open surface fraction between the cells as it would decrease the water transport rate between the cells.

6.4.2 Extruded Products

Extrusion processing is a high temperature short-time method for producing cellular solid cereal foams which involves consecutive steps of mixing, shearing and formation. Operational parameters (e.g., screw speed, temperature, and feed rate) and ingredient properties have an impact on degree of expansion, micro-/macrostructure and texture. During extrusion processing irreversible physicochemical changes occur at the polymer level such as denaturation of proteins and formation of starch–lipid, protein–lipid and protein–protein complexes (Sozer and Poutanen 2013). Extruded solid foams consist of a continuous starch matrix and a discontinuous protein phase. Nevertheless, there is an increasing demand to produce appealing extruded cereal foams with high dietary fibre content yet good structural and textural properties. This is a challenging engineering task as more than 10% addition of insoluble fibre such as bran interferes with the expansion creating dense structures with hard, non-crispy textures. In this part of the chapter, we will first provide examples from the literature related to starch-based extruded foam structures and then we will present how insoluble fibre addition affects structure. The link between structure and textural properties will be demonstrated based on noninvasive XMT imaging techniques and data interpretation.

6.4.2.1 Microstructure of Starch-Based Extruded Solid Foams

Agbisit et al. (2007) determined the relation between mechanical properties (e.g., compression modulus, crushing force and stress and crispness work) and microstructure (e.g., average cell diameter, cell wall thickness and cell number density) of cellular corn starch extrudates by SkyScan 1072 (Aartselaar, Belgium) desktop XMT (20–100 kV/0–250 μA; Agbisit et al. 2007). A moderate to high correlation ($r = 0.48–0.81$) was found between microstructural and mechanical properties. Gib-

son–Ashby model was used to understand foam mechanics and to associate microstructural properties to sensory properties. Gibson–Ashby model was simplified as:

$$\frac{t_{\text{wall}}}{l} = 1.4\,(1-\phi)\frac{\rho}{\rho_S} \tag{6.4}$$

where l is edge length, t_{wall} is wall thickness and ρ/ρ_s refers to relative density. Relative density value is less than 0.3 for true solid foams and more than 0.3 for isolated pores. Agbisit et al. (2007) suggested using a correction factor called drainage factor (Ø) due to drainage of solids from the walls to the edges which reflects the volume fraction of the solid material present in the cell edges (Eq. 6.4).

In general, extrudates have closed air cells varying in structural architecture based on operational parameters such as the amount of water feed and screw speed. Increasing screw speed gave increased cell diameter, decreased cell number density but had no effect on cell wall thickness. Increased cell diameter and decreased cell number density gives expanded extrudates as reported by Trater et al. (2005). Mechanical properties such as crushing force and crispiness work was negatively correlated with cell diameter by $r=-0.79$ and $r=-0.81$, respectively. Mechanical properties of starch-based extrudates were dependent on the combined effect of cell wall thickness and diameter. Extrudates with higher ratio of cell wall thickness/diameter (t_{wall}/D=thicker cell walls and smaller cell diameters) had higher compression modulus and crushing stress compared to the extrudates of lower t_{wall}/D (thinner walls and larger cell diameters; Agbisit et al. 2007). Babin et al. (2007) used synchrotron (European Synchrotron Radiation Facility, F-38, Grenoble) radiation to characterize the microstructure of starchy extrudates made of amylopectin (99%) and amylose (70%) rich corn starch and blend of corn starch containing 47 and 24% amylose in the mixture. Extrudate samples were scanned to produce 900 (for each scan) 2D representative images with a scanning time of 10 min. ImageJ (http://rsb.info.nih.gov/ij/) and Aphelion (ADCIS-SA, 14-France) softwares were used to analyse 3D images. To eliminate the edge effect, artefacts and cutting damage, VOI was selected at the centre of the sample (Fig. 6.4). Due to good contrast between void and solid phase (two distinct peaks in the picture), determination of the threshold value for segmentation was easier.

Average cell size, cell wall thickness distributions and their average volumic values were determined using 3D granulometry analysis of highly contrasted 3D image. Average cell size and average cell wall thickness of extrudates made from various maize starches (high amylose and waxy) varied between 0.2–5 and 0.08–63 mm, respectively. Despite the same relative density the extrudates exhibited different microstructures determined by XMT and further data analysis. Coarse (larger cells) structures had high average cell size (inhomogeneous distribution) along with thicker cell walls which yielded less mechanical resistance.

Pore size distribution of starch-based corn flour extrudates was determined and compared by MRI and XMT imaging (Horvat et al. 2014). Extrudates with different pore sizes were produced by varying mechanical energy input (163-170-247 Wh/kg; Fig. 6.5). Commercial cabinet cone-beam XMT (μCT 50, Scanco Medical AG,

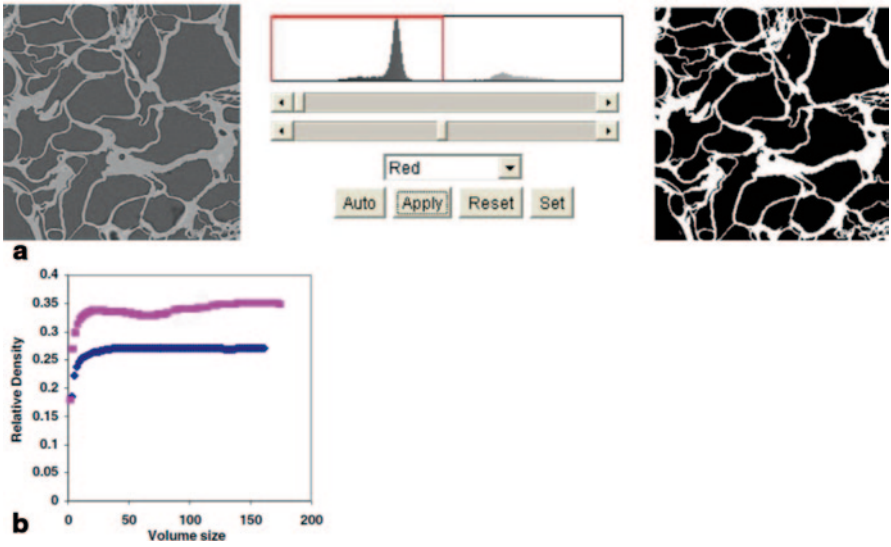

Fig. 6.4 2D. **a** Illustration of thresholding of *XMT* image obtained with synchrotron facility at *ESRF;* **b** determination of representative volume element *(RVE)* for different (*pink* and *dark blue*) sample. (Adapted with permission from Babin et al. (2007))

Brüttisellen, Switzerland) was used, where cone beam X-ray generated from a 4 µm focal-spot X-ray tube. Reconstructed projected images (1233 slices) of 1536 × 1536 matrix were obtained with a 15.05 mm field of view. A sample holder of inner diameter of 14 mm was used to place the sample inside the XMT. A cylindrical region of Ø×(14 × 12) mm was scanned at 9.8 µm resolution (= voxel size). Scanning time (4.5 s) was same for all samples at 55 kVp (6 W). This study showed that starch-based extrudates could have different pore size distribution even with similar expansion indices. Mechanical properties of extruded products are influenced by both

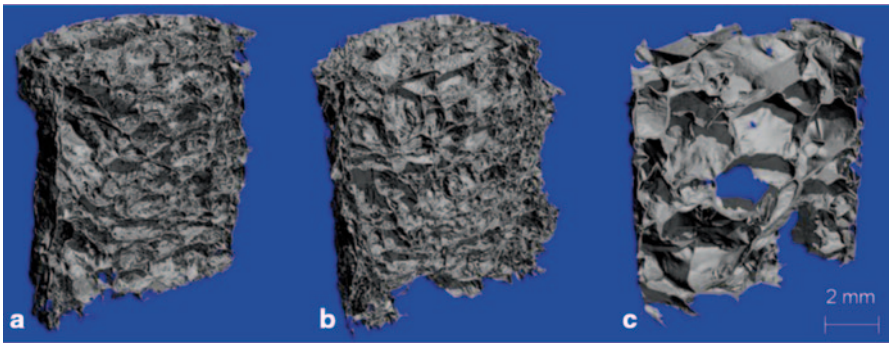

Fig. 6.5 Reconstructed *XMT* images showing different pore structures at *SME* of **a** 247 Wh/kg, **b** 170 Wh/kg and **c** 163 Wh/kg. (Adapted with permission from Horvat et al. (2014))

expansion and porosity which can be used to predict sensory responses. Even with different spatial resolution and acquisition technique both MRI and XMT techniques showed same trends. Volume distribution ranges varies between 0.5–100 mm^3 and 0.5–200 mm^3 for MRI and XMT, respectively. In both techniques, largest pores and thicker cell walls were obtained with a specific mechanical energy (SME) input of 163 Wh/kg. Due to better spatial resolution and limit in data processing step XMT could detect more small pores than MRI (e.g., 0.01 mm^3 in XMT vs. 0.1 mm^3 in MRI). In general, the cell wall thicknesses distributed between 0.01and 0.1 mm, a cell wall thickness of 0.025 mm was mainly observed. The sample extruded at 163 Wh/kg SME had thicker cell walls with a maximum at 0.04 mm.

6.4.2.2 Microstructure of Dietary Fibre Added Extruded Solid Foams

Robin et al. (2010; 2011a, b, c; 2012a, b) made an extensive study on structural and textural effects of wheat bran supplemented extruded solid foams. The authors used 1172 desktop μCT for scanning and CTAn software for data processing (Skyscan, Kontich, Belgium). Grey level images were segmented at 40 and shrink-wrap function was used to adjust to the surface of the extruded pellets through which VOI was selected. The ratio of the volume of pores to the extrudate volume was termed as porosity. Radial expansion anisotropy was found in structures with large and fewer number of cells. Expanded structures with minimal number of cells showed less stress during rupture being less hard in texture. Stress in rupture and density was highly positively correlated. Increased amount of insoluble fibre content in the starchy matrices formed compact structure with higher number of small cells and high surface porosity due to the early burst of air cells at the die exit (Fig. 6.6) which further reduces overall expansion. Wheat flour extrudates with different added bran can have identical porosity but may differ in hardness based on bran addition level, the dimension and orientation of bran within the cell wall (Robin et al. 2012a, b).

Fig. 6.6 3D *XMT* image of refined wheat flour-based extrudates with different levels of added wheat bran (0, 25 and 50%) processed at same extrusion condition (screw speed of 400 rpm, 18% feed moisture and 120 °C). (Adapted with permission from Robin et al. (2011b); Robin et al. (2012b))

The effect of fibre addition on structural and mechanical properties of extruded solid foams strongly depends on the type of fibre sources. For instance, addition of 15% wheat bran into corn flour can significantly decrease the sectional expansion which is associated with increased bulk density (Robin et al. 2012b). On the other hand, addition of same level of soluble fibre such as inulin or guar gum under similar processing conditions does not alter sectional expansion but increase bulk density which is associated with reduced porosity (Robin et al. 2012b). However, Chanvrier et al. (2013; 2014) showed that porosity and average cell size of the extrudates decreased with increased amount of total dietary fibre content regardless of the fibre sources, while opposite trends were reported for hardness. Addition of fibre had less impact on cell wall thickness (Chanvrier et al. 2014). In these studies, two types of base recipes were produced from whole wheat flour and corn flour by adding up to 32% of wheat bran (insoluble dietary fibre) and oat bran (soluble dietary fibre) with extrusion conditions of; feed rate:15 kg/h, temperature profile (90-135-150-160 and 135 °C) and screw speed: 400 rpm. XMT imaging was done with 1172 MCT system (Brüker MicroCT, Kontich, Belgium). Image processing was done using same approaches of Robin et al. (2010). A linear increase of porosity vs. average cell size was reported for both whole wheat- and corn-based extrudates (Chanvrier et al. 2014). In general, crispiness increased with increasing number of pores in the matrix. Corn-based extrudates had lower porosity (59−90%) compared to wheat recipe (82−92%). The average cell sizes varied between 150–600 and 600–1200 µm for corn- and whole wheat-based extrudates, respectively. At wide range of porosity, the number of acoustic events and total energy had a strong link with microstructural attributes (Fig. 6.7). However, when the range became narrow,

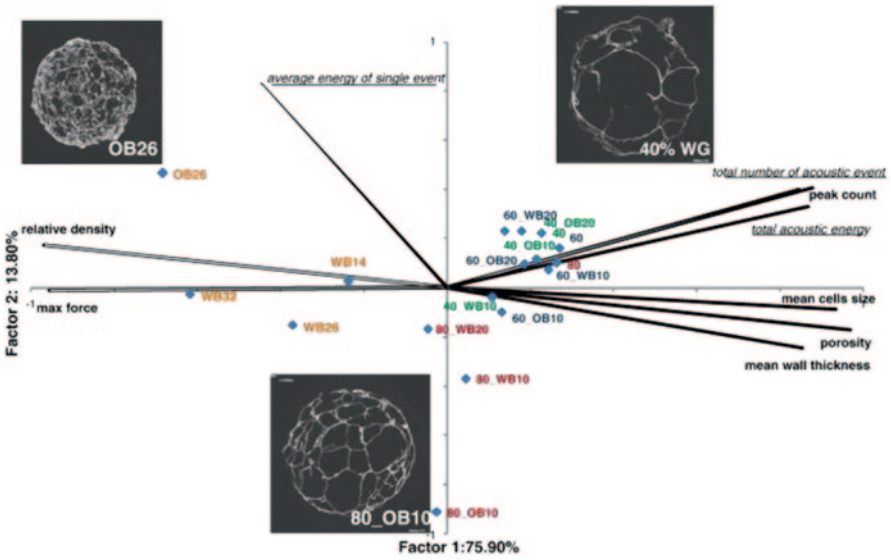

Fig. 6.7 Principal component analysis (*PCA*) of texture, acoustic and structure data of extrudates made of corn and wheat with varying porosity between 55 and 90%. *XMT* images of wheat- and corn-based recipe (*OB*=oat bran; *WB*=whole grain wheat flour). (Adapted with permission from Chanvrier et al. (2014))

the acoustic properties were only linked to number of peaks obtained by mechanical fracture. Therefore, crisp sound produced during the acoustic measurements depended on the organization of cell wall and their ability to break.

The effect of soluble dietary fibre; guar gum (0–10%) addition on physical (texture, expansion, density and pasting), microstructural and starch digestibility of various flour types (potato, corn, rice and wheat) was investigated by Parada et al. (2011). Microstructural analysis was done with SkyScan1072 XMT (SkyScan, Aartselaar, Belgium) with 40 kV/100 setting for better contrast. Extrudates (diameter: 10–18 mm) were rotated 180° with a step size of 0.9° per image. Image reconstruction was done with volumetric reconstruction software Version 2.1, Skyscan). Filtered back-projection algorithm using a cone-beam (Feldkamp) reconstruction was utilized in reconstruction software with a reconstruction time of 4.7 s/cross section. After reconstruction entire cylindrical sample was captured by a set of 2D slices. VOI consisted of 30 consecutive slices from the central portion of each sample. The height of each VOI ranged between 1.6 and 7.2 mm. Several slices of each VOI maintained a constant distance. Threshold value of 35 set to differentiate between void and solid matter in each 2D image. Depending on the image quality, a median rank filter was applied in a 3×3 pixel area followed by a smoothing operation. Microstructural parameters were influenced both by flour type and fibre percentage. Trabecular separation (mm) and trabecular thickness (mm) were affected by fibre percentage. Decreasing effect for degree of anisotropy was reported with increasing percentage of fibre in potato-, rice- and wheat-based extrudates but remained unchanged in corn-based extrudates. Increasing the fibre addition level increased the number of air cells, trabecular number (mm^{-1}), percent matrix volume (%) and matrix surface density (mm^{-1}). Addition of guar gum increased contact area per unit volume of the extrudates and produced weaker, less hard structures. In this study, microstructure of extrudates was related to starch digestibility. The greater the contact area the greater was the accessibility of the matrix for digestive enzyme and the extrudates became more rapidly digestible.

Effect of particle size reduction on the microstructural properties of high fibre extrudates was studied by Alam et al. (2014). Extrudates were made from rye bran varying in particle size (coarse: 440; medium: 143 and fine: 28 μm) with a twin screw extruder. Rye bran has 39−48% total dietary fibre, 13−28% starch and 14−18% protein which enables its extrusion without adding further starch. The interrelation between microstructural (porosity, cell wall thickness/cell diameter ratio and fragmentation index), mechanical (e.g., hardness and crispiness), macro-structural (expansion, specific length and piece density) properties was studied. Decreasing the particle size (440 to 28 μm) significantly improved crispiness by increasing expansion, air cell size and porosity. Microstructural analyses were performed by Skyscan 1172 XMT device (Aartselaar, Belgium) operated at a voltage and current of 40 kV/250 μA to obtain optimum contrast between void and solid matrix. Samples (triplicate of 10 mm radial cut) were rotated over 180° with angular increment 0.7° during the scanning with a pixel size of 11.65 μm to obtain optimum resolution. Total scanning time was 18 min. NRecon reconstruction software (v. 1.6.6) was used to convert 2D cross-section images into 3D image. Beam hardening correction

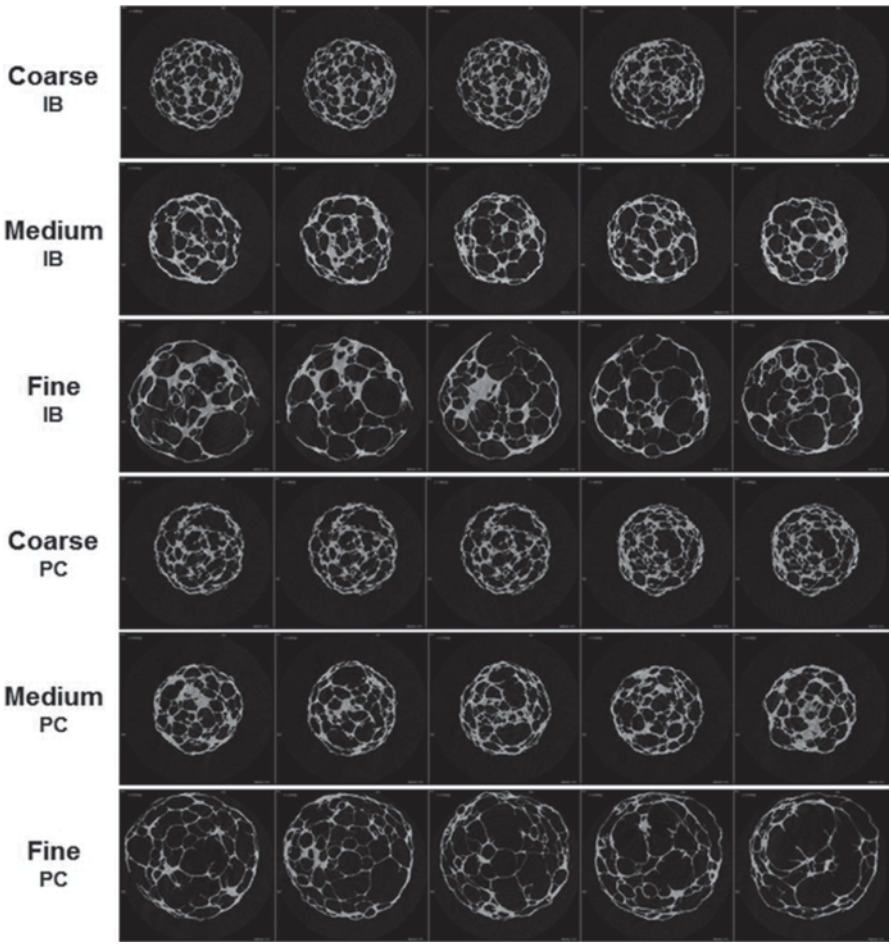

Fig. 6.8 2D *XMT* images of rye bran (particle sizes of coarse: 440 μm, medium: 143 μm and fine: 28 μm) extrudates processed with 17% feed moisture in two different hydration regimens (*IB* = In barrel–water feed and *PC* = Preconditioning) at a screw speed of 500 rpm at 130 °C. (Adapted with permission from Alam et al. (2014))

was set to 40% to minimize artefacts. CTAn software (v. 1.12, Skyscan, Belgium) was used to calculate the microstructural parameters.

It is clear from the representative images (Fig. 6.8) that particle reduction increased the average cell diameter (ranged between 0.49 and 1.17 mm; highest for fine bran) and expansion rate. Reducing particle size from 440 to 28 μm increased the porosity from 64.4 to 83.9%. Early rupture of the precursor air cells caused more small air cells in coarse- and medium-particle-sized rye bran extrudates (≈2800–4000) as compared to fine extrudates (≈1000). The effect of particle size was more profound on cell diameter than on cell wall thickness. Microstructural parameters of coarse and medium-sized bran extrudates were not affected by hydration regi-

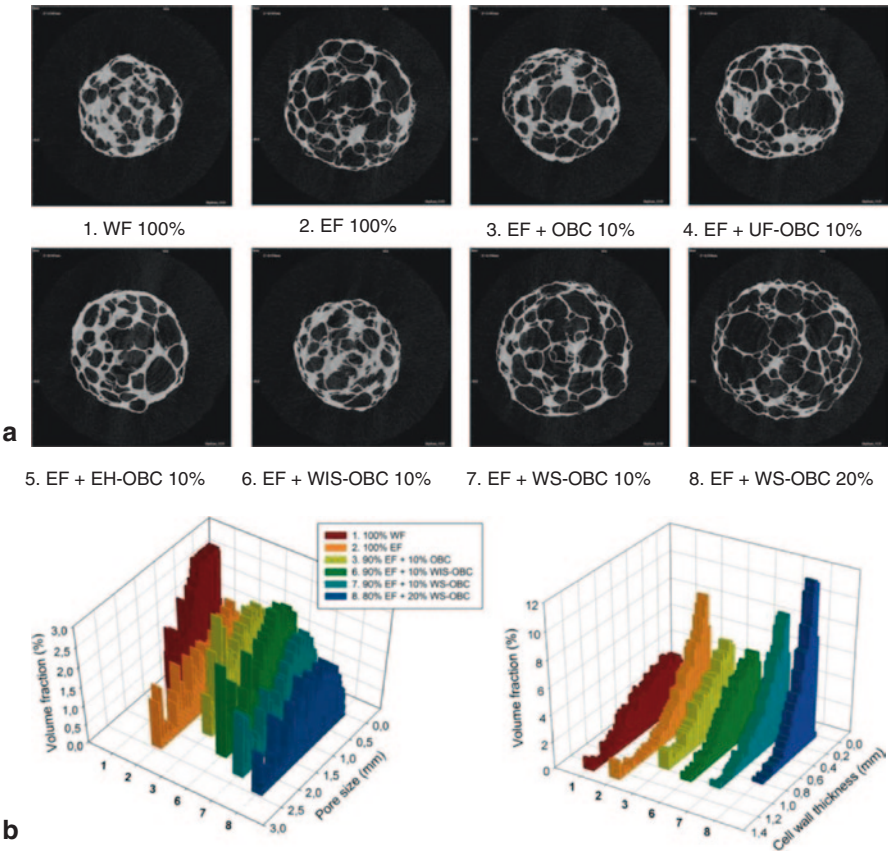

Fig. 6.9 **a** 2D *XMT* cross-section images of extrudates made of different oat ingredients: *WF* wholegrain oat flour, *EF* endosperm oat flour, *OBC* oat bran concentrate, *UF* ultra-fine, *EH* enzyme hydrolysed, *WIS* water insoluble, *WS* water soluble. **b** Pore size and cell wall thickness distributions of the oat extrudates. Data of samples 4 (EF + UF-OBC 10%) and 5 (EF + EH-OBC 10%) exhibited similar results to that of sample 3 (EF + OBC 10%) thus not shown in the plot. (Adapted with permission from Sibakov et al. (2014))

men but preconditioning resulted increased porosity by 6% and cell wall thickness/cell diameter ratio by 50%. Higher connectivity of the pores was confirmed by low fragmentation index values (−0.8 and −4.5 L mm).

Sibakov et al. (2014) studied the effect of differently treated oat bran concentrate (OBC) into 90% defatted oat endosperm flour (EF) extrudates made by twin screw extruder. XMT analyses were performed using similar protocol as of Alam et al. (2014). Representative XMT images are shown in Fig. 6.9a. They reported that extrudates made of untreated OBC (213 μm) had lower porosity (65% vs. 69 and 71%) compared to the extrudates made of fine (32 μm) and enzyme-hydrolysed OBC (111 μm). Addition of 10% OBC increased (0.34–0.42 vs. 0.32 mm) the cell wall thickness compared to 100% EF. The 10% addition of water insoluble OBC

(70 μm) into EF reduced the porosity from 75 to 59%, while the addition of 10% water soluble OBC (37 μm) did not affect the porosity. However, further increase in water-soluble OBC increased the porosity and for 20% addition level porosity reported to be 81%. Moreover, a decreasing trend was observed for average cell wall thickness when increasing the content of water-soluble OBC. The number of small pores was higher in case of water-insoluble OBC added extrudates than that of water-soluble OBC extrudates (10 20%). Thick cell walls with small pore sizes were reported for all treated OBC extrudates except 20% water-soluble OBC added extrudates. Hundred percent whole grain oat flour extrudates had narrowest pore size distribution with small porosity together with large cell wall distribution including mostly thick cell walls. However, extrudates with 20% water-soluble OBC had wider pore size distribution with larger pores and thinner cell walls (Fig. 6.9b). Hence, the microstructural properties of oat bran added endosperm oat flour extrudates depend mainly on the solubility of DF.

6.4.2.3 Microstructure of Protein-Enriched Extruded Solid Foams

Microstructural properties of corn starch extrudates enriched with whey protein isolate (WPI; 0, 6, 12 and 18%) processed at two different water feed (23 and 27%) levels were determined with XMT (Cheng et al. 2007). Increasing the level of WPI increased the foaming effect thus increased the cell density. In general, incorporation of protein gave greater number of smaller cells with thinner cell wall, regardless of water addition level. The effect of water feed on microstructural properties such as average cell diameter, average cell wall thickness and cell number density was not consistent throughout the experiments except cell wall thickness. Cell wall thickness increased from (0.04–0.07) to (0.09–0.27 mm) by increasing amount of water feed from 23 to 27% which further increased hardness (Cheng et al. 2007). Cho and Rizvi (2009) used supercritical fluid extrusion (SCFX) technology for pregelatinized corn-starch-based extrudates supplemented with WPI (0, 3, 6, 12, and 18%). A desktop XMT (Model 1072, 20–100 kV/0–250 μA, SkyScan, Belgium) used to analyse microstructure by setting the voltage 40 kV and resolution 100 μA. Skyscan software was used to produce a set of 2D images to capture whole sample. Later the set of 2D images was partitioned to get the VOI, which consisted of 15 consecutive 2D slices with a constant distance between the slices. Image analysis was performed using one fourth of the cross-sectional area of each 2D slices. Cell perimeter, solid and void areas were calculated using a threshold value of 35, from each slices. Scion Image for Windows (Scion Corporation, MD) was used for the calculation. The analysed microstructural parameters were: average cell diameter, cell wall thickness, void fraction, polydispersity index, cell density per unit total extrudate volume, and cell number density per unit solid volume.

Increasing the level of WPI in SCFX extrudates resulted in lower cell density and reduced volumetric expansion as denaturation of WPI reduced melt viscosity. At highest level of WPI (18 wt%) and SC-CO_2 level (0.75 wt%), the average cell size reduced (600 μm → 310 μm) exceptionally due to heterogeneous nucleation

depending on the blowing agent and on the feed formulation. The cell number density per unit total extrudate volume and cell number density per unit solid volume both decreased with the increasing amount of WPI except 18 % WPI at 0.75 wt% SC-CO_2. On the other hand, the cell number density increased with the increasing amount of SC-CO_2 for each WPI level due to the increased number of gas nucleation.

6.5 Summary and Conclusions

The successful use of XMT in other fields of science (e.g., medical, agricultural, biological and material science) has led its further application in food structure characterization. Cellular solid structures have great impact on sensory properties and associated with also textural-mechanical properties. XMT is able to present rigorous quantitative information related to cellular architecture of solid foods such as cell size and distribution, cell wall thickness, cell connectedness and porosity both in 2D and 3D. The accurate microstructural characterization of cellular solid foods would also help food engineers and scientists to understand and develop links between structure–mechanical–sensory properties. Based on these and the use of numerical simulation technologies together with modelling approaches can be used to design novel food structures and textures. Furthermore, the noninvasive XMT technology does not require tedious sample preparation methods compared to other microscopy technologies such as light microscopy or confocal scanning light microscopy. The continuous development in data processing and equipment manufacturing technologies will enable the use of XMT technology for in-line or on-line food structure analysis during processing.

References

Agbisit R, Alavi S, Cheng E, Herald T, Trater A (2007) Relationships between microstructure and mechanical properties of cellular cornstarch extrudates. J Texture Stud 38(2):199–219

Alam SA, Järvinen J, Kirjoranta S, Jouppila K, Poutanen K, Sozer N (2014) Influence of particle size reduction on structural and mechanical properties of extruded rye bran. Food Bioprocess Tech 7:2121–2133

Babin P, Della Valle G, Dendievel R, Lourdin D, Salvo L (2007) X-ray tomography study of the cellular structure of extruded starches and its relations with expansion phenomenon and foam mechanical properties. Carbohyd Polym 68(2):329–340

Baltsavias A, Jurgens A, Van Vliet T (1999) Fracture properties of short-dough biscuits: effect of composition. J Cereal Sci 29(3):235–244

Barigou M, Douaire M, Morris V, Groves K (2013) X-ray micro-computed tomography for resolving food microstructures. In: Morris VJ, Groves K (eds) Food microstructures: microscopy, measurement and modelling. Woodhead, Cambridge, p 246–272

Betz O, Wegst U, Weide D, Heethoff M, Helfen L, LEE W, Cloetens P (2007) Imaging applications of synchrotron X-ray phase-contrast microtomography in biological morphology and

biomaterials science. I. General aspects of the technique and its advantages in the analysis of millimetre-sized arthropod structure. J Microsc 227(1):51–71
Bhatnagar S, Hanna MA (1996) Effect of talc on properties of cornstarch extrudates. Starch-Starke 48(3):94–101
Biswas S, Dubreil L, Marion D (2001) Interfacial behavior of wheat puroindolines: study of adsorption at the air–water interface from surface tension measurement using Wilhelmy plate method. J Colloid Interf Sci 244(2):245–253
Chanvrier H, Gumy J, Blank I (2009) Food solid foams made from cereals: assessment of the structure of extruded rice by X-ray tomography. Paper presented at the SkyScan user meeting, Bruker microCT, Ghent, 22–24 April 2009
Chanvrier H, Desbois F, Perotti F, Salzmann C, Chassagne S, Gumy J, Blank I (2013) Starch-based extruded cereals enriched in fibers: a behavior of composite solid foams. Carbohyd Polym 98(1):842–853
Chanvrier H, Jakubczyk E, Gondek E, Gumy J (2014) Insights into the texture of extruded cereals: structure and acoustic properties. Innov Food Sci Emerg 24:61–68
Chassagne-Berces S, Leitner M, Melado A, Barreiro P, Correa EC, Blank I, Gumy J, Chanvrier H (2011) Effect of fibers and whole grain content on quality attributes of extruded cereals. Procedia Food Sci 1:17–23
Chaunier L, Della Valle G, Lourdin D (2007) Relationships between texture, mechanical properties and structure of cornflakes. Food Res Int 40(4):493–503
Chaunier L, Chrusciel L, Delisée C, Della Valle G, Malvestio J (2008) Permeability and expanded structure of baked products crumbs. Food Biophys 3(4):344–351
Cheng E, Alavi S, Pearson T, Agbisit R (2007) Mechanical–acoustic and sensory evaluations of cornstarch–whey protein isolate extrudates. J Texture Stud 38(4):473–498
Chevallier S, Réguerre A, Bail A L, Della Valle G (2014) Determining the cellular structure of two cereal food foams by X-ray micro-tomography. Food Biophys 9:219–228
Cho K, Rizvi S (2009) 3D microstructure of supercritical fluid extrudates I: melt rheology and microstructure formation. Food Res Int 42(5):595–602
Curry TS, Dowdey JE, Murry RC Jr (eds) (1990) Christensen's physics of diagnostic radiology. Lippincott Williams & Wilkins, Pennsylvania
De Mesa NJE, Alavi S, Singh N, Shi Y, Dogan H, Sang Y (2009) Soy protein-fortified expanded extrudates: baseline study using normal corn starch. J Food Eng 90(2):262–270
De Roos KB (2007) Selecting the right flavourings for a food product. In: Taylor AJ, Hort J (eds) Modifying flavour in food. Woodland, Cambridge, p 243–273
Devi NL, Shobha S, Tang X, Shaur SA, Dogan H, Alavi S (2013) Development of protein-rich sorghum-based expanded snacks using extrusion technology. Int J Food Prop 16(2):263–276
Dubreil L, Compoint J, Marion D (1997) Interaction of puroindolines with wheat flour polar lipids determines their foaming properties. J Agr Food Chem 45(1):108–116
Esveld D, van der Sman R, Witek M, Windt C, van As H, van Duynhoven J, Meinders M (2012) Effect of morphology on water sorption in cellular solid foods. Part II: sorption in cereal crackers. J Food Eng 109(2):311–320
Frisullo P, Conte A, Del Nobile M (2010) A novel approach to study biscuits and breadsticks using X-Ray computed tomography. J Food Sci 75(6):E353–E358
Gaines C, Finney P (1989) Effects of selected commercial enzymes on cookie spread and cookie dough consistency. Cereal Chem 66:73–78
Gondek E, Jakubczyk E, Herremans E, Verlinden B, Hertog M, Vandendriessche T, Verboven P, Antoniuk A, Bongaers E, Estrade P (2013) Acoustic, mechanical and microstructural properties of extruded crisp bread. J Cereal Sci 58(1):132–139
Hedjazi L, Martin C, Guessasma S, Della Valle G, Dendievel R (2014) Experimental investigation and discrete simulation of fragmentation in expanded breakfast cereals. Food Res Int 55:28–36
Herremans E, Chassagne-Berces S, Chanvrier H, Atoniuk A, Kusztal Z, Bongaers E, Verlinden BE, Jakubczyk E, Estrade P, Verboven P, Nicolaï B (2011). Possibilities of X-ray nano-CT for internal quality assessment of food products. Paper presented at the 11th International Congress on Engineering and Food (ICEF), Athens, 22–26 May 2011

Hicsasmaz Z, Clayton JT (1992) Characterization of the pore structure of starch based food materials. Food Struct 11(2):115–132
Horvat M, Guthausen G, Tepper P, Falco L, Schuchmann HP (2014) Non-destructive, quantitative characterization of extruded starch-based products by magnetic resonance imaging and X-ray microtomography. J Food Eng 124:122–127
Jones D, Chinnaswamy R, Tan Y, Hanna M (2000) Physiochemical properties of ready-to-eat breakfast cereals. Cereal Food World 45(4):164–168
Karkle EL, Alavi S, Dogan H (2012a) Cellular architecture and its relationship with mechanical properties in expanded extrudates containing apple pomace. Food Res Int 46(1):10–21
Karkle EL, Keller L, Dogan H, Alavi S (2012b) Matrix transformation in fiber-added extruded products: impact of different hydration regimens on texture, microstructure and digestibility. J Food Eng 108(1):171–182
Kelkar S, Stella S, Boushey C, Okos M (2011) Developing novel 3D measurement techniques and prediction method for food density determination. Procedia Food Sci 1:483–491
Kiani H, Sun D (2011) Water crystallization and its importance to freezing of foods: a review. Trends Food Sci Tech 22(8):407–426
Kirjoranta S, Solala K, Suuronen J, Penttilä P, Peura M, Serimaa R, Tenkanen M, Jouppila K (2012) Effects of process variables and addition of polydextrose and whey protein isolate on the properties of barley extrudates. Int J Food Sci Tech 47(6):1165–1175
Kotwaliwale N, Kalne A, Singh K (2010) Radiography, CT and MRI. In: Jha SN (ed) Nondestructive evaluation of food quality- theory and practice. Springer, Berlin, pp 101–140
Kotwaliwale N, Singh K, Kalne A, Jha SN, Seth N, Kar A (2014) X-ray imaging methods for internal quality evaluation of agricultural produce. J Food Sci Tech 51(1):1–15
Lim KS, Barigou M (2004) X-ray micro-computed tomography of cellular food products. Food Res Int 37(10):1001–1012
Maache-Rezzoug Z, Bouvier J, Allaf K, Patras C (1998) Effect of principal ingredients on rheological behaviour of biscuit dough and on quality of biscuits. J Food Eng 35(1):23–42
Mamlouk H, Guessasma S (2013) Finite element simulation of the compression behaviour of airy breakfast cereals. Innov Food Sci Emerg 19:190–203
Mohammed I, Charalambides M, Williams J, Rasburn J (2014) Modelling the microstructural evolution and fracture of a brittle confectionery wafer in compression. Innov Food Sci Emerg 24:48–60
Parada J, Aguilera JM, Brennan C (2011) Effect of guar gum content on some physical and nutritional properties of extruded products. J Food Eng 103(3):324–332
Pareyt B, Talhaoui F, Kerckhofs G, Brijs K, Goesaert H, Wevers M, Delcour JA (2009) The role of sugar and fat in sugar-snap cookies: structural and textural properties. J Food Eng 90(3):400–408
Pauly A, Pareyt B, Lambrecht MA, Fierens E, Delcour JA (2013a) Impact of puroindolines on semisweet biscuit quality: a fractionation-reconstitution approach. Cereal Chem 90(6):564–571
Pauly A, Pareyt B, Fierens E, Delcour JA (2013b) Wheat (*Triticum aestivum L*. and *T. turgidum L. ssp. durum*) kernel hardness: i. Current view on the role of puroindolines and polar lipids. Compr Rev Food Sci F 12(4):413–426
Penttilä PA, Suuronen J, Kirjoranta S, Peura M, Jouppila K, Tenkanen M, Serimaa R (2011) X-ray characterization of starch-based solid foams. J Mater Sci 46(10):3470–3479
Pitts KF, Favaro J, Austin P, Day L (2014) Co-effect of salt and sugar on extrusion processing, rheology, structure and fracture mechanical properties of wheat–corn blend. J Food Eng 127:58–66
Plews AG, Atkinson A, McGrane S (2009) Discriminating structural characteristics of starch extrudates through X-ray micro-tomography using a 3-D watershed algorithm. Int J Food Eng 5(1). doi:10.2202/1556-3758.1513
Primo-Martín C, Van Dalen G, Meinders M, Don A, Hamer R, Van Vliet T (2010) Bread crispness and morphology can be controlled by proving conditions. Food Res Int 43(1):207–217
Robin F, Engmann J, Pineau N, Chanvrier H, Bovet N, DellaValle G (2010) Extrusion, structure and mechanical properties of complex starchy foams. J Food Eng 98(1):19–27

Robin F, Dubois C, Curti D, Schuchmann HP, Palzer S (2011a) Effect of wheat bran on the mechanical properties of extruded starchy foams. Food Res Int 44(9):2880–2888
Robin F, Dubois C, Pineau N, Schuchmann HP, Palzer S (2011b) Expansion mechanism of extruded foams supplemented with wheat bran. J Food Eng 107(1):80–89
Robin F, Dubois C, Schuchmann HP, Palzer S (2011c) Supplementation of extruded foams with wheat bran: effect on textural properties. Procedia Food Sci 1:505–512
Robin F, Dubois C, Pineau N, Labat E, Théoduloz C, Curti D (2012a) Process, structure and texture of extruded whole wheat. J Cereal Sci 56(2):358–366
Robin F, Schuchmann HP, Palzer S (2012b) Dietary fiber in extruded cereals: limitations and opportunities. Trends Food Sci Tech 28(1):23–32
Rodríguez-García J, Laguna L, Puig A, Salvador A, Hernando I (2013) Effect of fat replacement by inulin on textural and structural properties of short dough biscuits. Food Bioprocess Tech 6(10):2739–2750
Sibakov J, Kirjoranta S, Alam SA, Kokkonen H, Jurvelin J, Jouppila K, Poutanen K, Sozer N (2014) Effects of native and modified oat bran on extrudates made of defatted oats. Food Bioprocess Tech. doi:10.1007/s11947-014-1425-4
Sozer N, Poutanen K (2013) Fibre in extruded food products. In: Delcour JA, Poutanen K (eds) Fibre-rich and wholegrain foods—improving quality. Woodland, Cambridge, p 226–272
Sozer N, Bruins R, Dietzel C, Franke W, Kokini JL (2011a) Improvement of shelf life stability of cakes. J Food Quality 34(3):151–162
Sozer N, Dogan H, Kokini JL (2011b) Textural properties and their correlation to cell structure in porous food materials. J Agr Food Chem 59(5):1498–1507
Trater A, Alavi S, Rizvi S (2005) Use of non-invasive X-ray microtomography for characterizing microstructure of extruded biopolymer foams. Food Res Int 38(6):709–719
Van Dalen G, Nootenboom P, Van Vliet LJ, Voortman L, Esveld E (2007a) 3D imaging, analysis and modelling of porous cereal products using X-ray microtomography. Image Anal Stereol 26:169–177
Van Dalen G, Nootenboom P, Van Vliet LJ (2007b) 3D Imaging and analysis of porous cereal products using X-ray microtomography. Paper presented at the 12th International Congress for Stereology (ICS XII), Saint-Etienne, 30 August–7 September
Vidal FP, Letang JM, Peix G, Cloetens P (2005) Investigation of artefact sources in synchrotron microtomography via virtual X-ray imaging. Nucl Instrum Meth B 234(3):333–348
Voogt JA, Hirte A, Meinders MB (2011) Predictive model to describe water migration in cellular solid foods during storage. J Sci Food Agr 91(14):2537–2543
Wilderjans E, Kerckhofs G, Lagrain B, Brijs K, Wevers M, Delcour J (2010) Baking gradients cause heterogeneity in starch and proteins in pound cake. Cereal Chem 87(5):475–480
Wu F (2004) Theory of resistor networks: the two-point resistance. J Phys A-Math Gen 37(26):6653
Yang N, Fisk ID, Linforth R, Brown K, Walsh S, Mooney S, Sturrock C, Hort J (2012) Impact of flavour solvent on biscuit micro-structure as measured by X-ray micro-computed tomography and the distribution of vanillin and HMF (HPLC). Eur Food Res Technol 235(6):1083–1091
Zhang L, Nishizu T, Kishigami H, Kato A, Goto K (2013) Measurement of internal shrinkage distribution in spaghetti during drying by X-ray μCT. Food Res Int 51(1):180–187
Zhu L, Shukri R, De Mesa-Stonestreet NJ, Alavi S, Dogan H, Shi Y (2010) Mechanical and microstructural properties of soy protein–high amylose corn starch extrudates in relation to physiochemical changes of starch during extrusion. J Food Eng 100(2):232–238

Chapter 7
Microstructure of Gluten-Free Baked Products

Ilkem Demirkesen Mert, Gulum Sumnu and Serpil Sahin

7.1 Introduction

Celiac disease, which is a chronic inflammatory intestinal disorder, occurs in susceptible people due to the inappropriate immune response to certain grain proteins in wheat, barley, rye, and possibly oat. This immunologic reaction causes damage to the villi, tiny, hairlike projections in the small intestine that absorbs nutrients including iron, folic acid, calcium, and fat-soluble vitamins. Therefore, people with celiac disease should eliminate gluten protein from their diet completely (Demirkesen et al. 2010a). However, gluten is an essential protein to form viscoelastic network in dough. Therefore, eliminating gluten from the products causes some quality problems such as insufficient rise in volume, relatively firmer texture, poor flavor, and rapid staling. In this respect, gluten replacement is still one of the most challenging tasks for many scientists and manufacturers. They seek alternative flour types to wheat flour such as rice, corn, chestnut, chickpea, soybean and sorghum flour, and pseudocereals such as buckwheat and amaranth.

In order to overcome the problems associated with the lack of viscoelasticity, some additives such as starches (Moore et al. 2004; Sanchez et al. 2002), hydrocolloids (Demirkesen et al. 2010a; Ribotta et al. 2004; Schober et al. 2008; Sciarini et al. 2010), emulsifiers (Demirkesen et al. 2014a, b, c; Nunes et al. 2009a; Turabi et al. 2008), enzymes (Moore et al. 2006; Renzetti et al. 2008, 2010; Renzetti

G. Sumnu (✉) · I. D. Mert · S. Sahin
Department of Food Engineering, Middle East Technical University, 06800 Ankara, Turkey
e-mail: gulum@metu.edu.tr

I. D. Mert
e-mail: Ilkemdemirkesen@gmail.com

S. Sahin
e-mail: serp@metu.edu.tr

N. Sozer (ed.), *Imaging Technologies and Data Processing for Food Engineers,*
Food Engineering Series, DOI 10.1007/978-3-319-24735-9_7

and Arendt 2009a, b), proteins (Ahlborn et al. 2005; Gallagher et al. 2003; Marco and Rosell 2008; Moore et al. 2004; Nunes et al. 2009b; Schober et al. 2004; Van Riemsdijk et al. 2011), and/or fiber sources (Mariotti et al. 2009; Sabanis et al. 2011) are required to be used. Recently, sourdough breadmaking technique (Moore et al. 2007; Moroni et al. 2011; Schober et al. 2007; Zannini et al. 2012a), infrared–microwave combination baking (Demirkesen et al. 2011, 2013, 2014a, c), and high hydrostatic pressure (HHP) treatment (Hüttner et al. 2009; Stolt et al. 2001; Vallons et al. 2010, 2011; Vallons and Arendt 2009) have been used as potential methods in gluten-free technology. The type of components present, the interactions among them, and the structural organization define the physicochemical (rheology, optics, stability), sensory, nutritional, and transport properties of foods (Aguilera and Germain 2007). These properties are largely affected by the structure of foods varying from the molecular to macroscopic levels.

In line with the general trend in food industry, the quality of gluten-free products is also evaluated manually by trained inspectors, which is tedious, costly, and lacks objectivity, consistency, and efficiency (Du and Sun 2004). There is a great need for more reliable tests and new methods of monitoring product quality (Rafiq et al. 2013). Computer-based image-processing techniques, however, offer the advantage of qualification and quantification of structural features that provide understanding of basic mechanisms of physicochemical changes. These techniques also offer flexibility, accuracy, consistency, and repeatability at relatively low cost in application while eliminating the subjectivity of manual inspections (Du and Sun 2004).

Examination of the macrostructure of gluten-free products gives information about the external attributes such as size, shape, color, and surface texture. Image analysis methods based on a large variety of macroscopic techniques such as charge-coupled device (CCD) and scanning have widely been applied for the quantitative description of macrostructure. The inventions made on food-structure imaging provide deeper information about quality attributes of gluten-free products. Foods are complex multicomponent systems. The majority of structural elements are below the 100-μm range, and therefore it is problematic to detect them in their natural or transformed states (Aguilera 2005; Aguilera and Germain 2007). However, application of special image acquisition techniques such as light microscopy (LM), scanning electron microscopy (SEM), transmission electron microscopy (TEM), confocal laser-scanning microscopy (CLSM), atomic force microscopy (AFM), magnetic resonance imaging (MRI), ultrasonic imaging and X-ray microtomography (X-ray μCT) present potential solutions to the problems for observations of microstructural features of food products. A number of studies have been conducted to evaluate the quality of gluten-free products (Demirkesen et al. 2010a; Nunes et al. 2009a; Turabi et al. 2008). Digital images that were captured using digital scanners have been widely analyzed to characterize the macrostructure of gluten-free products such as bread, cake, biscuit, and pasta (Demirkesen et al. 2013; Mariotti et al. 2011; Turabi et al. 2010). In order to understand the influence of different functional ingredients, microscopic techniques such as LM (Hüttner et al. 2009), SEM (Ahlborn

et al. 2005; Alvarez-Jubete et al. 2010; Hager et al. 2012; Hüttner et al. 2009; Marco and Rosell 2008; Sabanis and Tzia 2011; Schober et al. 2008; Vallons et al. 2010; Vallons et al. 2011), and CLSM (Alvarez-Jubete et al. 2010; Moore et al. 2004, 2006; Renzetti et al. 2008, 2010; Vallons et al. 2010; Vallons and Arendt 2009) have also been used for the observation of the quality attributes of gluten-free dough/batters and baked products. In recent studies, SEM images have been assessed to obtain not only qualitative but also quantitative information on crumb characteristics of gluten-free breads and cakes (Demirkesen et al. 2013; Turabi et al. 2010). In a recent study, X-ray μCT has also been used for quantitative characterization of bread crumbs by creating 3D representation of the inside structure of bread from 2D image slices (Demirkesen et al. 2014b). In this study, the microscopic changes of gluten-free breads by using X-ray μCT were pointed out, and the crumb microstructure of breads was related to their textural properties.

The aim of the present chapter is to illustrate important imaging techniques and their applications for gluten-free baked products and to summarize the advantages and disadvantages of these techniques. Macro- and microstructural changes of gluten-free baked products by using various imaging techniques and the influence of different functional ingredients and prospective methods on microstructure of gluten-free dough/batters and/or products were also reviewed.

7.2 Structural Analysis of Bakery Products

The quality of a baked product, which depends on appearance, texture, volume, and sensory properties, is significantly affected by its structure from molecular to macroscopic levels (Zghal et al. 1999). Thus, understanding of macro- and microstructure by image analysis techniques is critical. The obtained information from image analysis provides the conversion of the food system complexity to numerical data that will be analyzed to improve the understanding of structure–function relationships of materials (Chanona-Perez et al. 2008).

Application of special image acquisition techniques such as several microscopy, scanning, and spectrometric techniques that allow visualization of changes in structure at both macroscopic and microscopic levels without intrusion have been applied as convenient tools for image acquisition (Demirkesen et al. 2013; Falcone et al. 2006). In recent years, image analysis based on various macroscopic and/or microscopic techniques (e.g., flatbed scanning, SEM, X-ray μCT) has been used as a quantitative tool for description of baked product structure (Datta et al. 2007; Farrera-Rebollo et al. 2012; Kelkar et al. 2011; Ozkoc et al. 2009; Ronda et al. 2009; Rouillé et al. 2005; Sanchez-Pardo et al. 2008; Sapirstein et al. 1994; Zayas 1993; Zghal et al. 2002), which further on was adapted for the characterization of gluten-free products (Demirkesen et al. 2013, 2014b; Mariotti et al. 2011; Schober et al. 2008; Sozer 2009; Turabi et al. 2010).

7.2.1 Macrostructure of Gluten-Free Bakery Products

Macrostructural analysis provides information about the external attributes of food materials such as size, shape, color, and surface texture. Image analysis methods based on a large variety of macroscopic techniques such as CCD and scanning have widely been applied for quantitative evaluation of the macro- and microstructure of food products. Quantitative examination of crumb of baked products, such as measuring gas cell sizes and their distribution, can be done by image analysis to provide structural information.

CCD camera, which converts light into electrical charges, is a cost-effective way for image acquisition. It is commonly included in digital still and video cameras (Du and Sun 2004). It has the ability to produce high-quality and low-noise images with lots of pixels and excellent light sensitivity. It has widely been applied to examine physical characteristics and quality of food. The multiple uses of CCD cameras can be applied when it is difficult to evaluate food quality in ordinary spectral region. CCD cameras can be connected to microscopes and flatbed scanners in order to obtain images in digital form (Du and Sun 2004).

The most widely applied imaging technique in macrostructural food research is flatbed scanning. The use of a flatbed scanner for image acquisition and the assessment of appearance and/or color offer all the advantages of previously investigated camera-based systems. In addition, the acquisition of 2D images by flatbed scanning offers some advantages over camera-based systems such as being fast, easy to use, economical, robust, independent of the external light conditions, and providing good accuracy. However, one of the disadvantages of this technique is the lack of a standardized technique for food evaluation. The differences in methodologies such as scanning resolution and the range of air cells also result in different data for similar products (Farrera-Rebollo et al. 2012). Hence, comparing information among published reports is challenging. The most common use of flatbed scanners in the area of cereal research is for characterization of bread crumb structure (Demirkesen et al. 2014b). Pore size, pore distribution, wall thickness, and number of pores were measured for quantitative characterization of gluten-free bread crumb (Demirkesen et al. 2013, 2014b; Schober et al. 2008; Van Riemsdijk 2011; Zayas 1993). In addition, scanners were used for image acquisition of other types of baked products such as cake and biscuit (Ronda et al. 2009; Turabi et al. 2010). The sample images of scanned gluten-free cake and bread are shown in Figs. 7.2 and 7.4.

7.2.2 Image Analysis Process

Image analysis process includes the following five steps: image acquisition, preprocessing, segmentation, object measurement, and classification (Du and Sun 2004).

7.2.2.1 Image Acquisition

Images, which are the spatial representations of objects, stored as matrixes of columns *(x)* by rows *(y)* containing thousands of cells known as pixels. Each pixel consists of a numerical value that is called digital number (Falcone et al. 2006). Image acquisition, which is the first stage of the image analysis process, is the capture of an image in digital form. In order to obtain high quality from a captured image, lighting conditions are an important prerequisite of image acquisition and have a critical role on the improvement of the accuracy and the success of image analysis (Du and Sun 2004). The use of several different image acquisition techniques allows the observation of the structure of food from macroscopic to microscopic level and the translation of images into digital form. CCD camera, flatbed scanners, X-ray μCT, ultrasonic imaging and MRI are widely used image acquisition techniques.

7.2.2.2 Preprocessing

Preprocessing of the raw images is used to enhance the quality of the original images and hence to obtain correct information for image processing. For this purpose, the correction of geometric distortions, removal of distortions and noise, gray-level correction, correction of blurring, etc., are applied analysis steps in preprocessing. Based on the size of the pixel neighborhood, which is used for the calculation of a new pixel, there are two different types of image preprocessing approaches used in food quality evaluation: pixel preprocessing and local preprocessing.

Pixel preprocessing, which is a simple but important image-processing technique, converts an input image into an output image, where each output pixel is fitted directly to the input pixel having the same coordinates, but the values are changed according to the specified transformation function (Aguilera and Germain 2007; Du and Sun 2004). The most applied pixel preprocessing method in food quality evaluation is color space transformation. Although most of the color images are commonly obtained as 24-bit RGB (24 bits: 8 red, 8 green, 8 blue) images, most programs are capable of operating on gray scale (8 bit, monochrome; Falcone et al. 2006), in which images use only 1 byte of 8-bit data per pixel instead of 3 bytes. In addition, the byte still consists of values of 0 (black) to 255 (white), to represent 256 shades of gray. Therefore, the transformation of the RGB digital color image either in a gray-scale image or in three monochrome images (monochrome red, monochrome green, and monochrome blue) is the first stage after image acquisition. However, RGB cannot present all the colors that people can see, and people do not perceive color as a combination of red, green, and blue. Therefore, it is not the most adequate space for color representation, and it is preferable to transform the RGB color space into one of the more representative color spaces for the analysis of foods such as the Commission Internationale de l'Eclairage (CIE) Lab color space (Aguilera and Germain 2007). CIE contains a larger scale than the RGB space. It is device independent and presents a more consistent color measurement regardless

of the device used to acquire the image. The CIE chromaticity diagram is a 2D plot and utilizes three coordinates to locate a color in a color space, which are CIE XYZ, CIE L*a*b*, and CIE L*C*h*. For color analysis, the RGB image is transformed into XYZ tristimulus values, which are assigned to the red, green, and blue curves, respectively. The CIE XYZ data are then converted to the CIE L*a*b* coordinates, where L* reflects the luminance or lightness component, a* indicates the content of red or green, and b* defines the content of yellow and blue (Aguilera and Germain 2007). Hue, saturation, intensity (HSI) color space has also been used for the discrimination of different parts of food material. Intensity is indicated by brightness and moves from 0 to 1 as colors become brighter. Like HIS, hue, saturation, lightness (HSL) and hue, saturation, value (HSV) color spaces are known as human-oriented color spaces. They are two similar sets of coordinates that distinct the gray-scale brightness (L for luminance or V for value) from the hue which moves from 0 to 1, representing color variation from red, yellow, green, cyan, blue, magenta and back to red, and the saturation which moves from 0 to 1 with the increasing amount of black in the color.

Local preprocessing uses a small neighborhood of a pixel in an input image to eliminate nonuniform illumination and obtain a new brightness value in the output image. It can be also regarded as a filtering step, and different types of filters are used as a function of the noise magnitude (Falcone et al. 2006). Edge enhancement and noise reduction in the input images are needed before binarization since they may cause errors in the processing of images. Binarization is the transformation of the color or gray-level image into a black-and-white image. Binarization allows relating a value of black or white to each pixel. After binarization, the image will be ready for the extraction of artifacts and noise and to apply other functions. Then, the binary image can be used for quantitative analysis (Falcone et al. 2006).

7.2.2.3 Image Segmentation

Image segmentation is the process of partitioning the digital image into objects and background. Since the subsequent measurements depend on the accuracy of this operation, it is usually considered the most important step in the image analysis process (Aguilera and Germain 2007). It may be done either manually or automatically (Falcone et al. 2006). Based on different approaches, the techniques used in image segmentation can be classified into three categories: thresholding-based, region-based, and edge-based segmentation. Among these methods, the thresholding-based and region-based are the most widely applied methods (Du and Sun 2004).

Thresholding-Based Segmentation

Thresholding-based segmentation is the simplest way to perform segmentation, and it is the most commonly employed segmentation technique in image-processing applications. This method is based on a threshold value to turn a gray-scale image into a binary image, in which all the pixels that form part of the objects present (foreground) are set to black, while the background pixels are set to white (Aguilera

and Germain 2007). In this way, the object can be distinguished from the remaining part of an image. Thresholding works efficiently when different regions in an image have a different frequency distribution, and the objects of interest have uniform interior gray level. If the image consists of several objects with different surface characteristics, multiple thresholding can be applied for segmentation (Aguilera and Germain 2007).

Region-Based Segmentation
Region-based segmentation is a method used to determine the region directly, and thus algorithms are used to group the neighboring pixels within one region having similar values. It can be categorized as region growing-and-merging and region splitting-and-merging. In region growing-and-merging method, pixels or sub-regions are grouped into larger regions based on a set of homogeneity criteria, while in region splitting-and-merging, the image is successively divided into smaller and smaller regions until certain criteria are satisfied (Du and Sun 2004). Although it is computationally more expensive, it has the capability to use several image properties directly and simultaneously to determine the final boundary location that makes it a powerful approach in the segmentation of food products.

Edge-Based Segmentation
In edge-based segmentation, an edge filter is applied to the image to determine whether the pixels are on edge or not, depending on the filter output. A numerical test for image gradient or curvature, or other properties to classify pixels, is used in this technique (Aguilera and Germain 2007).

7.2.2.4 Object Measurement

Object measurement is the stage used for quantifying the individual features of each object. These features can be classified into four classes such as size (area, perimeter, length, and width), shape (roundness, elongation, compactness, etc.), color, and texture (smoothness, coarseness, graininess, etc.; Du and Sun 2004).

7.2.2.5 Classification

The aim of this step is the discrimination of multiple objects from each other within an image. It comprises a broad range of decision-theoretic approaches to the identification of objects by classifying them into one of the individual categories, comparing the measured features of the new object with those of a known object or other known criteria. A wide variety of approaches, such as the statistical, fuzzy, and neural network methods, are used to classify image objects (Du and Sun 2004). In statistical classification, probability models are used to classify objects. The fuzzy classification method categorizes objects into classes without defined boundaries, and thus the degree of similarity of the considered object with respect to the others can provide more information about the confidence of the class assignment.

Artificial neural network methods use statistical methods with the machine-learning objective of emulating human intelligence (Du and Sun 2004).

7.2.3 Microstructure of Bakery Products

Physical properties of bakery products are strongly related to structural organization of foods at molecular, microscopic, and macroscopic levels. In particular, microstructure and interactions of food components critically contribute to the transport, physical, and sensory properties of foods and hence determine their texture (Falcone et al. 2006). Image analysis techniques (e.g., electron microscopy (EM), CLSM, MRI, AFM, X-ray), which are a convenient and useful key to qualify and quantify the characteristics of crumb structure, can be used to observe the microstructure of gluten-free baked products (Demirkesen et al. 2013). The selection of the most suitable image acquisition technique is influenced by several factors such as the physical properties of the sample, magnification and resolution level requirement, and equipment availability (Aguilera and Germain 2007). One of the main limitations of these microscopic techniques is optical illusion (Du and Sun 2004). Furthermore, sample preparation artifacts are another challenge for the application of microscopic techniques. However, the application of a variety of different image analysis techniques to the same sample and comparing results that were obtained by applying these techniques may be a solution for this problem (Falcone et al. 2006).

LM provides specific staining of different chemical components of a food (proteins, fat droplets, etc.), which makes it a suitable imaging technique for investigating multicomponent or multiphase foods, such as cereal-based foods. LM has low magnifications and resolutions as compared to EM. Thus, the internal structures of micro-components cannot be observed by LM. In order to enhance the contrast of specific structures on samples, bright-field illumination, phase contrast, differential interference contrast, and polarizing light are commonly used methods (Aguilera and Germain 2007). In this method, image acquisition is created by connecting a CCD camera to the microscope objective lens. In the study of Hüttner et al. (2009), both SEM and LM imaging techniques were used to determine the impact of HHP on the microstructure of oat batters and to explain the changes in the major flour components, starch and protein. SEM micrograph revealed that the starch granules of batters treated at 500 MPa were swollen and slightly disintegrated. Treatment at increasing pressures also affected oat batter proteins, as revealed by bright-field microscopy (Fig. 7.1).

EM gives information about tomography, morphology, and composition. EM uses a beam of electrons as the illumination source instead of light. Thus, the images are obtained by projecting the electrons through a thin specimen. The differences in the affinity of heavy metals such as ruthenium, lead, uranium, and osmium allow the differentiation of structure components. Colorful micrographs cannot be obtained, but the colors can be added to the micrographs (Falcone et al. 2006). Since it works under vacuum conditions, sample preparation procedures such as

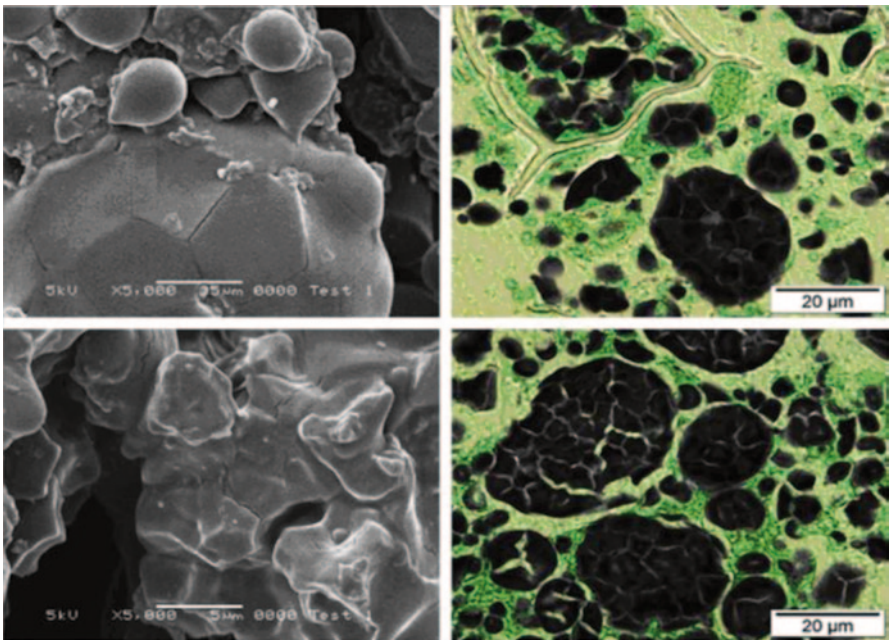

Fig. 7.1 SEM *(left)* and bright-field microscopy *(right*; proteins are stained in *green* and starch in *brown)* analysis of untreated oat batters *(first row)* and oat batters treated at 500 MPa *(second row)*. (For the interpretation of colors in the figure legend, the reader is referred to the web version of the chapter. Reprinted from Hüttner et al. 2009, copyright 2009, with permission Elsevier)

dehydration, freezing, or freeze-drying are required, and they may cause artifacts. EM is categorized into TEM and SEM. Compared with LM, SEM and TEM allow a higher resolution. TEM increase magnifications up to over 10,000 allowing the observation of smaller structures. However, it has many drawbacks. For the application of TEM, samples have to be cut extremely thin for observation (50–100 nm), and that may cause artifacts. Moreover, samples have to be extremely dry and strong enough to resist damage from the electron beam that requires high vacuum conditions during observation. The maximum magnification levels of an LM are about 1000×, while TEM can reach magnifications levels of up to over 10,000×. The magnification levels of SEM, on the other hand, are between that of LM and TEM, and it can magnify from 20 to 10,000× (Aguilera and Germain 2007). SEM is one of the most important image analysis techniques since it provides the combination of high magnification, large depth of focus, great resolution, and fast and easy sample observation (Demirkesen et al. 2013). SEM also offers the detailed observation of either whole samples or surface/internal structure of samples. Images can be recorded at various magnifications with one objective lens. However, the cost of this method is relatively higher. Furthermore, the sample's surface should be coated in order to avoid charging, and that requires a special training. Different characteristics of particulate structures can be determined by the combination of different

imaging techniques such as LM, TEM, SEM, and CLSM (Falcone et al. 2006). In the study of Langton et al. (1996), LM was used to observe pores, and TEM was used to evaluate particle size, while SEM revealed how the particles were linked together. Up to date, some SEM studies have been assessed to determine the changes that occur during baking qualitatively (Ozkoc et al. 2009; Polaki et al. 2010; Rosell and Santos 2010; Sanchez-Pardo et al. 2008). In recent studies by Demirkesen et al. (2013) and Turabi et al. (2010), SEM has been used to obtain quantitative information on macro- and microstructure of gluten-free breads and cakes. These will be discussed further in Sects. 7.4.1, 7.4.2, and 7.6.2.

Concerning sample preparation, CLSM represents a suitable alternative imaging technique since it requires a minimum sample preparation compared to EM. One of the other advantages of this method is providing the optical slicing of the sample. Thus, as opposed to LM, TEM, and SEM, it is a noninvasive technique. The topographic information can be obtained from a set of confocal images taken over a range of focal planes. A 3D topographical map of the object is obtained from a series of optical slices of the images at different focus positions. It provides volumetric data, which can be very easily quantified. It works best when it is used to provide extraordinary thin, in-focus, high-resolution optical sections through a thick specimen (Aguilera and Stanley 1999). It also provides specific staining of food components. However, CLSM has a high cost. Up to date, CLSM has been used to evaluate the 3D structure and protein network of gluten-free doughs and breads (Moore et al. 2004, 2007; Renzetti et al. 2008; Schober et al. 2007).

MRI, which is also known as nuclear magnetic resonance (NMR) imaging (NMRI), or magnetic resonance tomography (MRT), has found widespread applications in food quality evaluation as a nondestructive and noninvasive imaging technique. The working principle of MRI is based on the absorption and emission of energy in the radio frequency range of the electromagnetic spectrum, and thus it provides image contrast on the basis of the molecular ability (Falcone et al. 2006). Images are acquired based on the absorption or emission of energy by the atomic nuclei in an external magnetic field, and they are created from the Fourier transform of the signal. It also uses physicochemical properties of water to obtain images (Kelkar et al. 2011). MRI allows the collection of images of the system undergoing changes as a function of time from a unique specimen (Prior-Cabanillas et al. 2007). The signal of each voxel varies based on the physical properties of the sample such as proton density, relaxation times, temperature, diffusion, flow, and local differences in magnetic susceptibility (Mariette et al. 2012). MRI can be used to acquire 2D and even 3D images of food material without any preliminary sample preparation. It gives information about the 3D distribution of water, fat, and salt content of food material. It is usually applied in water-containing materials in order to monitor the variation of water content with time (Oztop 2010). It can also be applied to study the transport of solvents into solid systems in real time. Heat and mass transfer within food materials can be studied by MRI (Mariette et al. 2012). Another application of MRI is to understand and follow up the physicochemical changes during food processing. In addition, NMR parameters such as relaxation time and diffusion coefficient can be used for the definition of the interactions among water

and other molecules, which provides information about the physical and chemical properties of food material (Clarke and Eberhardt 2002). However, the main disadvantage of this expensive technique is that it can be used only for such food materials which have sufficient water content (13 %≤). There are limited studies on MRI of gluten-free baked products (Lodi and Vodovotz 2008). In the study of Lodi and Vodovotz (2008), water and other components of the gluten-free bread matrix were characterized in fresh and stored soy and soy-almond bread samples using a variety of thermal and magnetic-resonance-based techniques. In this study, it has been suggested that changes in water and lipid mobility reflected the microscopic basis of the different loaf quality attributes of soy and soy-almond breads.

AFM is a powerful and revolutionary method that enables information in nanoscale. AFM produces an image by scanning with a sharp stylus, which is attached to a flexible cantilever, across the sample surface. The tip is brought into contact with or close to the sample, and the surface is scanned beneath the tip. When the sample is raster scanned (zigzag movements), the change in surface topography or in probe-sample forces causes the cantilever to deflect (Leite and Herrmann 2005; Yang et al. 2007). The deflection of the cantilever is determined by using laser light reflected off the back surface of the cantilever onto a position-sensitive photodiode detector. Due to that deflection, a line-by-line image of the sample is produced (Leite and Herrmann 2005). Thus, images are created as a result of the measurement of the magnitude of a multitude of forces interacting between the probe and surface of the sample (Yang et al. 2007). AFM can be operated with or without feedback control modes. In feedback control mode, positioning piezo responds to any changes in force and changes the tip-sample separation to restore the force to a predetermined value. As a result of this topographical or height mode, an image can be created. The operation of AFM is done in constant-height or deflection mode in without-feedback mode. Contact, noncontact, and tapping modes are the three basic operation modes in AFM. In contact mode, the tip is attached to the end of the cantilever, and it maintains contact with the sample surface at all times. In noncontact mode, an alternating current (AC) signal is obtained from the cantilever as a result of the cantilever oscillation at a frequency that is slightly above the cantilever's resonance frequency. In tapping-mode AFM, the tip attached to the end of the oscillating cantilever intermittently contacts the surface of the sample at the lowest point of the oscillation (Yang et al. 2007). High resolution, ease of use, and simple sample preparation are the advantages of AFM. In addition, the specimen can be imaged in air or liquid. Furthermore, AFM imaging method provides information about the individual molecules of a material, and it can be used for imaging biological nonconducting materials (Falcone et al. 2006).

Ultrasound is a sound wave having a frequency higher than the hearing limit of the human ear (~20 kHz; Awad et al. 2012). Ultrasound can be used to inspect internal features. The images are created as a result of high-frequency sound waves that are translated into information. The ultrasonic velocity, attenuation coefficient and the acoustic impedance are essential physical factors that depend on the composition and microstructure of a material. The relationship between measured ultrasonic parameters and microstructural properties of a material can be created by a

calibration curve or, theoretically, by using equations that relate the propagation of ultrasound through the material (Falcone et al. 2006). Therefore, 2D images and 3D images are generated. As opposed to light-scattering studies, which require the dilution of food material, ultrasound can measure concentrated food properties, and this allows the analysis of nonhomogeneous foods such as solidifying fats, dynamically changing dairy food systems, dough, and emulsions (Falcone et al. 2006). Ultrasound technology is nondestructive, rapid, and easily modified for on-line measurement. On the other hand, one of the disadvantages of ultrasound technology is that it can be used for imaging concentrated and optically opaque materials. In addition, the presence of small gas bubbles in a sample can weaken the ultrasound, and the signal from the bubbles may interfere with the signals obtained from other components. Moreover, it has limited use for complex biochemical and physiological events. Furthermore, design and development of efficient power ultrasonic systems, which support large-scale operations, are needed (Awad et al. 2012). Based on frequency range, the applications of ultrasound in food industry can be categorized as low- and high-energy ultrasound. Low-energy ultrasound is also known as low-power, low-intensity ultrasound, and it has frequencies higher than 100 kHz at intensities below 1 W/cm^2. High-energy ultrasound, on the other hand, has intensities higher than 1 W/cm^2 at frequencies between 20 and 500 kHz. In bakery industry, it has been applied for online dough quality control (Ross et al. 2004), characterization of the fermentation phase during breadmaking (Elmehdi et al. 2003; Skaf et al. 2009), defining the changes in wheat flour dough consistency induced by proteins and gelatinization of the starch (García-Álvarez et al. 2011), for estimation of the textural characteristics of bakery products such as bread, cakes, crackers, and wafers (Petrauskas 2007; Povey and Harden 1981), and for evaluating rheological characteristics of dough (Fox et al. 2004; Gómez et al. 2008; Salazar et al. 2004). Although there is no literature focusing on the use of ultrasound imaging for gluten-free baked products, we believe that this imaging technology could be applied also for this type of products.

X-ray μCT, which is usually used in medical applications, uses ionizing radiation in the form of X-rays. The major advantage of this nondestructive and powerful imaging technique is the ability to generate cross-sections of the 3D image of an object from a large series of 2D images taken around a single axis of rotation (Kelkar et al. 2011). Another advantage of this technique is its ability to produce the contrast-enhanced imaging without any sample preparation that helps to overcome typical artifacts in the visualization of structure. In addition, the final image results can be recorded by 3D rendering, by 2D slices, or projections following arbitrary directions, and these images can be stored digitally (Besbes et al. 2012; Falcone et al. 2004, 2005; Primo-Martín et al. 2010; Wang et al. 2011). This method also provides greater spatial resolution of X-ray microscopy over other types of microscopes. X-rays have the ability to penetrate through food materials and, in most cases, to capture 3D details of the inner microstructure. However, most other existing microscopes have the ability to focus only at the object surface or a transmission image through a thin section; thus, the internal 3D structure can only be

obtained invasively (Lim and Barigou 2004). X-ray μCT imaging technique requires an X-ray source, a rotation stage, and a radioscopic detector, and analysis is made by scanning the sample under different viewing angles. This imaging method has been used for quantitative characterization of bakery products such as bread, cake, cookie, and muffin (Besbes et al. 2012; Falcone et al. 2004, 2005; Lape et al. 2008; Lim and Barigou 2004; Pareyt et al. 2009; Primo-Martín et al. 2010; Wang et al. 2011), to study the bubble structure of aerated food products, and to obtain quantitative information on the number and size of bubbles present (Babin et al. 2006; Bellido et al. 2006). Demirkesen et al. (2014b) used X-ray μCT to study the effects of different gums and gum blends additions on the crumb structure of gluten-free breads. In this study, microscopic changes of gluten-free breads were related to textural properties of breads.

7.3 Celiac Disease and the Role of Gluten in Baked Products

Celiac disease (gluten-sensitive entropathy), is a multi-symptom, autoimmune disorder, which is triggered by the response of the body's immune system to prolamins found in wheat (gliadin), rye (secalin), barley (hordein), and their crossbreeds (Bower 2006). When people with celiac disease consume gluten, their immune system generates antibodies against this protein causing damage to the tiny hairlike projections in the small intestine; in severe cases, the lesion extends to the ileum colon (Demirkesen et al. 2014a). Hence, a permanent withdrawal of gluten from the diet of celiac patients is required throughout their life span. Recent studies showed that celiac disease is more common than previously reported, and the incidence is 1:100−30:100 in the general population of Europe and the USA (Catassi et al. 2002).

Bread is one of the most important basic items of the human diet. Wheat, which is the major cereal in breadmaking, consists of starch (70–75%), water (14%), proteins (10–12%), and non-starch polysaccharides (2–3%), particularly arabinoxylans and lipids (2%; Goesaert et al. 2005). Wheat flour consists of two groups of proteins: non-gluten proteins, which have either no or just a minor role in breadmaking, and the gluten proteins, which have a major role. Non-gluten proteins, which represent 15–20% of the total protein content of wheat, are mainly present in the outer layers of the wheat kernel. These proteins are mostly structural proteins and genetically related to the major storage proteins in legumes and in the cereals of oats and rice. Gluten is the major storage of protein in wheat and contributes 80–85% of the total wheat protein. They are found in the endosperm cells of the mature wheat grain, where they form a continuous matrix around the starch granules (Van Der Borght et al. 2005). It is essential to form a strong protein network for the desired viscoelasticity to obtain high-quality breads. Therefore, the quality and quantity of gluten have critical role in the quality of breads. Glutenin and prolamin

are the major fractions of gluten. Glutenin molecule is linked by intermolecular disulfide bonds, giving a network structure. In contrast, monomeric gliadin molecule is linked by intramolecular disulfide bonds, creating a globular confirmation for the the proteins (Tronsmo et al. 2002). Therefore, while prolamin provides viscous properties and extensibility in a dough system, polymeric glutenin is responsible for the elastic and cohesive properties of the dough (Gujral and Rosell 2004). Together, the two are important for crumb structure of cereal-based products, and the relative proportions of gliadin and glutenin affect the overall quality. When flour is mixed with water, gluten proteins provide cohesive viscoelastic properties to the dough that is responsible for retaining gas produced during fermentation and oven rise, so a high volume and soft texture can be obtained.

Consumer expectations for gluten-free breads are greatly influenced by traditional bread attributes. Therefore, gluten-free product developers should determine their aims based on wheat bread. Gluten-free dough formulations tend to contain higher water level, so it resembles a batter rather than dough, and they cannot be shaped like wheat dough. Thus, mixing is done mechanically, often in a kitchen mixer or in a mixer using a batter attachment (Lazaridou and Billiaderis 2009). While traditional wheat bread production consists of mixing, bulk fermenting, dividing, proofing, and baking, gluten-free bread production steps are only mixing, proofing, and baking. Furthermore, gluten-free dough formulations need shorter proofing and baking times than their wheat counterparts (Arendt et al. 2008). Studies showed that the standard farinograph curve for a gluten-free dough mixture requires longer time to reach the consistency of 500 Brabender unit (BU) and a continuous increase in consistency during mixing time (Lazaridou and Billiaderis 2009). This result suggested that gluten-free dough has poor dough characteristics for baking with relaxing stretchable properties and with limited machinability, which creates handling problems during mixing. Due to the handling problems of gluten-free dough, researchers have used quality measurements such as volume, texture, and macro- or microstructural analysis of crumb to evaluate the effect of water absorption and mixing time on structure instead of using farinograph measurements. Wheat dough is a colloidal system with a continuous phase containing hydrated biopolymers and a dispersed phase consisting of CO_2. On the other hand, gluten-free dough is a colloidal system with starch particulates that make up the continuous phase and water constituting the dispersed phase (Dobraszczyk et al. 2001). Although, starch gelatinization provides some structure to gluten-free dough, it is not enough to provide resistance to shear and entrapment of CO_2. Thus, the rate of CO_2 release in gluten-free dough is higher (22 μmol/min) than that in wheat dough (5 μmol/min) at 23 °C (He and Hoseney 1991). As a result, manufacturers and scientists have tried to decrease CO_2 diffusion of gluten-free dough to obtain high volume, good crumb structure and flavor, and longer shelf life from the gluten-free breads. For this purpose, they are especially focused on the use of additives such as hydrocolloids, emulsifiers, enzymes, protein sources, and fibers.

7.4 Cereal Sources for Gluten-Free Products

Since gluten creates a continuous protein network, which helps to retain gas produced from yeast fermentation and oven rise, gluten-free baked products on the market are of poor quality with low volume and poor texture and flavor. Moreover, they lack the adequate amount of vitamins, minerals, and fiber that deteriorates the nutritionally unbalanced diet of celiac sufferers (Bardella et al. 2000; Demirkesen et al. 2010b). For these reasons, producing high-quality gluten-free products is one of the most challenging issues for cereal food technologists and scientists (Demirkesen et al. 2010b; Moore et al. 2007). Traditionally, most gluten-free products have been produced by replacing wheat flour by alternative flours (rice, corn, chestnut, chickpea, soy, soybean and sorghum flour, pseudocereals such as buckwheat and amaranth, etc.) as well as by using some additives (e.g., starches, hydrocolloids, emulsifiers, enzymes, protein, and/or fiber sources) to mimic the viscoelastic properties of gluten (Demirkesen et al. 2010b).

7.4.1 Rice Flour

Rice flour is the most suitable cereal flour for preparing gluten-free products due to its several noteworthy characteristics: It is natural, hypoallergenic, colorless, and has a bland taste. It contains a very low amount of protein, sodium, and fat, and a high amount of easily digested carbohydrates. Rice has a very low amount of prolamins (2.5–3.5 %) (Demirkesen et al. 2010a). It can also be used in combination with other types of gluten-free flours. Despite its numerous advantages, rice proteins have poor functional properties. Moreover, they are insoluble because of their hydrophobic nature, and this prevents the formation of viscoelastic structure in dough (Rosell and Collar 2007). As a consequence, rice products have low volume, firm texture, short shelf lives, and they stale rapidly. Several studies in the literature have demonstrated the potential use of rice flour for the development of gluten-free products (Ahlborn et al. 2005; Demirkesen et al. 2010a, b, 2011, 2014a, b, c; Moore et al. 2006; Rosell and Collar 2007; Sivaramakrishnan et al. 2004; Turabi et al. 2008). There are various studies in the scientific literature that show the application of different imaging tools for the evaluation of macroscopic and microscopic characteristics of gluten-free baked products containing rice flour (Demirkesen et al. 2013, 2014b; McCarthy et al. 2005; Turabi et al. 2010). In these studies, researchers used different gums, enzymes, and dietary fibers to develop gluten-free formulations. Turabi et al. (2010) studied the effects of different gums (xanthan, guar, LBG, k-carrageenan and xanthan–guar gum blend) on the macro- and microstructure of gluten-free rice cakes. The cakes were baked by using two different baking methods: conventional and infrared–microwave combination baking. In order to characterize the cake crumbs quantitatively, flatbed scanner and SEM were

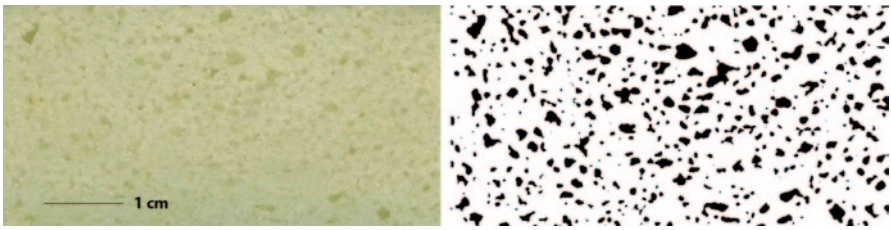

Fig. 7.2 **a** Scanned image of rice cake containing xanthan gum. **b** Binarized image of this cake. (Reprinted from Turabi et al. 2010, copyright 2010, with permission Elsevier)

used as imaging tools. Scanned images were used to observe the macrostructure of gluten-free rice cakes, while the microstructure of cakes was examined by using SEM images. During the preprocessing step, the scanned images of the cake crumb (Fig. 7.2a) were converted into binarized images (Fig. 7.2b).

Image analysis software ImageJ was used for quantitative analysis of pores. The pore area fraction values of the macrostructure of cake crumbs were significantly affected from both gum type and baking mode. Cakes baked in infrared–microwave combination oven had higher porosity than those baked in conventional oven. The addition of xanthan and xanthan–guar gum blend gave higher pore area fractions than the other gums when they were baked in infrared–microwave combination oven. The higher porosity values of cake crumbs were related to the entrapment of more air bubbles in batters containing these gums due to their higher viscosity values. To obtain microstructural information about rice cakes, SEM images of cake crumbs at 30× magnification were used (Fig. 7.3).

Pore area fraction values of these images were analyzed by image analysis. It was found that cakes containing xanthan gum and xanthan–guar gum blend and baked in infrared–microwave combination oven had higher pore area fractions as compared to other formulations. This result was in agreement with the data obtained for the macrostructure of cake crumbs. The authors hypothesized that the variation in dielectric properties of gums might affect the porosity of cake crumbs. High dielectric properties of the batters might cause more interaction between the cake batters and microwaves and hence higher gelatinization. Thus, it was postulated that the higher porosity of cakes containing xanthan was due to higher dielectric properties of xanthan than the other gums (Turabi et al. 2010). Different hydrocolloids were added in gluten-free bread formulations based on rice flour and cornstarch in order to investigate their effects on dough rheology and bread quality (Sabanis and Tzia 2011). In this study, concentrations of ingredients (cornstarch, rice flour and hydroxypropylmethylcellulose (HPMC)) were optimized for a fiber-enriched gluten-free bread formulation. SEM images of dough samples were used to show the structural integrity of hydrocolloid-containing gluten-free bread crumbs. The SEM micrographs of xanthan-gum-containing dough samples showed a large number of very small gas cells in an interrupted hydrocolloid–starch matrix, presenting a dense structure. On the other hand, a continuous matrix that was obtained between starch and HPMC exhibited a more aerated structure. The baking and sensory

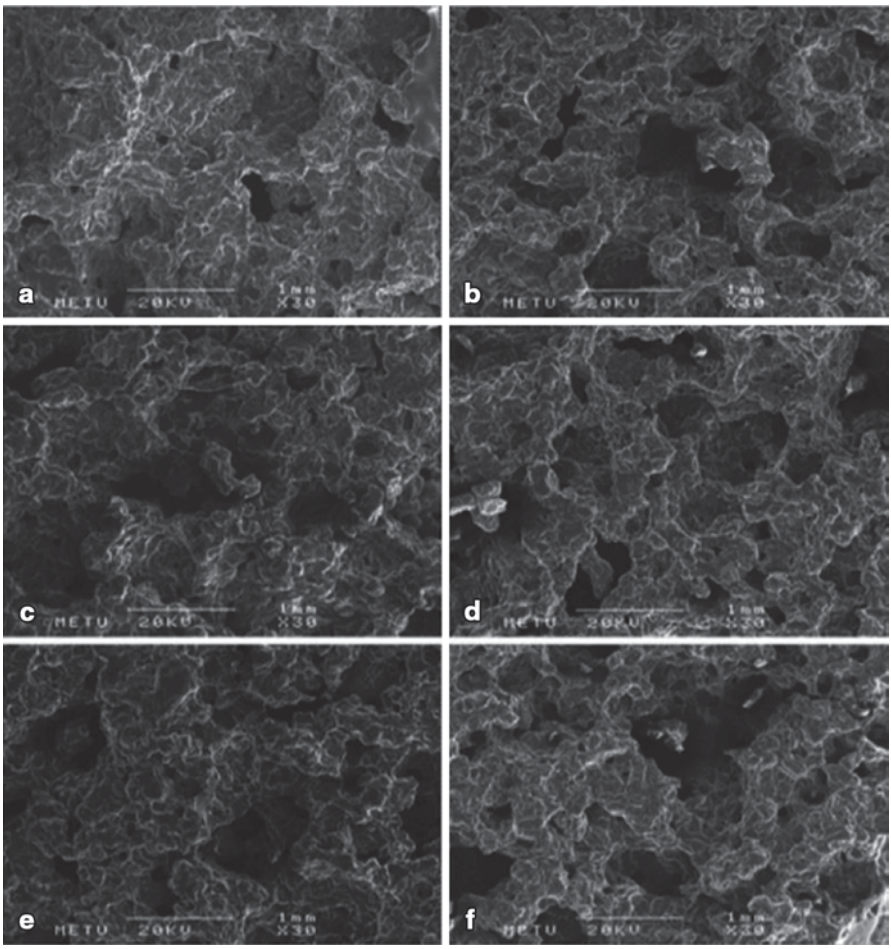

Fig. 7.3 SEM micrographs (30×) for cakes baked in conventional oven (**a** control, **b** xanthan, **c** guar, **d** xanthan–guar, **e** locust bean, **f** kappa-carrageenan). (Reprinted from Turabi et al. 2010, copyright 2010, with permission Elsevier)

tests indicated that the addition of HPMC resulted in higher loaf volume, uniform and finely grained crumb texture, better color, longer shelf life, and higher sensory scores, and thus HPMC was found to be the most effective gum in structuring gluten-free rice cakes.

7.4.2 Chestnut Flour

Chestnut flour has high-quality proteins with essential amino acids (4–7%), a relatively high amount of sugar (20–32%), starch (50–60%), dietary fiber (4–10%),

and a low amount of fat (2–4%). It also includes some important vitamins, minerals, and phenolics (Blaiotta et al. 2012; Chenlo et al. 2007; Sacchetti et al. 2004). Besides its health and nutritional benefits, the ingredients of chestnut flour may provide some functional properties to the dough. While the fiber content of chestnut flour may assist the emulsifying, stabilizing, texturizing, and thickening properties of dough, the sugar content of chestnut flour may improve the color and flavor properties of gluten-free products when it is used at a certain level (Demirkesen et al. 2013). Demirkesen et al. (2013) studied the effects of the replacement of rice flour with chestnut flour and xanthan–guar gum blend emulsifier–diacetyl tartaric acid ester of mono- and diglycerides (DATEM) mixture addition on the macro- and microstructure of rice breads baked in different types of ovens (conventional and infrared–microwave combination ovens). In this study, flatbed-scanned and SEM pictures were analyzed by image analysis program in order to obtain quantitative information about the macro- and microstructure of gluten-free breads. The scanned images of gluten-free bread samples prepared with different formulations and baked in different ovens are depicted in Fig. 7.4.

Control breads, which were prepared without using chestnut flour and gum-emulsifier blend had heterogeneous crumb structure with their larger pores. This result was related to insufficient air incorporation of dough during the fermentation and baking processes due to its low viscosity and viscoelastic properties. The higher fiber content of chestnut flour improved the viscoelastic properties of dough leading to entrapment of more air bubbles. Therefore, even in the lack of additives, the replacement of rice flour with chestnut flour prevented the formation of very large pores (Fig. 7.4c and g). Hydrocolloids enhanced bread quality by improving water absorption and viscoelastic properties of dough, and emulsifiers lowered the surface tension of dough leading to the subdivision of the entrapped air bubbles into more and smaller bubbles during mixing. Therefore, when xanthan–guar gum blend–DATEM mixture was incorporated into dough, the pores of gluten-free breads were found to be smaller and more uniform in size (Fig. 7.4b, d, f, h). The high internal heat generation in infrared–microwave combination baking produced higher internal pressure, which created a puffing effect, and this puffing effect resulted in the formation of looser and more porous structure. Consequently, among all gluten-free breads, the most homogenous structure was obtained in the presence of chestnut flour, xanthan–guar gum blend–DATEM mixture addition, and infrared–microwave combination baking (Fig. 7.4). The pore area fractions of gluten-free breads prepared with different formulations and baked in different ovens based on scanned images are presented in Fig. 7.5.

The lowest pore area fraction values were obtained from control breads. However, the replacement of rice flour with chestnut flour increased the pore area fractions of breads. Furthermore, the incorporation of xanthan–guar gum–DATEM mixture and the use of infrared–microwave combination oven resulted in higher pore area fraction values. Therefore, the qualitative information based on scanned images was found to be in agreement with the quantitative data obtained by image analysis. In order to obtain quantitative information about the microstructure of breads, SEM images at magnification of 20× were used for the image analysis. Similar to scanned images, the highest pore area fraction values were obtained from breads

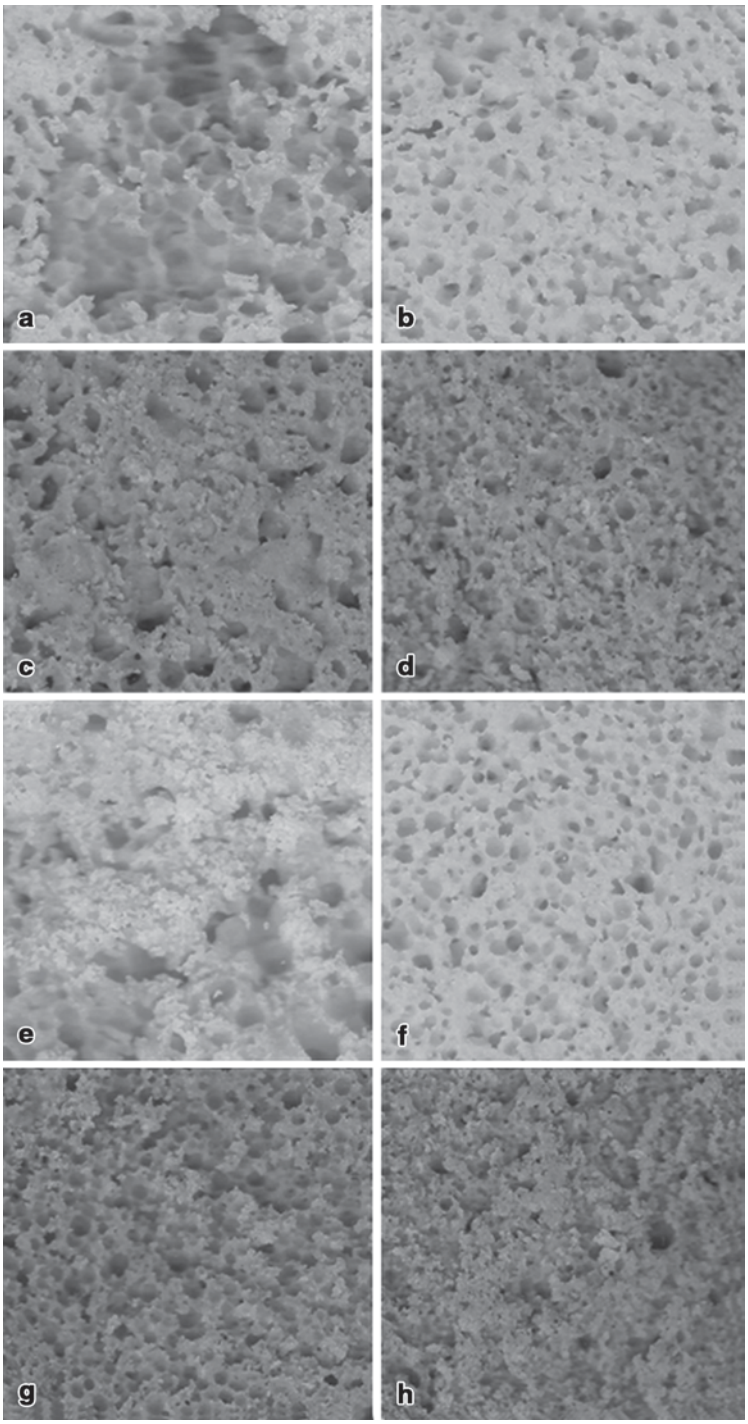

Fig. 7.4 Scanned images of different gluten-free bread formulations baked in different ovens. **a** Rice bread baked in a conventional oven. **b** Rice bread containing xanthan–guar gum blend–DATEM mixture and baked in a conventional oven. **c** Chestnut-rice breads baked in a conventional

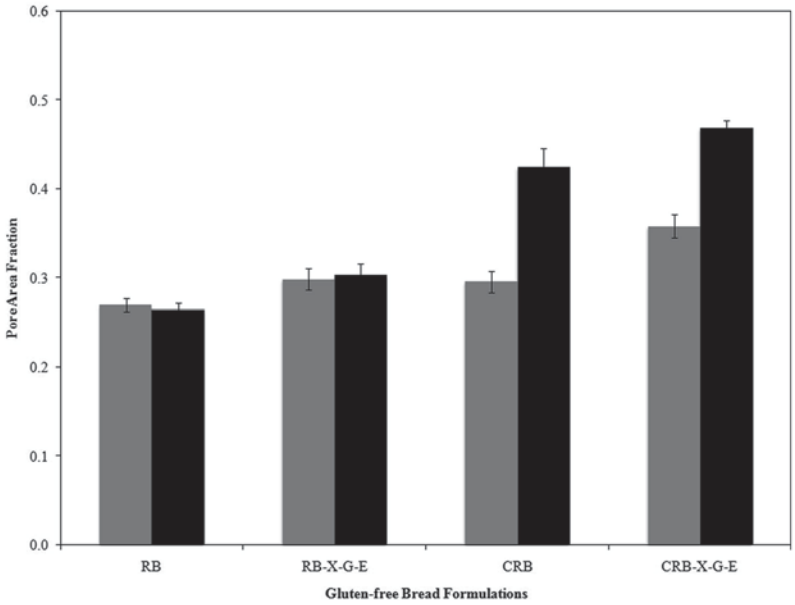

Fig. 7.5 Based on scanned images, pore area fractions of different gluten-free bread formulations baked in conventional *(gray)* and infrared–microwave combination ovens *(black)*. (*RB* rice bread, *RB-X-G-E* rice bread containing xanthan–guar gum blend–DATEM mixture, *CRB* chestnut-rice bread, *CRB-X-G-E* chestnut-rice bread containing xanthan–guar gum blend–DATEM mixture). (Reprinted from Demirkesen et al. 2013, copyright 2013, with permission Springer)

formulated with chestnut flour with xanthan–guar gum blend–DATEM mixture addition and baked in an infrared–microwave combination oven (Fig. 7.6).

In this study, SEM pictures of the bread crumbs at 1000× magnification were also obtained (Fig. 7.7). Control breads, especially conventionally baked ones, had less-developed pores due to the entrapment of insufficient amount of air bubbles into the dough (Table 7.1 and Fig. 7.7a, e). More homogenous structure was obtained in breads prepared with the replacement of rice flour with chestnut flour (Table 7.1 and Fig. 7.7c, d, g, h).

The enhancement of viscosity and decrease in starch-protein binding in the presence of fiber might lead to the formation of more homogenous structure. It was also suggested that the significant relationship between starch granule size and gas retention might also affect final crumb appearance. Flours that have larger starch

oven. **d** Chestnut-rice bread containing xanthan–guar gum blend–DATEM mixture and baked in a conventional oven. **e** Rice bread baked in an infrared–microwave combination oven. **f** Rice bread containing xanthan–guar gum blend–DATEM mixture and baked in infrared–microwave combination oven. **g** Chestnut-rice breads baked in an infrared–microwave combination oven. **h** Chestnut-rice bread containing xanthan–guar gum blend–DATEM mixture and baked in an infrared–microwave combination oven. (Reprinted from Demirkesen et al. 2013, copyright 2013, with permission Springer)

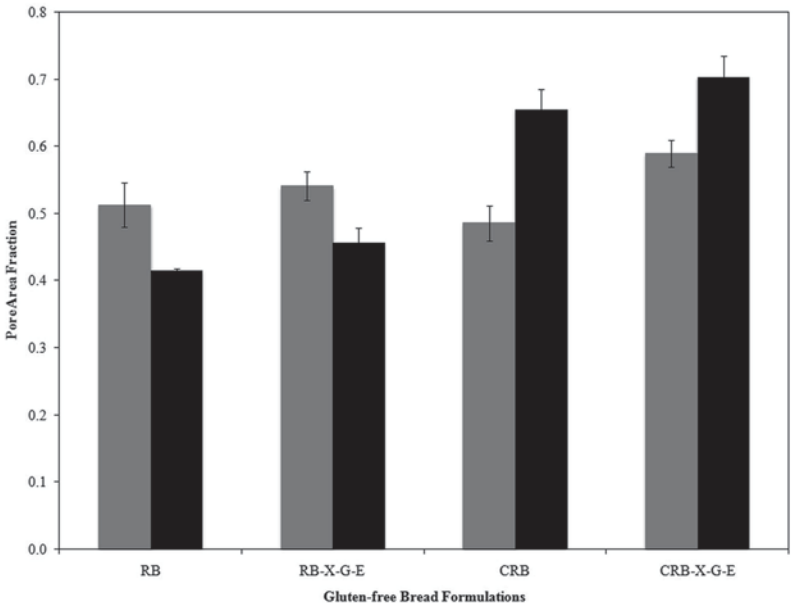

Fig. 7.6 Based on SEM, pore area fractions of different gluten-free bread formulations baked in conventional *(gray)* and infrared–microwave combination ovens *(black)*. (*RB* rice bread, *RB-X-G-E* rice bread containing xanthan–guar gum blend–DATEM mixture, *CRB* chestnut-rice bread, *CRB-X-G-E* chestnut-rice bread containing xanthan–guar gum blend–DATEM mixture). Magnification: 20×. (Reprinted from Demirkesen et al. 2013, copyright 2013, with permission Springer)

granules, like chestnut starch granules, might release more amylose during baking since they contain more amylose as compared to small rice granules. Thus, a film-like structure was formed by the interaction between that amylose and protein which might coalesce less during the baking of chestnut-flour-containing breads. Like scanned images of breads, SEM images also showed that among all breads prepared without any additives, the most homogenous structure was obviously obtained from breads formulated with chestnut flour and baked in an infrared–microwave combination oven (Fig. 7.7g). More homogenous pore distributions were observed in gluten-free breads containing xanthan–guar gum blend–DATEM mixture (Fig. 7.7b, d, f, h).

7.4.3 Sorghum Flour

Sorghum is a member of the grass family of Graminae and tribe Andropoggonae. It is regarded as a primary ingredient in bread in most urban areas due to its easier growing conditions and low prices (Arendt and Moore 2006). Although, sorghum is reported to have very similar chemical composition to maize, it has slightly lower protein (11–12%) and starch digestibility. Furthermore, sorghum flour is also

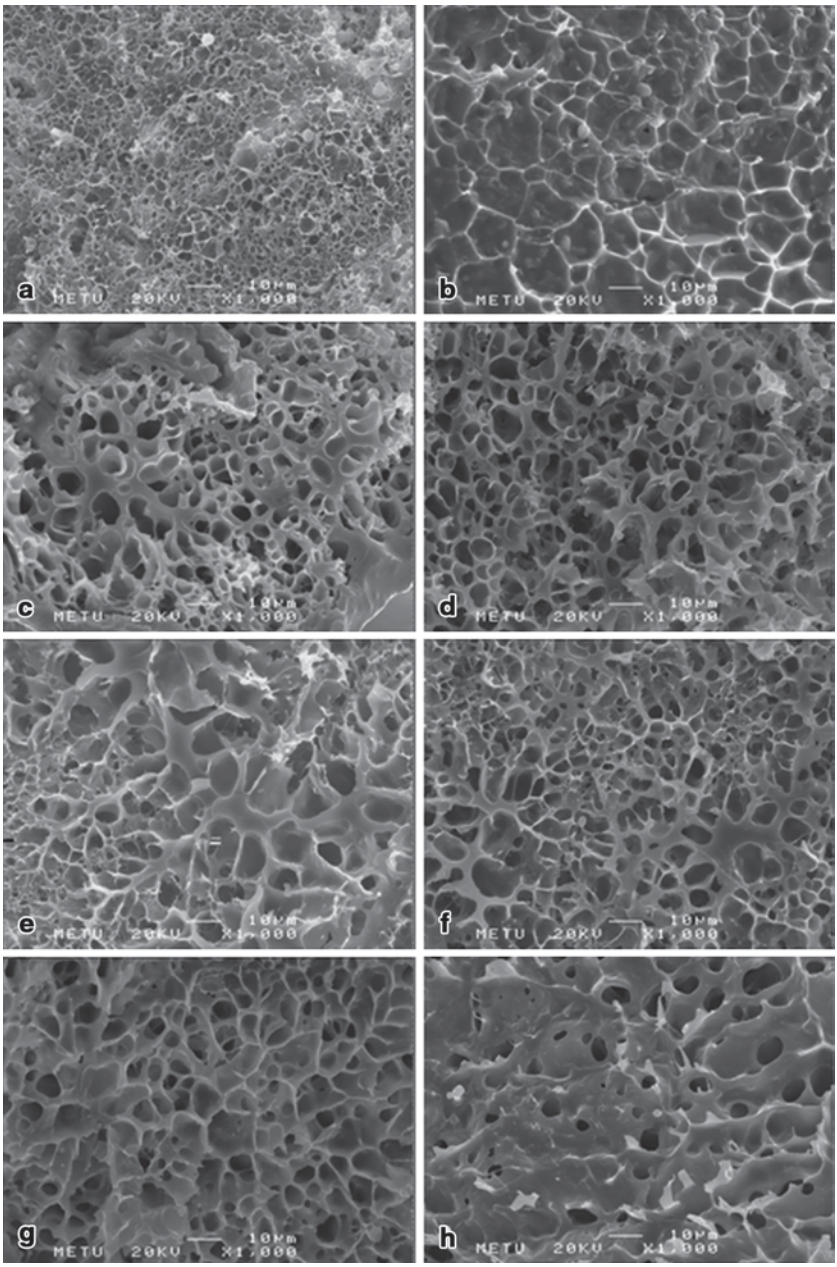

Fig. 7.7 SEM micrographs of the outside of gluten-free bread crumb samples baked in different ovens. **a** Rice bread baked in a conventional oven. **b** Rice bread containing xanthan–guar gum blend–DATEM mixture and baked in a conventional oven. **c** Chestnut-rice breads baked in a conventional oven. **d** Chestnut-rice bread containing xanthan–guar gum blend–DATEM mixture and baked in a conventional oven. **e** Rice bread baked in an infrared–microwave combination oven. **f** Rice bread containing xanthan–guar gum blend–DATEM mixture and baked in an infrared–

Table 7.1 Pore area distribution of gluten-free breads prepared with different formulations and baked in different ovens. (Reprinted from Demirkesen et al. 2013, copyright 2013, with permission Springer)

Number of pores					
Range of pore area (mm^2)	Oven type	RB-X-G-E	RB	CRB-X-G-E	CRB
	Conventional				
0–5		161	98	278	339
5–10		62	23	54	32
10–20		24	18	28	24
>20		3	11	1	5
Total number of pores		250	150	361	400
	Infrared–microwave combination				
0–5		259	271	291	292
5–10		54	25	27	26
10–20		16	23	26	25
>20		0	5	17	19
Total number of pores		329	324	361	362

RB rice bread, *RB-X-G-E* rice bread containing xanthan–guar gum blend–DATEM mixture, *CRB* chestnut-rice breads, *CRB-X-G-E* chestnut-rice bread containing xanthan–guar gum blend–DATEM mixture

neutral in flavor and light in color. As in the case of maize and millet, the protein content of sorghum is not considered to have a large role in creating structure in foods. However, sorghum proteins are reported to form cross-links with themselves or with other constituents during processing as well as cooking that directly impact the functional properties of dough and the quality of sorghum-based products (Hamaker and Bugusu 2003). Gluten-free breads made from sorghum present technical difficulties. Thus, very limited studies have been conducted on gluten-free sorghum dough and bread characteristics. Schober et al. (2004) evaluated crumb characteristics of gluten-free breads made from different sorghum varieties by digital image analysis and texture profile analysis (TPA). Significant differences in crumb structure in terms of number of pores, pore size, and hardness were found and were related to differences in kernel hardness and damaged starch. It has been postulated that a coarse and open crumb structure might provide less resistance to the probe during TPA, thus resulting in softer crumb. In a recent study of Hager et al. (2012), crumb grain characteristics of gluten-free breads prepared with sorghum, oat, buckwheat, rice, maize, quinoa, and teff flours were investigated by image analysis. SEM was also used for the observation of microstructure of dough and bread samples, while a C-cell bread imaging system was used for the quantitative description of the crumb grain characteristics. Digital image analysis revealed that

microwave combination oven. **g** Chestnut-rice breads baked in an infrared–microwave combination oven. **h** Chestnut-rice bread containing xanthan–guar gum blend–DATEM mixture and baked in an infrared–microwave combination oven. Magnification: 1000×. (Reprinted from Demirkesen et al. 2013, copyright 2013, with permission Springer)

several gluten-free samples prepared with quinoa, teff, maize, and buckwheat were characterized by a dense structure with a low number of cells as a percentage of a slice area. On the other hand, breads made from oat and rice had an open aerated structure with a higher number of cells. The SEM images of the breads also reflected a more aerated crumb structure of oat and rice breads, and this result was found to be in accordance with the macrostructure observations obtained by image analysis. By regarding the results of both digital image analysis and quality tests (specific volume, crumb hardness, springiness, loaf height, and sensory), the authors concluded that only breads produced from oat flour had a similar quality to wheat bread.

7.4.4 Pseudocereal Flours

Buckwheat, amaranth, and quinoa are classified as pseudocereals, and their seeds show similarity with true cereals in terms of their function and composition. Pseudocereals contain a high amount of starch (52–69 %), which make them important energy sources. The protein content of pseudocereals ranges approximately from 11 to 18 %. Pseudocereals are also rich in sources of good-quality protein with the acceptable levels of essential amino acids, and the structural characteristics of these proteins influence their techno-functional properties. They also have a high amount of dietary fiber and lipids rich in unsaturated fats. Moreover, they contain adequate levels of important micronutrients, such as minerals and vitamins, and significant amounts of other bioactive components (Alvarez-Jubette et al. 2010). Due to their excellent nutritional value, the latest studies have focused on the use of pseudocereals in the formulation of high-quality, healthy, gluten-free products. In the study of Alvarez-Jubette et al. (2010), technological characteristics (i.e., batter and baking properties) of pseudocereals (amaranth, quinoa, and buckwheat) as ingredients in the production of gluten-free breads were evaluated. In this study, SEM images were used to evaluate properties of flours. CLSM images obtained from the baked breads were used to obtain qualitative information about microstructure (Fig. 7.8).

On the other hand, C-cell bread imaging analysis was conducted on the bread slices to obtain quantitative information (Fig. 7.9).

SEM images of the flours indicated that the size of flour particles had significant differences, and the smallest particle size was observed in potato starch and wheat flour, followed by rice, buckwheat, amaranth, and quinoa flours. The results for the crumb grain analysis of the baked breads showed that the largest number of cells was obtained from buckwheat bread, followed by quinoa, control, and amaranth breads. The smallest cell volume was found in gluten-free control bread, followed by quinoa, amaranth, and buckwheat breads. The cell wall was the thinnest in quinoa bread, followed by control, buckwheat, and amaranth breads in increasing order. Significant variations were obtained between CLSM images of different breads (Fig. 7.8). Starch gelatinization, which was characterized by fusing starch granules together and losing their original structure, occurred at a greater degree in the gluten-free control bread compared with the pseudocereal-containing gluten-free

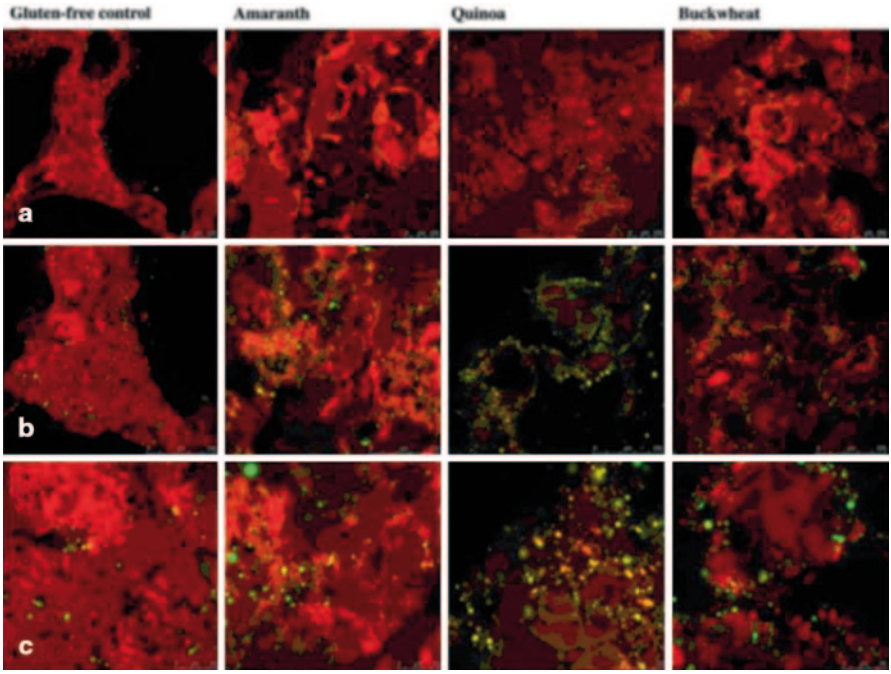

Fig. 7.8 Confocal laser-scanning micrographs of gluten-free control, amaranth, quinoa, and buckwheat breads. Scale bars row **a** 0–250 μm, **b** 0–250 μm, **c** 0–50 μm. (Reprinted from Alvarez-Jubete et al. 2010, copyright 2010, with permission Springer)

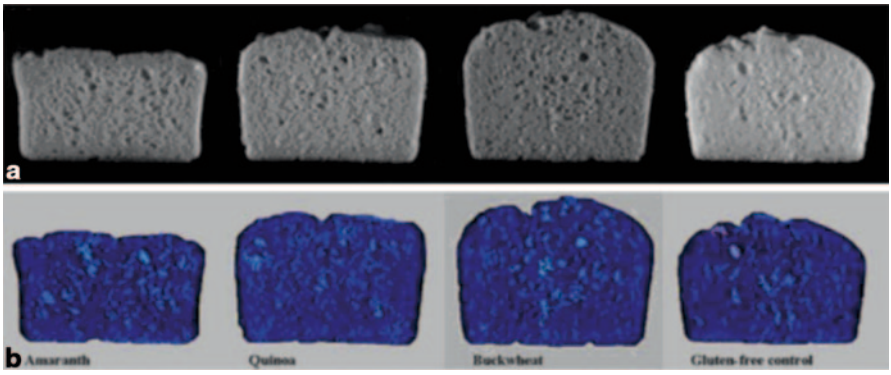

Fig. 7.9 Raw (**a**) and cell (**b**) images of amaranth, quinoa, buckwheat, and gluten-free control breads. (Reprinted from Alvarez-Jubete et al. 2010, copyright 2010, with permission Springer)

breads. Pseudocereal-containing gluten-free breads had a more homogenous structure with less gas voids and a more even distribution of fat, protein, and starch. The pseudocereal-containing breads were characterized by a noticeably softer crumb texture that was attributed to the presence of natural emulsifiers in the pseudocereal flours and confirmed by the CLSM images (Fig. 7.8). Thus, the authors suggested

the application of pseudocereal flours as feasible ingredients in the manufacture of good-quality and healthy gluten-free breads.

7.5 Ingredients and Additives Used to Improve the Structure of Gluten-Free Baked Products

Nowadays, the use of additives, which have the ability to mimic the viscoelastic properties of gluten, has commonly been applied in the gluten-free industry. Hydrocolloids have been widely used in the gluten-free bakery industry since they can improve dough viscoelasticity, enhance moisture retention, improve gas holding, texture, and shelf life as well as retard starch retrogradation, modify gelatinization of starch and act as fat replacer in formulations (Arendt et al. 2008). There has been growing interest in the use of hydrocolloids as gluten substitutes in gluten-free bread formulations (Acs et al. 1997; Anton and Artfield 2008; Brites et al. 2010; Demirkesen et al. 2010a, b; Demirkesen et al. 2011, 2013, 2014a, b, c; Gambus et al. 2001; Leray et al. 2010; Peressini et al. 2011; Ribotta et al. 2004). The most commonly used hydrocolloids in the gluten-free industry are xanthan gum, guar gum, locust bean gum (LBG), HPMC, and carboxymethylcellulose (CMC).

McCarthy et al. (2005) optimized a gluten-free bread formulation based on rice flour, potato starch, HPMC, and skim milk powder using a response surface methodology. Crumb structure was evaluated using a digital image analysis system. The crumb grain parameters used in this study were as follows: number of small cells ($0.05 < x < 4.00$ mm^2), number of large cells (> 4.00 mm^2), number of cells/cm^2 (including small and large cells), and mean cell area in mm^2. Both sides of three central slices of each loaf were used for crumb grain measurements (60×60 mm cropped scanned images of the crumb), yielding 24 images per formulation in the optimization experiment and 12 images per replicate in the shelf-life trial. It has been stated that increasing HPMC and water level decreased crumb firmness and increased specific volume. However, high levels of HPMC and water had adverse effects on crumb structure by reducing the number of cells per unit area. When optimized bread formulation was used, the resulting bread was found to be comparable with a wheat bread in terms of mean cell area, but was still lower in terms of number of cells/cm^2. Schober et al. (2008) showed that the addition of HPMC resulted in a regular, fine, gluten-free crumb, a round top, and good aeration. HPMC also stabilized gas bubbles. CLSM revealed finer zein strands in the dough when HPMC was present. Sciarini et al. (2010) conducted a study to assess the influence of the addition of different hydrocolloids (carrageenan, alginate, xanthan gum, CMC, and gelatin) on gluten-free batter properties and bread quality and to obtain information about the relationship between dough consistency and bread quality. Images analysis was done using ImageJ software. Cell average area (mm^2) and number of cells per square millimeter were determined (0.15 and 10.00 mm^2 were the lower and upper area limit values, respectively, for being considered as cells by the software). The ratio of small cells ($0.15 < x < 2.00$ mm^2) to large cells ($2.00 < x < 10.00$ mm^2)

was calculated. The highest consistency and specific volume were observed for xanthan-containing batters and breads. The addition of xanthan gum enhanced crumb, thus leading to the formation of a more aerated structure with increased cell size and reduced shrinkage. Xanthan gum incorporation also decreased crumb firmness and retarded staling.

In addition to hydrocolloids, emulsifiers are also commonly used in bakery products to assist blending and emulsification of ingredients, to enhance the properties of the shortening, and to obtain a softer crumb. Moreover, they enhance dough-handling ability; improve rate of water absorption; provide greater tolerance to resting and fermentation; improve crumb structure and loaf volume; increase uniformity in cell size; advance gas retention resulting in lower yeast requirements, better oven spring, and faster rate of proof; and provide longer shelf-life of bread (Stampfli and Nersten 1995). Although the synergic interaction between hydrocolloids and emulsifiers is well known, there are limited publications on the use of both hydrocolloids and emulsifiers in gluten-free bread formulations (Demirkesen et al. 2010a, b, 2011, 2013, 2014a, b, c; Nunes et al. 2009a; Onyango et al. 2009). Demirkesen et al. (2014b) examined the effects of adding the emulsifier DATEM and different gums (xanthan, guar, LBG, agar, methylcellulose (MC), CMC and HPMC) and gum blends (xanthan–guar and xanthan–LBG) on crumb structure of gluten-free breads by X-ray μCT. In this study, porosity, number of pores, average pore size, aspect ratio, and roundness of pores were used as parameters to describe the internal structure of the crumbs, and the characteristics of the crumb structure were related to the hardness, cohesiveness, and springiness of breads. 2D and 3D X-ray μCT images of gluten-free bread samples prepared with the addition of different gums or different gum blends indicated that in the lack of hydrocolloids and the emulsifier DATEM, control breads had a very open sponge-like structure (Figs. 7.10 and 7.11). The crumb structures of gluten-free breads prepared with MC and agar showed similarity to the control bread crumb structure. It was observed that these breads exhibited heterogeneous structures with lots of void spaces (open pores). The reason for undesirable, heterogeneous crumb appearances of these breads might be related to the nonuniform distribution of open pores as well as the wide distribution of closed cells in breads. In addition, control, MC, and agar were not capable of providing high viscosity and viscoelastic structure to dough during mixing, which might be another reason for their heterogeneous crumb appearance with nonuniformly distributed void spaces (Figs. 7.10a–c and 7.11a–c). On the other hand, except MC and agar, the presence of a relatively higher number of smaller pores of gluten-free breads prepared with additives provided the capture of more gas bubbles and moisture in their closed pores, resulting in finer crumb structure (Figs. 7.10d–j and 7.11d–j). Porosity, number of pores, averages size of pores, aspect ratio, and roundness values of pores are shown in Table 7.2.

Among all gluten-free breads, gluten-free breads prepared with the addition of MC, agar, and no additives had the highest porosity values with the lowest number of pores, which indicated a nonuniform crumb structure with very large pores. The highest average areas of pores observed for these breads were related to the interconnection between all gas cells (Table 7.2, Figs. 7.10a–c and 7.11a–c).

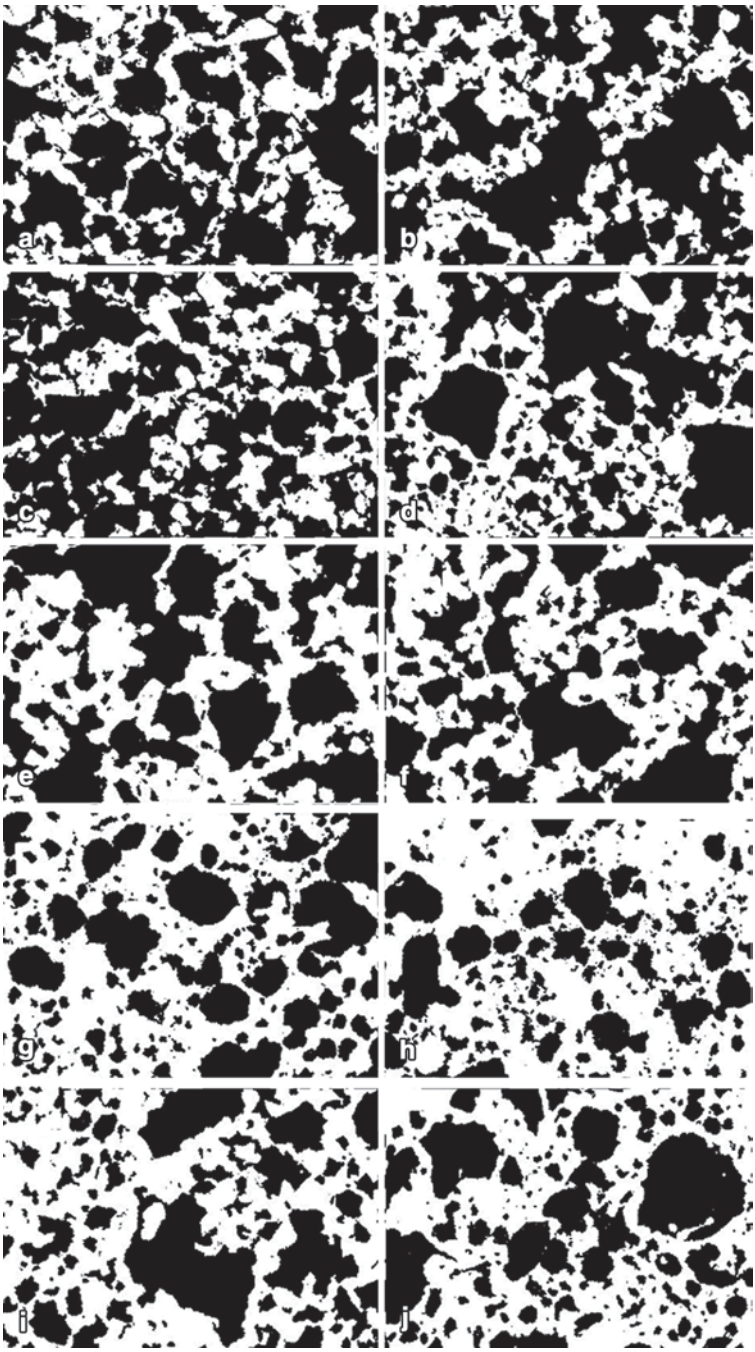

Fig. 7.10 2D X-ray μCT images of gluten-free bread slices prepared with different gums or gum blends. **a** Control breads. **b** Breads prepared with methylcellulose. **c** Breads prepared with agar. **d** Breads prepared with locust bean. **e** Breads prepared with guar. **f** Breads prepared with xanthan. **g** Breads prepared with carboxymethylcellulose. **h** Breads prepared with hydroxypropylmethylcellulose. **i** Breads prepared with xanthan–locust bean gum blend. **j** Breads prepared with xanthan–guar gum blend. (Reprinted from Demirkesen et al. 2014b, copyright 2014, with permission Elsevier)

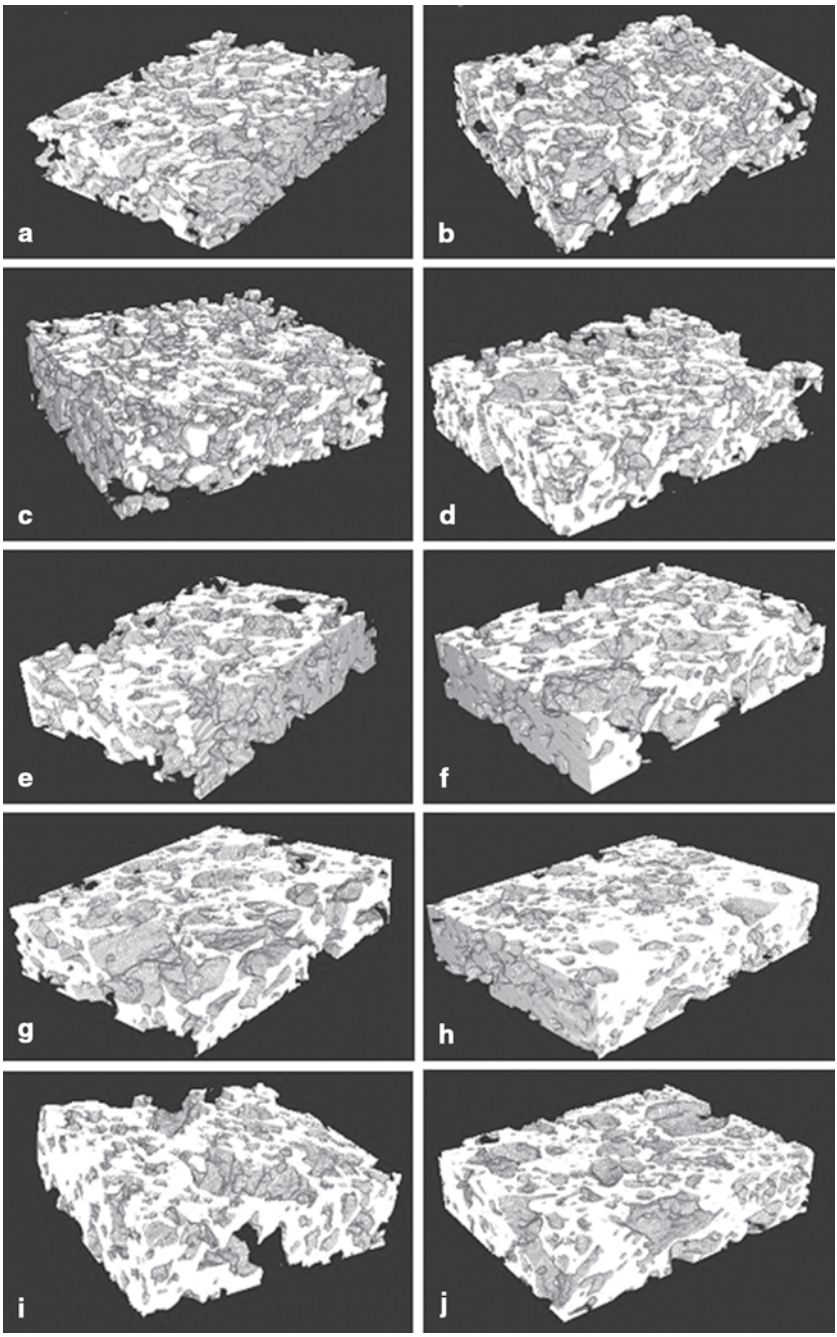

Fig. 7.11 3D X-ray μCT images of gluten-free bread samples prepared with different gums or gum blends. **a** Control breads. **b** Breads prepared with methylcellulose. **c** Breads prepared with agar. **d** Breads prepared with locust bean. **e** Breads prepared with guar. **f** Breads prepared with xanthan. **g** Breads prepared with carboxymethylcellulose. **h** Breads prepared with hydroxypropylmethylcellulose. **i** Breads prepared with xanthan–locust bean gum blend. **j** Breads prepared with xanthan–guar gum blend. (Reprinted from Demirkesen et al. 2014b, copyright 2014, with permission Elsevier)

Table 7.2 Quantification of the porous structure per slice thickness (0.036 mm) and per identical size (~0.688 cm^3) of the gluten-free bread samples prepared with different gums or gum blends. (Reprinted from Demirkesen et al. (2014b), copyright 2014, with permission Elsevier)

Gluten-free bread samples	Porosity values of identical size (~0.688 cm^3)		Number of pores per 1.85 cm^2 area		Average size of the pore (cm^2)	
		SE		SE		SE
Control	0.568[a]	1.65	8.56[c]	3.079	0.165[a]	1.20
MC	0.629[a]	2.05	5.10[c]	2.015	0.298[a]	2.07
A	0.602[a]	1.72	3.99[c]	1.091	0.478[a]	4.26
LBG	0.539[b]	1.21	11.0[b]	1.094	0.088[b]	0.19
G	0.510[b]	1.34	11.4[b]	2.096	0.083[b]	0.24
X	0.453[c]	0.98	13.9[a]	2.052	0.055[c]	0.13
CMC	0.471[c]	1.16	15.5[a]	1.092	0.050[c]	0.09
HPMC	0.382[c]	0.87	14.3[a]	2.006	0.040[c]	0.07
X-LBG	0.502[c]	1.76	12.3[a]	2.047	0.071[b]	0.18
X-G	0.423[c]	1.18	14.4[a]	2.073	0.047[c]	0.15

Analysis was done in duplicate. Pores > 0.01 cm^2 considered. Values are means of 100 slices
SE standard error of 100 slices *MC* methylcellulose, *A* agar, *LBG* locust bean gum, *G* Guar gum, *X* Xanthan, *CMC* carboxymethylcellulose, *HPMC* hydroxypropyl methylcellulose
[a, b, c] Formulations having different letters are significantly different ($p \leq 0.05$)

A significant negative correlation between porosity and number of pores ($r = -0.90$) and a positive correlation between porosity and average size of pores ($r = 0.80$) were also found in that study. This result also indicated the noticeable effect of void spaces on porosity of crumb structure. As opposed to breads containing MC and agar and control breads, the lowest porosity, the lowest average pore area, and the highest number of pores were observed for gluten-free breads prepared with the addition of xanthan, CMC, xanthan–guar, xanthan–LBG, and HPMC. A negative correlation observed from the data between number of pores and average size of pores ($r = 0.94$) indicated the finest crumb structure of these breads with the highest number of smaller pores. The aspect ratio of all the bread samples, which expresses the relationship between the width of the pore and its height, was found to be under 2, representing the ellipsoidal nature of the pores. The roundness of pores in gluten-free bread samples prepared with different additives was found to be between 0.559 and 0.637 indicating their noncircular shape.

Recently, enzymes such as amylase, cyclodextrin glycosyltransferases (CGT), transglutaminase (TG), glucose oxidase (GO), laccase, and proteases have been successfully used in the gluten-free baking industry in order to improve dough-handling ability and water-binding capacity as well as texture and shelf life of products. Since the proteins in cereals except wheat gluten do not aggregate to continuous network in dough at room temperature, protein functionality can be modified by cross-linking. Recently, protein-cross-linking enzymes, such as TG, have been used in the gluten-free industry since they are responsible for the formation of a protein network—through the formation of intra- and intermolecular cross-links between the polypeptide chains. TG is responsible for the formation of new covalent cross-links in proteins via lysine and glutamine residues. It can be applied as a protein

modifier, and it is able to modify the functional characteristics of a wide range of proteins, such as casein and albumen from milk, animal protein from eggs and meat, soy protein, and wheat protein (Arendt et al. 2009). Moore et al. (2006) evaluated the impact of TG at different levels (0, 0.1, 1, and 10 U of TG/g of protein) on the quality of gluten-free bread prepared by rice flour, potato starch, corn flour, xanthan gum, and various protein sources (skim milk powder, soy flour, and egg powder). For image analysis, the images of the bread were captured using a flatbed scanner and supporting software. Brightness levels were adjusted, and a square field of view was evaluated for each image, which in turn captured the majority of the crumb area of each individual slice of bread. The crumb grain feature chosen was the number of cells per square centimeter in digital photographs. From the image analysis based on the scanned images, it was observed that TG inclusion increased the number of cells per square centimeter of bread crumbs when milk and egg powder were used. This result suggested an improvement in the crumb structure due to protein cross-linking. Image characteristics of breads were also evaluated by using CLSM. CLSM images indicated that no differences could be detected between the microstructure of batters containing TG and their controls, and no orientated protein network was visible within these batters. The microstructure of the breads indicated that TG application improved continuity in the protein network within skim–milk- and egg-powder-containing gluten-free breads. It was concluded that it is possible to form a protein network in gluten-free bread with the addition of TG, but the efficiency of the enzyme changes depending on both the protein source and the level of TG concentration. To promote protein cross-linking, Renzetti et al. (2008) studied the incorporation of 0.1 and 10 U of TG into six different gluten-free cereals (brown rice, buckwheat, corn, oat, sorghum, and teff). CLSM was used to observe the modifications caused by TG on the microstructure of batters and breads made with brown rice or buckwheat (Figs. 7.12 and 7.13).

The microscopy images of control buckwheat and brown rice batters, which were incubated for 30 min and prepared without addition of any enzyme revealed a homogeneous distribution of proteins in the system (Fig. 7.12). The incorporation of 10 U of TG after 30 min incubation resulted in buckwheat and brown rice proteins appearing to be distributed in aggregates. 180 min of incubation caused larger protein agglomerates formation in the system, and no differences could be detected for the other cereal batters. The incorporation of 10 U of TG enhanced the continuity of the protein phase in breads (Fig. 7.13).

The result of the study indicated that upon the addition of TG, the rheology of batters and the quality of breads from buckwheat, rice, and corn flour improved, but no improvement occurred when oat, teff, and sorghum flours were used (Renzetti et al. 2008). Thus, it was suggested that TG can be successfully applied to gluten-free flours to improve their breadmaking potentials by promoting network formation, but the protein source is a key element in determining the impact of the enzyme. The use of CLSM confirmed the improvements brought by TG on the microstructure of batters and breads. The impact of the different levels of laccase, GO, and protease on the breadmaking performance of gluten-free oat flour was also tested (Renzetti et al. 2010). The addition of laccase and protease enzymes significantly

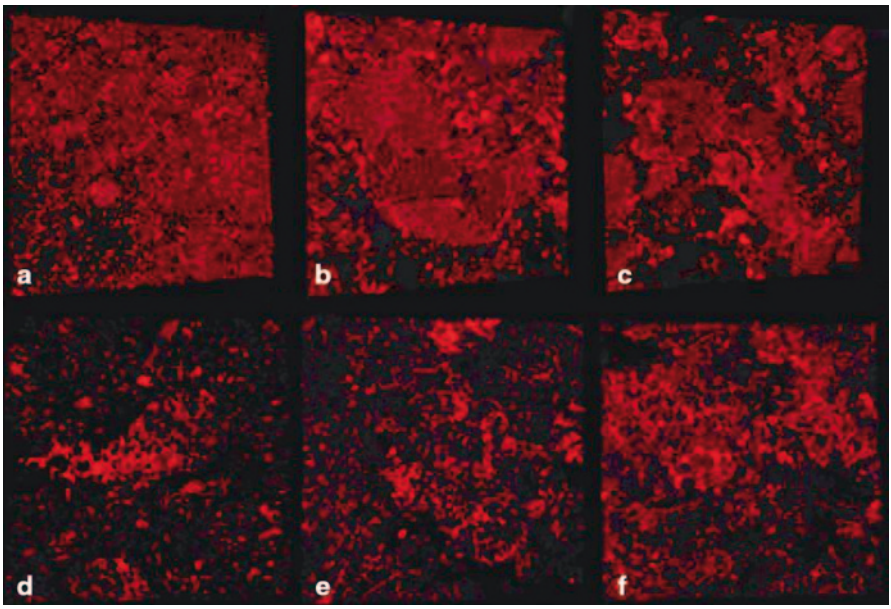

Fig. 7.12 3D elaboration of confocal laser-scanning microscopy (CLSM) images of buckwheat (BW) and brown rice (BR) batters (40× magnification): **a** BW control (0 U of enzyme) after 30 min at 301 C, **b** BW 10 U of transglutaminase (TG) batter after 30 min at 301 C, **c** BW 10-U batter after 180 min at 301 C, **d** BR control (0 U of enzyme) after 30 min at 301 C, **e** BR 10 U of TG batter after 30 min at 301 C, **f** BR 10-U batter after 180 min at 301 C. Proteins appear *red*. With increasing incubation time, the proteins in the batter change from a homogeneous dispersion (**a** and **d**) to protein aggregates (**b** and **c, e** and **f**). (Reprinted from Renzetti et al. 2008, copyright 2008, with permission Elsevier)

enhanced the quality of oat bread as the enzymes increased the specific volume and decreased crumb hardness and chewiness. The improved quality of breads upon the addition of these enzyme preparations was attributed to their noticeable levels of endo-β-glucanase side activity. CLSM of bread crumbs revealed that the addition of GO resulted in larger protein aggregates in the bread crumbs, and these globular aggregates negatively affected the breadmaking performances of oat bread. In contrast, protease addition showed the presence of smaller protein clusters dispersed in the system, resulting in oat breads of the best textural quality. Renzetti and Arendt (2009a) studied the impact of GO and protease on the breadmaking performance of four different gluten-free flours (buckwheat, corn, sorghum, and teff). GO enhanced corn and sorghum bread quality by increasing specific volume and reducing collapsing at the top. The improvements of the bread quality were related to the aggregation of the dispersed protein structures as revealed by CLSM and resulted in enhanced continuity of the protein phase and elastic-like behavior of corn and sorghum batters. In another study of Renzetti and Arendt (2009b), the effect of protease treatment was investigated on the baking properties of brown rice bread.

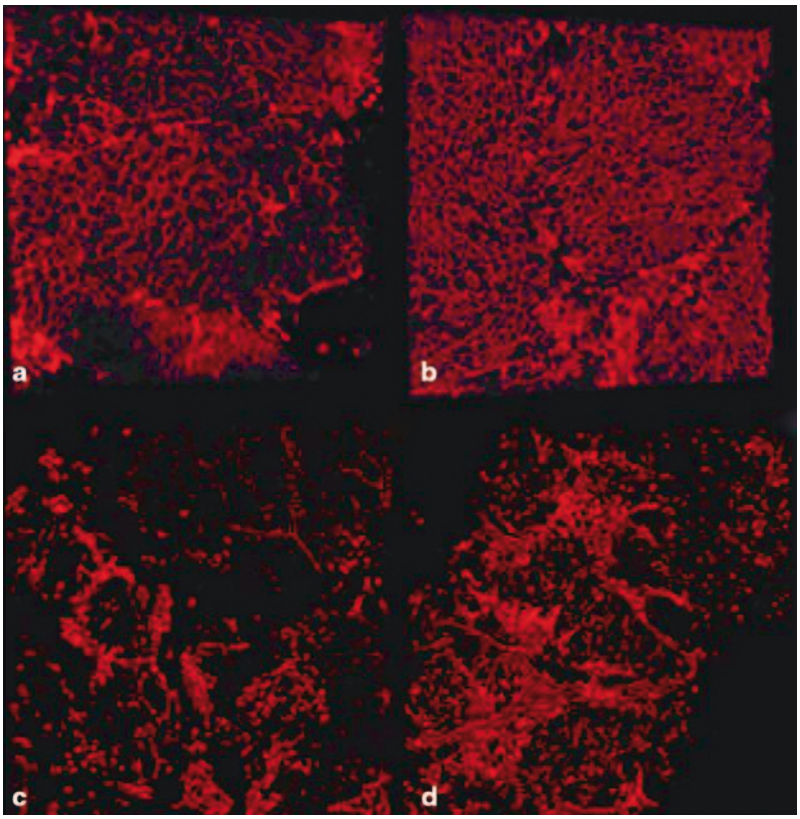

Fig. 7.13 3D elaboration of confocal laser-scanning microscopy (CLSM) images of buckwheat (BW) and brown rice (BR) bread crumb (40× magnification): **a** BW control bread (0 U of enzyme), **b** BW 10 U of transglutaminase (TG) bread, **c** BR control bread (0 U of enzyme), **d** BR 10 U of TG bread. Proteins are stained *red* together with yeast cells, which appear *round shaped*. For BW, the control bread shows a continuous protein network, characteristic only of BW breads. The addition of the enzyme results in a crumb with a strengthened, finer-meshed protein network. For BR, the control bread shows the absence of any kind of protein network. The addition of the enzyme enhances the continuity of the protein phase. (Reprinted from Renzetti et al. 2008, copyright 2008, with permission Elsevier)

It was shown that protein degradation could be beneficial in improving the bread-making performances of brown rice flour, by increasing the specific volume of the bread and decreasing crumb hardness and chewiness. CLSM images confirmed that the gelatinized starch phase was the main structuring component in protease-treated breads.

In order to improve both the nutritional and functional properties of gluten-free products, the replacement of gluten with protein sources such as dairy, egg, soy, and maize has long been used in gluten-free baking technology (Ahlborn et al. 2005; Gallagher et al. 2003; Marco and Rosell 2008; Nunes et al. 2009b; Schober et al.

2004; Van Riemsdijk et al. 2011). The incorporation of two important milk proteins, caseins and whey proteins, has been established in gluten-free baking industry in order to increase water absorption and, therefore, enhance the handling properties of the batter and bread characteristics. Besides, supplementing the gluten-free formulation with high-protein-content dairy powders also increases the protein content of the breads (Gallagher et al. 2003). Schober et al. (2004) tested the influence of milk proteins and rice starch on crumb structure (pore size, number of pores, and crumb hardness) by using digital image analysis and TPA. Bread slices were scanned by a flatbed scanner and digital image analysis of the crumbs was performed using a digital image analysis system. Mean cell area and total number of cells were selected as crumb structure features. It was found that the addition of milk proteins and rice starch in gluten-free sorghum breads resulted in the formation of more open structure and hence decreases in the number of cells per square centimeter. The more open structure provided less resistance to the probe during TPA, and thus softer textures were obtained from the bread supplement with milk proteins. Moore et al. (2004) produced gluten-free breads using dairy protein sources. Due to its high resolution and ability to scan through thick samples, CLSM proved to be very useful in detecting the desirable protein structure elements of bread crumb. From CLSM images it was observed that the dairy-based gluten-free bread crumb had a network-like structure, which resembled a gluten network in wheat bread crumb. This study showed that the formation of a continuous protein phase and film-like structures was critical for an improved quality of gluten-free bread based on starch retrogradation. Ahlborn et al. (2005) compared the microstructure of wheat bread with low-protein starch bread and with gluten-free bread supplemented with egg proteins and milk proteins by SEM. Both low-protein starch bread and gluten-free bread contained xanthan gum and HPMC. It was observed that both cell diameter and lamellae thickness were larger in the rice and low-protein starch breads as compared to wheat bread. SEM images made it possible to see a web-like structure in gluten dough and gluten bread. On the other hand, in the low-protein starch bread, coalescence of the gas cells as evidenced by larger cell diameters and thicker lamellae was observed. The results of this study demonstrated that the combinations of rice, tapioca, egg, and milk proteins with xanthan gum and HPMC could create a bicontinuous matrix with starch fragments, similar to gluten. Nunes et al. (2009b) indicated the successful use of low-lactose dairy powders in gluten-free recipes. In this study, the impacts of different low-lactose dairy ingredients (sodium caseinate, milk protein isolate, whey protein isolates, and whey protein concentrate) on gluten-free dough rheology and bread quality were determined. Better quality in terms of specific volume and hardness is attained with whey proteins. CLSM images showed that the microstructure of casein-containing breads was dominated by a starch phase, where no protein network could be observed, while the incorporation of whey protein formed a protein network. It has been noted that the differences in thermal stability of casein and whey protein might play a major role in the resulting microstructure of the bread crumbs containing casein or whey protein.

7.6 Methods to Improve the Microstructure of Gluten-Free Products

As stated before, producing high-quality gluten-free products is one of the most challenging issues for cereal technologists and scientists. Up to date, most gluten-free products have been produced by replacing wheat flour by alternative flours as well as using some additives to mimic the viscoelastic properties of gluten. In order to meet the rising demand of celiac patients for high-quality products, sourdough technology, infrared–microwave combination baking, and HHP treatment have also lately been studied as potential methods in gluten-free technology.

7.6.1 Sourdough Technology

Sourdough, which is a mixture of flour and water fermented with lactic acid bacteria (LAB) and/or yeast, is used to improve the quality of wheat breads (Moroni et al. 2009). In order to meet the rising demand of celiac patients for high-quality and healthier products, this old biotechnological process has recently been applied as a new approach in gluten-free breadmaking. It has been stated that the problems associated with gluten-free dough and bread characteristics may be overcome by the application of sourdough. By the application of this technology, the rheological properties of gluten-free dough as well as the quality of gluten-free breads in terms of volume, texture, crumb structure, flavor, and nutritional value may be improved (Moroni et al. 2011; Schober et al. 2007; Zannini et al. 2012a). The positive effects of sourdough on the retardation of the staling process and protecting gluten-free bread from mold and bacterial spoilage have also been demonstrated by researchers (Moore et al. 2007).

Moore et al. (2007) conducted a study on the effects of adding different strains of LAB on gluten-free sourdough, batter, and bread. As controls, chemically acidified (80% lactic acid and 20% acetic acid) and nonacidified batters/breads were used. CLSM, which presents advantages to produce optical sections through a 3D specimen without damaging the structure, was used to observe microscopic changes. Digital image analysis was used to characterize the crumb structure. The images of the bread were captured using a flatbed scanner, and the number of cells was chosen as the crumb structure characteristic. CLSM showed remarkable structural changes in sourdough over time due to the action of the LAB. As compared to the initial microstructures of sourdoughs, smaller and more scattered proteins within starch granules were observed in microimages of sourdoughs at 24 h. This result indicated that the protein particles in sourdough-containing breads were degraded over the fermentation process. Since the degradation was found to be less obvious in gluten-free sourdough, it was concluded that gluten-free sourdoughs did not exhibit oriented protein network or degraded network, which is generally seen in wheat-based sourdough systems. The microimages of gluten-free breads indicated

that gluten-free breads prepared with 20% sourdough incorporation had a higher amount of aggregated and larger particles as compared to nonacidified control gluten-free breads. The pore walls in both nonacidified control and gluten-free batters prepared with 20% sourdough incorporation were characterized by the presence of large denatured soy globules and gelatinized starch granules. Moreover, none of the breads had network formation. Therefore, the control and the breads prepared with the addition of 20% sourdough did not indicate any significant difference in terms of loaves volume and height, number of cells, or mean cell area. However, the addition of sourdough delayed the onset of staling, which showed that the addition of sourdough in gluten-free bread formulation may improve the quality of the resulting bread. Schober et al. (2007) used sourdough fermentation in order to improve the quality of gluten-free sorghum breads. Flatbed scanning images were used to examine the microstructure of breads, while CLSM was applied to understand the microstructure that contributes to bread quality. In the case of sourdough breads, the height of breads was significantly improved. This might be due to the stronger starch gel in sourdough breads. For a further understanding of the mechanisms, the authors compared bread crumbs prepared with the addition of HPMC with those of sourdough breads at microscopic level and also included chemically acidified bread crumb to address the effect of acidification alone. CLSM revealed aggregated protein in both gluten-free breads prepared with HPMC and chemically acidified gluten-free breads. In the case of chemically acidified breads, protein aggregation might be attributed to poor solubility of sorghum proteins at acidic pH values. However, in the case of breads prepared with sourdough fermentation, only small isolated patches of protein bodies embedded in matrix protein remained. Thus, the authors suggested that unlike protein bodies, the specific sourdough fermentation of this study could degrade some other proteins, which would otherwise aggregate upon baking as in the case of bread crumb prepared with the addition of HPMC. The authors concluded that as opposed to gluten proteins, aggregated proteins in the case of gluten-free breads prepared with HPMC and chemically acidified gluten-free bread were clearly not associated with improved bread quality. In contrast, proteins in sourdough-containing breads can no longer cross-link, and therefore they do not aggregate upon baking, which may be attributed to the improved quality of sourdough bread.

7.6.2 Infrared–Microwave Combination Baking Technology

Microwave heating offers a number of advantages such as energy efficiency, faster heating, space saving, precise process control, selective heating, and food with high nutritional quality, but microwave-baked products do not meet with consumer acceptance because of their quality problems (Sumnu 2001). Infrared–microwave combination heating provides selectivity that improves moisture distribution inside food by heating the surface of a food faster. Therefore, moisture can be easily removed from the surface of the product, and the food remains crisp (Datta et al.

2005). This technology combines the browning and crisping advantages of near-infrared heating and the time-saving and energy efficiency advantages of microwave heating. The advantages of infrared–microwave combination heating over microwave heating have been realized over the past few years. Previous attempts have been made to overcome the problems associated with microwave baking, and in these studies the combination of microwave heating with infrared heating has been successfully used by several researchers (Datta et al. 2007; Demirekler et al. 2004; Keskin et al. 2004, 2005; Sakiyan et al. 2011; Sumnu and Sahin 2005). This baking technology may also be a good alternative to conventional baking to produce gluten-free products with comparable quality but in shorter times (Demirkesen et al. 2011, 2013, 2014a, c; Sumnu et al. 2010; Turabi et al. 2008). In recent studies, the images obtained by a flatbed scanner and SEM were used to obtain qualitative and quantitative information about the macro- and microstructure of gluten-free bread and cake products (Demirkesen et al. 2013; Turabi et al. 2010). In the study of Demirkesen et al. (2013), both quantitative and qualitative information were obtained related to the macro- and microstructure of gluten-free breads prepared with rice and chestnut flour and xanthan–guar gum blend–DATEM mixture addition, and baked in conventional and infrared–microwave combination ovens. Quantitative information about crumb cells of the scanned images and SEM micrographs at a magnification of 20× were obtained using Image J software. Binarized images were used for quantitative analysis of pores. Crumb structures of gluten-free bread samples were analyzed by calculating pore area fraction, pore size distribution, and mean roundness values by this software. As discussed before, the macrostructure images of gluten-free breads, which were obtained by the help of a scanner, showed that gluten-free breads baked in infrared–microwave combination oven were looser and more porous (Fig. 7.4). The puffing effect that occurred during infrared–microwave combination baking also increased the pore area fraction values and the total number of pores of gluten-free breads (Fig. 7.5). It has been demonstrated that baking method also affected the pore size distribution of breads significantly. Infrared–microwave combination baking increased the number of small pores in rice breads but large pores in chestnut-rice breads (Fig. 7.5). The quantitative data obtained by SEM images showed that infrared–microwave combination baking resulted in higher pore area fraction values (Fig. 7.6). It has been shown that gluten-free breads baked in an infrared–microwave combination oven had more starch granules, which did not lose their identity and did not disintegrate completely (Fig. 7.7). The authors hypothesized that shorter processing time during infrared–microwave combination baking might affect swelling and gelatinization and lead to incomplete disintegration of starch granules. Turabi et al. (2008) also used flatbed-scanned and SEM images to obtain quantitative and qualitative information on the macro- and microstructure of gluten-free rice cakes containing different types of gums and baked in different ovens. Macrostructure of gluten-free cakes indicated that infrared–microwave combination baking provided more porous structure to cakes, which may be caused by higher pressure gradient during the infrared–microwave combination baking mechanism. Infrared–microwave combination baking increased the pore area fraction values and the total number of pores of gluten-free

cakes and resulted in the formation of pores having larger area. From SEM images it was also observed that conventionally baked cakes showed more starch granule deformations (Fig. 7.3), while cakes baked in an infrared–microwave combination oven had granular starch residues and deformed starch structure together. The studies of Demirkesen et al. (2013) and Turabi et al. (2010) demonstrated that there was a close relationship between the quantitative information obtained from the macro- and microstructure of gluten-free products.

7.6.3 High Hydrostatic Pressure Technology

HHP technology, which consists in applying pressures between 100 and 1000 MPa to foods, creates new structures and textures by modifying functional properties of biopolymers such as proteins and starches (Zannini et al. 2012b). Therefore, HHP may offer a good alternative for enhancing the viscoelasticity of gluten-free doughs and the quality of resulted bakery products. Moreover, this alternative nonthermal technology may prevent the necessity of the use of additives in gluten-free products. It has been stated that HHP treatment induces starch swelling and gelatinization without the disruption of granule integrity that offers advantages over products such as high moisture retention, improvement of gas retention capacity of the batter, hence increased volume, and enhanced shelf life of baked products. HHP also alters the structure and functional properties of proteins which may be due to its pronounced effect on the folded–unfolded equilibrium of proteins, on the weakening of electrostatic and hydrophobic interactions, and on the thiol–disulphide exchange reactions resulting in the disruption of non-covalent interactions within proteins, with subsequent reformation of intra- and intermolecular bonds within or between proteins (Vallons et al. 2011). Recent studies showed that HHP could be utilized as a potential tool to improve the functionality of gluten-free products (Hüttner et al. 2009; Stolt et al. 2001; Vallons et al. 2010, 2011; Vallons and Arendt 2009).

In the study of Vallons and Arendt (2009), the effect of HHP treatment on structural properties of sorghum starch was evaluated by using rheological and microscopic techniques. In addition, pressure-induced gelatinization of sorghum starch was compared with heat-induced gelatinization of sorghum starch. CLSM was used to determine the loss of birefringence during gelatinization. CLSM pictures showed loss in birefringence of starch granules at high-pressure and temperature treatment but preservation of granular structure upon pressure and temperature treatment. In order to obtain finer details about the effect of pressure and temperature on the starch granule morphology, SEM analysis was used. Both CLSM and SEM images revealed that granular integrity was retained within the gelatinization interval in the presence of pressure and temperature changes. It was also observed that there were no significant differences between the microstructure of the pressure-treated samples and the temperature-treated samples within the gelatinization intervals. In order to evaluate the potential use of pressure-treated sorghum in the production of sorghum breads, another study was conducted on the application of high-pressure

processing of sorghum batters (Vallons et al. 2010). The impacts of high pressure on the structure of sorghum breads were examined by SEM. The untreated batter and batter treated at low pressures did not show visual differences. However, at higher-pressure treatment, starch granules became swollen and deformed, while their granular structure remained intact. The results of this study suggested that pressure treatment has the potential to delay staling in gluten-free products. In another study, the effect of HHP on the microstructure properties of three gluten-free batters made from buckwheat, white rice, and teff was examined (Vallons et al. 2011). SEM was used to observe the changes in the microstructure of the batters induced by the HHP treatment. Clearer changes were observed in the buckwheat images. Although, most granules retained their granular shape after treatment with 600 MPa, they were swollen, deformed, and collapsed. In the case of the microstructure of the gluten-free batters made from rice and teff, the effects of HHP on the granule structures were found to be less obvious; however, the structure of the batters looked smoother after HHP treatment. These structural changes in batters showed the noticeable effect of HHP treatment on the modifications occurring in starch and proteins. Hüttner et al. (2009) conducted a study on the effects of HHP on the microstructure of oat batters. SEM and bright-field microscopy were used to examine the structural changes of batters through HHP treatment. It was observed that both proteins and starch granules were affected by the HHP treatment, and higher pressures resulted in more noticeable changes in the structures of batters. Both bright-field microscopy and SEM revealed that higher pressures led to swollen and slightly disintegrated starch granules of batters and a more continuous distribution of proteins (Fig. 7.1). In another study, Hüttner et al. (2010) examined the use of HHP as a tool to improve the breadmaking performance of oat four. SEM and bright-field microscopy were used to investigate the effect of HHP treatment on the oat batter constituents. Both protein and starch were affected by HHP treatment, and more evident alterations were observed with higher-pressure treatment. Although the majority of oat starch granules retained their granular structure, modifications in their surface appearance such as swelling and slight disintegration of some granules were found to be visible. As compared to the untreated oat batter, more continuous distribution of proteins with higher-pressure treatment was observed. It was suggested that HHP treatment could be successfully applied for the improvement of oat flour functionality and bread quality by selecting the suitable pressure levels and amounts of flour. Protein modification and changes in the moisture distribution positively influenced the quality by retarding the staling of oat bread.

7.7 Conclusion

Gluten is responsible from the formation of the basic structure necessary for the appearance, texture, flavor, and shelf life of many baked products; therefore, eliminating gluten from the products causes quality problems. Replacing gluten in gluten-free products requires the use of alternative flour types to wheat flour

as well as several functional ingredients such as starches, hydrocolloids, emulsifiers, enzymes, protein, and/or fiber sources. In addition, sourdough breadmaking technique, infrared–microwave combination baking, and HHP treatment have been used as potential methods in gluten-free technology. The physicochemical, sensory, nutritional and, transport properties of foods are largely affected by the structure of foods varying from molecular to macroscopic levels. Although quantitative description of baked products is generally done by image analysis methods based on macroscopic techniques, microstructural analysis provides more detailed information about quality attributes of multicomponent sophisticated food products.

Recently, LM, SEM, CLSM, MRI, and X-ray μCT have been the popular techniques used in image acquisition for the quality of dough/batters and gluten-free baked products. Since CLSM has the ability to produce optical sections of a 3D specimen without damaging the structure and provides specific staining of components, it has been extensively used as a valuable tool in gluten-free baked products in order to provide deeper understanding of the role of ingredients and their interactions in the microstructure of gluten-free batters and breads. SEM imaging technique has recently been used to obtain quantitative information about crumb characteristics of gluten-free breads and cakes. As a powerful imaging technique, X-ray μCT has been recently used for quantitative characterization of gluten bread crumbs by creating 3D representation of bread structure from 2D image slices. In the future, widespread application of novel and powerful imaging techniques for the examination of the microstructure of gluten-free products can provide deeper knowledge about the quality attributes of gluten-free baked products.

References

Acs E, Kovacs Z, Matuz J (1997) Possibilities of producing low-protein, gluten-free bread. 1. Structure formation. Novenytermeles 46:227–234

Aguilera JM (2005) Why food microstructure? J Food Eng 67:3–11

Aguilera JM, Germain JC (2007) Advances in image analysis for the study of food microstructure. In: McClements DJ (ed) Understanding and controlling the microstructure of complex foods. Woodhead Publishing in Food Science, Technology and Nutrition, Cambriedge, UK, pp 261–287

Aguilera JM, Stanley DW (1999) Examining food microstructure. In: McClements DJ (ed) Microstructural principles of food processing and engineering. Aspen Publishing, Gaithersburg, pp 19–21

Ahlborn GJ, Pike OA, Hendrix SB, Hess WM, Clayton SH (2005) Sensory, mechanical, and microscopic evaluation of staling in low-protein and gluten-free breads. Cereal Chem 82:328–335

Alvarez-Jubete L, Auty M, Arendt EK, Gallagher E (2010) Baking properties and microstructure of pseudocereal flours in gluten-free bread formulations. Eur Food Res Technol 230:437–445

Anton AA, Artfield SD (2008) Hydrocolloids in gluten-free breads: a review. Int J Food Sci Nutr 59:11–23

Arendt EK, Moore MM (2006) Gluten-free cereal based products. In: Hui YH, Rosell CM, Gómez M (eds) Bakery products: science and technology Blackwell Publishing, USA, pp 471–497

Arendt EK, Morrissey A, Moore MM, Dal Bello F (2008) Gluten-free breads. In: Arendt EK, Dal Bello F (eds) Gluten-free cereral products and beverages, 1st edn. Academic, Oxford, pp 289–321

Arendt EK, Renzetti S, Dal Bello F (2009) Dough microstructure and textural aspects of gluten-free yeast bread and biscuits. In: Gallagher E (ed) Gluten-free food science and technology, 1st edn. Wiley, West, Sussex, pp 107–130

Awad TS, Moharram HA, Shaltout OE, Asker D, Youssef MM (2012) Applications of ultrasound in analysis, processing and quality control of food: a review. Food Res Int 48:410–427

Babin P, Della Valle G, Chiron H, Cloetens P, Hoszowska J, Pernot P (2006) Fast X-ray tomography analysis of bubble growth and foam setting during breadmaking. J Cereal Sci 43:393–397

Bardella MT, Fredella C, Prampolini L, Molteni N, Giunta AM, Bianchi PA (2000) Body composition and dietary intakes in adult celiac disease patients consuming a strict gluten-free diet. Am J Clin Nutr 72:937–939

Bellido GG, Scanlon MG, Page JH, Hallgrimsson B (2006) The bubble size distribution in wheat flour dough. Food Res Int 39:1058–1066

Besbes E, Jury V, Monteau JY, Le Bail A (2012) Characterizing the cellular structure of bread crumb and crust as affected by heating rate using X-ray microtomography. J Food Eng 115:415–423

Blaiotta G, Di Capua M, Coppola R, Aponte M (2012) Production of fermented chestnut purees by lactic acid bacteria. Int J Food Microbiol 158:195–202

Bower SL (2006) What is celiac disease. In: Bower SL, Sharrett MK, Plogste S (eds) Celiac disease: a guide to living with gluten intolerance, 1st edn. Demos Medical Publishing, New York, pp 1–9

Brites C, Trigo MJ, Santos C, Collar C, Rosell CM (2010) Maize based gluten-free bread: influence of processing parameters on sensory and instrumental quality. Food Bioprocess Technol 3:707–715

Catassi C, Fornaroli F, Fasano A (2002) Celiac disease: from basic immunology to bedside practice. Clin Appl Immunol Rev 3:61–71

Chanona-Perez J, Quevedo R, Jimenez Aparicio AR, Gumeta Chavez C, Mendoza Perez JA, Calderon Dominguez G, Alamilla-Beltran L, Gutierrez- Lopez GF (2008) Image processing methods and fractal analysis for quantitative evaluation of size, shape, structure and microstructure in food materials. In: Gutierrez-Lopez GF, Barbosa-Canovas GV, Welti-Chanes J, Parada-Arias E (eds) Food engineering: integrated approaches. Springer, New York, pp 277–286

Chenlo F, Moreira R, Pereira G, Silva CC (2007) Evaluation of the rheological behaviour of chestnut (castanea sativa mill) flour pastes as function of water content and temperature. Electron J Environ Agric Food Chem 6:1794–1802

Clarke AR, Eberhardth CN (2002) Microscopy techniques for materials science, 1st edn. CRC Press LLC 2000, USA, pp 375–377

Datta AK, Greedipalli SSR, Almeida MF (2005) Microwave combination heating. Food Technol 59:36–40

Datta AK, Sahin S, Sumnu G, Keskin O (2007) Porous media characterization of breads baked using novel heating modes. J Food Eng 79:106–116

Demirekler P, Sumnu G, Sahin S (2004) Optimization of bread baking in halogen lamp-microwave combination oven by response surface methodology. Eur Food Res Technol 219:341–347

Demirkesen I, Mert B, Sumnu G, Sahin S (2010a) Rheological properties of gluten-free bread formulations. J Food Eng 96:295–303

Demirkesen I, Mert B, Sumnu G, Sahin S (2010b) Utilization of chestnut flour in gluten-free bread formulations. J Food Eng 101:329–336

Demirkesen I, Sumnu G, Sahin S, Uysal N (2011) Optimization of formulations and infrared-microwave combination baking conditions of chestnut-rice breads. Int J Food Sci Technol 46:1809–1815

Demirkesen I, Sumnu G, Sahin S (2013) Image analysis of gluten-free breads prepared with chestnut and rice flour and baked in different ovens. Food Bioprocess Technol 6:1749–1758

Demirkesen I, Sumnu G, Sahin S, Eroğlu MM (2014a) Quality of gluten-free bread formulations baked in different ovens. Food Bioprocess Technol 7:619–626

Demirkesen I, Kelkar S, Campanella OH, Sumnu G, Sahin S, Okos M (2014b) Characterization of structure of gluten-free breads by using X-ray microtomography: relationship between microstructure and quality characteristics. Food Hydrocoll 36:37–44

Demirkesen I, Campanella OH, Sumnu G, Sahin S, Hamaker B (2014c) A study on staling characteristics of gluten free breads prepared with chestnut and rice flours. Food Bioprocess Technol 7:806–820

Dobraszczyk BJ, Campbell GM, Gan Z (2001) Bread: a unique food. In: Dobraszczyk BJ, Dendy DAV (eds) Cereals and cereal products: technology and chemistry. Aspen Publishers, USA, pp 182–232.

Du CJ, Sun DW (2004) Recent developments in the applications of image processing techniques for food quality evaluation. Trends Food Sci Technol 15:230–249

Elmehdi HM, Page JH, Scanlon MG (2003) Monitoring dough fermentation using acoustic waves. Food Bioprod Process 81:217–223

Falcone PM, Baiano A, Zanini F, Mancini L, Tromba G, Montanari F (2004) A novel approach to the study of bread porous structure: phase-contrast X-ray microtomography. Food Eng Phys Prop 69:38–43

Falcone PM, Baiano A, Zanini F, Mancini L, Tromba G, Dresossi D (2005) Three-dimensional quantitative analysis of bread crumb by X-ray micro-tomography. Food Eng Phys Prop 70:265–272

Falcone PM, Baiano A, Conte A, Mancini L, Tromba G, Zanini F, Del Nobile MA (2006) Imaging techniques for the study of food microstructure: a review. Adv Food Nutr Res 51:205–263

Farrera-Rebollo RR, Salgado-Cruz MP, Chanona-Pérez J, Gutiérrez-López GF, Alamilla-Beltrán L, Calderón-Domínguez G (2012) Evaluation of image analysis tools for characterization of sweet bread crumb structure. Food Bioprocess Technol 5:474–484

Fox P, Smith PP, Sahi S (2004) Ultrasound measurements to monitor the specific gravity of food batters. J Food Eng 65:317–324

Gallagher E, Gormley TR, Arendt EK (2003) Crust and crumb characteristics of gluten free breads. J Food Eng 56:153–161

Gambus H, Nowotna A, Ziobro R, Gumul D, Sikora M (2001) The effect of use of guar gum with pectin mixture in gluten-free bread. Electron J Pol Agric Univ 4:1–13

García-Álvarez J, Salazar J, Rosell CM (2011) Ultrasonic study of wheat flour properties. Ultrasonics 51:223–228

Goesaert H, Brijs K, Veraverbeke WS, Courtin CM, Gebruers K, Delcour JA (2005) Wheat flour constituents: how they impact bread quality, and how to impact their functionality. Trends Food Sci Technol 16:12–30

Gómez M, Oliete B, García-Álvarez J, Ronda F, Salazar J (2008) Characterization of cake batters by ultrasound measurements. J Food Eng 89:408–413

Gujral SG, Rosell CM (2004) Improvement of the breadmaking quality of rice flour by glucose oxidase. Food Res Int 37:75–81

Hager AS, Wolter A, Czerny M, Bez J, Zannini E, Arendt EK, Czerny M (2012) Investigation of product quality, sensory profile and ultrastructure of breads made from a range of commercial gluten- free flours compared to their wheat counterparts. Eur Food Res Technol 235:333–344

Hamaker BR, Bugusu BA (2003) Overview: sorghum proteins and food quality, Paper 8. Proceedings of Afripro—workshop on the proteins of sorghum and millets: enhancing nutritional and functional properties for Africa, Pretoria, South Africa

He H, Hoseney RC (1991) Gás retention of different cereal flours. Cereal Chem 68:334–336

Hüttner EK, Dal Bello F, Poutanen K, Arendt EK (2009) Fundamental evaluation of the impact of high hydrostatic pressure on oat batters. J Cereal Sci 49:363–370

Hüttner EK, Dal Bello F, Poutanen K, Arendt EK (2010) Fundamental study on the effect of hydrostatic pressure treatment on the bread-making performance of oat flour. Eur Food Res Technol 230:827–835

Kelkar S, Stella S, Boushey C, Okos M (2011) Developing novel 3D measurement techniques and prediction method for food density determination. Procedia Food Sci 1:483–491

Keskin SO, Sumnu S, Sahin S (2004) Bread baking in halogen lamp-microwave combination oven. Food Res Int 37:489–495

Keskin SO, Ozturk S, Sahin S, Koksel H, Sumnu G (2005) Halogen lamp-microwave combination baking of cookies. Eur Food Res Technol 220:546–551

Langton M, Aström A, Hermansson A-M (1996) Texture as a reflection of microstructure. Food Qual Preference 7:185–191
Lape AD, Jensen S, Jeor VS, Lendon CA (2008) Use of X-ray micro computed tomography in the evaluation of bread crumb structure. Microsc Microanal 14:700–701
Lazaridou A, Billiaderis CG (2009) Gluten-free doughs: rheological properties, testing procedures-methods and potential problems. In: Gallagher E (ed) Gluten-free science and technology, 1st edn. Wiley, West, Sussex, pp 52–83
Leite EL, Herrmann PSP (2005) Application of atomic force spectroscopy (AFS) to studies of adhesion phenomena: a review. In: Drelich J, Mittal KL (eds) Atomic force microscopy in adhesion studies. VSP, Leiden-Boston, pp 3–43
Leray G, Oliete B, Mezaize S, Chevallier S, De Lamballerie M (2010) Effects of freezing and frozen storage conditions on the rheological properties of different formulations of non-yeasted wheat and gluten-free bread dough. J Food Eng 100:70–76
Lim KS, Barigou M (2004) X-ray micro-computed tomography of cellular food products. Food Res Int 37:1001–1012
Lodi A, Vodovotz Y (2008) Physical properties and water state changes during storage in soy bread with and without almond. Food Chem 110:554–561
Marco C, Rosell CM (2008) Breadmaking performance of protein enriched, gluten-free breads. Eur Food Res Technol 227:1205–1213
Mariette F, Collewet G, Davenel A, Lucas T, Musse M (2012) Quantitative MRI in food science and food engineering. Encyclopedia of Magnetic Resonance. doi:10.1002/9780470034590emrstm1272
Mariotti M, Lucisano M, Pagani MA, Ng PKW (2009) The role of corn starch, amaranth flour, pea isolate, and Psyllium flour on the rheological properties and the ultrastructure of gluten-free doughs. Food Res Int 42:963–975
Mariotti M, Lametti S, Cappa C, Rasmussen P, Luciano M (2011) Characterisation of gluten-free pasta through conventional and innovative methods: evaluation of the uncooked products. J Cereal Sci 53:319–327
McCarthy DF, Gallagher E, Gormley TR, Schober TJ, Arendt EK (2005) Application of response surface methodology in the development of gluten-free bread. Cereal Chem 82(5):609–615
Moore MM, Schober TJ, Dockery P, Arendt EK (2004) Textural comparisons of gluten-free and wheat-based doughs, batters, and breads. Cereal Chem 81:567–575
Moore MM, Heinbockel M, Dockery P, Ulmer HM, Arendt EK (2006) Network formation in gluten-free bread with the application of transglutaminase. Cereal Chem 83:28–36
Moore MM, Juga B, Schober TJ, Arendt EK (2007) Effect of lactic acid bacteria onproperties of gluten-free sourdoughs, batters, and quality and ultrastructure ofgluten-free bread. Cereal Chem 84:357–364
Moroni AV, Dal Bello F, Arendt EK (2009) Sourdough in gluten-free bread-making: an ancient technology to solve a novel issue? Food Microbiol 26:676–684
Moroni AV, Dal Bello F, Zannini E, Arendt EK (2011) Impact of sourdough on buckwheat flour, batter and bread: biochemical, rheological and textural insights. J Cereal Sci 54:195–202
Nunes MHB, Moore MM, Ryan LAM, Arendt EK (2009a) Impact of emulsifiers on the quality and rheological properties of gluten-free breads and batters. Eur Food Res Technol 228:633–642
Nunes MHB, Ryan LAM, Arendt EK (2009b) Effect of low lactose dairy powder addition on the properties of gluten-free batters and bread quality. Eur Food Res Technol 229:31–41
Onyango C, Unbehend G, Lindhuaer MG (2009) Effect of cellulose-derivatives and emulsifiers on creep-recovery and crumb properties of gluten-free bread prepared from sorghum and gelatinised starch. Food Res Int 42:949–955
Ozkoc SO, Sumnu G, Sahin S (2009) The effects of gums on macro and micro-structure of breads baked in different ovens. Food Hydrocoll 23:2182–2189
Oztop MH, Rosenberg M, Rosenberg Y, McCarthy KL, McCarthy MJ (2010) Magnetic Resonance Imaging (MRI) and relaxation spectrum analysis as methods to investigate swelling in whey protein gels. J Food Sci 75:508–515

Pareyt B, Talhaoui F, Kerckhofs G, Brijs K, Goesaert H, Wevers M, Delcour JA (2009) The role of sugar and fat in sugar-snap cookies: structural and textural properties. J Food Eng 90:400–408
Peressini D, Pin M, Sensidoni A (2011) Rheology and breadmaking performance of rice-buckwheat batters supplemented with hydrocolloids. Food Hydrocoll 25:340–349
Petrauskas A (2007) Evaluation of porous food products by using ultrasonic methods. Ultragarsas (Ultrasound) 62:20–27
Polaki A, Xasapis P, Fasseas C, Yanniotis S, Mandala I (2010) Fiber and hydrocolloid content affect the microstructural and sensory characteristics of fresh and frozen stored bread. J Food Eng 97:1–7
Povey MJW, Harden CA (1981) An application of the ultrasonic pulse echo technique to the measurement of crispness of biscuits. Int J Food Sci Technol 16:167–175
Primo-Martín C, van Dalen G, Meinders MBJ, Don A, Hamer RH, van Vliet T (2010) Bread crispness and morphology can be controlled by proving conditions. Food Res Int 43:207–217
Prior-Cabanillas A, Barrales-Rienda JM, Frutos G, Quijada-Garrido I (2007) Swelling behavior of hydrogels from methacrylic acid and poly(ethylene glycol) side chains by magnetic resonance imaging. Polym Int 56:506–511
Rafiq A, Makroo HA, Sachdeva P, Sharma S (2013) Application of computer vision system in food processing—a review. Int J Eng Res Appl 3:1197–1205
Renzetti S, Arendt E (2009a) Effects of oxidase and protease treatments on the breadmaking functionality of a range of gluten-free flours. Eur Food Res Technol 229:307–317
Renzetti S, Arendt E (2009b) Effect of protease treatment on the baking quality of brown rice bread: from textural and rheological properties to biochemistry and microstructure. J Cereal Sci 50:22–28
Renzetti S, Dal Bello F, Arendt EK (2008) Microstructure, fundamental rheology and baking characteristics of batters and breads from different gluten-free flours treated with a microbial transglutaminase. J Cereal Sci 48:33–45
Renzetti S, Courtin CM, Delcour JA, Arendt EK (2010) Oxidative and proteolytic enzyme preparations as promising improvers for oat bread formulations: rheological, biochemical and microstructural background. Food Chem 119:1465–1473
Ribotta PD, Ausar SF, Morcillo MH, Perez GT, Beltramo DM, Leon AE (2004) Production of gluten-free bread using soybean flour. J Sci Food Agric 84:1969–1974
Ronda F, Gómez M, Caballero PA, Oliete B, Blanco CA (2009) Improvement of quality of gluten-free layer cakes. Food Sci Technol Int 15:193–202
Rosell CM, Collar C (2007) Rise based products. In: Hui HY (ed) Handbook of food products manufacturing. Wiley-Interscience, Hoboken, pp 523–523
Rosell CM, Santos E (2010) Impact of fibers on physical characteristics of fresh and staled bake off bread. J Food Eng 98:273–281
Ross KA, Pyrak-Nolte LJ, Campanella OH (2004) The use of ultrasound and shear oscillatory tests to characterize the effect of mixing time on the rheological properties of dough. Food Res Int 37:567–577
Rouillé J, Valle GD, Devaux MF, Marion D, Dubreil L (2005) French bread loaf volume variations and digital image analysis of crumb grain changes induced by the minor components of wheat flour. Cereal Chem 82:20–27
Sabanis D, Tzia C (2011) Selected structural characteristics of HPMC-containing gluten-free bread: a response surface methodology study for optimizing quality. Int J Food Prop 14:417–431
Sabanis D, Lebesi D, Tzia C (2011) Effect of dietary fibre enrichment on selected properties of gluten-free bread. LWT Food Sci Technol 42:1380–1389
Sacchetti G, Pinnavaia GG, Guidolin E, Dalla-Rosa M (2004) Effects of extrusion temperature and feed composition on the functional, physical and sensory properties of chestnut and rice flour-based snack-like products. Food Res Int 37:527–534
Sakiyan O, Sumnu G, Sahin S, Meda V, Koksel H, Chang P (2011) A study on degree of starch gelatinization in cakes baked in three different ovens. Food Bioprocess Technol 4:1237–1244

Salazar J, Turó A, Chávez JA, GarcIa MJ (2004) Ultrasonic inspection of batters for on-line process monitoring. Ultrasonics 42:155–159
Sanchez HD, Osella CA, de la Torre MA (2002) Optimisation of gluten-free bread prepared from cornstarch, rice flour and cassava starch. J Food Sci 67:416–419
Sanchez-Pardo ME, Ortiz-Moreno A, Mora-Escobedo R, Chanona-Perez JJ, Necoechea-Mondragon H (2008) Comparison of crumb microstructure from pound cakes baked in a microwave or conventional oven. LWT Food Sci Technol 41:620–627
Sapirstein HD, Roller R, Bushuk W (1994) Instrumental measurement of bread crumb grain by digital image analysis. Cereal Chem 71:383–391
Schober JT, Messerschmidt M, Bean SR, Park SH, Arendt EK (2004) Gluten-free bread from sorghum: quality differences among hybrids. Cereal Chem 82:394–404
Schober TJ, Bean SR, Boyle DL (2007) Gluten-free sorghum bread improved by sourdough fermentation: biochemical, rheological, and microstructural background. J Agric Food Chem 55:5137–5146
Schober TJ, Bean SR, Boyle DL, Park S (2008) Improved viscoelastic zein–starch doughs for leavened gluten-free breads: their rheology and microstructure. J Cereal Sci 48:755–767
Sciarini LS, Ribotta PD, León AE, Pérez GT (2010) Effect of hydrocolloids on gluten-free batter properties and bread quality. Int J Food Sci Technol 45:2306–2312
Sivaramakrishnan HP, Senge B, Chattopadhyay PK (2004) Rheological properties of rice dough for making rice bread. J Food Eng 62(9):37–45
Skaf A, Nassar G, Lefebvre F, Nongaillard B (2009) A new acoustic technique to monitor bread dough during the fermentation phase. J Food Eng 93:365–378
Sozer N (2009) Rheological properties of rice pasta dough supplemented with proteins and gums. Food Hydrocoll 23:849–855
Stampfli L, Nersten B (1995) Emulsifiers in bread making. Food Chem 52:353–360
Stolt M, Oinonen S, Autio K (2001) Effect of high pressure on the physical properties of barley starch. Innov Food Sci Emerg Technol 1:167–175
Sumnu G (2001) A review on microwave baking of foods. Int J Food Sci Technol 36:117–127
Sumnu G, Sahin S (2005) Baking using microwave processing. In: Schubert H, Regier M (eds) The microwave processing of foods. Woodhead Publishing Limited, Cambridge, pp 119–141
Sumnu G, Koksel F, Sahin S, Basman A, Meda V (2010) The effects of xanthan and guar gums on staling of gluten-free rice cakes baked in different ovens. Int J Food Sci Technol 45:87–93
Tronsmo KM, Faergestad EM, Longva A, Schofield JD, Magnus EM (2002) A study of how size distribution of gluten proteins, surface properties of gluten and dough mixing properties relate to baking properties of wheat flours. J Cereal Sci 35:201–214
Turabi E, Sumnu G, Sahin S (2008) Optimization of baking of rice cakes in infrared microwave combination oven by response surface methodology. Food Bioprocess Technol 1:64–73
Turabi E, Sumnu G, Sahin S (2010) Quantitative analysis of macro and microstructure of gluten-free rice cakes containing different types of gums baked in different ovens. Food Hydrocoll 24:755–762
Vallons KJR, Arendt EK (2009) Effects of high pressure and temperature on the structural and rheological properties of sorghum starch. Innov Food Sci Emerg Technol 10:449–456
Vallons KJR, Ryan LAM, Koehler P, Arendt EK (2010) High pressure–treated sorghum flour as a functional ingredient in the production of sorghum bread. Eur Food Res Technol 231:711–717
Vallons KJR, Ryan LAM, Arendt EK (2011) Promoting structure formation by high pressure in gluten-free flours. LWT-Food Sci Technol 44, 1672–1680
Van Der Borght A, Goesaert H, Veraverbeke WS, Delcour J (2005) Fractionation of wheat and wheat flour into starch and gluten: overview of the main processes and the factors involved. J Cereal Sci 41:221–237
Van Riemsdijk LE, Van der Goot AJ, Hamer RJ, Boom RM (2011) Preparation of gluten-free bread using a meso-structured whey protein particle system. J Cereal Sci 53:355–361
Wang S, Austin P, Bell S (2011) It's a maze: the pore structure of bread crumbs. J Cereal Sci 54:203–210

Yang H, Wang Y, Lai S, An H, Li Y, Chen F (2007) Application of atomic force microscopy as a nanotechnology tool in food science. J Food Sci 72:65–75

Zannini E, Pontonio E, Waters DM, Arendt EK (2012a) Applications of microbial fermentations for production of gluten-free products and perspectives. Appl Microbiol Biotechnol 93:473–485

Zannini E, Jones JM, Renzetti S, Arendt EK (2012b) Functional replacements for gluten. Ann Rev Food Sci Technol 3:227–245

Zayas IY (1993) Digital image texture analysis for bread crumb grain evaluation. Cereal Foods World 38:760–766

Zghal MC, Scanlon MG, Sapirstein HD (1999) Prediction of bread crumb density by digital image analysis. Cereal Chem 76:734–742

Zghal MC, Scanlon MG, Sapirstein HD (2002) Cellular structure of bread crumb and its influence on mechanical properties. J Cereal Sci 36:167–176

Chapter 8
Molecular Organization and Topography of Prolamin Protein Films

Jarupat Luecha and Jozef L. Kokini

8.1 Introduction

8.1.1 Zein and Gluten Proteins

Wheat, maize, and rice are the most important cereal crops accounting for more than 70 % of the world cereal production in 2012. Nonfood utilization of these cereals increased rapidly particularly as a result of an escalation in feed production and industrial uses (GIEWS, 2012). Although storage cereal proteins constitute only about 10–12 % of the cereal mass, they play an important role in food production, feed production, and industrial uses. For instance, wheat proteins are not only nutritionally important for human consumption but also functionally essential for the viscoelasticity of bread dough, bread, and pasta.

Prolamins are among the major storage proteins that are found in wheat, barley, rye, maize, sorghum, and millet. Prolamins can be defined as protein fractions that are soluble in the mixture of alcohol/water in the presence of reducing agents (Shewry and Halford 2002; Shewry and Tatham 1990). The water insoluble property of prolamins mainly results from the high content of hydrophobic amino acids and glutamines and the low content of polar amino acids (Lagrain et al. 2010). A wheat prolamin and a maize prolamin both have been studied extensively for nonfood applications as they are biodegradable materials from renewable resources. Moreover, several studies on their thermoplastic properties have shown that they can be exploited for nonfood applications, including adhesives, coatings, and packaging materials (Shukla and Cheryan 2001; Lawton 2002; Hernandez-Munoz et al.

J. L. Kokini (✉)
Department of Food Science, Purdue University, West Lafayette, IN, USA
e-mail: jkokini@purdue.edu

J. Luecha
Division of Food Technology, Mahidol University Kanchanaburi Campus, Kanchanaburi, Thailand
e-mail: jarupat.lue@mahidol.ac.th

N. Sozer (ed.), *Imaging Technologies and Data Processing for Food Engineers,*
Food Engineering Series, DOI 10.1007/978-3-319-24735-9_8

2003; Roy et al. 1999; Lagrain et al. 2010; De Graaf 2000). In addition, the industrial uses of maize prolamins have grown dramatically due to ethanol production from maize, leaving behind the protein-rich byproducts to be used as animal feed and for industrial uses (Aithani and Mohanty 2006).

Prolamins of Maize

Zein is the main prolamin found in maize. Zein proteins can be classified according to the way they aggregate in aqueous ethanol at various concentrations in the presence of reducing agents into α-zein, β-zein, and δ-zein. Alpha-zein is the most abundant fraction which contains electrophoretic bands at a molecular weight of 19,000 and 21,000 (Esen 1986). The α-helical structure dominates the secondary structure of α-zein rather than the β-sheet structure in aqueous ethanol solution (Shewry and Tatham 1990). Several studies have shown that zein in aqueous solution forms ellipsoidal aggregates with both hydrophilic and hydrophobic molecular planes (Argos et al. 1982; Matsushima et al. 1997; Shewry and Tatham 1990).

Prolamins of Wheat

Prolamins are well known to be responsible for the viscoelastic properties of wheat gluten (WG) in bread dough (Kuktaite et al. 2011; He et al. 2013). The prolamins of wheat can be classified into the low-molecular-weight gliadins (Mw~36,000–44,000) and higher-molecular-weight glutenins (Mw~67,000–88,000) (Shewry and Tatham 1990). Gliadins contribute to the flowability of gluten while glutenins contribute to the ability of gluten to stretch. Gliadins are monomeric proteins that can be fractionated into four groups: α-, β-, γ-, and ω-gliadins, with the ω-gliadins being the only group that does not contain cysteine residues (Shewry and Halford 2002). The sulfur-rich gliadins are responsible for the inter- and intramolecular cross-links via disulfide bonds. The structure of high-molecular-weight unit was proposed to be a loose spiral of several organized β-turns, resulting in the rod shape of the whole structure (Shewry and Tatham 1990).

8.1.2 Prolamin Proteins as Promising Biodegradable and Edible Packaging Films from Renewable Resources

Petroleum-based synthetic polymer plastics accounted for 13% of the solid waste generated in the USA in 2011 (EPA 2011), the major portion coming from packaging applications (Aithani and Mohanty 2006). Their advantages include high durability, ease of handling at industrial scale, low gas permeability, and ease of disposal. However, their disadvantages include difficulty to biodegrade, resulting pollution, and the fact that they are derivatives of raw materials from limited fossil resources that will vanish in the next century if not sooner (Zhang and Mittal 2010). For these reasons, bio-based renewable materials such as hydrophobic proteins from cereals and legumes are gaining increasing attention as they are biodegradable and offer a sustainable solution (Johansson et al. 2012). In addition to their biodegradable and renewable properties, bio-based materials such as starch, cellulose, and proteins are

also considered edible films. Edible films are used as edible coatings, edible wrap, separable layers between food components to prevent moisture migration, and edible plastic bags/pouches to contain foods (Hernandez-Izquierdo and Krochta 2008). Protein films are particularly interesting as edible packaging films because of the diversity of the amino acid side chains varying from polar to nonpolar functional groups, thus allowing diverse chemical functionalization (Zhang and Mittal 2010; Lagrain et al. 2010; De Graaf 2000).

In addition to their nutritional and food-processing value, prolamins have become potentially promising biodegradable and edible packaging films (Lagrain et al. 2010; De Graaf 2000). However, the major drawback of these prolamin films is that their mechanical and barrier properties as well as processability are inferior to petroleum-based packaging films (Taylor et al. 2013). The brittleness of prolamin films can be reduced by the addition of plasticizers to suppress their glass temperature. The effects of the addition of plasticizers such as glycerol, polyethylene glycol, propylene glycol, and oleic acid on the mechanical and barrier properties of prolamin films have been studied extensively (Xu et al. 2012; Jagadeesh et al. 2013; Lawton 2004; Ghanbarzadeh et al. 2007). Most findings indicate that the flexibility of prolamin films increased as the plasticizer content increased. The hydrophobic plasticizers were found to increase the water vapor permeability of the zein films (Ghanbarzadeh et al. 2007; Xu et al. 2012). The efficacy of the plasticization depends on the compatibility between the plasticizers and the prolamin proteins. Besides the addition of plasticizers, the cross-linking reaction as well as lamination with other film layers has been used as techniques to improve physical properties of the prolamin films (Sessa et al. 2007; Gu et al. 2013). Nanocomposite prolamin films showed improved tensile strength, barrier properties, and thermal resistance with the degree of enhancement dependent on film fabrication processes (Luecha et al. 2010; Guillard et al. 2013; Ture et al. 2012; Sozer and Kokini 2009).

8.1.3 Manufacture and Functionality of Protein Films

Prolamin proteins can be formed into freestanding films by several film-forming techniques that share three main steps: breaking intermolecular bonds, arranging and orienting the mobile polymer chains to the desired conformation, and allowing the newly formed bonds to stabilize and form the three dimensional network (Jerez et al. 2007). Normally, the film fabrication techniques can be categorized into two main processes: wet process and dry process (Hernandez-Izquierdo and Krochta 2008). In wet processing, prolamins are dissolved in common solvents, then the solution is cast on a nonsticky surface. The freestanding film is peeled off the surface after most of the solvent is removed. The strength of prolamin films obtained from this process is affected by the inefficient organization of protein polymer chains after the removal of solvents. The dry process depends on the thermoplastic properties of prolamins at low moisture/plasticizer content as found in compression/injec-

tion molding and extrusion (Hernandez-Izquierdo and Krochta 2008; Luecha et al. 2010; Shi et al. 2009; Reddy and Yang 2013; Taylor et al. 2013).

State diagrams have been developed for several proteins including zein, gliadin, gluten, soy protein, the 7S and 11S fractions of soy protein, and others as a function of moisture/plasticizer content and temperature (Kokini et al. 1994). The state diagram of prolamins provides useful information for designing film fabrication processes. It was reported that at the moisture content of 25–35 %, zein displayed a networking reaction zone caused by disulfide exchange in the temperature range between 65 and 160 °C and behaved as an entangled polymer at temperatures below 65 °C (Madeka and Kokini 1996). In contrast, the reaction zone began at 120 °C for gluten with moisture content of 20 % (Toufeili et al. 2002). In the reaction zone, the plasticized prolamins begin to unfold and lose their native structures as a result of the breakdown of hydrogen bonds, thus allowing chemical reaction with cross-linking reagents, antimicrobial agents, or nanomaterials to take place. If mechanical shear is also applied using extrusion, the molecular mobility of prolamins increases, thus promoting an exposure of the protein reactive sites (Lagrain et al. 2010).

The dry process is preferred to the wet process because it is the leading industrial process that is commonly used to produce packaging films at low-cost and faster production rates (Hernandez-Izquierdo and Krochta 2008; Reddy and Yang 2013; Taylor et al. 2013). Although prolamin protein films have been studied extensively, the utilization of prolamin protein films in the packaging industry is still very limited. This might be due to the fact that the prolamin films are outperformed by the synthetic film counterparts. Therefore, the internal microstructure of prolamin films would provide rich information on the spatial distribution and the interaction of the prolamin films at molecular level throughout the fabrication processes and help design films with improved physical properties with the potential to compete favorably with their synthetic counterparts. The study of their structure is vital for the development of the prolamin films with desired mechanical properties, barrier properties, and special functionalities.

8.2 Structural Development and Characterization of the Topography of Protein Films Using Imaging Technologies

The mechanism of film formation of prolamin proteins has remained unclear. Using advanced imaging technologies, it is possible that better understanding of the formation of prolamin films might be achieved, and this might lead to enhancement of their permeability and mechanical properties among other properties. Among advanced imaging technologies, atomic force microscopy (AFM) is a powerful imaging tool that can assess precisely three-dimensional high-resolution images at the nanoscale of individual molecules as well as protein arrays and membranes at conditions comparable to physiological conditions (Alessandrini and Facci 2005). AFM allows probing of chemical characteristic of the surface (McMaster et al.

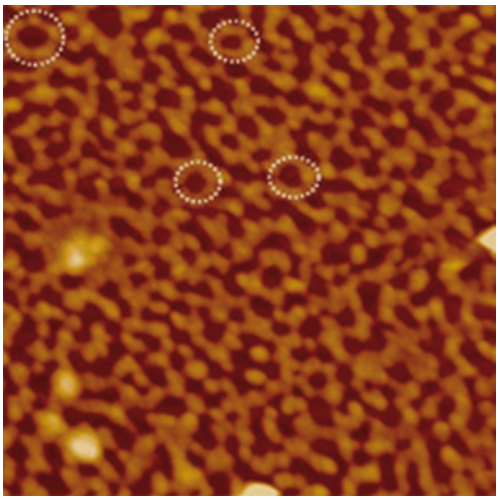

Fig. 8.1 The meshwork of joined rods of zein from dilute solution is the foundation of film formation. The *white circles* are the doughnut-shape joined rods. Scan size: 1000 × 1000 nm, z scale: 20 nm. (Reproduced with permission from Guo et al. 2005)

1999) and has become a preferred tool among other imaging techniques particularly for biological samples mainly due to the fact that it allows imaging of nonconductive materials (Alessandrini and Facci 2005). AFM with tapping mode has been used extensively to probe the surface topography of the thin prolamin films fabricated from solution on solid surfaces. The information gained can be related to the mechanism of film formation through the behavior of monolayers and thin films.

A well-studied example includes zein protein films that were prepared from dilute solution on mica surface using solvent-casting technique. The molecular arrangement was observed in air by AFM in the tapping mode (Shi et al. 2009; Panchapakesan et al. 2012). After solvent evaporation, increasing zein protein concentration caused protein aggregation resulting in various rod-like shapes of dumbbell, pole, and branched structures on the surface. The formation of rod-like meshwork nanosized structures with a diameter of joined rods of 50 nm and the gaps between joined rods of less than 100 nm represents the initial mechanism of film formation as it can be seen in Fig. 8.1. The formation of the meshwork led to good mechanical and gas barrier properties for zein films (Guo et al. 2005). The tapping mode AFM with Nanoscope software was also used to characterize the surface roughness at nanoscale of zein films prepared from different types of solvent cast on solid surfaces. The zein films prepared from 95 % ethanol showed rougher surface morphology as observed at the z scale of 60 nm, while the ones prepared from acetic acid were 20 times smoother (Fig. 8.2). The surface roughness at the nanoscale was influenced by the concentration of ethanol but not by the concentration of acetic acid (Shi et al. 2009).

AFM can also be used for monitoring the inter- and intramolecular interactions. The measurement of the cantilever deflection in relation to the motion of the tip is used in this approach. Once the tip is in contact with the sample then pulled back, the deflection occurs due to van der Waal forces between the tip and the sample as indicated by the negative force in the force curve. According to Hooke's law, the

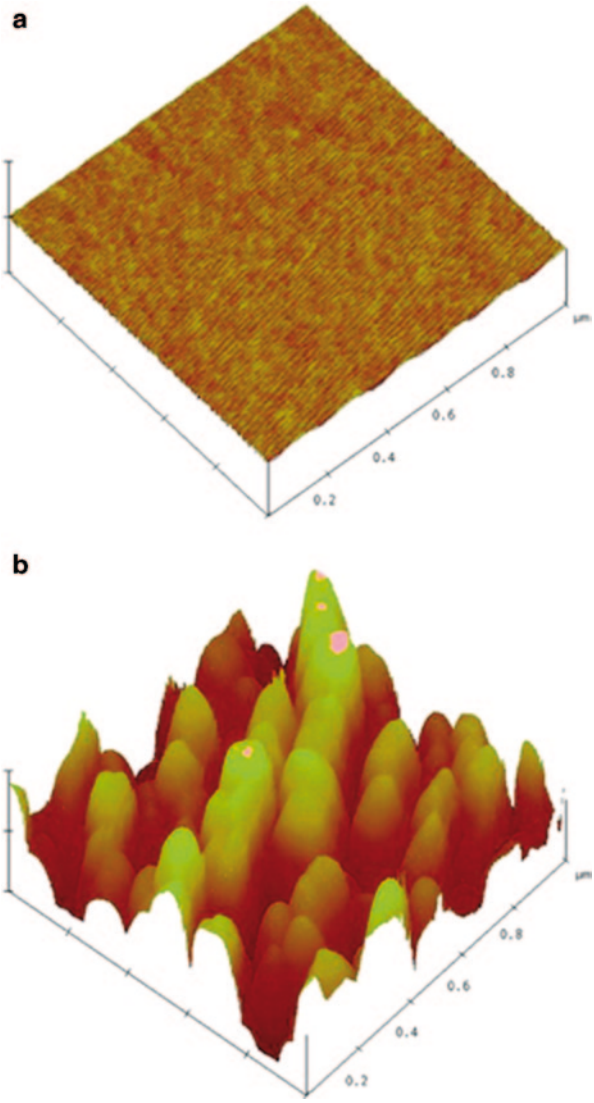

Fig. 8.2 The surface morphologies of zein films prepared from different solvents: **a** acetic acid and **b** 95% aqueous ethanol. The scan size was 1 ×1 μm with z scale of 60 nm. (Reprinted with permission from Shi et al. 2009). (Copyright (2009) American Chemical Society)

adhesive force between the tip and the sample can be calculated (Alessandrini and Facci 2005). These types of measurement were used to probe the changes from glassy to rubbery states of zein films (Panchapakesan et al. 2012). It was found that an increase in adhesive force was related to the increase in the molecular mobility of zein due to the transition from glassy state to rubbery state. As clearly shown in Fig. 8.3, the adhesive force increased as the water activity of the zein film increased. It was suggested that an increase in adhesive force was an additional capillary force that resulted from high water content in the sample. The authors also confirmed the results with measurement of the glass transition temperature using differential

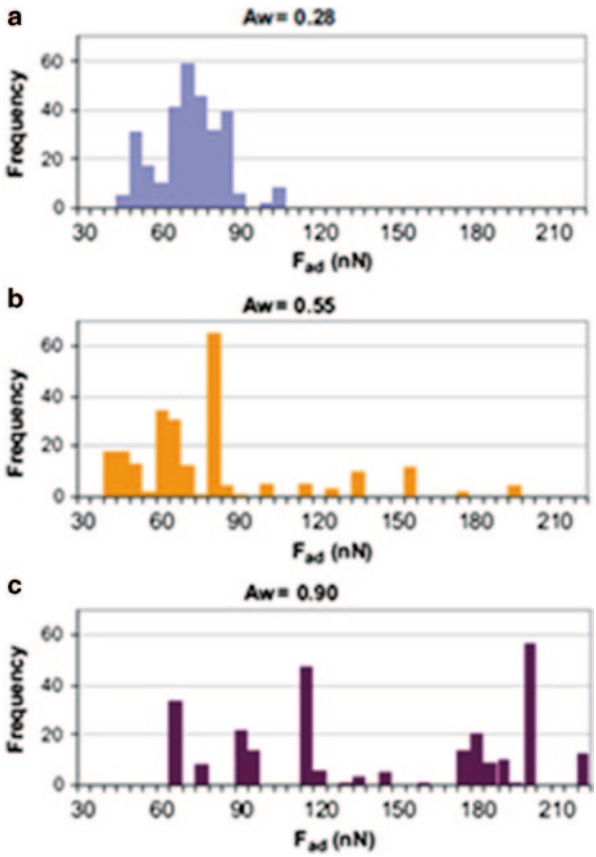

Fig. 8.3 Histograms of adhesive force of zein films at **a** Aw = 0.28, **b** Aw = 0.55, and **c** Aw = 0.90. (Reproduced with permission from Panchapakesan et al. 2012)

scanning calorimetry. Moreover, the topographical images suggested that the zein film microstructure produced on the basis of solvent casting technique strongly depended on how zein aggregated onto the solid surface, as shown in Fig. 8.4. The behavior of zein in different solvents also greatly influenced the aggregation, while the purity of zein proteins had little impact on the surface morphology of zein films (Panchapakesan et al. 2012).

The mixture of α-gliadin and ω-gliadin at various ratios were formed as Langmuir–Blodgett (LB) films—a monolayer of amphiphilic molecules built up on a solid surface (Schwartz, 1997), and AFM with tapping mode was used for investigating the microphases of the mixed gliadin films (McMaster et al. 1999). AFM topographical images of mixed gliadins showed two distinct morphologies as a result of the difference in structures and properties of the two gliadins. The rod-shaped ω-gliadin lacks cysteine, resulting in inter- and intra-hydrogen bonding. In contrast, the spherical α-gliadin is more hydrophilic resulting in greater adhesion with the hydrophilic tip surface. The visualization of monolayer film formation at the molecular level obtained by AFM provided detailed information on structural formation of wheat prolamins (McMaster et al. 1999).

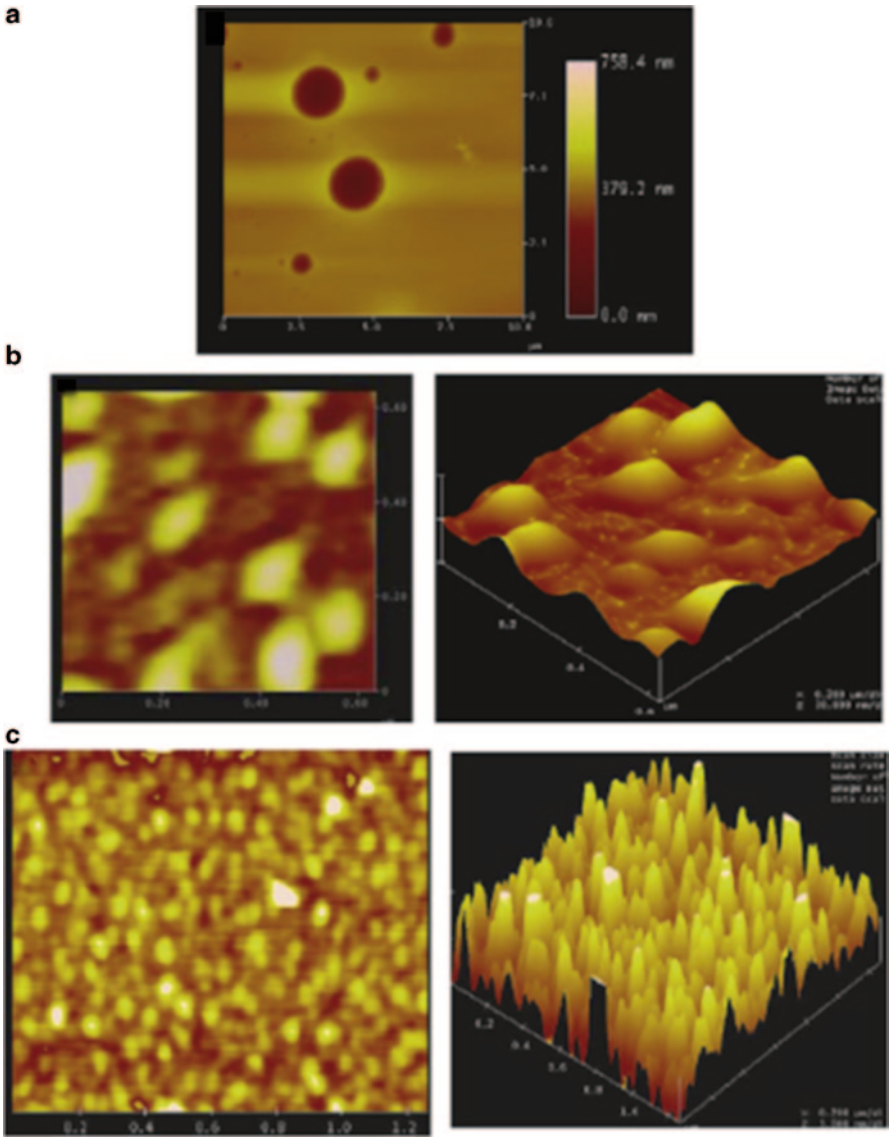

Fig. 8.4 The topographical images of zein films fabricated by **a** solvent casting (10 mm scan of 16% w/v cast zein film, data scale = 758.4 nm, top view), **b** dropped deposition (1 mg/ml, data scale = 30 nm top view and 3-D image), and **c** spin-casting (1 mg/ml, data scale = 10.0 nm top view and 3-D image). (Reproduced with permission from Panchapakesan et al. 2012)

Haward et al. (2010) developed the direct real-time imaging of wheat prolamins monolayer formation using AFM with a liquid cell. In this work, the sulfur-rich γ-gliadin and sulfur-poor ω-gliadin were model proteins for the continuous observation of protein adsorption from solution on hydrophilic (mica) and hydropho-

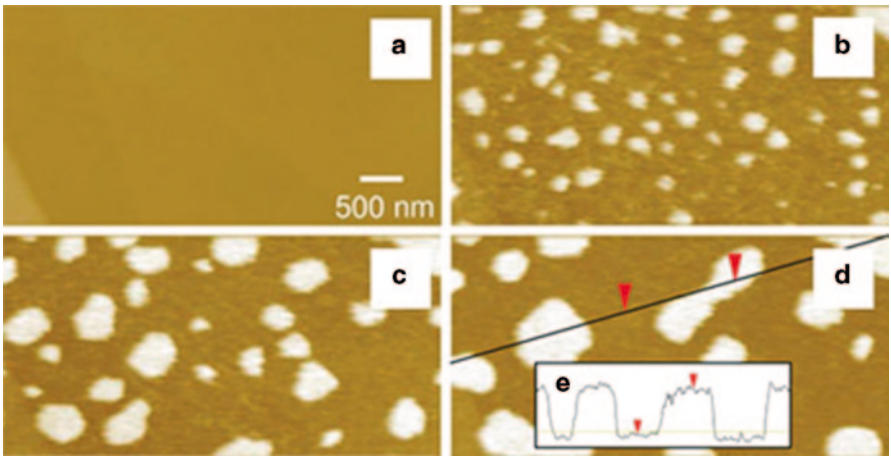

Fig. 8.5 Sequence of images of γ-gliadin adsorption onto graphite; **a** graphite surface imaged under 1 % acetic acid; **b** protein aggregation 1676 s after injection of protein; **c** 1932 s after injection of protein; and **d** 2444 s after injection of protein. The data scale = 0–40 nm (**e**). A topographical profile along the crosswise line in (**d**). (Reproduced with permission from Haward et al. 2010)

bic (graphite) solid surfaces. The surface morphology and the interaction on the different surfaces of each individual gliadin were observed. Figure 8.5 shows the time-lapse AFM images of hydrophobic γ-gliadin absorbed onto graphite surface. However, when mixed, the two gliadins interact strongly resulting in an alteration of the surface morphology. This finding supported the understanding of the interactions of wheat prolamins in the hydrated state (Haward et al. 2010).

The morphology of prolamin films is highly influenced by solvent, protein fractions, moisture content, etc., all that causes protein aggregation. Moreover, the platform that is used for growing the prolamin film also affects the surface topography. AFM also clearly allows the monitoring of the formation in these environments with the possibility of an observation in real time. The force-deformation curve allows the investigation of molecular mobility at the surface of prolamin films. However, it is noteworthy to consider that the structural development of the prolamin films that has been assessed by AFM were the films that were prepared from solvent. The mechanism of structural development of the prolamin films prepared by a solvent-free technique such as extrusion might be challenging to observe using AFM.

8.3 Characterization of Physical Properties of Protein Films Using Imaging Technologies

As potential food-packaging materials, prolamins in film form have the ability and properties to serve food packaging's main functions, which are protection of food from chemical and physical damages as well as from impurity and prevention of

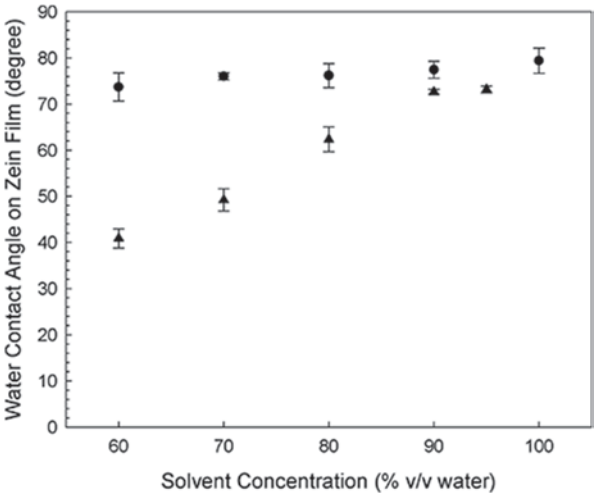

Fig. 8.6 The water contact angles of zein films prepared from aqueous acetic acid and aqueous ethanol at different levels of concentration (v/v). (Reprinted with permission from Shi et al. 2009). (Copyright (2009) American Chemical Society)

flavor and moisture loss. Generally, the properties of interest for characterization of packaging materials are mechanical properties and gas permeability, which can be measured using conventional methods. These important properties are influenced by the morphology of the prolamin protein. Hence, the information of the molecular orientation of prolamin protein after processing usually is related to the functional properties of the prolamin films. Imaging techniques including AFM, confocal laser scanning microscopy (CLSM), and Fourier transform infrared spectroscopy (FTIR) have been used together extensively to complement one another for structure and functionality characterization. These imaging techniques offer unique and powerful insights into the microstructure as well as molecular orientation which strongly influence the functionality of the prolamin films.

One of the important properties of prolamin films is their water vapor permeability related to the surface properties of the films. AFM was used in a combination with a surface contact angle analyzer to evaluate their surface properties (Shi et al. 2009). As aforementioned, zein films fabricated from different solvents displayed significantly different surface properties. The smooth films prepared from acetic acid had higher hydrophobicity than the rougher surface films prepared from ethanol. Furthermore, the hydrophobicity/hydrophilicity of the surface of zein films was evaluated by water contact angle measurement. The zein films made from aqueous acetic solvent were more hydrophobic than the one from aqueous ethanol solvent (Fig. 8.6, Shi et al. 2009).

The mechanical properties of freestanding prolamin films are related to the protection functionality of packaging films. The conventional method to measure the mechanical properties is the tensile measurement. Typically, the film sample is pulled apart at a constant rate, and the breaking force is measured. However, it is interesting to observe the micro-cracks that usually occur before breaking to gain better understanding of the mechanism of mechanical property development of prolamin films. Figure 8.7 shows time lapsed microimages of zein film samples in red, fluosphere® in green, and micropores in black. The film samples were stretched at

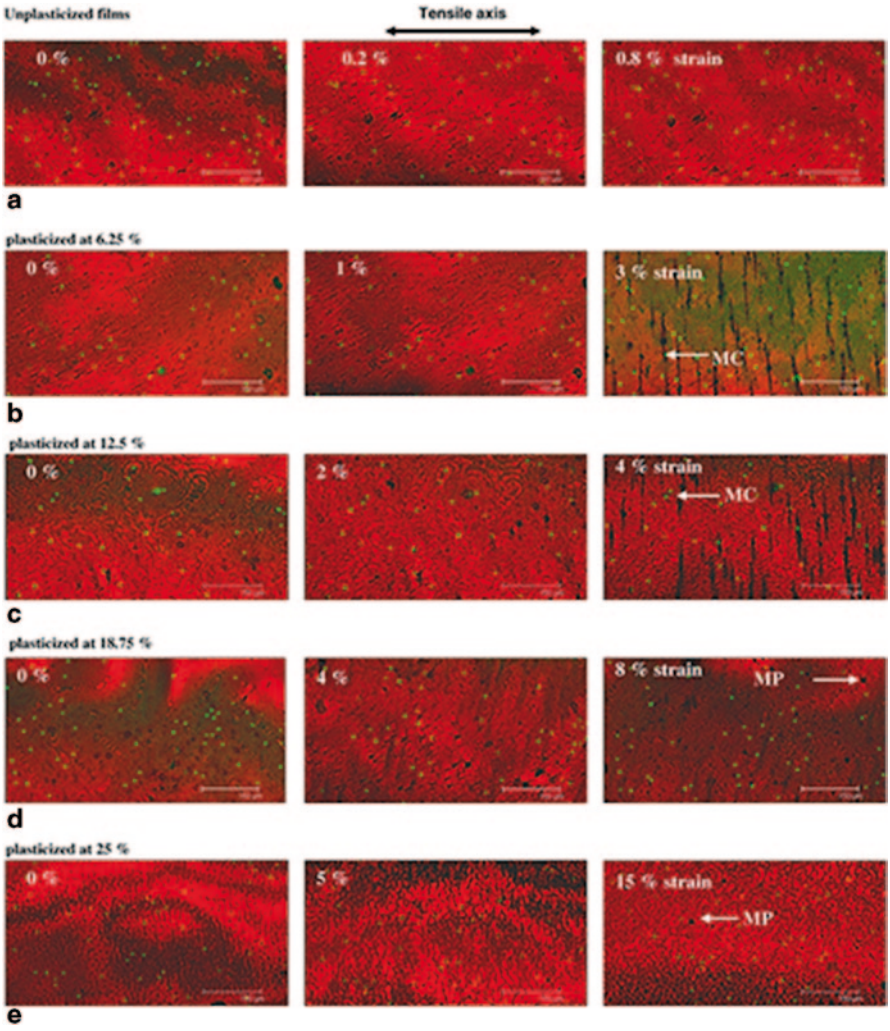

Fig. 8.7 CLSM micrographs of un-plasticized (**a**) and plasticized (**b**, **c**, **d**, and **e**, at 6.25, 12.5, 18.75 and 25 % (w/w)) solvent-cast zein films at different strain levels. The bar is 150 micrometer. MC stands for micro-cracks and MP for micropores. (Reproduced with permission from Emmambux and Stading 2007)

a fixed rate along the tensile axis as confirmed by the separation of the green dots. The images were taken at several strains to observe the micro-cracks. It is well known that un-plasticized zein film is very brittle. At small strains, the zein film structure remained unchanged (Fig. 8.7a). It can be seen that as the concentration of plasticizer increases, the micro-cracks were observed at lower strain, suggesting the plasticizers decreased the development and propagation of the micro-cracks (Fig. 8.7a–e). The excellent agreement between the observations related to micro-cracks as a function of plasticizer content from CLSM images measurement and

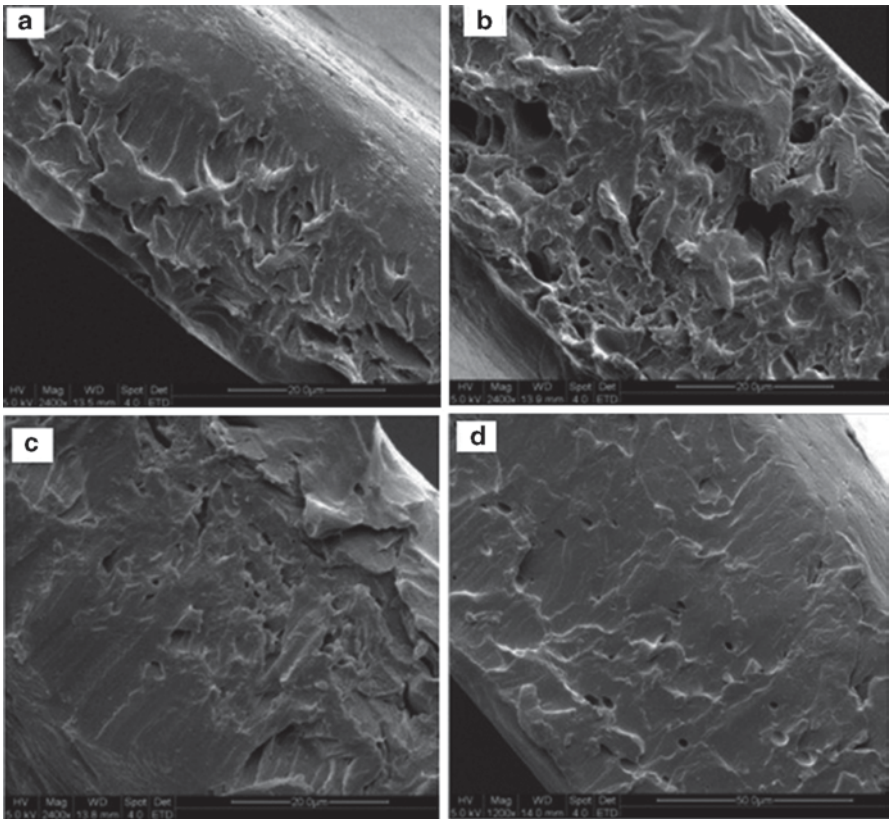

Fig. 8.8 The cross-sectional SEM images of zein films with different plasticizers at the fixed amount of 20 wt.%: **a** control (no plasticizers added), **b** oleic acid, **c** glycerol, **d** oleic acid + glycerol (3:1). (Reprinted with permission from Xu et al. 2012, pp.). (Copyright (2012) American Chemical Society)

the change in the glass transition temperature using dynamic mechanical analysis (DMA) was also shown in this study (Emmambux and Stading 2007).

The effects of the combination of hydrophilic and hydrophobic plasticizers on the physical properties of zein films were also observed by Xu et al. (2012). They showed interesting synergistic impact of the duo plasticizers on the mechanical properties including the tensile strength and elongation at break, the same trend Emmambux and Stading (2007) observed as a function of plasticizers. Especially at the ratio of 3:1 of oleic acid and glycerol (at total weight of plasticizers = 20 %), zein improved both the tensile strength and elongation at break compared to plasticized zein film with single plasticizer. In general, as the plasticizer content increases, the elongation at break increases with a decrease in tensile strength. The authors also evaluated the supramolecular structure of the plasticized zein films using the SEM. It was found that only the oleic acid-plasticized zein film had non-smooth cross section. Fig. 8.8 shows SEM images with some pores and empty spaces, suggesting

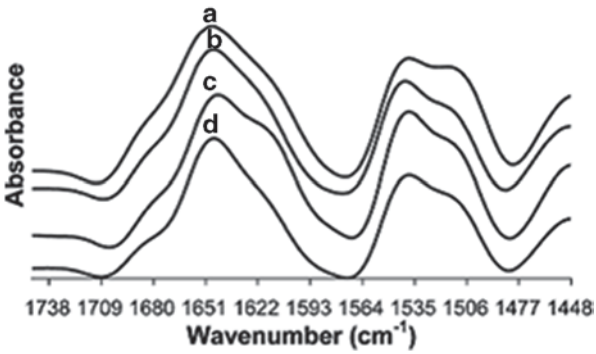

Fig. 8.9 An overlay of FTIR spectra of cast zein films: dehydrated zein films (**a**), zein film plasticized with 40% glycerol (**b**), with 12.8% water (**c**), and with 2-mercaptoethanol (**d**). (Reprinted with permission from Gillgren et al. 2009)

the molecular confinement of oleic acid in the interior of zein molecules. Whereas, the un-plasticized, glycerol-plasticized, and the glycerol-oleic acid-plasticized zein films had rather smooth cross sections with considerably less pores. According to SEM results, the oleic acid molecules are confined within the internal zein molecules resulting in strengthening of zein film against tension, while glycerol acted as filler to the pores and empty spaces without further modification to the molecular arrangement of zein films. No evidence of secondary structure modification by these plasticizers was found based on FTIR measurement. Further investigation is required in order to understand the mechanism of the synergistic effects of the two different plasticizers (Xu et al. 2012).

The plasticization effects of water and polyols on the mechanical properties of zein film have been studied extensively. FTIR was used together with DMA to study the interaction of zein and plasticizers at the molecular level (Gillgren et al. 2009). The glass transition temperature decreased as the plasticizer content increased. Water showed greater impact on the reduction in the glass transition temperature than glycerol, whereas the 2-mercaptoethanol showed no impact.

In order to understand the plasticization effect at the molecular level, FTIR was used. Figure 8.9 shows FTIR spectra of zein films with different plasticizers. The amide I (1652–1657 cm^{-1}) and amide II (1521-1525 cm^{-1}) bands are of interest for determination of protein secondary structure (Jackson and Mantsch 1995). The spectra intensity at amide I band and amide II band were lower for the plasticized zein films in comparison to the dehydrated one. The amide II band is generally influenced by the hydrogen bonding environment. Zein film plasticized with glycerol or water both showed a lower peak intensity at amide II band, indicating the molecular modification by the plasticizers. In contrast to other plasticizers, 2-mercaptoethanol slightly affected the zein protein conformation. Thus, the FTIR results were in accordance with the DMA results (Gillgren et al. 2009).

The film formation processes, the formulation, and the relative humidity had a great impact on the physical properties of freestanding zein films. The mechanical properties of extruded zein ribbons were tested at machine direction as well as at transverse direction to observe the directional dependency of the mechanical strength of extruded zein ribbons (Selling and Sessa 2007). It was found that

the tensile strength and elongation at break when tested at the machine direction were significantly greater than at the transverse direction. The authors suggested that this finding was a result of molecular orientation during the extrusion. In this work, the FTIR was used to gain insight into the microstructural information of the zein ribbons. The amide I and amide II bands are of interest for characterization of secondary structure of protein. The FTIR normal spectra of the extruded zein ribbons measured at the two directions were similar, while the secondary derivative of the FTIR spectra showed some differences, suggesting the molecular orientation of the two directions was slightly different. Moreover, the authors investigated the birefringence of the zein ribbons. They found that there was a birefringence of the zein ribbons, thus confirming that the molecular orientation of zein ribbons were direction-dependent (Selling and Sessa 2007).

In wheat, the final extruded film properties can be defined from the molecular orientation of the high molecular mass complex polymer of monomeric gliadins and glutenins via disulfide cross-links (Tatham and Shewry 2000). In the recent works, the effects of base and extrusion temperature on the molecular organization of platicized WG protein films were studied (Kuktaite et al. 2011). While the authors measured the molecular dimensions of the aggregated WG protein in the films using X-ray diffraction (XRD), they confirmed the molecular interaction between glutenins and gliadins using CLSM (Kuktaite et al. 2011). The diffraction patterns suggested that at the extrusion temperature higher than 90 °C, the NaOH induced the formation of tetragonal structure, whereas NH_4OH led to the formation of supramolecular structure of hexagonal-closed-packed organization. In order to visualize the molecular interaction between the components of WG including high-molecular-weight glutenin subunits (HMW-gs), the low-molecular-weight glutenins subunits (LMW-gs), and gliadins, the film samples were immunostained with a series of antibodies for CLSM measurement. It is important to note that a series of monoclonal and polyclonal antibodies that are specific to each individual WG protein component were used in this study, although the immunostaining technique will not be discussed here. Figure 8.10a–c shows CLSM images of plasticized WG films extruded at 105 °C, while Fig. 8.10c shows CLSM image of platicized WG protein extruded at 120 °C with the presence of NH_4OH. Figure 8.10a–b showed the individual gliadins (red) distribution in common extruded WG films with the presence of individual area of low-molecular-weight glutenin subunits (green), while Fig. 8.6c showed the region where there was some overlapping of the gliadin area and the low-molecular-weight glutenin subunits (yellow). It can be seen in Fig. 8.10c that the films with the presence of NH_4OH showed more uniform overlapping yellow area, indicating the intimate interaction between glutenins and gliadins. The interaction of the two components was the re-polymerization via covalent bonds. The authors suggested that the hexagonal-closed-packed organization as a result of the intimate interaction between major protein components may perhaps result in an increase in mechanical properties and a decrease in oxygen permeability of the WG films (Kuktaite et al. 2011).

Moreover, the CLSM was also used to probe the effects of urea acting either as denaturant or plasticizer in an alternative solvent-free and base-free process for a

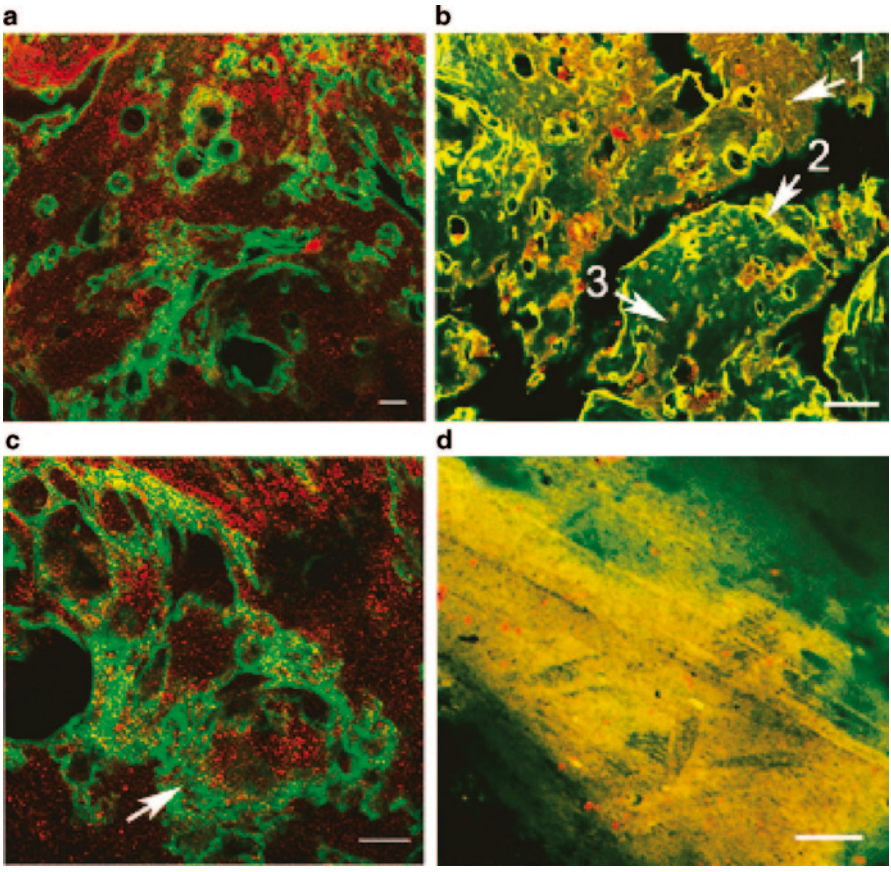

Fig. 8.10 CLSM images of (**a**–**c**) glycerol plasticized wheat gluten (WGG) film extruded at 105 °C and (**d**) 7.5-NH_4OH-1.5-salicylic acid (WGG) extruded at 120 °C; wheat gluten proteins immunostained with two antibodies directed to the LMW-gs *(green)* and gliadins *(red)* (**a**, **b**); WG proteins immunostained with two antibodies directed to LMW-gs peptide *(green)* and gliadins *(red)* (**c**, **d**). **a** Overview of individual areas of gliadins and HMW-gs. **b***Arrow* indicates an area with major HMW-gs and to minor scattered gliadins. **c** An overlapping binding site of antibodies directed to gliadins and LMW-gs *(yellow color)*; gliadin-rich region *(reddish, arrow 1)*, overlapping gliadin and LMW-gs region *(yellow, arrow 2),* and LMW-gs-rich region *(greenish, arrow 3)*. **d** A thorough mixture of gliadins and LMW-gs; scale 10 μm. (Reproduced with permission from Kuktaite et al. 2011)

better environmentally friendly extruded WG film production (Ture et al. 2012). They found that the addition of urea was similar to the addition of plasticizers in terms of the influences on the mechanical and barrier properties of WG films. The immunostaining techniques were used specific to HMW-gs. They found that with the presence of urea, the aggregation of high HMW-gs occurred and separated partly from gliadins which led to the formation of sheet structure. Thus, the CLSM with the advanced immunostaining technique is a powerful tool that allows us to visually assess the WG protein film formation at the molecular level.

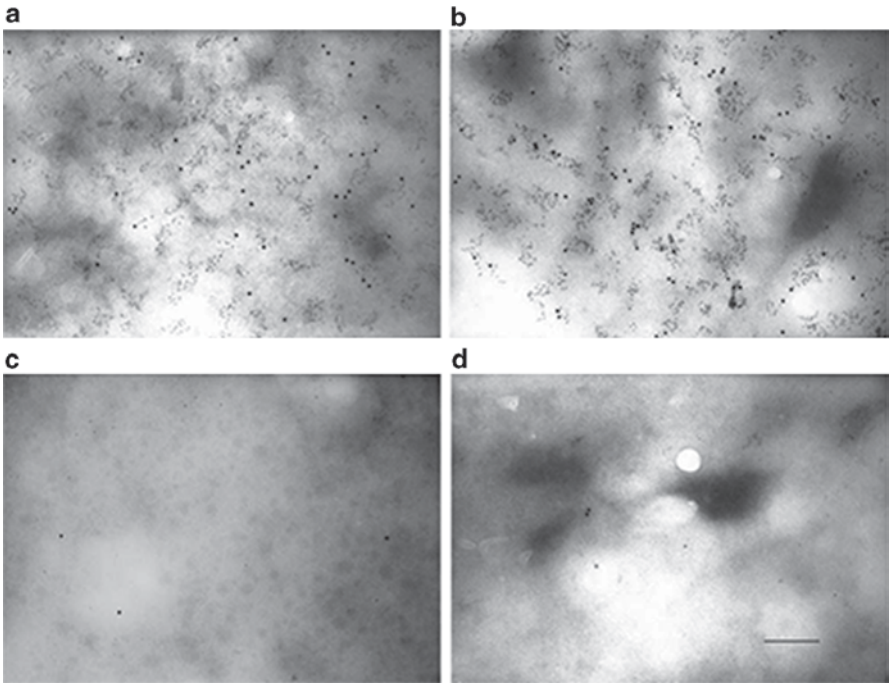

Fig. 8.11 Transmission electron microscopy (TEM) images of immunolocalized wheat gluten proteins with large 10-nm gold particles indicating high molecular weight (HMW) glutenins and small 2-nm gold particles indicating gliadins. **a** Glycerol-plasticized wheat gluten (control) film treated with two primary antibodies; **b** glycerol-plasticized wheat gluten with urea film treated with two primary antibodies; **c** control film and control labeling without primary antibodies; **d** glycerol-plasticized wheat gluten with urea film, control labeling without primary antibodies; scale bar = 100 nm. (Reproduced with permission from Kuktaite et al. 2012)

Urea also induced a hexagonal-closed-packed organization to gluten films similar to NH_4OH confirmed by XRD (Kuktaite et al. 2012). TEM was used to gain insights about the morphology of the urea-treated WG protein films in parallel with the XRD results. Immunolabeled gold particles specifically bound to HMW glutenins and gliadins were employed to increase the contrast of biological samples. Gold nanoparticles were well distributed and localized within WG allowing the geometrical structure and inter-grain spacing in gluten aggregates to be revealed. However, the expected hexagonal structure was not visually observed. It can be seen in Fig. 8.10a–c that the immunolabeled gold nanoparticles were distributed bi-continuously in both samples with or without urea. Untreated gold nanoparticles used as negative controls were also observed in the samples (Fig. 8.11c–c). The cloudy area is evidence of protein denaturation (Kuktaite et al. 2012). This study shows the advancement in molecular localization in bio-based films using inorganic gold nanoparticles.

The molecular organization of prolamin protein films strongly influences the properties and functionalities of the freestanding films. With advanced imaging

technologies, the relationship between the molecular orientation of the films and their properties can be well established, thus providing rich information for improvement in film processing for specific packaging applications.

From the aforementioned, conferring to the physical property of prolamin films, the following can be summarized. The gas/water permeability of the prolamin films were related to the surface properties of the films. The AFM and SEM are two main imaging techniques that can provide supportive evidence for surface properties. Moreover, with the progressive molecular localized labeling technology, it allows the visualization of the molecular arrangement of each protein component of prolamins at ease by using CLSM. The CLSM with tensile testing equipment allows visual observation of the beginning of the rupture, thus detecting the mechanical properties at molecular level, at each applied strain. The self-assembly of the free-standing prolamin films can be further monitored using TEM with gold nanoparticle assisted. Nonetheless, chemical bonding as a result of film processing can be assessed by means of FTIR.

8.4 Characterization of the Physical Properties of Composite Biofilms by Microstructural Analysis

Several studies have been focusing on improvement of the properties of prolamin films by mixing prolamin proteins with additive materials. In this chapter, the composite laminates and nanocomposites of biomaterials from natural origin are mainly emphasized. The composite films can be prepared by mixing two or more different materials together before forming into films for the purpose of enhancing mechanical properties and permeability. If the additive used owns at least one dimension at the nanometer scale, it is called nanocomposite. Composite laminate is also another film-enhancement approach. Normally, at least two thin layers made from different biomaterials with desirable property are thermally compressed for a short period of time, resulting in the unified one piece of laminate films. The lamination helps reduce leakage, thus it is also a promising method to improve gas barrier property. The interaction among composite materials as well as the laminated materials at the molecular level is worth investigating to gain an understanding on the molecular composition at the interface in which it will lead to better process manipulation for desirable biocomposite packaging films.

Recently, two or more bio-based materials have been used as an alternative way for the production of environmentally friendly biocomposite films. Zein–chitosan composite films were prepared by mixing solution of each material at different ratios and formed into films similar to solvent-casting technique (Escamilla-Garcia et al. 2013). The chitosan film alone is very transparent, and as the percentage of chitosan increased in the zein–chitosan composite, the transparency of films increased. The increase in zein fraction resulted in an increase in elasticity and softness. Water vapor permeability decreased as the percentage of zein increased. The morphology of the composite was observed using AFM, and the higher the zein

concentration, the higher was the surface roughness for biocomposite films. The interaction of the composite materials at the molecular level was characterized using Raman spectroscopy. The standalone zein film and standalone chitosan film showed individual characteristic peaks as shown in Fig. 8.12. Zein film showed spectra (Fig. 8.11a) with characteristic peaks at 1448 cm^{-1} (glutamine), 525 cm^{-1} (cysteine), 848/828 cm^{-1}(tyrosine), 1525 cm^{-1}(lysine), and 998/620 cm^{-1}(phenylalanine). Chitosan showed sharp peaks (Fig. 8.11c) at amide band I at 1665 cm^{-1}, amide band III at 1262 cm^{-1},and polysaccharide peak at 1111 cm^{-1}. The Raman spectra of the composite films (Fig. 8.10c) displayed some shifted peaks compared to the single films with different peak intensity as well as disappearance of some peaks compared to zein film, especially the cysteine and lysine peaks. This was hypothesized to be due to the interaction at the molecular level between chitosan reactive site and zein reactive site, possibly the formation of O=S=O and C=O=S, which are the peaks at 1066 $cm^{-1}$and 823 cm^{-1}, respectively (Escamilla-Garcia et al. 2013).

Aside from an observation of the chemical interaction between the composite materials using Raman spectroscopy, SEM is also a vital tool that allows visualizing the morphology of the composite films. The soy protein isolate films were laminated with a thin zein layer using compression mold. The tensile properties improved, while the zein layer induced brittleness to the laminates. Zein film alone is very brittle compared to soy protein isolate as zein owes lower molecular weight than soy protein isolates. To gain more supportive information, the microstructure of the laminates was monitored on the cross section of the tested failure films. The three-dimensional SEM image showed the sharp and smooth surface zein layer which is the characteristic of brittle films. In contrast, the cross section of soy protein isolate layer contained ridges-and-valleys which is the characteristic of ductile films (Pol et al. 2002).

Other than composites, the blending technique has been used for a production of novel biomaterials. Starch and zein, the two components as a model of unpurified corn flour, were studied for the compatibilization as potential biomaterials for packaging (Leroy et al. 2012). In this work, the authors analyzed CSLM images using “mathematical morphology” for particle size evaluation of the starch–zein blends at several ratios with ionic compatibilizer or glycerol. The protein molecular orientation was visible as white on the black background of starch, thus creating textural images that enabled mathematical evaluation of particle size distribution of the surfaces of the blended film. It was found that the co-continuous morphology at 50:50 starch–zein ratio showed the greatest amount of small grains according to the mathematical morphology. The higher the amount of the starch, the more zein aggregates and vice versa. The ionic liquid not only acted as a compatibilizer for starch and zein, but also as a plasticizer, resulting in rather smoother film surfaces compared to the samples plasticized by glycerol.

Plasticized WG film was laminated with polylactic acid (PLA) using compression molded methods for the applications in paper/board coatings (Cho et al. 2010). It was found that by laminating WG films with PLA, the migration and loss of glycerol to environments over time was reduced significantly, thus prolonging WG desired functional property. This study also found that lamination promoted

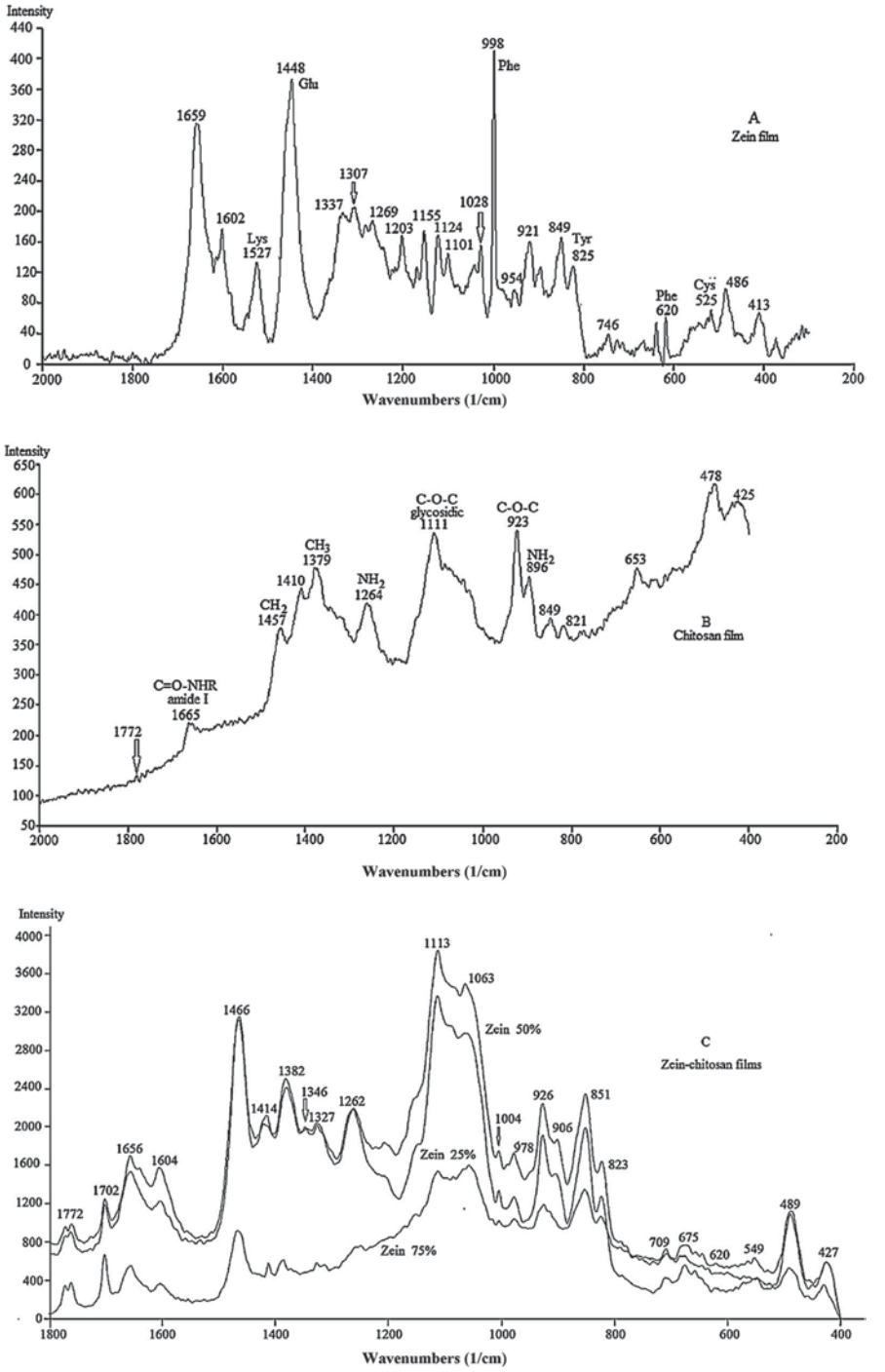

Fig. 8.12 Raman spectroscopy of zein, **a**; chitosan, **b**; zein–chitosan, **c** formulations. The *arrows* only indicate the position of the peaks at certain wave number. (Reproduced with permission from Escamilla-Garcia et al. 2013)

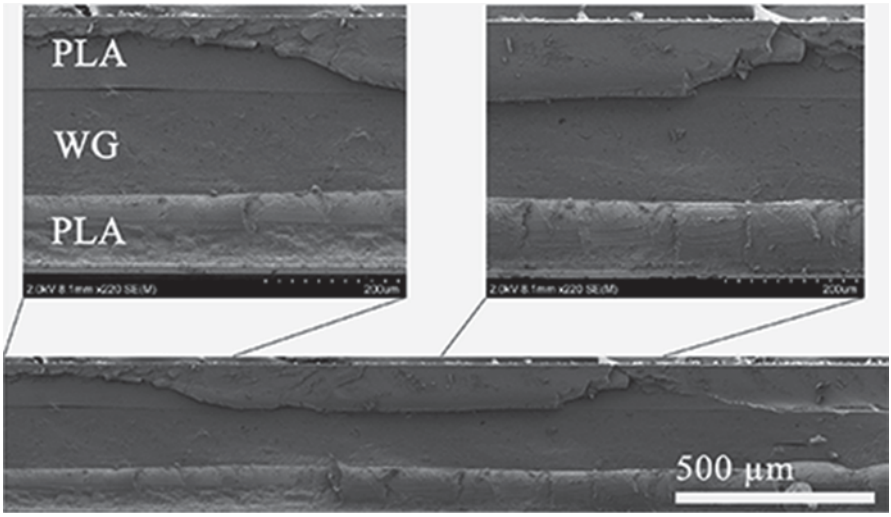

Fig. 8.13 Field emission– scanning electron microscopy (SEM) images of the cryo-fractured surface of the wheat gluten/polylactic acid (WG/PLA) laminate film. (Reproduced with permission from Cho et al. 2010)

mechanical properties as well as gas barrier properties, especially showing profound oxygen barrier property. In this work, the field emission SEM was employed to investigate the quality of lamination. As clearly shown in Fig. 8.13c, the WG sheet was homogeneously sandwiched with PLA thin layers with uniform thickness. The clear interface where WG layer and PLA layer were laminated was a result of different conductive effects of WG and PLA layers. However, the observation at higher magnification at the interface (seam) would interestingly offer the information on bonding or molecular union of the two layers at the interface.

As aforementioned, polymer nanocomposites have gained remarkable amount of attention in the past decades as a promising technique for production of packaging materials with improved functional properties. The composite nanomaterials commonly used are inorganic nanosilicates (nanoclays). The attractive benefit of incorporating the nanoclays in polymer matrix is that the barrier properties as well as the mechanical properties of the nanocomposites can be enhanced dramatically with small amount of nanoclays. However, the process and the compatibility between nanoclays and the base polymers and the amount of nanoclays addition govern the degree of improvement that is usually related to the dispersion of nanoclays in polymer matrix. Since nanoclays are crystalline inorganic materials, XRD together with transmission electron microscopy (TEM) are the characterization techniques that provide information on the degree of nanoclay dispersion.

WG is one of the plant-derived biopolymers that has been modified by using montmorillonite (MMT) in several approaches (Olabarrieta 2006; Tunc et al. 2007; Angellier-Coussy et al. 2008). In general, for solvent cast films, as the percentage of nanoclays increases up to 5 %, the tensile strength of the WG nanocomposite films

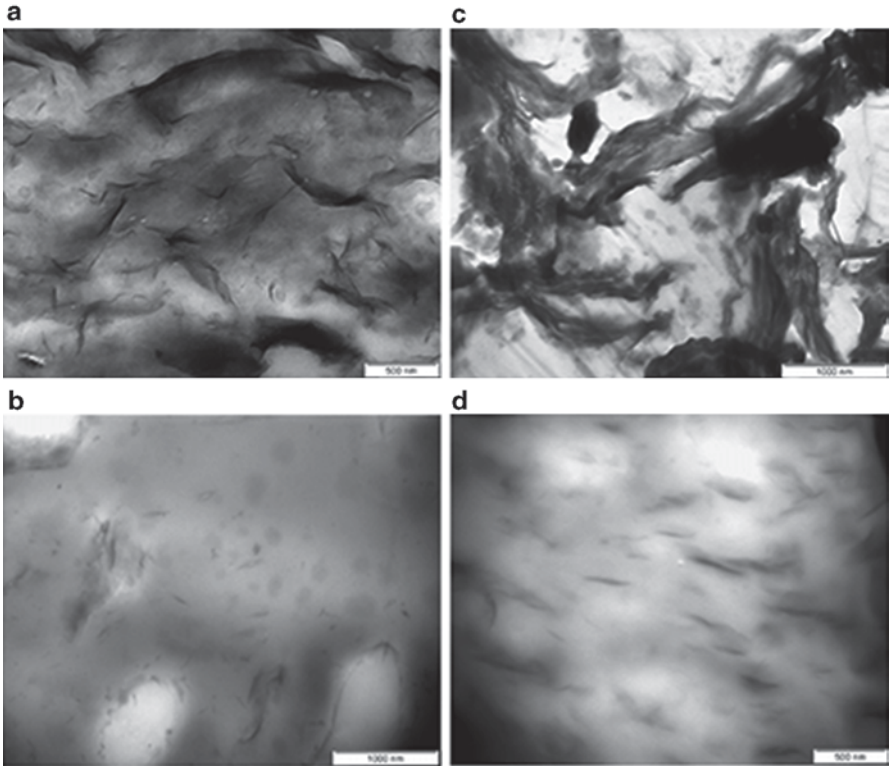

Fig. 8.14 Transmission electron micrographs of **a** the pH 11 with pristine nanoclay wheat gluten (WG) film (4.5 wt.% clay), **b** the pH 11 with modified nanoclay WG film (4.5 wt.% clay), **c** the pH 4 with pristine nanoclay WG film (4.5 wt.% clay), and **d** the pH 4 with modified nanoclay WG film (4.5 wt.% clay). (Reproduced with permission from Olabarrieta 2006)

increases while the elongation at break decreases. The water vapor permeability decreases as the nanoclay loading increases, which depends also on the degree of nanoclay dispersion. TEM provides images of the degree of nanoclay dispersion in WG nanocomposite films prepared from solvent casting at different pH as shown in Fig. 8.14. It was found that pH and modification of nanoclays played a major role in controlling the degree of nanoclay dispersion. The black streaks are nanoclays that are on the bright WG background. The WG nanocomposite films prepared at pH 11 with modified nanoclays showed fully delaminated nanoclay platelets with good dispersion. This result was in good agreement with physical properties such that the greatest improvement in mechanical and barrier properties among other samples (Olabarrieta 2006).

Similar investigation was on zein-modified nanoclay nanocomposite films. It was also found that the process played a major role in controlling the degree of physical properties improvement. Although the TEM images showed that zein nanoclay nanocomposite films prepared from both techniques had a combination of intercalated and exfoliated nanocomposite structures (Fig. 8.15), the blown films

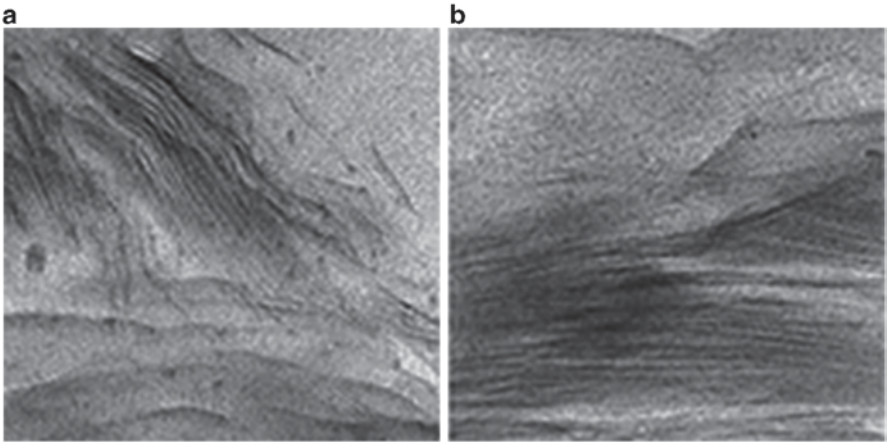

Fig. 8.15 The nanocomposite structures of zein nanoclay hybrid films at 5 wt.% nanoclay as viewed by TEM; **a** prepared by solvent-casting technique, **b** prepared by extrusion-blowing technique. (Reproduced with permission from Luecha et al. 2010)

showed more directional nanoclay-platelets arrangement that can be controlled by further improving the extrusion process (Luecha et al. 2010).

It is worth mentioning that in case of biocomposites including laminates, TEM and SEM play an important role in the investigation of the quality of the biocomposites that is in association with the properties of the final biocomposite films. TEM is widely used to probe the distribution of inorganic nanomaterials in the prolamin matrix. However, the sample preparation of biofilms for TEM measurement would be challenging.

8.5 Summary, Conclusions, and Recommendations

Imaging technologies have become essential for material characterization and also in the study of prolamin films for packaging applications. The use of potent imaging tools including AFM and CLSM enables us to investigate the molecular orientation of prolamin proteins during the formation of the films. AFM can be used to understand the mechanism of the protein conformational change at the beginning of film formation based on processing conditions. Moreover, the relationship between the microstructure/topography and the physical properties as well as functional properties can be well understood using the imaging tools in complement with other film functional property evaluation methods. SEM is used for obtaining the three-dimensional images of the films at sub-micrometer scale, thus providing surface topography of the films as well as the interface between laminates. On the other hand, TEM is used for visual investigation of the distribution of nanoparticles in prolamin nanocomposite films. However, sample preparation techniques for TEM and SEM can be complicated for biological samples, thus no exception for prolamin

films. Molecular localization techniques have become simple due to fast progress in biological imaging. Such advancement enables CLSM to visualize the molecular orientation and arrangement of the prolamin protein films. Nevertheless, the immunostaining agents specific to each prolamin can be expensive. The observation of new inter- and intramolecular chemical interaction, as far as the loss of the bonding of the films is considered, can be investigated using FTIR or Raman spectroscopy.

The imaging tools have become essential for material characterizations that provide rich information on the microstructure of prolamin proteins; coupling these powerful tools with specific functions would provide more insight into the physical properties locally at the molecular level. Moreover, the investigation of film formation in real time will initiatively open up several research challenges, especially in relation to mechanical and barrier properties of films. It is suggested that one should contemplate the pros and cons of each imaging tool and the relevant information in selecting the most appropriate imaging technique.

References

Aithani D, Mohanty AK (2006) Value-added new materials from byproduct of corn based ethanol industries: blends of plasticized corn gluten meal and poly(epsilon-caprolactone). Ind Eng Chem Res 45:6147–6152

Alessandrini A, Facci P (2005) AFM: a versatile tool in biophysics. Meas Sci Technol 16:R65

Angellier-Coussy, H., Torres-Giner, S., Morel, M. H., Gontard, N., Gastaldi, E. (2008). Functional properties of wheat gluten/montmorillonite materials with respect to formulation and processing conditions. App Polym Sci, 107, 487–496

Argos P, Pedersen K, Marks MD, Larkins BA (1982) A structural model for maize zein proteins. J Biol Chem 257:9984–9990

Cho SW, Gallstedt M, Hedenqvist MS (2010) Effects of glycerol content and film thickness on the properties of vital wheat gluten films cast at pH 4 and 11. J App Polym Sci 117:3506–3514

De Graaf LA (2000) Denaturation of proteins from a non-food perspective. J Biotechnol 79:299–306

Emmambux M N, Stading M (2007) In situ tensile deformation of zein films with plasticizers and filler materials. Food Hydrocoll 21:1245–1255

EPA (2011) Municipal solid waste in the United States. http://www.epa.gov/osw/nonhaz/municipal/pubs/MSWcharacterization_fnl_060713_2_rpt.pdf. Accessed 20 Feb 2014

Escamilla-Garcia M, Calderon-Dominguez G, Chanona-Perez JJ, Farrera-Rebollo RR, Andraca-Adame JA, Arzate-Vazquez I, Mendez-Mendez JV, Moreno-Ruiz LA (2013) Physical and structural characterisation of zein and chitosan edible films using nanotechnology tools. Int J Biol Macromol 61:196–203

Esen A (1986) Separation of alcohol-soluble proteins (zeins) from maize into three fractions by differential solubility. Plant Physiol 80:623–627

Ghanbarzadeh B, Oromiehie A, Musavi M, Falcone P, D-Jomeh Z, Rad E (2007) Study of mechanical properties, oxygen permeability and AFM topography of zein films plasticized by polyols. Packag Technol Sci 20:155–163

GIEWS, Global information and early warning system on food and agriculture (2012) http://www.fao.org/docrep/016/al993e/al993e00.pdf. Accessed 20 Feb 2014

Gillgren T, Barker SA, Belton PS, Georget DM R, Stading M (2009) Plasticization of zein: a thermomechanical, FTIR, and dielectric study. Biomacromolecules 10:1135–1139

Gu L, Wang M, Zhou J (2013) Effects of protein interactions on properties and microstructure of zein-gliadin composite films. J Food Eng 119:288–298

Guillard V, Chevillard A, Gastaldi E, Gontard N, Angeillier-Coussy H (2013) Water transport mechanisms in wheat gluten based (nano) composite materials. Eur Polym J 49:1337–1346

Guo YC, Liu ZD, An HJ, Li MQ, Hu J (2005) Nano-structure and properties of maize zein studied by atomic force microscopy. J Cereal Sci 41:277–281

Haward SJ, Shewry PR, Miles MJ, McMaster TJ (2010) Direct real-time imaging of protein adsorption onto hydrophilic and hydrophobic surfaces. Biopolymer 93:74–84

He J, Penson S, Powers S, Hawes C, Shewry P, Tosi P (2013) Spatial patterns of gluten protein and polymer distribution in wheat grain. J Agri Food Chem 61:6207–6215

Hernandez-Izquierdo VM, Krochta JM (2008) Thermoplastic processing of proteins for film formation—a review. J Food Sci 73:R30–R39

Hernandez-Munoz P, Kanavouras A, Ng PK, Gavara R (2003) Development and characterization of biodegradable films made from wheat gluten protein fractions. J Agric Food Chem 51:7647–7654

Jackson M. and Mantsch, H. H. (1995). The use and misuse of FTIR Spectroscopy in the determination of protein structure. Crit Rev Biochem Mol Biol, 30, 95–120

Jagadeesh D, Kumar BP, Sushakara P, Prasad CV, Rajulu AV, Song JI (2013) Preparation and properties of propylene glycol plasticized wheat protein isolate novel green films. J Polym Environ 21:930–936

Jerez A, Partal P, Martinez I, Gallegos C Guerrero A (2007) Protein-based bioplastics: effect of thermo-mechanical processing. Rheol Acta 46:711–720

Johansson C, Bras J, Mondragon I, Nechita P, Plackett D, Simon P, Svetec DG, Virtanen S, Baschetti MG, Breen C, Clegg F, Aucejo S (2012) Renewable fibers and bio-based materials for packaging applications—a review of recent developments. Bioresources 7:2506–2552

Kokini, J. L., Cocero, A. M., Madeka, H., de Graaf, E. (1994). The development of state diagrams for cereal proteins. Trends Food Sci Tech. 5, 281–288

Kuktaite R, Plivelic T, Cerenius Y, Hedenqvist M, Gallstedt M, Marttila S, Ignell R, Popineau Y, Tranquet O, Shewry P, Johansson E (2011) Structure and morphology of wheat gluten films: from polymeric protein aggregates toward superstructure arrangements. Biomacromolecules 12:1438–1448

Kuktaite R, Plivelic TS, Ture H, Hedenqvist M S, Gallstedt M, Marttila S, Johansson E (2012) Changes in the hierarchical protein polymer structure: urea and temperature effects on wheat gluten films. RSC Adv 2:11908–11914

Lagrain B, Goderis B, Brijs K, Delcour JA (2010) Molecular basis of processing wheat gluten toward biobased materials. Biomacromolecules 11:533–541

Lawton JW (2002) Zein: a history of processing and use. Cereal Chem 79:1–18

Lawton JW (2004) Plasticizers for zein: their effect on tensile properties and water absorption of zein films. Cereal Chem 81:1–5

Leroy E, Jacquet P, Coativy G, Reguerre AL, Lourdin D (2012) Compatibilization of starch–zein melt processed blends by an ionic liquid used as plasticizer. Carbohydr Polym 89:955–963

Luecha J, Sozer N, Kokini JL (2010) Synthesis and properties of corn zein/montmorillonite nanocomposite films. J Mater Sci 45:3529–3537

Madeka H, Kokini JL (1996) Effect of glass transition and cross-linking on rheological properties of zein: development of a preliminary state diagram. Cereal Chem 73:433–438

Matsushima N, Danno G, Takezawa H, Izumi Y (1997) Three-dimensional structure of maize alpha-zein proteins studied by small-angle X-ray scattering. Biochim Biophys Acta 1339:14–22

McMaster TJ, Miles MJ, Wannerberger L, Eliasson AC, Shewry PR, Tatham AS (1999) Identification of microphases in mixed alpha- and omega-gliadin protein films investigated by atomic force microscopy. J Agri Food Chem 47:5093–5099

Olabarrieta I, Gallstedt M, Ispizua I, Sarasua JR, Hedenqvist MS (2006) Properties of aged montmorillonite–wheat gluten composite films. J Agri Food Chem 54:1283–1288

Panchapakesan C, Sozer N, Dogan H, Huang QR, Kokini JL (2012) Effect of different fractions of zein on the mechanical and phase properties of zein films at nano-scale. J Cereal Sci 55:174–182

Pol H, Dawson P, Acton J, Ogale A (2002) Soy protein isolate/corn-zein laminated films: transport and mechanical properties. J Food Sci 67:212–217
Reddy N, Yang YQ (2013) Thermoplastic films from plant proteins. J App Polym Sci 130:729–738
Roy S, Weller C, Gennadios A, Zeece M, Testin R (1999) Physical and molecular properties of wheat gluten films cast from heated film-forming solutions. J Food Sci 64:57–60
Schwartz DK (1997) Langmuir-Blodgett film structure. Surf Sci Rep 27:245–334
Selling GW, Sessa DJ (2007) Sample preparation and testing methods affect the physical properties and evaluation of plasticized zein. Ind Crop Prod 25:266–273
Sessa DJ, Mohamed A, Byars JA, Hamaker SA H, Selling GW (2007) Properties of films from corn zein reacted with glutaraldehyde. J App Polym Sci 105:2877–2883
Shewry PR, Halford NG (2002) Cereal seed storage proteins: structures, properties and role in grain utilization. J Exp Bot 53:947–958
Shewry PR, Tatham AS (1990) The prolamin storage proteins of cereal seeds: structure and evolution. Biochem J 267:1–12
Shi K, Kokini JL, Huang QR (2009) Engineering zein films with controlled surface morphology and hydrophilicity. J Agri Food Chem 57:2186–2192
Shukla R, Cheryan M (2001) Zein: the industrial protein from corn. Ind Crop Prod 13:171–192
Sozer N, Kokini JL (2009) Nanotechnology and its applications in the food sector. Trends Biotechnol 27:82–89
Tatham AS, Shewry PR (2000) Elastomeric proteins: biological roles, structures and mechanisms. Trends Biochem Sci 25:567–571
Taylor J, Anyango JO, Taylor JRN (2013) Developments in the science of zein, kafirin, and gluten protein bioplastic materials. Cereal Chem 90:344–357
Toufeili I, Lambert IA, Kokini JL (2002) Effect of glass transition and cross-linking on rheological properties of gluten: development of a preliminary state diagram. Cereal Chem 79:138–142
Tunc, S., Angellier, H., Cahyana, Y., Chalier, P., Gontard, N., Gastaldi, E. (2007). Functional properties of wheat gluten/montmorillonite nanocomposite films processed by casting. J Membrane Sci.289, 159–168
Ture H, Blomfeldt TOJ, Gallstedt M, Hedenqvist MS (2012) Properties of wheat-gluten/montmorillonite nanocomposite films obtained by a solvent-free extrusion process. J Polym Environ 20:1038–1045
Xu H, Chai YW, Zhang GY (2012) Synergistic effect of oleic acid and glycerol on zein film plasticization. J Agri Food Chem 60:10075–10081
Zhang HK, Mittal G (2010) Biodegradable protein-based films from plant resources: a review. Environ Prog Sustain Energy 29:203–220

Chapter 9
Assessment of Internal and External Quality of Fruits and Vegetables

Natalia Hernández-Sánchez, Guillermo P. Moreda, Ana Herre-ro-Langreo and Ángela Melado-Herreros

9.1 Introduction

Worldwide production and trade of fruits and vegetables is steadily increasing in line with the consumer awareness for a healthy diet. Thus, there is a demand to fulfil the external and internal quality requirements for fresh fruits and vegetables sector. The concept of quality is a complex characteristic that determines the value or acceptance of the produce by the consumers (Piñeiro and Díaz Ríos 2004). Such quality comprises attributes as appearance, organoleptic characteristics, ripeness, safety and nutritional value. The external aspect is the primary attribute evaluated by the consumer, whereas other attributes such as taste, texture, juiciness or the absence of internal damages and/or disorders are only destructively assessed through their senses (López Camelo 2004) once the produce is purchased. For industrial processing, the internal attributes are of major importance for establishing the storage conditions and for deciding the optimum use in alternative processes.

A critical aspect that differentiates fruits and vegetables from other commodities is their perishability. Their high water content together with their usually highly permeable pericarp triggers metabolic processes as well as growth of microorganisms, resulting in both qualitative and quantitative losses. Besides, these produces are especially prone to developing damages caused by impacts and scratches.

N. Hernández-Sánchez (✉) · G. P. Moreda · Á. Melado-Herreros
Physical Properties Laboratory-Advanced Technologies in Agri-Food (LPF-TAGRALIA), Technical University of Madrid, 28040 Madrid, Spain
e-mail: n.hernandez@upm.es

G. P. Moreda
e-mail: guillermo.moreda@upm.es

Á. Melado-Herreros
e-mail: angela.melado@upm.es

A. Herre-ro-Langreo
Irstea, UMR ITAP, 361 Rue J.F. Breton, 34196 Montpellier Cedex 5, France
e-mail: anahelangreo@gmail.com

N. Sozer (ed.), *Imaging Technologies and Data Processing for Food Engineers,* Food Engineering Series, DOI 10.1007/978-3-319-24735-9_9

Therefore, the development of methodologies that bring insight into the quality attributes at an early stage in the postharvest process in a nondestructive manner is a major challenge for the horticultural sector. In this chapter, advances in the most important imaging techniques that can be applied to fruit and vegetable inspection are addressed. The review begins with the external inspection, dominated by the use of computer vision, which analyses morphological features and surface attributes. Then, inspection goes through the pericarp and reaches the closest inner layers by the application of hyperspectral imaging, which provides complementary information by analysing both external and internal attributes. At this location, the microscale inspection is achieved by optical coherence tomography (OCT), which performs high resolution imaging of the microstructure. Two techniques are finally reviewed as being capable of evaluating the most internal regions, providing cross-sectional images of the complete sample at both macro- and microscale. X-ray imaging is based on the contrast arising from the differences in the atomic number, density and thickness of the internal structures and tissues, revealing morphological and structural aspects. For the magnetic resonance imaging (MRI), the image contrast can be weighted in several resonance parameters, which broadens the field of applications. Therefore, in addition to morphological and structural features, the chemical composition and tissue characteristics of different nature can be studied.

9.2 Computer Vision

Computer vision is a technology for acquiring and analysing an image of a real scene (Fig. 9.1) by computers to obtain information about objects in the scene. According to Sun (2008), the aim of computer vision is recognising objects and extracting quantitative information from digital images in order to provide objective, rapid,

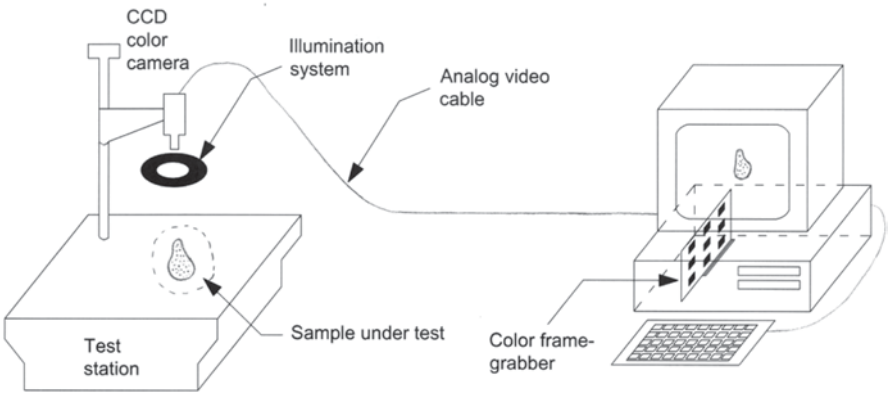

Fig. 9.1 Components of a conventional computer vision system. Alternatively, the frame grabber can be inside the camera, with video cable from camera to computer carrying a digital signal. (Redrawn with permission from Sun 2008. © 2008 Academic Press)

noncontact and nondestructive quality evaluation. A computer vision system generally consists of five basic components: illumination, a still camera or a video camera, an image digitiser, computer hardware and software (Fig. 9.1). The terms computer vision and machine vision are used interchangeably in the literature. Computer vision is based on image processing and analysis, two powerful tools common to other sensing technologies. The most promising branch of computer vision is spectral imaging, which combines spatial and spectral information from computer vision and spectroscopy, respectively (Kim et al. 2007).

External quality traits of fruits and vegetables include size, shape, surface texture, surface colour and surface defects. Computer vision systems measure the reflectance of an object but also the range or distance from the camera to the object surface (Ruiz-Altisent et al. 2010). While reflectance data are essential and irreplaceable for colour and defect inspection, size, shape and surface texture can be alternatively evaluated from range data. When only reflectance data are managed, the term used is 2D computer vision.

Segmentation is the first step in image analysis to subdivide an image into meaningful regions, and it directly affects the subsequent image analysis outcomes (Mizushima and Lu 2013). More specifically, the aim of image segmentation is the partition of the image into a set of regions which are uniform with respect to some property, such as grey level, texture, colour or depth. These regions are the so-called segments (Fig. 9.2). The simplest form of segmented image is the binary image, which includes only two segments: pixels of fruit and background pixels. Typically, 0 is assigned to the scene background pixels and 1 to the pixels of fruit. Four different approaches to segmentation are thresholding based, region based, edge based, and classification based.

9.2.1 Size and Shape

From a binary image, fruit size can be estimated as perimeter, area (Fig. 9.3) or several diameters (Fig. 9.2). According to fresh fruit marketing standards in force in many countries worldwide, apple size is given by the maximum diameter of the equatorial section. Blasco et al. (2003) calculated diameter from the image out of four images in which the stem cavity was nearest to the centroid of the fruit (Fig. 9.2), because this implies that the polar axis is approximately orthogonal to the image plane.

Unlike equatorial diameter or mass, fruit volume is not a sizing parameter in marketing standards. However, volume estimation is required for calculating fruit density, which is an important parameter for food technologists. For example, starch content has a major influence on the cooking and processing properties of potatoes (Hoffmann et al. 2005), and there is a close correlation between the density of the potato tuber and its starch content. Martynenko (2011) calculated instantaneous volume during convective drying of ginseng roots. Assuming cylindrical geometry, they computed surface area from projected area. Then, they used an empirical relation to compute volume from surface area.

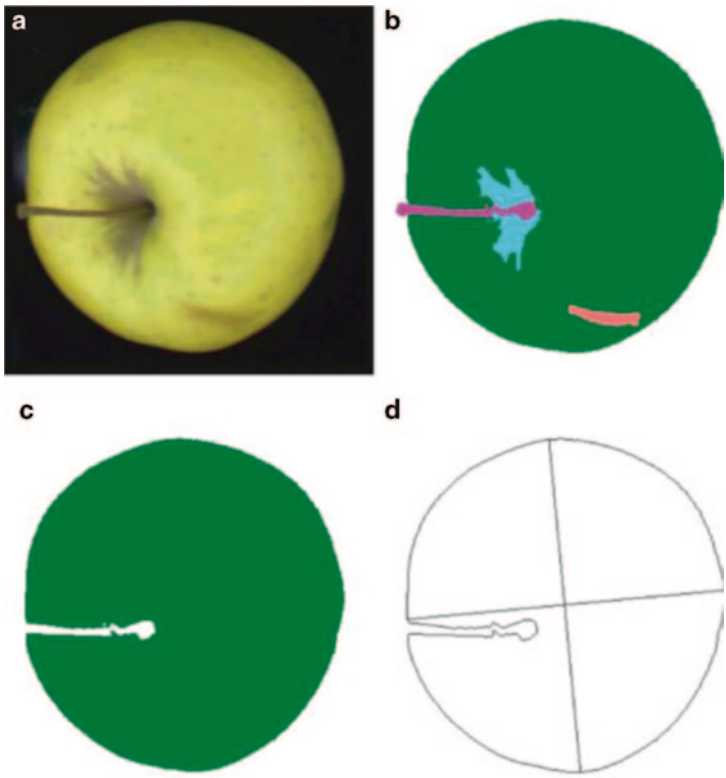

Fig. 9.2 **a** Original image captured by the camera. **b** Segmented image showing the sound skin *(green),* the russeting *(cyan),* the stem *(purple)* and the damage *(pink)* regions. **c** Region containing all the classes except the stem and the background, used to calculate the size. **d** Image showing how the size was estimated. (Reprinted with permission from Blasco et al. 2003. © 2003 Silsoe Res. Inst.)

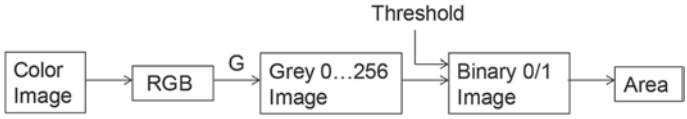

Fig. 9.3 Image segmentation for size feature extraction. (Reprinted with permission from Martynenko 2011. © 2008 Springer)

Fruit shape determination is important in many food industries. For example, top quality cans of mandarin segments should not contain more than 5 % of partially broken segments. Blasco et al. (2009) detected broken mandarin segments based on their lack of symmetry. Regular-shaped potato tubers are desirable because the irregular ones cause a great deal of losses during peeling and subsequent processing (El Masry et al. 2012). Moreover, French fries manufacturers prefer long-oval or long tuber with a length of at least 50 mm. For the production of crisps (chips), round tubers are required with a diameter range of 40–60 mm (NIVAP Holland

2014). Tomato processing companies are interested in developing varieties which carry oblong, almost square-shaped fruit, in order to pack them more efficiently (Moreda et al. 2012). Some companies might be interested in developing extremely elongated tomatoes shaped like cucumbers. These fruits would be very advantageous when preparing sliced tomatoes for hamburgers, as less ends would have to be thrown away (Espinoza 2003). Sometimes, ill-shaped specimens present protruding zones that contain low-quality tissue. Thus, the presence of neck in a cucumber is undesirable, because of the absence of fleshy tissue that makes it useless for the consumer (Fanourakis and Tzifaki 1993). Likewise, the protruding zone in pear-shaped or 'sheepnosed' grapefruit is a peel disorder characterised by a coarse rind or thick albedo (Syvertsen et al. 2005). Heat and mass transfer coefficients which are crucial for majority of unit operations are also dependent on the shape and surface area of the object (Goñi et al. 2007).

The process leading to shape classification can be divided into following steps: image capturing; preprocessing, e.g. noise filtering, segmentation, feature value extraction or shape description; eventual compression of the feature set and finally comparison and classification. Sometimes two or more steps are merged into one, e.g. simultaneous segmentation and feature extraction. Some examples of segmentation techniques are level set methods and edge detectors like the Sobel gradient operator (Fig. 9.4) and active contours or 'snakes'. According to Duda et al. (2000), and classification is somewhat arbitrary: An ideal feature extractor would yield a feature vector that makes the job of the classifier trivial; conversely, an omnipotent classifier would not need the help of a sophisticated feature extractor. There are different approaches for classification, from simple thresholding to parametric (Bayes, linear discriminant analysis) and nonparametric (artificial neural network, k-nearest neighbours) techniques.

In 2D computer vision, fruit shape can be evaluated in three major ways: First and simplest, as a simple combination of size features (Okayama et al. 2006); second, using only contour data and hence contour-based methods, and third, using all fruit pixels or region-based methods (Moreda et al. 2012). Region-based methods include medial axis or skeleton technique, and several types of moments (Gui and Zhou 2010). Contour-based shape description methods include shape signature (Jarimopas and Jaisin 2008), chain code (Nandi et al. 2012), Bézier curves, Fourier

Fig. 9.4 Date with slight skin delamination. Lighter pixels in image **a** correspond to loose delaminated skin. Comparing **a** with **d,** we can observe the good performance of Sobel gradient operator as an edge detector. (Reprinted with permission from Lee et al. 2008. © 2007 Elsevier)

(Menesatti et al. 2008), wavelet (Riyadi et al. 2008) and fractal analyses, amongst others. El Masry et al. (2012) discriminated well-shaped potatoes from misshapen ones with an in-line sorting success rate of 96.2 % by using simple combination of size parameters together with Fourier descriptors as shape features.

9.2.2 Surface Texture

Wang et al. (2007) found that produce surface characteristics affect both product quality and safety. For example, *Escherichia coli* more preferentially attaches itself to coarse, porous or injured surfaces than uninjured surfaces of fruits.

Lee et al. (2008) tackled dates classification according to degree of delamination. Delaminated skin is synonym with loose skin. They argued that thresholding segmentation was not suitable for the detection of skin delamination. Instead, they used the Sobel gradient operator to detect the edges of greatest contrast (Fig. 9.4).

Wrinkles in apple skin are a visible indicator of fruit senescence. Dunn (2007) developed 2D computer vision algorithms to classify citrus fruits according to peel roughness. Jafari et al. (2012) addressed indirect estimation of citrus peel thickness through image analysis of peel surface texture. They hypothesised that fruits with coarser surface texture would have a thicker peel, and vice-versa. They obtained an r^2 of 0.958 when correlating coarseness with peel thickness. Peel thickness was calculated from a fruit cross-section image, as the ratio of peel area to total fruit area.

9.2.3 Surface Colour

Colour is an important quality attribute that dictates the quality and value of many fruit products (Kang et al. 2008). The perceived colour of objects depends on three factors: the spectral distribution of the illuminant, the spectral reflectance of scene surfaces, and the spectral response of the imaging sensor. The colour of a particular pixel in an image is expressed by three coordinates in a colour space. The primary colours red, green and blue (RGB) are the most widely used in computer vision. When inspected objects have very different colours, sometimes simple ratios between RGB values can discriminate between them, thus saving processing time. Blasco (2009) used the R/G ratio to discriminate four classes of pomegranate arils, with a success rate of 90 %, similar to the one obtained by human visual inspection.

One drawback of RGB colour spaces is that they are device dependent. This means that different devices produce different RGB values for the same pixels in a scene (Cubero et al. 2011). If reproducibility is required, then CIE L*a*b* colour space should be used. Calculation of colour coordinates can be performed in two ways: First, by imaging a colour reference standard template card with declared XYZ values (Kang et al. 2008); and second, by measuring the same target both with a colorimeter and with the computer vision system (Matiacevich et al. 2013). Fathi et al. (2011), in a work aimed to predict colour changes during osmotic dehydration

of kiwifruit slices, converted RGB coordinates into L*a*b* to ensure colour reproducibility. They observed that chromatic parameter a* reflected most colour change, with increased a* values associated to increasing osmotic temperature, which shows diminishing of green colour of dehydrated kiwifruit slices.

9.2.4 Surface Defects

Inspection of fruit surface defects is of utmost importance, both for marketing and safety reasons. With regard to fresh produce market, fruit category is diminished when blemished area exceeds a given percentage of the fruit surface. From the packing industry point of view, identification of the type of defect is a key aspect (Cubero et al. 2011), since some defects are more problematic than others. The presence of dark and brown spots due to natural defects or injuries in raw potatoes will lead to surface defects in chips, with likely rejection by consumer (Mendoza et al. 2007). In banana, surface blemishes known as senescent spotting are an indicator of fruit overripeness. Quevedo et al. (2008) proposed fractal dimension as a potential method for determining banana ripening at the final ripening stage. With regard to safety, Wang et al. (2007) reported higher attachment rate of microorganisms to injured tissue of fruits.

Slaughter et al. (2008) reported the appearance of a visible small dot pattern on an orange peel after a frost. They used ultraviolet (UV) fluorescence properties of the dots to assess the level of freeze damage, and concluded that black rooms currently used in packinghouses to detect and remove fungal infected oranges could also be used to remove freeze-damaged fruits. It just would need inspectors be trained to look at yellow small dot pattern, apart from pink reflections typical of fungal disease. Of course, in the automated version of the system, both fungal and freeze detection could be performed using computer vision.

With regard to blemish detection, unsupervised segmentation methods (thresholding and flooding algorithms on monochrome images and Mahalanobis distance in the RGB space) give good results for mono-colour fruits. For bicolour fruits, supervised techniques are usually used (Sun 2008).

A recurrent research issue in apple blemish detection is achieving that the stem cavity and the calyx are not confused with a blemish by the computer vision system. Jiang et al. (2009) argued that 2D near infrared (NIR) imaging was unable to discriminate stem end calyx from true defects. They proposed 3D surface reconstruction of apples, using the shape-from-shading algorithm, and obtained a 90.15 % detection rate.

9.3 Hyperspectral Imaging

Hyperspectral (HS) imaging stands on the edge between image analysis and spectroscopy. These two technologies are widely used for the assessment of fruit and vegetables quality (Nicolaï et al. 2007; Huang et al. 2008; Cubero et al. 2011). HS images provide both spatial and electromagnetic spectral information of a material.

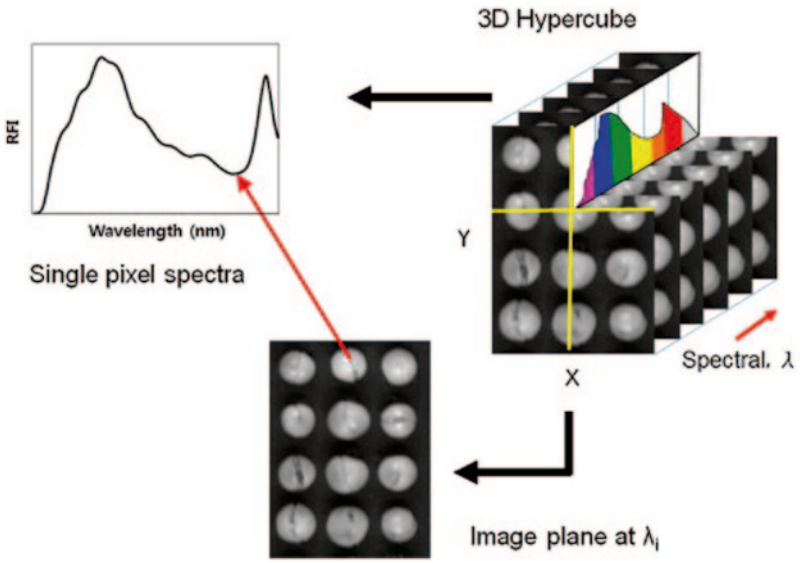

Fig. 9.5 Schematic representation of HS imaging hypercube of cherry tomatoes showing the relationship between spectral *(axis λ)* and spatial dimensions *(axis X and Y)*. (Cho et al. 2013)

A typical HS system consists of a light source, a wavelength dispersion device and a detector (Wu and Sun 2013). The emitted light interacts with the surface of the sample and the area detector measures the spectra resulting from this interaction. As it is further explained in the application examples, the ability of the sample in absorbing or scattering the exciting light can be related to both chemical and physical properties. In addition, the spatial information of the image, the spatial distribution of these spectra, can be used to identify objects and object attributes such as shape, size, texture, etc. Electromagnetic spectral information is acquired for each pixel of the image. As a result, 3D images are obtained: two dimensions provide spatial information and one dimension provides spectral information of the scene (Wu and Sun 2013). As schematically represented in Fig. 9.5 by Cho et al. (2013), an HS image can be regarded as a set of images, each one acquired at a narrow band of wavelengths (waveband).

When the spectral image is composed of a few wavebands (usually less than ten wavebands, not necessarily contiguous), it is generally termed as "multispectral" (MS), while "HS" imaging, generally accounts for images containing continuous spectral information in a certain wavelength range.

Image acquisition technologies are different for HS and MS imaging. Detailed discussion on these technologies is out of the scope of this book chapter, but updated information can be found elsewhere (Boldrini et al. 2012; Wu and Sun 2013). Concerning the evaluation of fruits and vegetables quality, it is important to note that MS technology is significantly cheaper and faster than HS, while HS imaging provides complete spectral information, facilitating the chemical characterisation of each pixel of the image (Boldrini et al. 2012).

Regarding the spectral range, most applications of MS and HS imaging for fruits and vegetables evaluation focuses on NIR and visible (VIS) regions of electromagnetic spectrum. Nevertheless, the same principles can be used on UV ranges (Al-Mallahi et al. 2010) or combined with fluorescence technologies (Cho et al. 2013), or thermal imaging (Baranowski et al. 2012).

9.3.1 External Quality

HS imaging is measured on the surface of the samples, and it is thus especially adequate for the assessment of external quality, such as bruising or external damages.

Evaluation of bruising damages by HS imaging were extensively reviewed by Opara and Pathare (2014). Recent applications of HS imaging for bruise damage evaluation are found both in fruits: apples (Peng et al. 2012; Baranowski et al. 2013), kiwis (Lü et al. 2011) and pears (Zhao et al. 2010), and vegetables: especially mushrooms (Gowen et al. 2008; Esquerre et al. 2012).

A clear example illustrating the challenges faced by this kind of application is presented by Gowen et al. (2008). In this work, HS images acquired from 400 to 1000 nm were used to assess bruise damage on mushrooms. A fix intensity threshold (0.1) on the images acquired at 720 nm was used to segment mushrooms from the image background. Two spectral preprocessing treatments: Multiplicative scatter correction (MSC) and mean normalisation (MN) were applied to correct the spectral variability (scattering) produced by the curvature of the mushroom volume, shown in Fig. 9.6. Bruised areas were enhanced through a principal components analysis (PCA), which reduced the spectral information of the image from 71 original images (one for each acquired waveband) to a single informative image, related

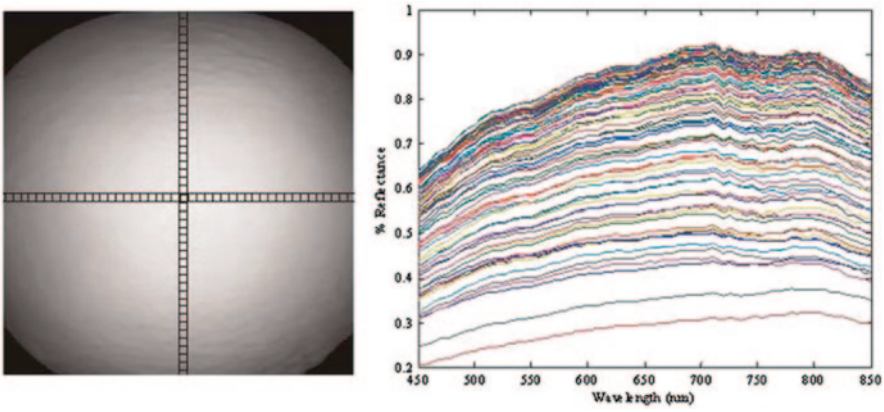

Fig. 9.6 Effect of mushroom curvature on spectrum. Each square on the *left hand side* image represents a region on the surface of an undamaged mushroom, from which an average spectrum was calculated, as shown in the plot on the *right hand side*. (Gowen et al. 2008)

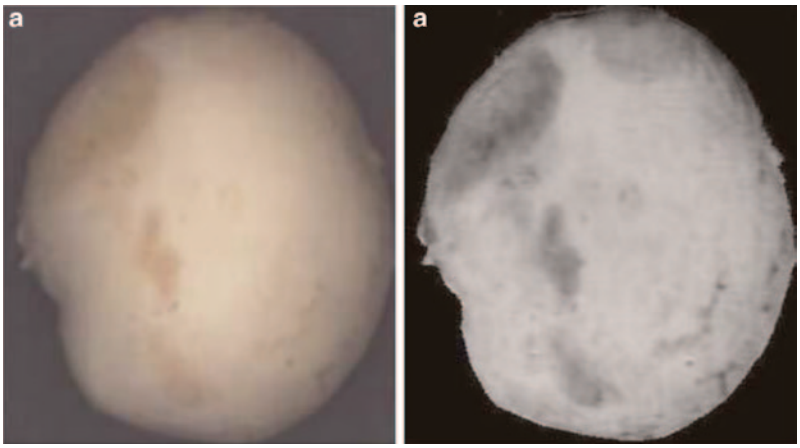

Fig. 9.7 **a** RGB image of damaged mushroom. **b** Virtual image obtained after multiplying the image hypercube by PC 1 loading vector arising from PCA analysis of sample of 600 spectra representing undamaged (n¼300) and bruise-damaged (n¼300) mushroom tissue. (Gowen et al. 2008)

to bruising damage (Fig. 9.7). Spatial information was used to avoid misclassification of mushroom borders, using a roundness metric algorithm to exclude the classification of thin elongated areas as bruises. Finally, PCA allowed the classification of each pixel as sound or bruised tissue. Mushrooms were classified as sound or damaged according to the estimated percentage of bruised area, obtaining between 83 and 100 % of correct classification, depending on the batch and variations of the PCA approach.

Other external defects can be also characterised through HS imaging. Li et al. (2011) used HS imaging between 400 and 1000 nm to detect various common defects in oranges (insect damage, wind scarring, thrips scarring, scale infestation, canker spot, copper burn, heterochromatic stripe and phytotoxicity). Images were evaluated through PCA, and both loadings and PC images were analysed for interpretation. This analysis led to the identification of three specific wavebands, best related with the studied fruit damages, and a waveband ratio (875/691 nm) to differentiate calix/stems from defects. Up to 95.4 % of the defects were detected by this imaging system.

9.3.2 Internal Quality

The evaluation of internal quality is also an extended application of HS imaging. When measuring small fruits such as grapes and blueberries (Baiano et al. 2012; Leiva-Valenzuela et al. 2013), HS imaging can facilitate the automation of the measurements procedure, allowing to measure complete spectral information of several samples at the same time or even of moving samples on a processing line (Boldrini et al. 2012). In bigger samples such as melons (Sugiyama and Tsuta 2010), HS

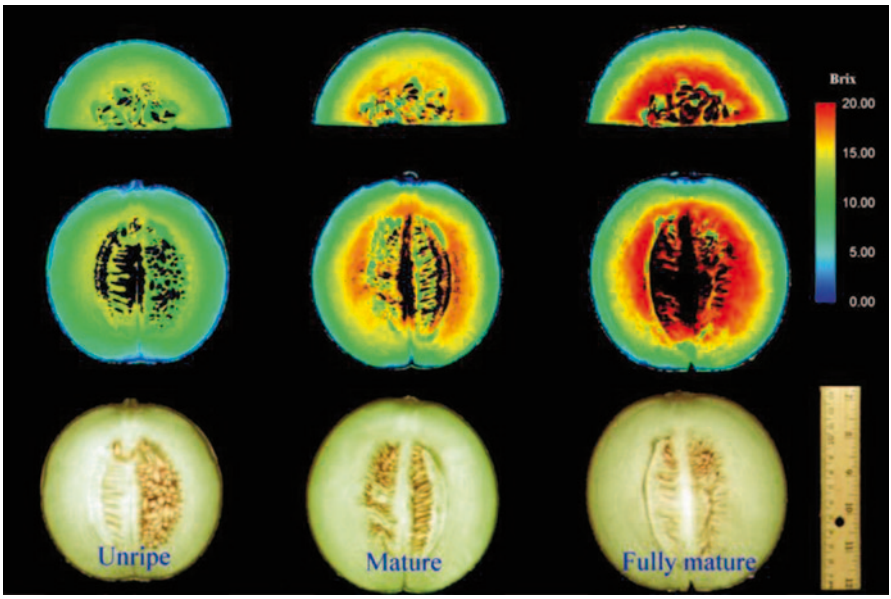

Fig. 9.8 Sugar distribution map for *unripe, mature* and overripe melons. (Sugiyama and Tsuta 2010)

imaging can allow to map the spatial distribution of quality attributes, as soluble solids content (Fig. 9.8).

A recent example of this kind of application is presented by Baiano et al. (2012). This work studies several physico-chemical and sensory indexes of seven cultivars of table grapes, three red and four white, through HS imaging (400–1000 nm). Samples were randomly sorted in two batches: 50 % of the samples were used for model calibration and 50 % for validation of the model. Average spectra were computed for each grape. Mean centre correction (spectral preprocessing) and partial least squares regression (PLSR) modelling was applied to estimate the physico-chemical indexes. Two PLS models were computed, one for red and one for white varieties. A single PLS model per variety group (red or white) obtained good estimations on pH (coefficients of determination were 0.80 and 0.90 for white and red grapes, respectively), total acidity (0.95 and 0.82) and soluble solids content (0.94 and 0.93). No correlation was found with the sensory data.

Spectral scattering is also recently being applied on machine vision systems for the assessment of internal quality in several fruits, such as apple (Mendoza et al. 2011) or peach (Cen et al. 2012). In contrast to reflectance spectroscopy, spectral scattering differentiates and measures separately the scattering and the absorption coefficients of the samples. Scattering coefficients are influenced by fruit tissue density, cell composition and extra- and intracellular structures, while absorption coefficients relate to chemical composition. Further information on the basic principles of light scattering techniques is exposed by Zhelev and Barudov (2005). Applying this technique on a spatially resolved system (HS imaging-based

spatially resolved), Cen et al. (2012) obtained good estimations of several quality attributes of peaches. Correlation coefficient for firmness, SSC, skin lightness and flesh lightness was 0.749 (standard error of prediction or SEP = 17.39 N), 0.504 (SEP = 0.92 °Brix), 0.898 (SEP = 3.45), and 0.741 (SEP = 3.27), respectively. These results compared favourably to acoustic and impact firmness measurements, whose correlations with destructive measurements were 0.639 and 0.631, respectively.

9.3.3 Quality Evolution

HS imaging is a powerful tool to evaluate quality evolution on fruits and vegetables in processes such as ripening or senescence during postharvest (Lorente et al. 2012; Wu and Sun 2013). As shown in Fig. 9.9, NIR and VIS spectra can provide detailed information on the evolution of physical and chemical properties during these processes (Rajkumar et al. 2012). Spatial information (Fig. 9.10) facilitates the correct and representative sampling of the spectra and allows observing the spatial evolution of ripening or senescence processes (Lleó et al. 2011).

As presented by Rajkumar et al. (2012), optimal wavelengths for predicting quality attributes related with ripeness can be inferred from the variation of VIS–NIR spectra (400–1000 nm) at different ripening stages. The spectral evolution can be interpreted according to physiological processes related with ripeness, such as chlorophyll degradation, observed around the chlorophyll absorption peak, at 680 nm, or moisture content at 800–970 nm (Fig. 9.9). The identification of these key wavebands for specific products is important because it facilitates the application of spectral imaging on fruit-sorting systems: It allows using MS imaging systems, significantly cheaper and quicker than HS imaging, for the evaluation of fruit ripeness. In this regard, Lleó et al. (2011) proposed and tested several spectral indexes to

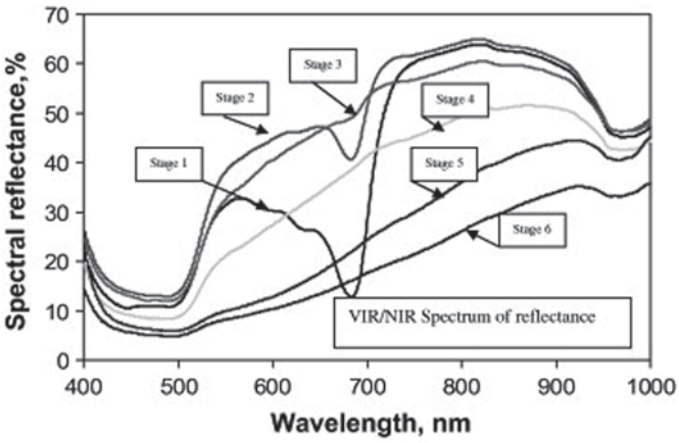

Fig. 9.9 HS reflectance of *VIR/NIR spectrum* at different maturity stages of banana fruits stored at 20 °C. (Rajkumar et al. 2012)

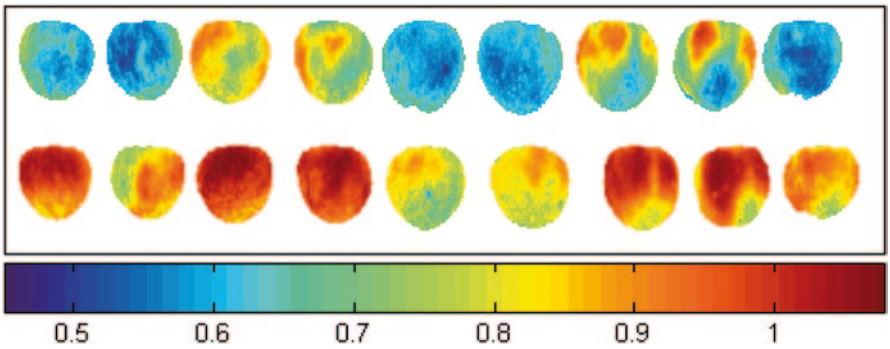

Fig. 9.10 Spectral index images (Ind2) for nine fruits before *(first line of the image)* and after *(second line)* commercial ripening process. *Blue* corresponds to the most unripe areas and *red* to the ripest. (Lleó et al. 2011)

evaluate peach ripeness through MS imaging. The proposed indexes were conceived both to detect the evolution of peach spectra along commercial ripening process and to avoid multiplicative and/or additive spectral effects (typically removed through spectral preprocessing when the complete spectra are available). Five spectral indexes based on the combination of wavelengths close to the chlorophyll absorption peak at 680 nm were considered. Between these indexes, Ind2, which corrects both multiplicative and additive spectral effects, was appointed as the best performing on description of ripening. This index was able to differentiate ripening regions and their evolution within the fruits (Fig. 9.10) and was unaffected by the spherical shape of the fruit.

Similar principles apply to the monitoring of fruits or vegetables senescence during shelf life. Recent applications of HS imaging on this field can be found on rocket (Løkke et al. 2013), spinach (Diezma et al. 2013), mushrooms (Taghizadeh et al. 2010) and apples (Cen et al. 2013).

An interesting application is presented by Lara et al. (2013). In this work, spinach evolution during storage was monitored through the packaging films. HS images (400–1000 nm) were taken at different stages of the storage period (21 days at 4 °C). The effect of the packaging films on the spectra was corrected through spectral preprocessing (radiometric correction). As in the case of ripening, spectral changes could be interpreted according to physiological processes related to leaf degradation: a shift on the red edge spectra, associated with ageing of the leaves, and an increase in global reflectance and slope of the spectra, associated with water loss.

9.3.4 Contaminants

Other extended application of HS imaging for the evaluation of fruit and vegetables is the detection of contaminants, such as *E. coli* (Siripatrawan et al. 2011) and faecal contamination (Kang et al. 2011; Teena et al. 2013). This subject has been recently

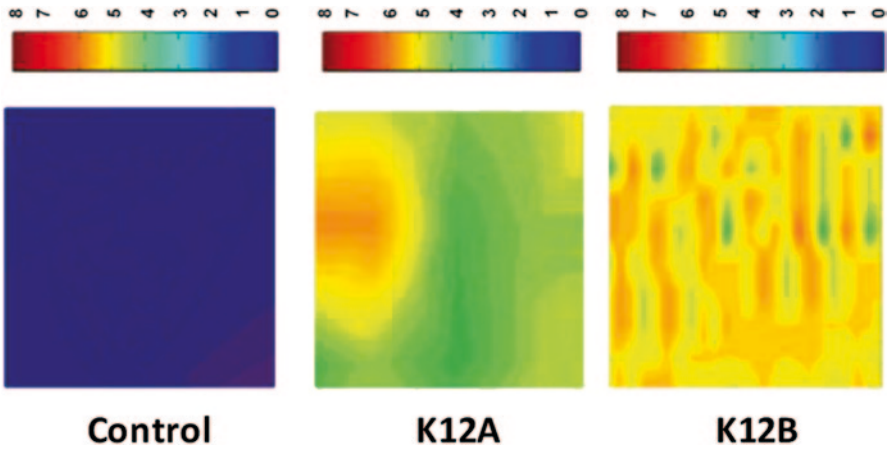

Fig. 9.11 Prediction map of *E. coli* contamination determined using artificial neural network (ANN) algorithm. The colour corresponds to the number of *E. coli*, expressed as Log (CFU/g). (Siripatrawan et al. 2011)

reviewed by Dale et al. (2013). Siripatrawan et al. (2011) present a clear example of the potential of HS imaging for assessing food safety on fresh products. In this work, HS imaging (400–1000 nm) is used to estimate *E. coli* contamination on packaged fresh spinach. HS images were first simplified through PCA, then artificial neural networks (ANN) was used to predict and map microbial contamination (Fig. 9.11). The coefficient of determination between measured and estimated microbial cell count was 0.97.

9.4 Optical Coherence Tomography

OCT is a nondestructive and noncontact imaging technique, in which the sample is commonly illuminated with light in the NIR. The result is the acquisition of high-resolution one-, two- and three-dimensional image data in the real time. The technique is based on the physical phenomenon of white light interferometry (WLI) (Huang et al. 1991). OCT performs high-resolution, cross-sectional tomographic imaging of the internal microstructure in materials and biological systems by measuring backscattered or backreflected light (Fujimoto et al. 2010). It enables an excellent axial (depth) resolution (Drexler et al. 1999). The image contrast in OCT is caused by inhomogeneities in the refractive index of the sample material (Verboven et al. 2013). Traditionally, OCT has been applied to animal and human tissues. Nevertheless, Loeb and Barton (2003) anticipated that botanical subjects, such as fruit and vegetables, are ideal candidates for OCT technique due to the presence of large fluid-filled vacuoles that provide greater contrast and inspection depth than animal and human tissues. Only in the recent years, OCT has been applied to the fruit and vegetables.

9.4.1 Internal Quality

Meglinski et al. (2010) used OCT to monitor defects and rots in onion. They imaged the skins and outer laminae (concentric tissue layers) of intact whole onion bulbs at the near-surface zone, up to 0.5 mm with approximately 1 μm spatial resolution. Ford et al. (2011) also investigated diseases in stored onions. They obtained images with a depth resolution of 7 μm, a lateral resolution of 10 μm and a depth about 0.5 mm. Cell-level structure of healthy stored onions was compared to that of onions affected by fungal neck rot *(Botrytis allii)* and bacterial fort rot (*Pseudomonas* spp.). They found evident differences between different sites in the onion bulb and also between healthy and diseased tissue. Continuing with this work, Landahl et al. (2012) obtained OCT images, corresponding to a lateral dimension of 4 mm and depth of 0.3 mm, of onion bulbs which were stored for 3.5 months at 4 °C and bulbs stored for 1 month at 20 °C. Half of the onions were treated with 100 μl sterile water and the other half were inoculated with conidial solution containing *B. allii*. Finally, the bulbs were cut and photographed. After that, a number of laminae from 5 to 9 were measured with OCT. Image processing was applied to automatically extract useful features. The cell areas and centroids were computed after enhancing, filtering and segmenting the original images. OCT images showed differences between healthy and diseased tissue, as neck rot affected tissue showed detachment of inner cell walls and the average cell size was smaller. Also, cells were found less round-shaped. OCT provided images to a depth of about 0.5 mm.

In apples, Rizzolo et al. (2013) utilised OCT to characterise the tissue of air-dried (noOSMO) and osmo-air-dried (OSMO) rings. They prepared apple rings from 'Golden Delicious' apple cultivar. Different mature stages were selected according to the absorption coefficient measured at 670 nm by time-resolved reflectance spectroscopy (TRS), stored in air for 5 months and subjected to air-drying with and without osmodehydration pretreatment. Images were obtained with 2 μm of axial resolution. OCT distinguished between OSMO and noOSMO air-dried rings, since noOSMO samples showed a dense structure and thus a limited penetration depth, while the OSMO samples showed loose surface structure with large inclusions of air (Fig. 9.12). Differences in mechanical characteristics between them seem to be a surface effect.

Also in apples, Verboven et al. (2013) visualised microstructure of peel by means of OCT in different cultivars ('Braeburn', 'Arlet', 'Royal Gala' and 'Ida Red'). OCT allowed the visualisation of the surface topology including cracks in the wax, surface roughness and lenticels. Depth scans with OCT revealed the cellular structure down to a few hundred of micrometres into the fruit.

On fruit, OCT has been used for nondestructively characterised rind breakdown disorder (RBD) in mandarins (Maguwaza et al. 2013). Histological changes associated with the development of a progressive RBD were evaluated by using fruits with different damage levels. These fruits were selected from a batch stored for 8 weeks at 8 ± 0.5 °C. The images were obtained of fruit rind to a depth of about 1.1 mm. It was found that the oil glands stayed intact in unaffected fruit and gradually collapsed in RBD-affected fruit. At advanced stages of the disorder, the collapsed oil glands became increasingly deformed and flattened.

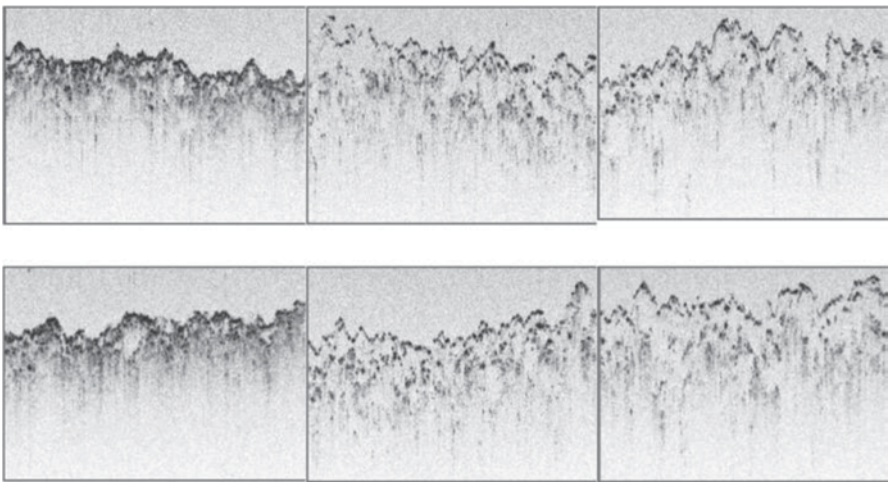

Fig. 9.12 Examples of OCT images of the surface of noOSMO, OSMO1 and OSMO2 dried apple rings from fruit for the most differing fruit in the batch (R1, LeM; R20, MoM). *OCT* optical coherence tomography. (Image size 5×0.88 mm^2)

Loeb and Barton (2003) applied OCT to imaging botanical subjects like sectioned kiwifruit, orange flesh, orange peel, lettuce leaves and intact cranberries. They concluded that this is a suitable technique for botanical imaging since features at the tissue and cellular level were identified, such as parenchyma cell vacuoles and endosperm in kiwifruit tissue, outer integument in kiwifruit seeds, juice vacuoles and membranes of juice sac in orange or oil glands and epidermis flavedo on orange peel among others. Authors also imaged cranberries at different ripeness stages, judged by flesh colour. They found repeatable differences in the OCT images of ripe and unripe berries.

9.5 X-Ray Imaging

X-ray imaging is based on the attenuation that an X-ray beam experiences when passing through a sample. The transmitted photons are usually registered by arrays of photodiodes or a charge-coupled device. In order to obtain a 2D image, the sample moves transversally to the beam (Fig. 9.13). Then, the image is compiled for further analysis.

In X-ray imaging systems, the representative parameters are the tube voltage and the tube current of the X-ray source. The tube voltage produces the acceleration of the electrons from the cathode to the anode, so that when they decelerate the X-rays are produced. An increase in the tube voltage involves an increase in the maximum energy of the beam and in the total amount of radiation, which allow the inspection of increasing depths. The tube current is the stream of electrons between the cathode and the anode, which determines the total amount of radiation, without affecting the

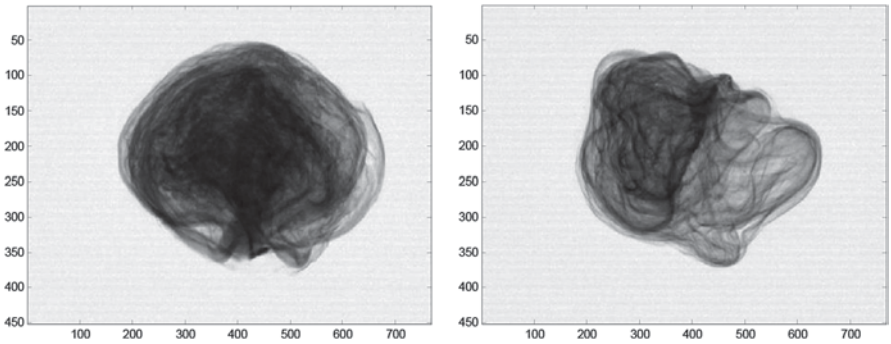

Fig. 9.13 X-ray images of lettuces acquired at a source voltage of 60 keV and a current of 7 mA while conveyed at 0.46 m/s. On the *left* a high-quality, compact and round-shaped sample, and on the *right* a low-quality, loose and no round-shaped sample. (Courtesy of Multiscan Technologies S.L. (www.multiscantechnologies.com))

maximum energy. The tube current is set so as to assure that enough photons reach the detectors.

Image contrast is a result of the presence of internal regions with different attenuation coefficients. Such differences are enhanced as the energy of the X-ray beam decreases and, therefore, contrast is improved. When using a low-energy beam (50–500 keV) for the inspection of products with low atomic number, the attenuation is governed by the photoelectric effect. This is the case of the horticultural produces, which mainly comprise hydrogen, carbon and oxygen. Consequently, the image contrast arises from differences in atomic number, density, and thickness. The higher the latter characteristics, the higher will be the attenuation.

Transmission X-ray imaging can be thought of as a projection of the sample onto a plane. Thus, internal structures may be masked when they are along the same linear trajectory of the photons. In many cases, the assessment of internal quality in fruits and vegetables requires more detailed image resolution. Therefore, studies have been developed by using the X-ray computed tomography (CT), which produces cross-sectional images of the sample. In CT, the source of X-rays rotates at steps of a certain angle around the sample, registering transmitted photons at each step. Reconstruction of the image is performed by applying algorithms such as the filtered back projection, so that small volumes of tissue are depicted as pixels in the image. Pixel intensity is measured in Hounsfield units, being the water attenuation the zero value. Positive values correspond to compounds with higher absorption when compared to water, whereas negative values correspond to lower absorption.

9.5.1 Internal Quality

X-ray CT images have been used to study the internal browning (IB) in apples. Herremans et al. (2013a, b) analysed the microstructural arrangement of cells and intercellular spaces of ‘Braeburn’ apples. Such characteristics have a major effect

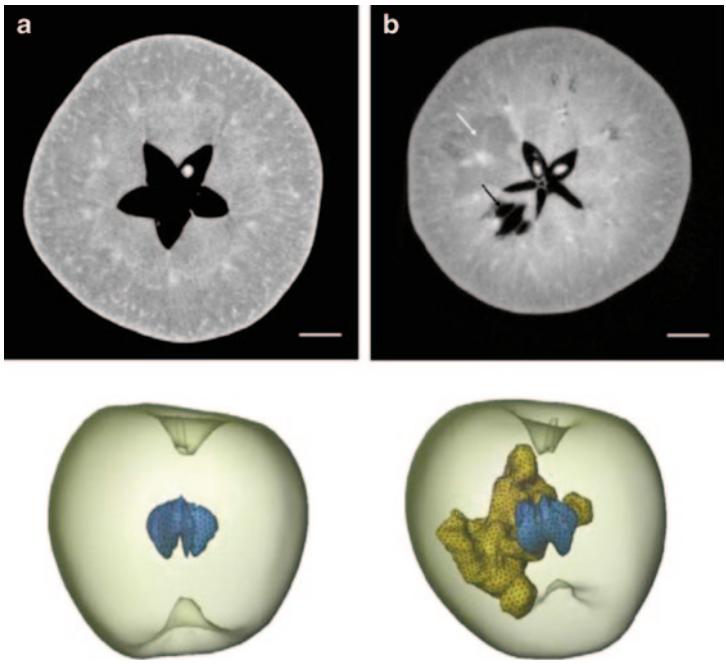

Fig. 9.14 X-ray CT images of virtual apple cross-section *(top)* of a healthy fruit (**a**) and a BBD-affected sample, manifested as dehydrated tissue *(white arrow)* with the formation of cavities (*black arrow,* **b**). The scalebars in the cross-sectional CT images measure 1 cm. 3D geometry of a healthy and affected apple *(bottom)*. The air in the core *(blue)* and tissue affected by BBD *(yellow)* are shown as meshed volumes. (Herremans et al. 2013b)

on the transport of the respiratory gasses oxygen and carbon dioxide, which may induce IB. X-ray micro-CT images of cylindrical samples of outer, middle and inner cortex tissues were obtained with 4.83 μm^3 voxels at 58 keV. Microstructure was characterised by extracting morphometric parameters such as porosity, anisotropy and connectivity from the images previously segmented by Otsu's algorithm. These parameters successfully classified the 97% of the tissue samples (Herremans et al. 2013a). Closely related to this study 'Braeburn' apples were monitored during the development of internal disorders under storage brown-inducing conditions (1% O_2, 5% CO_2) (Fig. 9.14). Samples of apple cortex tissue were imaged by micro-CT with 4.8 µm pixel size at 58 keV, whereas CT images were obtained of intact apples with 82.6 µm pixel size at 85 keV (Herremans et al. 2013b). The tissue microstructure allowed solving a microscale gas exchange model by using the finite volume method on a voxel-based mesh. The apparent gas diffusion coefficients were calculated and subsequently used to solve the diffusion–respiration process in a macroscale structure containing sound, brown and cavity-filled tissues to simulate the oxygen profiles. A combined multiscale model was constructed, which revealed to be useful for predicting storability of fruit. This study verified that under sub-optimal gas conditions oxygen concentrations drop; that the disorder expands as a

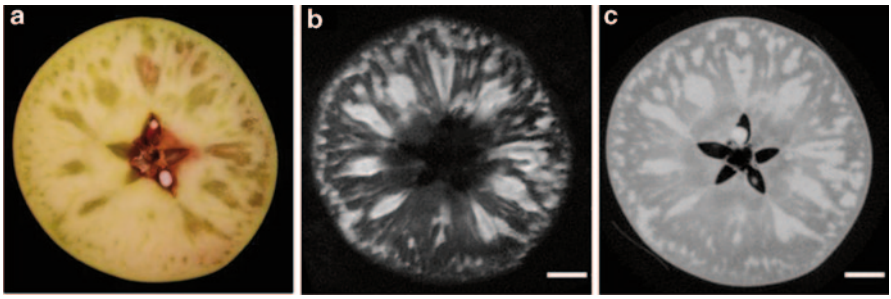

Fig. 9.15 Visual evaluation of watercore disorder in Rebellón apple after cutting the fruit at the equator (**a**) and the corresponding MRI (**b**) and CT images (**c**). The MRI image was exactly matched to the CT image because we obtained 3D data. The photograph is from approximately the same, however obviously not identical, position. Scale bars measure 10 mm. (Herremans et al. 2014)

result of the decrease in oxygen diffusivity; and that a dense tissue structure induces low-oxygen diffusivity and, hence, browning disorder.

X-ray CT images have been used to define watercore in apples. Such disorder is characterised by water-soaked and glassy areas appearing in the flesh, where sorbitol-rich solutions are accumulated in the intercellular spaces. The associated changes in the microstructure and the increasing density are revealed in the X-rays images (Fig. 9.15). The porosity decreases significantly as the pores in the affected tissue are almost absent, thus likely filled with water (Herremans et al. 2014). X-ray CT images operating at a source voltage of 80 keV and a current of 100 μA were obtained from entire apples of different cultivars along with X-ray micro-CT images from cylindrical tissue samples. Authors proposed different image-processing techniques to extract discriminant parameters between sound and affected samples. Firstly, images were segmented by applying Otsu's algorithm and then grey-level histograms were generated. An analysis of variance (ANOVA) showed that the mean and the variance of the grey levels in the affected apples were significantly different ($p < 0.05$) from the healthy apples. Secondly, two grey-level thresholds were computed to divide the pixels into the underlying populations. An adaptive threshold was computed by the maximum entropy method, which obtained a percentage of correctly classified samples of 68%. A global threshold was computed from the signal of the population of affected pixels, which achieved an 89% of correct classification.

For dried fruits, X-ray CT images have been used to evaluate the microstructure of air-dried and osmo-air-dried apple rings, and to study the relationships between the microstructure features and the crispness of dried apple rings in relation to fruit maturity (Rizzolo et al. 2013). Measurements were performed at 55 keV source voltage and 181 μA current with a pixel resolution of 2.44 μm. The skeleton of dried apple tissue could be accurately detected in X-ray CT images because of the high contrast with the pore space. A threshold was applied to segment skeleton and then morphometric parameters were computed. The analysis revealed that the osmotic

pretreatment increased porosity and tissue-specific surface area and decreased pore anisotropy, tissue thickness, tissue anisotropy and tissue intersection surface. Regarding maturity, it was found that tissue-specific surface area, tissue thickness and tissue fractal dimension depended on maturity class. For air-dried samples, only porosity was influenced by maturity. An analysis of principal components highlighted relationships between some morphometric parameters and acoustic characteristics as well as mechanical characteristics.

Leónard et al. (2008) used X-ray microtomography to investigate tissue microstructure of dried banana when conventional drying techniques such as low-pressure superheated steam drying and vacuum drying were assisted with far-infrared radiation (FIR). The study was focused on porosity, which is a major quality parameter in dried products. 2D X-ray micro-CT images were obtained with a pixel size of 15 μm at 60 kV and 167 μA. 3D images were reconstructed from 2D set. Banana skeleton appeared at high grey levels, whereas pore space appeared at low grey values. An automatic threshold based on maximisation of the interclass entropy was calculated in order to segment the skeleton. Remaining small black holes were removed by applying a closing filter. Then, the porosity was measured as the fraction of voxels of the image that belonged to the pores. FIR was found to modify the structure of the dried bananas by increasing their final porosity.

Nielsen et al. (2014) proposed a new approach based on X-ray dark-field radiography for the detection of microstructural changes due to freeze injuries. The advantage of this technique relies on its sensitiveness to structural differences on the micrometre scale. Both dark field and conventional transmission X-ray images were obtained of blueberries, blackberries and a piece of mandarin with different levels of injury (Fig. 9.16). The experiments were carried out using an X-ray grating interferometer, consisting of an X-ray phase grating, an analyser absorption grating, and a third grating to optimise spatial coherence. The source voltage and current were set to 40 keV and 150 mA, respectively, and the effective pixel size at the sample was 155 × 155 μm. The contrast between the frozen/defrosted tissue and the raw tissue was evaluated by computing a contrast-to-noise ratio (CNR) that took into account the mean and the variance of the signal intensity. The higher the CNR, the higher the contrast will be in between tissues. Variations in microstructure of frozen/defrosted tissue were clearly revealed by the highest CNR value computed in dark-field images. Authors suggested the ultra-small-angle scattering originated by the injured tissue as origin of the enhanced contrast.

Jiang et al. (2008) proposed the use of X-ray images to identify insect infestation in fruit (cavity or pest). Experiments were conducted in a specifically designed X-ray system at a scanning rate of 1.2 m/min in fruits such as citrus, peach and guava. The tube voltage was adjusted in the range of 40–90 keV and the tube current in the range of 110–250 μA to achieve the optimum contrast of the X-ray image. Authors developed an image segmentation procedure to overcome the difficulties due to shape or uneven thickness of fruit that appear when selecting a suitable global grey level threshold. The adaptive image segmentation algorithm was based on the analysis of the local pixels intensities and an iterative unsupervised threshold selection, with a final morphological filtering to remove suspicious small points.

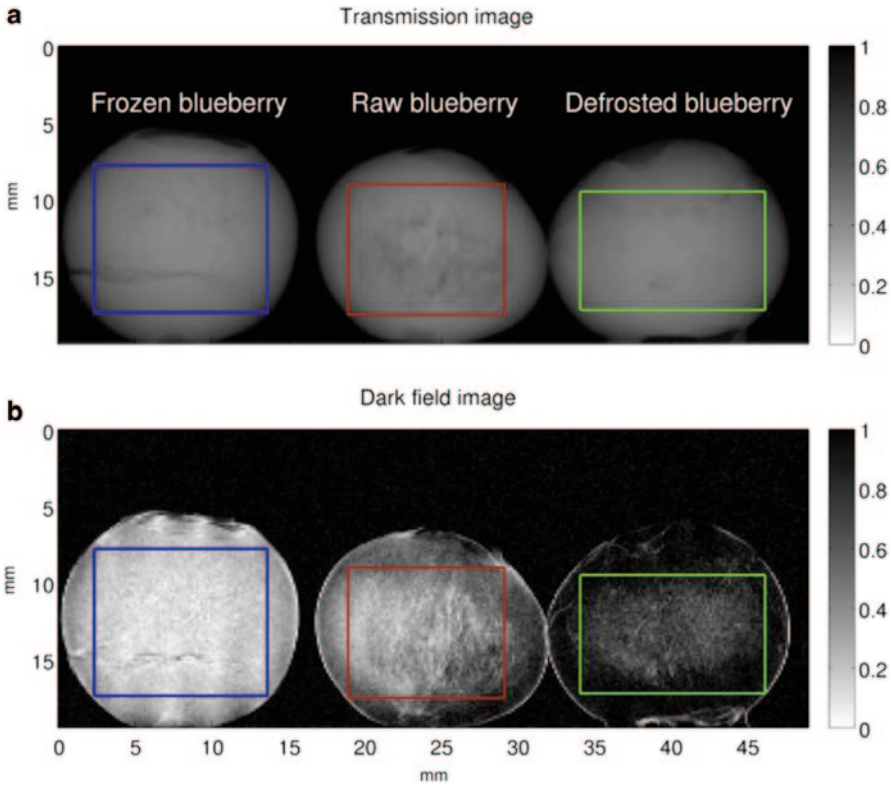

Fig. 9.16 X-ray images of blueberries in different states; frozen *(left),* raw *(middle)* and defrosted *(right)*. The regions used for calculating the CNR values are indicated. **a** Transmission radiogram. **b** Dark-field radiogram. (From Nielsen et al. (2014))

Segmentation parameters needed to be determined for each type of fruit. The sites of infestation were accurately identified. Further work involved the development of a prototype scanner system working at a scanning rate of 30 m/min with a detection rate up to 94% within the 4 days after pest implanted (Chuang et al. 2011).

Donis-González et al. (2014) characterised internal decay of chestnuts, internal defects in pickling cucumbers, translucency disorder in pineapples, and both pit presence and plum curculio infestation in tart cherries. 2D CT-X-ray images were acquired with a resolution of 1.289 pixel mm-1 using a scanner operating at 120 keV and 170 mA for chestnuts, cucumbers and cherries; and at 120 keV and 240 mA for pineapples. Different circular regions of interest were defined within the image, each one containing a characteristic tissue under study. Hounsfield units of each region were averaged. Mean values entered an ANOVA, and a Tukey post hoc test identified significant differences at 95% confidence level. For chestnuts, significant differences were found between all the tissues: healthy kernel, pellicle, decayed kernel and void space. For tart cherries, curculio-infested pulp and pit fragments were significantly different from healthy pulp, pit embryo and void space.

For pineapple, translucent pulp was significantly different from healthy and core tissues; void space was found different as well. For pickling cucumber, healthy pulp was significantly different from defective tissue and natural void spaces. Such results reinforce the potential of this technique for nondestructive inline sorting whenever procedures become more time- and cost-effective.

9.6 Magnetic Resonance Imaging

MRI is a technique based on the nuclear magnetic resonance phenomenon, which involves that some nuclei, such as ^{1}H, ^{13}C or ^{31}P, have a magnetic moment that precess at the so-called Larmor frequency (ν_0) when placed within the action of a magnetic field. The ν_0 value is both nuclei and magnetic field strength dependent. Under such conditions, an excitation pulse of radiofrequency makes all the magnetic moments in the sample precess synchronised. An electromotive force is induced in a receiver coil so that the signal is registered as an alternating voltage. At a first stage, the intensity of the signal is proportional to the abundance of the nuclei. After excitation, the magnetic moments recover their equilibrium state while they lose phase coherence, and hence, the signal decays along time. The former process is characterised by the spin-lattice or longitudinal relaxation time (T_1), and the latter by the spin–spin or transversal relaxation time (T_2). The T_1 is affected by sample characteristics such as molecular motion, molecular size, molecular complexity and viscosity, whereas the T_2 is affected by molecular motion, chemical exchange, cell morphology and size, cell compartmentation, membrane permeability, tissue microstructure and diffusion (Hernández-Sánchez et al. 2009). In order to obtain an MR image, magnetic field gradients are generated along perpendicular directions so that the precession frequency of the nuclei is spatially codified in two or three dimensions. Signal decodification is performed by applying the fast Fourier transform algorithm. Series of excitation pulses are applied, repetition and echo time being the representative parameters of image sequences. By managing such parameters, the image contrast can be weighted in nuclei density, T_1, T_2 or diffusion. Therefore, valuable information on the sample characteristic affecting such NMR parameters is revealed. For fruit and vegetable studies, ^{1}H MRI is applied since hydrogen is the most abundant nuclei.

9.6.1 Internal Quality

The characterisation of intercellular spaces in relation to microstructural properties by applying MRI is useful to understand several phenomena that affect postharvest quality or shelf life of apple (Musse et al. 2010), since the gas-filled intercellular spaces are considered as the pathways for gas transport.

Defraeye et al. (2013) applied MRI at high magnetic field strength, 11.7 T, for tissue characterisation of ‘Braeburn’ apple cultivar. Authors studied the effect of fertilisation

treatment, storage time and IB-inducing storage conditions on the microstructure of the inner and outer cortex tissue. Proton density (PD) and T_2 values were obtained from a multi-spin echo sequence (TR = 3000 ms and TE from 7 to 112 ms); self-diffusion coefficient (DC) was computed from a diffusion echo sequence (TR = 2300 ms and TE = 13.5 ms). Circular regions of interest were defined in the images, from which average and standard deviation of PD, T_2 and DC were computed. An ANOVA revealed the parameters with significant differences. Inner tissue showed higher PD, T_2 value and DC when compared to the outer tissue. No effect was detected for different fertilisation treatments. For storage, PD increased along the time, which was tentatively attributed to the tissue degradation due to IB that may alter water bounding. As for IB, the affected tissue had higher PD, T_2 and DC values than the healthy tissue, being especially useful for disorder identification of the DC.

The early detection of internal quality problems of fruits may allow accomplishing a successful postharvest treatment. In this sense, Melado-Herreros et al. (2013) assessed watercore development in apples with MRI and related watercore incidence with the location of the fruit in the canopy. Rapid acquisition with relaxation enhancement (RARE) sequence was used to acquire T_2-weighed images (TR = 5000 ms and TE = 60 ms) at 4.7 T. Damaged areas were detected within the images by using an interactive segmentation method. Then, the area of affected tissue (μm^2), the total area of apple tissue (μm^2) and the Euler number, which is an indicator of the connectivity of a 3D structure and topology, were computed (Fig. 9.17). MR images revealed that apples from the top of the tree showed higher proportion of radial development of the disorder (84 %) when compared to the apples from the bottom (65 %), and a more extended affected area (about 5 % higher). The Euler number showed that apples with block development of watercore were grouped in Euler numbers between −400 and 400 with a limited evolution; and for apples with radial development, the Euler number was highly negative, up to −1439. Positive Euler numbers correspond to unconnected objects which, in this case, corresponded to a slightly affected fruit. Large negative Euler numbers correspond to complex segmented shapes with highly connected areas.

Herremans et al. (2014) compared the capability of MRI and X-ray to identify watercore disorder in different apple cultivars (Fig. 9.15). An MRI spin echo sequence (TR = 5000 ms and TE_{eff} = 62.7 ms) was used to acquire T_2-weighted images at 4.7 T. Image processing is summarised in the corresponding X-ray section. Watercore appeared as high-intensity regions showing better contrast when compared to X-ray images. However, performance was slightly lower as the accuracies of the disorder identification were 79 % for the maximum entropy method and 73.5 % for the global threshold.

Hernández-Sánchez et al. (2007) studied IB in pears by means of NMR and MRI in order to develop a nondestructive procedure for on-line disorder identification. The effect of the tissue microstructure on the transverse relaxation rate ($1/T_2$) was assessed by NMR relaxometry. The water diffusion through magnified local gradients as a result of the membrane alteration, tissue disintegration and water evaporation was the main cause of the increasing rates in affected tissues, as confirmed by the higher diffusion coefficient computed by the T_2-diffusion correlation

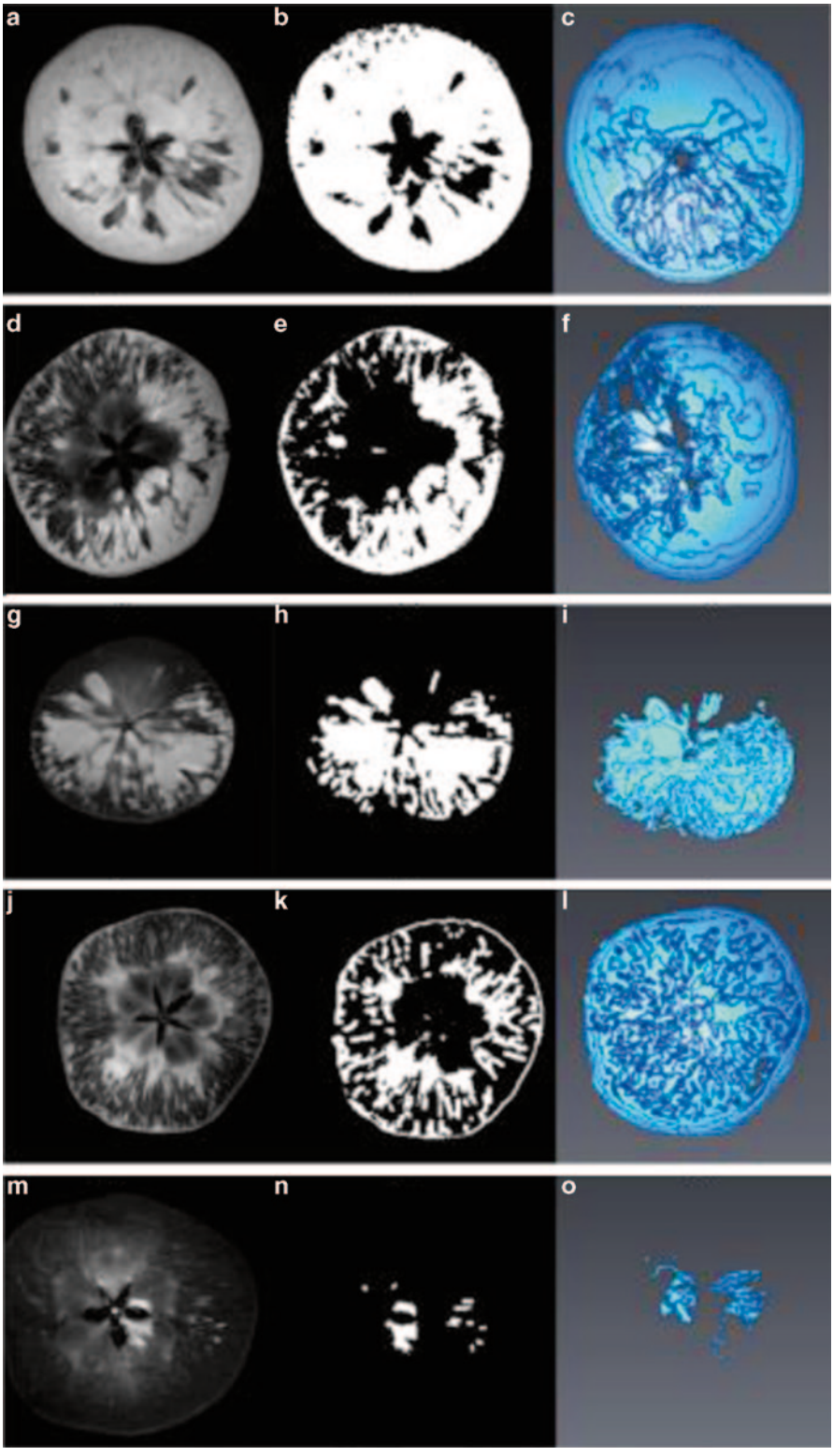
a
b
c
d
e
f
g
h
i
j
k
l
m
n
o

spectroscopy. At a macroscopic level, such microscopic information was used to optimise coronal fast low angle shot MR images, effective transverse relaxation weighted (TR = 11 ms and TE = 3.7 ms) and proton density (PD) weighted (TR = 7.6 ms and TE = 2.5 ms), with total acquisition times of 484 and 703 ms respectively. Pears were imaged at 54 mm/s conveyor belt speed. Histogram features were automatically extracted after motion artefact correction (Hernández-Sánchez et al. 2005). Features included coefficient of variation for signal intensity, skewness, kurtosis and percentage of accumulated pixels for selected histogram categories. An ANOVA was used to select those parameters that enabled disordered fruit identification, which entered a discriminant analysis. Discriminant functions correctly classified up to 94 and 96% of the fruit and showed that a minimum value of 12% of tissue affected by breakdown was always clearly identified.

Textural properties of potatoes are important for consumers, and, thus, there is a need for developing sensors enabling grading and sorting of potatoes according to their convenience for marketing, long-term storage or processing (Thybo et al. 2004a). MR images have illustrated both the spatial distribution and the abundance of water within potato tubers (Thybo et al. 2003). Thybo et al. (2004a) studied the quality attributes of cooked potatoes such as hardness, cohesiveness, adhesiveness, mealiness, graininess and moistness by MRI. MR T_1-weighted spin echo images (TR = 600 ms and TE = 10 ms) were obtained from a layer in the middle of the tuber samples with a 7 T system. Several image texture features were computed. Those derived from the first-order histogram were related to average level of intensity, variation of intensity, symmetry and flatness of histogram; those from image gradient map were related to the borders between light and dark pixels; those from co-occurrence matrix (COM) estimated joint probability of two pixels having particular intensities; those from run-length matrix (RLM) were related to the number of times that the picture contains a run of certain length; and finally, the parameters of autoregressive model described relations of grey-level intensities between neighbouring pixels. The radial directive structure in a potato did not place any problems on the features robustness. A principal component analysis (PCA) on image texture features grouped the potato samples according to variety, storage and dry matter variation. Such grouping was similar to that obtained from the PCA on the sensory data provided by a panel test. Partial least square regression (PLSR) showed that perception of hardness and adhesiveness can be predicted from the full set of MR image features, achieving correlation coefficients of 0.86 and 0.72, respectively. For moistness, a 0.69 correlation coefficient was found. Furthermore, individual image features were used to predict texture attributes. The COM features were the most significant for the prediction of hardness, adhesiveness and moistness. Besides, PLSR revealed that different MR-image structures, which were identify by RLM features, were relevant for the individual sensory texture attributes. In contrast, MR images were not able to predict specific gravity.

Fig. 9.17 MR images, (**a**), (**d**), (**g**), (**j**) and (**m**), segmented images (**b**), (**e**), (**h**), (**k**) and (**n**) and 3D reconstruction (20 slices) of the segmented area of the tomography (**c**), (**f**), (**i**), (**l**) and (**o**) of four images with different Euler number. Euler number (**a–c**) = 137 (watercore damage = 67.51%); Euler number (**d–f**) = −583 (watercore damage = 49.50%); Euler number (**g–i**) = −137 (watercore damage = 45.43%); Euler number (**j–l**) = −1275 (watercore damage = 35%); Euler number (**m–o**) = 30 (watercore damage = 0.43%). (From Melado-Herreros et al. (2013))

Thybo et al. (2004b) successfully assessed the applicability of MRI to the detection of internal bruise and spraing disease in potatoes. Authors underlined the need of a prompt identification of affected samples prior to storage or industrial processing. In their study, MR images were obtained on a 7 T system with different weightings: PD-weighted images (TR = 200 ms, TE = 3.1 for bruised potato and TE = 2.9 for spraing-affected potatoes); T_1-weighted images (TR = 50 ms and TE = 3.1 ms for bruised potato and TE = 2.9 for spraing-affected potatoes); T_2-weighted images (TR = 3 s and TE = 40 ms); and T_2 map (TR = 3.4 s and TE set to 16, 32, 48, 64 and 80 ms). Increasing knowledge on chemical and anatomical causes was achieved when interpreting the signal intensities within MR images. The low signal in the PD-weighted images indicated that the inner tissue of the bruises was very dry. The high signal in T_2-weighted images combined with the high relaxation time in T_2 maps revealed the migration of the water to the edges of the bruises, which are surrounded by a relatively dry shell. The regions with spraing development showed similar characteristics than bruise spots as containing relatively less water than their surroundings. T_1-weighted images revealed a large darker area surrounding the spraing spots, which authors attributed to the presence of the virus without visible symptoms (Fig. 9.18).

The sensory texture properties in tomato are of great importance for determining the end-use quality, as stated by Musse et al. (2009a). These authors investigated structural aspects affecting the texture such as cell morphology, arrangement and air bubble content in tomato fruit, by means of MRI. Measurements were performed on a 0.2 T system. Spin echo (SE) images (TR = 200 ms and TE = 15 ms) were obtained to analyse macroscopic morphological aspects. The air distribution was studied with two spoiled GE images (flip angle = 40°, TR = 1 s, TE_1 = 9 ms and TE_2 = 40 ms). T_1 and T_2 maps as well as macrovision images provided explanation of the observed results when different processes worked in opposite directions. Regions of interest were drawn manually from the T_2 maps that corresponded to a homogeneous region in each type of tissue and then translated to the other images to compute average intensity. An ANOVA identified those tissues significantly different. SE images provided contrast adequate to identify outer and radial pericarp, placenta, locular tissue and seeds. Variation in signal intensity between the placenta and the locular tissue were related to PD differences. GE images revealed that the placenta and core tissues had higher air bubble content than other tissues, which involved higher susceptibility effects driving signal loss due to the diffusion of the water molecules through local magnetic field gradients. MRI also indicated that cells of the outer pericarp were significantly larger than cells of the core and placenta, which accounted for the lower relaxation times when compared to other tissues.

The capabilities of the MRI showed in the previous work were applied to monitor the postharvest ripening of tomato fruit (Fig. 9.19). Musse et al. (2009b) obtained quantitative MR images at 0.2 T during 3 weeks. SE and GE provided similar identification of main structural tissues as well as air spaces. The contrast in SE images was found to change considerably throughout ripening mainly as a result of the decreasing relaxation times and of the development of the air bubbles in the outer pericarp. SE images revealed air spaces close to seeds and permitted the

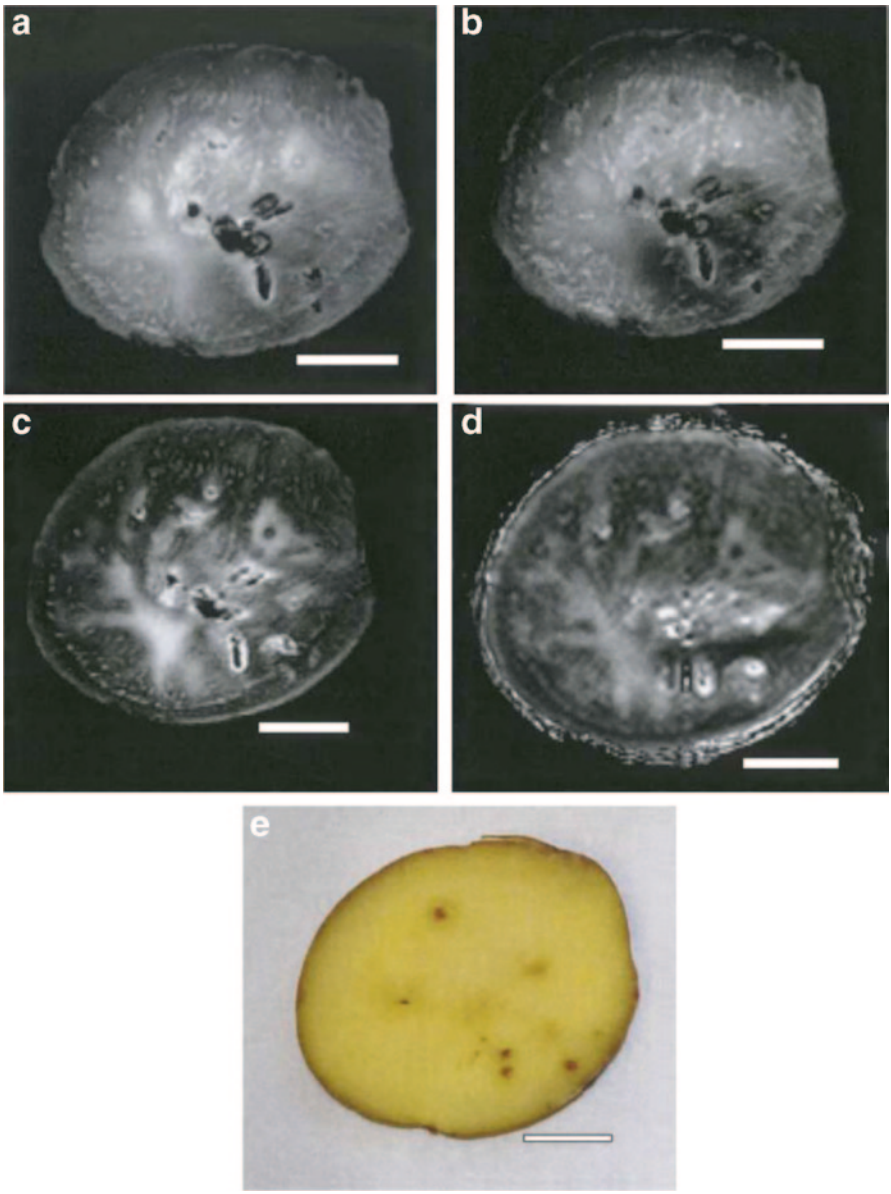

Fig. 9.18 **a** Proton-, **b** T1- and **c** T2-weighted images, **d** a T2 map and **e** digital photograph of a potato with spraing (Bar = 1 cm). (From Thybo et al. (2004b))

estimation of their shrinkage during the ripening period. The development of the bubbles in the outer pericarp during ripening was estimated from the GE images and supported by macrovision imaging.

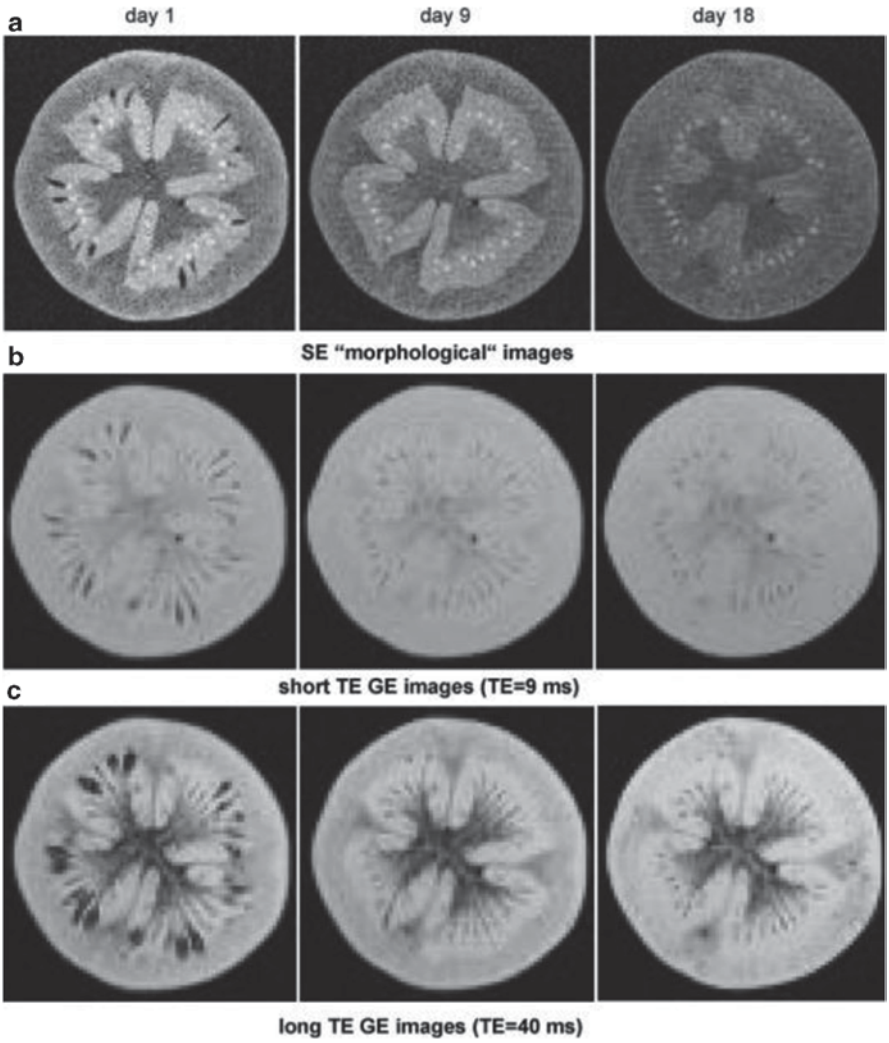

Fig. 9.19 Typical "morphological" SE image (**a**) along with short TE (**b**) and long TE (**c**) GE images of a tomato fruit at three different ripening stages. From Musse et al. (2009b)

Milczarek et al. (2009) focused on the development of an in-line method based on MRI to detect damaged pericarp in processing tomatoes. These authors proposed a new approach to determine the optimal MR pulse sequences for damage assessment, the so-called multivariate image analysis (MIA) method of partial least squares (PLS). MIA relies on the combination of the information extracted from a variety of weighted MR images that provides the best characterisation of the problem under study. In this work, MIA was used to determine which MR images to use among a set of 13 congruent MR images, and in what manner to use them.

Experiments were conducted at 1 T in an industrial-grade MR imaging system. The images were created by varying key parameters in the following sequences: fast spin echo (FSE), gradient recalled echo (GRE), fast low-angle shot (FLASH), and Turbo FLASH. For each tomato, a partial-annular ROI was segmented containing only the pericarp tissue. Membrane conductivity was selected as indicator of membrane integrity affected by a mechanical damage. The pixels in the ROIs were assigned a value between 0 (no damage) and 1 (extensive damage), corresponding to the conductivity score for that sample. A PLS model with eight latent variables was selected for conductivity score prediction. The model included only the sequences with the strongest influence, that is, FSE sequence with receiver gain of 10 and Turbo FLASH sequences with inversion times of 400, 800, 1000 and 1200 ms showed high performance with root mean square error of calibration and validation of 0.16 and 0.17, respectively. Lower resolution was proposed as a strategy to accomplish time shortening for in-line implementation under a production environment. The conductivity scores predicted by the model are arranged in an image providing a damage prediction image. The analysis of the histogram of such image would be useful to predict the level of damage and thus to direct the fruit on to steam peeling or off the line for other uses. Moreover, the PLS model could be used to optimise the contrast between sound and damaged tissue by selecting the best MR image parameters.

MRI has also been applied to assess the chemical and physical changes that appear in tomatoes in relation to the harvesting season (Ciampa et al. 2010). MRI experiments were performed on a 7 T system with the following sequences: GE (TE = 3.927 ms and TR = 60.0 ms); T_2 weighted multi-slice-multi-echo (MSME; TE = 30.0 ms and TR = 6000.0 ms); T_1 weighted MSME (TE = 30 ms and TR set from 6000 to 15.464 ms). Relaxation times T_2 and T_1 were fitted by mono-exponential decay curve. For each image, several morphological zones were identified as showing different signal intensities. Then, the thickness of pericarp, endocarp, T_2 and T_1 were analysed by an ANOVA, which found significant differences between periods of harvesting. For the external spherical crown of pericarp, both its thickness and the T_2 gradually decreased from winter to summer. As for the inner spherical crown of pericarp, the thickness also decreased, whereas T_2 increased towards summer. As for the endocarp, T_2 values showed more significant differences with an increase in the summer season. In addition, a decreasing gradient of water molecules content was observed from the inner to the outer portion of tomato fruit harvested during summer. The increased water to solid ratio accounted for the increase of T_2 values. The T_1 relaxation time presented variations higher than those of T_2, which were associated with metabolic processes, and were reflected in the MR images contrast. T_1 was higher in summer for both endocarp and pericarp. All samples harvested during winter and spring showed a darker spherical white crown covering the placenta cavities. This tissue was tentatively related to the accumulation of metabolic compounds resulting from stressing conditions such as exposition to low temperatures, which would decrease T_1 values. According to these results, the identification of internal variations derived from harvesting season is feasible by means of MRI.

Khoshroo et al. (2009) highlighted the interest of the pomegranate trade on the basis of its antimicrobial, antiviral, anticancer, potent antioxidant and antimutagenic properties which are associated to a proper ripening process, whose evaluation requires the use of a technique capable of nondestructive internal inspection. MRI was used to classify pomegranate, according to maturity and internal defects, into semi-ripe, ripe, overripe and internal defective groups. The experiments were performed on a 1.5 T system with 2D T_2-weighted MR spin echo sequence (TR = 3910 ms and TE = 60 ms). Texture analysis of regions of interest in MR images was applied to extract discriminant image features. From the grey level COM, the following features were calculated for four main directions (0°, 45°, 90° and 135°): angular second moment, contrast, sum of squares, correlation, inverse difference momentum, sum average, sum variance, sum entropy, entropy and difference variance. From the pixel RLM, the following features were extracted from four principal directions (0°, 45°, 90° and 135°): short-run emphasis, long-run emphasis, grey-level nonuniformity, run-length nonuniformity, and fraction (run percent). Such features entered a discriminant analysis. For COM features, the classification accuracy for semi-ripe, ripe, overripe and internal defects class was 100, 93.13, 94.89 and 95 %, respectively. For RLM features, the corresponding accuracy was 95, 94.66, 83.95 and 87.5 %, respectively. When both type of features were combined, the classification accuracy increased. The model based on the 11 most significant features achieved an accuracy of 100, 98.47, 100 and 95 %, respectively.

In a subsequent study, Khoshroo et al. (2011) proved the usefulness of texture features extracted from T_1-weighthed MR images to predict a maturity parameter such as the total soluble solid (TSS) content. The experiments were performed at 1.5 T with a 2D spin echo sequence (TR = 800 ms and TE = 18 ms). The texture features derived from COM and RLM were used as input in a multilayer perceptron neural network. The best architecture of the network contained 14 neurons in the hidden layer that satisfied the condition of preventing overtraining. The correlation coefficient between measured TSS and predicted TSS for the training data and testing data were 0.93 and 0.90, respectively.

Zhang and McCarthy (2012) assessed the applicability of MRI to the characterisation and detection of black heart in pomegranate. Experiments were conducted at 1 T. T_2-weighted fast spin echo images were acquired for healthy and affected pomegranates (TE_{eff} = 500 ms, TR = 8000 ms). Transverse relaxation time was measured using a Carr–Purcell–Meiboom–Gill sequence (TE = 1 ms and 8000 echoes). Image analysis consisted in the definition of a square region of interest (ROI) and the subsequent extraction of statistical features of the signal intensity, including mean, median, mode, standard deviation, skewness, kurtosis and coefficient of variation. Thereafter, a classification model was developed by applying a partial least square-discriminant analysis to the signal features.

The analysis of the signal in T_2-weighted images and of the T_2 relaxation distribution in arils provided valuable information for disorder identification. In the T_2-weighted MR images, the arils with black heart showed lower signal than the healthy ones, which was an indicator of the water loss (Fig. 9.20). Such image

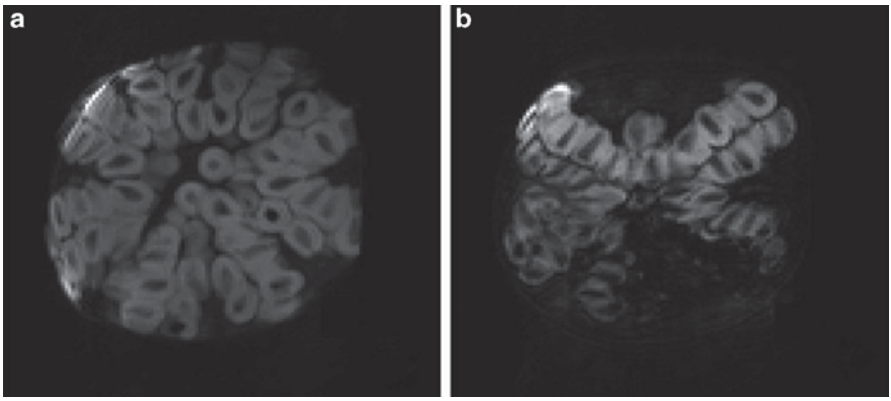

Fig. 9.20 Example MR images of **a** a healthy pomegranate and **b** a pomegranate with black heart. From Zhang and McCarthy (2012)

contrast was related to the change in cell integrity after infection and the subsequent decreasing of T_2, which was confirmed by NMR relaxometry measurements. For severely infected tissues, the voids were registered as regions with extremely low signal. T_2 spectra revealed the presence of several subcelullar structures characterised by different T_2 relaxation times. The assignment of the peaks to such structures was developed on the basis of the expected water mobility and water binding, which was reinforced by a paramagnetic ion tracer experiment. For healthy tissue, three peaks were found corresponding to cell wall, cytoplasm and vacuole, with increasing T_2 times, respectively. As for black heart tissue, these peaks were shifted to shorter T_2 values. In addition, cytoplasm and vacuole peaks tended to merge highlighting the effect of the damage on the membrane permeability. Moreover, a fourth component appeared which was assigned to extracellular water. The variation introduced in the image contrast as a result of the effect of the black heart in the tissue integrity provided high-discriminant image histogram features. The PLS-DA model achieved 92 % accuracy in detecting the presence of the damage. Such performance together with the use of a low magnetic field strength revealed the great potential of the methodology.

Zhang and McCarthy (2013) investigated the capability of MRI to predict common indicators of fruit maturity and palatability in pomegranates, such as soluble solids content, total titratable acidity, pH and Brix/acid ratio. A 1 T MRI system was used to obtain six images with varying contribution to total signal intensity from PD, T_1 and T_2 relaxation rates, and diffusion rate. MR images showed enough contrast to distinguish the main structures, i.e. arils, seeds and rind. Such structures appeared with varying signal intensity depending on the image weightings, which was indicative of a proper contribution of the intrinsic NMR parameters to the image contrast. For each image, an ROI was selected that contained the internal structures of the sample and excluded the periphery. Then, statistical features of the signal intensity of the ROI were calculated, including mean, median, mode, variance, standard deviation, skewness, kurtosis, range and coefficient of variation.

PLS regression was applied to the 54 features of the 6 images in order to generate corresponding prediction models for the four chemical properties. The best performance was achieved for predicting titratable acidity, pH and soluble solids/acidity levels, with R^2 of 0.54, 0.6 and 0.63, respectively. In addition, the residual prediction deviation indicated that the models were satisfactory for sorting purpose, which requires rough assessment of fruit quality instead of accurate quantification, as stated by the authors. T_2-weighted fast spin echo, diffusion weighted image and spin echo image with short TE and moderate TR were consistent in their important contribution to each model.

Freeze injury in citrus is characterised by the occurrence of both dehydration and hollows, which are well-known sources of image contrast when obtaining MR images. Hernández-Sánchez et al. (2004) studied the applicability of the MRI technique to identify freeze-injured oranges under on-line conditions. FLASH images (TR = 12.2 ms, TE = 3.8 ms and pulse angle = 10°) were obtained at 4.7 T while conveying the fruits at 0, 54 and 90 mm/s belt speeds. The affected tissue appeared as a region of hypointense signal as a result of the reduction in PD due to dehydration, and of the decrease in T_2^* caused by the local field gradients at the interfaces between juicy and dehydrated structures. The lower mobility of the water in the central axis accounted for its registered hypointense signal. In order to perform an automatic image segmentation, authors developed an iterative process to obtain two adaptive signal thresholds, where the number of pixels comprising each segmented region was computed at each step until convergence was reached. The first threshold separated the fruit from the background, and the second one segmented the healthy regions. Thresholds were addressed at each belt speed from undamaged fruits. The ratio between the signal hypointense region and the total fruit area in the sound samples was established as limit for discrimination. The threshold value increased from 10 % under static conditions to 20 and to 30 % at 54 and 90 mm/s belt speed, respectively, due to image blurring. Loss of image quality was driven by the axial location of the field of view together with the sample motion.

The detection of seeds in citrus is a major challenge for the industry. MRI has been proposed since seeds possess a solid-like structure that confers noticeable differences from the juicy pulp regarding different NMR weighting parameters. Such differences involve a straightforward contrast management and subsequent image processing. Hernández-Sánchez et al. (2005) investigated the detection of seeds under motion conditions by evaluating two different strategies. On the one hand, the acquisition of axial images requires ultrafast image sequences to avoid uncorrectable signal superimposing; on the other hand, the acquisition of coronal images requires the development of an algorithm to correct the motion artefacts caused by phase shift. In both strategies, acquisition conditions were the same with the above freeze study, only varying the field of view orientation. For the former, the results were similar, as the region containing the seeds and central axis appeared darker than the pulp. Likewise, the superimposition of signal arising from adjacent slices increased blurring artefacts. Despite the computation of a threshold and the extraction of morphological features from the hypointense region of interest, the discrimination of oranges with one single seed was not feasible. Therefore,

according to the alternative strategy an algorithm based on Fourier shift theorem was developed. Then, the correction of the motion artefacts was fully successful (Fig. 9.21).

In order to validate such results, a subsequent study was performed in mandarins (Hernández-Sánchez et al. 2006). The TR was shortened to 11 ms so that the total acquisition time was 703 ms. The morphological features extracted from the region containing the seeds and the central axis in dynamic images were not significantly different from those extracted from the static ones. The maximum radius and the perimeter of the seed-axis area, which showed significant differences between seed-containing and seedless mandarins (by ANOVA analysis), entered a discriminant

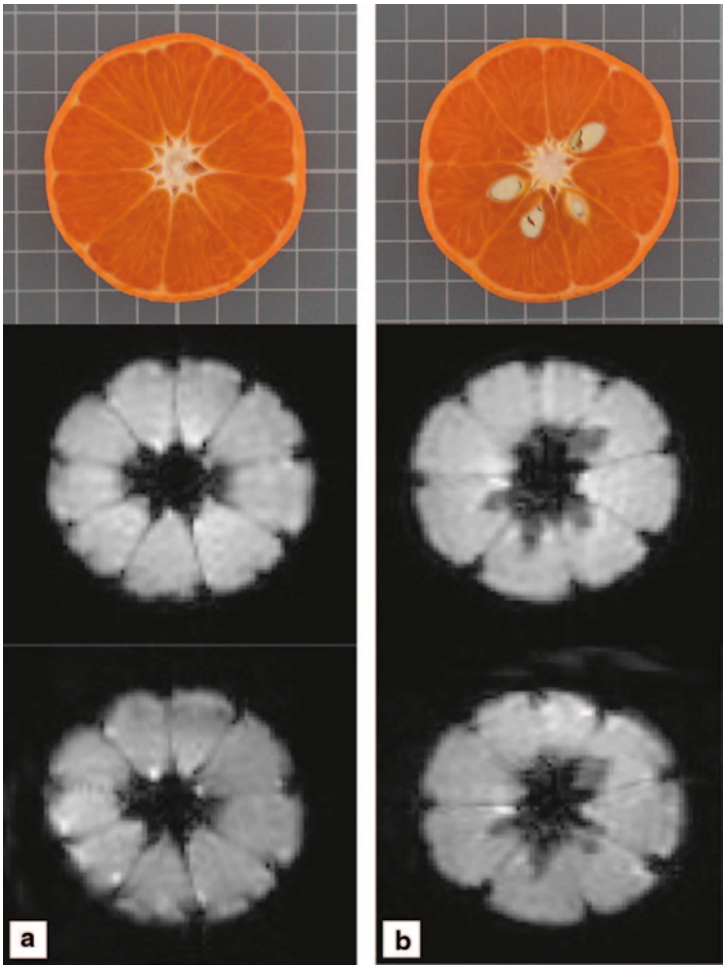

Fig. 9.21 Examples of seedless (**a**) and seed-containing (**b**) mandarins; *upper line* corresponds to *red, green and blue (RGB)* images; *middle line* to static magnetic resonance images, and *bottom line* to motion-corrected magnetic resonance images. From Hernández-Sánchez et al. (2006)

analysis to classify conveyed fruits. The percentages of correct classification into the corresponding category were 92.5 and 79.5% for seedless and seed-containing mandarins, respectively. These results need to be validated at lower magnetic field strength.

With the aim of improving the performance of the previous results, Barreiro et al. (2008) evaluated faster MRI sequences and more efficient segmentation procedures with stationary mandarins. The imaging experiments were performed at 4.7 T with a FLASH sequence and a spiral–radial (COMSPIRA sequence), which significantly shortened the acquisition times to 484 and 240 ms, respectively. The image segmentation procedures were based on simple region thresholding, on 1D histogram variance, and on 2D histogram variance (2DHV). Morphological parameters were then computed from the signal hypointense region. 2DHV provided the most promising results as the corresponding linear classification function achieved 100% accuracy using radial–spiral sequence and 98.7% accuracy with gradient echo images in discriminating mandarins with seeds.

The detection of internal freeze damage in pickling cucumbers has been studied using MRI (Kotwaliwale et al. 2012). Samples were imaged using a 9.4 T system at 0, 1, 3 and 6 days after inducing freeze injury. Relaxation times T_1 and T_2 were measured using a MEMS sequence (TE = 7.96 ms and TR from 0.05 to 2 s for T_1; TR = 2 s with 32 echoes spaced 10 ms apart for T_2). For quantitative analysis, T_1 and T_2 relaxation maps were constructed. PD images were acquired using a spin echo sequence (TE = 7.96 ms and a TR = 2 s). High-resolution FSE images were also acquired (TR = 2000 ms, an echo train length of 8 and an echo spacing of 10 ms). Texture profile analysis of the control and of the freeze-damaged samples was also carried out. Images provided five contrasting regions. Those images with the highest contrast were used for defining masks. Simple thresholds were used to segment cucumber tissue from the background and for gel around the seeds. Thresholding and morphological operations were applied to seed segmentation. The subsurface rind was segmented by disk eroding. Finally, the flesh portion was segmented by subtracting all the other masks. Then, the mean voxel intensities in both the T_2-weighted and PD images were computed for the different anatomical components. It was found that mean voxel intensities for all the freeze-damaged regions were always higher than the control samples. Accordingly, T_2 values were also higher. T_2 values were different between tissues and did not change significantly over the storage period. Despite T_2 and firmness values being significantly different for control and freeze-damaged tissues, there was no correlation between them.

As introduced by Taglienti et al. (2009), kiwifruit is prone to water loss with severe tissue degradation before any external symptom, such as shrivel and shrinking, becomes visible. MRI is especially suitable to evaluate structural changes in kiwifruit along storage period. Hence, these authors imaged fruits along 35 days for samples stored at 20 °C; and along 65 days for samples stored at 0 °C, with several imaging sequences using a 7 T MRI system: GEFI (TE = 2.445 ms and TR = 60.0 ms), MSME (TE = 17.5 ms and the TR = 6000.0 ms), RARE (TE = 12.0 ms and TR = 4500.0 ms, and rare factor = 64), and GE3D (TE = 1.472 ms and TR = 60.0 ms). The T_2-weighted

contrast of the MSME images highlighted five concentric regions: the intermediate was the brightest one corresponding to the tissue containing seeds (S_3), which would have weakly bound water; the internally adjacent region was slightly darker (S_4); the columnella appeared as the darkest region due to the strongly bound water within the highly fibrous structure (S_5); the two outer regions, which correspond to pericarp, showed low-signal revealing lower water mobility (S_1 and S_2), being slightly higher than the most external one probably as a result of a different interaction between cells and water. The PD-weighted contrast of the GEFI images revealed a highly homogeneous water distribution. Here, two regions were identified in the pulp. The brightest comprising the previous S_3 and S_4 regions. Along the storage period, samples at 0 °C experienced only slight changes. For samples, storage at 20 °C changes in the image contrast revealed a decrease in the fruit diameter and in the thickness of all regions. In addition, pericarp displayed a coarse contour, and the columnella experienced a morphological shrinking with increasing signal intensity, indicating higher amount and water mobility. The initial disintegration of the tissue observed by MRI corresponded to both a dramatic increase of ethylene production and a decrease of penetrometer force and firmness. In view of the contrast in GE3D images, authors suggested a possible migration process of water molecules from the inner zones towards the epicarp, which increased signal intensity; and an accumulation of water due to an evapotranspiration slower than the migration.

MRI has been used to investigate the changes of main compounds in olives during ripening and after processing (Brescia et al. 2007; Brescia and Sacco 2010). Authors proposed an alternative approach with a selective excitation pulse, the so-called chemical shift imaging. This technique takes advantage of the differences in the resonance frequency between water and oil protons, so that by managing the pulse parameters, the resulting image will display the selected proton pool. The imaging experiments were performed at 4.7 T with a spin echo imaging sequence by applying a chemical shift selective excitation pulse and a slice-selective refocusing pulse. The TR and TE were 8.2 ms and 2 s, respectively. This technique allowed monitoring the increase of oil content and the decrease of water content. Both compounds appeared concentrated around the endocarp, which authors related to the high porosity of this region. Water seemed to move from the inner mesocarp to outer mesocarp during ripening.

References

Al-Mallahi A, Kataoka T, Okamoto H, Shibata Y (2010) Detection of potato tubers using an ultraviolet imaging-based machine vision system. Biosystems Eng 105(2):257–265

Baiano A, Terracone C, Peri G, Romaniello R (2012) Application of hyperspectral imaging for prediction of physico-chemical and sensory characteristics of table grapes. Comput Electron Agric 87(0):142–151

Baranowski P, Mazurek W, Wozniak J, Majewska U (2012) Detection of early bruises in apples using hyperspectral data and thermal imaging. J Food Eng 110(3):345–355

Baranowski P, Mazurek W, Pastuszka-Woźniak J (2013) Supervised classification of bruised apples with respect to the time after bruising on the basis of hyperspectral imaging data. Postharvest Biol Technol 86(0):249–258

Barreiro P, Zheng C, Sun D-W, Hernández-Sánchez N, Pérez-Sánchez JM, Ruiz-Cabello J (2008) Non-destructive seed detection in mandarins: comparison of automatic threshold methods in FLASH and COMSPIRA MRIs. Postharvest Biol Technol 47:189–198

Blasco J (2009) Development of a machine for the automatic sorting of pomegranate arils based on computer vision. J Food Eng 90:27–34

Blasco J, Aleixos N, Moltó E (2003) Machine vision system for automatic quality grading of fruit. Biosytems Eng 85(4):415–423

Blasco J, Aleixos N, Cubero S, Moltó E (2009) Automatic sorting of satsuma segments using computer vision and morphlogical features. Comput Electron Agric 66:1–8

Boldrini B, Kessler W, Rebnera K, Kessler RW (2012) Hyperspectral imaging: a review of best practice, performance and pitfalls for in-line and on-line applications. J Near Infrared Spectrosc 20(5):483–508

Brescia AM, Sacco A (2010) Chapter 13—ripening of table olives: use of magnetic resonance imaging (MRI). In: Preedy VR, Watson RR (eds) Olives and olive oil in health and disease prevention. Elsevier Inc, San Diego, pp 109–116. ISBN 978-0-12-374420-3

Brescia MA, Pugliese T, Hardy E, Sacco A (2007) Compositional and structural investigations of ripening of table olives, Bella della Daunia, by means of traditional and magnetic resonance imaging analyses. Food Chem 105(1):400–404

Cen H, Lu R, Mendoza FA, Ariana DP (2012) Assessing multiple quality attributes of peaches using optical absorption and scattering properties. Trans ASABE 55(2):647–657

Cen H, Lu R, Mendoza F, Beaudry RM (2013) Relationship of the optical absorption and scattering properties with mechanical and structural properties of apple tissue. Postharvest Biol Technol 85:30–38

Cho B-K, Kim MS, Baek I-S, Kim D-Y, Lee W-H, Kim J, Bae H, Kim Y-S (2013) Detection of cuticle defects on cherry tomatoes using hyperspectral fluorescence imagery. Postharvest Biol Technol 76(0):40–49

Chuang C-L, Ouyang C-S, Lin T-T, Yang M-M, Yang E-C, Huang T-W, Kuei C-F, Luke A, Jiang J-A (2011) Automatic X-ray quarantine scanner and pest infestation detector for agricultural products. Comput Electron Agric 77:41–59

Ciampa A, Dell'Abate MT, Masetti O, Valentini M, Sequi P (2010) Seasonal chemical–physical changes of PGI Pachino cherry tomatoes detected by magnetic resonance imaging (MRI). Food Chem 122:1253–1260

Cubero S, Aleixos N, Moltó E, Gómez-Sanchís J, Blasco J (2011) Advances in machine vision applications for automatic inspection and quality evaluation of fruits and vegetables. Food Bioproces Technol 4:487–504

Dale LM, Thewis A, Boudry C, Rotar I, Dardenne P, Baeten V, Pierna JAF (2013) Hyperspectral imaging applications in agriculture and agro-food product quality and safety control: a review. Appl Spectrosc Rev 48(2):142–159

Defraeye T, Lehmann V, Gross D, Holat C, Herremans E, Verboven P, Verlinden B, Nicolai B (2013) Application of MRI for tissue characterisation of 'Braeburn' apple. Postharvest Biol Technol 75:96–105

Diezma B, Lleó L, Roger JM, Herrero-Langreo A, Lunadei L, Ruiz-Altisent M (2013) Examination of the quality of spinach leaves using hyperspectral imaging. Postharvest Biol Technol 85:8–17

Donis-González IR, Guyer DE, Pease A, Barthel F (2014) Internal characterisation of fresh agricultural products using traditional and ultrafast electron beam X-ray computed tomography imaging. Biosystems Eng 117:104–113

Drexler W, Morgner U, Kärtner F-X, Pitris C, Boppart SA, Li XD, Ippen EP, Fujimoto JG (1999) In vivo ultrahigh-resolution optical coherence tomography. Opt Lett 24(17):1221–1223

Dunn MT (2007) Applications of vision sensing in agriculture. Ph.D. dissertation. University of Southern Queensland

El Masry G, Cubero S, Moltó E, Blasco J (2012) In-line sorting of irregular potatoes by using automated computer-based machine vision system. J Food Eng 112:60–68

Espinoza M (2003) Researcher seeks to solve tomato shape riddle, develop new varieties. Ohio State University Extension. http://www.ag.ohio-state.edu/~news/story.php?id=2673. Accessed 28 Oct 2010

Esquerre C, Gowen AA, Downey G, O'Donnell CP (2012) Wavelength selection for development of a near infrared imaging system for early detection of bruise damage in mushrooms *(Agaricus bisporus)*. J Near Infrared Spectrosc 20(5):537–546

Fanourakis NE, Tzifaki EE (1993) Correlated inheritance of fruit neck with fruit length and linkage relations with 10 other characteristics of cucumber. Euphytica 65:71–77

Fathi M, Mohebbi M, Razavi SMA (2011) Application of image analysis and artificial neural network to predict mass transfer kinetics and color changes of osmotically dehydrated kiwi-fruit. Food Bioprocess Technol 4:1357–1366

Ford HD, Tatam RP, Landahl S, Terry LA (2011) Investigation of disease in stored onions using optical coherence tomography. Proc IV Int Conf Postharvest Unltd 2011:247–254

Fujimoto J-G, Pitris C, Boppart S-A, Brezinski M (2010) Optical coherence tomography: an emerging technology for biomedical imaging and optical biopsy. Neoplasia 2:9–25

Goñi SM, Purlis E, Salvadori VO (2007) Three-dimensional reconstruction of irregular foodstuffs. J Food Eng 82:536–547

Gowen AA, O'Donnell CP, Taghizadeh M, Gaston E, O'Gorman A, Cullen PJ, Frias JM, Esquerre C, Downey G (2008a) Hyperspectral imaging for the investigation of quality deterioration in sliced mushrooms *(Agaricus bisporus)* during storage. Sens Instrum Food Qual Saf 2(3):133–143

Gowen AA, O'Donnell CP, Taghizadeh M, Cullen PJ, Frias JM, Downey G (2008b) Hyperspectral imaging combined with principal component analysis for bruise damage detection on white mushrooms *(Agaricus bisporus)*. J Chemometr 22(3–4):259–267

Gui J, Zhou W (2010) Fruit shape classification using Zernike moments. Proc SPIE 7820:782015

Guo H, Tan Y, Li W (2014) Chapter 12: surface texture detection of double-feature apple based on computer vision. Proceedings of 3rd international conference on multimedia technology (ICMT 2013). Springer, Berlin, pp. 117–127

Hernández-Sánchez N, Barreiro P, Ruiz-Altisent M, Ruiz-Cabello J, Fernandez-Valle M (2004) Detection of freeze injury in oranges by magnetic resonance imaging of moving samples. Appl Magn Reson 26:431–445

Hernández-Sánchez N, Barreiro P, Ruiz-Altisent M, Ruiz-Cabello J, Fernandez-Valle M (2005) Detection of seeds in citrus using magnetic resonance imaging under motion conditions and improvement with motion correction. Concepts in magnetic resonance. Part B Magn Reson Eng 26B:81–92

Hernández-Sánchez N, Barreiro P, Ruiz-Cabello J (2006) On-line identification of seeds in Mandarins with magnetic resonance imaging. Biosyst Eng 95:529–536

Hernández-Sánchez N, Hills BP, Barreiro P, Marigheto N (2007) An NMR study on internal browning in pears. Postharvest Biol Technol 44:260–270

Hernández-Sánchez N, Barreiro P, Ruiz-Cabello J (2009) NMR for internal quality evaluation in horticultural products. In: Optical monitoring of fresh and processed agricultural crops. CRC Press, pp. 423–468. ISBN: 978-1-4200-5402-6

Herremans E, Verboven P, Bongaers E, Estrade P, Verlinden BE, Wevers M, Hertog MLATM, Nicolaï BM (2013a) Characterisation of 'Braeburn' browning disorder by means of X-ray micro-CT. Postharvest Biol Technol 75:114–124

Herremans E, Verboven P, Defraeye T, Rogge S, Ho QT, Hertog MLATM, Verlinden BE, Bongaers E, Wevers M, Nicolaï BM (2013b) X-ray CT for quantitative food microstructure engineering: the apple case. Nucl Instrum Methods Phys Res Sect B 324:88–94. http://dx.doi.org/10.1016/j.nimb.2013.07.035

Herremans E, Melado-Herreros A, Defraeye T, Verlinden B, Hertog M, Verboven P, Val J, Encarnación Fernández-Valle M, Bongaers E, Estrade P, Wevers M, Barreiro P, Nicolaï BM (2014) Comparison of X-ray CT and MRI of watercore disorder of differentapple cultivars. Postharvest Biol Technol 87:42–50

Hoffmann T, Wormans G, Fürll C, Poller J (2005) A system for determining starch in potatoes online. IAg Eng LUA LU of Ag 37(2):34–43. http://vddb.library.lt/fedora/get/LT-eLABa-0001:J.04~2005~ISSN_1392-1134.V_37.N_2.PG_34-43/DS.002.1.01.ARTIC. Accessed 21 July 2014

Huang D, Swanson EA, Lin CP, Schuman JS, Stinson WG, Chang W, Hee MR, Flotte T, Gregory K, Puliafito CA (1991) Optical coherence tomography. Science 254(5035):1178–1181

Huang H, Yu H, Xu H, Ying Y (2008) Near infrared spectroscopy for on/in-line monitoring of quality in foods and beverages: a review. J Food Eng 87(3):303–313

Jafari A, Zarazadeh MR, Fazayeli A (2012) Orange grading based on visual texture features. CIGR-AGENG 2012, Valencia

Jarimopas B, Jaisin N (2008) An experimental machine vision system for sorting sweet tamarind. J Food Eng 89(3):291–297

Jiang J-A, Chang H-Y, Ke-Han Wu, Ouyang C-S, Yang M-M, Yang E-C, Chen T-W, Lin T-T (2008) An adaptive image segmentation algorithm for X-ray quarantine inspection of selected fruits. Comput Electron Agric 60:190–200

Jiang L, Zhu B, Cheng X, Luo Y, tao Y (2009) 3D surface reconstruction and aanlysis in automated apple stem-end/calyx identification. Trans ASABE 52(5):1775–1784

Kang SP, East AR, Trujillo FJ (2008) Colour vision system evaluation of bicolour fruit: a case study with 'B74' mango. Postharvest Biol Technol 49:77–85

Kang S, Lee K, Son J, Kim MS (2011) Detection of fecal contamination on leafy greens by hyperspectral imaging. Procedia Food Sci 1(0):953–959

Khoshroo A, Keyhani A, Zoroofi RA, Rafiee S, Zamani Z, Alsharif MR (2009) Classification of pomegranate fruit using texture analysis of MR images. Agric Eng Int. XI:Manuscript 1182. (March 2009)

Khoshroo A, Keyhani A, Zoroofi RA, Yaghoobi G (2011) Nondestructive inspection of pomegranate maturity using magnetic resonance imaging and neural networks. CIGR Section VI international symposium on towards a sustainable food chain, food process, bioprocessing and food quality management. Nantes, France. April 18–20, 2011

Kim MS, Chen Y-R, Cho B-K, Chao K, Yang C-C, Lefcourt AM, Chan D (2007) Hyperspectral reflectance and fluorescence line-scan imaging for online defect and fecal contamination inspection of apples. Sens Instrum Food Qual Saf 1:151–159

Kotwaliwale N, Curtis E, Othman S, Naganathan GK, Subbiah J (2012) Magnetic resonance imaging and relaxometry to visualize internal freeze damage to pickling cucumber. Postharvest Biol Technol 68:22–31

Landahl S, Terry LA, Ford HD (2012) Investigation of diseased onion bulbs using data processing of optical coherence tomography images. Acta Hortic 969:261–270

Lara MA, Lleó L, Diezma-Iglesias B, Roger JM, Ruiz-Altisent M (2013) Monitoring spinach shelf-life with hyperspectral image through packaging films. J Food Eng 119(2):353–361

Lee D-J, Schoenberger R, Archibald J, McCollum S (2008) Development of a machine vision system for automatic date grading using digital reflective near-infrared imaging. J Food Eng 86:388–398

Leiva-Valenzuela GA, Lu R, Aguilera JM (2013) Prediction of firmness and soluble solids content of blueberries using hyperspectral reflectance imaging. J Food Eng 115(1):91–98

Leónard A, Blacher S, Nimmol C, Devahastin S (2008) Effect of far-infrared radiation assisted drying on microstructure of banana slices: an illustrative use of X-ray microtomography in microstructural evaluation of a food product. J Food Eng 85:154–162

Li J, Rao X, Ying Y (2011) Detection of common defects on oranges using hyperspectral reflectance imaging. Comput Electron Agric 78(1):38–48

Lleó L, Roger JM, Herrero-Langreo A, Diezma-Iglesias B, Barreiro P (2011) Comparison of multispectral indexes extracted from hyperspectral images for the assessment of fruit ripening. J Food Eng 104(4):612–620

Loeb G, Barton JK (2003) Imaging botanical subjects with optical coherence tomography: a feasibility study. Trans ASAE 46:1751–1757

Løkke MM, Seefeldt HF, Skov T, Edelenbos M (2013) Color and textural quality of packaged wild rocket measured by multispectral imaging. Postharvest Biol Technol 75:86–95

López Camelo AF (2004) Manual for the preparation and sale of fruits and vegetables. ISSN 1010–1365 FAO agricultural services bulletin 151 FAO 2004 ISBN 92-5-104991-2. http://www.fao.org/docrep/008/y4893e/y4893e00.htm#Contents

Lorente D, Aleixos N, Gómez-Sanchis J, Cubero S, García-Navarrete OL, Blasco J (2012) Recent advances and applications of hyperspectral imaging for fruit and vegetable quality assessment. Food Bioprocess Technol 5(4):1121–1142

Lü Q, Tang MJ, Cai JR, Zhao JW, Vittayapadung S (2011) Vis/NIR hyperspectral imaging for detection of hidden bruises on kiwifruits. Czech J Food Sci 29(6):595–602

Maguwaza LS, Ford HD, Cronje PJR, Opara UL, Landahl S, Tatam RP, Terry LA (2013) Application of optical coherence tomography to non-destructively characterize rind breakdown disorder of 'Nules Clementine' mandarins. Postharvest Biol Technol 84:16–21

Martynenko AI (2011) Porosity evaluation of ginseng roots from real-time imaging and mass measurements. Food Bioprocess Technol 4:417–428

Matiacevich S, Celis Cofré D, Silva P, Enrione J, Osorio F (2013) Quality parameters of six cultivars of blueberry using computer vision. Intl J Food Sci 2013:8

Meglinski IV, Buranachai C, Terry LA (2010) Plant photonics: application of optical coherence tomography to monitor defects and rots in onion. Laser Phys Lett 7:307–310

Melado-Herreros A, Muñoz-García M, Blanco A, Val J, Fernandez-Valle M, Barreiro P (2013) Assessment of watercore development in apples with MRI: effect of fruit location in the canopy. Postharvest Biol Technol 86:125–133

Mendoza F, Dejmek P, Aguilera JM (2007) Color and image texture analysis in classification of commercial potato chips. Food Res Intl 40:1146–54

Mendoza F, Lu R, Ariana D, Cen H, Bailey B (2011) Integrated spectral and image analysis of hyperspectral scattering data for prediction of apple fruit firmness and soluble solids content. Postharvest Biol Technol 62(2):149–160

Menesatti P, Costa C, Paglia G, Pallotino F, D'Andrea S, Rimatori V, Aguzzi J (2008) Shape-based methodology for multivariate discrimination among Italian hazelnut cultivars. Biosystems Eng 101:417–424

Milczarek R, Saltveit ME, Casey Garvey T, McCarthy MJ (2009) Assessment of tomato pericarp mechanical damage using multivariate analysis of magnetic resonance images. Postharvest Biol Technol 52:189–195

Mizushima A, Lu R (2013) An image segmentation method for apple sorting and grading using support vector machine and Otsu's method. Comput Electron Agr 94:29–37

Moreda GP, Muñoz MA, Ruiz-Altisent M, Perdigones A (2012) Horticultural produce shape determination using computer vision—a review. J Food Eng 108:245–261

Musse M, Quellec Sp, Cambert M, Devaux M-FO, Lahaye M, Mariette F (2009a) Monitoring the postharvest ripening of tomato fruit using quantitative MRI and NMR relaxometry. Postharvest Biol Technol 53:22–35

Musse M, Quellec Sp, Devaux M-FO, Cambert M, Lahaye M, Mariette FO (2009b) An investigation of the structural aspects of the tomato fruit by means of quantitative nuclear magnetic resonance imaging. Magn Reson Imaging 27:709–719

Musse M, De Guio FO, Quellec SP, Cambert M, Challois S, Davenel A (2010) Quantification of microporosity in fruit by MRI at various magnetic fields: comparison with X-ray microtomography. Magn Reson Imaging 28:1525–1534

Nandi CS, Tudu B, Koley C (2012). An automated machine vision based system for fruit sorting and grading. 6th International Conference on Sensing Technology, pp 195–200

Nicolaï BM, Beullens K, Bobelyn E, Peirs A, Saeys W, Theron KI, Lammertyn J (2007) Nondestructive measurement of fruit and vegetable quality by means of NIR spectroscopy: a review. Postharvest Biol Technol 46(2):99–118

Nielsen MS, Christensen LB, Feidenhans'l R (2014) Frozen and defrosted fruit revealed with X-ray dark-field radiography. Food Control 39:222–226

NIVAP Holland (Netherlands Potato Consultative Foundation) (2014) Tuber characteristics determining quality. http://www.nivaa.nl/uk/about_potatoes/agronomy/on_the_road_to_potato_processing/tuber_characteristics. Accessed 21 July 2014

Okayama T, Qiao J, Tanaka H, Kondo N, Shibusawa S (2006) Classification of shape of bell pepper by machine vision system. Agr Inf Res 15(2):113–122

Opara UL, Pathare PB (2014) Bruise damage measurement and analysis of fresh horticultural produce—a review. Postharvest Biol Technol 91:9–24

Peng Y, Zhao J, Dhakal S, Zhou T (2012) Real-time detection of natural bruises in apple surface using machine vision. ASABE, Dallas

Piñeiro M, Díaz Ríos LB (2004) Manual para multiplicadores. Servicio de Calidad de los Alimentos y Normas Alimentarias (ESNS) Dirección de Alimentación y Nutrición. FAO. http://www.fao.org/docrep/007/y5488s/y5488s00.htm#Contents

Quevedo R, Mendoza F, Aguilera JM, Chanona J, Gutiérrez-López G (2008) Determination of senescent spotting in banana *(Musa cavendish)* using fractal texture Fourier image. J Food Eng 84:509–515

Rajkumar P, Wang N, Eimasry G, Raghavan GSV, Gariepy Y (2012) Studies on banana fruit quality and maturity stages using hyperspectral imaging. J Food Eng 108(1):194–200

Riyadi S, Ishak AJ, Mustafa MM, Hussain A (2008) Wavelet-based feature extraction technique for fruit shape classification. In: Proceedings of 5th International Symposium on Mechatronics and its Applications (ISMA 08). IEEE

Rizzolo A, Vanoli M, Cortellino G, Spinelli L, Contini D, Herremans E, Bongaers E, Nemeth A, Leitner M, Verboven P, Nicolaï B, Torricelli A (2013) Characterizing the tissue of apple air-dried and osmo air-dried rings by X-CT and OCT and relationship with ring crispness and fruit maturity at harvest measured by TRS. Innov Food Sci Emerg Technol 24:121–130

Ruiz-Altisent M, Ruiz L, Moreda GP, Lu R, Hernández-Sánchez N et al (2010) Sensors for specialty crops. Comput Electron Agr 74:176–194

Siripatrawan U, Makino Y, Kawagoe Y, Oshita S (2011) Rapid detection of *Escherichia coli* contamination in packaged fresh spinach using hyperspectral imaging. Talanta 85(1):276–281

Slaughter DC, Obenland DM, Thompson JF, Arpaia ML, Margosan DA (2008) Non-destructive freeze damage detection in oranges using machine vision and ultraviolet fluorescence. Postharvest Biol Technol 48:341–346

Sugiyama J, Tsuta M (2010) Chapter 11—visualization of sugar distribution of melons by hyperspectral technique. In: Sun D-W (ed) Hyperspectral imaging for food quality analysis and control. Academic, San Diego, pp 349–368

Sun D-W (2008) Computer vision technology for food quality evaluation. Academic, San Diego

Syvertsen JP, Albrigo LG, Dunlop JM, Ritenour MA, Vachon RC (2005) Growth conditions, crop load and fruit size affect sheepnosing in grapefruit. Proc Fla State Hort Soc 118:28–34

Taghizadeh M, Gowen A, Ward P, O'Donnell CP (2010) Use of hyperspectral imaging for evaluation of the shelf-life of fresh white button mushrooms *(Agaricus bisporus)* stored in different packaging films. Innov Food Sci Emerg Technol 11(3):423–431

Taglienti A, Massantini R, Botondi R, Mencarelli F, Valentini M (2009) Postharvest structural changes of Hayward kiwifruit by means of magnetic resonance imaging spectroscopy. Food Chem 114:1583–1589

Taglienti A, Vanoli M, Cortellino G, Spinelli L, Contini D, Herremans E, Bongaers E, Nemeth A, Leitner M, Verboven P, Nicolaï BM, Torricelli A (2013) Characterizing the tissue of apple air-dried and osmo-air-dried rings by X-CT and OCT and relationship with ring crispness and fruit maturity at harvest measured by TRS. Innov Food Sci Emerg Technol. In Press

Teena M, Manickavasagan A, Mothershaw A, Hadi SE, Jayas DS (2013) Potential of machine vision techniques for detecting fecal and microbial contamination of food products: a review. Food Bioprocess Technol 6:1621–1634

Thybo AK, Andersen HJ, Karlsson AH, Donstrup S, Stodkilde-Jorgensen H (2003) Low-field NMR relaxation and NMR-imaging as tools in differentiation between potato sample and determination of dry matter content in potatoes. J Food Sci 36(3):315–322

Thybo AK, Szczypinski PM, Karlsson AH, Donstrup S, Stodkilde-Jorgensen HS, Andersen HJ (2004a) Prediction of sensory texture quality attributes of cooked potatoes by NMR-imaging (MRI) of raw potatoes in combination with different image analysis methods. J Food Eng 61:91–100

Thybo AK, Jespersenb SN, Lærkec PE, Stødkilde HJ (2004b) Nondestructive detection of internal bruise and spraing disease symptoms in potatoes using magnetic resonance imaging. Magn Reson Imaging 22:1311–1317

Verboven P, Nemeth A, Abera MK, Bongaers E, Daelemans D, Estrade P, Herremans E, Hertog M, Saeys W, Vanstreels E, Verlinden B, Leitner M, Nicolaï B (2013) Optical coherence tomography visualizes microstructure of apple peel. Postharvest Biol Technol 78:123–132

Wang H, Feng H, Luo Y, Zhang A (2007) Produce surface characteristics affect product quality and safety. ISHS Acta Hort 746:131–138 (Proc IC on Qual Manag Fresh cut produce. Eds.: S Kanlayanarat et al.)

Wu D, Sun D-W (2013a) Advanced applications of hyperspectral imaging technology for food quality and safety analysis and assessment: a review—part I: fundamentals. Innovative Food Sci Emerg Technol 19:1–14

Wu D, Sun D-W (2013b) Advanced applications of hyperspectral imaging technology for food quality and safety analysis and assessment: a review—part II: applications. Innovative Food Sci Emerg Technol 19:15–28

Zhang L, McCarthy MJ (2012) Black heart characterization and detection in pomegranate using NMR relaxometry and MR imaging. Postharvest Biol Technol 67:96–101

Zhang L, McCarthy MJ (2013) Assessment of pomegranate postharvest quality using nuclear magnetic resonance. Postharvest Biol Technol 77:59–66

Zhao J, Qin O, Chen Q, Wang JJ (2010) Detection of bruise on pear by hyperspectral imaging sensor with different classification algorithms. Sens Lett 8(4):570–576

Zhelev N, Barudov S (2005) Laser light scattering applications in biotechnology. Biotechnol Biotechnological Equip 19:3–8

Chapter 10
Microstructural Imaging of Chocolate Confectionery

Dérick Rousseau

10.1 Introduction

Chocolate making is a centuries-old process that relies heavily on the initial quality of the cocoa beans and their processing, ingredient mixing and refining as well as the meticulous control of cocoa butter (CB)/fat phase crystallisation. Perceived losses in quality frequently occur once packaged chocolate has left the factory floor. In the hands of the consumer, chocolate may be subjected to uncontrolled CB recrystallisation, often leading to loss of sensory quality. With this in mind, the focal point of this chapter is on the fat phase and on how its crystal and polymorphic stability is crucial for maintaining chocolate quality. Particular attention is paid to the repercussions of fat bloom on microstructure. The relationship between microstructure and two phenomena, migration and uncontrolled recrystallisation, is related to loss of shelf and sensory breakdown.

10.2 Background

Chocolate is defined as a solid-like mixture of CB and ground, roasted cacao seed, normally mixed with sugar, milk powder (if milk chocolate), emulsifier and vanilla processed to give a final product with a defined range of sensory and physical properties, including a smooth, melt-in-the-mouth texture, glossy surface and firm snap. Below 25 °C, it is solid and holds the other ingredients together, namely the sugar and cocoa powder, whereas at body temperature, it melts, enabling particles to flow past one another and form a smooth viscous suspension once in the mouth.

D. Rousseau (✉)
Department of Chemistry and Biology, Ryerson University, 350 Victoria St, KHE 327C, Toronto, ON M5B 2K3, Canada
e-mail: rousseau@ryerson.ca

N. Sozer (ed.), *Imaging Technologies and Data Processing for Food Engineers,*
Food Engineering Series, DOI 10.1007/978-3-319-24735-9_10

There are three main types of chocolate: milk, white and dark (plain) chocolate, with notable differences in composition existing between them. Dark chocolate consists primarily of sugar, CB and cocoa liquor. Milk chocolate also consists of sugar, CB and cocoa liquor but with added milk solids. Finally, white chocolate is made up of sugar, CB and milk solids (Lonchampt and Hartel 2004). In all three cases, the CB may in part be replaced with milkfat and/or CB equivalents (CBEs). With the possibility of fats of different origins present in the chocolate, it is more appropriate to speak of the fat phase rather than of CB only.

From a colloidal perspective, the dry ingredients—the cocoa mass (butter and liquor), sugar particles and milk powder, if present—are distributed within a continuous fat phase typically containing soy lecithin or polyglycerol polyricinoleate (a castor oil derivative) as emulsifier. These ingredients, when mixed, must be ground so that most of the particles are <30 μm in diameter. The sensory attributes of chocolate are strongly dependent on the size and distribution of the particles in the chocolate matrix, and the polymorphic form and morphology of the fat phase.

CB is an important ingredient for chocolate and other confectionery products. It can amount to up to ~30% (w/w) of chocolate and binds the other ingredients. CB exhibits brittleness below 20 °C, and begins softening at 30–32 °C if properly solidified. It is tasteless and shows sharp and complete melting near body temperature. It is nothing short of critical to the enjoyment of chocolate—it dictates its snap, gloss and sharp melting profile. However, it is also responsible for the development of fat bloom—the streaky, greyish coating sometimes seen on chocolate.

10.3 Fat Structure–Functionality Relationship

CB comprises three classes of triglycerides (TGs): saturated TGs, monounsaturated TGs and polyunsaturated TGs. The TG molecule consists of a glycerol backbone and three fatty acids, with the main fatty acids in CB being palmitic acid (saturated), oleic acid (monounsaturated) and stearic acid (saturated). Fat crystals consist of interacting TGs arranged in an asymmetrical tuning fork geometry, which then stack into lamellae with the tuning forks butting end to end.

CB is polymorphic, meaning that even if its fatty acid composition and positional distribution remain constant, it can exist in different crystal forms, each with a different thermodynamic stability. The three primary polymorphic forms in food fats, in order of increasing thermodynamic stability, are alpha (α), beta prime (β′) and beta (β). Viewed on end, the α-form subcell is hexagonal, the β′-form orthorhombic, while the β-form is triclinic. Crystal subforms include sub-α, β′1, β′2, pseudo-β′, sub-β, β1 and β2 (Himawan et al. 2006), though new developments in the next few years will surely bring new subforms to light. Depending on the degree and rate of undercooling, fats may crystallise directly into most of these polymorphs. Polymorph-polymorph transformations usually occur via a solid–solid transition or by melt-mediation. X-ray diffraction, used to identify crystal polymorphs, is based on the determination of the long and short spacings of crystals, that is, the fatty acid

subcell arrangement and lamellar spacing. The α-form has a single short spacing near 4.15 Å, the β′-form spacings at 3.8 and 4.2 Å, while the β form does not correspond to either of these forms and typically shows a single strong spacing at 4.6 Å (deMan 1992).

Each polymorph is associated with a different crystal morphology. α-crystals are the least stable and least densely packed and exist as small, fragile, transparent platelet crystals measuring ~5 μm in length. Given their lack of stability, α-crystals are not overly common, though they may exist in fats mixed with emulsifiers (Garti et al. 1998). No natural fats are stable in this form but almost all transform through it during a liquid–solid transition. Natural fats with a great compositional TG and fatty acid variety will exist as stable β′-crystals. In many cases, transformation from α to β′ is slower, and transformation to β is unlikely. β′-crystals are small, delicate needles measuring 1–2 μm in length. In native CB, the β′ form is generally transient. β-crystals have the highest melting point and a more compact crystal structure than the β′-form. Fats with little compositional variety such as CB are stable in this form. β-needles measuring upwards of 50 μm in length are possible.

Six polymorphs have been identified in CB (Wille and Lutton 1966), ranging from form I to form VI when using Roman nomenclature. The form V (β_2) polymorph is the desired CB polymorph, as its melting point is above room temperature and slightly below body temperature. It provides chocolate products with snap (ability to break apart easily), good demoulding properties (contraction) and a good quality finish in terms of colour and gloss. From the processor's perspective, the aim of the crystallisation regime employed during chocolate making, known as tempering, is to crystallise the fat phase into form V. Any other form will lead to inadequate organoleptic properties and/or a shortened shelf life, as bloom sets in early, often in days instead of months. In particular, presence of the form VI polymorph is undesirable, as it is closely associated with bloom formation. Given that this form is more thermodynamically stable, all CB-based fats eventually tend towards its formation.

CB is often mixed with other fats that are cheaper and/or retard fat bloom formation, namely CBEs and milkfat. CBEs are vegetable fats with similar chemical and physical characteristics to CB that can be used interchangeably with CB in any formulation. The greatest single advantage of CBEs is their ability to inhibit fat bloom, especially in dark chocolate, which is more vulnerable to it. The shortage in CB supply, variation in CB quality at harvest and its price have largely driven CBE development (Lipp et al. 2001). The EU Chocolate Directive 2000/36/EC adopted in 2003 allows the use of up to 5% of a compatible vegetable fat (Stewart and Kristott 2004). These fats include illipé, palm oil, sal, shea, kokum gurgi and mango kernel (Wilson 1999). A CBE must have a similar melting and crystallisation behaviour as well as fatty acid and TG composition that do not result in eutectic formation with CB. Also, the appearance and bloom-free shelf life of CBE-containing products should rival, if not better, that of CB-based products (Lipp and Anklam 1998).

Milkfat may be added to dark, milk and white chocolate as a fat bloom inhibitor. It is generally compatible with CB but does affect its crystallisation kinetics and the temperatures of its polymorphic transitions. It tends to soften chocolate when added in large amounts to the fat phase.

Milkfat is a mixture of more than 100,000 different TGs with a melting range between −40 and +40 °C. The presence of ~400 different fatty acids has been noted in milkfat (Deffense 1993). Such variety in composition is responsible for milkfat's unique physical properties, such as the sharp drop in solid fat content between refrigerator and room temperatures (DeMan 1961). Contrary to CB, milkfat is β′ stable, a direct consequence of its compositional variety. Milkfat likely retards bloom formation by slowing down the form V → VI transition via disruption of the effective packing of CB TGs into bilayers.

10.4 Chocolate Making

The basic processing steps necessary to develop the correct texture, flavour and CB fat crystal habit are (i) bulk ingredient mixing, (ii) refining, (iii) conching, (iv) tempering and (v) cooling. Prior to this, the cocoa must be harvested and treated so as to provide the desired starting materials (Beckett 2008).

10.4.1 Ingredient Mixing and Refining

The first step in making chocolate is the blending of ingredients, notably sugar, cocoa powder, the emulsifier and, of course, CB. These ingredients are sequentially weighed and mixed into a paste. These ingredients are blended and finely ground, during which time more CB is added. The chocolate ingredients are usually milled on a roll refiner, whose goal is to reduce the solid particles so that most are < 30 μm in size. Chocolate with larger particles leaves a gritty texture in the mouth, whereas particles that are too small will yield a texture that is pasty.

10.4.2 Conching

A conche is a scraped-surface mixer that optimises flavour development and turns the chocolate mass into a flowable liquid. Through shear and longitudinal mixing, acidic flavours and moisture in the cocoa mass are reduced. Upon entering the conche, not all sugar and cocoa particles will be coated with CB. Fat in the chocolate will be released from the agglomerated chocolate mass and spread to cover these particles so that they can flow easily. The final chocolate mass should have a viscosity deemed optimal for the ensuing tempering. Conching length will also play an influential role on the final smoothness, taste and quality of the chocolate. High-quality-chocolate conching is lengthy (e.g. 72 h), whereas lesser chocolates are conched 4–6 h. Conching is still not well understood, and the industrial time/temperature combinations used remain closely guarded secrets. Changes in conche

design and/or operating procedures may result in very different flavours and flow profiles. After the process is complete, the chocolate mass is stored at ~45–50 °C to ensure that no crystal or thermal memory remains.

10.4.3 Tempering

Using a well-defined temperature regime, the crystallisation behaviour of CB is controlled to develop form V nuclei and seed crystals. If crystallisation of the fat phase is uncontrolled, the final product will not possess acceptable organoleptic properties. Its surface and interior may then consist of fat crystals varying in polymorph and size (with some crystals visible to the naked eye), yielding a chocolate that lacks desirable gloss, texture and melting properties. Rather than having a melt-in-your-mouth character and a desirable snap, the chocolate may crumble and either be too soft or waxy in the mouth. In a typical tempering regime, the chocolate is initially maintained at 45–50 °C to fully melt all crystals and remove any crystal history. In the second stage, it is cooled to ~27 °C under agitation, which removes heat from the mixture and initiates crystallisation to promote the formation of unstable and stable crystal nuclei (i.e. forms II, IV and V). Afterwards, the chocolate is heated to ~31 °C to melt unstable polymorphs and ensure that only form V crystals remain. During the last stage, crystal growth is promoted under agitation and shearing. The temperatures mentioned will vary depending on the formulation of the chocolate, the type of tempering equipment used and the final application of the chocolate (e.g. enrobing vs moulded chocolate). This process can last from 10 to 12 min for moulded chocolates to 20–360 min for enrobing chocolates (Beckett 2008).

10.4.4 Moulding/Cooling/Storage

Chocolate is poured into preheated moulds that are vibrated to reduce air bubble formation. The chocolate sets in a cooling tunnel where temperature is meticulously controlled to ensure that no undue polymorphic transformations take place. As chocolate is very sensitive to temperature and humidity, subsequent storage is controlled (15–17 °C and relative humidity (RH) < 50 %).

10.5 Fat Bloom

This is the chief defect that afflicts chocolate confections. This physical imperfection makes the chocolate undesirable for consumers who expect a glossy surface and desirable colour. It is defined as the unwanted, uncontrolled recrystallisation or polymorphic transition of CB from form V crystals into form VI, normally caused

by the migration of lower-melting fats (e.g. in centre-filled products) and/or temperature fluctuations during storage. In its mildest form, it appears as an overall dulling of the chocolate surface. In its extreme form, the appearance of the chocolate deteriorates significantly with the development of distinct white patches. This defect is primarily a surface phenomenon that results from crystals measuring > 5 μm in length that diffuse light, yielding a greyish, chalky appearance. Such topographical changes are also indicative of significant changes in the bulk properties of the chocolate. There are different mechanisms that are thought to lead to bloom formation.

Mechanism 1 is related to the uncontrolled form IV → V polymorphic transition during tempering. This is a now a rare cause of bloom formation, as CB tempering is highly controlled. Mechanism 2 may lead to fat bloom due to the solid state form V → VI polymorphic transition. Similar to mechanism 1, contraction, polymorph packing density and migration will influence the possibility of bloom formation. This highly time- and temperature-dependent conversion occurs in properly tempered chocolate and may take months or years to manifest itself. In mechanism 3, the solid–liquid equilibrium in chocolate may impact the shelf life of the chocolate, particularly if it encounters temperature fluctuations. With slight temperature changes (e.g. ±2–3 °C), smaller or less dense fat crystals with lower melting points may melt and recrystallise in an uncontrolled manner, resulting in bloom crystals. With larger temperature fluctuations, well-tempered form V crystals may melt outright and recrystallise without retempering, and so form VI crystals will be promoted at the expense of form V crystals. This highly temperature-dependent process usually occurs once the chocolate has left the chocolate factory. Finally, mechanism 4 is limited to filled chocolates where the composition and melting properties of the fat phase in a soft centre filling substantially differ from that of the chocolate exterior. For example, chocolates with nut centres will bloom quite rapidly as the TGs in nuts (e.g. hazelnuts) are highly unsaturated and fully liquid at room temperature. The compositional gradient existing between the chocolate shell and the filling fat will lead to an exchange of material, as the fat phases attempt to reach compositional equilibrium.

10.6 Mixing Behaviour

A number of the aforementioned mechanisms will be influenced by the mixing behaviour between CB and other fats. Monotectic behaviour occurs when the higher-melting TGs of a fat are solubilised in liquid TGs. As a result, CB will be highly soluble in the TGs present in a filling fat, as they are normally liquid. Such behaviour is prevalent in mixed systems consisting of fats with widely different melting points and is considered unwanted.

In the chocolate itself, the phase behaviour of CB and other fats (i.e. milkfat, CBEs) must be understood and controlled to avoid bloom. If incompatibility between the TGs in the respective fats exists, rather than having an additive effect in terms of solid fat content (SFC), there will be a net lowering of the SFC when the fats are mixed. This is called a eutectic and may lead to bloom initiation, as the

higher liquid content will promote migration towards the surface of the chocolate, where uncontrolled crystallisation may occur.

10.7 Methods to Study the Microstructure of Chocolate

Many food companies are now realising the importance of microscopy-based approaches to optimise existing processes and to develop and control attributes in new food products, such as the spatial distribution of dispersed particulates, the morphology of crystals, droplet size distributions, etc. Microscopy techniques now used in both fundamental and applied research include polarised light microscopy to study fat crystal morphology and aggregation behaviour (Marangoni and McGauley 2003), fluorescence microscopy to study lipid migration (Marty et al. 2005), scanning electron microscopy (SEM) for the examination of crystal morphology and network structure (Kinta and Hatta 2006; Hicklin et al. 1985), magnetic resonance imaging to examine migration (Choi et al. 2007), atomic force microscopy (AFM) to investigate surface structure (Sonwai and Rousseau 2010; Smith and Dahlman 2005; Hodge and Rousseau 2002), laser microscopy to study surface roughness (Altimiras et al. 2007; Quevedo et al. 2005), confocal laser scanning microscopy (CLSM) to delineate the spatial distribution of particulates in chocolate (Auty et al. 2001; Dahlenborg et al. 2012) and X-ray tomography to assess structure in aerated confectionery products (Frisullo et al. 2010; Lim and Barigou 2004). Thus, from the standard light and electron microscopes of only a few decades ago, newer techniques have emerged and are increasingly being used in confectionery research.

The following section describes some microscopy techniques that may be used to characterise the microstructure of chocolate, specifically AFM, environmental scanning electron microscopy (ESEM), CLSM and optical profilometry. Though other techniques are certainly seeing use (e.g. magnetic resonance imaging), the present chapter focuses on these four techniques.

10.7.1 Atomic Force Microscopy

AFM belongs to a family of versatile instruments called scanning probe microscopes designed to measure the surface properties of materials. Its main use is to examine the surface morphology on a scale spanning from angstroms (e.g. carbon atoms) to ~100 μm (e.g. human hair). AFM has an effective magnification of range 500 to 10^8 times and offers resolution comparable to that of a transmission electron microscope. Unlike this technique, however, AFM generates images by 'feeling' the surface of a sample, using a sharp tip akin to a stylus on a record player. The term 'atomic force' results from its ability to measure forces in the range of interatomic forces in solids.

The anatomy of an AFM consists of three fundamental elements. The tip consists of an extremely sharp spike mounted onto the end of a cantilever. Tips are usually made from silicon or silicon nitride using semiconductor fabrication methods. The sharpness of the spike will strongly dictate the resolving ability of an AFM. The tip apex may be as small as 1 nm. It is the cantilever that allows the tip to move up or down and feel the contours of a sample's topography. Another important feature is the scanning mechanism, which controls the motion of the tip. The cantilever is controlled by a piezoelectric transducer capable of moving the tip at the atomic level in the *x-, y-* and *z-*. The third key element of an AFM is the detection mechanism. As an AFM tip scans the surface of a sample, its motion must be detected. The most common detection method is the optical lever system whereby a laser diode is focused onto the mirrored end of the cantilever. Deflections resulting from changes in tip–sample interactions change the reflection angle of the laser beam, and hence laser intensity, which is monitored by a position-sensitive detector capable of detecting angstrom-scale bending motions. The signal from the detector is converted to an image visible on a computer monitor where it can be digitally analysed. Besides imaging, sample–tip interactions are used to characterise force–distance relationships that exist where force measurements in the pico-Newton range are possible.

As an AFM generally has a *z*-axis deflection limit of ~10 μm, rough samples (e.g. very bloomed chocolate) cannot be imaged.

10.7.2 Environmental Scanning Electron Microscopy

ESEM is a technique capable of imaging non-conductive materials in their natural state. Quite comparable to high-vacuum SEM in many respects, the technique provides for neutralisation of electron-induced charge build-up by the ionisation of water vapour in the sample chamber. With ESEM, samples are not coated, and imaging is more dependent on sample rather than coating characteristics. Similar to SEM, an ESEM has a large depth of field, allowing a large amount of a sample to be in focus at one time.

SEM, and now ESEM, are instruments that see heavy usage in many research fields, including food science. The use of ESEM for chocolate research, however, has been limited, with little literature mentioning the use of this technique. SEM, on the other hand, has been used for decades. For example, in the 1970s SEM was used to investigate the different polymorphs of CB (Jewell 1972). More recently, ESEM and X-ray photoelectric spectroscopy were used to show that bloom composition on poorly tempered and well-tempered chocolate differed (James and Smith 2009).

10.7.3 Confocal Laser Scanning Microscopy

This established method is seeing increasing use in the food science and technology arena. In brief, CLSM represents the union of a centuries-old technique with much

more recent technology. Together, imaging software, fluorescent probes, and computer-controlled optical pathways have transformed the simple light microscope into a much more powerful technique. With CLSM, rather than using a lamp as with a conventional microscope, a laser source at a defined wavelength is focused by the objective lens onto a single point in the specimen plane. A subsequent X/Y raster scan of that plane produces an image. Through computer control, scans of a specific focal plane can be produced at set heights within the sample. This is one of the trademark features of CLSM—its capacity to obtain optical sections ('z-slices') of an image. By using image processing, sequential images can be assembled to yield 3-D representations of the structures studied. Reflected and fluorescent light (if the samples autofluoresce or if such stains are used) return via the illumination path and are focused at the confocal point located within a pinhole. Since the spot on the pinhole and the spot on the specimen are both located in the focal plane of the imaging lens, they are said to be confocal. These pinhole apertures limit the specimen focal plane to a confined volume of ~1 μm and block light from planes other than the focal plane. Relatively thick specimens (i.e. 100 μm) can thus be imaged by successively acquiring a series of thin sections (< 1 μm) along the optical (z) axis of the microscope.

10.7.4 Optical Profilometry

Though optical profilometry has been used in many fields to characterise the micron-scale topography of materials (e.g. microelectromechanical systems (MEMS), films, dermatology, concrete, etc.; Garbacz et al. 2006; Waits et al. 2005; Grove et al. 1989), very few published results describe its use for the study of food texture and topography. This technique provides rapid surface analysis by utilising light interferometry for high-resolution surface measurements (Wyant et al. 1984). In this technique, white light is focused on a sample using an interferometric lens that moves vertically through the focal plane. The light reflected from the surface recombines with a reference beam, and interference fringes are formed. The fringe pattern is captured on each pixel of a charge-coupled device (CCD) camera array and referenced to the vertical position of the lens, with the accompanying software generating a 2-D or 3-D profile. As it permits large scan sizes (e.g. ~3–4 mm^2), bigger surface features or periodicities are less likely to be overlooked than with AFM. However, optical profilometry performance somewhat depends on the reflectivity of the sample surface.

10.8 The Microstructure of Chocolate

To the naked eye, the surface of properly tempered chocolate should appear very smooth and glossy. At a microstructural level, it is rough and heterogeneous. As shown, the use of multiple microscopy techniques permits in-depth characterisation

of this soft material. The following sections highlight the microstructure of chocolate using AFM, CLSM, optical profilometry and ESEM.

10.8.1 Internal Microstructure of Chocolate

Chocolate is a multiphasic material whose internal structure is largely dictated by the crystallisation regime that the fat phase has undergone, the refining of the chocolate mass and, to a lesser extent, the conching that the dispersed particulates of sugar, cocoa and milk powder (if milk chocolate) have been subjected to. A simple means of assessing particle size in-situ is via CLSM. This technique often relies on fluorescent stains that contain fluorophores (the portion of the molecule responsible for fluorescence) for visualisation through differentiation of particles. Though very common in microbiology circles, the use of multiple stains sees comparatively little use in food science applications. Figure 10.1 shows the internal structure of milk chocolate recrystallised in the presence of two fluorescent stains, the oil-soluble Fluorol Yellow 088 and water-soluble Rhodamine B. Each possesses specific excitation and emission wavelengths, with the former preferentially partitioning towards more hydrophobic species, whereas the latter will be attracted to hydrophilic species within the chocolate. Clearly seen in the image is a network of individual particulates measuring 20–40 μm in length corresponding to the milk protein (blue), the fat network (yellow) and autofluorescent cocoa solids (red), with the dark regions representing the nonfluorescent sugar crystals.

If there is a disadvantage to CLSM in the context of chocolate microstructural analysis, it is that stains must be used. Stain incorporation is most easily achieved

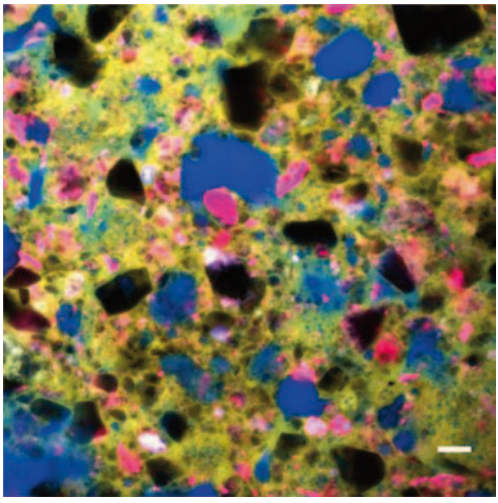

Fig. 10.1 Image of chocolate dual-stained with Fluorol Yellow 088 and Rhodamine B. Size bar = 10 μm

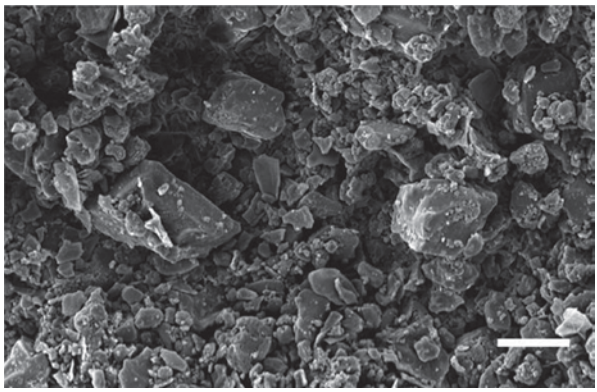

Fig. 10.2 Milk chocolate internal structure where the fat phase has been removed with petroleum ether. The dispersed particulates are clearly visible. Size bar = 20 μm

within melted chocolate that is then recrystallised. However, this process damages the innate spatial organisation of the structural elements generated during industrial chocolate making.

Of course, a clearer picture can be obtained by removing the fat phase and exploring the microstructure of the dispersed particulates in-situ. One approach is via solvent vapour extraction to remove sufficient CB from the chocolate for particulate network visualisation. Figure 10.2 shows the appearance of a defatted chocolate vis SEM. The backbone structure consisting of the dispersed particulates is clearly visible, with the sugar crystals being most obvious. These are surrounded by milk solids and cocoa powder particles, though it is difficult to differentiate between the two. In this regard, CLSM provides a distinct advantage over SEM given the specificity of the stains used.

10.8.2 The Surface Structure of Chocolate

To best understand the surface morphology of chocolate, a combined microscopy approach is best. In this section, AFM, optical profilometry and ESEM are used as complementary techniques to provide topographical information at different length scales. Figure 10.3 shows a 50 × 50 μm AFM scan of the surface structure of well-tempered commercial milk chocolate. A complex topography is visible, comprising a finely mottled, yet irregular texture, interspersed with obvious pits or pores. Furthermore, numerous embedded CB and sugar crystals are visible, partially covered by the continuous fat matrix.

Figure 10.4 shows a 20 × 20-μm AFM scan further exemplifying the presence of pores or pits on the surface of milk chocolate. A 2-D scan shows a pore at centre top (Fig. 10.4a) with the corresponding cross-sectional analysis revealing that it is 2–2.5 μm in depth (Fig. 10.4b). The surrounding surface morphology for this sample is of uniform roughness with the surface generally being no different in the immediate vicinity of the depression compared to the rest of the sample (Fig. 10.4c).

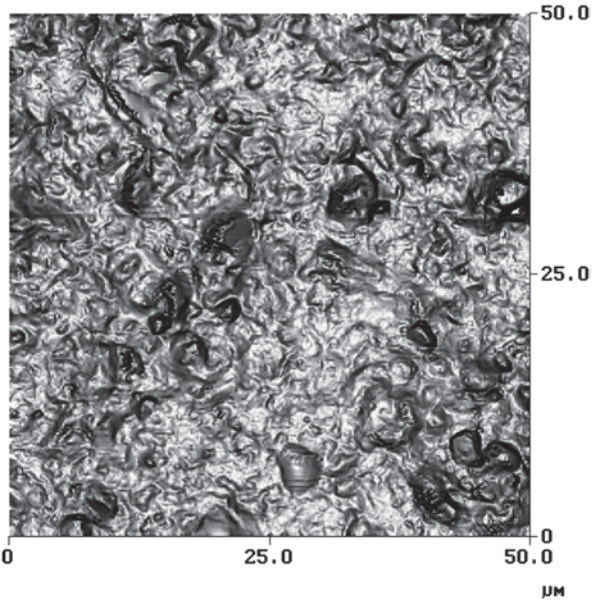

Fig. 10.3 Atomic force microscopy (AFM) images of milk chocolate surface showing a fine-textured surface. Scan size is 50 × 50 µm

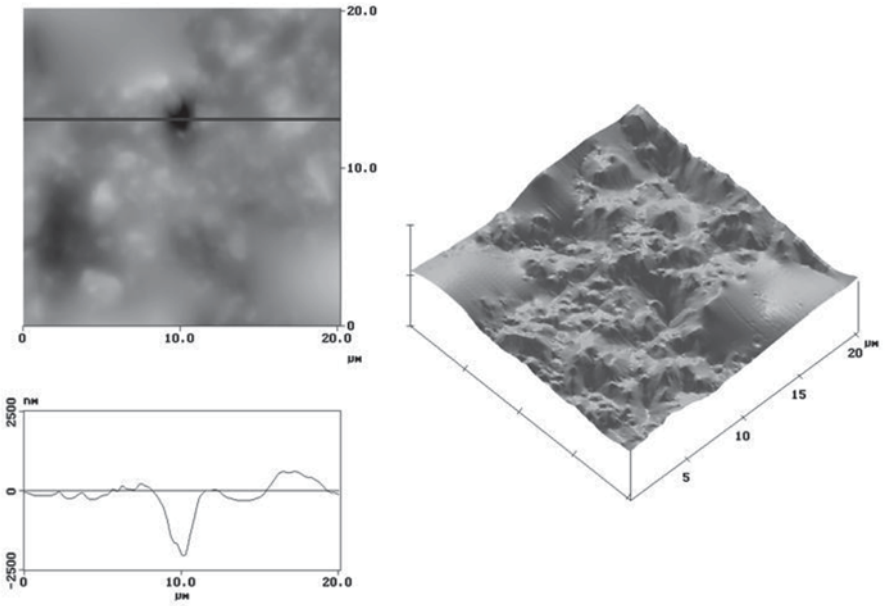

Fig. 10.4 Atomic force microscopy (AFM) images of milk chocolate surface showing fine-textured surface. **a** 2-D scan. **b** Cross-sectional analysis of a pore. **c** 3-D profile. Scan size is 20 × 20 µm

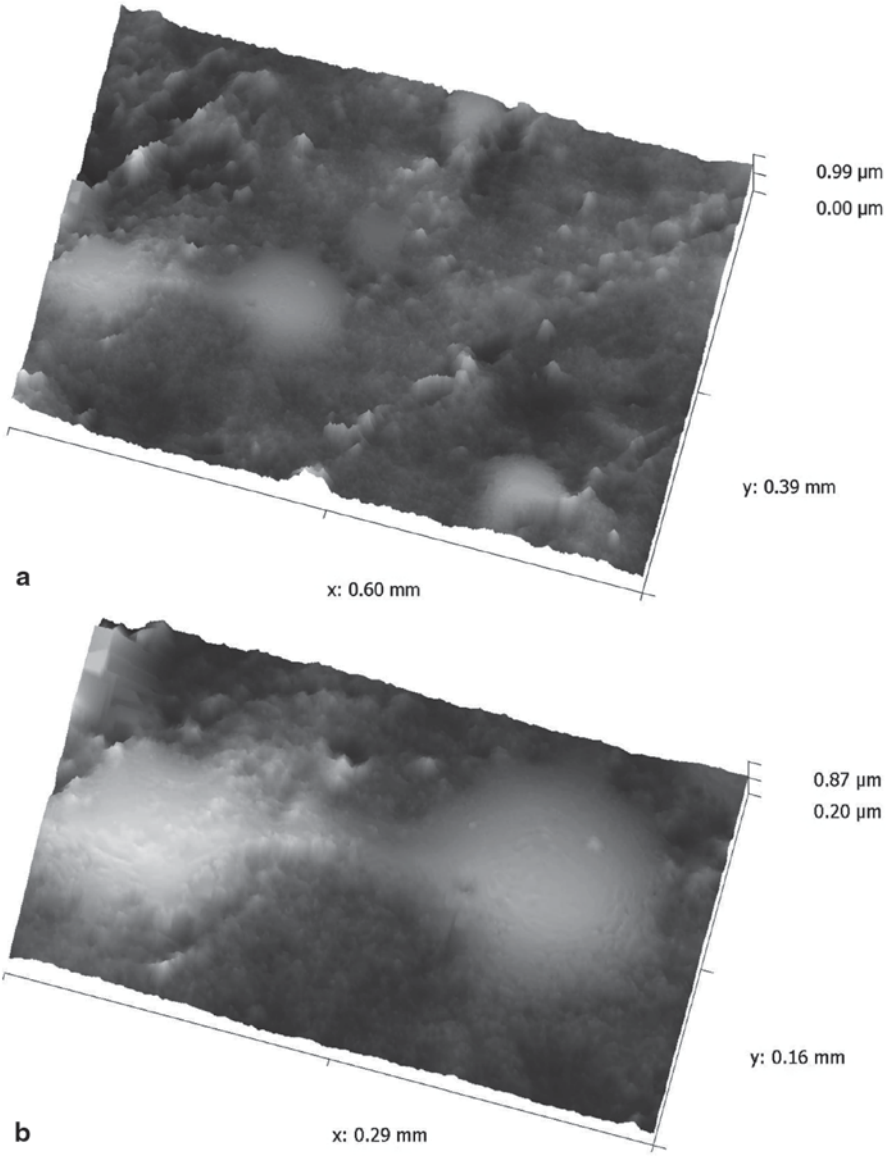

Fig. 10.5 Optical profilometry of the surface of poorly tempered chocolate. **a** 600 × 390-µm profile. **b** Close-up of the smooth regions visible at the *left* of the top image (290 × 160 µm)

However, an intriguing feature is the presence of distinct smooth zones. Extensive analysis has shown that these circular welled zones range in diameter from a few microns to upwards of 50 µm.

Optical profilometry yields microstructural information at a larger length scale. For example, Fig. 10.5a shows a 600 × 390 µm image of poorly tempered chocolate.

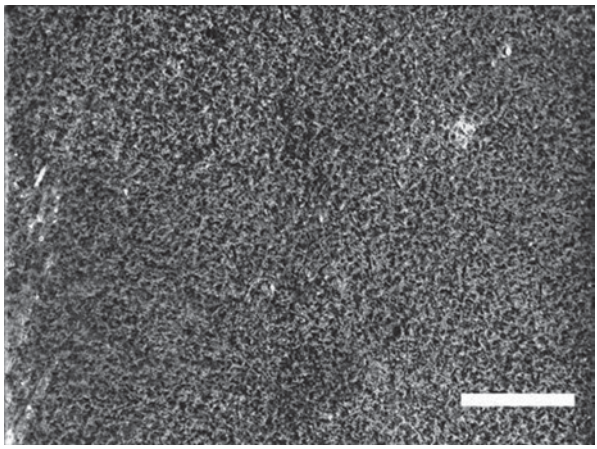

Fig. 10.6 Surface structure of plain chocolate as viewed using environmental scanning electron microscopy (ESEM). Note the presence of an extensive number of pores. Size bar = 100 μm

There are a number of surface features visible, including jagged ridges, smooth 'valleys', surface mounds and the possibility of surface pores. In this regard, the ability to provide a wide-scale perspective permits clear delineation of the variety of surface features present. Figure 10.5b shows a close-up of the smooth regions visible at the left of Fig. 10.5a (290 × 160 μm). These are thought to result from chocolate network contraction during cooling and the subsequent expulsion of lower-melting fat species through network imperfections, thereby resulting in 'softer' regions on the chocolate surface.

Finally, the surface of chocolate as imaged with ESEM (Fig. 10.6) shows a highly porous topography where the dark areas correspond to pores with diameters up to ~10 μm. Overall, these results clearly indicate that the surface of chocolate is porous, which is contrary to previous research where it was stated that chocolate does not contain surface pores with diameters greater than 0.4 μm (Loisel et al. 1997). Divergences in these results may be due to at least two factors: (i) the different techniques used (microscopy vs porosimetry) or (ii) chocolates of different origins and/or processed under dissimilar conditions. Numerous microscopy scans also indicate that pores likely number in the hundreds per cm^2, with these being randomly distributed on the surface of milk chocolate.

We now consider how pores form. During chocolate manufacture, tempering ultimately results in the contraction of the chocolate and the possible generation of pores and hairline cracks. Too fast a cooling rate may introduce these attributes on the chocolate, which in turn, may promote bloom formation. Thus, homogeneous heat release, resulting from even cooling, may reduce temperature gradients within chocolate (e.g. between the cooling and air-exposed surfaces), delaying blooming. A second possibility is that these pores are in fact small air bubbles (Dahlenborg et al. 2012). Though there is no conclusive evidence against this, the great variability in morphology and locations (e.g. beside a crystal) does not lend itself to this hypothesis. Furthermore, the cavities are not hemispherical as one would likely expect with bubbles.

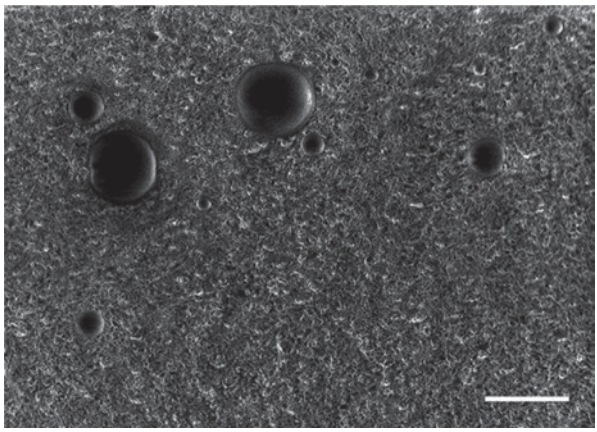

Fig. 10.7 Presence of air bubbles within chocolate. Note the large size distribution. Size bar = 250 μm

By manually snapping chocolate in two, air bubbles are seen within chocolate. With the broken face exposed, ESEM shows numerous air bubbles ranging in diameter from a few microns to ~0.5 mm (Fig. 10.7). These are likely the result of air incorporation in the chocolate during conching/mixing. Then, during moulding of the chocolate, as the CB solidifies, the air bubbles become entrapped within the matrix. Given their high internal pressure, they maintain their shape, as the fat phase crystallises around them. Large air bubbles are generally considered a sensory defect.

10.8.3 Post-processing Changes in Chocolate Microstructure

Most adverse changes take place in chocolate during post-processing storage where the manufacturer has no control over what happens to the chocolate. Bloom formation is most often generated due to mechanisms 3 and 4 mentioned earlier. This section is broken into three subsections: (i) the natural evolution in the microstructure of chocolate as a function of storage time, (ii) effects of temperature cycling, and (iii) impact of soft centre fillings on chocolate bloom.

10.8.3.1 Shelf Life of Chocolate

The shelf life of chocolate is dictated by when its organoleptic properties are no longer appealing to the consumer. Fat bloom is the leading cause of deterioration in chocolate. It leads to undesirable changes in appearance and is often associated with a slight hardening of the texture of the chocolate and an inappropriate melting profile, given form VI's higher melting point. Figure 10.8 shows two views of the surface topography of milk chocolate stored 30 weeks at room temperature. These images substantially differ from Fig. 10.3 where a finely mottled surface is seen. Figure 10.8a shows the topography of chocolate with small ridges and valleys. An

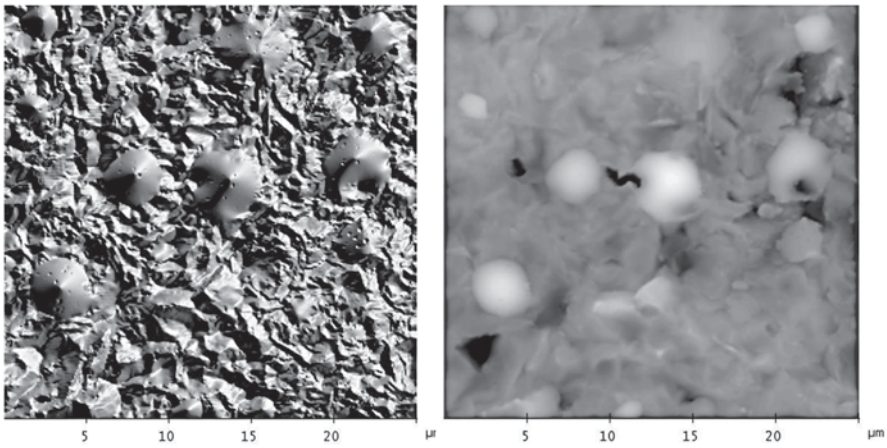

Fig. 10.8 Topography (**a**) and height (**b**) atomic force microscopy (AFM) scans of 30-week-old tempered chocolate. Scan size is 25 × 25 µm

intriguing feature is the formation of randomly distributed amorphous regions on the surface of the chocolate (as discussed earlier). The height image (Fig. 10.8b) shows that the amorphous zones protrude outwards from the surface of the chocolate. Also visible are deep pits (in black), at least several microns in depth. In certain cases, surrounding these amorphous zones are crystals that appear to grow forth from them with time. Figure 10.9 shows such an example where an amorphous zone acts as a 'nursery' for crystal growth. Compared with Fig. 10.5, where smooth

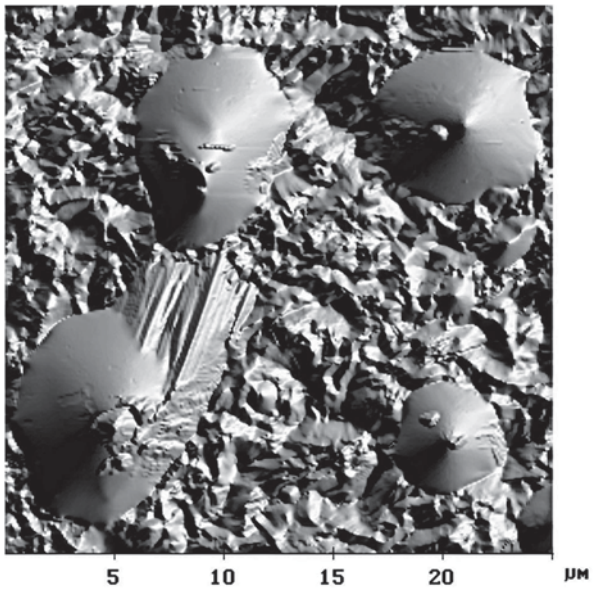

Fig. 10.9 Topography atomic force microscopy (AFM) scan of 30-week-old tempered chocolate showing evidence of crystal growth emanating from a welded zone. Scan size is 25 × 25 µm

welled zones are present, in Fig. 10.9 apparent solidification has taken place suggesting that this chocolate is not fresh, hinting that these welled zones may serve as micro-scale shelf life indicators.

10.8.3.2 Temperature Cycling

In properly tempered and stored chocolate, visible fat bloom may take months or years to set in. Temperature cycling has been used to promote polymorphic transitions in crystal structures, often in pharmaceutical applications and, to a lesser extent, in food products. With respect to chocolate, this approach has been used to accelerate fat bloom onset and growth (Hachiya et al. 1989; Bricknell and Hartel 1998). By tailoring the temperature gradients to take into account the distinct melting points of CB's key polymorphs, it is possible to determine how controlled recrystallisation and melting may significantly reorganise chocolate microstructure. The next section reports the influence of large temperature cycles on the surface microstructure of chocolate as observed via optical profilometry.

Larger temperature variations in storage temperatures (i.e. greater than 10 °C) can substantially accelerate the form V → VI polymorphic transition, particularly when such transitions and/or TG melting points are included within the temperature range of a fluctuation along with the repeated dissolution and (re)crystallisation of certain lipid species in the fat phase. Another element to consider is the exothermic nature of recrystallisation and associated polymorphic transitions, which may liquefy some of the surrounding fat around the crystals. Both scenarios can result in more liquid fat in the immediate periphery of existing crystals, leading to an acceleration of polymorphic transitions and evolution in microstructure.

Surface roughness, which may be considered an indicator of fat bloom formation, can be ascertained with techniques such as AFM and optical profilometry. The topography of a material such as chocolate can be described by numerous textural parameters, namely roughness, waviness (upon which roughness is superimposed), surface anisotropy (i.e. dominant direction or pattern in surface texture), atomic/molecular roughness and unique errors (e.g. scratches, imperfections; Howell and Behrends 2006).

Figures 10.10 and 10.11 show the impact of temperature cycling to 34 °C, with this temperature chosen, as it is above the form V polymorph melting point. Visually, cycling to this temperature did not lead to immediate visual bloom, though significant effects on microstructure and fat phase melting behaviour were noted. As viewed with optical profilometry, the initial chocolate topography was lightly mottled and consisted of small asperities (Fig. 10.10). As a result of cycling to 34 °C, the surface roughness of all samples increased, with the smallest rise seen after 1 cycle. Decomposition of the roughness into low- and high-frequency components revealed a significant contribution of waviness (the low-frequency component) to overall roughness (Fig. 10.11). Furthermore, with the fat phase fully molten, the backbone structure consisting of the dispersed particulates also contributed to overall roughness. Clearly, significant microstructural changes and deformation

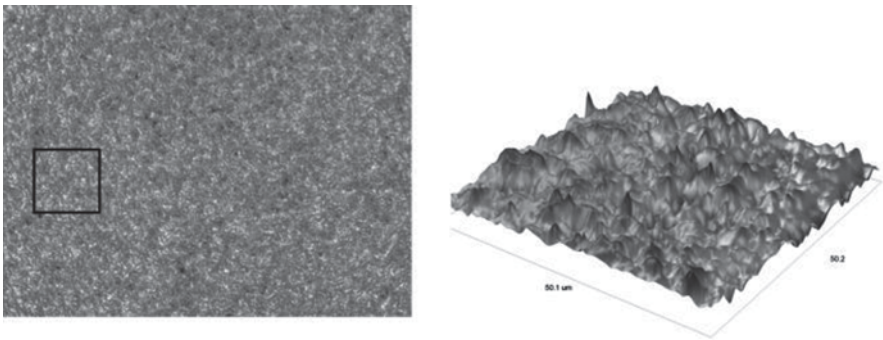

Fig. 10.10 Topography optical profilometry scan of properly tempered chocolate. Scan size is 290 × 160 μm

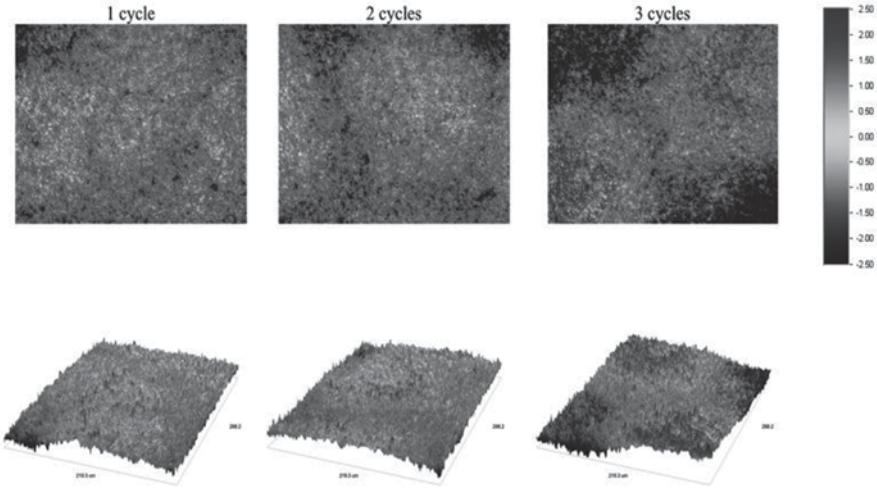

Fig. 10.11 Optical profilometry scan of milk chocolate temperature-cycled three times between 20 and 34 °C. *Top row*: 2-D scans; *bottom row*: corresponding 3-D scans. Scan size is 288 × 219 μm

take place within chocolate as a result of temperature fluctuations prior to the onset of visible surface fat bloom.

10.8.3.3 Influence of Microstructure of Diffusion of Soft Centre Fillings

The next section outlines the role of migrant fats in modifying the microstructure of chocolate. Initially, the ingress of hazelnut oil present within a simulated soft centre filling into a dark chocolate matrix stored at 26 °C is described. Subsequently, an example of the high-magnification morphology of fat bloom is shown, along with some mechanistic considerations regarding the transport mechanism of migration, crystallisation and bloom formation.

During the storage of filled confections, an exchange of TGs between the chocolate and filling may result in softening of the chocolate and a hardening of the filling, a flattening of the taste and often the formation of surface fat bloom (Miquel et al. 2001; Miquel and Hall 2002; Ziegleder and Schwingshandl 1998). Accounting for these phenomena, it has been proposed that an insufficient number of metastable form V crystals formed during tempering may lead to liquid fat being pumped to the surface, particularly if there are cracks and crevices present. Furthermore, given that less stable crystals will have lower melting points, they will be more likely to separate from the crystal network and migrate to the surface. Such melting may occur via an increase in temperature or from the energy released during recrystallisation of CB into a more stable polymorph. Liquid fat migration may also result from an increase in volume when CB melts, which forces liquid fat through pores and microfractures formed during crystallisation.

Mechanistically, diffusion has been the preferred theory to explain lipid migration in chocolate products (Miquel and Hall 2002; Ziegleder and Schwingshandl 1998). Initially, diffusion was thought to result from the difference in liquid fat content between the filling and the coating but has now been ascribed to a concentration gradient of TGs within some regions of the product (Ghosh et al. 2002). The exact mechanism(s) of fat migration in chocolate products still remain poorly understood, though recent progress is certainly being made (Motwani et al. 2011; Van der Weeën et al. 2013; Galdámez et al. 2009).

Insights on the influence of migrants on chocolate microstructure may be obtained via ESEM. Figure 10.12 demonstrates the influence of a filling fat on the surface and internal structure of a chocolate ‘shell’ with a filling fat composed of oil and icing sugar where microstructure was evaluated for 40 days. The surface of a fresh chocolate (Fig. 10.12a) is highly porous, with numerous pores present over the entire surface of the chocolate (similar to Fig. 10.6). After 40 days (Fig. 10.12b), the surface of the chocolate is fully covered in large crystals and was very soft and difficult to handle. These results demonstrated that the presence of a migrant fat substantially alters the crystallisation kinetics of the fat phase. A high-magnification view reveals the presence of a cone-like mound as well as a large individual crystal present on the surface of chocolate stored against a filling fat (Fig. 10.13). Cones observed were large, with some measuring over 100 μm in height. Similarly, sharp individual crystals protruded from the surface of the chocolate. Both of these may be considered defects that eventually lead to visible fat bloom once they attain a certain size, as they hamper the appearance and texture of the final product.

Previously, it was shown that chocolate is a particulate material with sugar crystals, milk protein and cocoa solids interspersed within a continuous fat phase consisting of crystalline and liquid fat (Figs. 10.1 and 10.2). In a soft-centre confection, the oil present in the filling will promote solubilisation of the CB/fat phase in the shell, thereby increasing the liquid oil content in the chocolate via an additive effect and through solid fat solubilisation. With increased fluidity, the lipid phase will be free to travel throughout the chocolate shell leading to a rearrangement of the network structure, not only in terms of solid crystal morphology and polymorphic behaviour but also in the spatial distribution of the cocoa and sugar particles. The cone-like structures almost certainly consist of a mixture of the filling fat and the fat

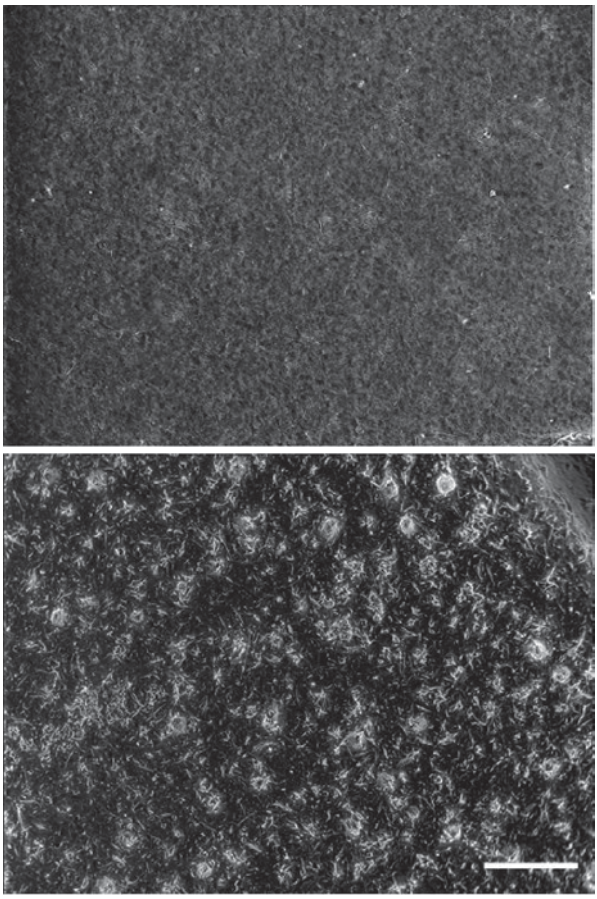

Fig. 10.12 Environmental scanning electron microscopy (ESEM) showing effect on chocolate surface topography of a filling fat–hazelnut oil mixture after 40 days. **a** Tempered chocolate on day 0. **b** Chocolate stored 40 days against filling. Size bar = 250 μm

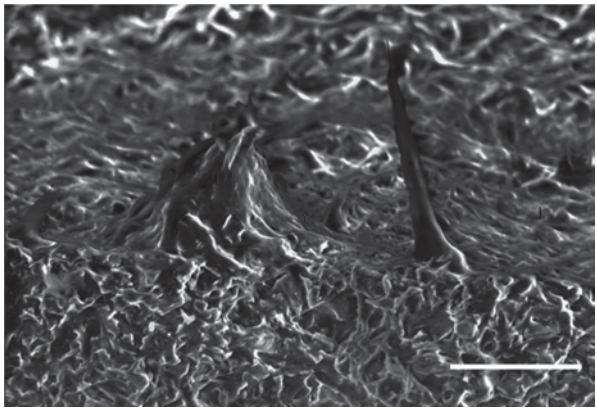

Fig. 10.13 Edge-on view showing crystal growth on the surface of chocolate stored 40 days at 26 °C. Note distinct morphologies. Size bar = 50 μm

in the shell, notably CB. This is a result of lipid migration from the filling through the chocolate shell, which, as it travels, solubilises some of the hard fat phase. This fluid mixture will then appear at the surface of the chocolate and manifest itself as cones. By contrast, individual crystals will consist of CB that has undergone uncontrolled recrystallisation. In this context, particle size has been shown to influence the rate of oil migration and fat bloom development in chocolate shells (Dahlenborg et al. 2015). Using non-fat particles in the chocolate (sugar and cocoa particles) of 15, 22 or 40 μm in size, the former showed higher rates of oil migration as well as the earliest development of surface fat bloom. This suggested that larger specific surface areas facilitated migration of filling oil, possibly due to a more heterogeneous and coarser crystal network with higher permeability.

10.9 Conclusion

Chocolate microstructure is integral to understanding and controlling chocolate's desirable sensory attributes. It is also central to elucidating the complex phenomena that lead to fat bloom initiation and propagation. In the future, new processing methods will continue to improve the way that chocolate is made, particularly as processors vie to ensure quality and minimise 'post-factory' deleterious changes such as bloom. In this context, the importance of microstructure should not be understated. Its role in ensuring top-quality chocolate will grow, particularly as processors continue to realise its importance in the structure–functionality relationship of chocolate.

Acknowledgements The author recognises funding from various government and industrial sources that have made this work possible. The contributions of Drs. Supratim Ghosh, Nicole Green and Sopark Sonwai are acknowledged.

References

Altimiras P, Pyle L, Bouchon P (2007) Structure–fat migration relationships during storage of cocoa butter model bars: bloom development and possible mechanisms. J Food Eng 80(2):600–610

Auty M et al (2001) Development and application of confocal scanning laser microscopy methods for studying the distribution of fat and protein in selected dairy products. J Dairy Res 68(3):417–427

Beckett ST (2008) The science of chocolate. 2nd edn. RSC Publishing

Bricknell J, Hartel RW (1998) Relation of fat bloom in chocolate to polymorphic transition of cocoa butter. J Am Oil Chem Soc 75(11):1609–1615

Choi YJ et al (2007) Oil migration in chocolate. Appl Magn Reson 32(1–2):205–220

Dahlenborg H et al (2012) Study of the porous structure of white chocolate by confocal Raman microscopy. Eur J Lipid Sci Technol 114(8):919–926

Dahlenborg H, Millqvist-Fureby A, Bergenståhl B (2015) Effect of particle size in chocolate shell on oil migration and fat bloom development. J Food Eng 146:172–181

Deffense E (1993) Milk fat fractionation today: a review. J Am Oil Chem Soc 70(12):1193–1201

DeMan J (1961) Physical properties of milk fat. Some factors influencing crystallization. J Dairy Res 28(2):117–122
deMan JM (1992) X-ray diffraction spectroscopy in the study of fat polymorphism. Food Res Int 25(6):471–476
Frisullo P et al (2010) Microstructural characterization of multiphase chocolate using X-ray microtomography. J Food Sci 75(7):E469–E476
Galdámez JR et al (2009) Oil migration in chocolate: a case of non-Fickian diffusion. J Food Eng 92(3):261–268
Garbacz A, Courard L, Kostana K (2006) Characterization of concrete surface roughness and its relation to adhesion in repair systems. Mater Charact 56(4–5):281–289
Garti N, Binyamin H, Aserin, A (1998) Stabilization of water-in-oil emulsions by submicrocrystalline α-form fat particles. J Am Oil Chem Soc 75(12):1825–1831
Ghosh V, Ziegler GR, Anantheswaran RC (2002) Fat, moisture, and ethanol migration through chocolates and confectionary coatings. Crit Rev Food Sci Nutr 42(6):583–626
Grove GL, Grove MJ, Leyden JJ (1989) Optical profilometry: an objective method for quantification of facial wrinkles. J Am Acad Dermatol 21(3):631–637
Hachiya I, Koyano T, Sato K (1989) Seeding effects on solidification behavior of cocoa butter and dark chocolate. I. Kinetics of solidification. J Am Oil Chem Soc 66(12):1757–1762
Hicklin J, Jewell G, Heathcock J (1985) Combining microscopy and physical techniques in the study of cocoa butter polymorphs and vegetable fat blends. Food Microstruct 4(2):241–248
Himawan C, Starov VM, Stapley AGF (2006) Thermodynamic and kinetic aspects of fat crystallization. Adv Colloid Interface Sci 122(1–3):3–33
Hodge SM, Rousseau D (2002) Fat bloom formation and characterization in milk chocolate observed by atomic force microscopy. J Am Oil Chem Soc 79(11):1115–1121
Howell D, Behrends B (2006) A review of surface roughness in antifouling coatings illustrating the importance of cutoff length. Biofouling 22(5–6):401–410
James BJ, Smith BG (2009) Surface structure and composition of fresh and bloomed chocolate analysed using X-ray photoelectron spectroscopy, cryo-scanning electron microscopy and environmental scanning electron microscopy. LWT—Food Sc Technol 42(5):929–937
Jewell GG (1972) Some observations of bloom on chocolate. Int Choc Rev 27(6):161–162
Kinta Y, Hatta T (2006) Composition, structure, and color of fat bloom due to the partial liquefaction of fat in dark chocolate. J Am Oil Chem Soc 84(2):107–115
Lim KS, Barigou M (2004) X-ray micro-computed tomography of cellular food products. Food Res Int 37(10):1001–1012
Lipp M, Anklam E (1998) Review of cocoa butter and alternative fats for use in chocolate—Part A. Compositional data. Food Chem 62(1):73–97
Lipp M et al (2001) Composition of genuine cocoa butter and cocoa butter equivalents. J Food Compos Anal 14(4):399–408
Loisel C et al (1997) Fat bloom and chocolate structure studied by mercury porosimetry. J Food Sci 62(4):781–788
Lonchampt P, Hartel RW (2004) Fat bloom in chocolate and compound coatings. Eur J Lipid Sci Technol 106(4):241–274
Marangoni AG, McGauley SE (2003) Relationship between crystallization behavior and structure in cocoa butter. Cryst Growth Des 3(1):95–108
Marty S et al (2005) Monitoring and quantifying of oil migration in cocoa butter using a flatbed scanner and fluorescence light microscopy. Food Res Int 38(10):1189–1197
Miquel ME, Hall LD (2002) Measurement by MRI of storage changes in commercial chocolate confectionery products. Food Res Int 35(10):993–998
Miquel ME et al (2001) Kinetics of the migration of lipids in composite chocolate measured by magnetic resonance imaging. Food Res Int 34(9):773–781
Motwani T, Hanselmann W, Anantheswaran RC (2011) Diffusion, counter-diffusion and lipid phase changes occurring during oil migration in model confectionery systems. J Food Eng 104(2):186–195

Quevedo R et al (2005) Surface roughness during storage of chocolate: fractal analysis and possible mechanisms. J Am Oil Chem Soc 82(6):457–462
Smith PR, Dahlman A (2005) The use of atomic force microscopy to measure the formation and development of chocolate bloom in pralines. J Am Oil Chem Soc 82(3):165–168
Sonwai S, Rousseau D (2010) Controlling fat bloom formation in chocolate—impact of milk fat on microstructure and fat phase crystallisation. Food Chem 119(1):286–297
Stewart I, Kristott J (2004) European Union chocolate directive defines vegetable fats for chocolate. Lipid Technol 16:11–14
Van der Weeën P et al (2013) A discrete stochastic model for oil migration in chocolate-coated confectionery. J Food Eng 119(3):602–610
Waits CM et al (2005) Microfabrication of 3D silicon MEMS structures using gray-scale lithography and deep reactive ion etching. Sens Actuators A: Phys 119(1):245–253
Wille RL, Lutton ES (1966) Polymorphism of cocoa butter. J Am Oil Chem Soc 43(8):491–496
Wilson E (1999) Chocolate, the 5% option… What if? Manufact Confect 79(11):47–51
Wyant J et al (1984) An optical profilometer for surface characterization of magnetic media. ASLE Trans 27(2):101–113
Ziegleder G, Schwingshandl I (1998) Kinetik der Fettmigration in Schokoladenprodukten. Teil III: Fettreif. Fett—Lipid 100:411–415

Chapter 11
Physical-Bioimaging Characterization of Nuts

Yang Tao, Xin Chen and Lu Jiang

11.1 Introduction

There are many kinds of nuts. In industrial-scale processing of nut food grades, the major tasks are to separate the nutmeats from their shells and sort them into quality grades. The finished products, either nutmeats or shells, can be used for food or industrial materials. The nutmeats are found in value-added foods such as ice cream or baked goods, while nutshells, such as those of walnuts, are useful for industrial polishing particles. When commercializing nutmeats, nuts are often characterized, sorted, and graded by their quality. Quality evaluation by sizes is usually simple. However, assessment on food safety for biological and physical hazards of nutmeats can be a challenge that goes beyond simple visual inspection.

Physical hazards include nut fragments, which are pieces of shells or foreign materials. Hard nuts and sharp fragments, such as walnut shell fragments, may pose a danger to teeth and a choking hazard for small children and the elderly. Mechanical and electronic methods are used for shell fragment removal. However, challenges exist in ensuring that the final nutmeat product is free of shell fragments. Imaging techniques are used to detect and sort out the fragments, though challenges still exist.

Y. Tao (✉) · X. Chen
Bioimaging and Machine Vision Labs, University of Maryland, 1426 Building 142, College Park, MD 20742, USA
e-mail: ytao@umd.edu

L. Jiang
Department of Radiology and Oncology, Johns Hopkins University, Baltimore, MD, USA

N. Sozer (ed.), *Imaging Technologies and Data Processing for Food Engineers,*
Food Engineering Series, DOI 10.1007/978-3-319-24735-9_11

11.2 Imaging Recognition of Physical Hazard in Nut Meats

Optical imaging techniques offer fast ways of high-throughput inspections by scanning materials on a moving conveyor. For varieties where the nut meat and shell have distinctive color contrasts, traditional color or near-infrared (NIR) imaging methods can be used to differentiate the shell fragments from the meat stream. However, for some nuts such as black walnuts, the nut meat and interior shell has little or no difference to the naked eye, mostly because the chemical compositions of the nutmeat skin and the inner surface membrane of the shell in contact with the meat are similar. Therefore, imaging characterization of the nutmeat and inner shell in these circumstances poses greater difficulties.

In this section, we will introduce an imaging modality using hyperspectral fluorescence analysis to classify the nut and shell fragments of black walnuts. The problem domain on imaging detection of black walnut is believed to be more complicated than most other nuts. Thus, the method herein may be applicable toward detecting other difficult-to-recognize nut categories or species.

11.2.1 Hyperspectral Fluorescent Imaging Analysis of Black Walnuts

Differentiating black walnut shell fragments from nutmeat is a challenging task even to the trained eye, because the two usually have very similar patterns in size, color, or texture. Figures 11.1 and 11.2 illustrate this similarity. Traditional optical imaging technologies (visible, infrared, backlighting, etc.) lack sufficient differen-

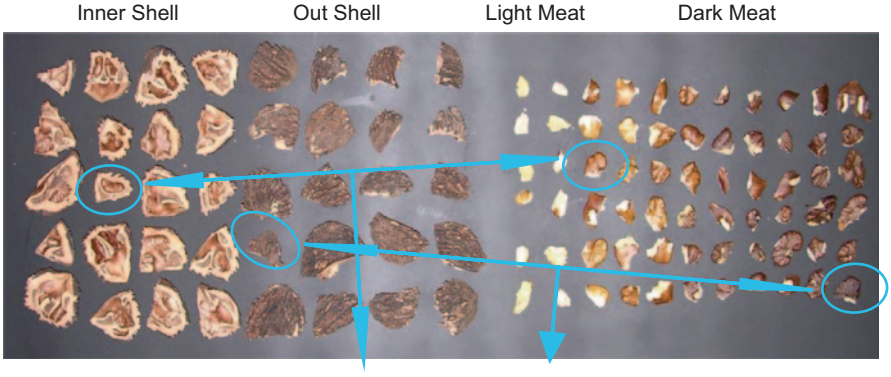

Similar patterns, though hard to distinguish from one another based on visible information.

Fig. 11.1 Four categories (inner and outer shell fragments, light and dark meats) have very similar patterns in size, color, or texture. Notice the similar patterns in the *circles*. All sizes are random after cracking the shells

Fig. 11.2 Machine-cracked black walnuts. *Left:* cracked nuts, *Right:* nutmeat. Visual sorting is very eye-intensive. Machine-cracked black walnuts were ready to use, but the broken kernels quickly oxidized within weeks

tiable information to classify between walnut shell and meat, and therefore are not solutions for the aforementioned problem.

We developed a hyperspectral fluorescence imaging approach to address this challenging problem. Figure 11.3 gives the spectral responses to four walnut sample categories, i.e., light meat, dark meat, inner shell, and outer shell. In the lower spectral range, especially 425–470 nm, differences exist among all four categories, while in the higher spectral range of 560–695 nm, significant differences appeared between light meat and other samples.

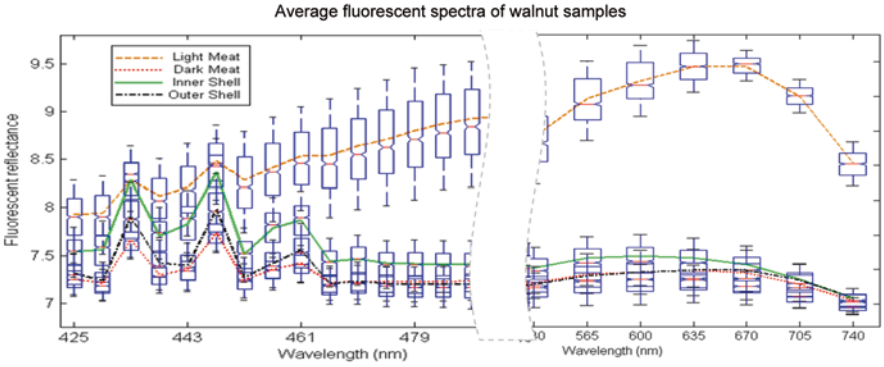

Fig. 11.3 Fluorescent spectral responses of four sample categories, averaged over 5496 data samples, where each pixel is represented by a 79-dimensional vector

11.2.2 Hyperspectral Detection Algorithms

Hyper-mixture model (HMM), Gaussian mixture model (GMM; Jiang et al. 2007b), and kernel function-based support vector machine (KF-SVM) classifiers were found effective as the base of our detection algorithm development. Here, we emphasized on the SVM approach for the object-based recognition (see results in 11.2.3 and 11.2.4). For the reviewer's convenience, this approach is briefly described herein.

The Kernel Function and Support Vector Machine (SVM) Classifiers The SVM classifier is expected to find the optimal hyperplane as a decision surface that correctly separates the sample data points from different classes (walnut shell and meat in this case), while maximizing the margins from the hyperplane to each class. The optimal hyperplane, *h,* that is searched in the input space can be defined by Eq. (11.1):

$$h = \Omega^T x + b \tag{11.1}$$

where x is the sample set including walnut meat and shell pixels, called input vector of the sample, Ω is the adaptable weight vector, b is the bias, and T is the transverse operator.

Suppose the input space vector $x_i \in \Re^n$, $i = 1, 2 \ldots l$ with its corresponding class label $y_i \in \{+1, -1\}$ in the two-class case, when $y_i = 1$ means the pixel belongs to meat category, otherwise when $y_i = -1$ means the pixel belongs to shell category, and l is the number of total input pixels. If all data points can be separated by a hyperplane, Eq. (11.1) must subject to the following condition:

$$y_i[(\Omega^T \cdot x_i + b] - 1 \geq 0. \tag{11.2}$$

According to Eqs. (11.1) and (11.2), the maximization problem was equal to solve the following problem:

$$\min \frac{1}{2}\|\Omega\|^2 = \frac{1}{2}(\Omega^T \cdot \Omega) \tag{11.3}$$

$$\text{Subject to } y_i[(\Omega^T \cdot x_i + b] - 1 \geq 0$$

Further, we can derive the following equation by using Lagrange multiplier method:

$$\max[\sum_{i=1}^{l} \alpha_i - \frac{1}{2}\sum_{i,j=1}^{l} \alpha_i \alpha_j y_i y_j (\Omega_i^T \Omega_j)] \tag{11.4}$$

$$\text{Subject to} \sum_{i=1}^{l} y_i \alpha_i = 0, \qquad \alpha_i \geq 0, i = 1, \cdots l$$

If the data points from different classes are not separable by a single hyperplane, that is, Eq. (11.2) does not hold for all data points, we need to add a slack variable into Eq. (11.2) to solve the classification problem. According to Eqs. (11.2, 11.3 and 11.4), the maximization problem above was equivalent to solve the following problem:

$$\min_{\Omega,b,\xi} \frac{1}{2}\Omega^T\Omega + C\left(\sum_{i=1}^{l} \xi_i\right) \tag{11.5}$$

$$\text{Subject to } 0 \le \alpha_i \le C, i = 1,\cdots,l$$

Where ξ_i is the slack variable, C is a user-specified positive parameter, and Ω is the weight vector.

To solve the maximization problem between walnut meats and walnut shells, a kernel function is introduced to the SVM (Jiang et al. 2007). The kernel function implicitly maps the input space, which may not be linearly separable, into an arbitrary high-dimensional feature space that can be linearly separable. Based on Eqs. (11.4) and (11.5), the maximization problem was equal to solve the following primal convex problem:

$$\min_{\Omega,b,\xi} \frac{1}{2}\Omega^T\Omega + C\left(\sum_{i=1}^{l} \xi_i\right) \tag{11.6}$$

$$\text{Subject to } y_i(\Omega^T \phi(x_i) + b) \ge 1 - \xi_i, \xi_i \ge 0, i = 1,\cdots,l$$

By mapping function ϕ, the input vector x_i is mapped from the input space $\Re^n$ into a higher dimensional feature space F. Thus, its corresponding dual problem is:

$$\min_{\alpha} \frac{1}{2}\alpha^T Q\alpha - e^T\alpha \; 0 \le \alpha \le C, i = 1,\cdots,l \tag{11.7}$$

$$\text{Subject to } y^T\alpha = 0$$

Where e is the vector of all ones, Q is an l by l positive semi-definite matrix and can be defined as:

$$Q_{ij} = y_i y_j K(x_i, x_j) \tag{11.8}$$

where $K(x_i, x_j) \equiv \phi(x_i)^T \phi(x_j)$ is the kernel matrix calculated by a specified kernel function $k(x, y)$, and subject to Mercer's condition, namely if for all $\varphi(x) \ne 0$ and $\int \varphi^2(x)\mathrm{d}x < \infty$, then $\iint K(x, x')\varphi(x)\varphi(x')\mathrm{d}x\mathrm{d}x' > 0$. α can be obtained by solving this dual problem.

Assuming the training vectors x_i were projected into a higher dimensional space by mapping φ, then the discriminant function of SVM was shown as follows:

Table 11.1 Three common kernel functions

Kernel name	Kernel equations
Polynomial kernel	$k(x,y)=<x,y>^{d}, \quad d \in R$
Gaussian kernel	$k(x,y)=exp(-\frac{\|x-y\|^2}{2\sigma^2}), \quad \sigma>0$
Sigmoid kernel	$k(x,y)=tanh(\kappa<x,y>+\vartheta) \quad \kappa>0, \vartheta \geq 0$

$$f(x)=\operatorname{sgn}(\sum_{i=1}^{l} y_i \alpha_i K(x_i,x)+b) \tag{11.9}$$

In general, three common kernel functions (Table 11.1) are widely used for SVM in the literature. Here we chose the Gaussian kernel to classify walnut points by pixel, namely meats and shells.

where d is the degree of freedom of polynomial kernel. σ is a parameter related with the width of Gaussian kernel. κ is the inner product coefficient in hyperbolic tangent function.

Based on the SVM of two categories, namely walnut meats and walnut shells, we can extend the SVM for four categories (light meat, dark meat, inner shell, and outer shell) to further improve classification accuracy by pixel. According to Eq. (11.9), we can construct the multi-class model as follows.

Suppose four categories exist in the sample set, namely light meat, dark meat, inner shell, and outer shell, respectively; the extended discriminant function of SVM is shown in Eq. (11.10):

$$\begin{cases} f^j(x)=\operatorname{sgn}(g^j(x)), j \in [1,M] \\ g^j(x)=\sum_{i=1}^{l} y_i \alpha_i^j K(x_i,x)+b^j \end{cases} \tag{11.10}$$

Where j is the index number of category, that is, $j=1$ for the light meat, $j=2$ for the dark meat, $j=3$ for the inner shell, and $j=4$ for the outer shell, and M=4, the number of total classes.

We need to convert the pixel-based classification results to object-based information, so that the rejection mechanism can follow actionable instructions. Pixel-based results (four categories) are transferred to object-based classification results (two categories, i.e., meat and shell) as follows.

To ensure the shell is not mistakenly classified as meat, we set two thresholds, T_{up} and T_{down}, to create a buffer category, named "uncertain" class. According to statistics, we used the following formulas to obtain the final results:

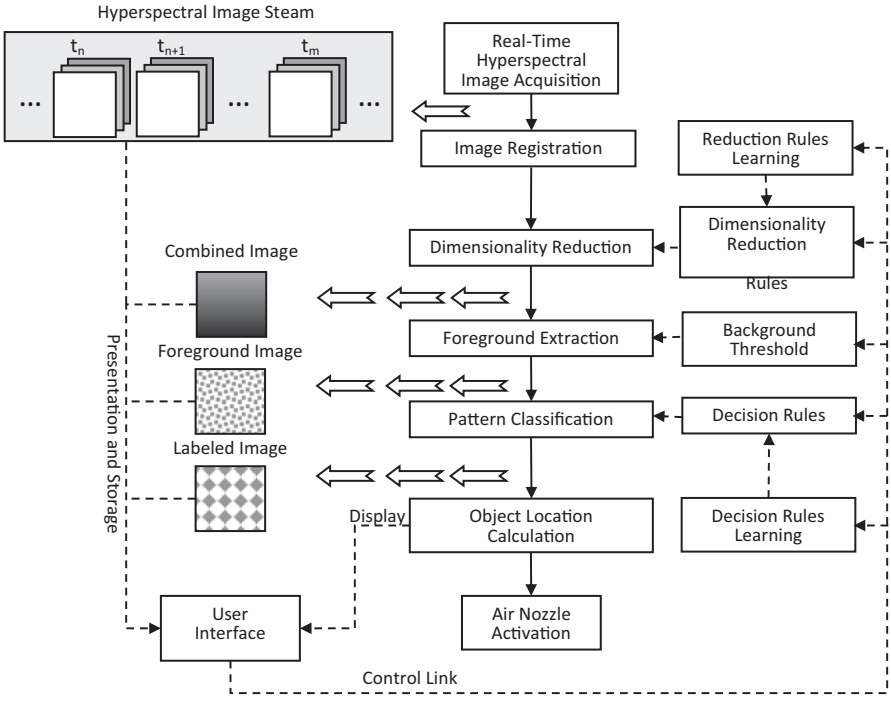

Fig. 11.4 The flow of the image analysis process

Suppose for an object in the image, $n1$ is the pixel number of light meat, $n2$ is the pixel number of dark meat, $n3$ is the pixel number of inner shell, and $n4$ is the pixel number of outer shell,

$$\begin{cases} if\ (n1+n2)/(n3+n4) < T_{\text{down}}, \text{the object is the shell} \\ if\ T_{\text{down}} < (n1+n2)/(n3+n4) < T_{\text{up}}, \text{the object is the uncertain} \\ if\ (n1+n2)/(n3+n4) > T_{\text{up}}, \text{the object is the meat.} \end{cases} \quad (11.11)$$

Finally, an object can be classified into three categories, namely *shell, meat*, or *uncertain object*, where uncertain can be checked manually or re-scanned by the machine.

The task of image processing is shown in Fig. 11.4, which gives six major steps in the image analysis process including image acquisition, image registration, band combination, foreground extraction, pattern classification, and object location calculation.

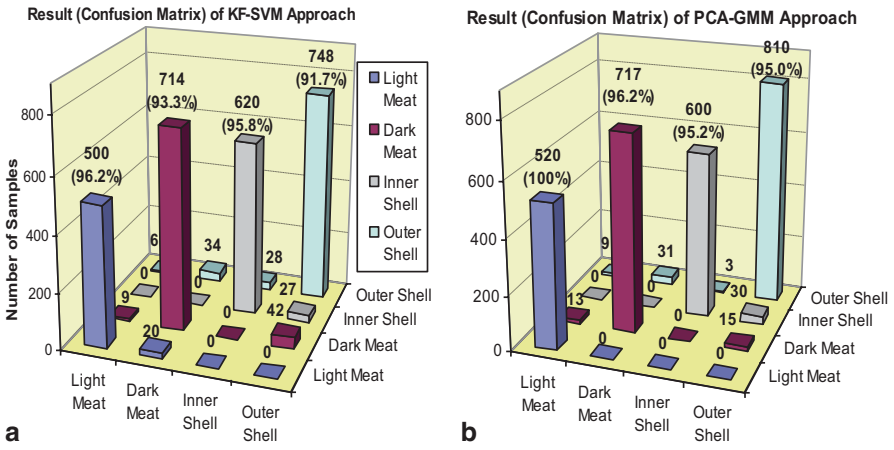

Fig. 11.5 Our early results (2008). The experimental results over a total of 5496 79-dimensional data vectors: **a** KF-SVM model and **b** PCA-GMM model. The PCA-GMM model has an overall total 96.3 % pixel-based recognition rate

11.2.3 Typical Classification Results

Figure 11.5 shows the results over 2748 independent testing 79-dimensional fluorescence spectra using Gaussian KF-SVM and principle component analysis-based Gaussian mixture model (PCA-GMM) (Jiang et al. 2007a, b). The high diagonal column indicates the four nut categories are mostly correctly classified. For cross-validation, independent tests were conducted twice using a total of 5496 sample vectors. The PCA-GMM method performs slightly better with a 96.3 % pixel-based recognition rate. Under this confidence level, each fragment can be further classified object by object, yielding a potentially 100 % accuracy, as shown in Fig. 11.6c.

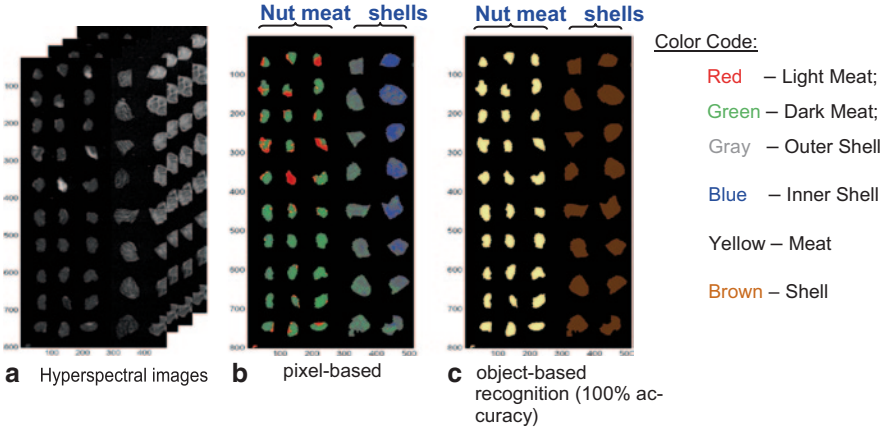

Fig. 11.6 Typical detection results. **a** Hyperspectral images; **b** Pixel-based recognition results; **c** Object-based recognition results

A typical image recognition result is shown in Fig. 11.6. Figure 11.6a depicts the scanned hyperspectral image cube. Through hyperspectral image processing PCA-GMM algorithms (Jiang et al. 2007b, 2010), the pixel-based classification result is shown in Fig. 11.6b, where each object's pixels are categorized or *colored* (at the accuracy or *confidence level* shown in Fig. 11.5). The red and green pixels indicate light and dark nutmeat, respectively, while the gray and blue pixels represent outer and inner shells, respectively. By further classifying, based on the dominant pixels for each object (object-based) with decision rules (e.g., scattered pixels are likely to be errors, and concentrated pixels are solid objects, etc.), the shell and meat objects are correctly differentiated, as shown in Fig. 11.6c, where the left three columns are meats and the two right columns are shells, respectively. All the samples in Fig. 11.6c are correctly labeled (100 % accurate), which demonstrates the effectiveness of hyperspectral imaging technology (Jiang et al. 2007a, b).

11.2.4 Hyperspectral Algorithm Adaptability to Nuts from Different Growing Regions

Cracked black walnuts and broken kernels became quickly oxidized within weeks. Consequently, the fluorescent characteristics may change accordingly. Additionally, different varieties and nuts from different growing regions may have certain variations in chemical compositions and moisture differences due to the climate and growing conditions. The samples used included 20–40 lb bags of roughly a dozen representative wild and planted black walnut tree varieties from nut growers and growers' associations from Eastern and Mid-Western regions (NY, PA, WV, OH, IN, MO, NE). Some of the samples were cracked by machine rollers, and others were whole walnuts. Both old and new crops were tested and fine-tuned in our detection algorithms to ensure that the imaging system under development is applicable to black walnuts of different cultivars and from different growing regions. Figures 11.7, 11.8, 11.9, 11.10, 11.11 and 11.12 show the hyperspectral imaging results of the nuts. The detailed algorithms can be seen in Jiang et al. (2007a, b, 2010).

Statistical analysis shows good detection results. The classification result of a batch test is shown in Fig. 11.11, which is improved over the earlier results shown in Fig. 11.12, both in accuracies of high detection rate for shells and high yield of meats. In Fig. 11.11, the detection of shell fragments is 100 % while recouping 94.6 % of nutmeat. Out of the 462 pieces of nutmeat, 17 (3.7 %) were classified as shell and 8 (1.7 %) classified as uncertain, respectively.

Note that the results of both years of crops showed that there was *no* single shell classified as meat. This result is significant because the meat bin will be virtually shell free (0 % of shell fragment in the meat bin). The results have achieved the designed goal.

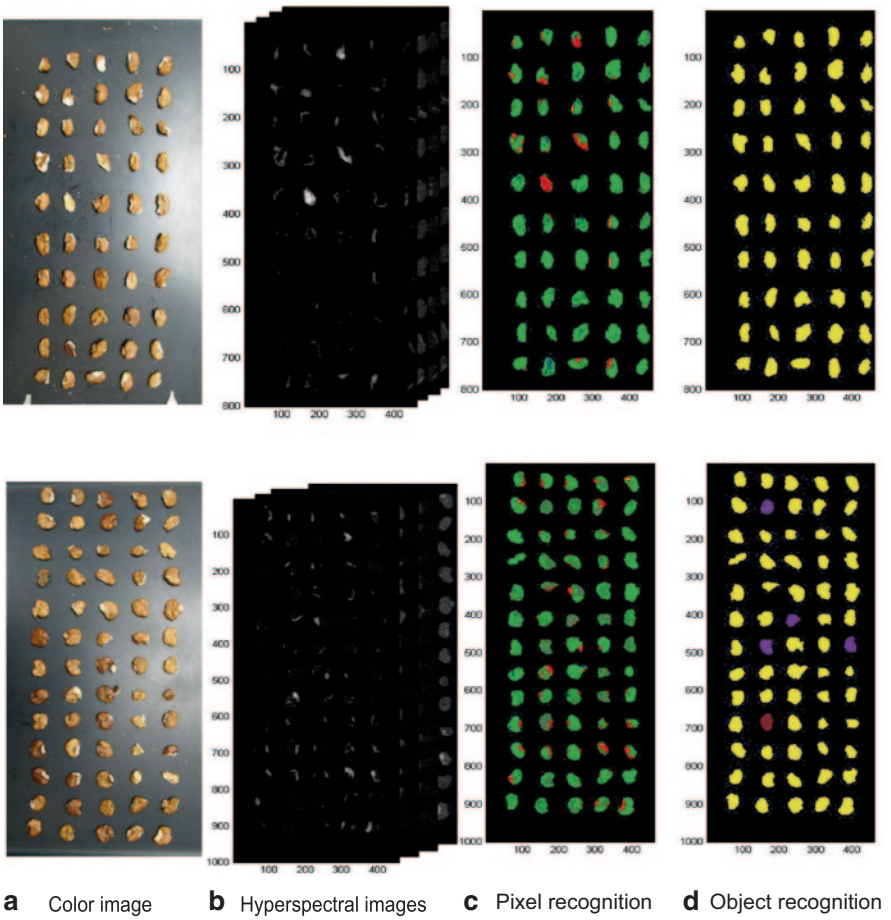

Fig. 11.7 Typical recognition of nutmeats, where **c** is the pixel-based recognition and **d** is the final object recognition. The *yellows* here are correctly recognized as meats. Four meats (shown in *purple*) were classified as uncertain, and one meat (shown in *brown*) was incorrectly classified as shell. Color code: *Red* light meat, *Green* dark meat, *Gray* outer shell, *Blue* inner shell, *Yellow* meat, *Brown* shell, *Purple* uncertain

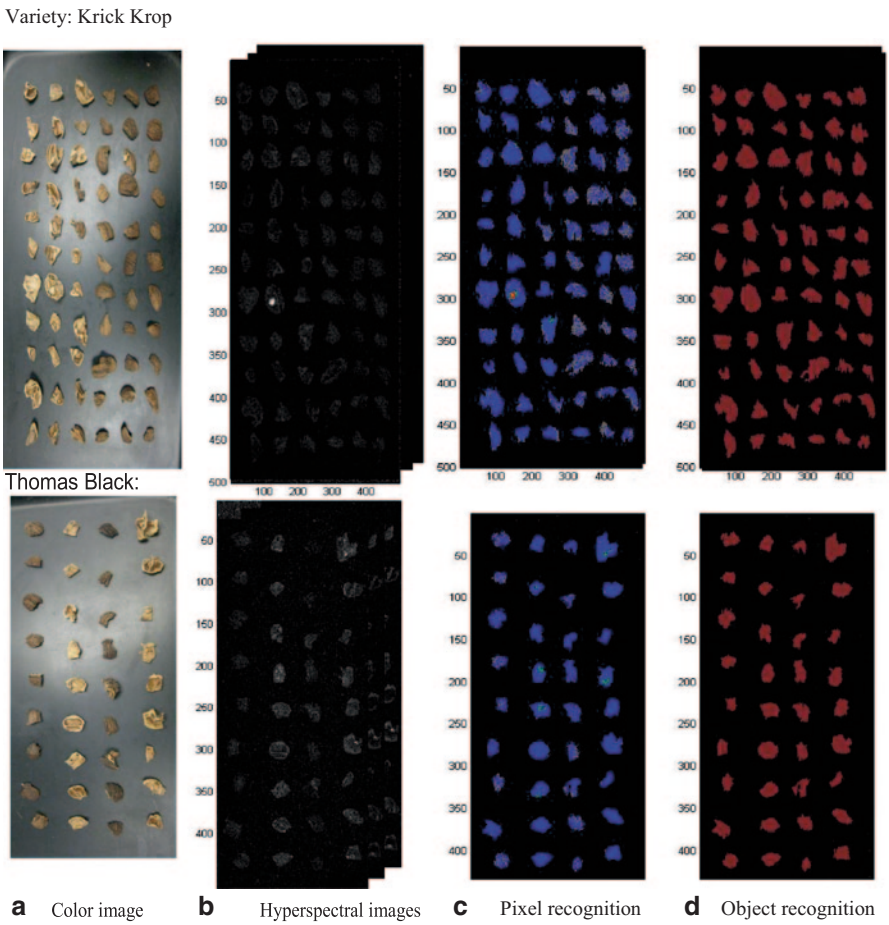

Fig. 11.8 Typical recognition of shell fragments, where **c** is the pixel-based recognition and **d** is the final object recognition. Varieties: *Top:* Krick Krop; *Bottom:* Thomas Black. Color code: *Red* light meat, *Green* dark meat, *Gray* outer shell, *Blue* inner shell, *Yellow* meat, *Brown* shell, *Purple* uncertain

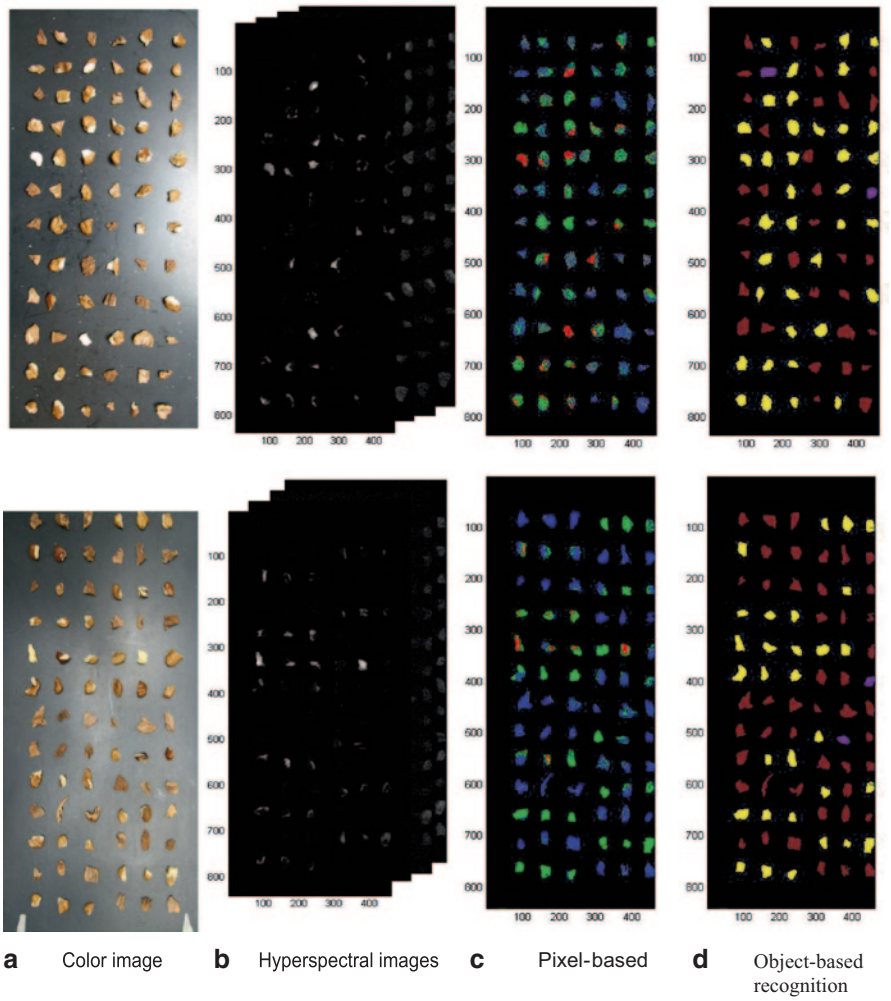

Fig. 11.9 Inspection of mixed shell fragments and nutmeat. Visual recognition is difficult. As seen in **d** object-based recognition, all shell fragments were correctly recognized (100 %) and all *yellow* objects are indicated correctly as nutmeats (shell fragment free). Four *purple* objects (from meats) were classified as uncertain. Color code: *Red* light meat, *Green* dark meat, *Gray* outer shell, *Blue* inner shell, *Yellow* meat, *Brown* shell, *Purple* uncertain

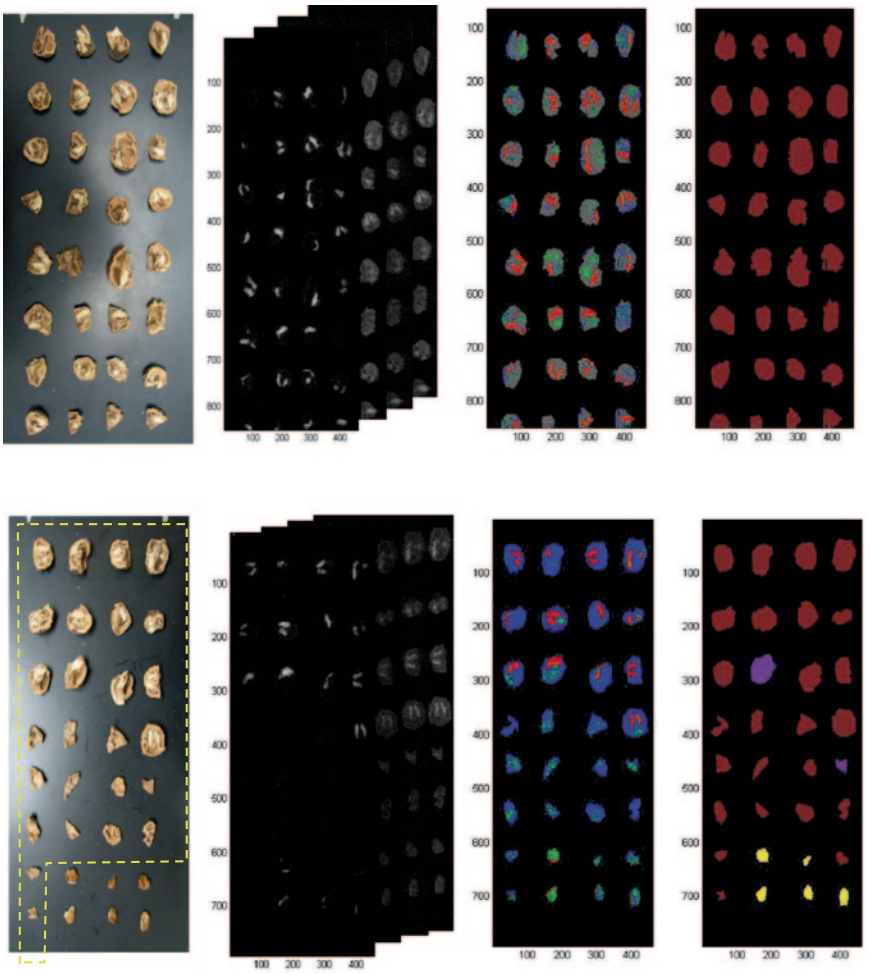

a Color images (These 6 are actual meats, all others are shells) **b** Hyperspectral images **c** Pixel-based **d** Object-based recognition

Fig. 11.10 Inspection of meats embedded in shells. If the nutmeat is still embedded in shells after cracking, the object will be classified and rejected as shells. As seen in **d** object-based recognition, all meat-shell fragments were recognized as shells or uncertain, but should never be recognized as meat. At the *bottom*, five actual meats were correctly recognized, and one meat was incorrectly classified as shell. Color code: *Red* light meat, *Green* dark meat, *Gray* outer shell, *Blue* inner shell, *Yellow* meat, *Brown* shell, *Purple* uncertain

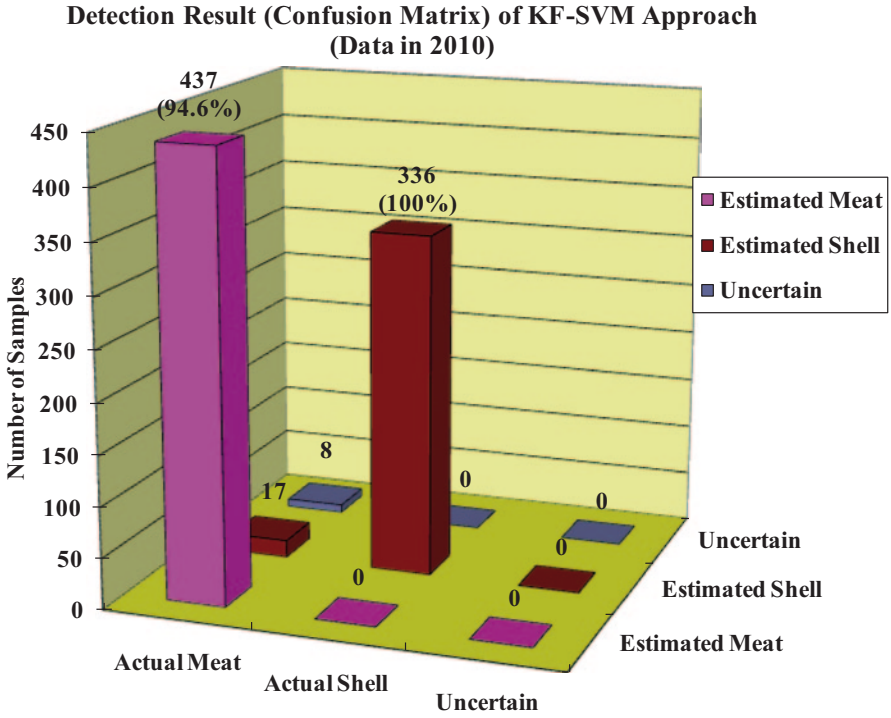

Fig. 11.11 Detection results (independent sample test). The detection rates are 100% for shells and 94.6% for meat. The remaining 5.4% of meat has been classified as shell (17 or 3.7%) and uncertain (8 or 1.7%). None of the shells were mistakenly classified as meat. The resulting meat bin is thus pure (free of shells)

11.3 Further Readings

Further readings on related fluorescent bioimaging characterization of nuts can be found in Zhu et al. 2007, Jiang et al. 2007a, and 2007b. Various hyperspectral imaging methods can be found in Jiang et al. 2010. A dark field imaging method and algorithms can be found in Jin et al. 2007 and 2008.

For biological substance analysis, researchers at the USDA Agricultural Research Services have a comprehensive program involving raw peanuts that ensures the proper processing or destruction of any high aflatoxin raw peanuts (Pearson and Schatzki 1998). Nut processors are required to inspect their lots for harmful biological substances such as mold and aflatoxin. The USDA provides the FDA with a copy of the certificate of analysis and the name of the applicant for each lot found to exceed 25 ppb aflatoxin (FDA 2001). Inspection is carried out through lab analysis of random samples. However, 100% inspection of all nut materials using optical and image processing techniques is preferred. Readers can explore those topics in literature.

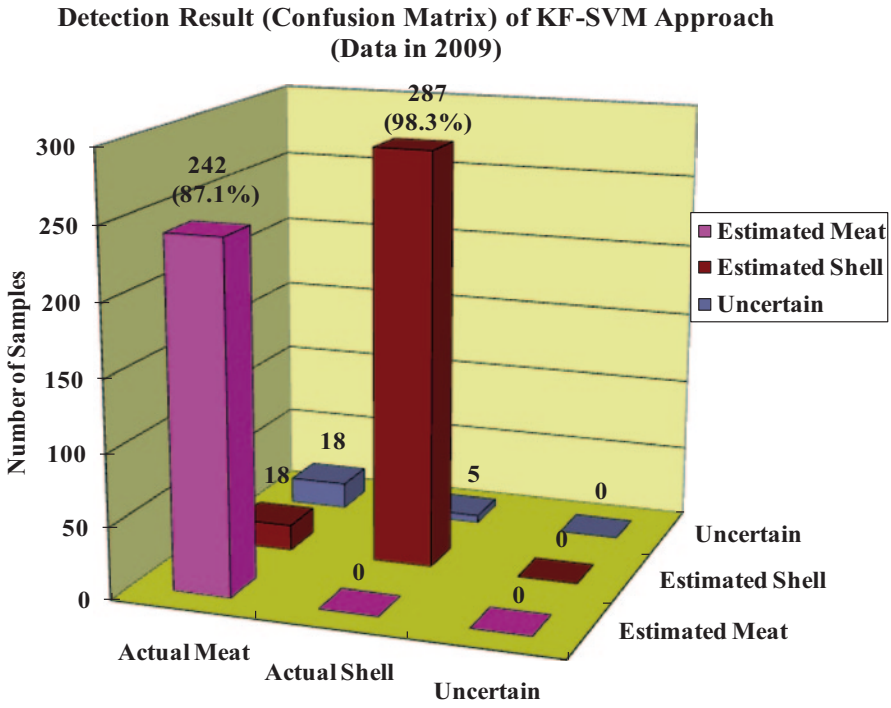

Fig. 11.12 Earlier detection results (independent sample test). The detection rates are 98.3% for shells and 87.1% for meat. Although there are meats and shells that have been classified as shell (18) and uncertain (18+5), no single shell (0%) was mistakenly classified as meat. This will keep the meat bin shell free (pure meat)

References

FDA (2001) (MOU, FDA 225-96-2001). http://www.fda.gov/ICECI/ComplianceManuals/CompliancePolicyGuidanceManual/ucm074598.htm

Jiang L, Zhu B, Jing H, Chen X, Rao X, Tao Y (2007a) Gaussian mixture model-based walnut shell and meat classification in hyperspectral fluorescence imagery. Trans ASABE 50(1):153–160

Jiang L, Zhu B, Rao X, Berney G, Tao Y (2007b) Discrimination of black walnut shell and pulp in hyperspectral fluorescence imagery using Gaussian kernel function approach. J Food Eng 81(1):108–117

Jiang L, Zhu B, Tao Y (2010) Hyperspectral image classification methods. 2010. In book: Hyperspectral imaging for food quality analysis and control. ISBN: 9780123747532. Chapter 3, pp 79–98

Jin F, Qin L, Rao X, Tao Y (2007) Walnut shell and meat classification using texture analysis and SVMs. Optics East 67610Q-67610Q-12

Jin F, Qin L, Jiang L, Zhu B, Tao Y (2008) Novel separation method of black walnut meat from shell using invariant features and a supervised self-organizing map. J Food Eng 88(1):75–85

Pearson TC, Schatzki TF (1998) Machine vision for automated detection of aflatoxin-contaminated pistachios. J Agric Food Chem 46:2248–2252

Zhu B, Jiang L, Jin F, Qin L, Vogel A, Tao Y (2007) Walnut shell and meat differentiation using fluorescence hyperspectral imagery with ICA-kNN optimal wavelength selection. Sens Instrum Food Qual Saf 1(3):123–131

Index

N. Sozer (ed.), *Imaging Technologies and Data Processing for Food Engineers*,
Food Engineering Series, DOI 10.1007/978-3-319-24735-9